5-2006

Secondary Electron Production and Transport Mechanisms By Measurement of Angle-Energy Resolved Cross Sections of Secondary and Backscattered Electron Emission from Gold

Jason T. Kite
Utah State University

Secondary Electron Production and Transport Mechanisms

By Measurement of Angle-Energy Resolved Cross Sections of Secondary and

Backscattered Electron Emission from Gold

Jason T. Kite

A dissertation submitted in partial fulfillment of the requirements for the degree

of

DOCTOR OF PHILOSOPHY

In

Physics

_____	_____
Dr. J. R. Dennison Major professor	Dr. D. Mark Riffe Committee member
_____	_____
Dr. John W. Raitt Committee member	Dr. Charles Swenson Committee member
_____	_____
Dr. Jan J. Sojka Committee member	Dr. Byron R. Burnham Vice Provost and Dean of Graduate Studies

Utah State University

Logan, Utah

2006

Secondary Electron Production and Transport Mechanisms

By Measurement of Angle- Energy- Resolved Cross Sections of Secondary and Backscattered Electron Emission from Gold

A dissertation submitted in partial fulfillment of the requirements for the degree

By

Jason T. Kite, Doctor of Philosophy

Utah State University

2006

Major Professor: Dr. J.R. Dennison

Department: Physics

Abstract: This work provides information about interactions that produce emitted electrons from polycrystalline Au. Emission energy- angle- dependent electron spectra from a polycrystalline Au surface have been measured at several incident electron beam energies. The range of incident energies (~100 eV to 2500 eV) extends from below the first crossover energy, through E_{max}, to above the second crossover energy. The conventional distinction between secondary electrons (SE) (<50 eV) and backscattered electrons (BSE) (>50 eV) is found to be crude for the investigation of electron yields using these energy-angle- resolved measurements. A more realistic boundary occurs at the local minima of the emission spectra; this feature is studied as a function of incident energy and emission angle. In addition, deviations observed in the angular resolved emission spectra from isotropic behavior suggests that residual signatures exist in the emission spectra resulting from the anisotropic SE production mechanisms. Based on the disparity between our observations and recent modeling of the emission spectra, the most recent theory and simulation studies may overestimate the occurrence of randomizing collisions of scattered secondary electrons in the model of the transport mechanism. Finally, description of extensive modification to instrumental and analysis methods are described, and their effectiveness is evaluated.

ACKNOWLEDGMENT

I would like to acknowledge Dr. J.R. Dennison for his advising and overseeing this work. He has influenced me to write (and rewrite) in a style, which is more like I am. I would like to acknowledge Dr. Mark Riffe for "bailing me out" so that this work could continue. Dr. W. John Raitt, Dr. Jan J. Sojka, Dr. Charles Swenson, Dr. James Wheeler, Dr. Charles Torre, Dr. David Peak, Dr. Edwards, Dr. Dwane Doty, and Dr. Ranganathan have been an encouragement and have kept me going in the proper direction. I express gratitude to Dr. John Wilson for believing my potential. I express gratitude towards Dr. Y. Gupta for reflecting scattering sentiment to change my direction towards the physics of reality.

I would like to acknowledge the Surface Science research group (Jodie Gillespi, Dr. Albert (Yen Wen) Chang, Dr. Rob Davies, Carl Ellsworth, Robert Franckowiak, Parker Judd, Spenser Nelson, Dr. Neal Nickels, Dr. Ali Sabbah, Ryan Hoffmann, John Abbott, Jerilyn Brunson, Joshua Hodges, A. Hunt, R. Spaulding, and especially Dr. Clint Thomson) for all of their work in the Materials Physics Group including modifications and upkeep to vacuum chambers. Quick acknowledgement is paid to Bill Fletcher for circuit design and materials, which cannot be reimbursed.

I would like to acknowledge Marilyn Griggs, Shawna Johnson, Melanie Oldroyd, Karalee Ransom, and Deborah Reece who have maintained order in the Physics Department.

I would like to acknowledge the NASA Space Environments and Effects Program for funding this work and the NASA Rocky Mountain Space Grant Consortium for my fellowship.

I also thank the people Larry and Sylvia Slate, Lt. Col. Johnny and Audrey Hays, Bill and Mary Ann Kincaid, Ken and June Nickelson, Mark and Shelley Kellis, Rich and Sandy Dawson (especially Matt Dawson), Virgil and Miriam, Mike and Trellys Henley, Jon and Char Lugger, Ron Batchelder, Harvey Cooper, and Sandra Malik for giving much room and board when funds were dire. Other memorable people have helped me with my psyche, Dr. Clarence Hibbs and Tauna Balahi, while completing this physics study.

CONTENTS

LIST OF TABLES

LIST OF FIGURES

Page

AR	angle-resolved
AI	angle-integrated
BSE	backscattered electron
CA	chamber apparatus
DAQ	data acquisition
EDX	energy-dispersive x-ray
ER	energy-resolved
ESA	electron-stimulated adsorption
ESD	electron-stimulated desorption
HV	high voltage
IP	inelastic peak
LET	low-energy tail
PE	primary electron
QM	quantum mechanical
RD	rotatable detector
RGA	residual gas analyzer
SE	secondary electron
SEE	secondary electron emission
SEM	scanning electron microscope
UHV	ultra-high vacuum
$\vec{E}$	ambient electric field
$\vec{B}$	ambient magnetic field
α	emission angle
E_B	incident electron beam energy
Φ_{RD}	sample bias
$d\Omega$	solid angle subtended by the RD

$\eta(x,E_0)$	average number of SE's produced per incident PE in a layer of thickness dx at a depth x below the surface
$f(x)$	probability for an SE to migrate to the surface from a depth x and escape
$\frac{-dE}{dx}$	average PE energy loss per unit path length (stopping power)
δ_{max}	maximum SE yield for a given material
E_{max}	incident energy at which δ_{max} occurs
φ_{RD}	detector position
E_e	emitted energy
δ	total SE yield
δ_{AER}	angle-energy-resolved SE yield
δ_{AR}	angle-resolved SE yield
δ_{ER}	energy-resolved SE yield
$\delta(\alpha')$	AR SE yield
$\delta(\alpha)$	SE angular distribution function
$\delta(E_e')$	energy-resolved SE yield
$\delta(E_e)$	SE energy distribution function
$\delta(\alpha',E_e')$	angle-energy-resolved SE yield
$\delta(\alpha',E_e)$	AR SE energy distribution function
$\delta(\alpha,E_e')$	energy-resolved SE angular distribution function
$\delta(\alpha,E_e)$	SE angle and energy distribution function
η	total BSE yield
$\eta(\alpha')$	AR BSE yield
$\eta(\alpha)$	BSE angular distribution function
$\eta(E_e')$	energy-resolved BSE yield
$\eta(,E_e)$	BSE energy distribution function

$\eta(\alpha', E_e')$	angle-energy-resolved BSE yield
$\eta(\alpha', E_e)$	AR BSE energy distribution function
$\eta(\alpha, E_e')$	energy-resolved BSE angular distribution function
$\eta(\alpha, E_e)$	BSE angle and energy distribution function
σ	total emitted electron yield (δ+η)
$\sigma(\alpha')$	AR total emitted yield
$\sigma(\alpha)$	emitted-electron angular distribution function
$\sigma(E_e')$	energy-resolved emitted-electron yield
$\sigma(E_e)$	emitted-electron energy distribution function
$\sigma(\alpha', E_e')$	angle-energy-resolved emitted-electron yield
$\sigma(\alpha', E_e)$	AR emitted-electron energy distribution function
$\sigma(\alpha, E_e')$	energy-resolved emitted-electron angular distribution function
$\sigma(\alpha, E_e)$	emitted-electron angle and energy distribution function

CHAPTER 1

INTRODUCTION

Fire and its involvement with solid materials has become more well known over the last few centuries. Recognizing that fire and its associated charge distribution is in fact a plasma; leads us to believe that scattering information can tell us something about the physics of a material's solid-plasma interface. It is amazing how waves of plasma could possibly overlap with solid as a shared space leading to an understanding of these effects in terms of quantized plasma oscillations, or plasmons. The following work describes an experiment for the study of the solid-plasma interface of polycrystalline gold in vacuum as normal incident electrons scatter from the surface.

.

1.1 Prognosis

The incidence of energetic primary electrons (PE's) on a surface induce electron emission from the surface. All of the emitted electrons, directly or indirectly, result from these incident PE's. Backscattered electrons (BSE's) originate from the PE undergoing elastic or inelastic collisions within the solid. Secondary electrons (SE's) originate via interactions of PE's or BSE's with electrons in the solid [Fig. 1-1] and are generally separated by the amount of kinetic energy they possess. Most SE's that leave the sample originate within a mean free path of their point of excitation, which is ~10-20 Å for metals [*Everhart and Chung, 1972*]. SE's are consequently very sensitive to surface conditions, composition, and crystal structure. The specific interactions that take place to produce BSE's and SE's can be investigated by studying the energy and angular resolved (ER and AR) distributions of all the electrons emitted from the surface [*Davies, 1999*]. In fact, the leading theorists in the field state that, "The maximum information about the SE emission process can be obtained by measuring the number of SE's emitted per second from 1 cm^2 of the surface with energy E in the direction Ω." [*Rösler and Brauer, 1981*]

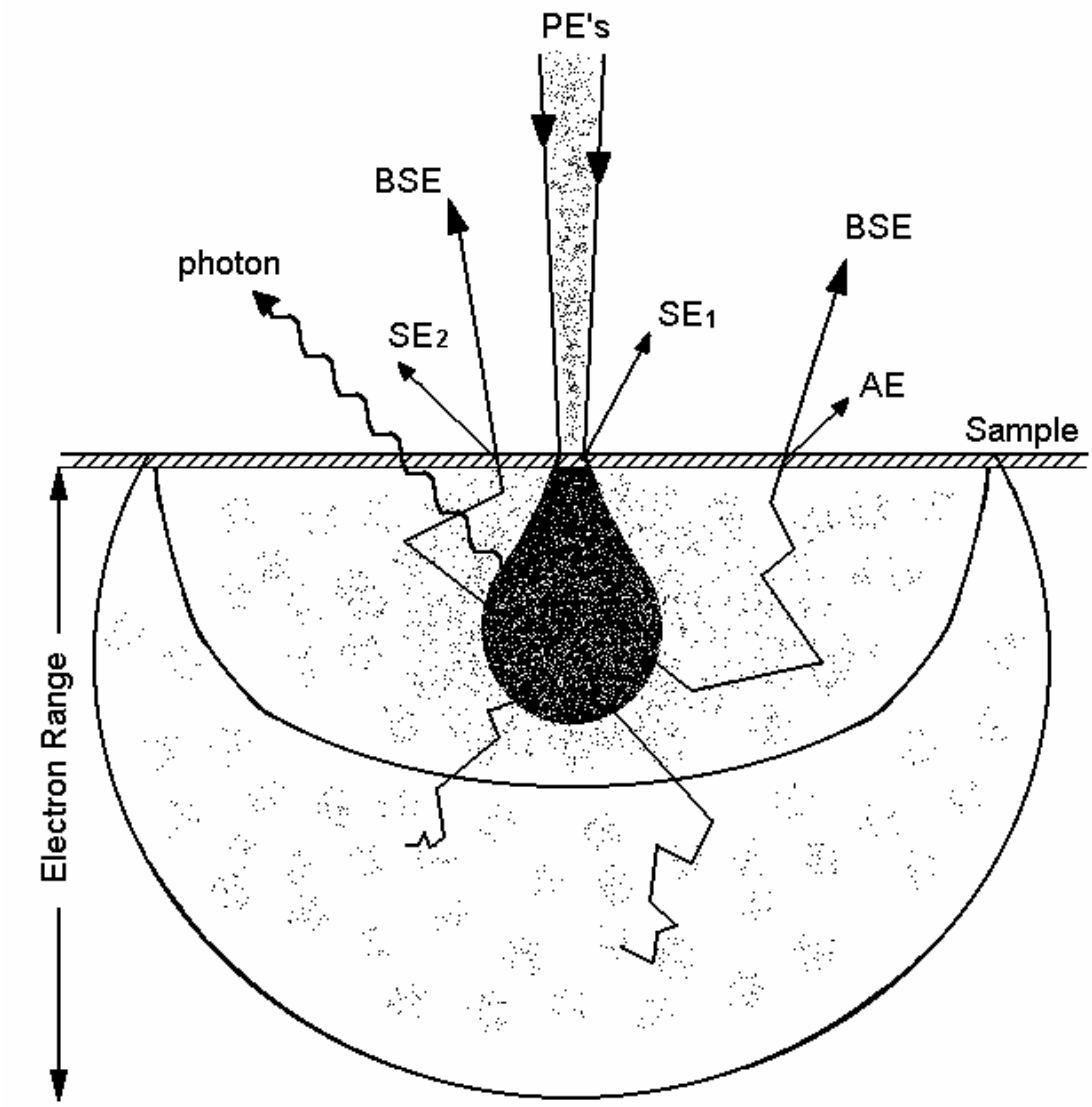

Figure 1-1 General diagram for electron bombardment onto a metallic surface, and electron emission from a metallic surface. Physical processes such as backscattered electrons (BSE), secondary electrons (SE_1) produced by primary electrons (PE), secondary electrons (SE_2) produced by BSE, Auger electrons (AE), and photons produced through inverse photoemission are shown. The shallow hatched area near the surface shows the depth of predominant SE production [*after Reimer, 1993*]. The shading shows the magnitude of the electron density.

1.2 Inspiration

I am fascinated by concepts that are seemingly incomprehensible. In addition, I am inspired by the challenge of finding ways in which a concept can be more clearly understood. One such concept, is how the process of emission leads to information about the "inner workings" of the bulk material. And further, that regardless of material, all measured quantities of charge were at some point a part of the emission process.

Of particular interest is the question of experimentally determining the origins of the emitted electrons present in the electron emission spectrum. Measured SE's are conventionally defined to have energies below 50 eV, though doubt has been cast on this arbitrary definition [*Davies, 1999, p. 164*]. Elastic electrons are emitted from the material with the same energy as the incident PE's. BSE's, believed to interact through combinations of elastic and inelastic interactions within the material, make up the rest of the emitted electrons. Unfortunately, most research scientists in this field restrict SE emission with dependencies on energy (E) and direction (Ω), which is imposing conservative boundaries contrary to the theorists' definition. A typical energy resolved spectrum [*Davies, 1999*] shows the ratio of incoming to outgoing electrons versus the energy of the emitted electron emission energy [Fig. 1-2]. There are three peak features; the SE peak, the BSE peak, and the elastic peak, which are shown separated by two valley features. The SE peak is fit with the Chung and Everhart model and the BSE peak is overlaid with an empirical exponential fit. The valley feature which divides the SE and BSE peak features is asymmetric and is characterized by a count minimum of approximately three orders of magnitude less than the SE peak (2 eV) [Fig. 1-2 inset] and one order of magnitude less than the BSE peak (1350 eV). This graph is intriguing because it shows the classical 50 eV demarcation (that many researchers use to delineate the SE's from the BSE's) as being at a significantly lower energy than the minimum energy of the dividing valley (450 eV).

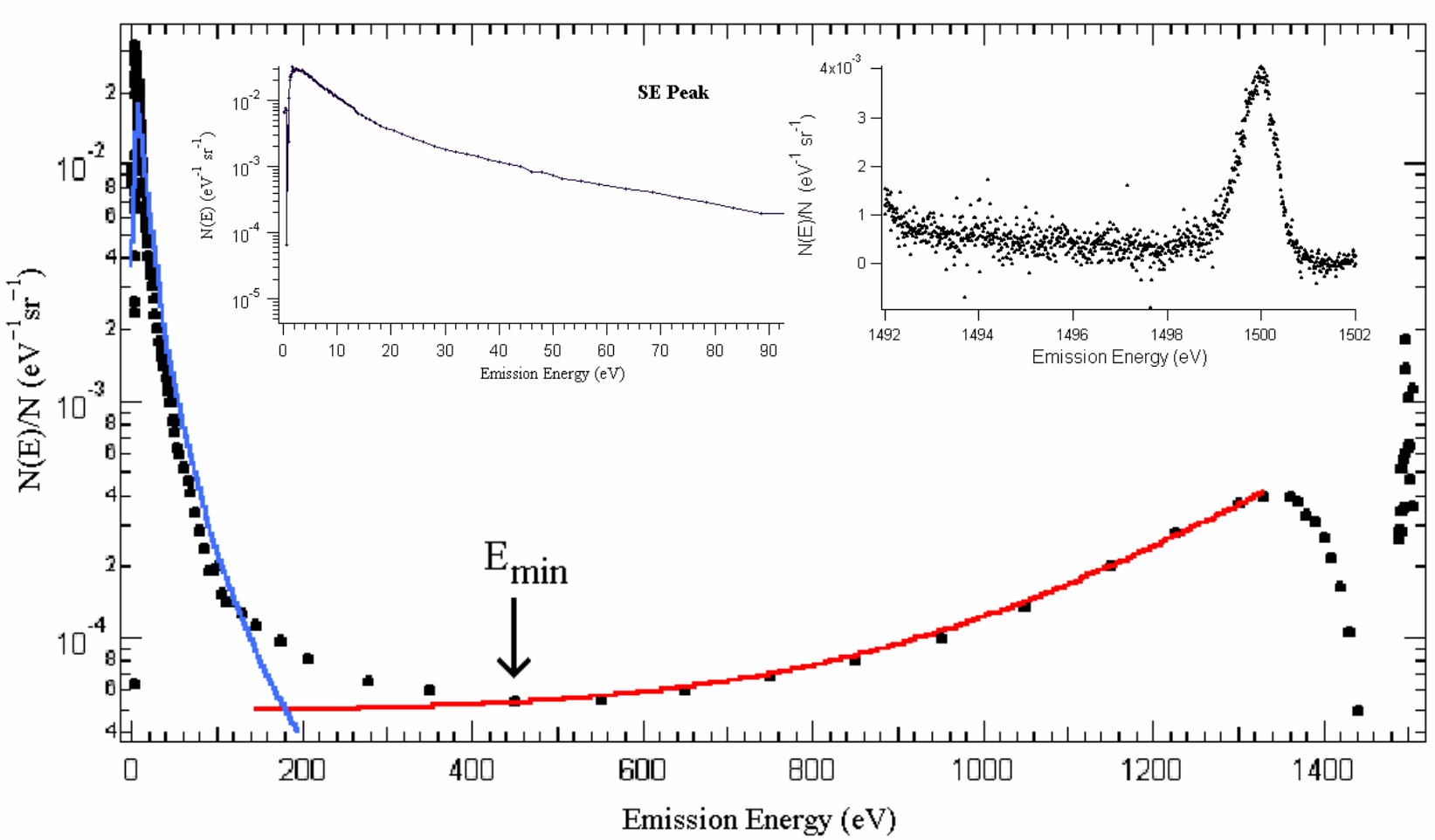

Figure 1-2 AR spectrum with log scale electron count vs. negative detector bias (emission energy). Primary energy is 1.5 keV at normal incidence on polycrystalline Au sample D6 at 17^{o} emission [Davies, 1999]. Blue line is a Chung and Everhart Fit. Red line is an empirical exponential fit.

Many technical applications use the accepted definition of 50eV as the dividing line for SE's. If in fact a more precise delineation can be determined, then it would further inspire those working on current applications to pursue similar advances in future technologies.

1.3 Applications

The general study of SE/BSE emission has many important applications. Three important charging phenomena directly related to SE emission are: (**i**) the detrimental effects associated with spacecraft charging and their applications [*DeForest, 1972; Froonincks, 1992; Katz, 1986; Garrett, 1987, 1981; Hastings, 1998; Wipple 1981; Davies 1996; Nickles, 1999*], (**ii**) the effects of high-voltage arcing and "snapover" [*Mandell, 1985; Hastings, 1989; Davies, 1997; Thompson, 2000*], and (**iii**) plasma-induced small-particle charging [*Chow, 1993*]. There are also three technological advances currently being investigated that are directly related to SE emission: (**i**) improved understanding and development of the electron microscope [*Seiler, 1983; Reimer, 1985, 1993*], (**ii**) electron-emission sources for the development of electron multipliers and flat-panel displays [*Kumar, 1995*], and (**iii**) plasma limiters deposited at the walls of nuclear fusion plasma devices [*Farhang, 1993*].

1.4 Objectives

As most theorists agree, this is best accomplished by measuring energy and angle resolved electron emission cross sections. The current theoretical prediction for the shape of the SE angular resolved spectra of metallic materials is cosine-like, which is a direct consequence of the supposition number of the SE's that are emitted are related to the path length they traverse through an energy dependent mean free path. For the remainder of this work, this specific angular cross section shape, in the direction normal from the surface, is referred to as isotropic. However, the preliminary experimental work by Davies [*1999*] led to a conclusion that the energy and angle resolved emission cross section measured for polycrystalline Au were not fully isotropic. Given this disparity, one or a combination of the following

must be true: the modeling parameters in the theory are not correct, the cross section measuring apparatus is not accurate, or the sample surface is not what we believe (polycrystalline).

This work will show that higher resolution measurements with reduced systematic errors confirm the observation of Davies that AR and ER SE cross sections of polycrystalline Au are not isotropic. Further, the near surface crystal structure orientation and domain size do not show any diffraction effects allowing the conclusion that the sample surface is well defined.

To probe the modeling parameters for inconsistencies, three experimental parameters are varied and observations of any changes in the cross sections are determined. The three parameters are the incident beam energy (E_b), the emission energy (E_e), and the emission angle (Ω). Comparing these cross section data helps to identify the extent to which the SE emission is dependent on each parameter. Once SE emission dependencies are identified, qualitative and quantitative information about the electrons produced within the material can be extracted. In order to isolate processes of energy exchange from energy transport within the material, the average penetration depth of incident PE's is examined. Energy exchange mechanisms can be reasonably isolated from the transport mechanism because the electron mean free path increases linearly with increasing energy for E > 100 eV [*Powell and Jablonski, 2000*]. Measuring the full AER distribution of polycrystalline Au, with a selection of PE beam energies, identifies the dependence of the production mechanism on E_b. By tracking the SE and BSE yields as the PE's energy changes is mapped to discrepancies in the linearity of the transport mechanism. This essentially provides production mechanism information as deviations from linearity.

PE incident energies of 100 eV, 500 eV, 600 eV, 700 eV, 900 eV, 1200 eV, 2000 eV, and 2500 eV were chosen to be evenly distributed around the maximum SE yield ($\delta^{Au}_{max} \approx 1.4$) which is located approximately at $E^{Au}_{max} \approx 650$ eV [Fig. 1-3, USU FatMan Chamber, *Clerc, 2005; CRC Handbook* E^{Au}_{max} = 880 eV*, 1991*]. The SE yield, measured using a hemispherical grid analyzer technique, is modeled using several current theories depicting information about the E_b dependence.

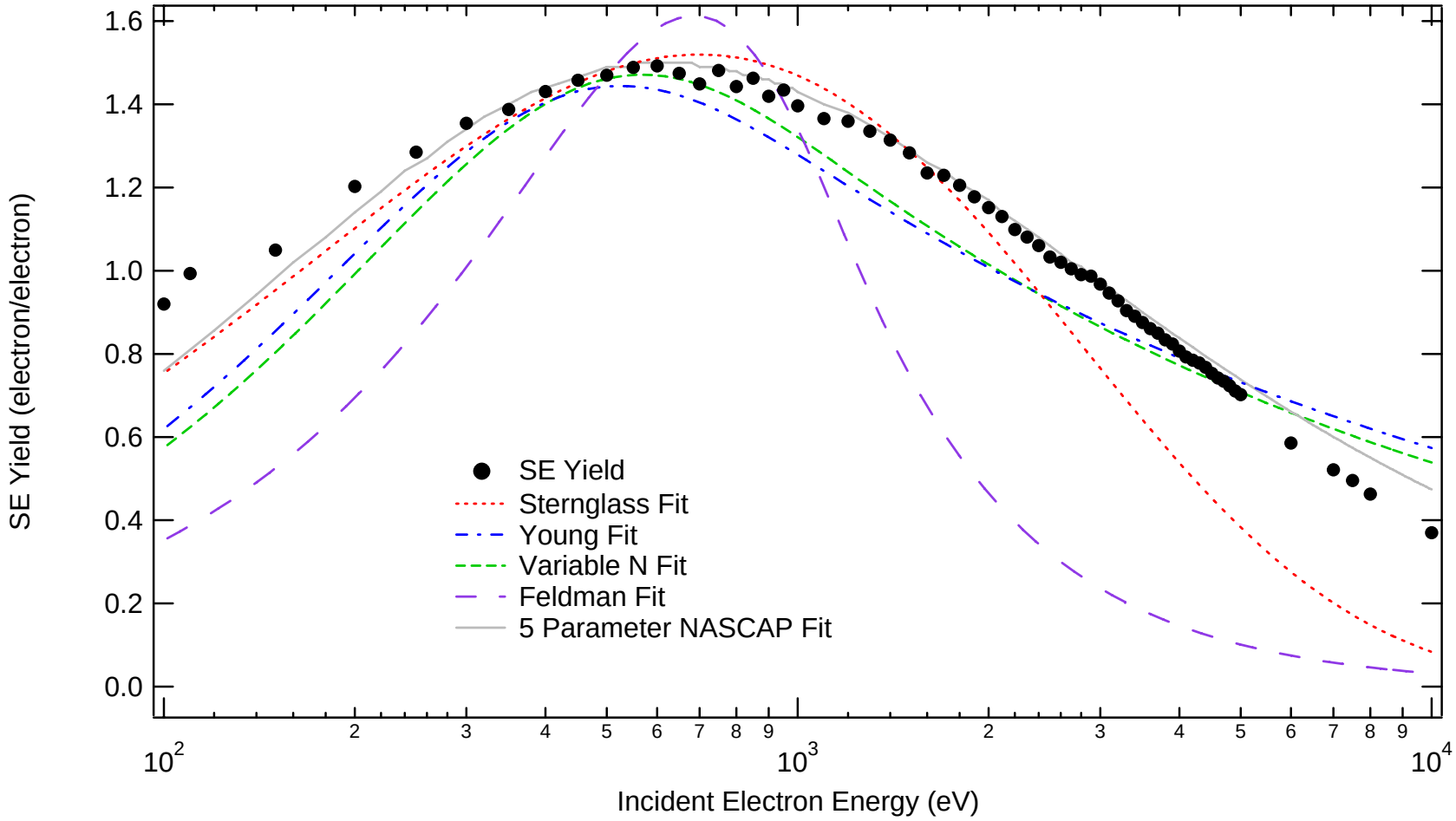

Figure 1-3 SE Yield of polycrystalline gold vs. log scale incident electron energy taken in the USU FatMan UHV chamber [*Clerc et. al., 2005*]. The various popular fits are included with the Variable N = 1.39 having the best physically explainable fit.

Varying the PE incident energy provides information about the natural dividing energy between emitted SE's and BSE's. For example in Fig. 1-2, the location of the valley minimum, $E_{min} \approx 450$ eV, is the natural dividing energy between SE's and BSE's for $E_b = 1500$ eV [*Davies, 1999, p. 166*]. A major goal is to determine the dependence of this natural dividing energy, E_{min}, on E_b. A further goal was to determine any dependence of E_{min} on Ω. Utilizing E_{min} as a better integration boundary for calculating SE and BSE yields focuses attention on the dependencies of SE and BSE yields on E_b and Ω. The extraction of production mechanism information from within the material is then addressed qualitatively by observing deviations of these yields from the best current theories.

The second objective of this work has been the progressive development of a new tool designated solely for the purpose of secondary electron emission (SEE) investigations. The "LittleBoy" ultrahigh vacuum (UHV) chamber, housed at Utah State University, is used for acquiring simultaneous angle- and energy- resolved electron emission measurements. Upgrades and other modifications to the LittleBoy chamber and its peripherals based on suggestions by Davies [*1999*] were made and thoroughly tested. These modifications and validations allowed newly acquired data so that the evaluation of fundamental secondary emitted electron (SEE) theory could be correctly assessed.

1.5 Synopsis

The sequence of material in this dissertation is as follows:

Chapter 2. A substantial review of the SEE literature was completed as a necessary part of this investigation. Based on this review, this chapter focuses particular attention on the theory of energy and angular distribution of SE's. A summary of nearly free electron materials with relation to SE production is included. The chapter concludes with a summary of the most current SEE observations for energetic electrons incident on polycrystalline gold.

Chapter 3. Details of the experimental apparatus are discussed. The most current modifications to the instrument are discussed along with their diagnostics. Also included are methods for analyzing data from measured quantities, with respective error analyses for energy spectra and angular distribution measurements presented in Chapter 5.

Chapter 4. Sample preparation and surface summary are given along with diagnostics related to contamination and surface structure.

Chapter 5. Angle-resolved measurements, spectra, and angular distributions are given and discussed. Beam energy and angle-resolved spectra are considered in detail, with results applied primarily to an assessment of instrument methods. The angle-resolved spectra and energy-resolved angular distributions presented are alternate ways to provide the same principal results of this investigation. Yields calculated using the experimental results presented in Chapter 5 are presented and discussed. The results are summarized and a comparison is made to the most current theory given in Chapter 2.

Chapter 6. A conclusion is given along with suggested improvements to the measurement apparatus and measurement technique. Further details and thoughts are presented regarding the continuation of this research emphasizing additional experimental studies and modeling simulations.

A specific structural notation is used throughout the text to refer to chapters, sections, and subsections. For example, [3.2 (a)], represents a reference to Chapter 3, Section 2, subsection (a). Since this document is to serve as a reference for professors and students as they endeavor to build on this work, results contained in the LittleBoy laboratory notebooks are cited within the text in the form [LB II, p. 32y], meaning LittleBoy lab book number II, yellow page 32.

CHAPTER 2

SECONDARY ELECTRON EMISSION

There are three different ways to classify emitted electrons. Emitted electrons can be classified by a net charge transfer, by their emission energy, or by their origin from the beam (either from primary incident or backscattered electrons) or from the sample (secondary electrons). The first classification describes electrons as pieces of charge without identity. The second classification describes electrons as a charged particles, which can be separated by characteristics of energy. The electrons emitted with low energy are classically termed secondary electrons (SE's) and with higher energy as backscattered electrons (BSE). The third classification describes electrons through the specific process by which they are created or modified. The production mechanism of an electron, a direct result of energy exchange, classifies an electron assuming no other energy exchange mechanism occurs prior to being emitted. Further classification allows for a convention of energy discrimination where low energy emissions (<50 eV) originate from the sample and higher energy emissions originate from the primary electrons (PE). Based on the emission of an electron, the reader will be lead through a historical perspective, then introduced to the basic semi-empirical theory and quantum mechanical theory, followed by a discussion of the importance of nearly free electron metals and backscattering concepts, and finally a review of previous observations and investigations of electron emission from Au.

2.1 Historical Perspective

Understanding charge and the process of its movement has been pondered for many centuries. Two kinds of charge (positive and negative) exist to oppose one another. Dividing negative charge into small packages, called electrons, was first presented to describe the atom a little over a century ago by J.J. Thompson. Probability charge distributions had no uniqueness for the electrons, and the identity of an

electron was improper to discuss because of the wave/particle duality first stated by De Broglie. Hiesenburg and Pauli took the next step to fix the identity crisis, with the uncertainty and exclusion principles, by investigating spin. The concept of non-localized electrons led to the conclusion that there are energy bands within materials. The manipulation of energy band gaps to organize electron densities within solid state semiconductors has given rise to the transistor. More recently, new ideas of classifying electrons as canonical ensembles dependent on certain thermodynamic variables have predicted both condensed matter and plasma state phenomena. For all practical purposes, electron scattering events can be classified in terms of their scattering histories. Following an electron through its life from creation to annihilation is feasible as long as certain stable environmental conditions exist. In the solid state, modeling can be accomplished through steps of processes.

2.2 Semi-Empirical Theory

The process through which a SE is produced can be modeled in three successive stages: the production of the SE in the bulk, the transport of the SE from the point of creation to the surface, and the emission of the SE from the surface. The vast majority of theoretical work has involved modeling SE emission with a standard semi-empirical theory developed by Salow and Bruining [*Dionne, 1973*] using an expression for the number of SE's produced per PE (or SE Yield, δ)

$$\delta^{(E)} = \int \left(-\frac{dE}{dx} \right) B e^{-x/\lambda} dx \tag{2.1}$$

Each of these three stages corresponds to a measured parameter. The "stopping power", -(dE/dx), describes the energy lost from the PE as it is transferred to the SE at a depth x; the mean-free-path of the

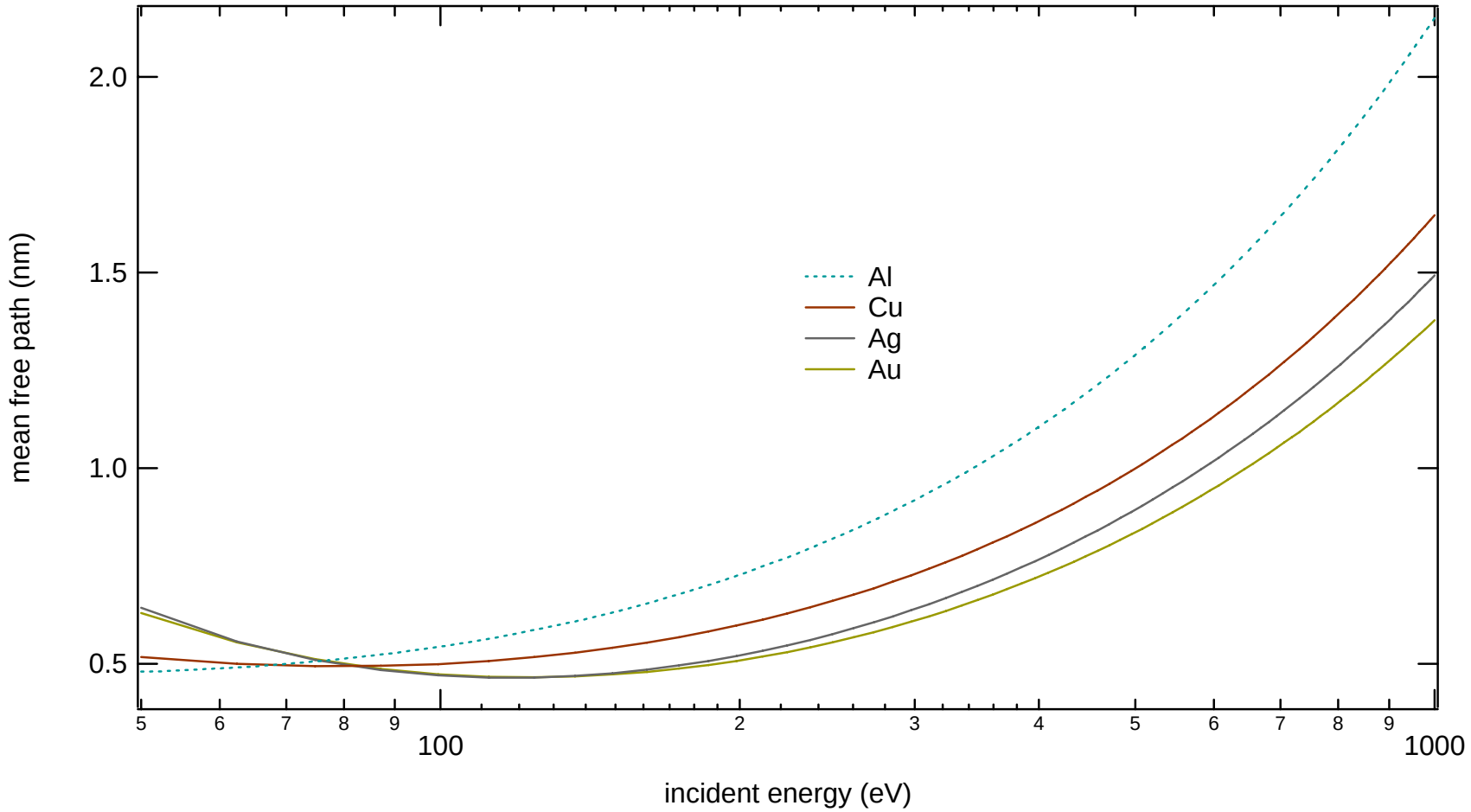

Figure 2- 1 Inelastic Mean free path for electrons traversing the metals Al (dots), Cu, Ag, and Au as a function of the incident energy on a logarithmic scale [*Powell and Jablonski, 2000*]. For the energy range studied here, the minimum penetration for Cu occurs at ~80 eV and electrons traverse Ag slightly more than Au.

SE, λ, [Fig. 2-1] parameterizes the SE transport to the surface; and the constant B is the probability that an SE escapes the surface. Improvements to the theory by Baroody [*1950*], Sternglass [*1950,1957*], Barut [*1954*], Lye and Dekker [*1957*], and Dionne [*1975*] have incorporated slightly different assumptions for the energy loss term, *E(x)*. For example, Sternglass uses the Bethe stopping power formula

$$\frac{dE}{dx} = F \cdot E^{-1} \ln\left(\frac{E}{I}\right) \tag{2.2}$$

where F and I are material dependent factors [*Kanter, 1961; Suszcynsky and Borovsky, 1992*]. Alternately, other semi-empirical theories [*Schou, 1988; Reimer, 1993*] model the stopping power in terms of a power law formula of the form

$$\frac{dE}{dx} = -A \cdot E^{1-n} \tag{2.3}$$

Using a stopping power exponent, of n = 1.45 typical for Au in the variable n power law model in Eq. 2.3, the cumulative fraction of the total number of SE's produced as a function of penetration depth, Eq. 2.4, is shown for various incident beam energies studied in this dissertation [Fig. 2-2]. Integration of Eq. 2.3 over a distance 0 to *R* and energy E_o to 0 yields

$$R = \frac{E_0^{\,n}}{An} \tag{2.4}$$

In the Chung and Everhart model [*Chung and Everhart, 1970*], the production of SE's as a function of depth x is assumed to be given by the inverse of the stopping power divided by the average energy lost by the PE in producing a SE, ε, so that from Eq. 2.1 the range, *R*, is related to E by

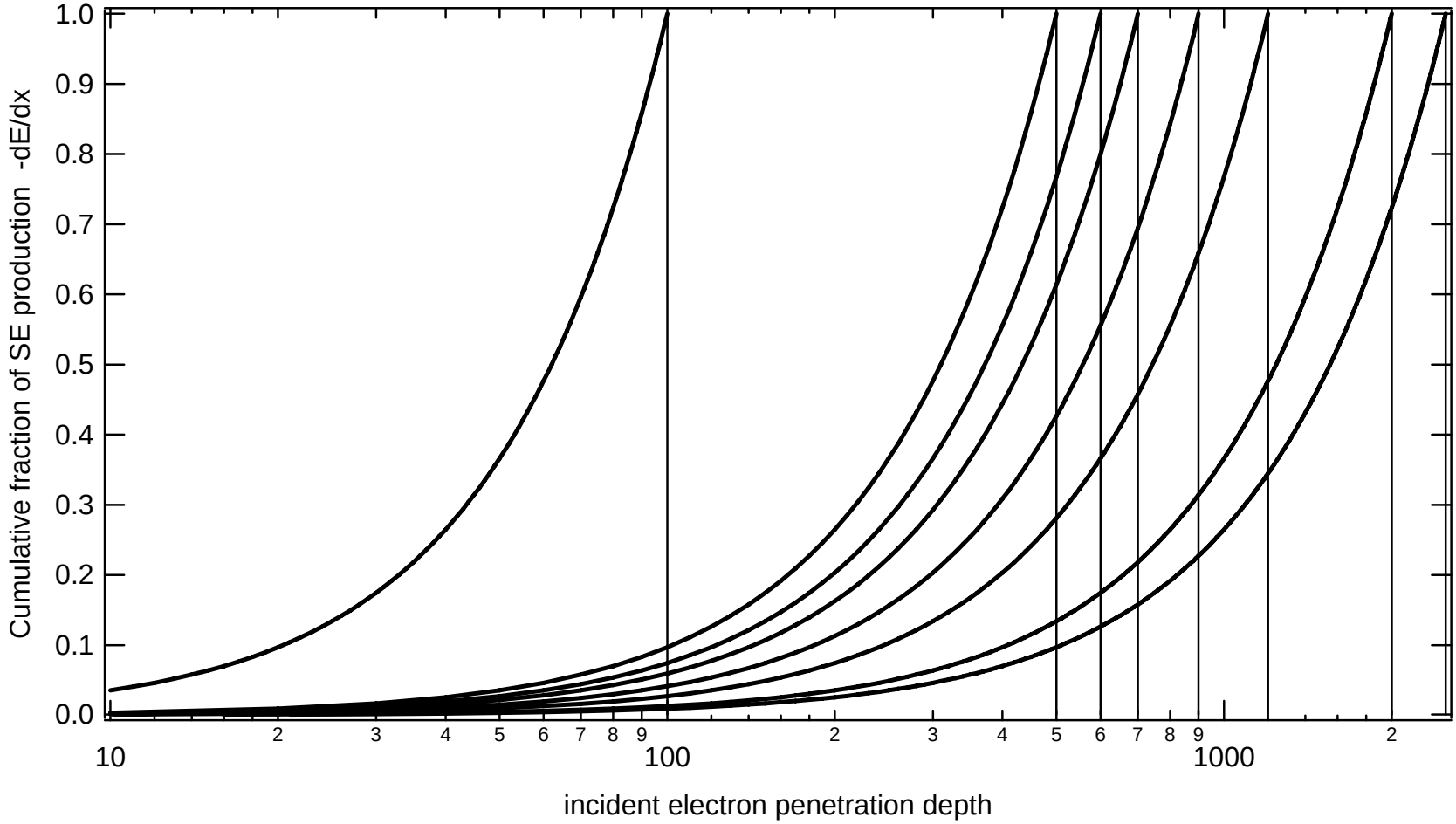

Figure 2- 2 A representation of the cumulative fraction of the total number of SE's produced as a function of penetration depth. A stopping power coefficient of n = 1.45 is used in Eqs. (2.1) through (2.3). The vertical lines represent the maximum incident electron penetration depth at each of the incident beam energies.

$$-\frac{dE}{dx} = \frac{1}{\varepsilon}\left(\frac{dR}{dx}\right)^{-1} \tag{2.5}$$

The integration of the stopping power in Eq. 2.5 from the incident surface to a depth R is equal to the energy of the PE's, E_o, divided by ε, or equivalently to the average number of SE's produced by a PE of energy E_o:

$$\int_0^R \frac{dE}{dx}dx = \frac{E_0}{\varepsilon} \tag{2.6}$$

The energy distribution of emitted SE's in the interval $E+dE$ is written in the Chung and Everhart theory [*Chung and Everhart, 1970*] [Fig. 1-2, blue] as

$$\frac{dN}{dE} = \frac{k}{E_0}\frac{(E - E_F - \phi)}{(E - E_F)^4} \tag{2.7}$$

where E_F is the Fermi energy, ϕ is the work function of the metal, and k is a material-dependent proportionality constant.

All of these semi-empirical theory variations assume an isotropic angular distribution as

$$\frac{dN(E_{SE})}{dE_e} = B\cos(\alpha) \tag{2.8}$$

(α measured from normal) of SE production mechanisms and therefore successfully account for the low energy features in the AR spectra [Fig. 1-2]. However, they are incomplete because they do not address details of the SE production mechanisms resulting from energy exchange within the solid. Accounting for different SE production mechanisms introduces an energy and/or angle dependence on λ and this interferes

with the mechanism of transport [Chap. 1.4]. A quantum mechanical theory is needed to address these production mechanisms as well as to investigate whether the AR emission distribution is indeed isotropic.

2.3 Quantum Mechanical Theory

The creation of the SE is most commonly addressed by considering that the majority of SE's are produced as a result of three types of PE energy exchange within the solid: (**i**) the excitation of valence electrons, (**ii**) the excitation of core electrons, and (**iii**) the electron excitation due to plasmon decay [*Amelio, 1970; Powell and Woodruff, 1972*]. Knowing the probability for producing an SE due to each of these energy exchange mechanisms allows one to calculate the transition probability between Bloch states within the solid sample. The resulting energy resolved (ER) and angular resolved (AR) distribution functions for these distinct production mechanisms [Fig. 2-3] can then be propagated to the surface using the Boltzmann transport equation [*Bindi, 1979*] or Monte Carlo techniques.

The full development of the quantum mechanical theories [Ono, *1978*] have been applied to SE production and simulated by Rösler and Brauer [*1981*] and Ganachaud and Cailler [*1979*]. The expression obtained for the angle- energy- distribution, $j(E,\Omega)$, is

$$j(E,\Omega) = \Theta[E'-W]\Theta[\cos\alpha - \cos\alpha_c]\left(1-\frac{W}{E'}\right)\sqrt{\frac{E'\cos^2\alpha'-W}{E'-W}}\Lambda(E')\sum_{\lambda}\psi_{\lambda}(E')P_{\lambda}(\cos\alpha) \quad (2.9)$$

where the primed variables designate the interior of the material and the unprimed variables designate the outer vacuum level. The Heavyside step function $\Theta[E'\text{-}W]$ is the energy constraint on the surface barrier with W, the Fermi energy plus the work function and E' > W is the condition for escape. The Heavyside step function, $\Theta[\cos\alpha - \cos\alpha_c]$, is the momentum constrain on the surface barrier where $\cos^2\alpha_c = W/E'$.

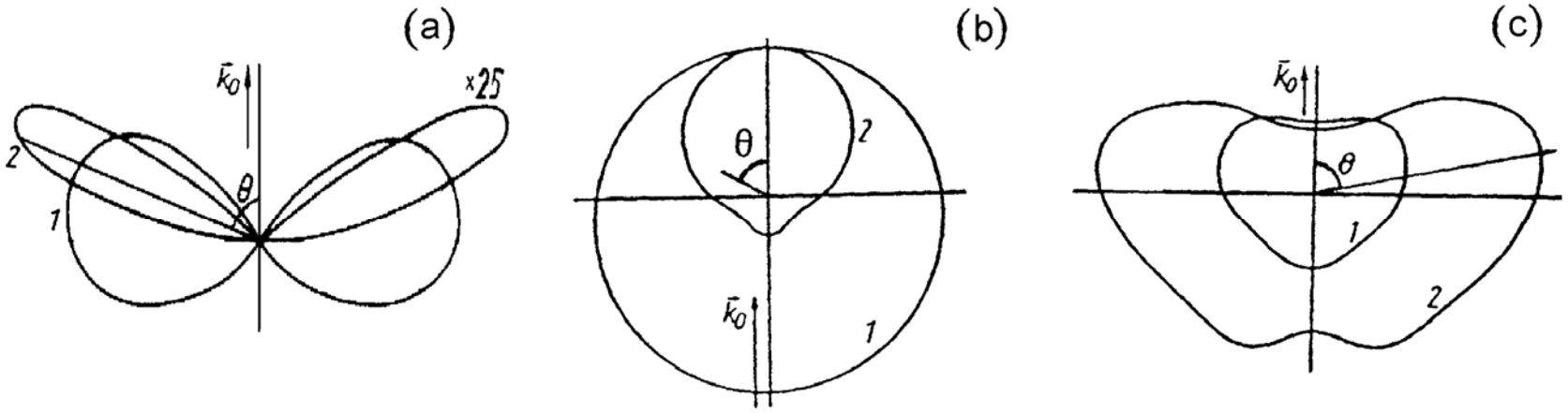

Figure 2- 3 Rosler and Brauer's cross sections for production mechanisms in aluminum. Angular dependence of excitation (a) by dynamical screened electron-electron scattering with a secondary electron energy of (1) 20 eV and (2) 200 eV (b) by core electron excitations with a secondary electron energy of (1) 50 eV and (2) 200 eV and (c) by plasmon decay with a secondary electron energy of (1) 20 eV and (2) 26 eV. Calculations assume a primary energy of 2 keV in aluminum [after *Rösler and Brauer, 1981*].

In polar coordinates, α and α' are connected by $(E + W)\cos^2\alpha' = E\cos^2\alpha + W$. The remaining terms in $j(E,\Omega)$ are the composite mean free path, $\Lambda(E')$, the excitation function $\psi_\lambda(E')$, and the Legendre polynomials $P_\lambda(\cos\alpha)$. Integration of $j(E,\Omega)$ over the emission energy provides the SE yield,

$$\delta(\Omega) = \int_0^{E_{SE}} j(E,\Omega)dE \tag{2.10}$$

where 50 eV has customarily been chosen as the upper energy boundary, E_{SE}.

The inner material variables can be expanded in terms of the outer vacuum level Legendre polynomials resulting in

$$\Lambda(E')\sum_\lambda \psi_\lambda(E')P_\lambda(\cos\alpha) = v(E')\hat{f}(E',\Omega') \tag{2.11}$$

where $v(E')$ is the electron velocity and $\hat{f}(E',\Omega')$ denotes the distribution function equal to the number of excited electrons, $E'>E_F$, above the Fermi energy, in 1 cm^3 for a unit primary current. In order to calculate $\hat{f}(E',\Omega')$, the respective Boltzmann transport equation is derived for the system of the excited electrons. In the stationary case, the following equation for the distribution function *f(k)*, with $E=(\hbar^2 k^2/2m)$ and $\Omega = \mathbf{k}/k \leftrightarrow \mathbf{k}$ (↔ indicates normalized volume), is equal to the number of excited electrons, written as

$$f(k)\sum_{\substack{k' \\ (k'>k_F)}} W_{k\to k'} = \frac{j_0 m\Omega}{\hbar k_0}\delta_{kk_0}\sum_{\substack{k' \\ (k'>k_F)}} W_{k_0\to k'} + \sum_{\substack{k' \\ (k'>k_F,k)}} f(k')\{W_{k'\to k} + W^s_{k',k}\} \tag{2.12}$$

where $W_{k\to k'}$ describes the transition probability from state **k** to state **k'**, $W^s_{k',k}$ is the probability of excitation by electron in state **k'** to the state **k**, and j_o is the primary current. Honing in on each of the three

major production mechanisms allows further approximations to be made to the dielectric function, transition matrix elements, and Bloch energies.

Though all production mechanisms are important, the quasi-inelastic region, usually observed in the high energy region of spectra, may have strong effects not easily observed in the lower energy regions of spectra. There are also some important approximations leading to the material chosen for modeling. For instance, the plasmon production mechanism contribution to the excitation function involves evaluating the model potential for plasmon damping in the long-wavelength limit. This involves using a well known dielectric function.

The extended zone scheme can be used to describe the interband transitions to determine the plasmon linewidth. The matrix element, which includes the Bloch integral and perturbed Bloch energies, $\hat{E}_k$, describes electronic structure for nearly free electron (NFE) metals quite well. However, relative differences between Al, Cu, Ag, Au and other NFE metals involve approximations to the D-band electronic structure. Utilizing perturbation theory and incorporating a model potential results in the well-known square root expressions for the Bloch energies and associated Bloch integral. The interband transitions are therefore governed by just a few nearest neighbors for small wave numbers of the plasmon linewidth. The excitation function, $S(k_o, k) = m/\hbar k_o W^s_{ko,k}$, written as a function of E_o, E_k, and $\cos\theta$, where $\theta = \pi - \alpha$ for normal incidence, becomes

$$S(E_0, E_k, \cos\theta) = \frac{4mk}{\pi^2\hbar^2 a_B^3 e^2 k_0^2 k_F^5} \sum_{[K]} n_{[K]} \int_{q_{\min}}^{q_c} dq \int_{E_k - E_F}^{Min\{E_k, \Delta_q\}} \frac{d\Delta}{|\varepsilon(q,\Delta)|^2} M_{[K]}(q, \Delta, \cos\theta) \qquad (2.13)$$

with the summation taken over $[K]$ sets of equal length reciprocal lattice vectors and $n_{[K]}$ given by the number of corresponding vectors in the plasmon linewidth. Integration over q uses a lower boundary $q_{min} = k_o - (k_o^2 - k^2 + k_F^2)^{1/2}$, and a conditional boundary, q_c. Integration over energy loss, $\Delta = E_{ko} - E_{ko+q}$, uses an upper boundary $\Delta_q = (\hbar^2 q/2m)(2k_o - q)$, which is necessarily larger than $E_k - E_F$. $M_{[K]}$ contains the Bloch integral information given by

$$M_{[K]}(q,\Delta,\cos\theta)=\frac{E_F k_F{}^3}{8\pi^2 q^3}\int d\varphi\int d\Omega_K\left|B^K\left(k,k+q+K\right)\right|^2\delta\left(\hat{E}_{k+q+K}-\hat{E}_k+\Delta\right) \qquad (2.14)$$

The result of Rösler and Brauer's calculation of the AR emission spectrum of aluminum is particularly interesting. Highly anisotropic angle dependent production distributions were found for the SE's produced by the three production mechanisms [Fig. 2-3]. However, Rösler and Brauer predicted isotropic (cosine) emission distributions for each production mechanism as well as a combined total [Fig. 2-4(a)] by adding the different SE production mechanisms and then transporting to the surface. This is most likely the result of an excessive amount of elastic collisions (with ions) occurring during transport to the surface in the modeling process. The transport of energy by exciton (electron-hole pair) and plasmon propagation using respective inelastic mean free path's gauge the number of lower ($<E_o$) energy scattering events. The elastic mean free path incorporates the density of the ion scatterers dictating the number of high energy scattering events. As decays and excitations occur through the predominant production mechanisms (sums over state k' in Eq. 2.12), the elastic scattering function effectively "washes out" any angle dependence that the inelastic scattering function propagates containing anisotropic excitation information (e.g., Eq. 2.13).

One might ask, "If the elastic scattering is slowly less intensified, which of the three predominant production mechanisms becomes most important?" The excitation of SE's due to plasmon decay is the most important excitation mechanism because it's scattering function is peaked 10 to 100 times the intensity of the electron-electron and electron-core excitation mechanisms, respectively. Though the plasmon decay seems to be important for the transport of internal SE's produced by electron-electron and core electron scattering, the energy (20 eV) at which the excitation function peaks is 15 and 25 eV less than the other two, respectively. This means that the intensity dominates production mechanism importance regardless of the excitation peak energy location [*Rösler and Brauer II, Fig. 10, 1981*].

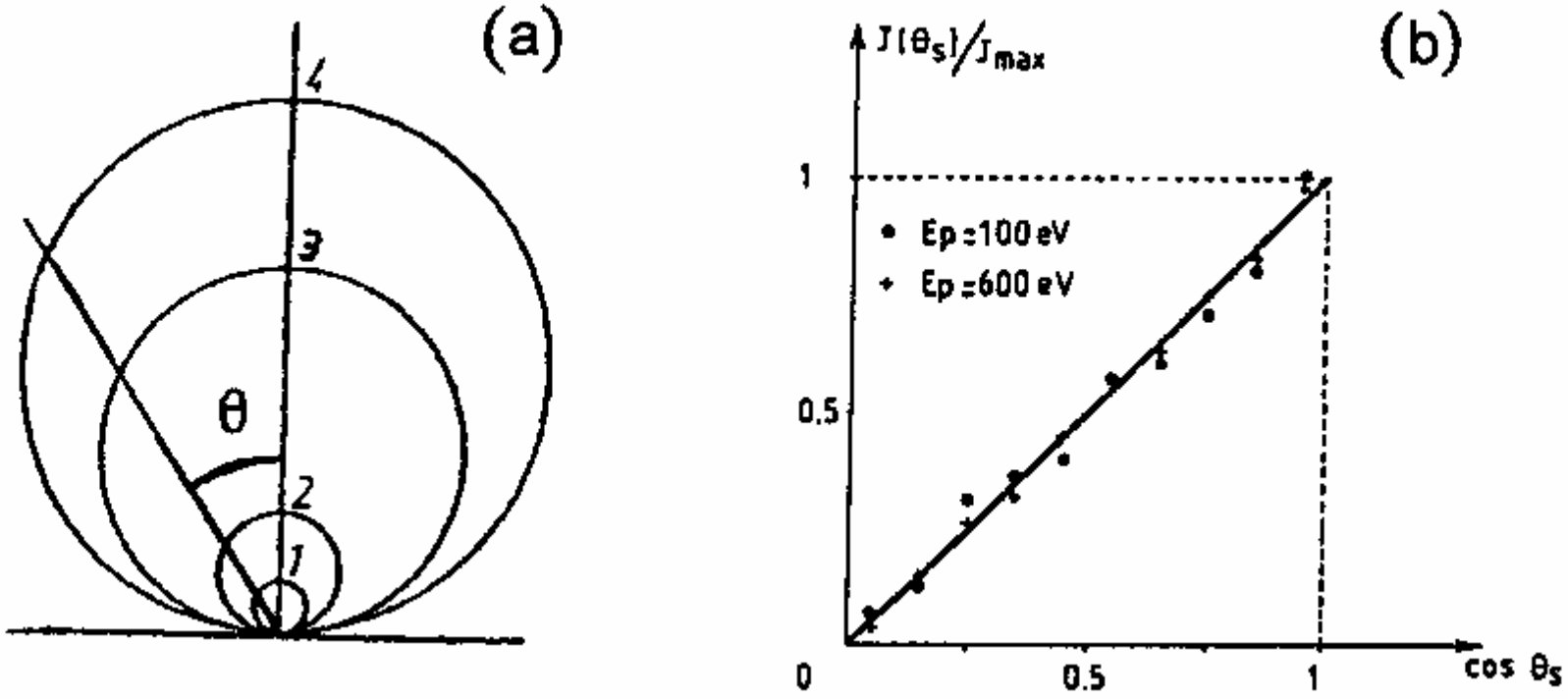

Figure 2- 4 AR electron emission distributions (a) at 2 eV emission energy for 2 keV PE's normally incident on polycrystalline Al. Contributions are from different excitation mechanisms (1) core electrons, (2) electron-electron, (3) plasmon decay, and (4) combined total. [after *Rösler and Brauer, 1981*]. (b) at 0 - 50 eV emission energy for 100 eV and 600 eV PE's normally incident on polycrystalline Al [after *Ganachaud and Cailler, 1979*]. Experimental data, • and +, are fitted to the cosine law [*Jonker, 1951; Jahrreiss and Oppel, 1972*].

Similarly, Ganachaud and Cailler also found an isotropic total emission distribution in the Al cross sections [Fig. 2-4(b)] using their unique **randium** (random ion position) and **jellium** (free electron gas) model. The important result relevant to my proposed study of these quantum mechanical SE theories is the prediction of highly anisotropic production distributions becoming isotropic during transport to the surface (Eq. 2.8).

Since the inelastic mean free paths are similar for various materials [Fig. 2-1], the sample material used in this study should provide similar cross section results. Referring back to Fig. 2-3, it would seem that the three predominant production mechanism cross sections for other materials should be similar. Simulations choose Al to model because its dielectric function is known to be dominated by bulk plasmon energy propagators (up to 10). Since Al is a nearly free electron (NFE) material, it is easier to make approximations of the dielectric function.

2.4 Nearly Free Electron Metals

As an aside, there is great interest in aluminum because much fine structure exists due to the strong electron-plasmon coupling (or energy exchange) in the material [*Henrich, 1973*]. Ganachaud and Cailler note that, "For Al, the characteristic loss spectra show peaks corresponding to the creation of one or several successive bulk plasmons (up to 10)." There has been much theoretical argument as to whether any other nearly-free-electron (NFE) metals have electron-plasmon coupling [*Henrich, 1973*]. Experimental evidence has shown that there are other NFE metals, which have electron-plasmon coupling [*Amelio, 1970*; *Haque and Kliewer, 1973*]. For example, Chung and Everhart state, "Low-q plasmon decay plays an important role in SE emission, which is not restricted to Al alone but should be valid in other NFE metals as well." [*Chung and Everhart, 1976, p. 4712*] Regardless of the implicit interest in electron-plasmon coupling, other NFE metals have production mechanisms similar to Al in that they are highly anisotropic. Since the inelastic mean free path for NFE metals is approximately the same for all the materials [*Powell,*

2000], the transport mechanism should also be similar. Therefore it is reasonable to infer an isotropic total emission distribution for the SE cross sections of other NFE metals.

2.5 Backscattering

The angular distribution for elastic and quasi-elastic scattering is unique due to the penetration depth of the bombarding electron. The theoretical angle distributions of quasi-elastic BSE's are given to compare to the results of the measured angle distributions. Theoretical elastic energy spectra are also quantitatively compared to measured elastic energy spectra using an energy emission dependent trend that is a combination of Gaussian and Lorentzian line shapes.

Theoretical formulations for electron backscattering are abundant in the literature [*Bishop, 1967; Jablonski et al., 1989, 1993; Jablonski, 1991*]. A concise, representative discussion of the treatment is given by Reimer [*1993*]. Generally, elastic and inelastic processes are considered. Elastic scattering arises from the attractive Coulomb potential of the nucleus, screened by an electron cloud (termed screened Rutherford scattering). The standard classical expression of the Rutherford scattering cross section for the unscreened Coulomb potential interaction between two electrons, $V(r) = q_e^2/r$ [*Sakurai, 1985*] is

$$\frac{d\sigma_R}{d\Omega} = \left(\frac{q_e^{\,2}}{4E}\right)^2 \left[\sin^2\left(\tfrac{\alpha}{2}\right)\right]^{-2} = \left(\frac{q_e^{\,2}}{4E}\right)^2 \left[1-\cos(\alpha)\right]^{-2} \qquad (2.15a)$$

α is the scattering angle in the lab frame and q_e is the elemental charge on the electron. For the screened Coulomb, or Yukawa potential interaction between two electrons $V(r) = q_e^2/r\, e^{-\mu r}$, the screened Rutherford cross section is

$$\frac{d\sigma_{SR}}{d\Omega} = \left(\frac{q_e^{\,2}}{4E}\right)^2 \left[\sin^2\left(\tfrac{\alpha}{2}\right) + \tfrac{\beta}{E}\right]^{-2} = \left(\frac{q_e^{\,2}}{4E}\right)^2 \left[1 - \cos(\alpha) + \tfrac{\beta}{E}\right]^{-2} \qquad (2.15b)$$

where $1/\mu$ is related to the range of the potential, $\beta = (\mu\hbar)^2/m_e$ and m_e is the mass of the electron [Bishop, 1967]. (Quantum mechanically, this expression is obtained as the first Born approximation to the Yukawa potential [*Sakurai, 1985*].) Based on a Rutherford scattering, including quantum mechanical electron exchange terms, the Mott cross section can be written in the form

$$\frac{d\sigma_{Mott}}{d\Omega} = \left(\frac{q_e^{\,2}}{4E}\right)^2 \left\{4\cos(\alpha)\left[\frac{1}{\sin^4(\alpha)} - \frac{1}{\sin^2(\alpha)\cos^2(\alpha)} + \frac{1}{\cos^4(\alpha)}\right]\right\} \qquad (2.16)$$

where a ratio between the Mott cross section and the unscreened Rutherford cross section [*Reimer, 1993*] is typically used. Inelastic scattering is due to intra- and inter-band transitions, surface and volume plasmon losses, single-electron excitations, and inner shell (core) ionizations [*Reimer, 1993*]. Detailed calculations utilizing this framework have been carried out by a number of authors and found to compare well with experiment [*Bishop, 1967; Jablonski et al., 1989, 1993; Jablonski, 1991; Reimer, 1993*].

It is known that the elastic peak for gold is a single peak having a characteristic gaussian shape on the high energy side (RD bias > E_b eV) and a Lorentzian shape due to electron-hole scattering on the low energy side (RD bias < E_b eV) [*Nazieres and de Dominicis, 1969*]. The theory used to fit the PE elastic peak spectra is of the Doniach and Sunjic [*Doniach and Sunjic, 1970*] type, shown in Eq. (2.17), having five parameters after removing background BSE features.

$$Elastic(E) = \left[BG + BGS \bullet E\right] + \frac{A \bullet \exp[(M-1) \bullet \ln 2 \bullet [\frac{(E - E_0)}{\beta - \alpha \bullet (E - E_0)}]^2]}{[1 + M \bullet [\frac{(E - E_0)}{\beta - \alpha \bullet (E - E_0)}]^2]} \qquad (2.17)$$

In this elastic peak equation, A is the peak amplitude, M is the magnification parameter (between 0 and 1), β is the Lorentzian width parameter, α is the Gaussian width parameter, and E_o is the PE elastic peak energy. Also included is the linear background term in square brackets, with BG as the high-energy background amplitude and BGS as the background slope. Note that when M = 0, only the Gaussian portion remains exemplifying the physical characteristics of the bombarding electrons. Also, when M = 1, the Gaussian portion vanishes and the Lorentzian portion portrays scattering information.

2.6 Previous Observations and Investigations of Gold

A summary of the relevant experimental AR cross section work on NFE and alkali metals is shown in Table 2-1. Five studies [*Kanter, 1957; Drescher, 1970; Jahrreiss and Oppel, 1971; Darlington and Cosslett, 1972; Massoumi, 1990*] were done in low-quality vacuums that limit the validity of the studies. Further, while each study has angle-resolved measurements, no study incorporates energy-resolved aspects of the SE yield. Four additional studies [*Jonker, 1951; Burns, 1960; Appelt, 1968; Davies, 1999*] have been made in ultra high vacuum (UHV), which significantly reduces unwanted contaminants such as water and oxides from surfaces. Only the study by Davies [*1999*] has angle resolved emission energy spectra [Fig. 2-5 and Fig. 2-6], while the remaining three studies resolve the SE and BSE energy dependence with large energy ranges. Each of these four studies have observed some deviation from an isotropic angular distribution. Burns [*1960*] and Appelt [*1968*] attribute relatively narrow deviations from isotropic angular distributions to diffraction or channeling effects for their single crystal samples. Broader deviations, observed by Appelt [*1968*] and Jonker [*1951*] for "polycrystalline" samples, are attributed to a preferred orientation of the micro-crystallites within the samples.

Table 2-1. Summary of Experimental AR studies on NFE metals.

Reference	Incident Electrons		Emitted Electrons				UHV	Materials studied					
	Energies	Angles	Low Energy (SE) Electrons	High Energy (BSE) Electrons	Uncertainty	Angles		Al	Au	Ag	Cu	Ni	Be
Davies 1999	1500 eV	0°	0-50 eV @ 1 eV step	200-1400 eV @ 100 eV step 1400-1480 eV 10 eV step 1480-1510 eV @ 1 eV step	±1 eV	17°, 24°, 38°, 53°, 65°, 73°, 76°	X		P				
Jonker 1951	25, 100, 450 eV	0°, 30°, 45°	1-6 eV, 10-15 eV, 20-25 eV, 5-15 eV, 45-55 eV	80-100 eV, 360-450 eV	±0.1 eV	♣20° to 90°	X					P	
Burns 1960	250, 500, 800 eV	0°, 25°, 45°	0-10 eV, 10-20 eV, 20-40 eV, 40-90 eV		6%	♣10° to 90°	X				C(001)	C(001)	
Appelt 1968	200, 400, 800 eV	0°	0.5-5.5 eV, 7.5-12.5 eV, 15-25 eV, 45-55 eV		±0.1 eV	♣	X				P, C(110)		
Kanter 1957	10, 30, 50, 70 keV	0°, 25°, 55°, 80°	0-50 eV	50 eV to incident Energy keV	5%	10°, 15° to 90° @ 15° steps		P	P	P	P		
Drescher 1970	10-100 keV	♣0° to 85°	___	___	___	♣		P	P		P		P
Jahrreiss and Oppel 1971	1, 1.4, 1.6, 1.8, 2, 3, 4, 5, 6, 8, 10, 12 keV	0°, 60°	0-50 eV	50 eV to incident Energy keV	1%	♣11° to 90°			P				
Darlington and Cosslett 1972	1-10 keV	0°		1-1.5 keV, 1.5-2 keV, 2-3 keV, 3-10 keV	5% - 15%	10° to 90° @ 10° steps		P		P	P		
Massoumi 1990	5-35 keV	0°	0-50 eV	50 eV to incident Energy keV	±4.8 keV	10° to 85° @ 5° steps		P	P	P	P		P

Notes: C – crystalline and P – polycrystalline.
♣ – Data taken over full angular range at small, unspecific increments.
All angles are from normal incidence.

The study by Davies [*1999*] on polycrystalline Au provides the most complete energy- and angle-resolved SE and BSE spectra, taken under UHV conditions. A cosine prediction has been compared with this available data, which comes from the re-organization of AR data [Fig. 1-2, other angles not shown] into sets of ER cross sections for the chosen energy resolutions [Fig. 2-5 and Fig. 2-6]. As can be seen, the SE cross sections show anisotropic behavior contrary to the predicted theory. Note that the BSE cross sections at the single energy resolutions of 450 eV and 600 eV most closely follow an isotropic distribution. These energies are very near the minimum counts in the AR spectrum of Figure 1-2 suggesting a single natural energy division between SE's and BSE's. Davies has hypothesized that the discrepancy is due to the fact that the transport modeling mechanism is most likely overestimating the randomizing elastic collisions and suggests several possible explanations for the anisotropic behavior. The following items are listed, referenced in Davies dissertation, and addressed within this dissertation.

a. The data may suggest that the studied Au samples are not entirely polycrystalline, but possess many micro-crystallites on the surface with possible preferred orientation [*Davies, 1999, 4.4(a), p.57*].
b. Stray electric and magnetic fields affect electron trajectories [*Davies, 1999, A.4, p190, C.3, p.210*]. Davies estimated that significant altercation of trajectories occurred for scattered electrons below about 8 eV.
c. Contamination [*Davies, 1999, 4.4(b), p.57, C.4, p.217*]
d. Detector misalignment [*Davies, 1999, C.1(a), p.198*]
e. Incident beam alignment [*Davies, 1999, 5.6(b), p.95*]
f. Charging of the RD and secondaries produced within the RD [*Davies, 1999, C.1(d), p.202, C.1(b), p.199*].

These potential problems are addressed in the dissertation and discussed in further detail. The effects of possible diffraction from (a) the polycrystalline sample and (b) the magnitude of stray electric

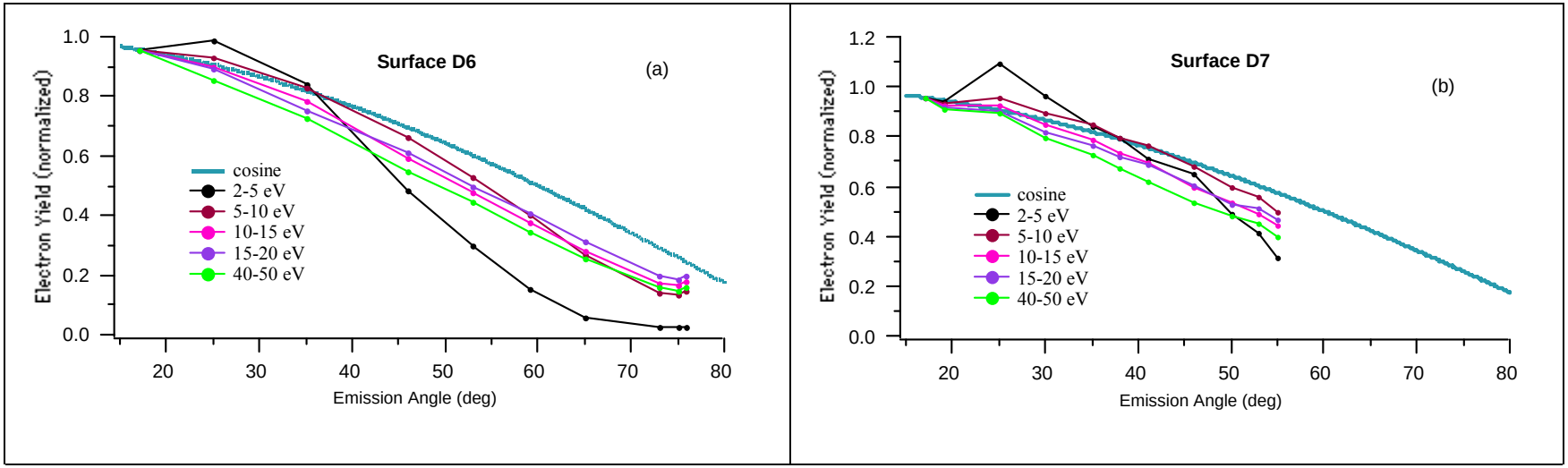

Figure 2- 5 SE cross sections for the energy resolutions 2-5 eV, 5-10 eV, 10-15 eV, 15-20 eV, and 40-50 eV on polycrystalline Au (a) surface D6 and (b) surface D7 with PE energy of 1500 eV at normal incidence. Lambert cosine law is shown in blue. [*Davies, 1999, p. 157*]

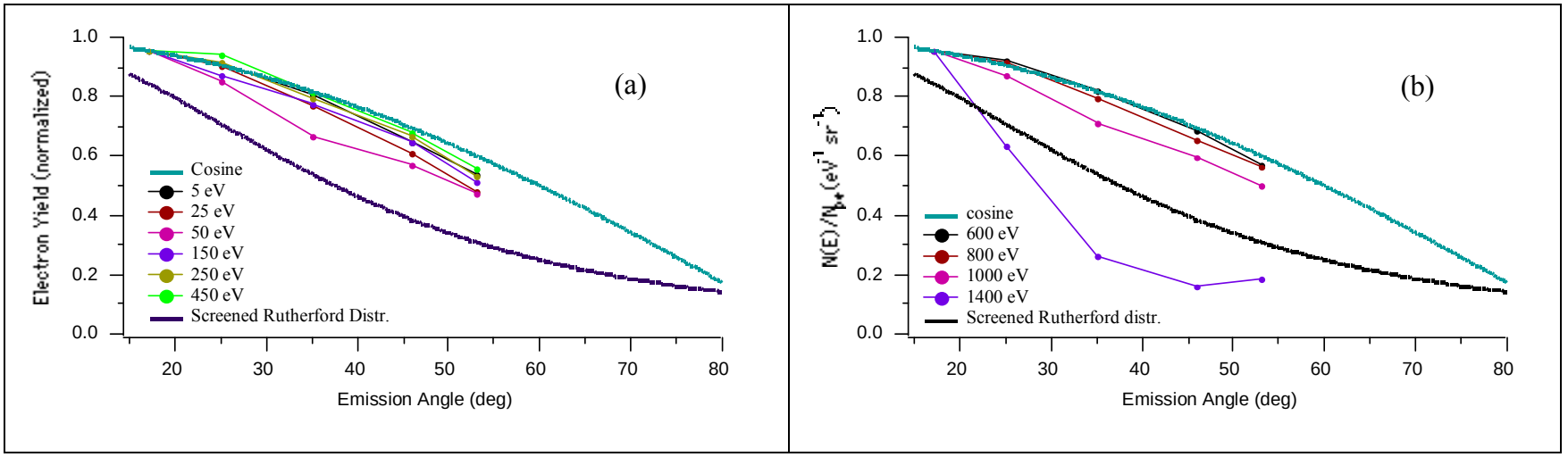

Figure 2- 6 Selected ER cross sections with PE energy of 1500 eV at normal incidence on polycrystalline Au sample D6 (a) 5 eV, 25 eV, 50 eV, 150 eV, 250 eV, 450 eV, (b) 600 eV, 800 eV, 1000 eV, 1400 eV. Cosine curve is shown in blue. [*Davies, 1999, p. 160,162*].

and magnetic fields is addressed by arranging the LittleBoy in a symmetric configuration [Appendix D] to test (3.2(f)) both the magnitude of diffraction and stray electric and magnetic fields. Contamination (c) is addressed by (3.2(d)) monitoring the lowered incident beam currents, hence reducing ESA. The possibility of the rotatable detector being misaligned (d) is addressed in 3.2(c). The possible misalignment of the incident electron beam (e) is addressed in Appendix A. The charging and secondary production within the rotatable detector (f) is addressed in 3.2(h).

2.7 Conclusion

Figures 2-5 and 2-6 have been re-plotted in a 3 dimensional AER distribution [Fig. 2-7]. Each spectrum contain minima (peaked at ~ 450 eV), which stresses that the natural dividing energy between SE's and BSE's most closely follows an isotropic distribution. Deviations are likely due to the modeling transport mechanism involving an overestimation of randomizing collisions. The best available simulations predict isotropic emission spectra which does not agree with the best data (anisotropic emission).

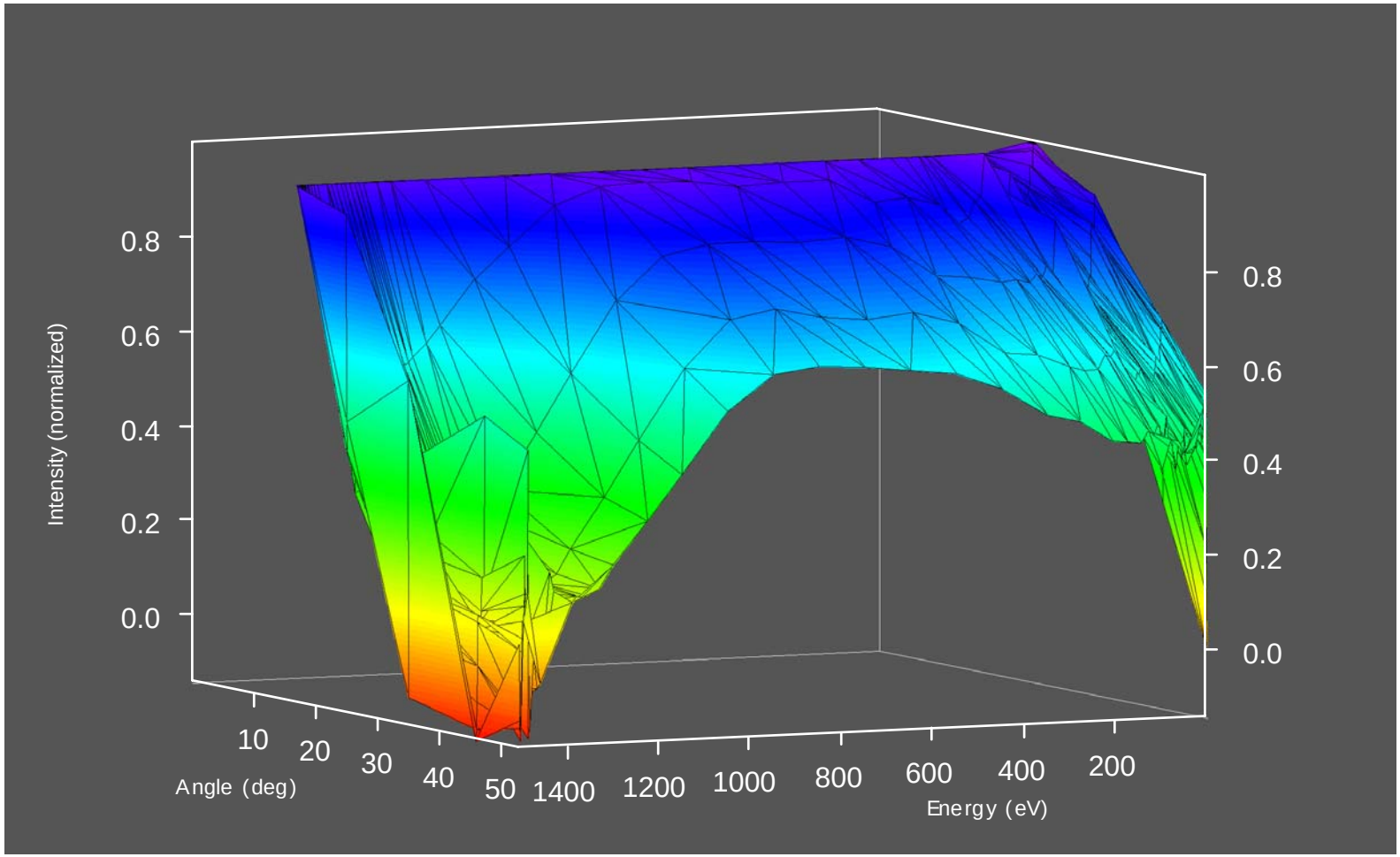

Figure 2- 7 Normalized AER distributions with PE incident energy of 1500 eV at normal incidence on polycrystalline Au sample D6 [Davies, 1999, p. 153].

CHAPTER 3

INSTRUMENTATION

After a flash of inspiration by Davies, the instrument, which contains the AER apparatus was dubbed the LittleBoy chamber. Prior to this flash, the measuring apparatus had been extensively analyzed [*Davies, 1996, 1999*], and is now dedicated for the sole purpose of probing scattered electrons in resolutions of angle and energy. The contents of this chapter include an overview of the equipment, an evaluation of modifications to the AER apparatus, and a detailed description of measured quantities, data acquisition procedure, and measurement techniques. The primary objective of this part of the dissertation work was to minimize errors in the data acquisition and analysis so that more accurate and precise energy and angle resolved emission spectra could be taken and compared to simulations.

3.1 EQUIPMENT OVERVIEW

The LittleBoy chamber is composed of an ultrahigh vacuum (UHV) chamber, an electron gun, a chamber apparatus, and some experimental electronics. The chamber apparatus contains a sample, two tertiary detectors, and a rotatable detector (RD) and is capable of measuring AER electron spectra. Detailed descriptions are found in Davies [*1996, 1999*].

3.1.(a) UHV Chamber

The UHV chamber is an ~25,000 cm^3 volume of standard stainless steel construction. Roughing is accomplished by a mechanically-backed turbomolecular pump, or by two cryosorption pumps cooled with liquid nitrogen; high-vacuum pumping is achieved with a magnetic ion pump, operated continuously and periodically supplemented by a water-cooled titanium sublimation pump (TSP). A 72-hour, 125 °C bake-out of the system routinely results in base pressures in the mid-10^{-11} Torr range. UHV absolute pressure measurement is accomplished independently with both a nude UHV ion gauge and a quadrupole mass spectrometer configured for total pressure measurement; these gauges typically agree to within less

(usually much less) than a factor of two.

3.1.(b) Electron Gun

The electron gun is constructed by Varian as a standard Pierce-type model that emits a constant flow of electrons from a tungsten filament and produces a beam in the 0.1-3 keV energy range. Recent enhancement of the beam current stability, beam shape and size, and beam current monitoring has optimized the performance of the electron gun. The FWHM thermal energy spread, ΔE, is ~0.3 eV. The beam current is controllable in the range ~10 to 300 nA, with a worst-case stability of ~5% over time scales on the order of seconds. Stability of the beam current improves with increasing beam current, but worsens with increasing beam energy, though degradation of the filament increases rapidly using energies less than 0.1 keV. For the beam currents and energies typical of this investigation, 10 nA — 300 nA and 0.1 — 2.5 keV respectively, beam stability is approximately 2% over time scales of minutes. Further details of the design and characteristics are given in Appendix A. The gun is mounted to the chamber on a 2 ¾'' conflat flange oriented 45° relative to the horizontal and aligned on the chamber center.

3.1.(c) Chamber Apparatus

The assembly housing the samples and rotatable detector, termed the *chamber apparatus* (CA), is depicted schematically in Fig. 3-1. The primary sample sits at the center of the chamber apparatus on a sample holder, and is flanked on either side by two tertiary samples. The primary and tertiary samples and their respective holders are mounted in the *sample block* which orients their surfaces 45° relative to the horizontal—perpendicular to, and directly facing the incident electron beam. The electron beam bombards the primary sample at normal incidence. The tertiary samples are located for the collection of scattered, returning current from the chamber interior (termed the *return current*). Incorporated inside the sample holder, mounted directly behind the primary sample, are a small resistive heater and thermocouple used for active temperature control and monitoring (27 °C < T < ~400 °C). Machined into the left center of the primary sample and holder is a large Faraday cup (2 mm dia. x 20 mm deep) into which the incident electron beam can be aligned for the purpose of beam profile and current measurement. The additional

Figure 3- 1 The Chamber Apparatus contains a sample, two tertiary detectors, and a rotatable detector.

presence of three smaller Faraday cups, machined into the primary sample above, below, and to the right of center, allow for precise positioning of the electron beam on the sample center. The sample center is located half-way between the left and right Faraday cups in the horizontal direction, and half-way between the top and bottom Faraday cups in the vertical direction.

Permanently aligned on the sample center is the rotatable detector (RD) [Fig. 3-2] allowing for angle-resolved measurements to be accomplished for a continuous range of emission angles relative to the sample normal. The RD is composed of an aluminum Faraday cup isolated with Teflon spacers and is encased in a stainless steel housing. This assembly is mounted to a support post that is subsequently mounted on a rotating plate [Fig. 3-1] capable of providing angular movement about the sample in the horizontal plane by means of a flexible cable connection to a rotary motion feedthrough. Throughout rotation, the RD remains aligned on the sample center at a distance of 74 mm to the Faraday cup (62 mm to the first aperture). At this distance, the solid angle subtended by the 1.5 mm first aperture is ~3.6×10^{-5} sr.

Since the sample is mounted at 45° relative to the horizontal and the RD is aligned at 59° relative to the horizontal, the relationship between the detector position and emission angle is highly nonlinear. Equal changes in the RD position, φ_{RD}, do not result in equal changes in the emission angle, α. Specifically, as the RD moves azimuthally about the sample [Fig. 3-3], from a detector position of $\varphi_{RD} = 0°$ to $\varphi_{RD} = 180°$ the emission (polar) angle, α, varies from $\alpha = 14°$ to $\alpha = 76°$. The nonlinear relationship between detector position and emission angle is reproduced in [Fig. 3-4].

The LittleBoy chamber has recently been upgraded with an automated RD-motion device (steppermotor). During the renovation, it was realized that the flexible cable that transfers rotational motion to the RD was torsionally damaged (3.2.(a)). The question of chamber symmetry with respect to the azimuthal angle, φ_s, with concerns towards non-uniform RD movement required that the chamber apparatus be arranged in a new configuration by relocation of a support post [Fig. 3-1, Fig. 3-3, and Fig. 3-8]. This alternative symmetrical configuration allows symmetric emission angle measurements from 53 degrees Clockwise to 53 degrees Counter-Clockwise. After the cable was replaced, the symmetrical configuration offered energy-resolved angular (EAR) distributions given in 3.2.(f). These provide critical diagnostic information about the ambient electric fields within the LittleBoy chamber and sample

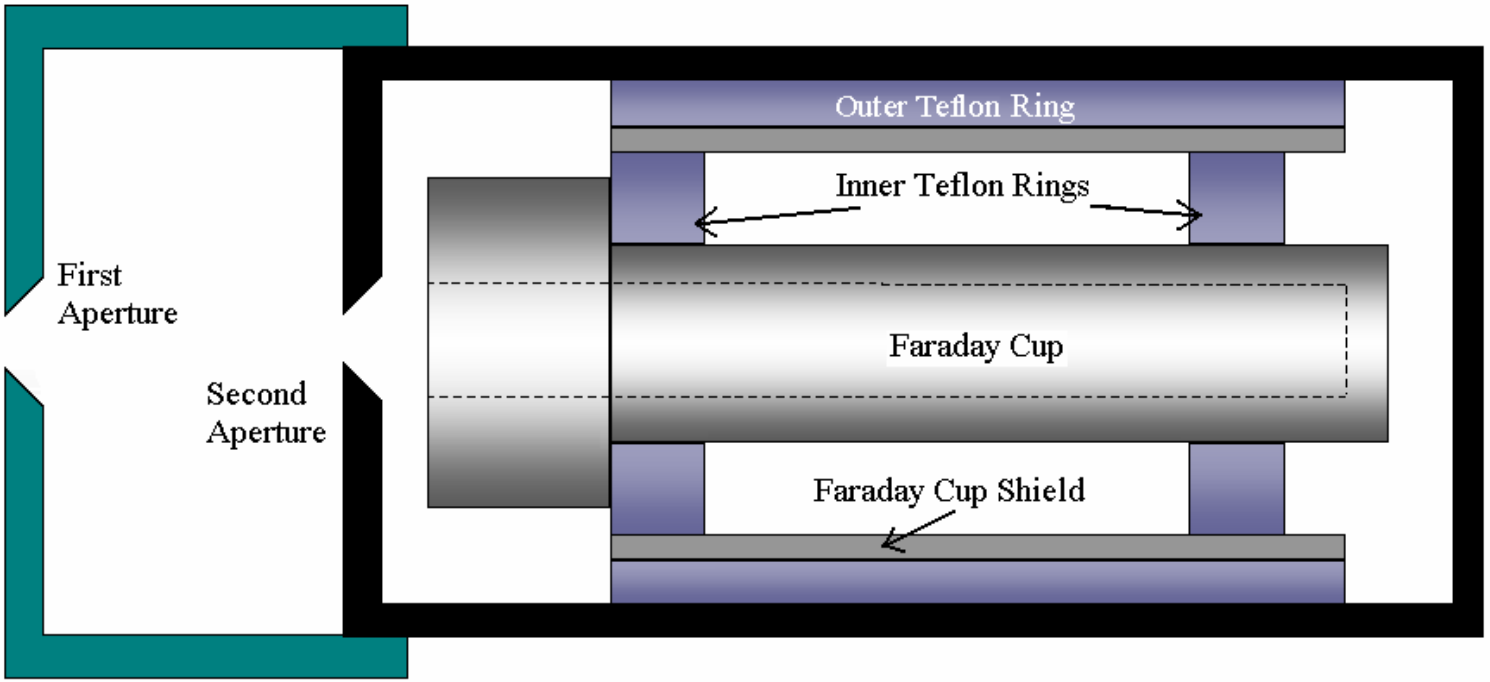

Figure 3- 2 Schematic depicting the rotatable detector, which includes two apertures, two Inner Teflon Rings, an Outer Teflon Ring, a Faraday Cup Shield, and a Faraday cup. The overall length and diameter of the rotatable detector are 4.5 cm and 3.6 cm, respectively.

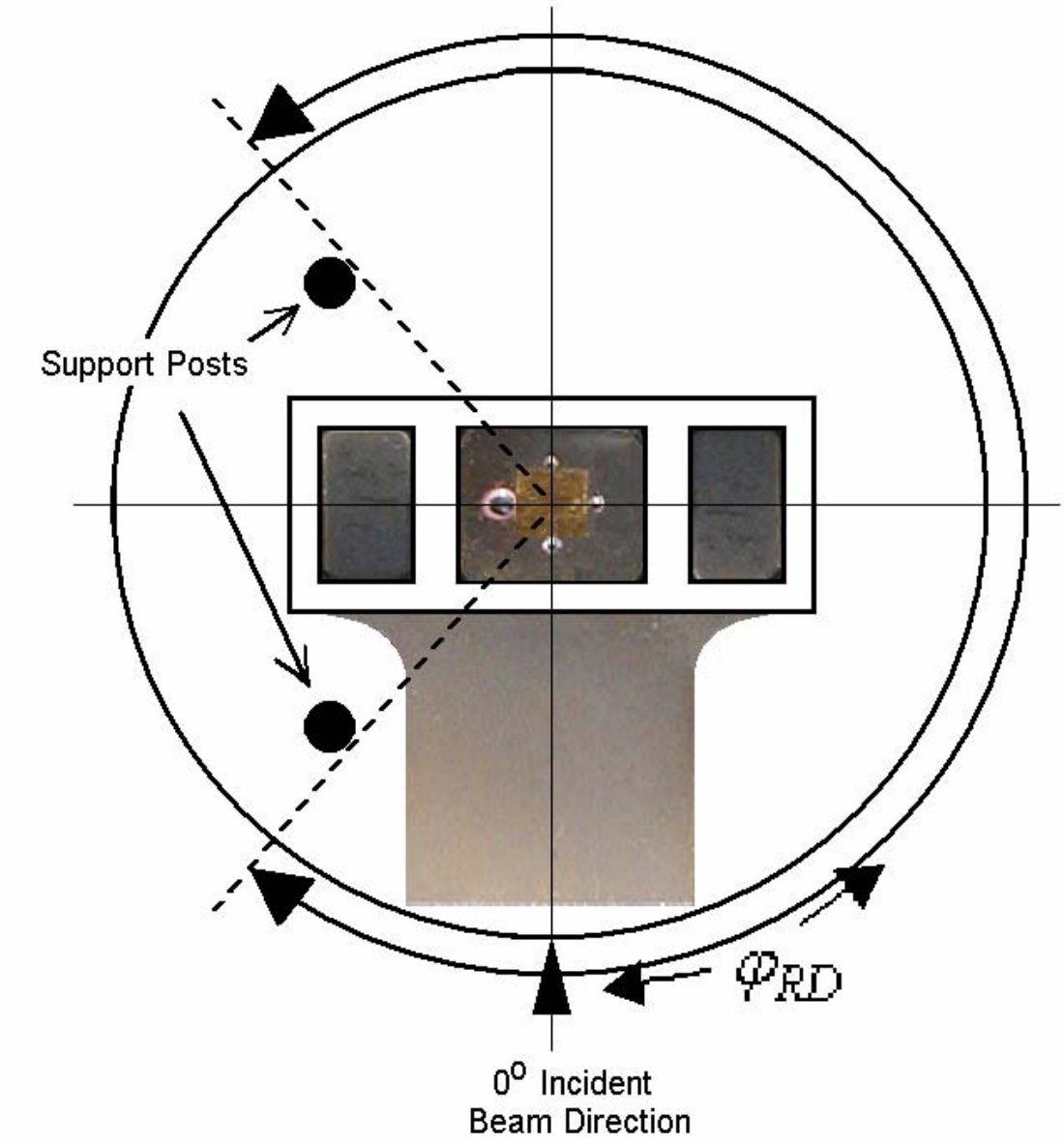

Figure 3- 3 The non-symmetric configuration for the chamber apparatus with support posts, which limit RD angle movement. The Primary Sample is flanked by two Tertiary Samples.

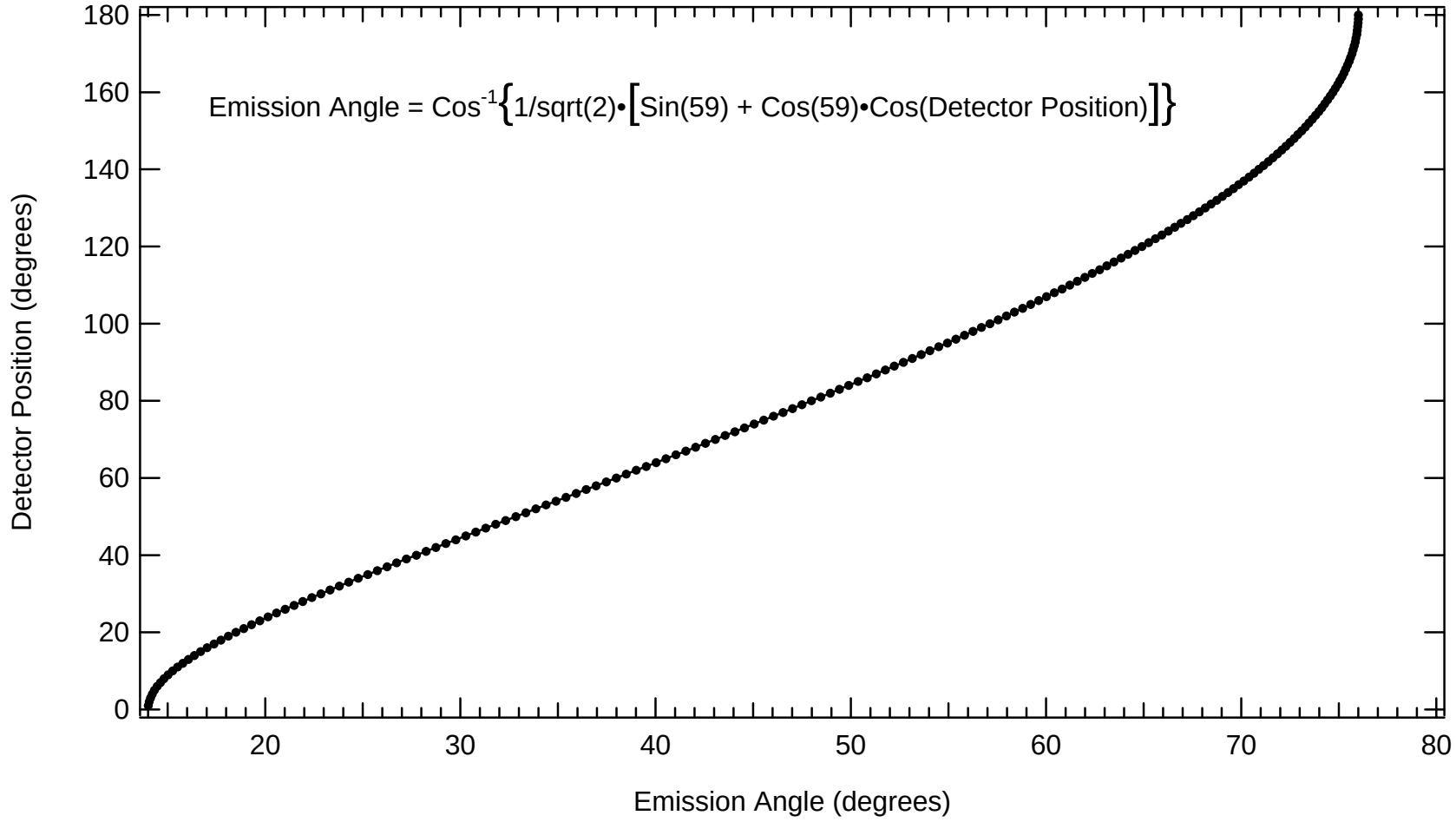

Figure 3- 4 Emission angle intercepted by the rotatable detector as a function of detector position.

characteristics such as morphology addressed in Chap. 4.

Enclosing the chamber apparatus is a cylindrical magnetic shield (not depicted in Fig. 3-1), constructed of 0.020" CO-NETIC μ-metal, reducing the earth's ~500 mG ambient magnetic field, $\vec{B}$, to ~4 mG in the region between the sample and the detector (measured with the chamber apparatus mounted inside the vacuum chamber). Such a reduction in $\vec{B}$ is necessary for the acquisition of low-energy (0-20 eV), angle-resolved spectra. [Note: While the average $\vec{B}$ in the 62-mm region between the sample and detector is very low, the presence of the sample heater (with nickel housing) produces a magnetic field magnitude of ~30 mG at the sample surface; this field drops below 10 mG after moving only a few millimeters away from the surface, and to only a few mG midway between the sample and the detector.]

The entire chamber apparatus is mounted in the vacuum chamber via a baffled rotational top feedthrough. One end of a rectangular bar is fixed to the "top plate" [Fig. 3-1], while the other is fixed to the ¼" diameter post protruding down from the top feedthrough with one setscrew. A vertical Z-axis caliper holds the rotational bearing, which provides rotation to the CA for purposes of sample sputtering and sample exchange. Two additional horizontal positioning micrometers, X and Y-axis, provide Cartesian alignment capability to the chamber apparatus. This arrangement allows for precise linear and rotational positioning of the sample within the LittleBoy chamber.

3.1.(d) Experimental Electronics Schematics

The experimental circuitry associated with the LittleBoy is composed of detectors, wires, meters, power supplies, and a computer. Because the measured signals are very small, extreme care is taken to minimize noise and leakage current in the current measurements. Detected electrical signals are transported by shielded wires to solid-state ammeters (electrometers) where measurement occurs. Each electrometer sends measurements to a PCI card (DAQBoard2000), which works in conjunction with a 233 MHz (Windows 98) personal computer. The software used to configure and control the LittleBoy is the LabVIEW 6.0 software by National Instruments. The experimental electronics schematic [Fig. 3-5] depicts the hierarchy of communication between the LabVIEW control software and its peripherals. Four signals

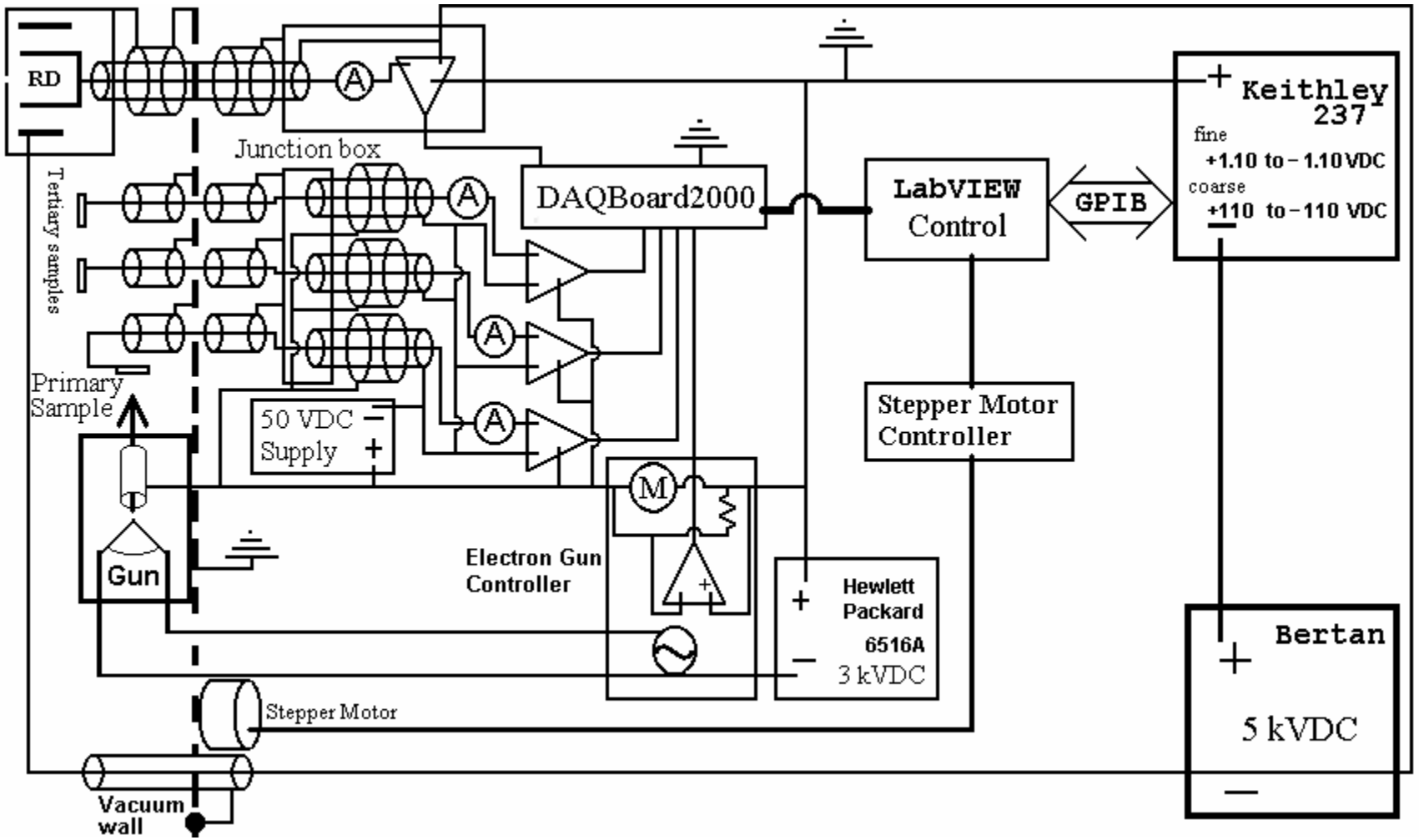

Figure 3- 5 The experimental electronic schematic includes detailed wiring of detectors, meters, power supplies, and peripherals. The vacuum chamber wall is the experimental ground and is represented by the thick dashed line.

are measured with electrometers, represented by a circumscribed letter A in Fig 3-5. Since each detector's electrometer floats at the same potential as the detector, an isolation amplifier, represented by a triangle, is used to convert the measured signal to chamber ground. The signal detected within the electron gun controller, represented by a circumscribed letter M, is of the analog type. The circuit within the electron gun controller is explained in detail in Appendix A.

The primary and tertiary sample coax wires exit the shielding can from the bottom [Fig. 3-1]. After the wires exit the LittleBoy chamber, a junction box aids in minimizing the noise of the signals before measurement [Fig. 3-5]. The 0 to 50 V power supply is used to bias the inner shield of a triax wire. Each of the three detectors possesses an independent, biasable triax wire. When no biasing is needed, the triax wire, isolation amplifier, and junction box are removed. The arrangement of the four insulators [Fig. 3-6] (inner triax insulation, outer triax insulation, coax insulation, and ceramic spacer) with respect to each detector assures that minimal leakage of the signal occurs prior to electrometer measurement.

The rotatable detector (RD) coax and triax wires exit from the top of the shielding can [Fig. 3-1]. The coax wire is used to bias the Faraday cup shield and the triax wire is used to transport the RD signal through the chamber wall. Immediately after exiting the top of the LittleBoy chamber, another triax wire transports the RD signal to the electrometer for measurement. The power supply used to bias the RD, the Keithley 237, is limited to ±1.1 kV [Fig. 3-7]. In order to exceed this limit, the Bertan 5 kV supply [Fig. 3-5] is used in series with the Keithley 237. Since both power supplies are used in series, the Bertan will be treated like a battery and the Keithley will be optimized utilizing coarse (±10 V) and fine (±0.01 V) energy ranges. Three insulators (outer Teflon ring, coax insulation, and outer triax insulation) maintain the bias on the Faraday cup shield and inner triax shield. Noise and current leakage is further reduced with the addition of the inner Teflon ring [Fig. 3-2]. The inner Teflon ring and inner triax insulation are responsible for making sure that all signal collected by the Faraday cup is measured. It is necessary to identify all possible paths for traveling currents because there is a possible loss of signal due to charge leakage. Since signal detected at the floating Faraday cup has two other possible alternate routes to travel to ground, it is

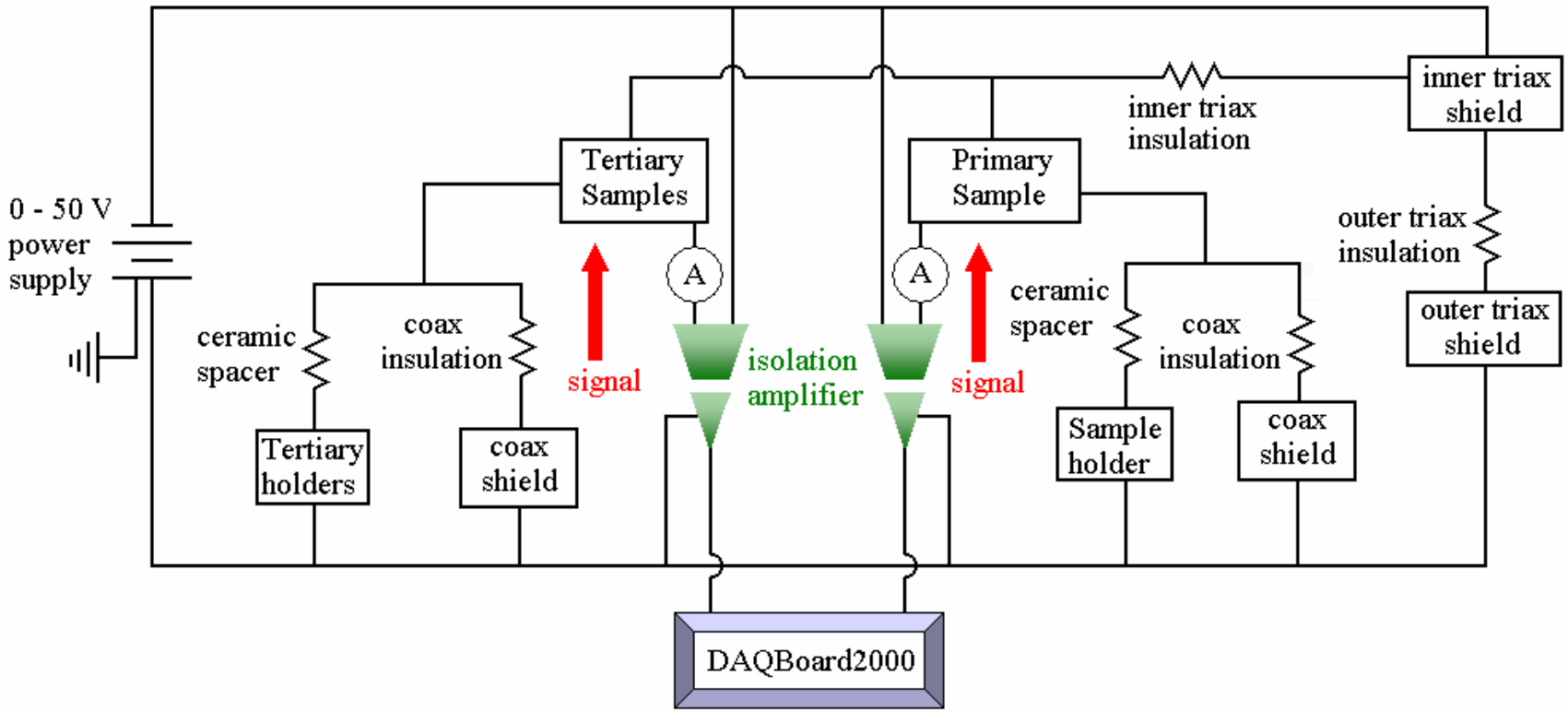

Figure 3- 6 Resistance diagram for the Primary and Tertiary Detectors.

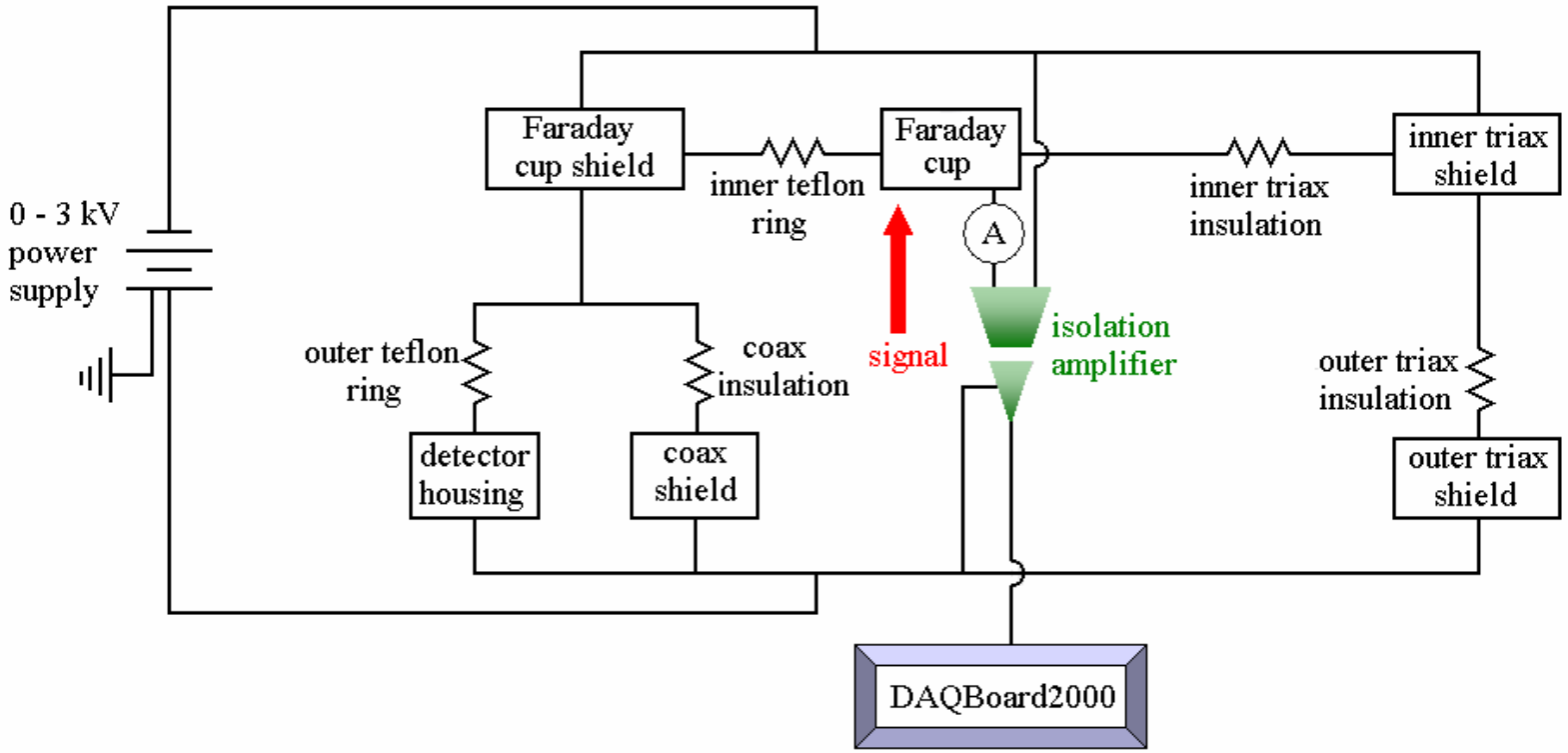

Figure 3- 7 Resistance diagram for the Rotatable Detector Faraday cup circuitry.

possible that some detected signal current does not get measured. With the electrometer and isolation amplifier disconnected and an AC power supply replacing the DC power supply, the RC time constant can be determined. The impedance matching of the inner Teflon ring and inner triax insulation assures that minimal signal loss occurs.

3.2 EVALUATION OF MODIFICATIONS TO THE AER APPARATUS

A preliminary study of AER spectra on polycrystalline gold was completed [*Davies, 1996, 1999 Chap. 3 and all appendices*]. Although his data have provided abundant information, there were limitations to his apparatus. Davies concluded the following limitation:

- The presence of ambient fields in the chamber apparatus caused distortions in the measured cross sections below the 10 - 15 eV range [*Davies, 1999, p. 170, 210*].
- Instabilities in the primary electron beam – most noticeably a 5 volt peak-to-peak ripple in the high voltage power supply – degraded energy resolution preventing identification of energy loss peaks near the elastic peak and prohibited the acquisition of Auger spectra used for surface characterization.
- Extraneous secondary electrons produced within the rotatable detector (RD) were observed and peaked at ~2 eV emission energy [*Davies, 1999, p. 200*].
- Surface charging within the RD caused anomalous measurements in the < 3 eV range [*Davies, 1999, p.203*].
- Lastly, there was a noticeable systematic error resulting from SE collection by the tertiary samples [*Chang, 2000*].

As a result of these limitations, several modifications to the LittleBoy apparatus have been made. A summary of changes completed and analysis of their effectiveness, as of January 26, 2001, is presented below, using a format listing order: **Problem**, **Action Taken**, **Evaluation**, and **Recommended Additional Action**.

3.2.(a) Angular Motion

Problem: The RD bearing has completely frozen on occasion due to the weight of the apparatus. [4-26-99, LB4-8y]

Action Taken: The rotating plate has been redesigned and replaced [5-5-99, LB4-10w] with a UHV compatible bronze-Al alloy that is harder than the aluminum used previously [5-5-99, LB4-7w].

Evaluation: The RD bearing no longer freezes.

Recommended Additional Action: No further steps are required.

Problem: The angular rotation of the RD was initially controlled by hand. The accuracy of the rotational measuring device was dependent on the choice of zero angle and the precision of the measuring device was related to the detector wheel gear ratio. The zero angle could not be set experimentally because the RD support post blocked the electron beam at zero angle. The zero angle had been determined by alignment to pre-measured markings placed on the magnetic shield made to move concurrently with the sample. This accuracy was ~0.05^{o}. The angle of the detector wheel was measured with an external measuring device (Huntington VF-106-3C) and had a resolution of 0.72^{o}. The angular precision of the detector wheel was theoretically determined by multiplying the precision of the angle markings on the measuring device by the gear ratio of the detector wheel (350^{o} :100 ticks X 1:12 = 0.292^{o}) [10-30-92, LBI 3y]. The precision was experimentally determined to be 0.286^{o} (90^{o}/315 ticks) [8-15-00, 53y]. The angular resolution was therefore no better than $0.286^{o} + 0.72^{o} / 12 = 0.346^{o}$.

Action Taken: A LabVIEW controlled stepper motor was developed by Nelsen, Chang, and Thomson to increase the accuracy of the angular rotation of the RD. A custom stepper motor mount was designed and constructed by Sabbah. The electronics used to control the stepper motor are detailed in Appendix B. The stepper motor is mounted to the chamber directly below the communications port, is connected to the rotational feedthrough, and provides complete automated angle resolved data [10-31-01, LB5 72w].

Evaluation: The angular precision of the new angle measuring device alone has been determined by Nelsen to be 0.001^{o}. In combination with the detector wheel gear ratio, the new predicted theoretical angular precision is $8.3x10^{-5\,o}$. This is a precision improvement of ~3500 times. The theoretically determined angular resolution of the RD (about 2^{o}) is calculated by knowing the RD aperture size and distance from the sample [*Davies, 1999, p. 29*]. This RD angular resolution is much greater than the theoretically predicted angular resolution of the RD rotational device (0.346^{o}). Therefore, further improvements to the RD should be considered before rotational device upgrades. There is no change to the accuracy because the "zero set" procedure is unchanged. Considerable improvement of the counting statistics has allowed two different angle step sizes to be utilized. The largest emission angle step size of 7° is used primarily for angle- energy- resolved results and the smallest emission angle step size of $1/20^{th}$ degree, is used for energy-resolved angular distribution results. The smallest emission angle step size has not been used extensively due to the large angular resolution of the RD.

Recommended Addition Action: No further steps are required.

Problem: There exists a new restriction of possible RD angular settings. This restriction was inherently due to the reassignment of a chamber apparatus support post. The support post nearest the front of the sample stage was relocated to the opposite side of the sample stage [Fig. 3-8]. This geometry is different from the non-symmetric [Fig. 3-3] in that φ_{RD} is limited to a smaller maximum angle. The reason for this arrangement was to take advantage of the right/left symmetry, which is used to determine the magnitude and effects of ambient electric fields existing in the chamber. The angle restriction for this configuration limits the possible RD settings to a maximum of 53° on either side of normal [5-9-99, LB5 10w].

Action Taken: After an ambient electric field study was accomplished, the chamber apparatus support post was reassigned to provide a non-symmetric angle configuration [Fig. 3-3] offering the maximum angular accessibility without compromising structural stability [2001].

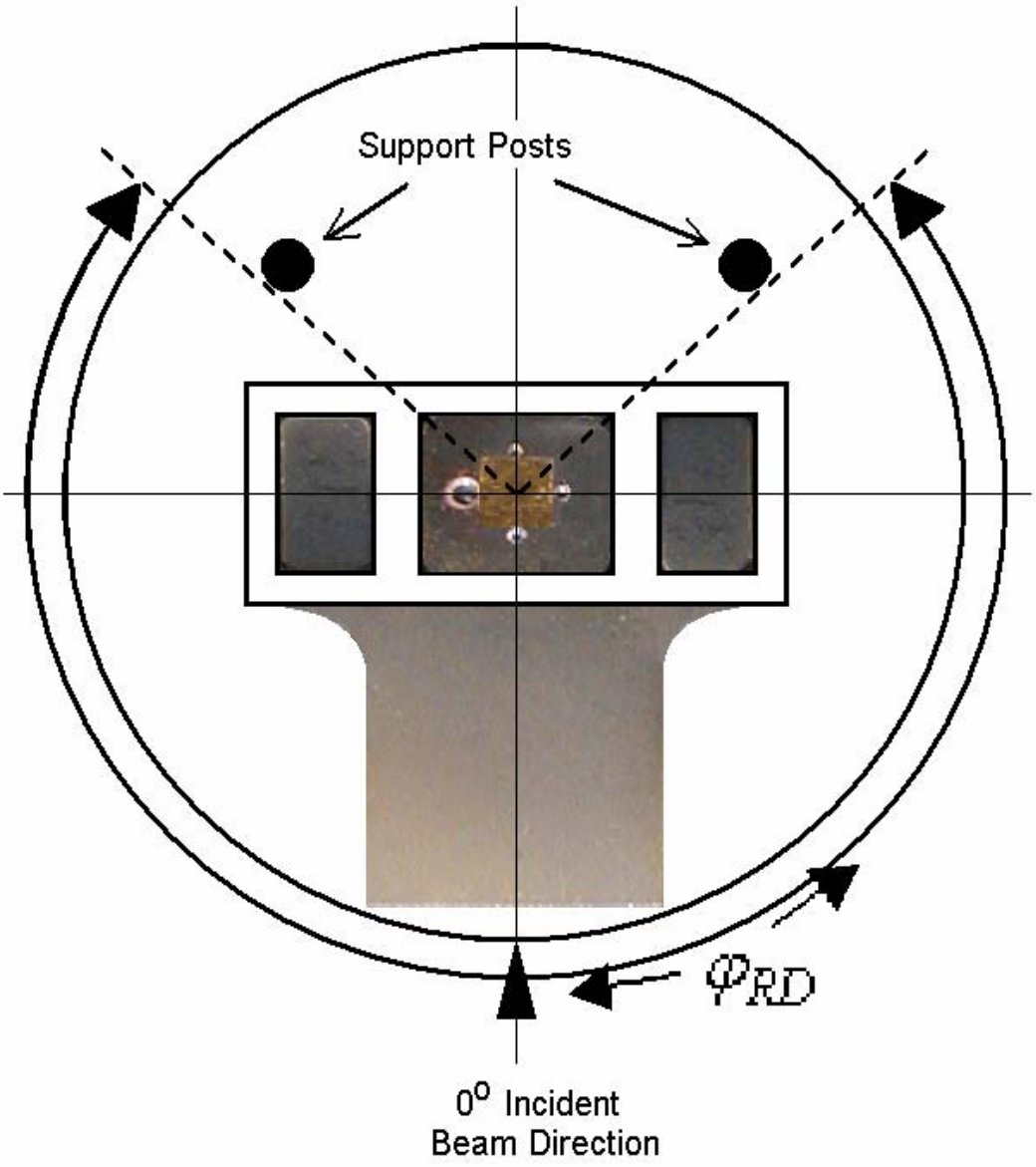

Figure 3- 8 Symmetric configuration for the chamber apparatus showing support posts, which limit RD angle movement.

Evaluation: By comparing angle resolved distributions in the symmetric configuration, concluding evidence was found that torsional damage to the stainless steel flex cable had occurred [Appendix D].

Recommended Addition Action: The stainless steel flex cable was replaced and tested. However, the flex cable is occasionally susceptible to damage due to the excessive torsional torque of the steppermotor. In order to prohibit further damage, software could be included to stop the RD. LabVIEW software has already been used to record each change in position of the steppermotor in the file "RDangle.txt". The locations of the support posts could be included in the software or a separate triggering switch within the chamber could be arranged to stop the steppermotor when contact is made with a post.

3.2.(b) Counting Statistics

Problem: The overall random error in the existing apparatus has been large enough to be a significant problem. This problem can be ameliorated by taking more counts at each energy bias of the RD. This modification improves the signal-to-noise ratio by taking higher counts for each RD energy bias setting.

Action taken: LabVIEW has been installed as the instrumentation and data acquisition software to replace the troublesome LabTech Notebook software [6-18-99, 18w, 42y]. A new data acquisition card (Iotech DAQboard2000) has been installed, with a higher resolution (16-bit) and a higher data through-put rate (200 kHz per channel nominal acquisition speed). In addition, a newly installed GPIB card (PCI-GPIB 4000) has enabled computer control and automation of the RD biasing voltage via LabVIEW [5-24-00 17w, 43w]. The electrical control schematic is shown in Fig. 3-5. A custom written LabVIEW VI program [Fig. 3-9] is the central processor of the data acquisition. The color-coded MonitorPressure.vi program measures four incoming signals from the LittleBoy chamber apparatus. Several LabVIEW programs have been written for the many purposes needed to measure and diagnose the LittleBoy chamber, which are summarized in Appendix C. The VI program controls the DAQboard2000 data sampler, the RD voltage

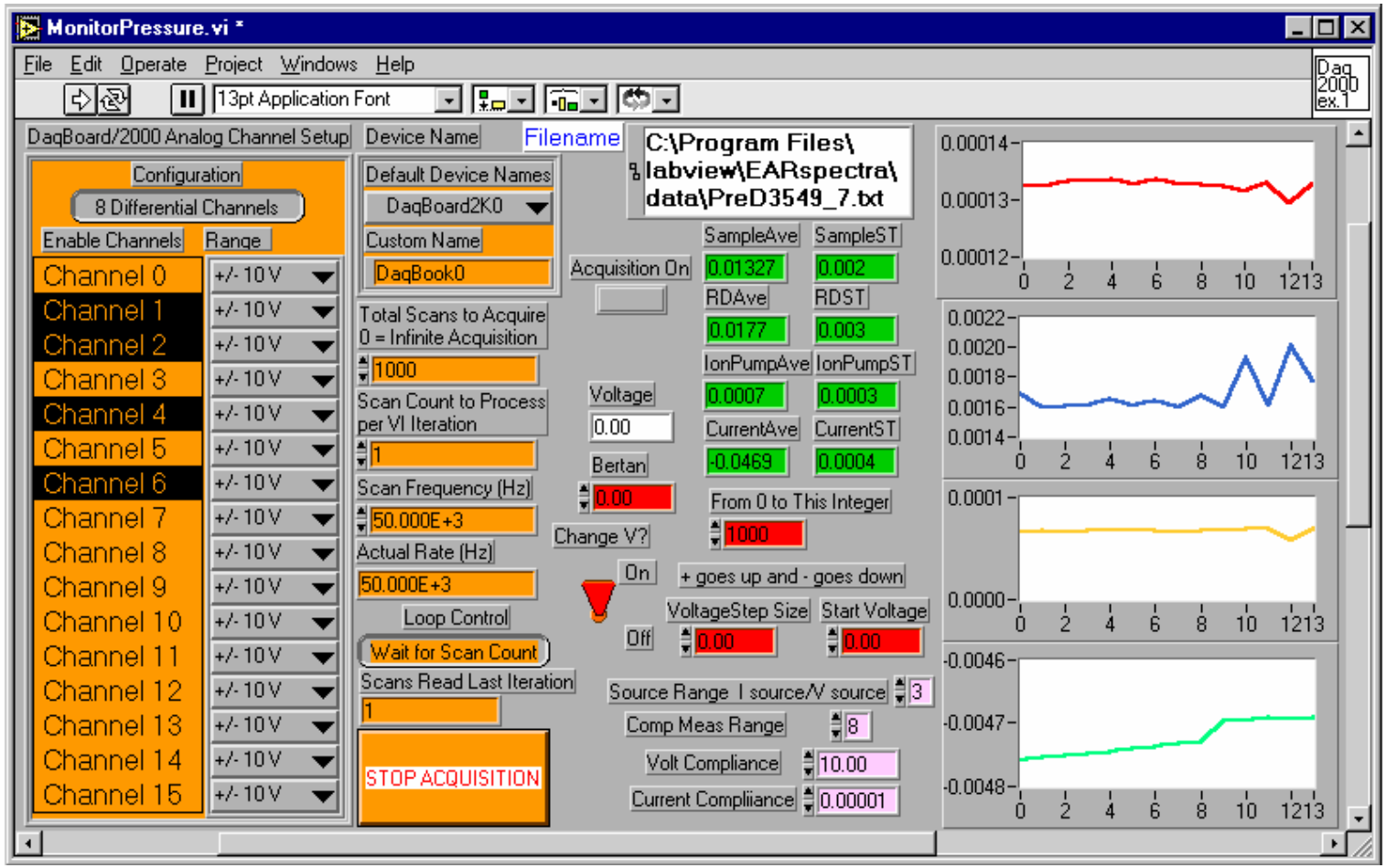

Figure 3- 9 LabVIEW VI program front panel used to monitor signals coming from the LittleBoy UHV chamber.

bias regulator via GPIB, and the RD rotational stepper motor controller [Appendix B]. Many of the VI programs also collect, average, and store the spectral data.

Evaluation: The implementation of LabVIEW via the DAQBoard2000 data acquisition card has increased the data collection using parallel data acquisition from 100 Hz (LabTech Notebook) to 66 kHz (DAQboard2000), which is an improvement of 660 times.

Recommended Additional Action: No further steps are required.

3.2.(c) Electron Beam Voltage Supply

Problem: A double peak was observed in the elastic portion of spectra with two peaks differing in energy by about 7 eV [Fig. 3-10]. The electron beam voltage supply within the electron gun controller was the suspected source of the AC ripple, which caused the double elastic peak.

Action Taken: The voltage supply within the electron gun controller has been replaced with a new voltage supply (Hewlett Packard 6516A). The replacement of the current regulating OP-AMP (OP177FP-Newark) [LB 47y, 6-22-00] along with the addition of a Zener diode [LB 46y, 6-18-00] in the stabilization circuit have increased the energy range of the electron beam to 100 – 2500 Volts. See Appendix A for specific details.

Evaluation: The voltage supply is stable with a ~10 mV ripple, but new data reveals the remaining double elastic peak [Fig. 3-11] with just a slightly better shape. The replaced electron beam voltage supply is not the cause of the double elastic peak.

Recommended Additional Action: The insertion of an automated voltage probe directly before the anode will assess the severity of the remaining AC voltage ripple. The voltage probe may also point to the cause of the remaining AC voltage ripple and will be installed before any further major chamber modifications.

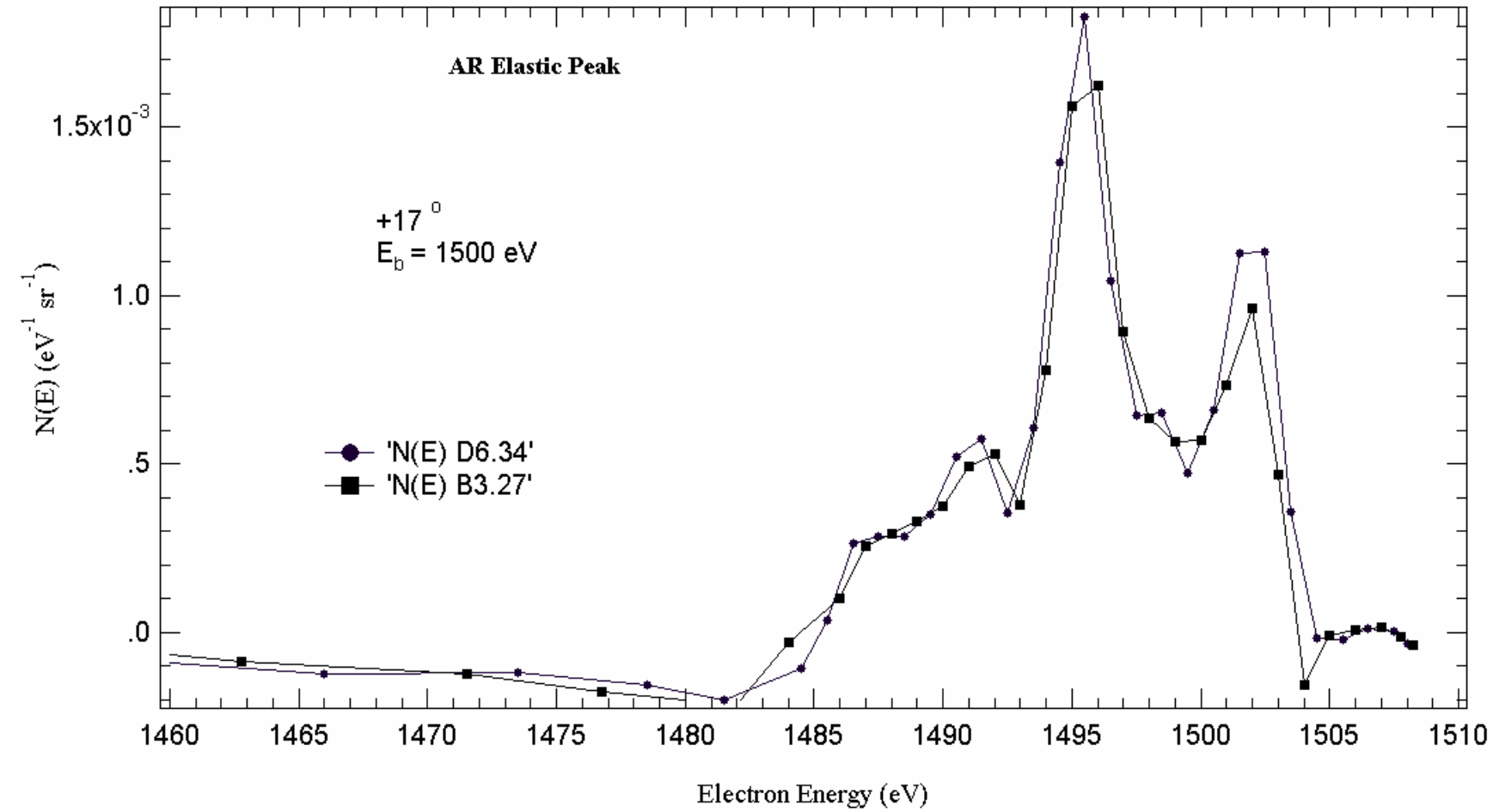

Figure 3- 10 Elastic peaks showing the double peak for surfaces D6 and B3.

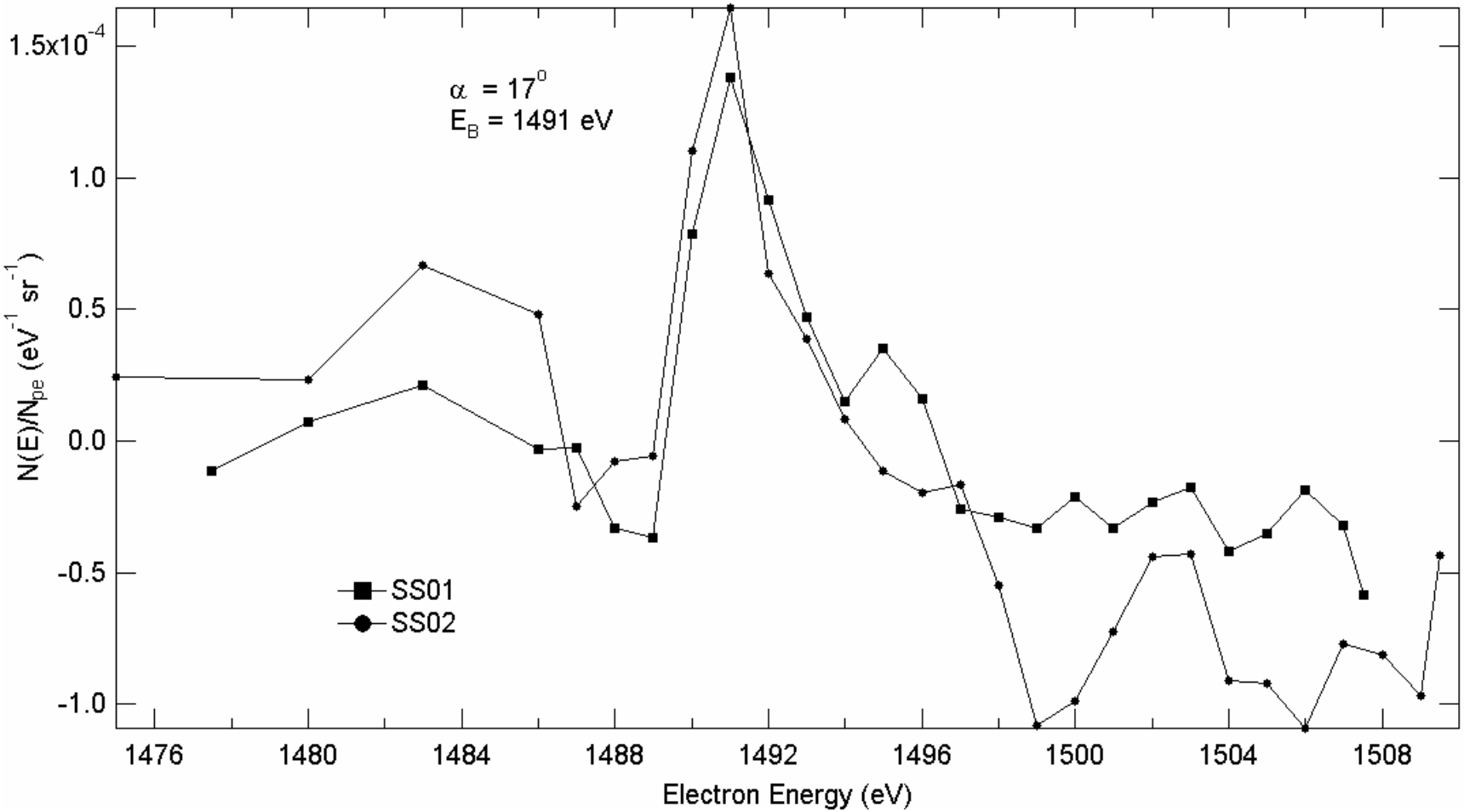

Figure 3- 11 Elastic peaks from Stainless Steel 316 showing double peak.

3.2.(d) Electron Beam Current Stability and Monitoring

Problem: The double elastic peak still existed along with a higher than desired beam current which could cause surface contamination via electron simulated adsorption [*Chang, 1999*].

Action Taken: An automated beam current ammeter [7-22-99] has been installed within the electron gun controller. See Appendix A for specific details. A new focusing extractor [6-14-00] has also been installed within the gun controller to more precisely control the beam current density.

Evaluation: The beam current monitor is in working condition and is automatically sampled by the DAQboard2000 [Fig. 3-5]. Since the output from beam current monitor is a voltage in the range 0 - 2 volts, 40nA minimum, no additional electrical conversion is needed. The DAQboard2000 now directly samples and monitors the electron beam controller's voltage, $V_{controller}$. The range of the $V_{controller}$ can be calibrated to the beam current, I_b, by direct measurement of the sample current, I_{sample}, via a grounded Faraday Cup.

A relationship exists between $V_{controller}$ and the beam voltage, E_b, the electron gun's deflectors, extractor, and focus controls. These relations exist because a portion of source electrons collide with one anode or another and return to ground through the analog meter. Therefore, the deflectors, extractor, and focus are only used prior to the beam current calibration and after a new beam energy setting. During one full spectral measurement, the E_b control remains constant. Since the $V_{controller}$ calibration involves aiming the electron beam into the Faraday Cup, relocation of the beam on the sample is accomplished by moving the sample (with the chamber apparatus) via micrometer adjustments on the top feedthrough. The data and analysis for the dependency of $V_{controller}$ on E_b is compiled in section 3.4 and used to optimize timing and determine error for absolute spectral measurement.

The beam current density is now controllable with the newly installed beam extractor to progressively decrease surface contamination effects. The Zener diode addition [Fig. A-5, CR10] has also lowered and stabilized the beam current. The beam current monitor, $V_{controller}$, [Fig 3-12, black] seems to

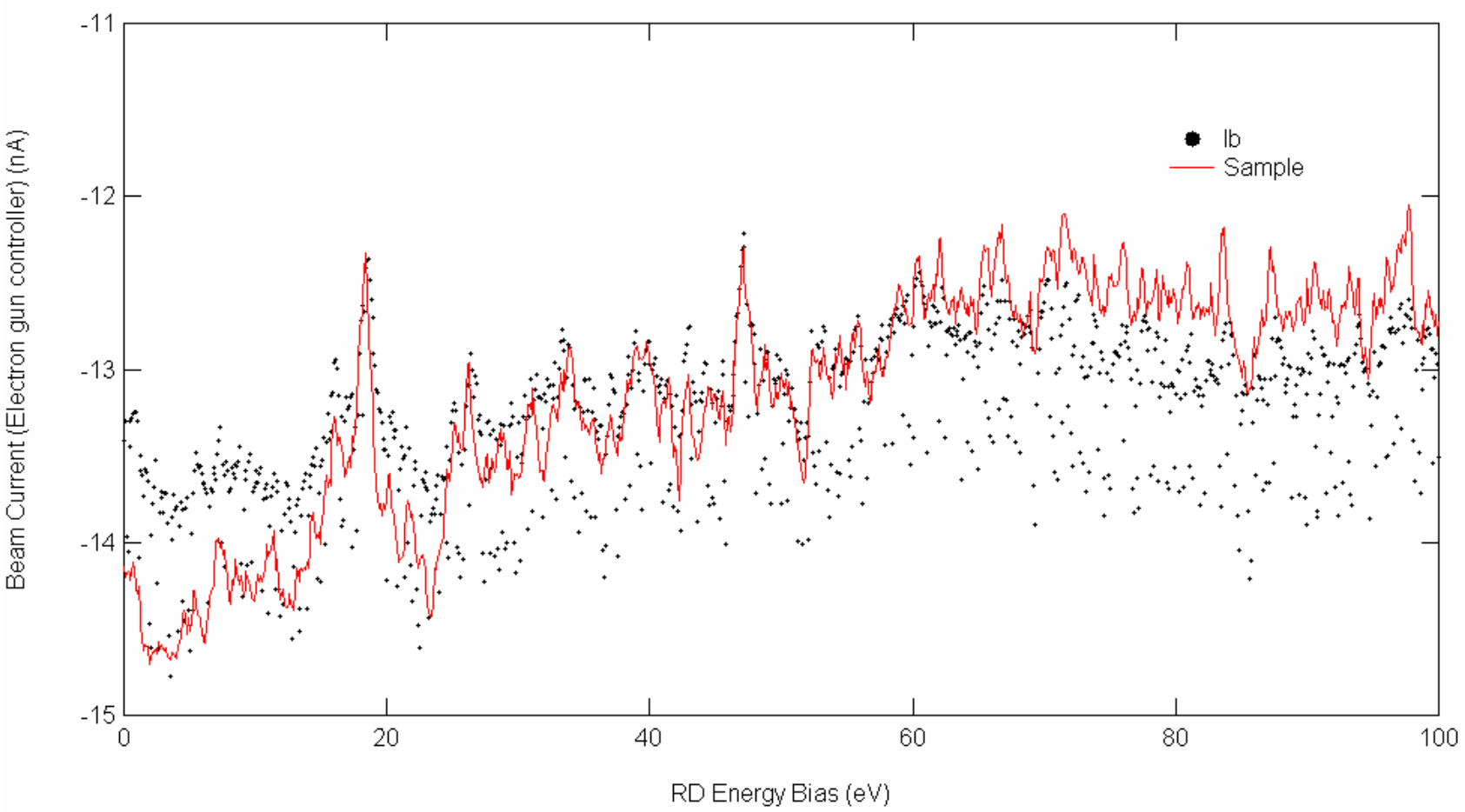

Figure 3- 12 The beam current monitor showing an unknown source of noise. Sample data are given for shape comparison.

show a source of unknown noise. This ambiguous noise does not affect any spectral result because averages of $V_{controller}$ over the duration of the experiment are used to calculate absolute yields (3.4.(c)).

Recommended Additional Action: Electrical relocation of the beam current monitor [Fig. A-6] inside the electron gun controller [Fig. 3-5] to float at the voltage of the electron beam, E_b, may alleviate the source of noise in the beam current monitor. It is common practice to measure beam profiles with the Faraday Cup by monitoring the current and the position of the beam at incremental distances from the Faraday Cup. Beam profiles should be taken to measure the beam density and the beam spot size after the relocation of the current monitor to determine any dependencies on E_b.

3.2.(e) Voltage Biasing of Rotatable Detector

Problem: In an effort to correct the double elastic peak problem, a thorough review has been conducted of the electronics for the RD high voltage bias scheme and the electron gun power supply. Modifications to the electron gun power supply were made first and are described in sections 3.2.(c) and 3.2.(d) on voltage and current monitoring and stability. In the RD high voltage bias scheme [Fig. 3-13] used by Davies [*Davies, 1999*], a precision GPIB-controlled 1.1 kV power supply (Keithley 237) was used to control a 5 kV high voltage power supply (Bertan 205A-05R) through the remote program input with x1000 amplification. This amplification has magnified an AC peak-to-peak ripple of about 20mV from the Keithley 237 resulting in a 20V ripple in the RD bias voltage. Comparison to the full width at half maximum (FWHM) of the elastic peak, 17 eV [Fig. 3-10 and Fig. 3-11], is quite good.

Action Taken: In order to more precisely control the RD bias voltage, a new biasing scheme was arranged. The Keithley 237 voltage supply is now used to directly float the Bertan voltage supply maintained at a constant voltage [Fig. 3-14]. Since the Bertan supply is no longer remotely controlled, it is set by hand to constant biases for acquiring spectral portions. These portions are then concatenated together to make a spectrum. The constant Bertan bias (increment) is determined by the choice of spectral portion via optimization the Keithley 237 bias (increment). The optimization is essentially an exchange of accuracy for precision and is controlled within the Keithley 237 computer. The Keithley 237 supply is a

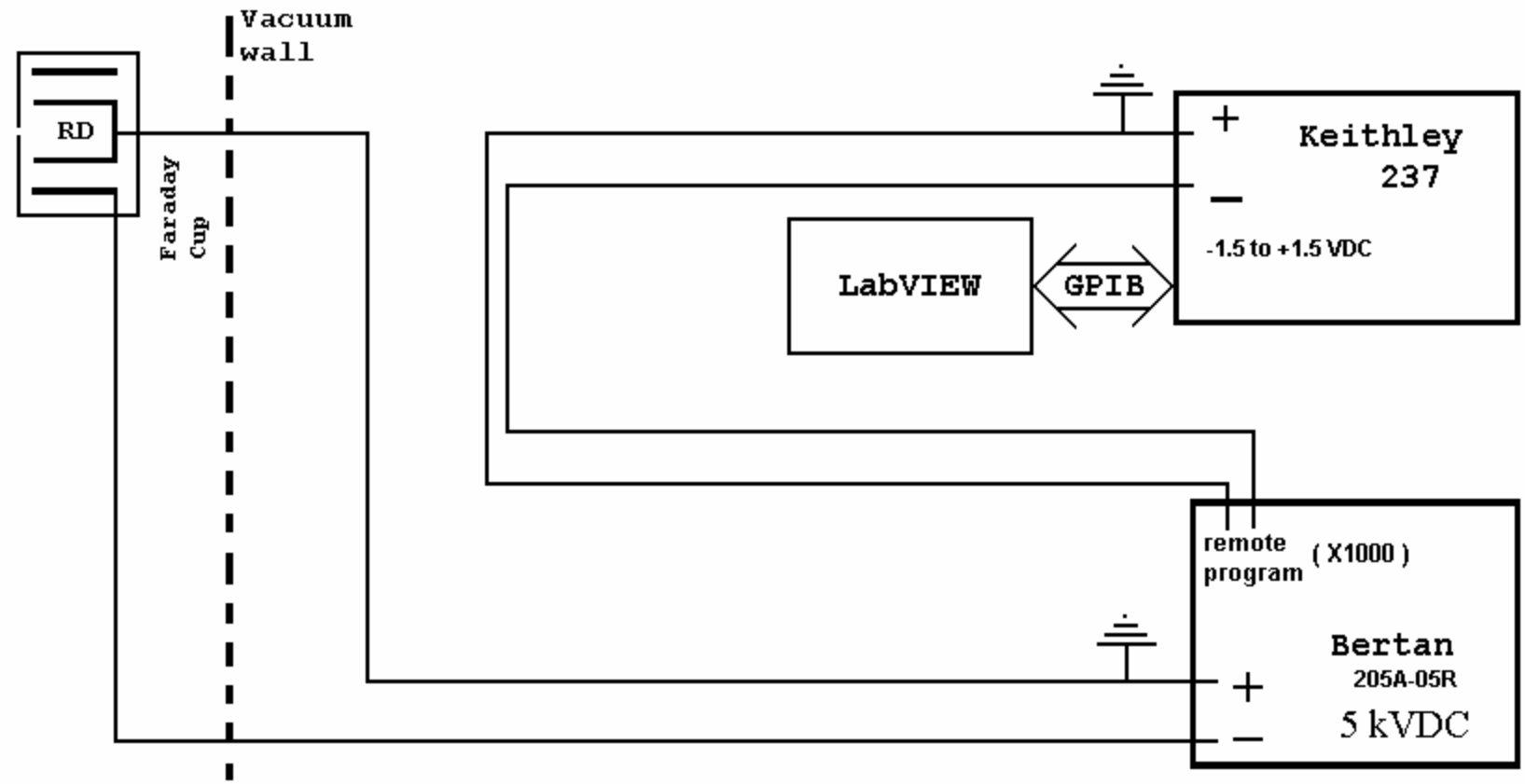

Figure 3- 13 Previous configuration of the RD biasing scheme using the remote program.

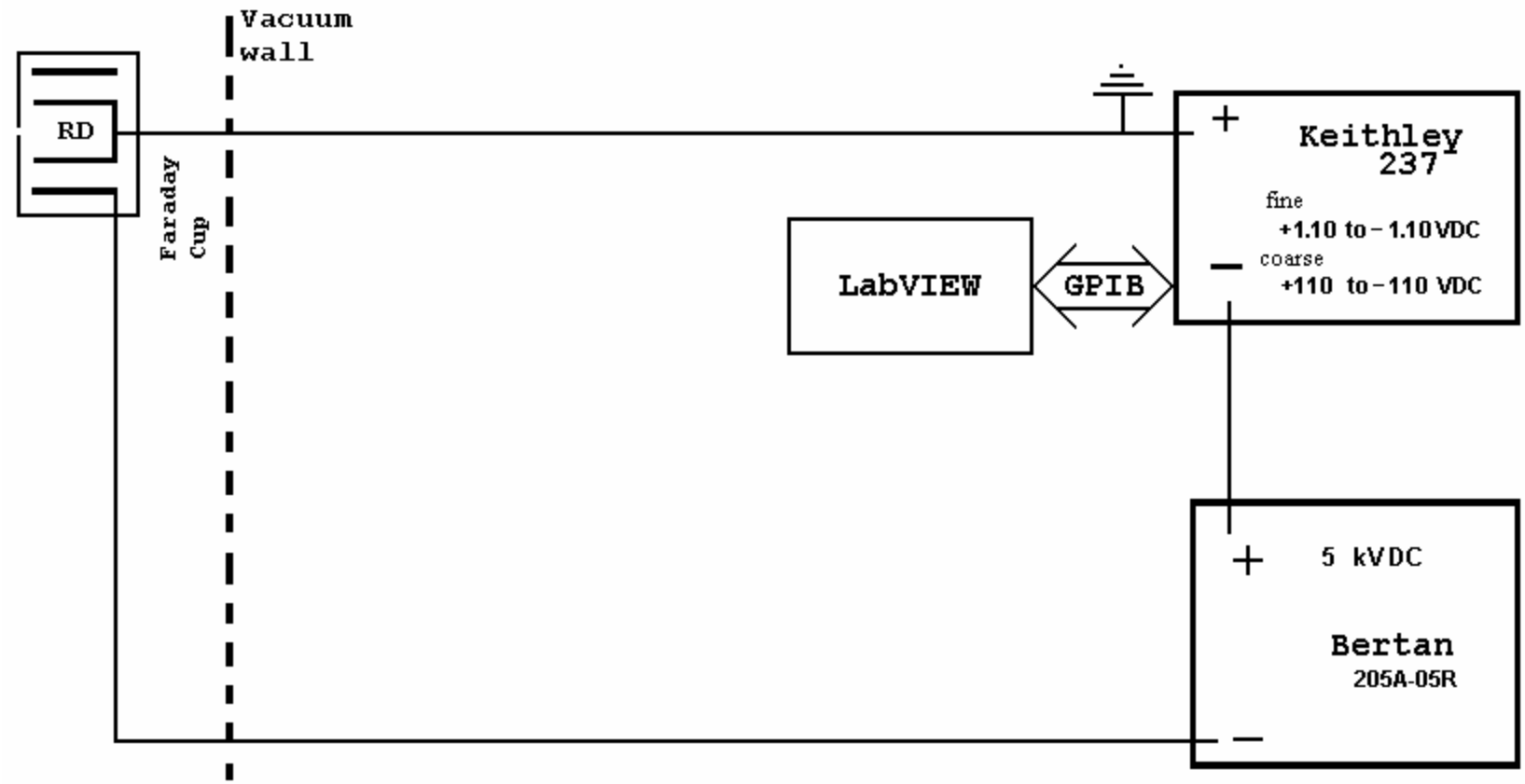

Figure 3- 14 RD biasing scheme of voltage supplies connected in series.

self-complying current monitor in source voltage output configuration. The current compliance setting regulates the output voltage for an optimum voltage precision. See Table C-1 for compliance setting details. Each different voltage precision has a specific operating voltage range. The three voltage range configurations for the Keithley 237 supply (±110 V, ±11 V, and ±1.1 V) correspond to coarse, fine, and extra-fine energy precisions. For each of the energy precisions, the Bertan supply is set at intervals of 200 V (e.g. E_bV, E_b-200 V, E_b-400 V, …, 0 V) for coarse 10 V step spectra, at intervals of 20 V (e.g. E_b-8 V and +8 V) for fine 1 V step spectra, and at intervals of 2.0 V (e.g. E_b V and 0 V) for extra-fine 0.1 V step spectra. For future reference, the accuracy in the RD bias, E_e, is taken from the Keithley 237 manual to be 0.033% + 0.024 V for 110 V range, 0.033% + 0.0024 V for 11 V range, and 0.033% + 0.00065 V for 1.1 V range. When including the accuracy of the Bertan supply, 0.005 V, the RD bias accuracies become 0.033% + 0.029 V for ±110 V range, 0.033% + 0.0074 V for ±11 V range, and 0.033% + 0.00565 V for ±1.1 V range. This leads to a standard deviation in the RD bias, ΔE_e, which is different for each Keithley 237 compliance setting. Hence an optimum compliance setting can be chosen for each spectral portion.

Evaluation: The infamous double peak is absent [Fig. 3-15] and no longer a problem. The nominal FWHM of the elastic peak is approximately 1 eV. Comparing to measured spectra utilizing the previous RD biasing scheme, a marked improvement of the FWHM by a factor of ~17 times is now achievable [refer to Fig. 3-10 and Fig. 3-11].

Using the symmetric RD angle configuration [Fig. 3-8], the elastic peak spectra for 5 different angles in both Clockwise (C) and Counter-Clockwise (CC) directions have been measured using the finest 0.01 eV resolution [Fig. 3-16 and Fig. 3-17] at 1.5 keV incident beam energy. Since the elastic peak has customarily been used to experimentally measure the energy resolution of the chamber apparatus, a more detailed analysis of the elastic peak shape and instrumental resolution follows.

The Doniach and Sunjic [*Doniach and Sunjic, 1970*] model (Eq. 2.16) is used to fit the elastic peak. The magnification parameter, *M*, gauges the amount of Gaussian and Lorentzian contributions to the elastic peak. The gaussian contribution amounts to the thermal characteristics of the electron gun filament

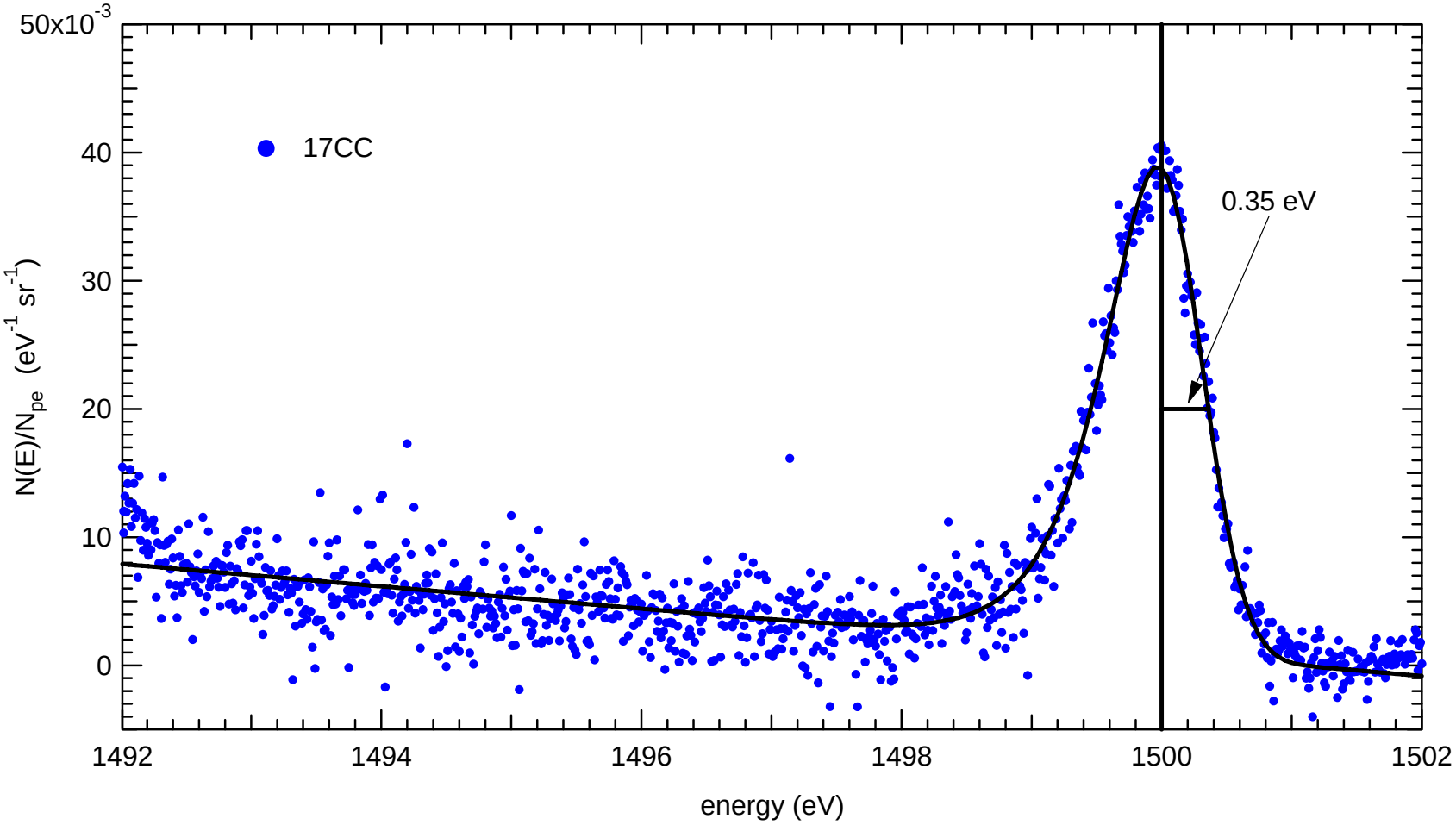

Figure 3- 15 Elastic Peak for 1500 eV incident beam energy at 17° Counter-Clockwise emission.

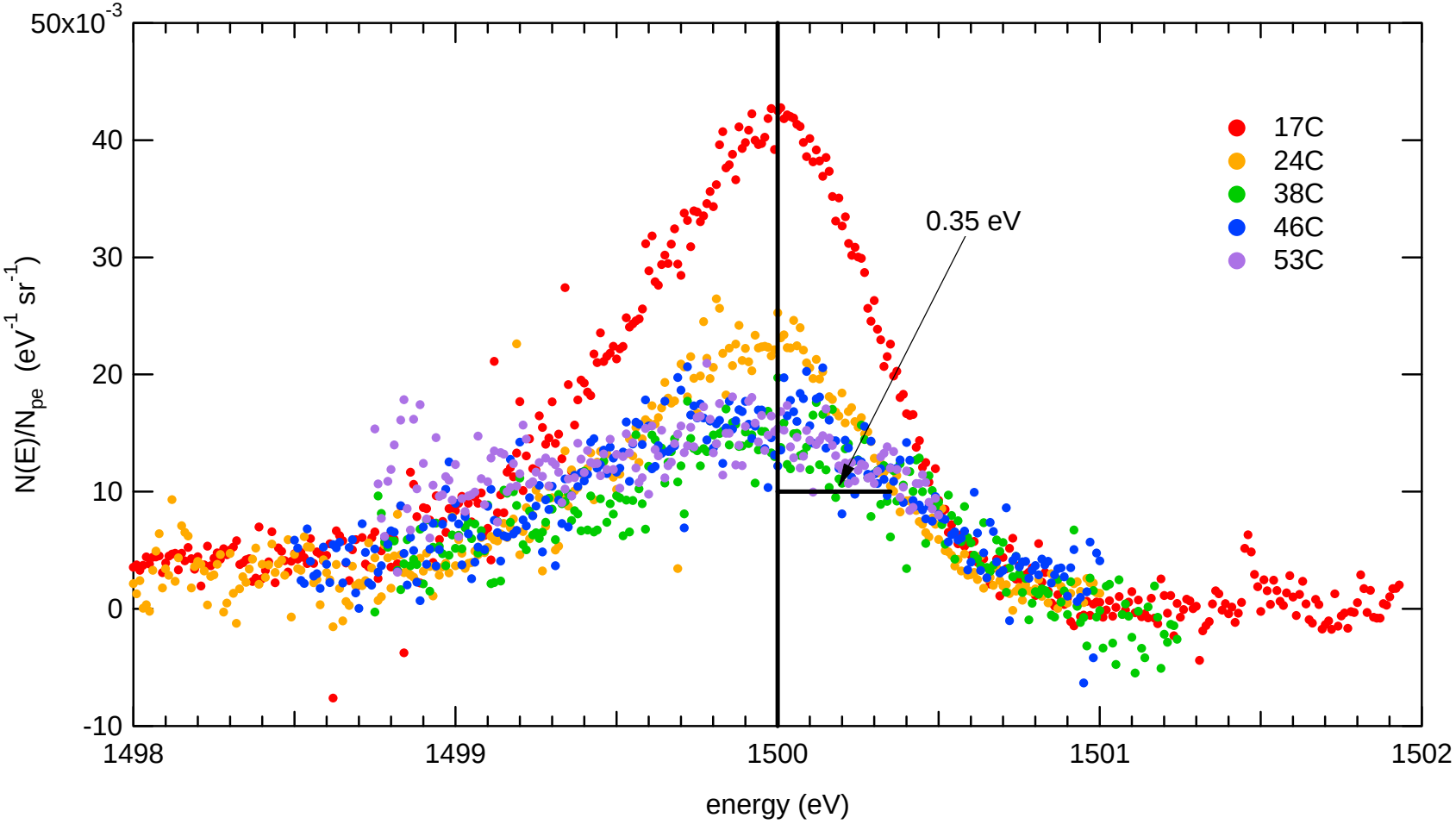

Figure 3- 16 Elastic Peak for 1500 eV Beam Energy with Clockwise emission.

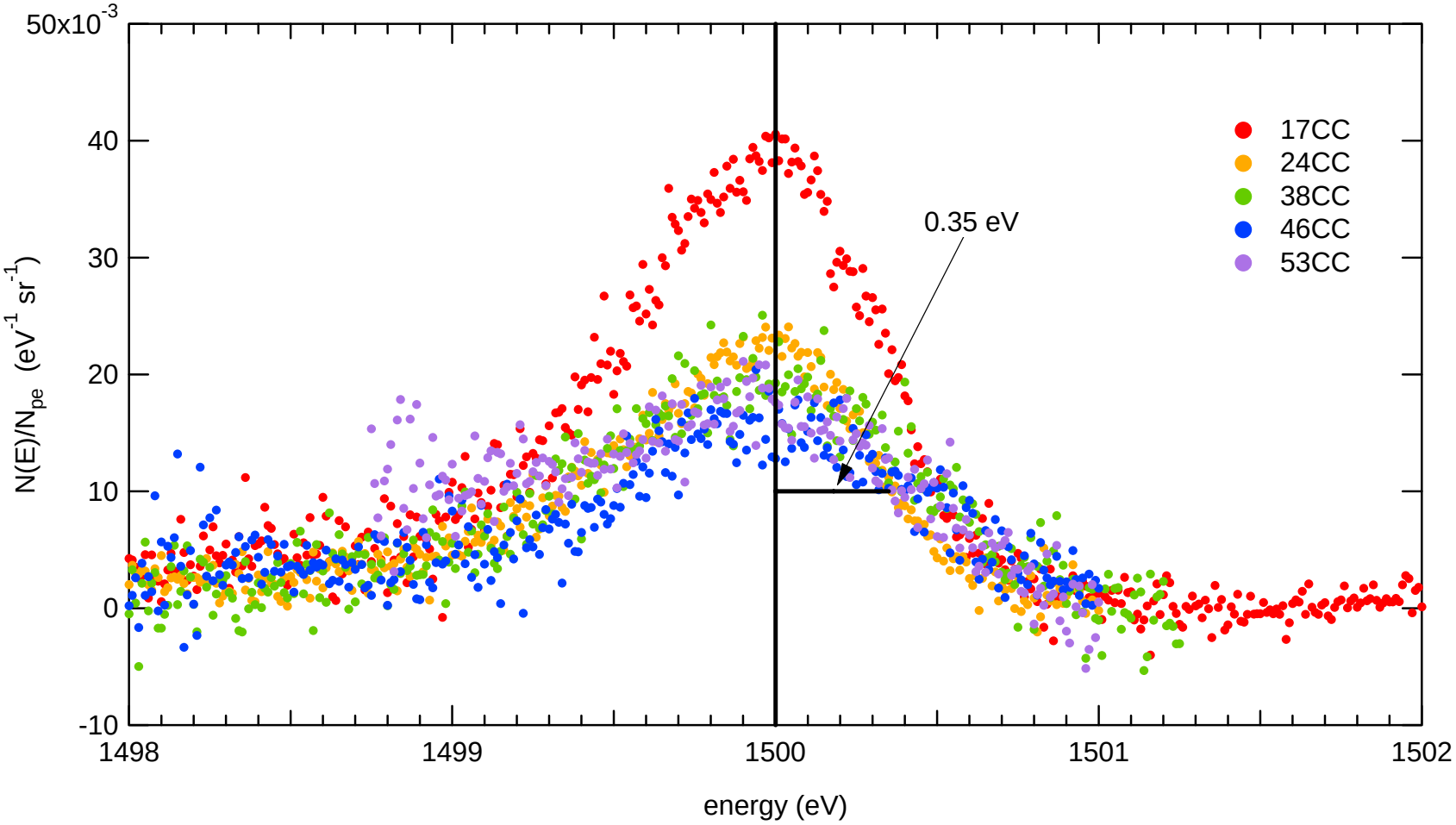

Figure 3- 17 Elastic Peak for 1500 eV Beam Energy with Counter-Clockwise emission.

and the Lorentzian contribution accounts for fractional energy exchange occurring within 1 eV of the elastic peak. The fitting parameters for the ten elastic peak spectra, measured at 1.5 keV, are listed [Table 3.1]. The magnification, gaussian, and Lorentzian parameters are plotted against emission angle [Fig. 3-18] for further analysis. The linear fit to parameter α shows no angular dependence exists. A qualitative comparison of linear and parabolic fits to parameter β shows there is a possible angular dependence not previously confirmed.

Table 3.1 Doniach and Sunjic Fitting Parameters for the 1.5 keV elastic peak spectra measured using the 0.01 V RD biasing resolution in the symmetrical configuration providing angular emissions of 17°, 24°, 38°, 46°, and 53°. Clockwise (C) and Counter-Clockwise (CC) are seen from the top of the LittleBoy chamber. The averages and standard deviation are also included.

angle	A(eV^{-1}*sr^{-1})	M	β	α	E_{PE} (eV)	BG(eV^{-1}*sr^{-1})	BG_{slope}(sr^{-1})
53CC	0.019	1.05	0.85	-0.53	1499.99	0.28	-0.0002
46CC	0.013	0	0.47	-0.06	1499.99	0.28	-0.0002
38CC	0.031	1.28	0.84	-0.17	1499.98	0.29	-0.0002
24CC	0.021	0.37	0.44	-0.19	1499.98	0.28	-0.0002
17CC	0.037	0.24	0.45	-0.13	1499.97	1.33	-0.0009
17C	0.039	0.16	0.43	-0.16	1499.99	1.33	-0.0009
24C	0.021	0.28	0.44	-0.1	1499.95	1.32	-0.0009
38C	0.020	0.96	0.85	-0.26	1500	0.29	-0.0002
46C	0.035	1.74	1.16	-0.23	1499.92	0.28	-0.0002
53C	0.006	0.7	0.34	-0.16	1499.91	0.28	-0.0002
average	0.024	0.68	0.63	-0.2	1499.97	0.59	-0.0004
stdev	0.01	0.57	0.27	0.1	0.03	0.5	0.0003

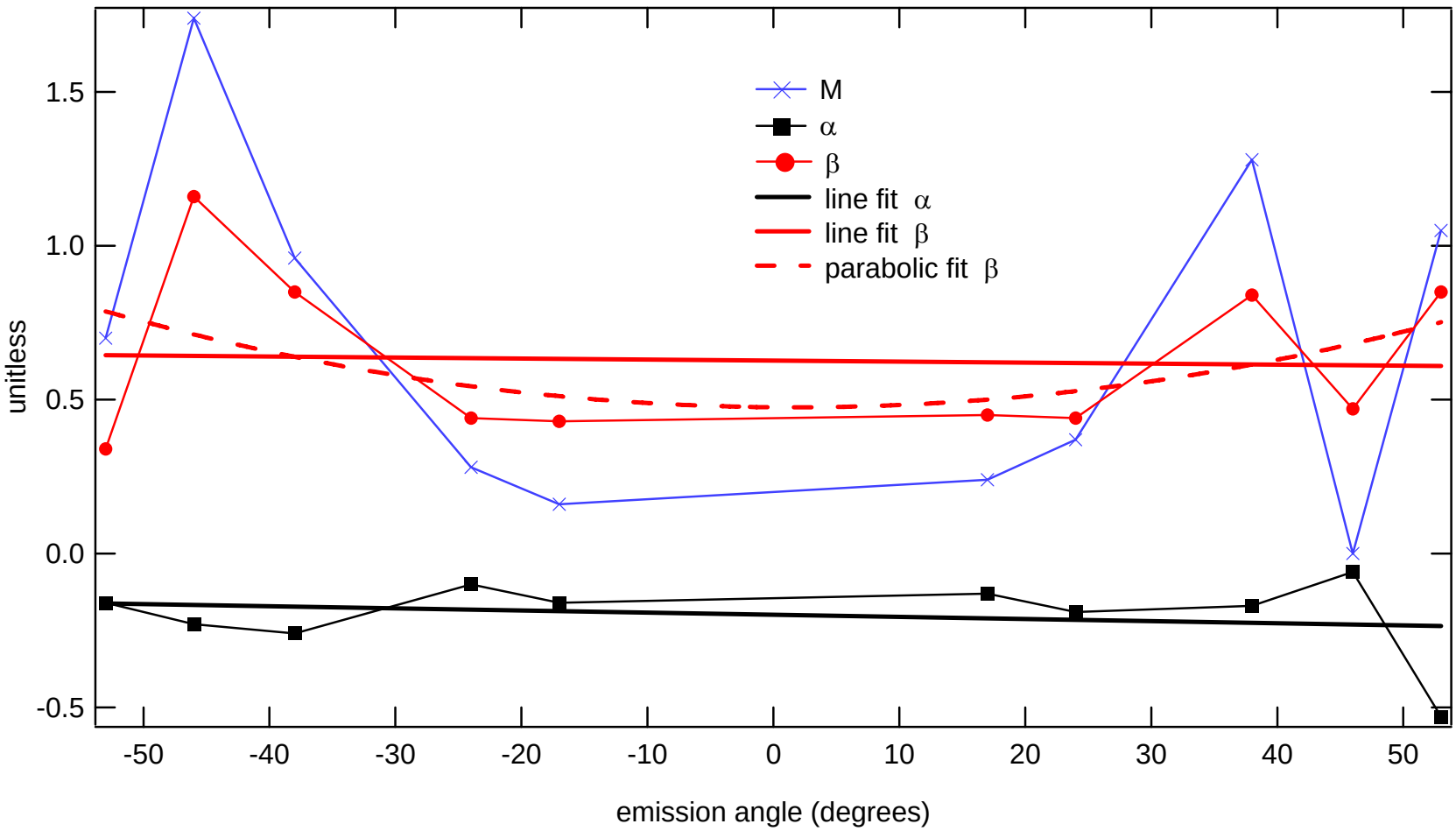

Figure 3- 18 Doniach and Sunjic fitting parameters M (magnification), β (Lorentizian), and α (gaussian) for 1.5 keV elastic peak fit with linear and parabolic trends.

There is no clear angular dependence on the gaussian parameter, but there is qualitative evidence that the Lorentzian parameters β and M may depend on emission angle [Fig. 3-18, β parabolic fit]. Comparisons of the half width at half maximum (HWHM = 0.35 eV) [Fig. 3-15, Fig. 3-16, and Fig. 3-17] to the nominal average Lorentzian HWHM ($\Gamma/2 = \beta/M^{0.5}/2 = 0.38 \pm 0.3$ eV) [Table 3-1] are within uncertainties.

There is an inherent width to the emitted electrons from the cathode tungsten filament in the electron gun. At higher currents the filament is reddish so photon energies are ~1 – 2 eV and thermionic emitted electrons peak at ~ 1 eV. At lower currents used in this study (10 to 50 nA), the filament temperature is much less, so that thermionic emitted electrons are on the order of 0.4 to 0.8 eV. Since the thermal kinetic energy is random, a spread in the emitted energies is observed by the gaussian characteristics of the elastic peak. The resolution of the RD must be less than this emitted energy spread. The energy resolution of the RD is determined both experimentally and theoretically. Based on the gaussian standard deviation analysis of these elastic peak data, the experimental energy resolution of the RD is less than 0.35 eV at 1500 eV. The theoretical energy resolution is determined by considering the pencil angle of the RD aperture and the distance between the first RD aperture and the sample [Fig. 3-2]. The estimated theoretical resolution of the RD is ~0.02% (0.0002 x 1500 eV = 0.3 eV) at the elastic peak energy [*Davies, 1999, p. 29, p. 199*].

Recommended Additional Action: To test for the dependence of the RD energy resolution on the electron beam energy, two other sets of elastic peak analysis should be made using beam energies greater and less than 1500 eV. In addition, Auger spectra can typically be resolved with retarding field hemispherical grids or electrostatic cylindrical mirror analyzers with ~20 eV energy resolution [*Tsutsumi, et. al., 2006*]. In these standard AES detectors, an AC biasing feedback scheme employing a lock-in amplifier is often used. Auger features have been detected without a lock-in amplifier and are addressed in Chapter 5. It may be necessary to use such a lock-in scheme concurrently with the new RD biasing scheme to probe Auger features with higher resolution.

3.2.(f) Ambient Field Distortions

Problem: The presence of ambient electric fields in the chamber apparatus caused distortions in the measured angle-resolved cross sections below the 10 - 15 eV range [*Davies, 1999, p. 170*]. The fields resulted from accumulated charge on insulating surfaces, particularly oxidized aluminum, which partially composes the chamber apparatus. The stray fields within the chamber apparatus can influence the trajectories of the lower energy emitted electrons.

Action Taken: To minimize these stray fields, colloidal micro-crystalline graphite (Aquadag^{TM}) has been used to coat most surfaces of the chamber apparatus. An Aquadag^{TM} coating was applied to the inside of the magnetic shield, to the sample holder and to the rotation apparatus [4-23-99, LB 7y]. This prevents dielectric surfaces such as oxidized aluminum from becoming charged and producing stray ambient fields. This modification is also beneficial in two other ways; the coating (1) makes the work function of almost all exposed surfaces approximately the same and (2) reduces the production of SE's from the chamber surfaces via BSE/chamber surface interactions since the SE and BSE yield of graphite is quite low [Farhang, 1993, ref. section 3.2.(g)].

Evaluation: In order to evaluate the extent to which the stray fields influence the measured angular distributions, a symmetry comparison is made between low energy SE emission spectra at Clockwise and Counter-Clockwise emission angles. Using the symmetric RD angle configuration [Fig. 3-8], the SE peak spectra for 5 different angles in both Clockwise (C) and Counter-Clockwise (CC) directions have been measured [Fig. 3-19 and Fig. 3-20] at 1.5 keV incident beam energy. The spectra are all peaked at approximately 3.5 eV. The critical emission energy below which the curves are inconsistent is determined by direct comparison [Figs. 3-21, 3-22, 3-23, 3-24, and 3-25]. Previous data [*Davies, 1999*] using the non-symmetric RD angle configuration [Fig. 3-3] is included for comparison.

Two plausible explanations should be made concerning the comparisons to previous data taken prior to the numerous improvements made to the LittleBoy apparatus. (1) Previous spectra were taken as a running average [*Davies, 1999*] while the RD was biased to increasing voltages. This sort of averaging tends to exaggerate past data values towards those in the step direction of RD voltage bias resulting in more

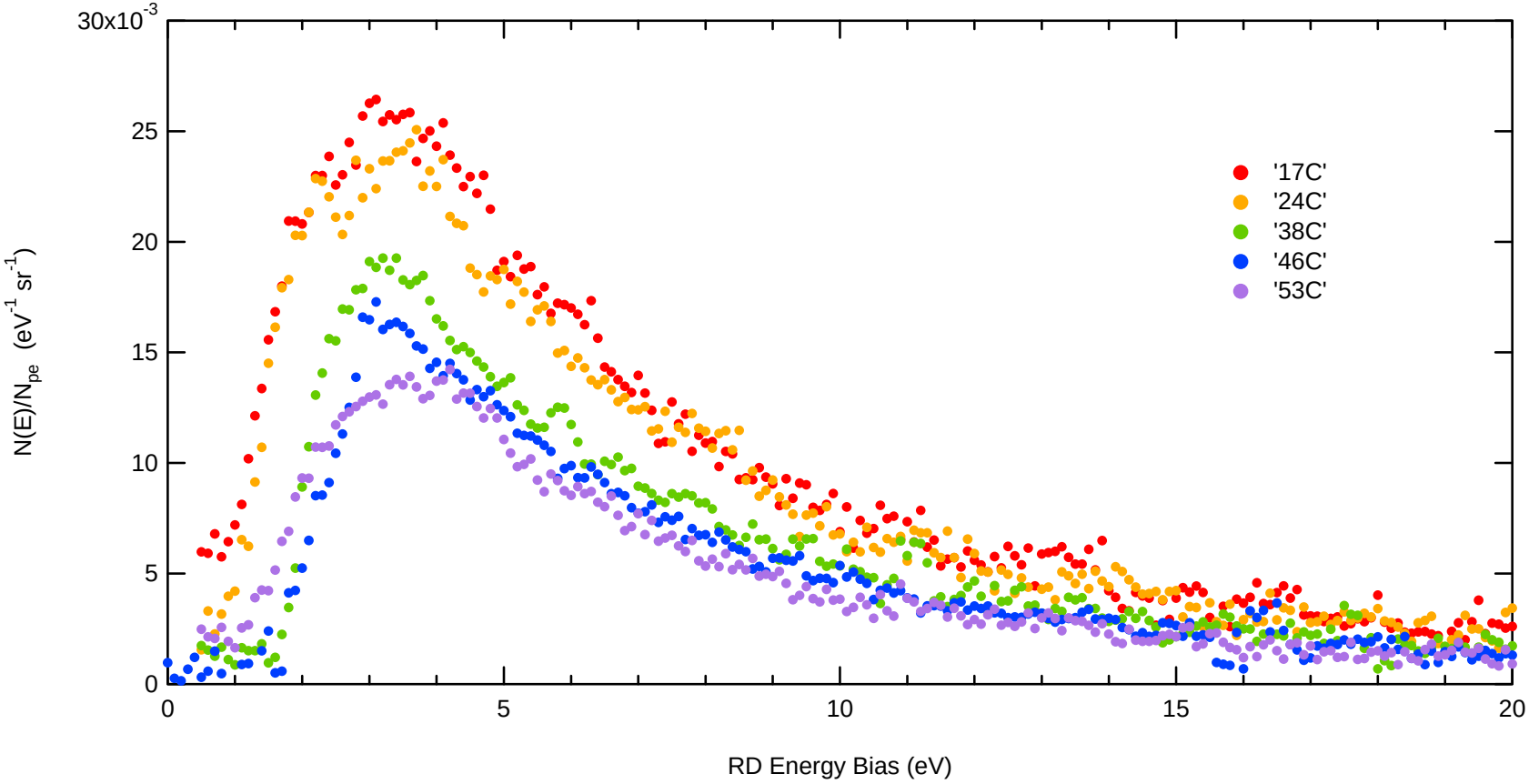

Figure 3- 19 SE spectra of polycrystalline Au at 1500 eV beam energy for clockwise emission.

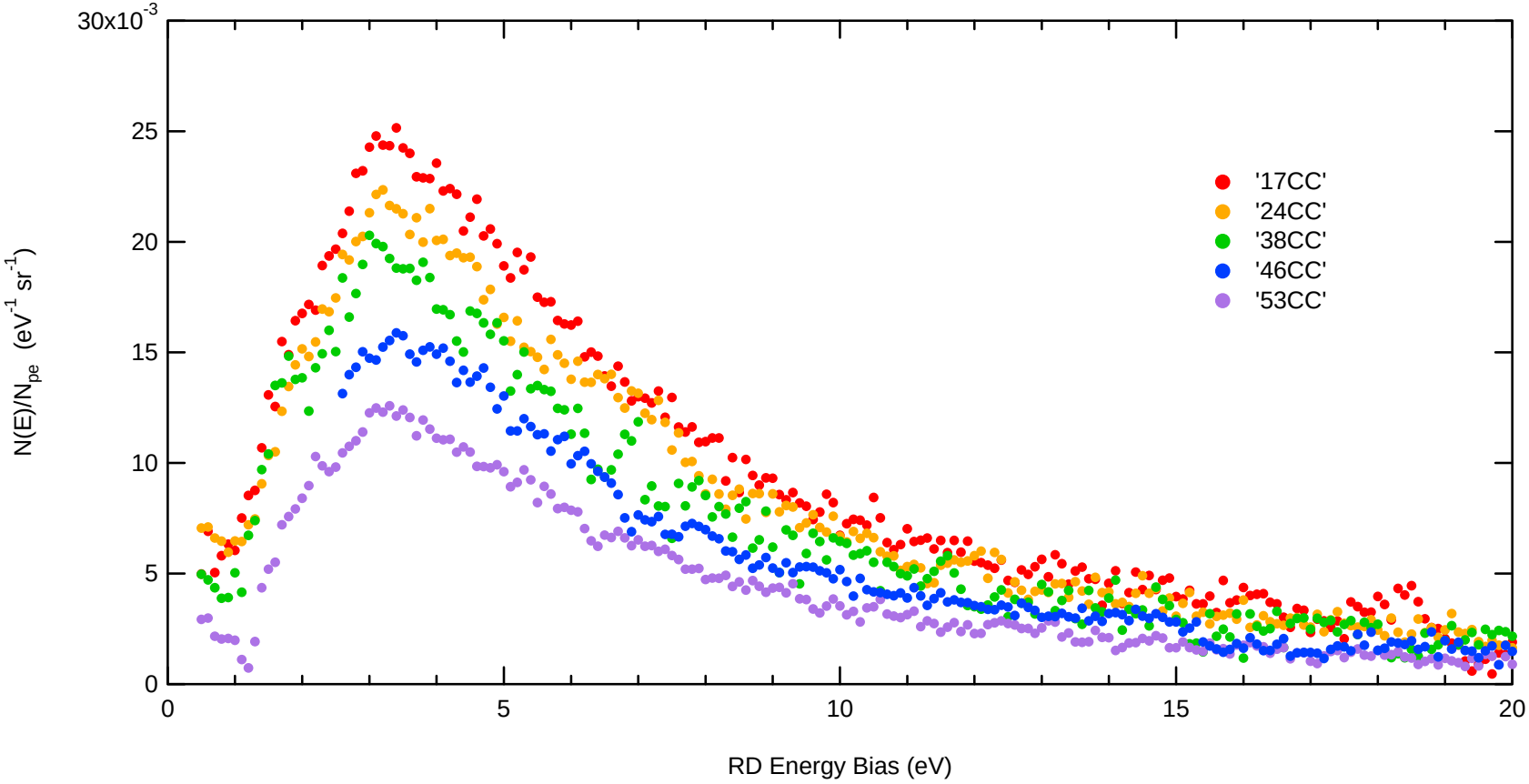

Figure 3- 20 SE spectra of polycrystalline Au at 1500 eV beam energy for counter-clockwise emission.

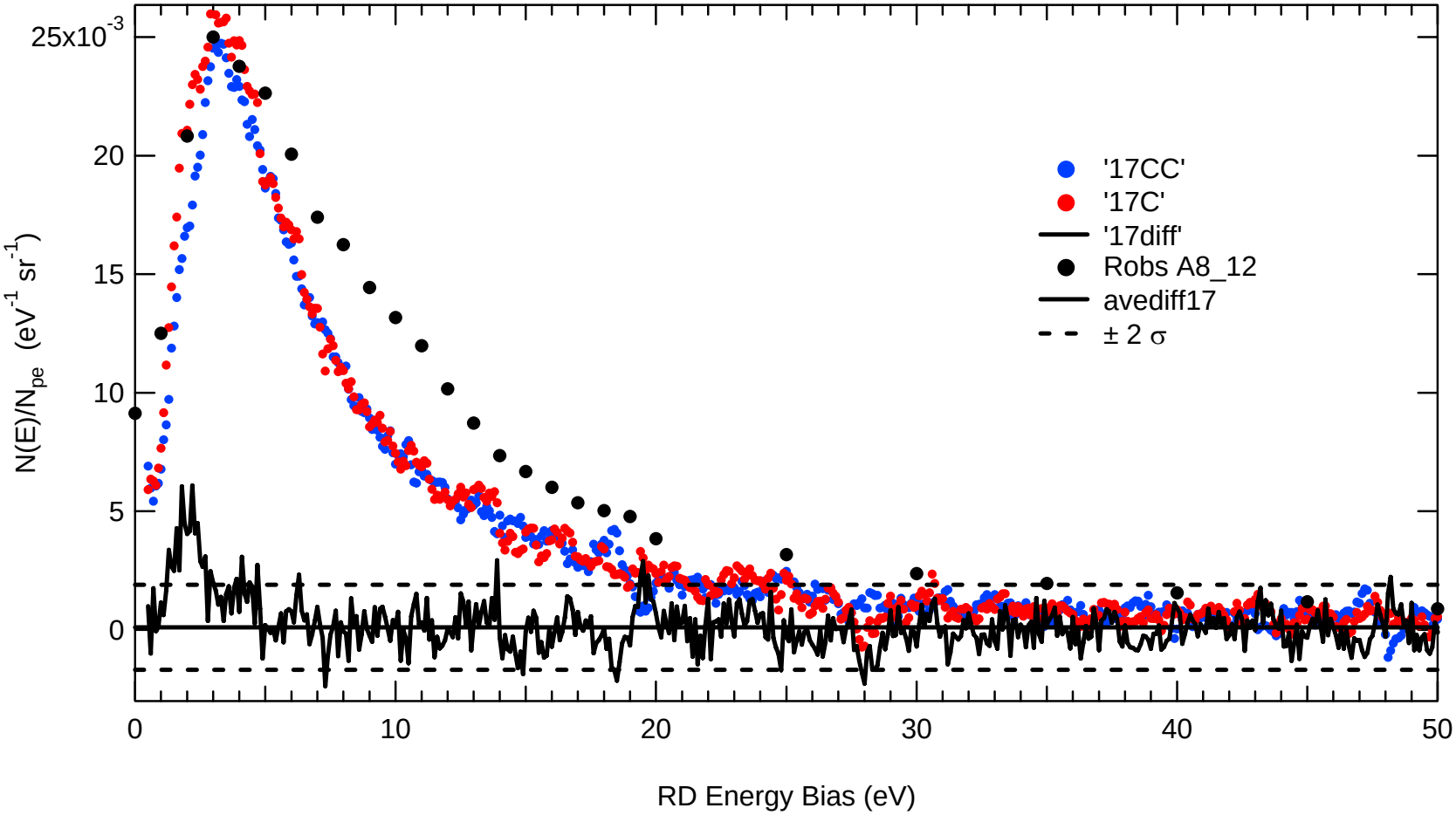

Figure 3- 21 SE Yield of polycrystalline Au at 17° emission for 1.5 keV incident beam energy with the difference shown in black. Davies data is shown in circles. The average of the difference in the two spectra is provided (solid black) along with 2X standard deviations above (dashed) and below (dashed) the average.

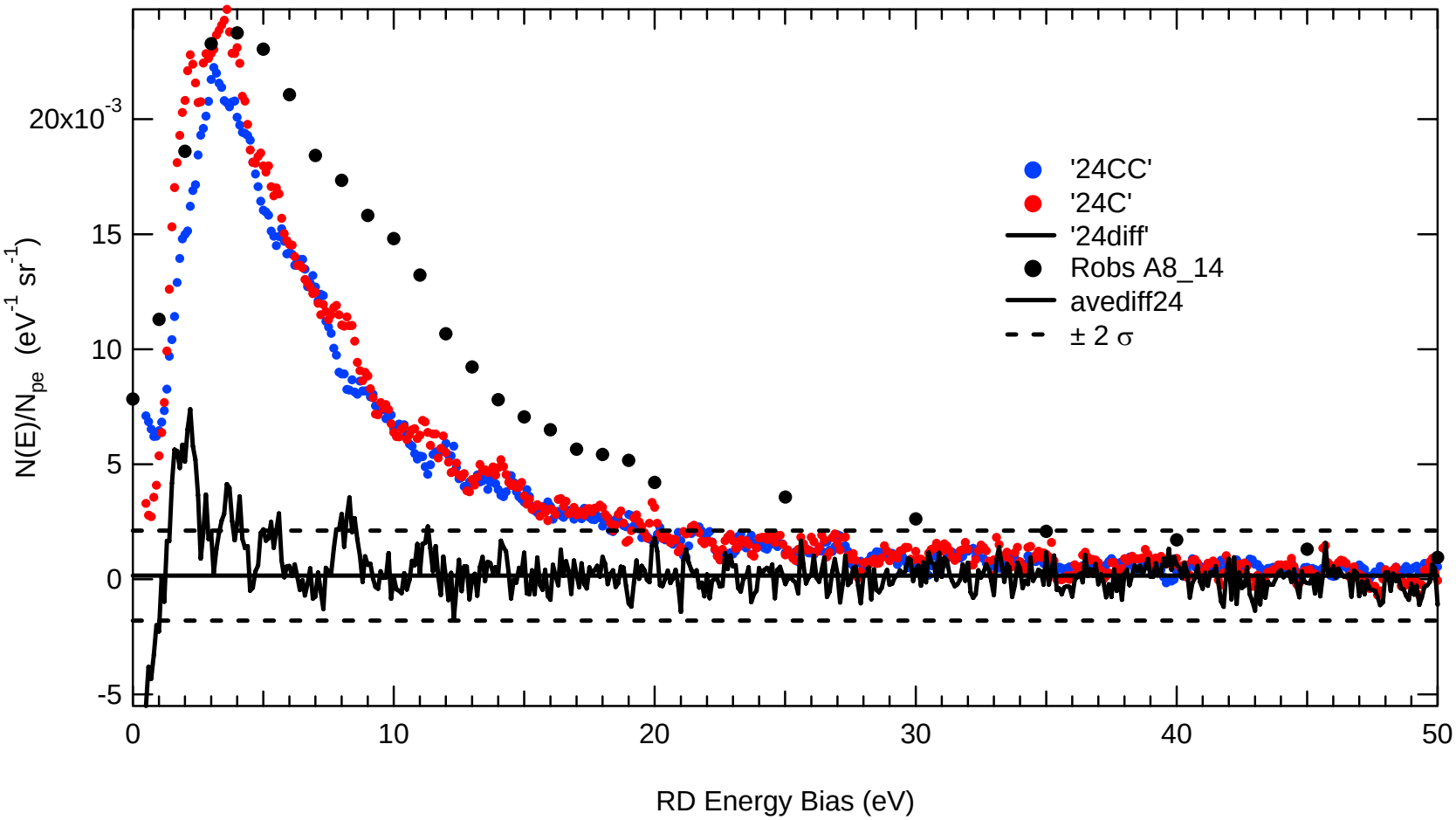

Figure 3- 22 SE Yield of polycrystalline Au at 24° emission for 1.5 keV incident beam energy with the difference shown in black. Davies data is shown in circles. The average of the difference in the two spectra is provided (solid black) along with 2X standard deviations above (dashed) and below (dashed) the average.

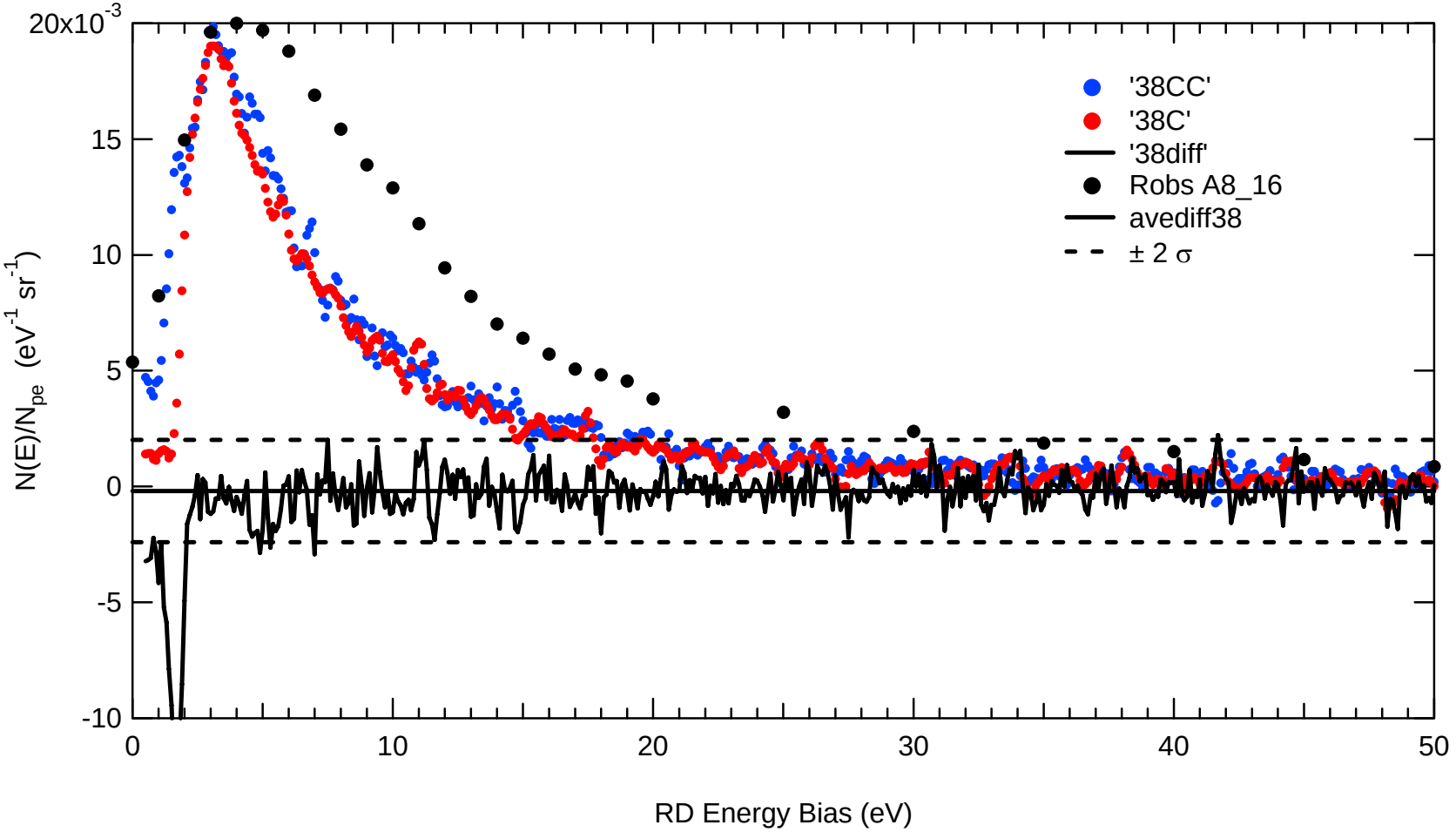

Figure 3- 23 SE Yield of polycrystalline Au at 38° emission for 1.5 keV incident beam energy with the difference shown in black. Davies data is shown in circles. The average of the difference in the two spectra is provided (solid black) along with 2X standard deviations above (dashed) and below (dashed) the average.

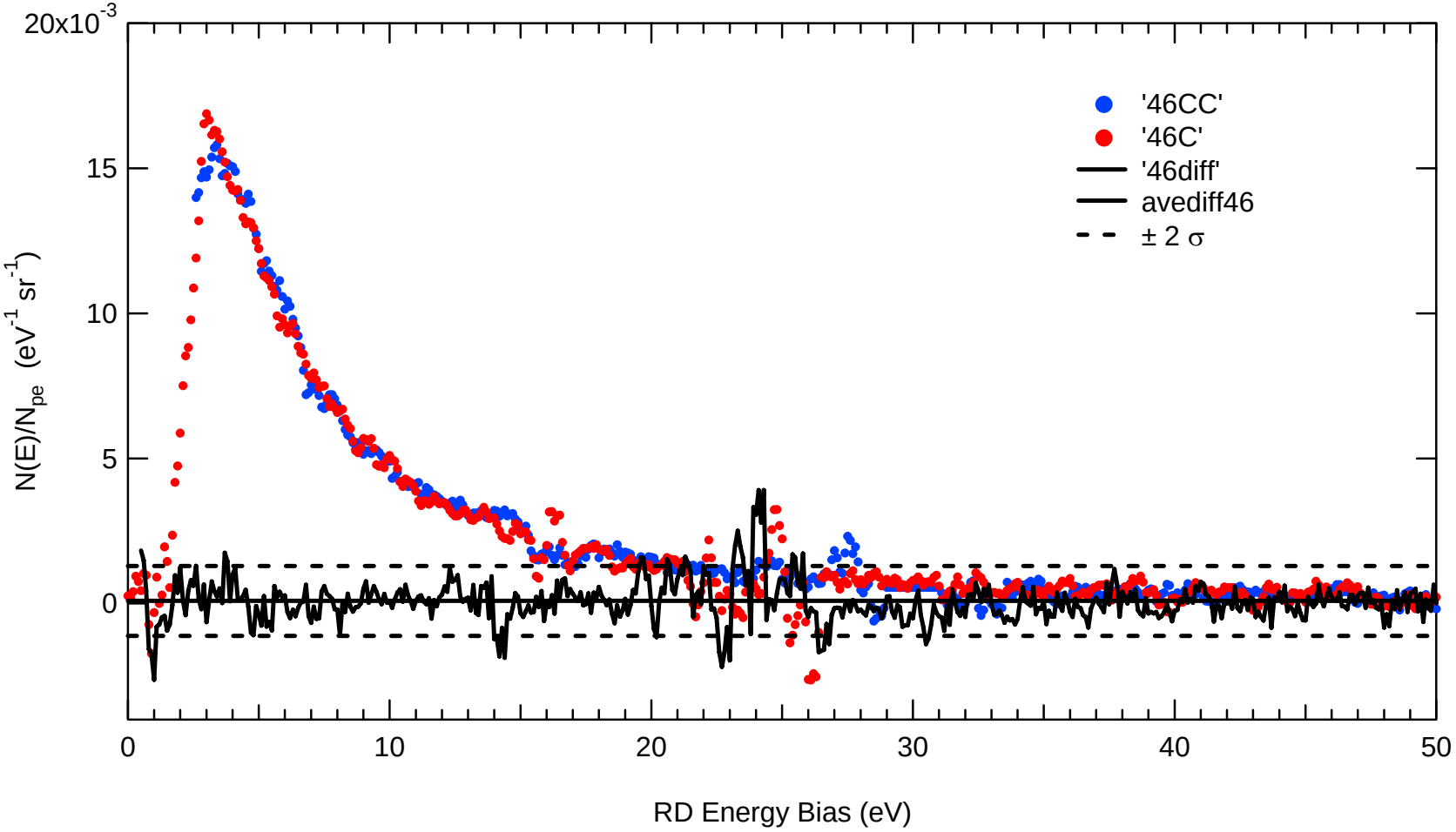

Figure 3- 24 SE Yield of polycrystalline Au at 46° emission for 1.5 keV incident beam energy with the difference shown in black. The average of the difference in the two spectra is provided (solid black) along with 2X standard deviations above (dashed) and below (dashed) the average.

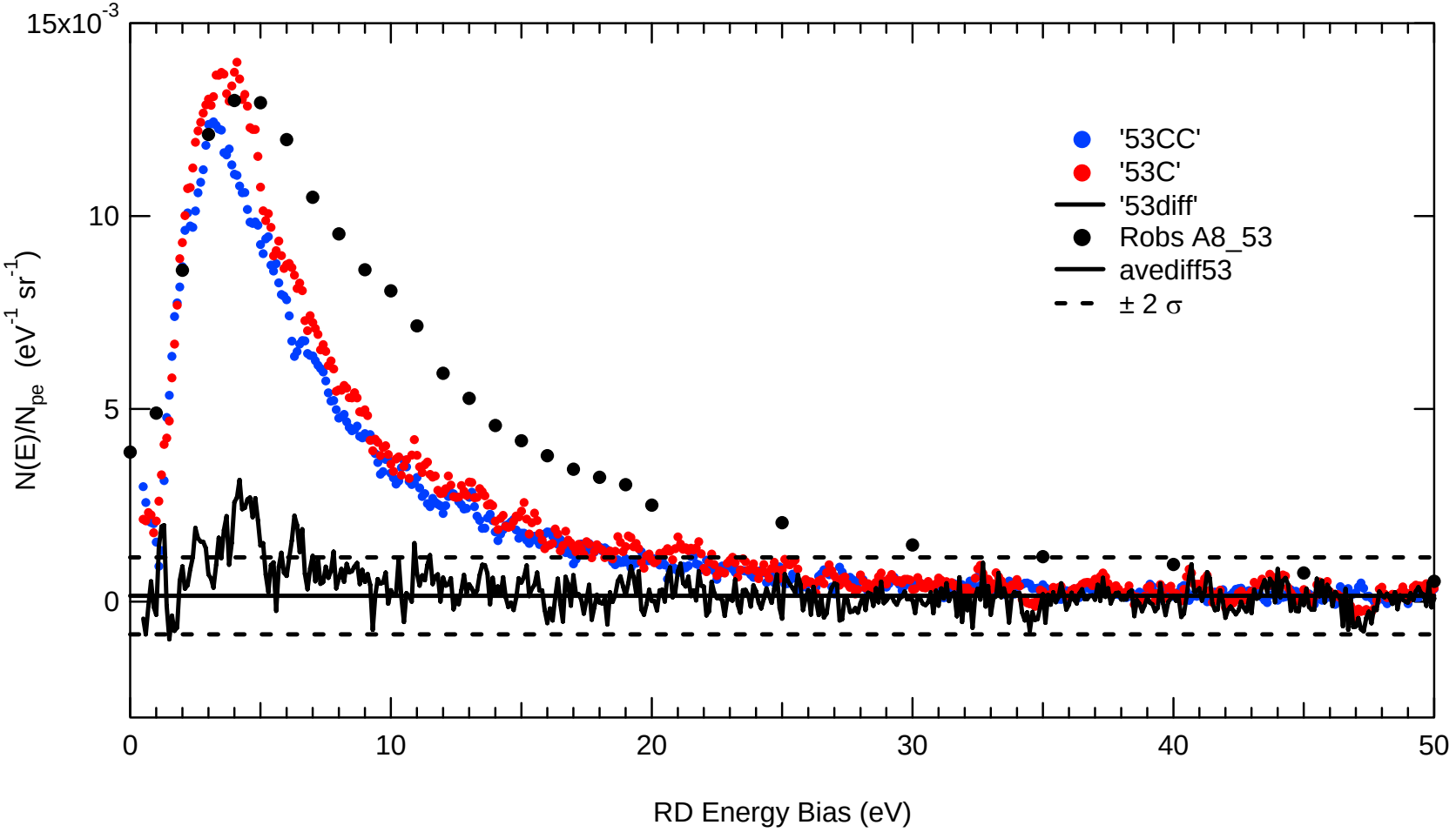

Figure 3- 25 SE Yield of polycrystalline Au at 53° emission for 1.5 keV incident beam energy with the difference shown in black. Davies data is shown in circles. The average of the difference in the two spectra is provided (solid black) along with 2X standard deviations above (dashed) and below (dashed) the average.

gradual changes in yield. The reason for this is because an increment RD bias presumes a decrement measured current in the RD. (2) Throughout the process of previous spectral measurement, the RD may have been accruing residual charge by current not measured by the floating ammeter resulting in RD charging. Any build-up of residual charge within the RD would leak away at a slower rate for a time decreasing current. Both of these explanations could be reasons for the differences in spectral shape seen in the 5 to 45 eV range.

In general, the shape comparisons of the Clockwise (C) to Counter-Clockwise (CC) SE spectra are very similar even at low energies. In fact, there is excellent absolute agreement [Fig. 3-26] at all energies above the SE peak, > 3 eV, in the electron emission spectra. The differences of the angle resolved SE spectra are void of shape and are similar to noise effects consistently contained within 2 standard deviations of the mean. The average fractional differences exceed 10% only below 2 eV [Fig. 3-27] in cases where the incident beam current was not consistent between angular spectrum counterpart. The percent difference spike shown for 38^{o} emission difference [Fig. 3-27, green], 1.6 eV, is known to be caused by the odd leading edge behavior of 38^{o} CC [Fig. 3-23, blue dots] where the incident beam current measured twice that of its angular counterpart, 38^{o} C. In addition, one average standard deviation of the mean, ~13%, enclosed all percent differences up to 14 eV in which case the signal-to-noise ratio worsens as RD count rates become less.

Recommended Additional Action: The beam current monitor within the electron gun controller should be checked for the source of noise or should be installed to float to the beam voltage just as the RD current monitor is floating at the voltage of the detected electrons.

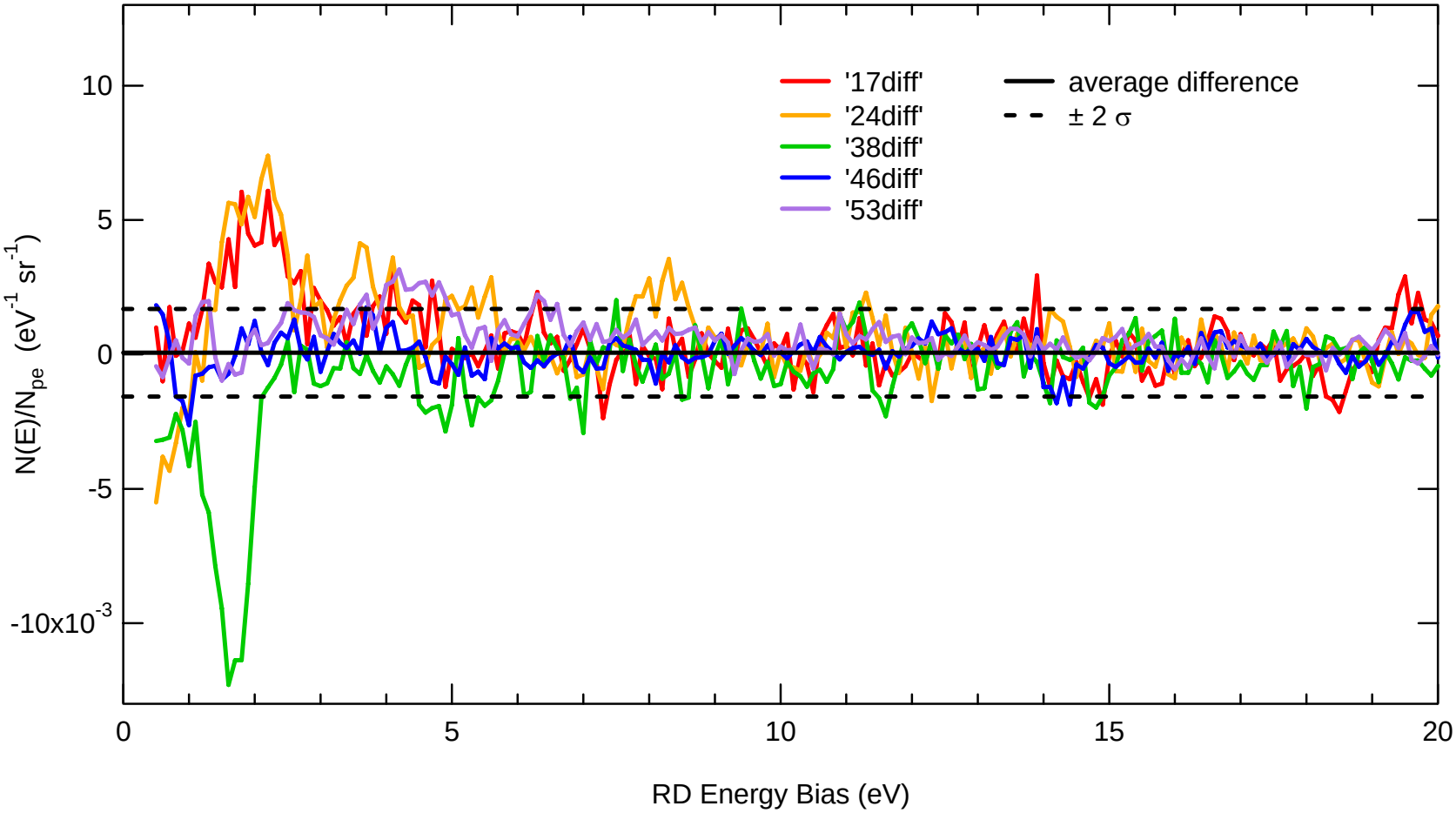

Figure 3- 26 Compiled difference SE spectra of polycrystalline Au for 1.5 keV incident beam energy. The average of the difference in each spectrum and it's symmetric counterpart is provided (solid black) along with two average standard deviations above (dashed) and below (dashed) the average.

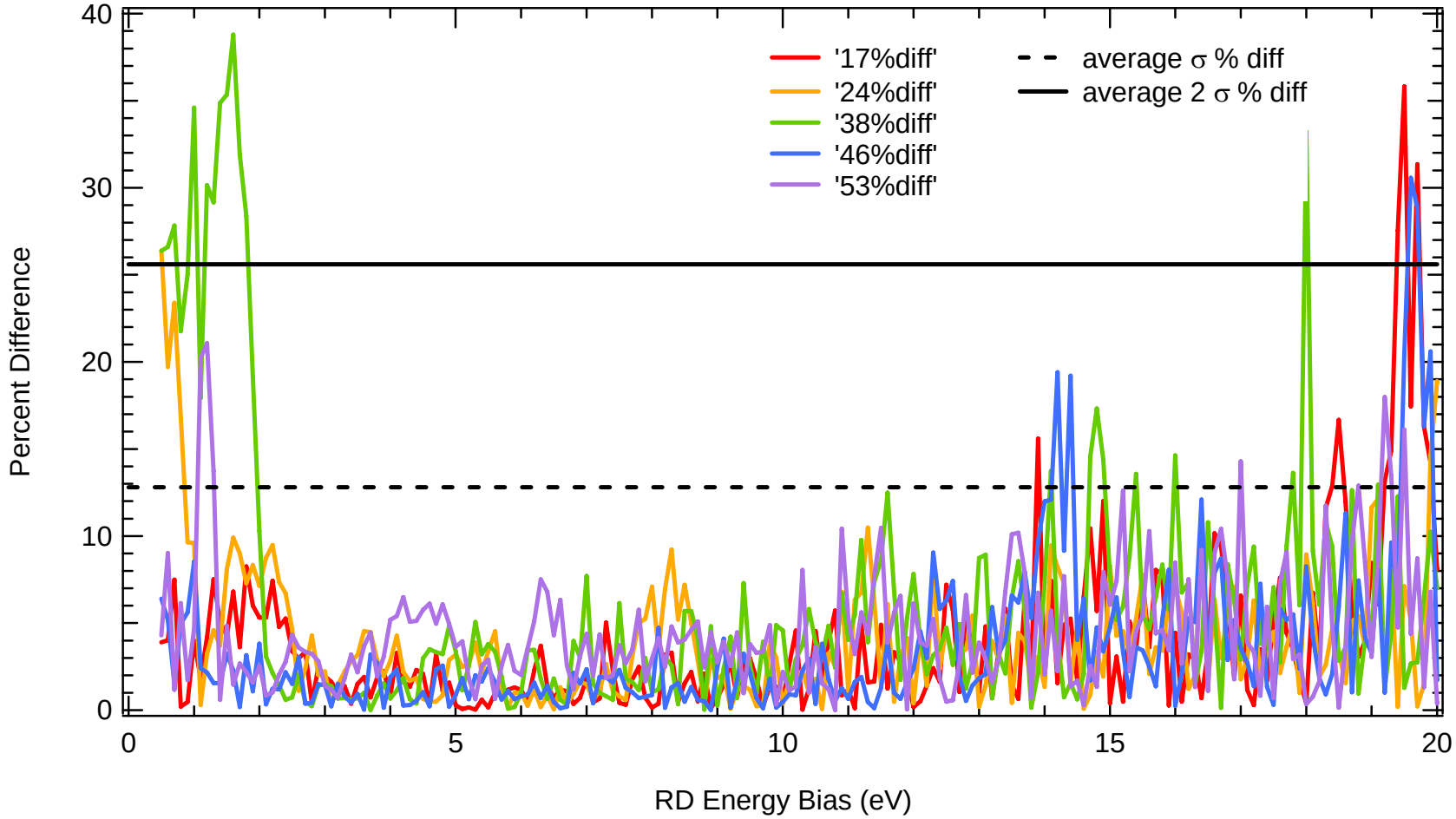

Figure 3- 27 Compiled percent difference SE spectra of polycrystalline Au for 1.5 keV incident beam energy. One and two average standard deviations of the mean are provided as percent differences of all five percent differences.

3.2.(g) Secondary Electron Production within the Chamber Apparatus

Problem: The production of unwanted SE's due to BSE collisions with the chamber apparatus has been problematic.

Action taken: An Aquadag^{TM} coating was applied to the inside of the magnetic shield, to the sample holder and to the rotation apparatus [4-23-99, LB 7y and Section 3.2.(f)].

Evaluation: The coating should reduce SE production by a factor of 2 to 5 since colloidal microcrystalline graphite has a very low SE yield of ~0.2 [*Thomas and Pattinson, 1970*] at 1500 volts. No evaluation has yet been done.

Recommended Additional Action: In order to evaluate the improvement of the Aquadag^{TM} coating, a comparison of the RD current with the tertiary current detectors will be made. This should be compared to previous yields taken by Davies.

3.2.(h) Secondary Electron Production within the Rotatable Detector

Problem: Davies has shown evidence of SE's that have been produced inside the RD.

Action taken: The problematic production of SE's within the RD has been measured [Fig. 3-28]. Two modifications have been made to the RD. Coating the inner surfaces of the detector with colloidal Aquadag^{TM} [4-23-99, LB 7y] greatly reduces SE production. Boring out the two collimator apertures of the RD reduces the probability for SE production with the 1st and 2nd collimator aperture edges [Fig. 3-2].

Evaluation: Comparison of the RD produced SE's can be measured by biasing the sample to -50 V. By sweeping the RD bias from 0 to –50 V, a spectrum of the SE's produced by the RD will be measured. The Aquadag coating has lowered the SE production by a factor of 20 [Fig. 3-29]. The reproducibility of this measurement is good [Fig. 3-30]

Recommended Additional Action: No additional action is required.

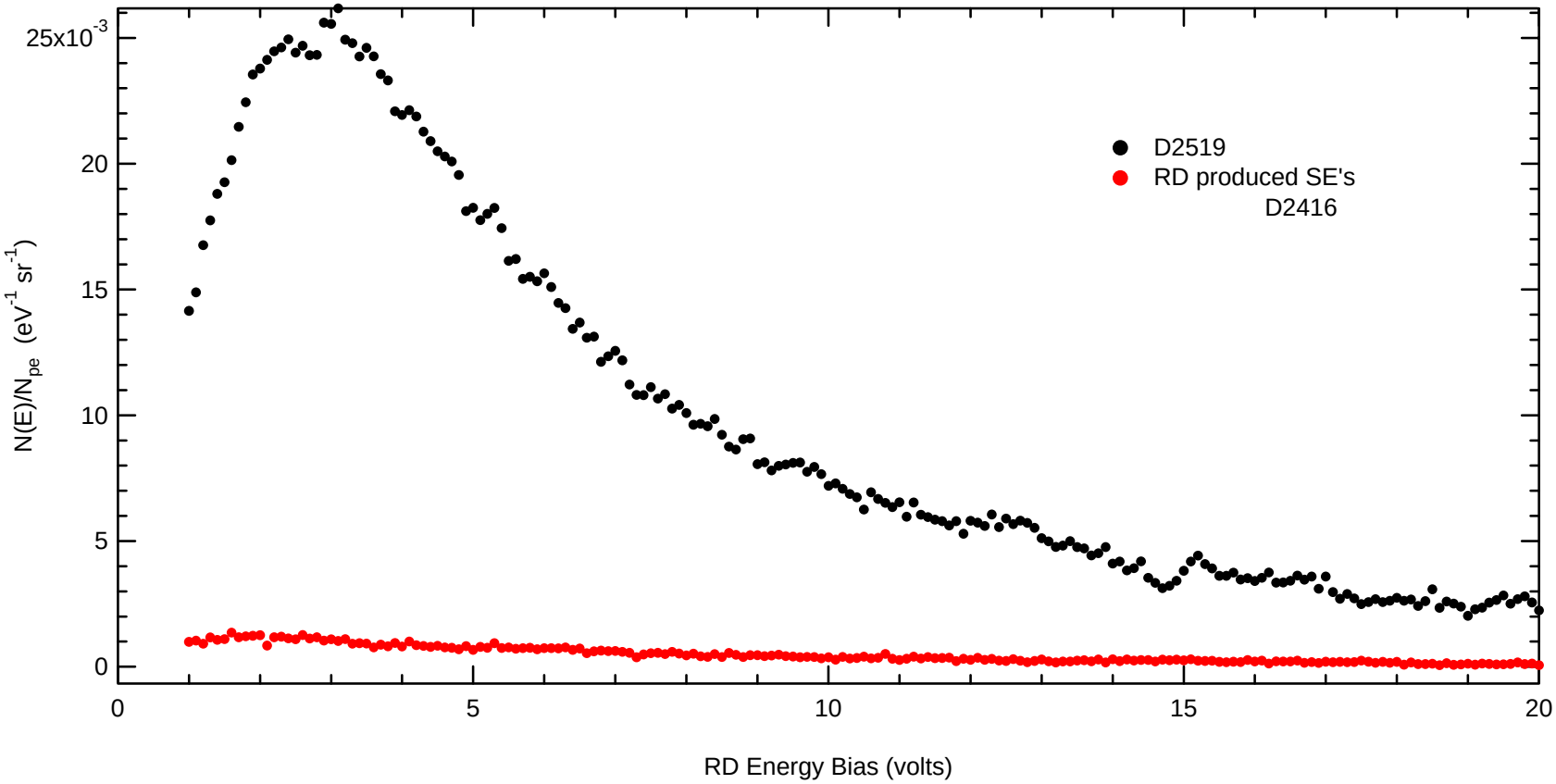

Figure 3- 28 RD produced SE's in red with SE spectra in black. Measurements were made after the aquadag coating.

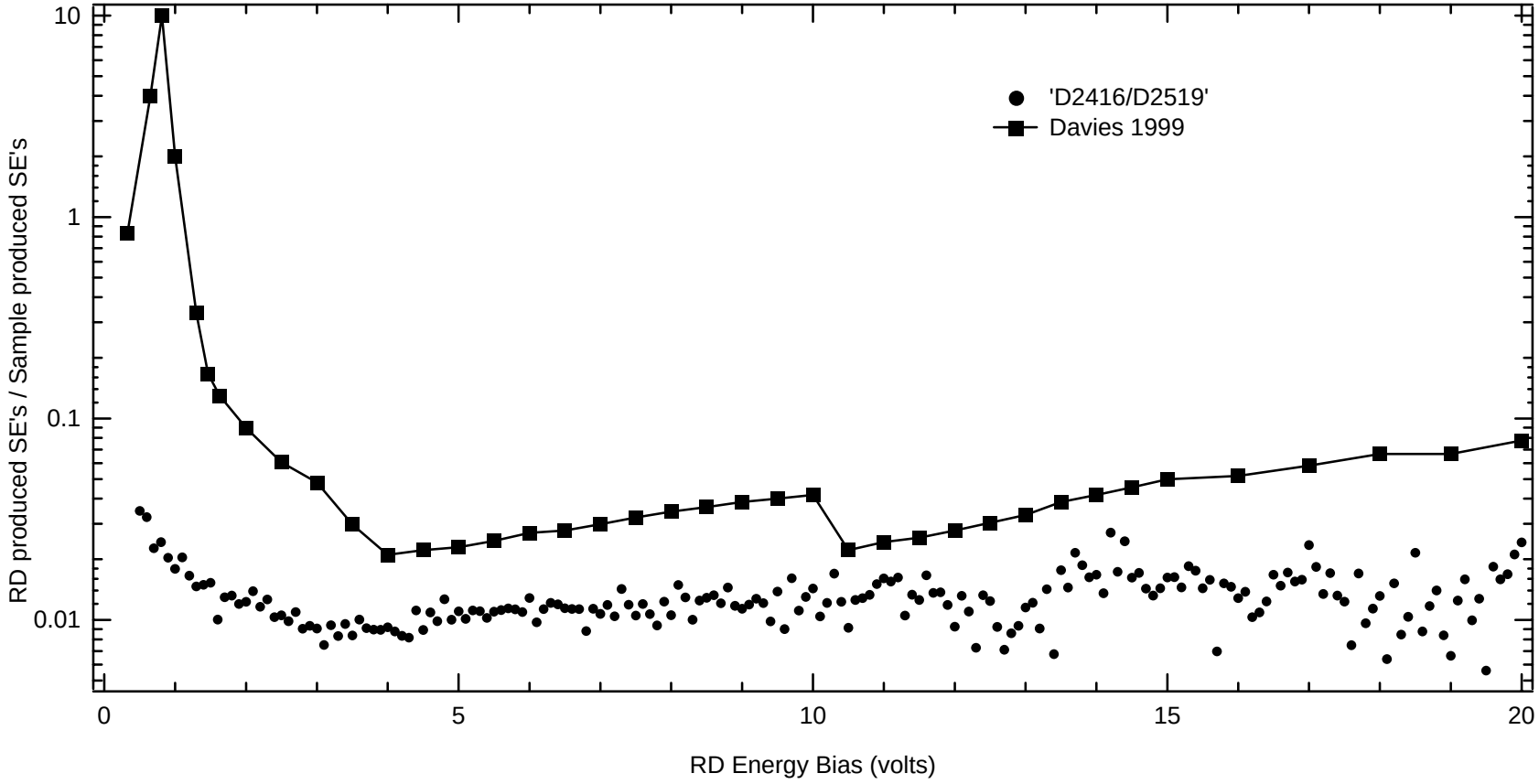

Figure 3- 29 Ratio of RD produced SE's to Sample produced SE's shown with circles. Davies measurement is shown with squares.

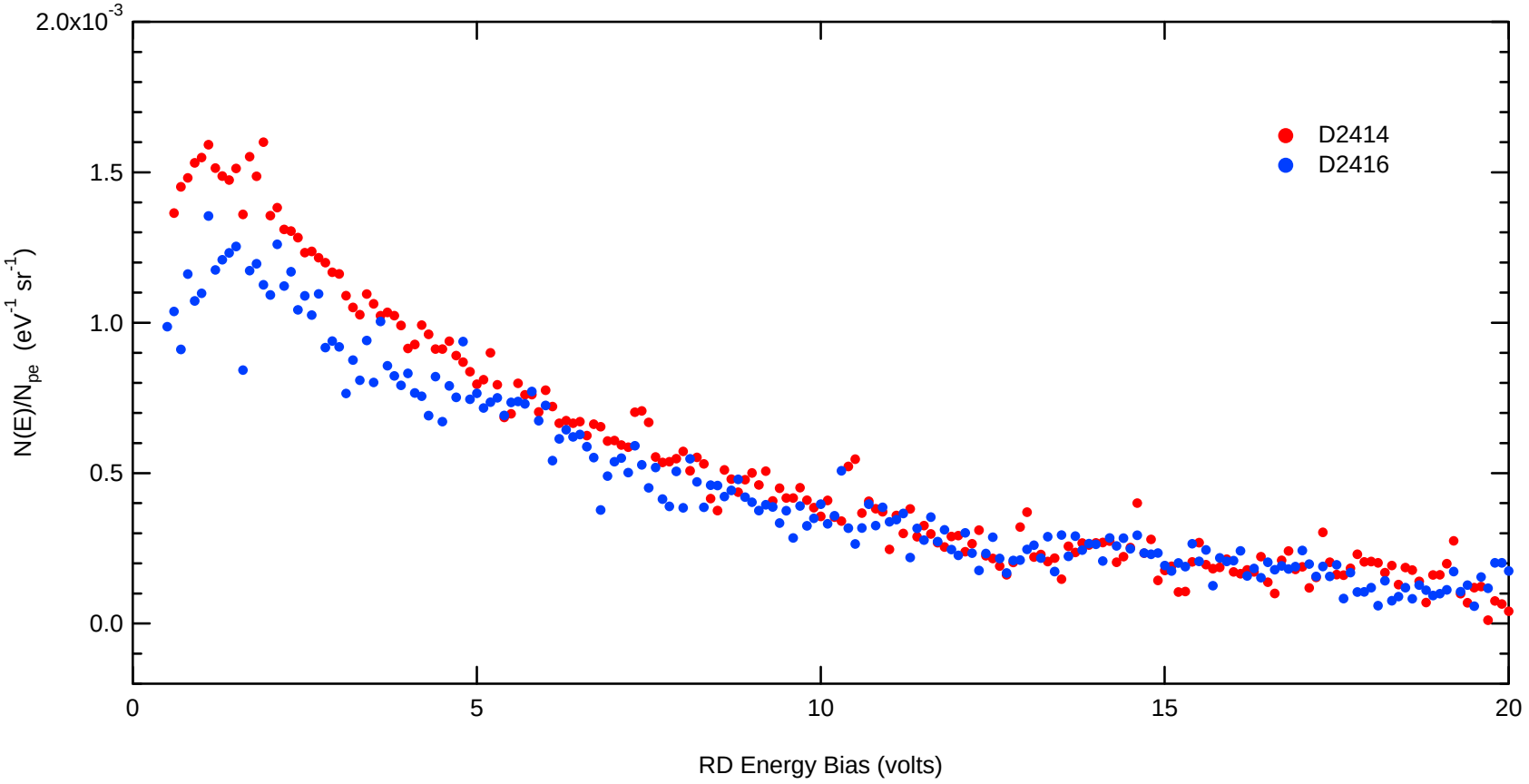

Figure 3- 30 Reproducibility of RD produces SE's. The two spectra have been taken ~20 hours apart.

3.2.(i) Data Analysis Algorithm

Problem: The original algorithm for differentiation [LB IV, 16y] may have included false information such as narrow fine structure and excluded important information such as broad Auger peaks (10-20 eV wide). The algorithm used by Davies for investigating data involved a derivative [Davies, p. 223] where the derivative was calculated between every other point regardless of the RD bias voltage increment size [*Davies, 1999, p. 222*]. A commercial smoothing Savitzky—Golay (SG) algorithm resulted in the AER spectra. The derivative process was not fully optimized, especially for data sets taken at different energy increments.

Action taken: A customized derivative algorithm has been developed with the IGOR analysis software (WaveMetrics) to validate the concatenation of spectral portions taken at varying resolutions of the RD voltage supply (Keithley 237). As addressed previously, each RD voltage resolution setting has a different associated precision, 3.2.(e), which is controlled by the Keithley 237 compliance setting. Since the RD voltage resolutions possess different amounts of standard deviation, comparison of derivative techniques is necessary. Coarse and fine data sets for an equal number of measurements per data point have been taken and then differentiated using the gaussian point—wise technique and the sliding point—wise technique.

In order to measure the amount of electric charge between two different energies, one must first count the charge collected in the RD while it is biased to two different biasing voltages. This energy, E_e, is defined to be the amount of charge able to decelerate over the potential of the bias setting. The RD bias rejects all charge with less energy than the bias setting and accepts (collects) all charge with energy greater than the bias setting. Recalling that charge per second is current, I, the ratio, N, of decelerated charge per second, I_{RD}, to that of the accelerated charge per second, I_b, exiting the electron gun can be plotted against E_e. Coarse and fine resolution data sets [Fig. 3-31] represent the electric charge measured at discrete steps of RD energy bias resolutions of 0.1 eV and 1 eV. Each error bar comes directly from the standard deviation of each measured point. Since the precision for every RD bias setting is dependent on the RD

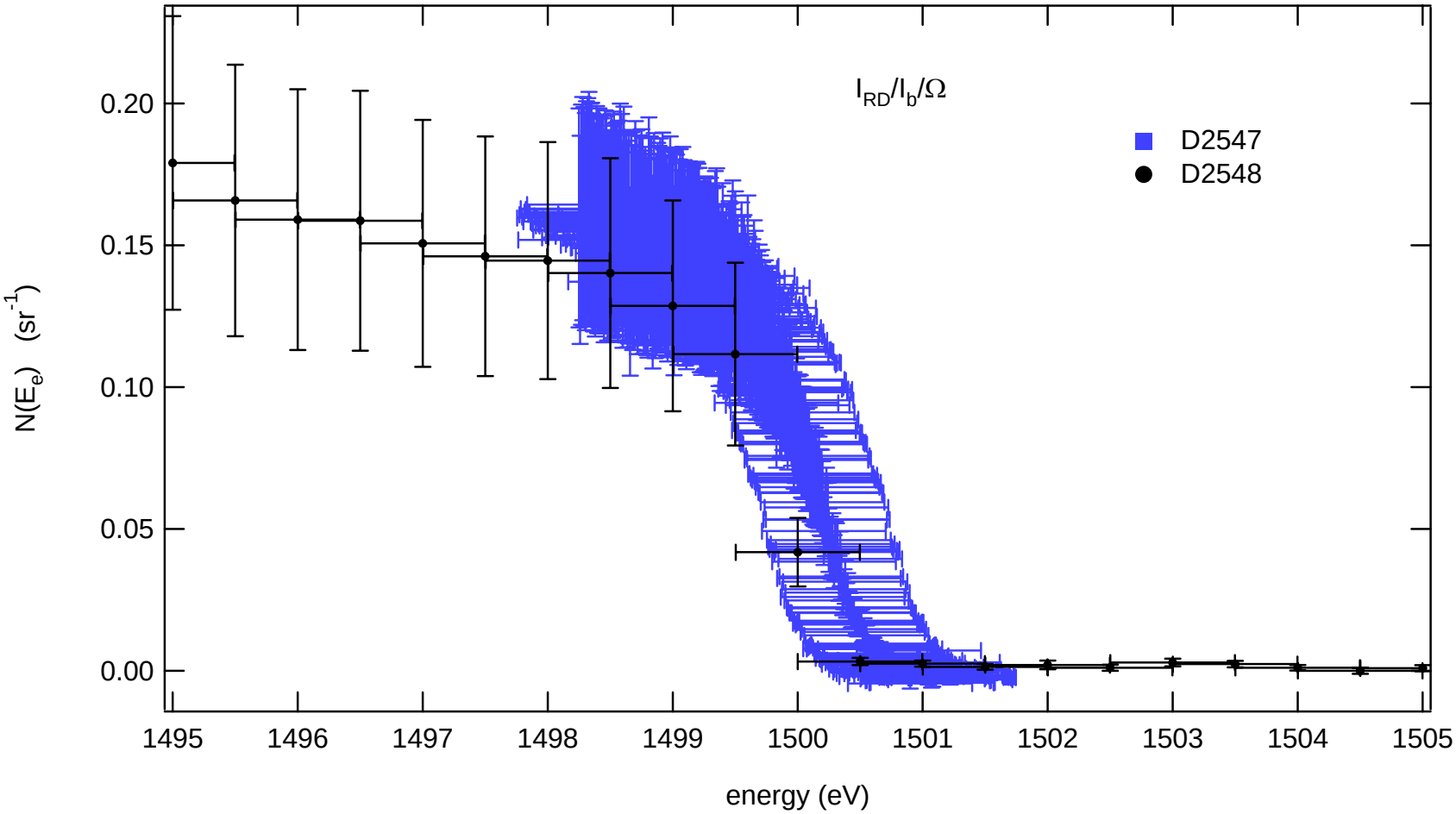

Figure 3- 31 Comparison of elastic pre—differentiated data using 0.1 eV (blue squares) and 1 eV (circles) resolutions.

bias [Fig. 3-32], it is reasonable to calculate the errors in quadrature from each derivative technique and compare them separately.

Since the difference of the two amounts of charge is the total amount of charge collected at *all* energies extending between the two different biases, then differentiation using the standard rise-over-run slope method is acceptable. Appropriate data resolution for a particular data range is calculated by matching the error bars of the fine resolution data to error bars of coarse resolution data. The point-wise gaussian derivative approach results in

$$\left.\frac{dN}{dE}\right|_{\mathrm{i+1}}^{\mathrm{gauss}} = \left.\frac{N_{i+1}-N_i}{E_{i+1}-E_i}\right|_{E=E_i} \tag{3.2}$$

The units follow as eV^{-1}*$steradian^{-1}$. The error in dN/dE is calculated in quadrature using the standard deviations of the RD bias data, σ_E [Fig. 3-32], and σ_N, [Fig. 3-33, dots], for each measurement point, i.

$$\sigma_{\frac{dN}{dE}} = \left.\frac{dN}{dE}\right|_{\mathrm{i+1}}^{\mathrm{gauss}} \times \left[\left(\frac{\sigma_{E_{i+1}}+\sigma_{E_i}}{E_{i+1}-E_i}\right)^2 + \left(\frac{\sigma_{N_{i+1}}+\sigma_{N_i}}{\mathrm{N}_{i+1}-\mathrm{N}_i}\right)^2\right]^{0.5} \tag{3.3}$$

Now the second derivative approach will be used to calculate each spectrum. The sliding point-wise derivative used to directly compare to the gaussian derivative results in

$$\left.\frac{dN}{dE}\right|_{\mathrm{i}}^{\mathrm{slide}} = \left.\frac{N_{i+n/2}-N_{i-n/2}}{E_{i+n/2}-E_{i-n/2}}\right|_{E=E_i} \tag{3.4}$$

where n is an even number less than the data range.

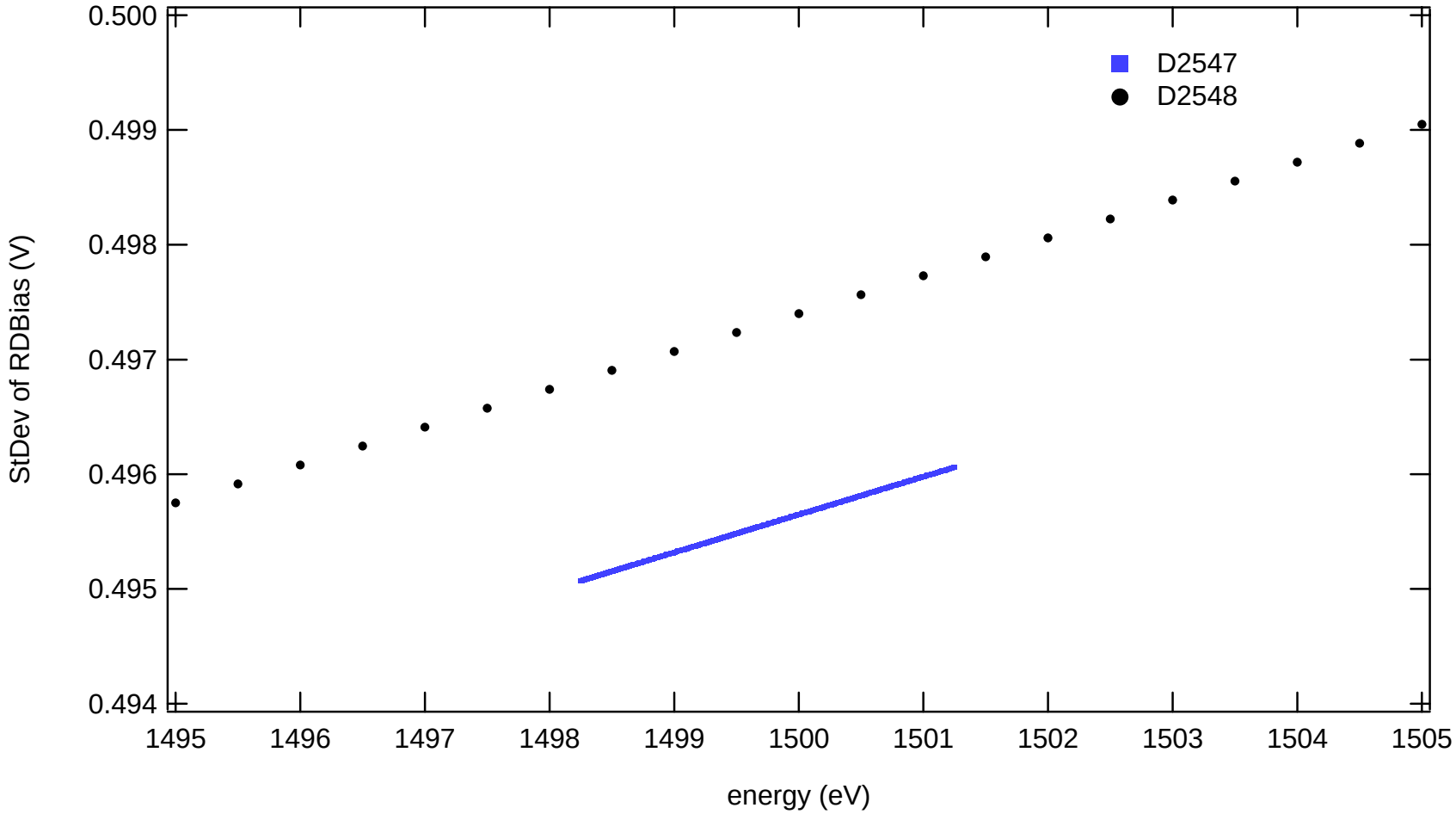

Figure 3- 32 Comparison of RD bias standard deviation for elastic data sets using the fine 0.1 eV (blue squares) and coarse 1 eV (circles) resolutions. These values are calculated from the voltage accuracy equation provided in the Keithley 237 manual and are used as the X-axis error bars in Fig. 3-31.

Errors calculated in quadrature from measured errors in $N_{i+n/2}$ and $N_{i-n/2}$ follow directly from the standard deviations of the RD bias, σ_E [Fig. 3-32], and σ_N, [Fig. 3-33, dots], for each measurement point, i.

$$\sigma_{\frac{dN}{dE}} = \left.\frac{dN}{dE}\right|_{i}^{slide} \times \left[\left(\frac{\sigma_{E_{i+n/2}} + \sigma_{E_{i-n/2}}}{E_{i+n/2} - E_{i-n/2}}\right)^2 + \left(\frac{\sigma_{N_{i+n/2}} + \sigma_{N_{i-n/2}}}{N_{i+n/2} - N_{i-n/2}}\right)^2\right]^{0.5} \tag{3.5}$$

where n is an even number less than the data range.

Integration (by Simpson's rule) of the derivative of the data with aims to calculate the error of the yield occurs with the area, A

$$A = (E_{i+1} - E_i) * N_{i+1} + \frac{1}{2}(N_i - N_{i+1}) * (E_{i+1} - E_i) \tag{3.6a}$$

becomes

$$A = \frac{1}{2}(E_{i+1} - E_i) * (N_{i+1} + N_i) \tag{3.6b}$$

but this is just the area of a triangle with width of the RD bias (V) and height of the yield ratio (1/eV*1/steradian). Thus, the error of the area or integral calculated in quadrature is

$$\frac{\sigma_A}{A} = \left[\left(\frac{\sigma_{E_{i+1}} + \sigma_{E_i}}{E_{i+1} - E_i}\right)^2 + \left(\frac{\sigma_{N_{i+1}} + \sigma_{N_i}}{N_{i+1} + N_i}\right)^2\right]^{0.5} \tag{3.7}$$

Shown in Fig. 3-33 are the standard deviations of the pre-differentiated data using the two different resolution data sets and the respective standard deviations (errorBSE) of the gaussian point-wise

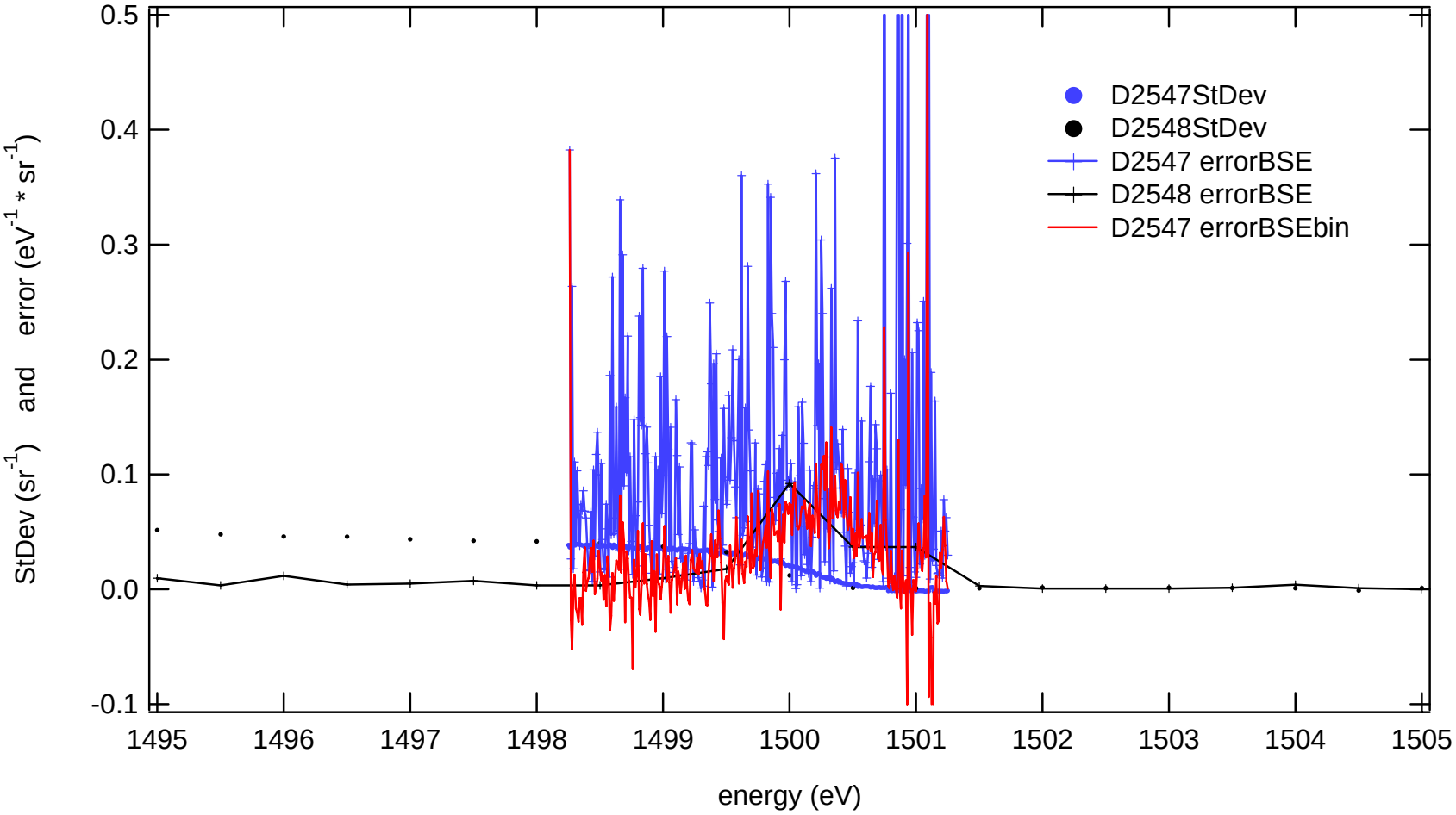

Figure 3- 33 Comparison overlay of Pre-Differentiated StDev and spectral error bars for elastic peak at E_b = 1.5 keV using 0.1 eV and 1 eV resolutions.

derivative (blue and black +'s) calculated using Eq. (3.3) and of the sliding point-wise derivative (red line) calculated with n = 50 using Eq. (3.5).

The two different resolutions of data show that the error in the voltage bias for the finer 0.1 eV resolution is much less than that of the coarser 1 eV resolution. Since the error bar for the finer 0.1 eV resolution is typically less [Fig. 3-33, red], it is used to match the error of the D2547 (black dots with lines).

The process of concatenating spectral portions of different resolutions involves the differentiation of pre-differentiated data resulting in the derivative (spectrum). The pre-differentiated data has an error in the RD bias energy. Upon concatenation, the error bar transition between the 1 eV and 0.1 eV spectra should almost match. The resulting spectra are then smoothed with the same commercial Savitzky-Golay smoothing algorithm. Each of the spectra have error bars on both the pre-differentiated and the differentiated data.

Fig. 3-34 shows the spectra produced at the 0.1 eV and 1 eV resolutions where the D2548 derivative at 1 eV point by point (with error bars) most closely matches the 0.1 eV resolution differentiated data (D2547) taken at every tenth point (error bars included in [Fig. 3-33, red]). Note: The small black points differentiated at 10 point increments are an order of magnitude wider and an order of magnitude smaller than those of the one point derivative (error bars included). This suggests that an appropriate voltage precision (Keithley 237 compliance) can be sought for the particular spectral feature of interest regardless of the existing RD resolution.

If the voltage precision is too small, a very noisy peak results [Fig. 3-34, blue x's]. If the voltage precision is too large, any small important details will be washed out with the averaging [Fig. 3-34, black dots with lines].

Evaluation: Though fine resolution SE spectra can be compared to previous work [Figs. 3-21, 3-22, 3-23, and 3-25], the different algorithms cannot be compared for extra-fine resolution because the old RD biasing scheme, 3.2.(e), provided large AC ripple magnification so that changing the compliance

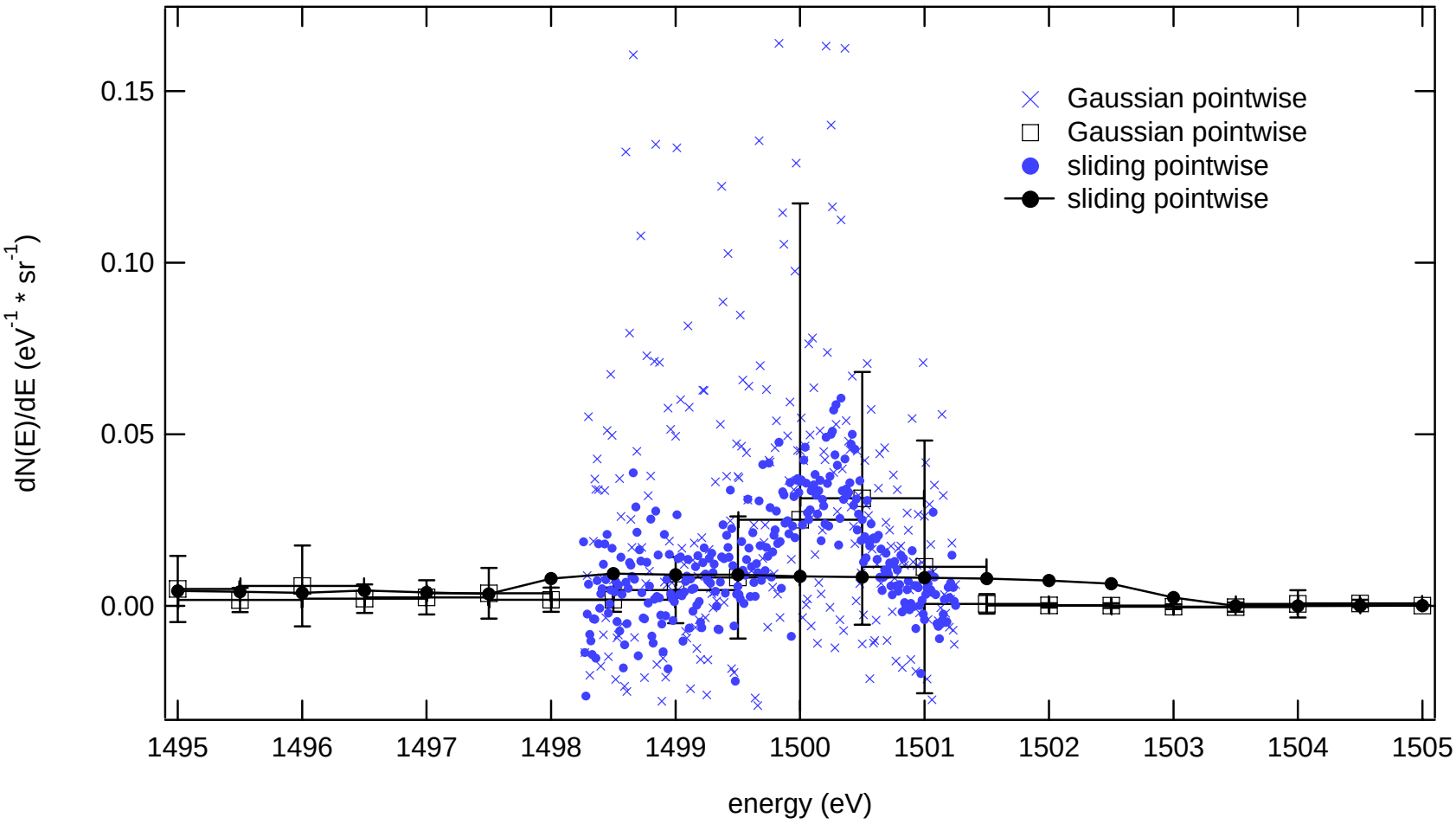

Figure 3- 34 Comparison of elastic spectra for the 0.1 eV (blue) and 1 eV (black) resolutions using the gaussian pointwise and sliding pointwise derivative techniques.

setting was not the weakest link. The BSE peaks can now be isolated for investigation and connected piece-wise to the coarse and fine resolution spectra.

The derivative resolution of the data will therefore be a measure of the precision of the RD, as long as the standard deviation of an individual energy bias measurement is sufficiently smaller than the sliding point-wise derivative size. The derivative has been chosen (0.5 eV) so that the standard deviation of each RD energy bias is the same as the standard deviation of the derivative data (~0.5 eV). The present theoretical resolution of the RD is 0.2 eV [*Davies, 1999, p. 199*]. Since the interest here is in broad features of polycrystalline materials, the overestimation of the voltage precision size is preferred. The sliding point-wise derivative has been calculated between every n = 50 points (0.01*50 = 0.5 eV), which yields the same result as a 0.5 eV gaussian point-wise derivative elastic peak data [Fig. 3-34, blue dots and black squares].

This new algorithm cannot be used on elastic peak data taken with the old RD biasing technique because the RD bias voltage increment (~1 eV) was never smaller than the resolution of the RD, so no comparison for improvement can be made. This is the reason Davies could not compare derivative procedures and the infamous double elastic peak could not be isolated for investigation.

The exclusive capability of the IGOR software (WaveMetrics) to run separate analysis routines (macros) and maintain organized information is advantageous. Incorporating the electron beam energy, E_b, as an additional variable in this study has also been straightforward due to the nicely organized help features. Three macros have been written to analyze the data. The first macro is used to parse the data, calibrate the data with the solid angle and multiply the data to average measurements of the beam current, I_b, using Eq. (3.7) to provide absolute spectra (3.4(b)). The second macro analyzes the data by differentiation, smoothing and/or curve fitting, (where needed) and in the determination of error. The third macro extracts yield results, consolidates the results, and stores the results in the correct beam energy folder.

Recommended Additional Action: No additional action is required

3.2.(j) Analysis Anomalies

Problem: There may be possible anomalies present in the AER spectra. Since these AER spectral measurements are absolute, the accuracy is much more well known than the precision. Hence, in many cases, smoothing is needed. In fact, for most cases, the correct amount of smoothing is required. Therefore, several resolutions were used to probe the precision. The comparison of spectra taken at different resolutions incorporated the comparison of corresponding error. The error in RD bias energy comes from the compliance setting of the Kiethley 237. Every different precision has a different compliance setting and visa versa, which provides the error on the X-axis. Error on the Y-axis is provided by the sliding point-wise derivative standard deviation calculated in quadrature (3.2(i)).

Action taken: A spectrum containing many ambiguous peaks is given [Fig. 3-35] at several different smoothing numbers. A commercial smoothing Savitzky-Golay (SG) algorithm is a type of least squares polynomial smoothing. The amount of smoothing is controlled by two parameters: the polynomial order and the number of points used to compute each smoothed output value. For this case, the polynomial order is always 2. The amount of smoothing for each E_b and resolution is provided (Table 3.2) along with the measured elastic energy used for comparing several E_b [Fig. 5-9].

Evaluation: The Elastic Peak Intensity is slightly different in magnitude for the 0.1 eV and 1 eV resolutions. However, the characteristic width of the elastic peak is different by an order of magnitude. The 0.1 eV resolution intensity is an order of magnitude greater than that of the 1 eV resolution intensities, but since the widths of the 1 eV resolution elastic peaks are an order of magnitude less than those of the 0.1 eV resolution, the product of the intensity by the width now become the important factor by which these two resolutions compare. The comparison itself is intertwined within the integrated areas of the elastic peaks measured using 0.1 eV and 1 eV resolutions [Fig. 5-10, linear yield] in the last section. Since the derivative process within the data analysis algorithm is the same, n = 20, for both energy resolutions (3.2(i), Fig. 3-34), the accuracy of dN(E)/dE determine the optimum n [Fig. 3-33, black +'s and red line]. In other words, the standard deviations of N(E) [Fig. 5-11] should determine the instrument accuracy and the standard deviations of dN(E)/dE, with appropriately optimized n, should determine the instrument

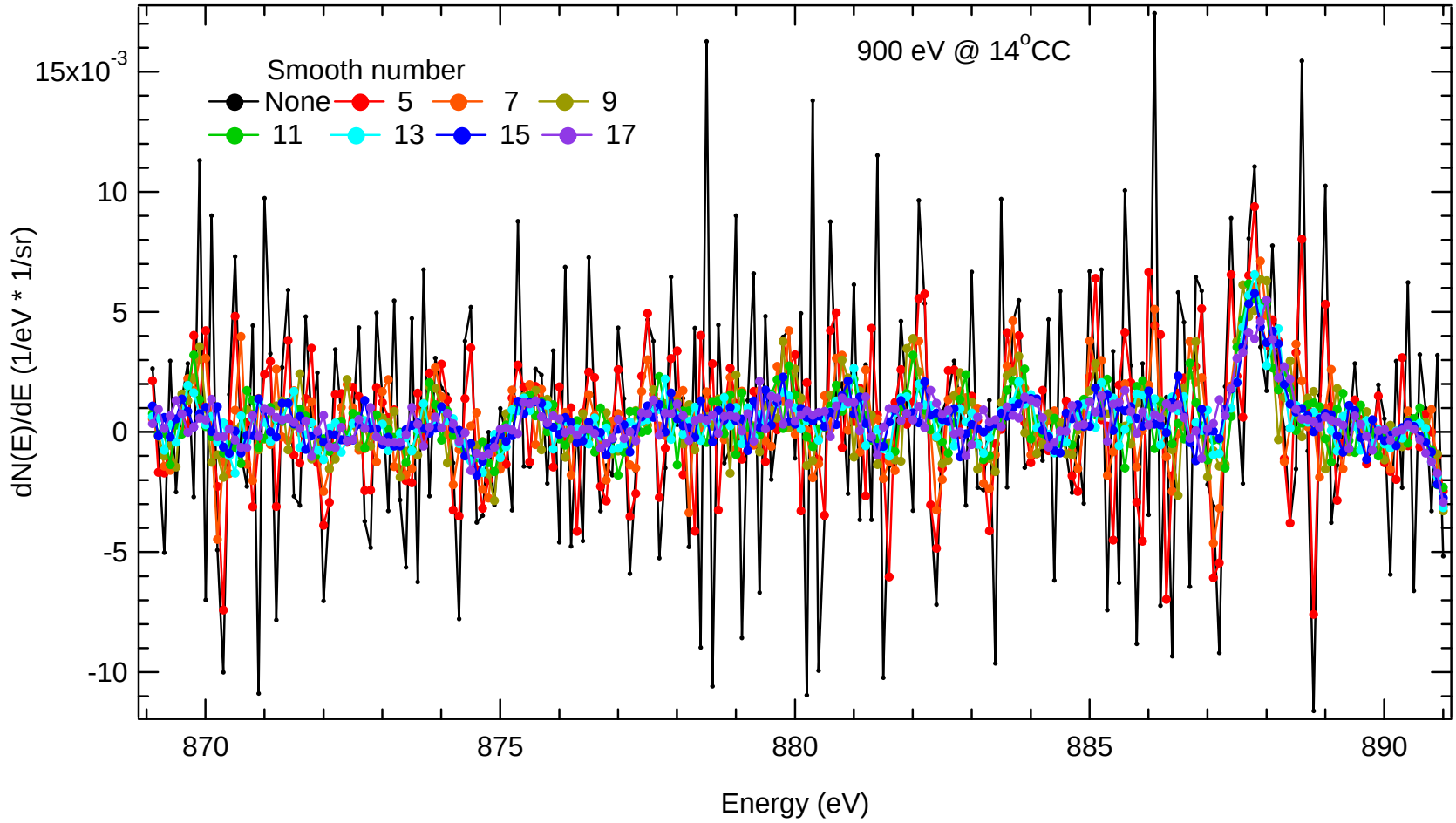

Figure 3- 35 Smoothing parameter using the second order Savitzky-Golay algorithm for several number of points (smooth number) taken on the elastic peak at 900 eV incident beam energie and 14° Counter-Clockwise emission using the 0.1 eV resolution.

resolution. Since the uncertainty in the measurement carries through the derivative process, it is important to also provide the Savitzky-Golay smoothing numbers for all spectra.

Smoothing numbers are unique for both N(E) and dN(E)/dE. The smoothing number for N(E) is used when extracting absolute yield values and the smoothing number for dN(E)/dE is used when extracting absolute intensities of peak and minimum features.

Recommended Additional Action: No additional action is required.

Table 3.2 Smooth Numbers utilized with the Savitsky-Golay type 2 Smoothing Algorithm are provided below. The pre-differentiated data, N(E), and the associated spectra, dN(E)/dE, have unique smoothing numbers for the three RD energy resolutions. The "elastic energy" column, used for both the 1 eV and 0.1 eV resolutions (zag dividers), signifies overlap in optimum n determination and smoothing number.

	10 eV resolution		1 eV resolution			0.1 eV resolution	
E_b (eV)	N(E) smooth number	dN(E)/dE smooth number	N(E) smooth number	dN(E)/dE smooth number	elastic energy (eV)	N(E) smooth number	dN(E)/dE smooth number
100	*	*	21†	*	102.3	7	5
500	11	11	25	25	494.4	25	11
600	11	none	19	25	594.4	*	*
700	none	13	19	25	694.4	*	*
900	none	13	19	7	888.2	25	11
1200	none	9	19	15	1189.5	25	11
2000	none	11	19	7	1981.3	7	11
2500	none	17	21	11	2475.5	11	11

* no measurement made

† Though no measurement was made for E_b = 100 eV at 1 eV resolution, a facsimiles was constructed by choosing every tenth data point of the 0.1 eV resolution.

3.3 MEASURED QUANTITIES

Two distinct types of electron scattering measurements are of interest in this investigation. The angle-resolved yields, $\delta(\alpha')$, and the energy resolved yields, $\delta(E_e')$, are calculated by measuring specific quantities from the instrument. An explanation of the notation used and a brief review of the yield definitions are presented.

3.3.(a) Notation

Throughout the remainder of this work, variables followed by parameters in parentheses represent functions, while variables followed by *primed* parameters in parentheses represent functions evaluated at a specific value; thus, the presence of a prime denotes a specific (though arbitrary) parametric value. For example, $\delta(\alpha)$ is a function describing the dependence of the angle-resolved (AR) SE yield on α (*i.e.*, the SE angular distribution function), and $\delta(\alpha')$ is the value of that function evaluated at $\alpha=\alpha'$ (i.e., the AR yield at $\alpha = \alpha'$): $\delta(\alpha') \equiv \delta(\alpha)\big|_{\alpha=\alpha'}$. Also note that the presence of a primed parameter in a variable indicates that this variable is a little piece of a "parent" variable—*i.e.*, a differential yield; for example, the angle-resolved SE yield $\delta(\alpha')$ is a little piece of the total SE yield, δ, and the angle-energy-resolved yield $\delta(\alpha', E_e')$ is a little piece of the AR yield, $\delta(\alpha')$, a little piece of the energy-resolved yield, $\delta(E_e')$, and a very little piece of δ. On occasion, a more suggestive notation with the presence of a *"d"* or *"d^2"* in the variable—*e.g.*, $d\delta(\alpha')$, $d^2\delta(\alpha', E_e')$, etc.—is used to emphasize the differential nature of a variable. As used in this work, the two notations are interchangeable:

$$d\delta(\alpha') \Leftrightarrow \delta(\alpha')$$

$$d^2\delta(\alpha', E_e') \Leftrightarrow \delta(\alpha', E_e')$$

etc.

3.3.(b) Definition

Each of the definitions presented in this section have been developed in detail in *Davies* [1996, 1999]. Presented here, is a summary of that work with an upgrade in notation to include the additional incident beam energy parameter, E_b. Figure 3-36 depicts the physical situation under investigation: an incident beam of energetic electrons is normally incident on a conducting sample, producing SE's (with energies *defined* to be from 0 to 50 eV) and BSE's (with energies defined to be 50 eV to E_b) which leave the sample surface in an electron spray. The symmetric distribution of this spray has been tested with respect to the azimuthal angle, φ_e, for both high energy (section 3.2.(e)) and low energy (section 3.2.(f)) electron emissions. The dependence of this spray on the emission angle, α', has presumably been thought to follow the form of the Mott law for high energy emissions and to follow the form of the Lambert cosine law for low energy emissions. The percentage, or yield, is the number of scattered electrons per incident electron. The following definitions of the total, angle-resolved and energy-resolved yields are now presented:

Total SE Yield, δ: the total number of SE's, N_{se}, produced per incident PE, at all energies (0 to 50 eV) and at all emission angles (0 to 4π steradians). Referring to Fig. 3-36, this would be all SE's passing through the entire hemispherical surface, divided by the total number N_{pe} of incident PE's,

$$\delta = \frac{N_{se}}{N_{pe}} \tag{3.8}$$

Angle-Resolved SE Yield, $\delta(\alpha'; E_b')$: the number of SE's produced per incident PE, per unit solid angle (measured in steradians), about a given emission angle α' and beam energy, E_b. Referring to Fig. 3-36,

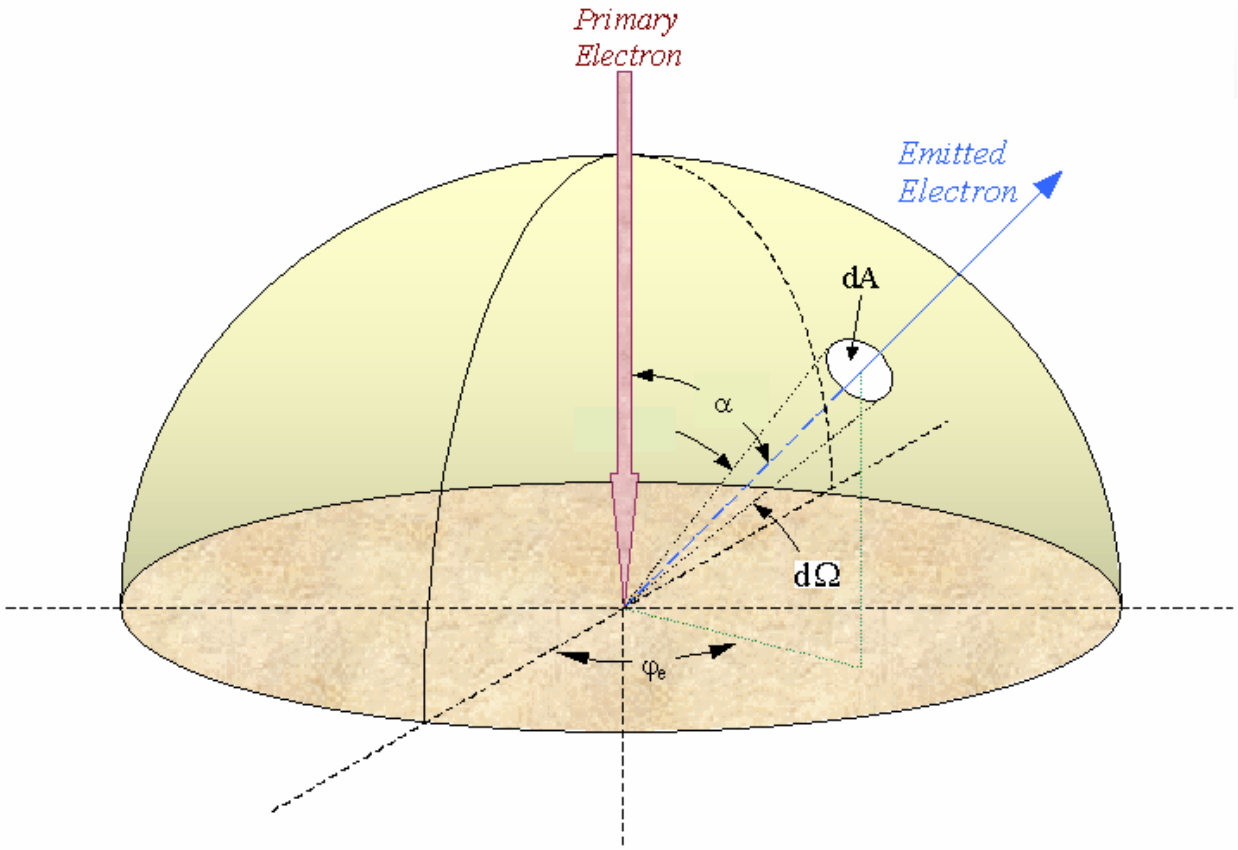

Figure 3- 36 Schematic depicting the experimental geometry of normally incident primary electrons shown in red and surface emitted electron shown in blue [*Davies, 1999*].

define $dN_{se}(\alpha';E_b')$ to be the number of SE's passing through the area element *dA* (centered on α' and subtending the solid angle $d\Omega$); $\delta(\alpha';E_b')$ can then be written

$$\delta_{AR} \equiv \delta(\alpha';E_b') = \frac{1}{N_{pe}} \frac{dN_{se}(\alpha';E_b')}{d\Omega} \tag{3.9a}$$

Implicit in Eq. (3.9a) is the assumption that $\delta(\alpha';E_b')$ is independent of φ_e. Also, it is important to note that in this context, $dN_{se}(\alpha';E_b')/d\Omega$ represents the form of a scattering cross section. Defining $\rho_{se}(\alpha';E_b')$ to be the number of SE's emitted per unit solid angle at $\alpha = \alpha'$ and beam energy E_b, we have $dN_{se}(\alpha';E_b') = \rho_{se}(\alpha';E_b')\,d\Omega$ (where, again, we are assuming the SE emission to be independent of φ_e). Clearly $\rho_{se}(\alpha';E_b')$ will be proportional to the total number of incident electrons: $\rho_{se}(\alpha';E_b') = N_{pe}\,\delta(\alpha';E_b')$, where $\delta(\alpha';E_b')$ represents the constant of proportionality for the case $\alpha = \alpha'$. Substituting, we can write

$$dN_{se}(\alpha';E_b') = N_{pe}\,\delta(\alpha';E_b')\,d\Omega \tag{3.9b}$$

which is just a rearrangement of Eq. (3.9a), but with the desirable feature of being completely unambiguous mathematically.

Energy-Resolved SE Yield, $\delta(E_e';E_b')$: the number of SE's produced per incident PE, per unit energy (measured in eV), about a given emission energy E_e' and beam energy, E_b'. Referring to Fig. 3-36, define $dN_{se}(E_e';E_b')$ to be the number of SE's passing through the entire hemispherical surface with energies in some small energy range E_e' to $E_e' + dE_e$. We can then write

$$\delta_{ER} \equiv \delta(E'_e; E'_b) = \frac{1}{N_{pe}} \frac{dN_{se}(E'_e; E'_b)}{dE_e} \tag{3.10a}$$

or, as in the previous definition, the less mathematically ambiguous form

$$dN_{se}(E'_e; E'_b) = N_{pe}\, \delta(E'_e; E'_b)\, dE_e \tag{3.10b}$$

Angle-Energy-Resolved SE Yield, $\delta(\alpha, E'_e; E'_b)$: the number of SE's produced per incident PE, per unit solid angle (measured in steradians), per unit energy (measured in eV), about a given emission angle α' and emission energy E'_e, with incident beam energy E'_b. Referring to Fig. 3-36, define $d^2N_{se}(\alpha', E'_e; E'_b)$ to be the number of SE's passing through the area element *dA,* centered on α′, with energies in the range E'_e to $E'_e + dE_e$; then we can write

$$\delta_{AER} \equiv \delta(\alpha', E'_e; E'_b) = \frac{1}{N_{pe}} \frac{d^2N_{se}(\alpha', E'_e; E'_b)}{d\Omega\, dE_e} \tag{3.11a}$$

or

$$d^2N_{se}(\alpha', E'_e; E'_b) = N_{pe}\, \delta(\alpha', E'_e; E'_b)\, d\Omega\, dE_e \tag{3.11b}$$

Corresponding definitions for the backscattered yields η, $\eta(\alpha'; E'_b)$, $\eta(E'_e; E'_b)$, and $\eta(\alpha', E'_e; E'_b)$ are completely analogous to those presented above.

Finally, it is sometimes useful to speak of the *total electron yield*, σ, emitted from a surface, which is simply the sum of the SE and BSE yields. Thus, we have

$$\sigma = \delta + \eta$$

$$\sigma(\alpha'; E'_b) = \delta(\alpha'; E'_b) + \eta(\alpha'; E'_b)$$

$$\sigma(E'_e; E'_b) = \delta(E'_e; E'_b) + \eta(E'_e; E'_b)$$

$$\sigma(\alpha', E'_e; E'_b) = \delta(\alpha', E'_e; E'_b) + \eta(\alpha', E'_e; E'_b)$$

There are four defined peak features and three defined minimum features in the AER spectra presented. The four peak features are the Elastic Peak, the Plasmon Peak, the BSE Peak and the SE Peak in order of decreasing emission energy. The three minimum features (transitions) separate peak features in the following way. The Elastic-Plasmon Minimum Boundary separates the Elastic Peak from the Plasmon Peak, the Elastic-BSE Minimum Boundary separates the Elastic Peak from the BSE Peak, and "E_{min}" separates the BSE Peak from the SE Peak.

Shown below are the specific quantities measured from a typical angle-resolved energy spectrum [Fig. 3-37]. These are the peaks and valleys that will be addressed in Chapter 5. The mathematical nomenclature is given for each peak and transition valley. Each has associated with it an intensity value (Y-axis) and an energy value (X-axis). The ordering (outline) of Chapter 5 follows a production origin structure where the elastic peak is discussed first to confirm that the incident beam energy can be used as a variable to parameterize this study. Referring back to section 3.2(i), the 0.1 eV and 1 eV resolutions provide comparing information about the elastic peak. However, the broad BSE peak was not measured using the 0.1 eV resolution because it would have taken too much time. In addition, the 1 eV resolution was not fine enough to decipher the first plasmon peak. So, when yield information is calculated for the different peaks, a decision must be made about the boundaries of the peak. For instance, the plasmon yield did not include the elastic peak and the BSE yield supposedly included the plasmon and elastic peaks even though they were not deciphered at the coarsest 10 eV resolution. The associated table provides the labels and nomenclature for each specific portion of the spectrum Table 3.3. Relationships between the relevant spectral elements and yields are discussed in the measurement technique section (3.5).

Attention is now turned to the data acquisition procedure used to measure these quantities with the LittleBoy instrument.

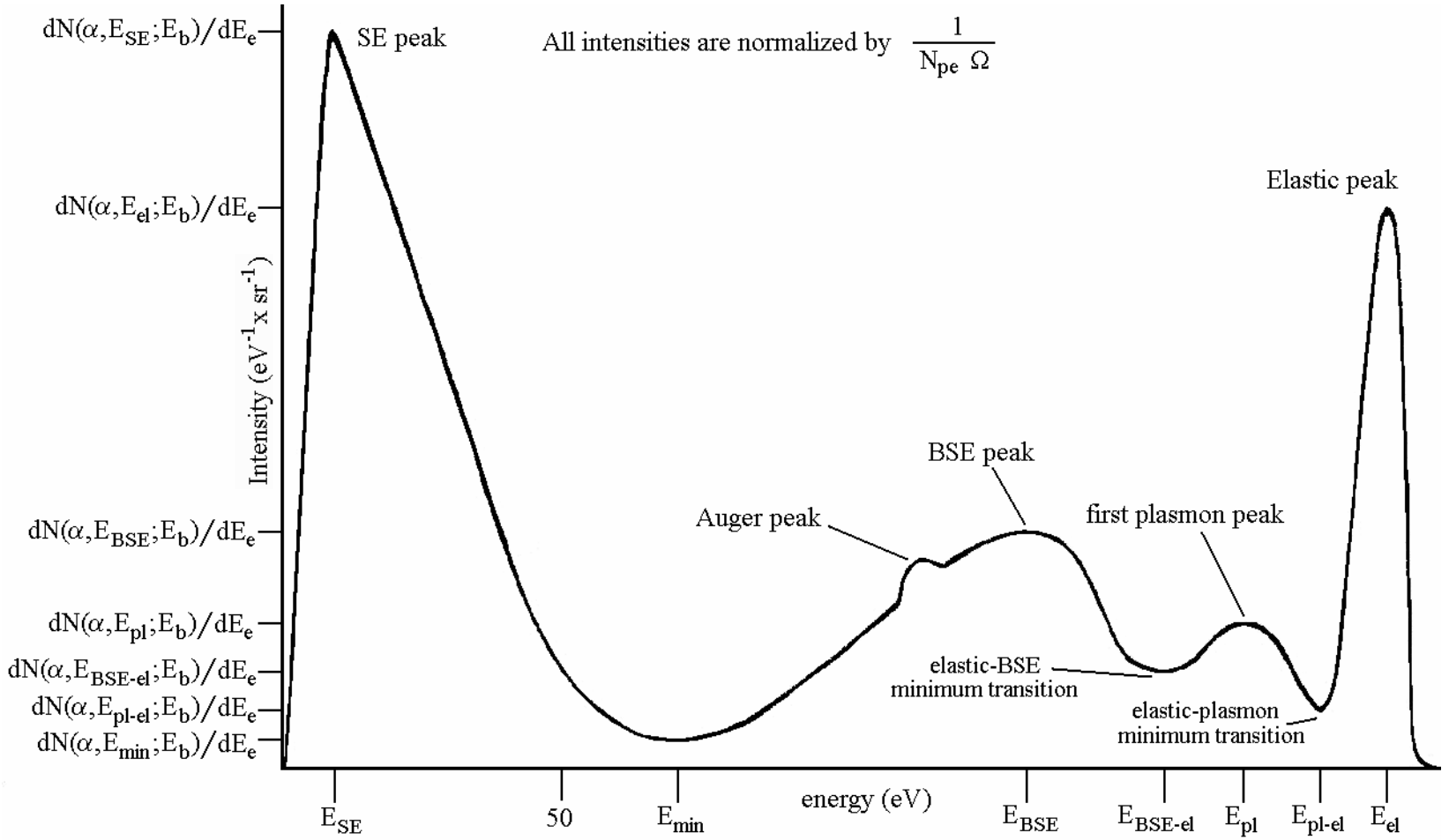

Figure 3- 37 Typical angle-resolved energy spectrum depicting the labeling and nomenclature of peaks and valleys. The energy positions are distorted for emphasis.

Table 3.3 Spectral and Integrated Yield Labels

Feature	Spectral label	Nomenclature	Dissertation Section	Limits (eV or ^{o})
Elastic Peak				
	ElasticPeakEnergy	E_{el}	5.1.(a)	
	ElasticPeakIntensity	$dN(\alpha,E_{el};E_b)/dE_e$	5.1.(b)	
	ElasticPeakYield	$\delta(\alpha,E_{el};E_b)$	5.1.(d)	$E_{pl\text{-}el}$ to E_b
First Plasmon Peak				
	PlasmonPeakEnergy	E_{pl}	5.2.(a)	
	PlasmonPeakIntensity	$dN(\alpha,E_{pl};E_b)/dE_e$	5.2.(b)	
	PlasmonPeakYield	$\delta(\alpha,E_{pl};E_b)$	5.2.(d)	$E_{BSE\text{-}el}$ to $E_{pl\text{-}el}$
BSE Peak				
	BSEPeakEnergy	E_{BSE}	5.3.(a)1	
	BSEPeakIntensity	$dN(\alpha,E_{BSE};E_b)/dE_e$	5.3.(a)2	
	BSEYield (50 eV)	$\eta_{50}(\alpha,E_{BSE};E_b)$	5.3.(c)1	50 to E_b
	BSEYield (E_{min} eV)	$\eta_{Emin}(\alpha,E_{BSE};E_b)$	5.3.(c)2	E_{min} to E_b
SE Peak				
	SEPeakEnergy	E_{SE}	5.4.(a)1	
	SEPeakIntensity	$dN(\alpha,E_{SE};E_b)/dE_e$	5.4.(a)2	
	SEYield (50 eV)	$\delta_{50}(\alpha,E_{SE};E_b)$	5.4.(b)1	0 to 50
	SEYield (E_{min} eV)	$\delta_{Emin}(\alpha,E_{SE};E_b)$	5.4.(b)2	0 to E_{min}
	SEYield (20 eV)	$\delta_{20}(\alpha,E_{SE};E_b)$	5.4.(b)4	0 to 20
Auger signature				
	AugerEnergy	E_{AES}	5.4.(d)	
	AugerIntensity	$dN(\alpha,E_{AES};E_b)/dE_e$	5.4.(d)	
Elastic/Plasmon Minimum Transition				
	Elastic_PlasmonMinEnergy	$E_{pl\text{-}el}$	5.5.(b)1	
	Elastic_PlasmonMinIntensity	$dN(\alpha,E_{pl\text{-}el};E_b)/dE_e$	5.5.(b)2	
Elastic/BSE Minimum Transition				
	Elastic_BSEminEnergy	$E_{BSE\text{-}el}$	5.5.(c)1	
	Elastic_BSEminIntensity	$dN(\alpha,E_{BSE\text{-}el};E_b)/dE_e$	5.5.(c)2	
E_{min} Transition				
	EminEnergy	E_{min}	5.5.(a)1	
	EminIntensity	$dN(\alpha,E_{min};E_b)/dE_e$	5.5.(a)2	
Angle Integrated BSE Yield		$\eta_{ER}(\alpha,E_{BSE};E_b)$	5.3.(c)5	50 to E_b E_{min} to E_b
Angle Integrated SE Yield		$\delta_{ER}(\alpha,E_{SE};E_b)$	5.4.(b)5	0 to 50, E_{min}, 20
AR SE Yield		$\delta_C(\alpha;E_b)$	5.4(c)	0 to 50,450
E_bR Total Yield		$\sigma_C(E_b)$, $\sigma_F(E_b)$	5.6	0 to E_b
AR Total Yield		$\sigma_C(\alpha;E_b)$	5.7	0 to 90
		$\sigma_N(\alpha;E_b)$	5.9	0 to 90
AE_bR Total Yield		$\sigma_C(E_b;\alpha)$		0 to E_b

3.4 DATA ACQUISITION PROCEDURE

Values in the AER spectra are determined by the ratio of outgoing electrons from the sample to incoming electrons to the sample.

$$\frac{d^2N(\alpha', E_e'; E_b')}{d\Omega\, dE_e} = \frac{I_{RD}}{I_{beam}} \qquad (3.12a)$$

In Eq. (3.6a), I_{RD} is the current from the scattered electrons entering the Rotatable Detector and I_{beam} is the primary beam current hitting the sample. The uncertainty in the AER cross section should then follow directly from the uncertainties in I_{RD} and I_{beam}. I_{RD} is measured directly while measuring $d^2N/d\Omega dE_e$ as discussed below. I_{beam} can only be measured accurately with a Faraday cup.

3.4.(a) Previous Data Acquisition Procedure

Direct measurement of I_{beam}, using a Faraday Cup, cannot be made simultaneously with the measurement of an AER data point. Davies employed a method whereby I_{beam} was measured directly using a Faraday Cup, immediately before and after measuring each AER data [Davies 1999, p.42, p. 221]. The average of the two beam currents $<I_{beam}>_{M=2}$ was used in Eq. (3.6a) so that

$$\frac{I_{RD}}{I_{beam}} = \frac{< I_{RD} >_N}{< I_{sample} >_N} \bullet \frac{< I_{sample} >_M}{< I_{beam} >_M} \qquad (3.13)$$

where averages are taken over N measurements per AER data and <, > symbols indicate averaging. The N index was typically 100 including a running average. Since I_{sample} is equal to I_{beam} while the incident electron beam is in the Faraday Cup, a resulting normalization of the spectral data occurred.

3.4.(b) Beam Current Scales with Controller Voltage

In a slightly different approach, the uncertainty in I_{beam} measurements can be reduced using a method of indirectly measuring I_{beam} and simultaneously measuring I_{RD} and I_{sample}. It has been found that the I_{beam} scales in direct proportion to the controller voltage, $V_{controller}$, [Fig. 3-38] for all beam energies.

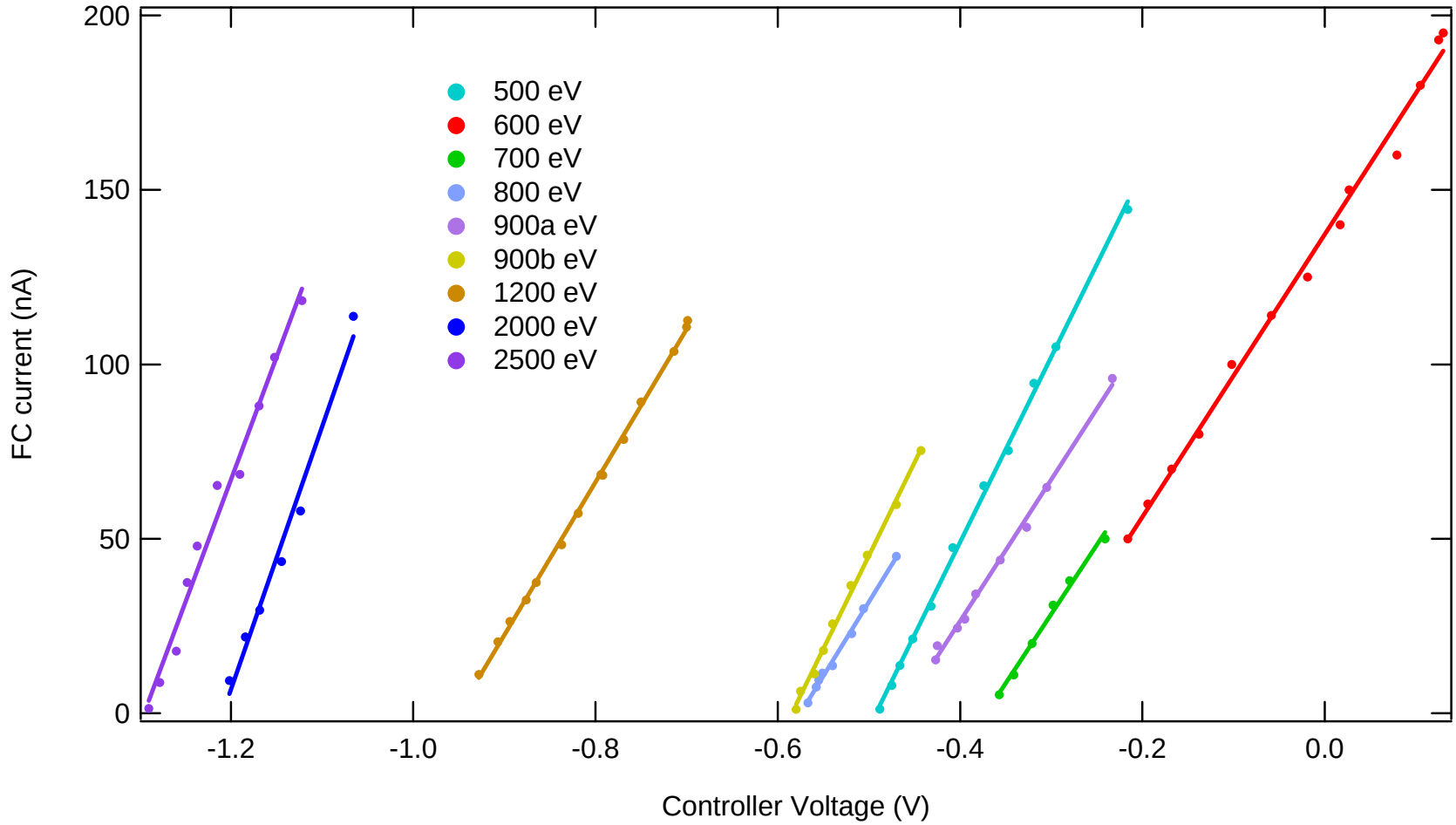

Figure 3- 38 Beam Current vs. Controller Voltage for several incident beam energies. Line fits are included.

Thus a simultaneous measurement of $V_{controller}$ is the optimal approach for determining the amount and sequencing of count data and rate due to the short term jitter [Fig. 3-12] and long term drift [Fig. E-1] within the electron gun controller. Using the following linear relationship,

$$< I_{beam} >= \alpha(E_b) + \beta(E_b) * < V_{controller} > \tag{3.14}$$

$V_{controller}$ can be scaled to I_{beam} by direct measurement using a Faraday Cup, immediately before and after measuring each AER data Eq. (3.14). There is a dependence of the proportionality constants (α and β) on incident beam energy, E_b. The consolidation of the linear relationship between I_{beam} and $V_{controller}$ showing the slope, β, and intercept, α, versus the beam energy, E_b, is shown in Fig. 3-39. The uncertainties in $\alpha(E_b)$ and $\beta(E_b)$ are evaluated by least-squares-fitting technique and participate in the error analysis. Substitution of Eq. (3.13) and Eq. (3.14) into Eq. (3.12a) results in

$$\frac{d^2N(\alpha', E_e'; E_b')}{d\Omega\, dE_e} = \frac{< I_{RD} >_N}{< I_{sample} >_N} \bullet \frac{< I_{sample} >_M}{\alpha(E_b) + \beta(E_b) * < V_{controller} >_M} \tag{3.12b}$$

In practice, long-term variations (drift) in $V_{controller}$ during the experiment introduce deviations into Eq. (3.12b) as indicated previously in Fig. 3-12. Since $V_{controller}$, I_{RD}, and I_{sample} are simultaneously measured as averages over N, additional averaging of the second term in Eq. (3.6b) is used to calculate the ratio $<I_{sample}>_M/<I_{beam}>_M$ so that M is some multiple of N. This effectively separates the treatment of the first and second half of the Eq. (3.12b). Choice of the correct multiple, L, minimizes the drift introduced into the $V_{controller}$ signal and presents the operational formula for AER cross section point.

$$\frac{d^2N(\alpha', E_e'; E_b')}{d\Omega\, dE_e} = \frac{< I_{RD} >_N}{< I_{sample} >_N} \bullet < \frac{< I_{sample} >_N}{\alpha(E_b) + \beta(E_b) * < V_{controller} >_N} >_L \tag{3.12c}$$

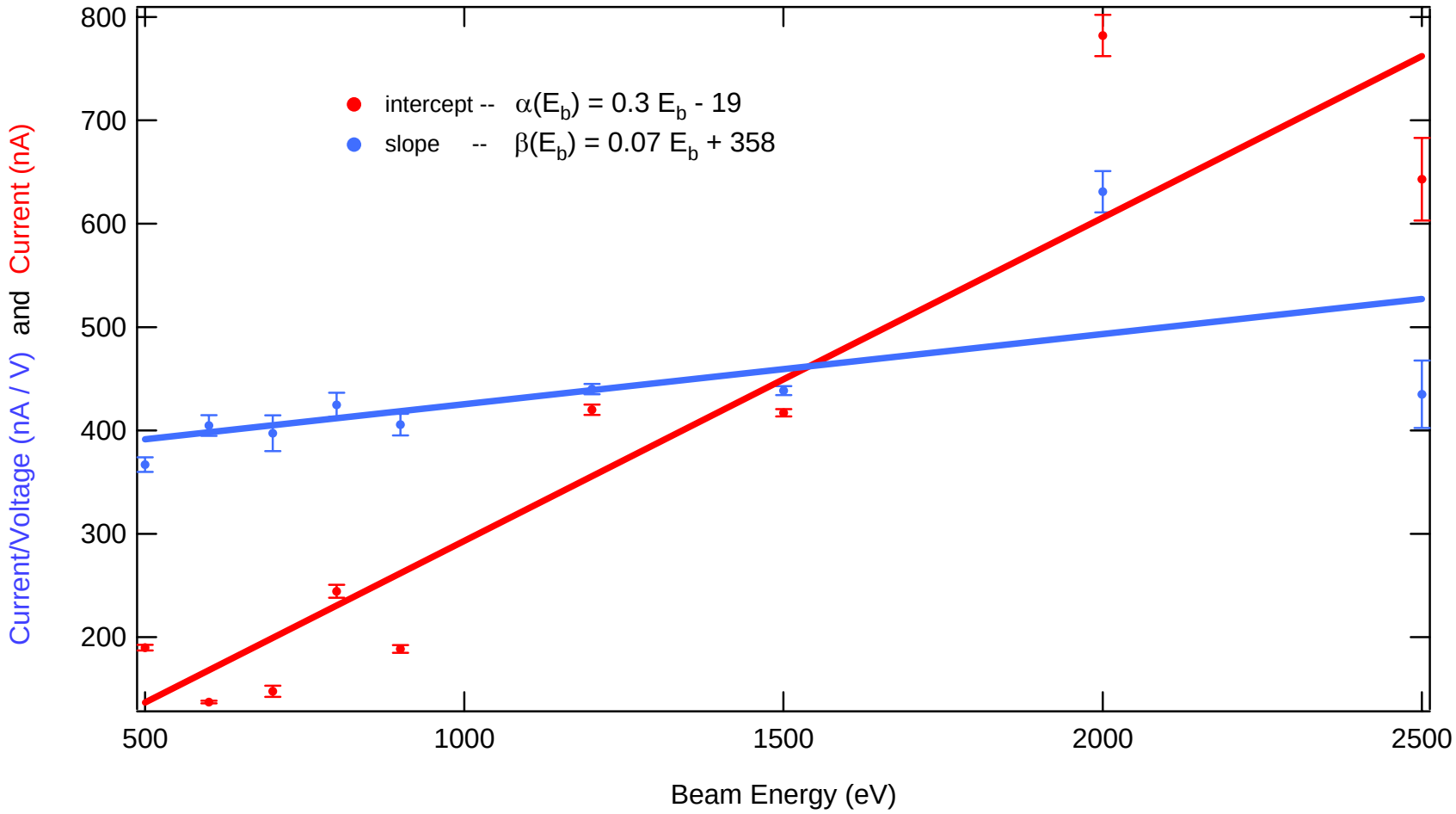

Figure 3- 39 Slopes and Intercepts of Beam Current to $V_{controller}$ data. Line fits of the intercept and slope are also provided.

Averaging over the second term in Eq. (3.12c) provides absolute AER data, where N is typically 10^3 taken over a time period of 10^1 sec and L is typically 10^2 taken over a time period of 10^3 to 10^4 sec. The proportionality constants of the I_{beam} to $V_{controller}$ relation are provided. The linear relationship of the intercept proportionality constant, $\alpha(E_b) = 0.3\ E_b - 19$, falls outside of all the error bars of the data. The linear relationship of the slope proportionality constant, $\beta(E_b) = 0.07\ E_b + 358$, falls within the error bars of the lower beam energy data. These proportionality constants give a glimpse of the inner workings of the gun controller circuit detailed in Appendix A. In order to optimize the timing range, the counting indices N and L are determined in the following section.

3.4.(c) Determination of Quantities of Data

An experiment was conducted to determine the optimum quantities of data, N, for a given E_e, α, and E_b. I_{sample} was measured as an analog-out voltage signal from an electrometer by the DAQboard2000. A linear relationship between I_{sample} and V_{sample} was assumed because of the constancy of the Kiethley 160 Operational Amplifier range. Figure 3-40 shows five data files taken with varying counting statistics of voltage samplings per set. Several sets make up a file. Each set is comprised of varying amounts of samplings, N. The number of samples per set varied from $N = 10^0$ to $N = 10^4$. The set sampling rate and delay time between sets were held constant at 66kHz and 1ms respectively. These normalized data showed a decrease of approximately 7% in 20 minutes as the sample current drifted. The normalized standard deviation calculated by the computer for each data set is shown as an error bar. The means of these normalized standard deviations for 10^0, 10^1, 10^2, 10^3, and 10^4 voltage readings per set grows steadily from 0 to 1.5% [Fig. 3-41, blue squares]. Here, the "drift" is associated with the long-term noise. The standard deviation of the mean, SDOM, was also calculated for each file for comparison. The sample SDOM remained constant at 0.2 nA [Fig. 3-41, red circles]. In order to determine the "jitter", or short-term noise, the first derivative's standard deviation of the mean was calculated. A comparison was made for each file's first derivative's SDOM, which decreased steadily from 1.26 nA/s to 0.04 nA/s [Fig. 3-41, green diamonds].

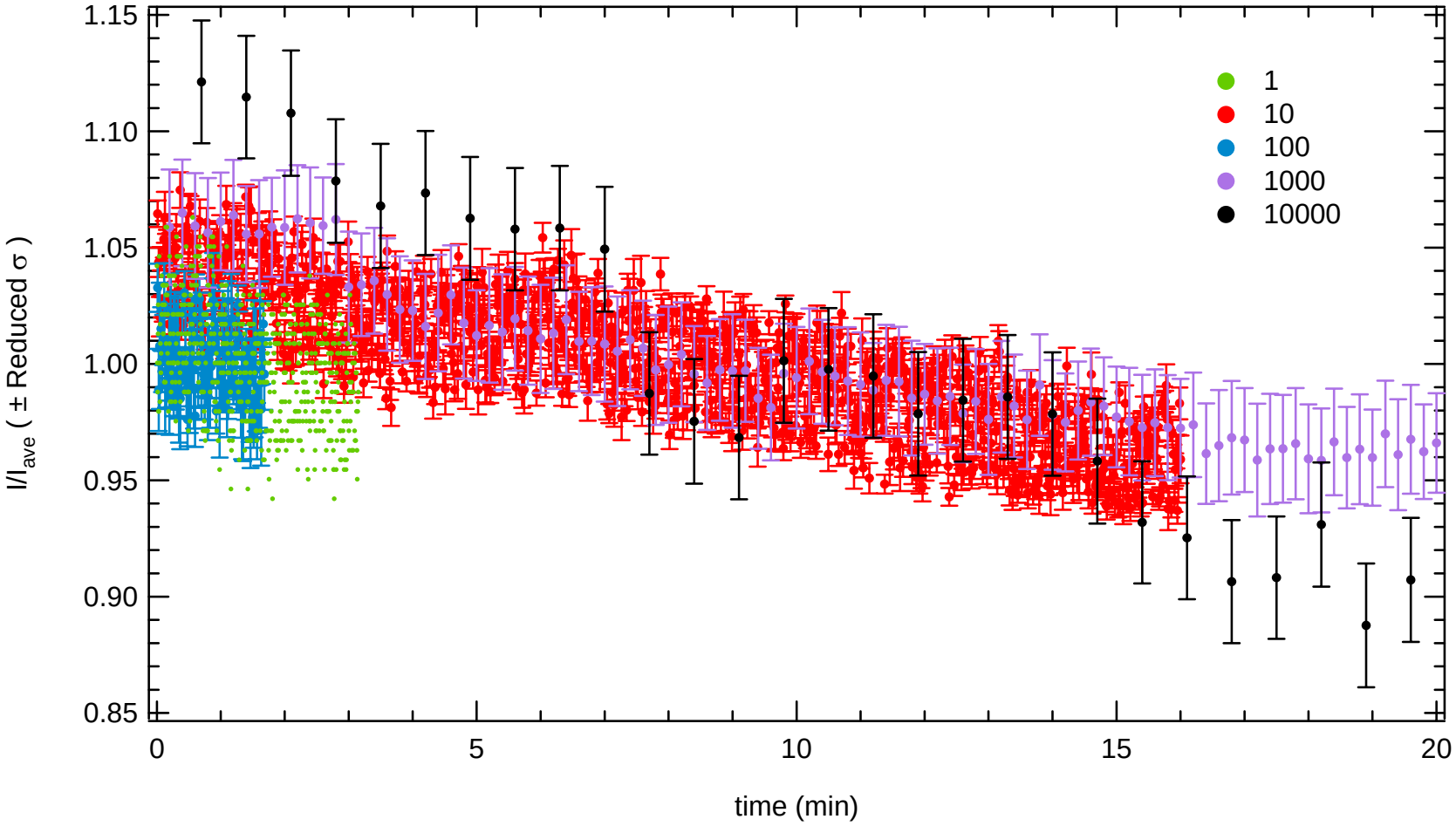

Figure 3- 40 Sample current data given in I/I_{ave} with error bars of σ/I_{ave} with sampling size per set varying in order of magnitude from 1 to 4.

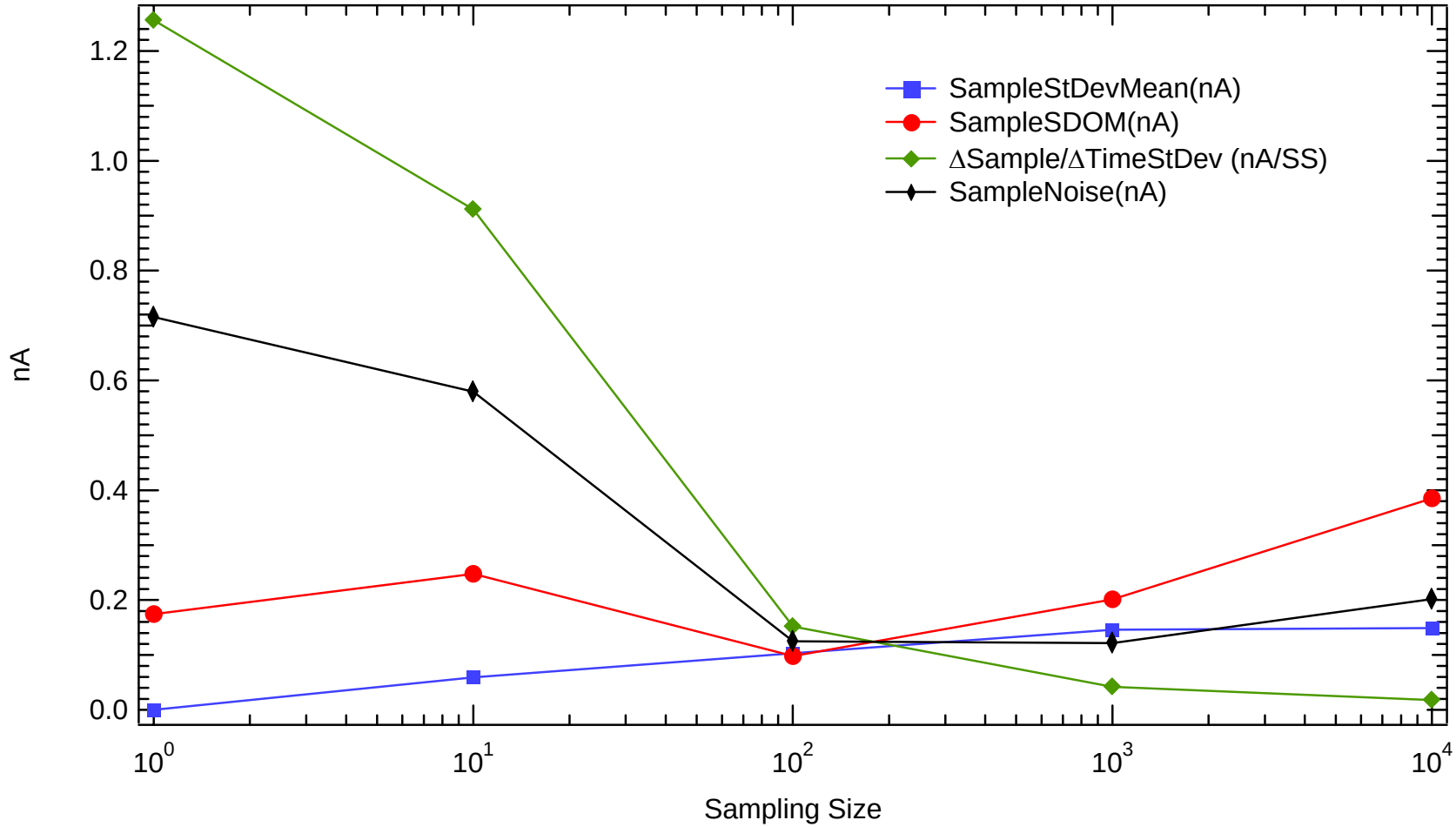

Figure 3- 41 Results showing the mean of SampleStDev, Sample Standard Deviation of the mean, the St Dev of the derivative in nA/SS, and SampleNoise in nA.

The sample noise was calculated as the average of the "drift" noise and the "jitter" noise [Fig. 3-41, black diamonds]. In order to minimize the uncertainty in I_{sample}, and hence optimize the sampling size, N, the sample noise minimum was found. The number of samplings per set is an optimum between sampling sizes of 10^2 and 10^3.

Corresponding measurements for the $V_{controller}$ signal are shown in Fig. 3-42. The respective statistical results for the $V_{controller}$ signal [Fig. 3-43] conclude an optimum near the 10^3 sampling size. For the remainder of this work, both the I_{sample} and $V_{controller}$ signals have been taken using identical sampling sizes of 10^3, which gives a 10 second acquisition time per AER measurement.

Since the counting statistics for $V_{controller}$ are a minimum at 10^3 sampling size, then the averaging index, L, should be limited to the size of the bias range provided by the Keithley 237 biasing scheme. In order to be consistent with the computer automation of the biasing scheme, averages over each angle for the entire bias range of the Kiethley 237 data range will determine the counting index, L = 220.

All of the angle-resolved energy spectra presented here are "pieced" together. This is done because the instrument is entirely automated except for the Bertan biasing voltage. The "mini"-spectra for all 12 angles are measured together for one programmed Keithley bias range. After the Bertan voltage is changed, then the overlapping "mini"-spectra for all 12 angles is repeated and "pieced" next to the previous "mini"-spectra. The process is repeated until the entire energy range, $0 < E_e < E_b$, is measured.

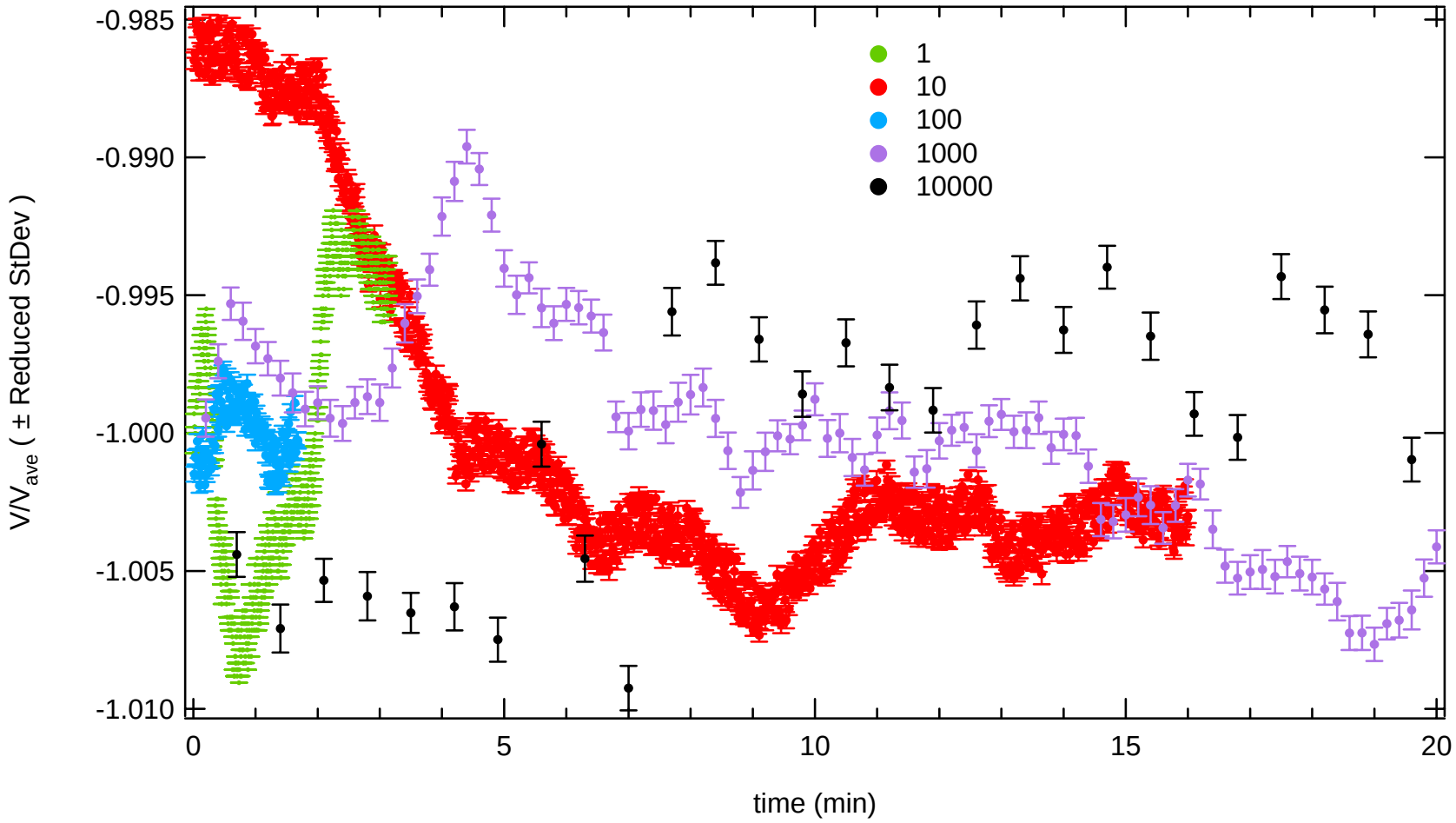

Figure 3- 42 Beam current controller voltage with error bars of StDev/V_{ave} for varying samples per average.

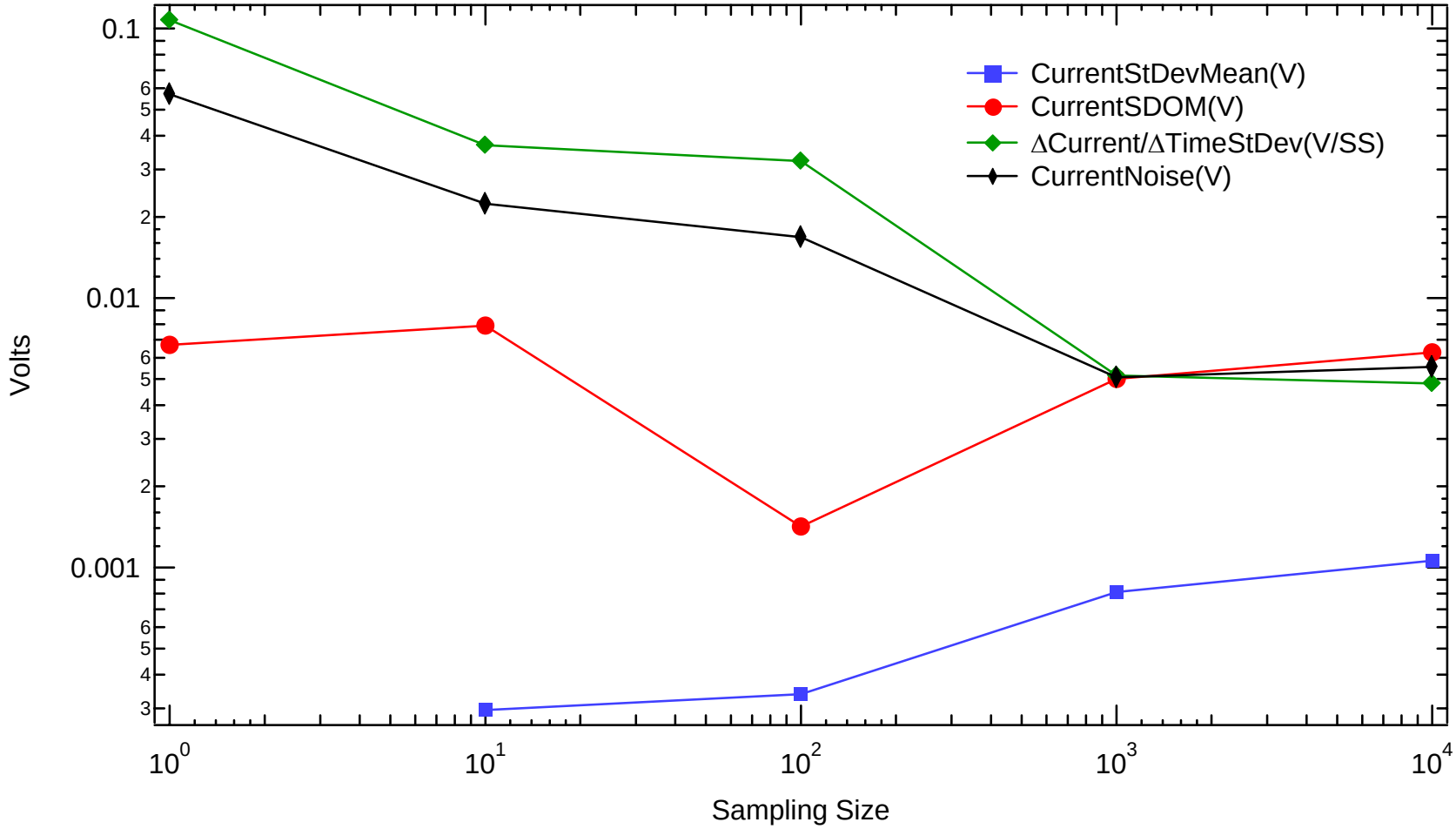

Figure 3- 43 Results of the CurrentAveStDev, CurrentReducedAveStDev, and CurrentNoise in volts and the StDev of Δcurrent/Δtime in volts/SampleSize.

3.5 MEASUREMENT TECHNIQUES

Determinations of all of the quantities described above are obtained via the measurement of net currents reaching various surfaces—under varying conditions of electrical bias—within the chamber apparatus. Net currents measured are those reaching the primary and tertiary samples at biases of 0 V and +50 V, and that reaching the Faraday cup inside the RD, with the Faraday cup biased anywhere between 0 V and $-E_b$ V. Since the angle-energy-resolved yields are the most fundamental quantities in this investigation—from which all other quantities can, in principle, be calculated—the measurement technique for their determination is presented first followed by an ad-hoc calculation for the incident beam energy resolution. Specific procedures for acquiring data with these techniques are now presented.

3.5.(a) δ_{AER} Determination

For a given emission angle α', determination of $\delta(\alpha', E_e'; E_b')$ is accomplished through RD current measurements performed at successively larger negative detector biases, Φ_{RD}, as follows: biasing the detector negatively serves to reject those electrons with energies $E_e < e\Phi_{RD}$ (for e the electron charge, in Coulombs, and Φ_{RD} the detector bias, in volts); one can then determine the current d^2I_{12} due to secondaries with energies between E_1 and E_2 (centered on α') via the relation $d^2I_{12} = dI_{\phi 1} - dI_{\phi 2}$. If we define $E_{e12} = (E_1 + E_2)/2$, we can then calculate $\delta(\alpha', E_e'; E_b')$ via

$$\delta(\alpha', E_e', E_b') = \frac{1}{I_B} \frac{d^2 I_{12}}{d\Omega_{RD}\, dE_{e12}} \tag{3.15}$$

for I_B the beam current, $d\Omega_{RD}$ the solid angle subtended by the detector, and $dE_{e12} = e(\Phi_{RD1} - \Phi_{RD2})$ the energy interval $E_1 - E_2$.

We now note that measurement of $\delta(\alpha', E_e'; E_b')$ at a fixed α' for a sufficient number of energies in the range $0 \le E_e' \le E_b$ eV, constitutes an angle-resolved energy *spectrum*, denoted

$\delta(\alpha', E_e; E_b')$. The absence of the prime on E_e is intended to emphasize the word *spectrum* as function-like. The differential yield, $\delta(\alpha', E_e'; E_b')$, is a number. Though measurements of the energy-resolved angular distribution, $\delta(\alpha, E_e'; E_b')$, have been measured (appendix D), it is the angle-resolved energy spectra, $\delta(\alpha', E_e; E_b')$, that constitute the most important results of this investigation. Given a sufficient number of these AR spectra one can in principle determine the simultaneous energy-resolved angle distribution function. Finally, repeating this process for several beam energies, the angular distribution and energy distribution of yields as a function of beam energy, $\delta(\alpha', E_e'; E_b)$, can be calculated. All of the differential yields, $\delta(\alpha', E_e'; E_b')$, with respect to their variable resolutions provide the maximum amount of information one can extract about the scattered electron population from the LittleBoy.

3.5.(b) δ_{AR} Determination

For a given emission angle α', direct determination of $\delta(\alpha'; E_b')$ is accomplished through RD current measurements performed at varying detector biases. The direct measurement of the angle-resolved yield, $\delta(\alpha'; E_b')$ can also be calculated from the angle-resolved spectrum via

$$\delta(\alpha'; E_b')_{calc} = \int_0^{50eV} \delta(\alpha', E_e; E_b')\, dE_e \tag{3.16}$$

where the integration can be performed analytically if a sufficiently accurate fit to the spectrum is found, or numerically by computing the area under the $\delta(\alpha', E_e'; E_b')$ vs E_e curve. It is important to emphasize that Eqs. (3.15) and (3.16) represent two distinct (though not quite independent) methods of obtaining $\delta(\alpha', E_b')$; the two results can therefore be compared and their level of agreement used as one means of gauging the consistency of measurements obtained with the RD.

The calculation of $\delta(\alpha'; E_b')$ for a sufficient number of angles allows for the construction of an angular yield distribution, $\delta(\alpha; E_b')$. This distribution can also be determined via the angle-energy distribution function by integrating over the appropriate energy range of 0-50 eV:

$$\delta(\alpha, E_b') = \int_0^{50eV} \delta(\alpha, E_e, E_b')\, dE_e \tag{3.17}$$

3.5.(c) δ_{ER} Determination

Unlike the other quantities under discussion, $\delta(E_e'; E_b')$ is unique in that it cannot be directly measured with this instrument; in principle, however, it can be calculated from angle-energy-resolved yields via

$$\delta(E_e'; E_b') = 2\pi \int_0^{\pi/2} \delta(\alpha, E_e'; E_b') \sin\alpha \, d\alpha\,, \tag{3.18}$$

given $\delta(\alpha', E_e'; E_b')$ for a sufficient number of emission angles. The integral can then be calculated analytically if a suitable expression for the function $\delta(\alpha, E_e'; E_b')$ can be found, or numerically by computing the area under the $\delta(\alpha', E_e'; E_b')$ vs α curve.

As above, note that calculation of $\delta(E_e'; E_b')$ for a sufficient number of energies in the range $0 \le E_e' \le 50$ eV constitutes an *integrated* SE spectrum, $\delta(E_e; E_b')$—*i.e.*, integrated over all emission angles—or one might prefer to call it an energy distribution function. This angle-integrated spectrum could also be calculated via the angle-energy distribution function by integrating over all emission angles:

$$\delta(E_e, E_b') = 2\pi \int_0^{\pi/2} \delta(\alpha, E_e; E_b') \sin\alpha \, d\alpha \tag{3.19}$$

(where we have assumed the distribution symmetric with respect to the azimuthal angle φ).

3.5.(d) Determination of the Total SE Yield

The total SE yield is determined by direct measurement of δ described by Eq. (3.9), the total SE yield can be calculated from the angle-resolved yields via

$$\delta_{calc1} = 2\pi \int_0^{\pi/2} \delta(\alpha; E_b') \sin\alpha \, d\alpha \tag{3.20}$$

given $\delta(\alpha'; E_b')$ for a sufficient number of angles, or from the angle-resolved spectra via

$$\delta_{calc2} = 2\pi \int_0^{50eV} \int_0^{\pi/2} \sigma(\alpha, E_e; E_b') \sin\alpha \, d\alpha \, dE \tag{3.21}$$

given $\sigma(\alpha', E_e'; E_b')$ for a sufficient number of angles and energies. Here, it is important to note the method for determining δ described by Eq. (3.15) is entirely independent of that described by Eqs. (3.16) and (3.17): δ_{meas} is obtained with primary and tertiary sample current measurements, while δ_{calc1} and δ_{calc2} are derived via data obtained with the RD.

CHAPTER 4

SAMPLE

Data used to characterize and define the sample material provided in this investigation are the most current information available to date. The devotion of an entire chapter assures confidence in conclusions drawn from the data taken on the specific sample material. The material for the sample has already been chosen and characterized and will now be shown. A broader range of information about the sample material will be investigated to verify the purity, depth profile, morphology, and condition of the material at its surface. The preparation of the sample and its surface provides predictable evolution of the sample, concluding that the boundary conditions are well known.

The process of secondary electron emission (SEE) is essential for determining a valid preparation procedure involving processes of chemical cleaning, electron bombardment, sputtering, and annealing. Issues addressing SEE from the sample surface are presented in the following order: choice of sample material, sample information, and surface preparation. Comparison to previous measurement and theory are provided along with systematic error determination of SEE and a brief conclusion.

4.1 Choice of Sample Material

There are four major reasons for choosing the appropriate material for this investigation. The first two reasons are related to the capabilities of the instrument addressed in chapter 3 and the last two reasons are based on proposed desires addressed in chapters 1 and 2. The selection of a sample material for this investigation was based on the following:

- the need to further verify and evaluate the instrument and methods;
- the absence of *in situ* surface characterization capabilities;
- the desire to perform new energy- and angle- resolved (EAR) SEE measurements; and

- the desire to accomplish some level of theoretical evaluation based on the measurements in these experimental results.

Weighing in these considerations, polycrystalline gold has been chosen to serve as the appropriate material for study in this investigation. In addition, there are a number of advantages that polycrystalline gold offers:

.

i) Previous δ and η determinations, performed by other investigators, are readily available in the literature and in reasonable agreement with one another [*Davies*, 1999; *Thomas and Pattinson*, 1970; *Kanter*, 1957; *Holliday and Sternglass*, 1957; *Reimer and Drescher*, 1977]. Comparison of total, SE, and BSE yields obtained in previous work by Davies, along with results obtained in the literature are therefore an important means of instrument verification.

ii) Gold has no known physisorbed or chemisorbed contaminants (no oxidation). Gold is therefore relatively easy to clean and to keep clean, allowing some measure of confidence in surface condition—an important consideration given our present inability to perform *in situ* surface characterization.

iii) Gold remains essentially uncharacterized with respect to angle-resolved SE spectra. However, the preparation of samples by Davies present an opportunity for additional contribution of new measurements to the field.

iv) Finally, there exist a number of theoretical SEE and backscattering formulations, applicable to gold, in need of experimental evaluation [*Chung and Everhart*, 1974; *Rösler and Brauer*, 1981a; *Gannachaud and Callier*, 1979a; *Jablonski et al*., 1989, *Jablonski*, 1991; *Jablonski et al*., 1993].

Several Au samples obtained commercially from the Aldrich Company have been cut from a piece of 0.127-mm thick, 4N purity Au foil. Data used to characterize and define the Au sample material for this investigation were collected from 4 identical Au samples. The Au samples were approximately 1 x 1 cm.

4.2 Sample Information

The pristine Au sample is very pure, however the unprepared surface is not optimum for immediate investigation due to contaminant impurities, polycrystalline size variance, and surface roughness. The Au sample material has been characterized extensively at the science facilities located at Utah State University. Much of the information used to define and characterize the sample material are *ex situ* measurements. The density and trace analysis, morphology, and surface condition provide the best bulk and surface properties available for identifying general information of the Au sample material.

4.2.(a) Trace analysis

Elemental trace analysis of the high purity sample was accomplished using Atomic Adsorption/Inductively Coupled Plasma Emission Analysis at USU Soil Science Laboratory. Elemental resolution of the instruments is ~3 ppm. Specific traces of Ag measure 10 ppm, and all other trace measurements of Cu, Pd, and Si are less than the resolution of the instrument.

4.2.(b) Morphology

The morphology of the sample surface has been measured with optical microscopy using an Intel Q3X microscope at 10x, 60x, 100x, and 200x magnification [Fig 4-1]. At these low resolutions, the average surface roughness is estimated to be <10 μm over a surface area of 1 mm^2. Over larger surface areas, the sample surface is shown to be generally smooth, though long thin scratches (~ 2 mm to 10 mm) on the surfaces are visible. These long parallel surface scratches are clearly evident measuring ~50 μm apart. A higher resolution Olympus BX41 microscope containing Mitutoyo lenses has surveyed the surface and recorded, with a Nikon D70 digital camera, magnifications of 150x, 300x, 750x, and 1500x [Fig. 4-2] to provide comparative surface morphology. With the higher powered microscope, average surface roughness can be estimated to be <0.1 μm over a surface area of 1 mm^2. Among the few present scratches

(a)

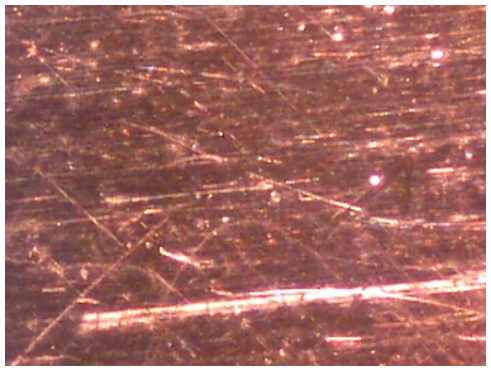

(b)

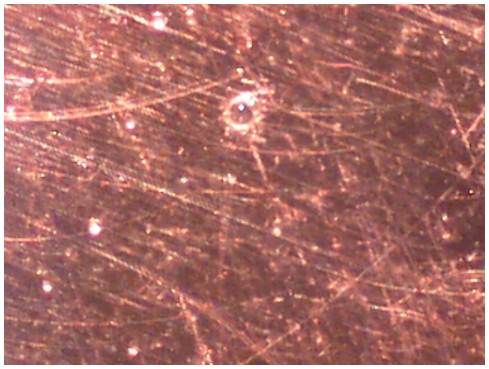

(c)

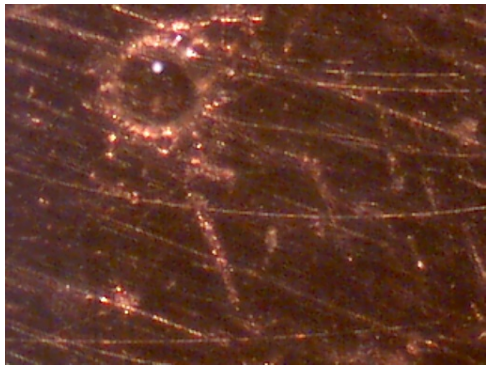

(d)

Figure 4-1 Optical micrograph images of the sample gold material. (a) Image using Intel QX3 microscope at 10x magnification showing an image of size 15 mm (h) x 23 mm (w). (b) Image using Intel QX3 microscope at 60x magnification showing an image of size 2.3 mm (h) x 3.1 mm (w). (c) Image using Intel QX3 microscope at 100x magnification showing an image of size 1.30 mm (h) x 1.90 mm (w). (d) Image using Intel QX3 microscope at 200x magnification showing an image of size 0.65 mm (h) x 0.95 mm (w).

(b)

(b)

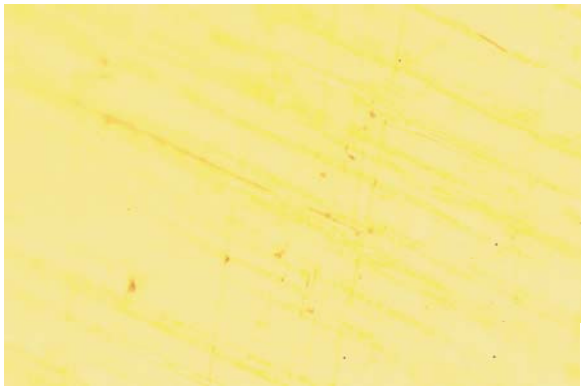

(c)

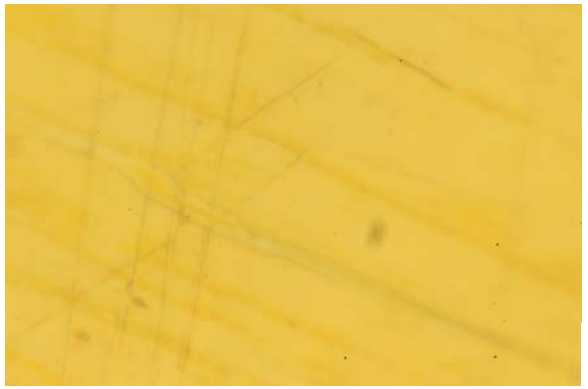

(d)

Figure 4-2 Optical micrograph images of the sample gold material. (a) Image using Olympus BX41 microscope at 150x magnification showing an image of size 0.64 mm (h) x 0.98 mm (w). (b) Image using Olympus BX41 microscope at 300x magnification showing an image of size 0.32 mm (h) x 0.49 mm (w). (c) Image using Olympus BX41 microscope at 750x magnification showing an image of size 0.13 mm (h) x 0.20 mm (w). (d) Image using Olympus BX41 microscope at 1500x magnification showing an image of size 0.06 mm (h) x 0.10 mm (w).

(~5 μm apart), small features, on the scale of 0.1 μm are visible in the images.

The STM image of polycrystalline gold [Fig. 4-3] measured at the USU surface science laboratory is shown to have an RMS surface roughness of ~8 nm. The maximum peak-to-peak vertical displacement for the 1.96 μm^2 sample surface is 78 nm. The included surface histogram depicts the largest occurring number of vertical displacements at ~ 30.0 nm with average occurring number of vertical displacements at 32.6 nm.

4.2.(c) Surface Condition

Surface contamination was measured within the FatMan chamber at the USU surface science laboratory using a Varian Auger Electron Spectrometer (AES) operating at 2 keV with a beam current of ~ 1 μA and a 20 μm diameter beam spot [Fig. 4-4]. Only the top ~1 nm of the sample is probed with AES. Resolution for contamination is ~0.1 monolayer. The relative amount of surface contamination is estimated from analysis of the integrated area of each feature in the measured AES curves, based on the relative sensitivity of each peak as studied in the most current research [*Tsutsumi et. al., 2006*]. The thickness of contamination was determined from the relative amounts (integrated peak heights) of bulk material versus contaminates in combination with estimated electron mean free paths for Auger electrons [Lindau]. For clean, unsputtered samples, carbon contamination was observed, with relative concentration of (51± 5) %, when compared with the gold peak. The surface contamination layer was estimated to be ~1.4 ± 1 monolayers or ~0.2 ± 0.1 nm thick. For sputtered samples, carbon was observed, with relative concentration of (16 ± 2) %, when compared with the gold peak. The surface contamination layer was estimated to be ~(0.3 ± 0.2) monolayers or ~(0.05 ± 0.05) nm thick.

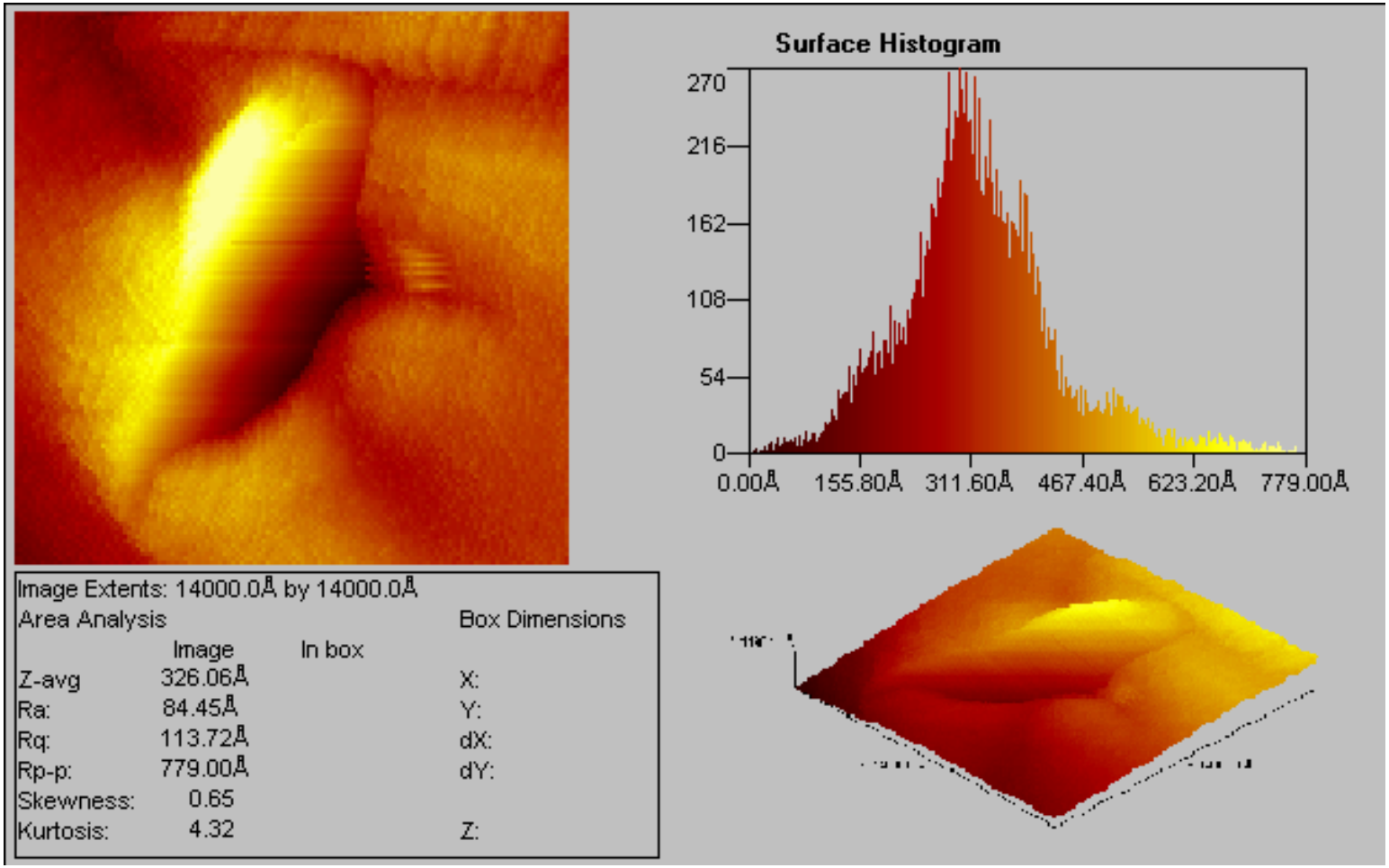

Figure 4-3 Scanning tunneling microscope (STM) image of the polycrystalline Au sample material. The sample size is 1.4 μm x 1.4 μm with a maximum peak-to-peak vertical displacement of 78 nm and an RMS surface roughness of ~8 nm.

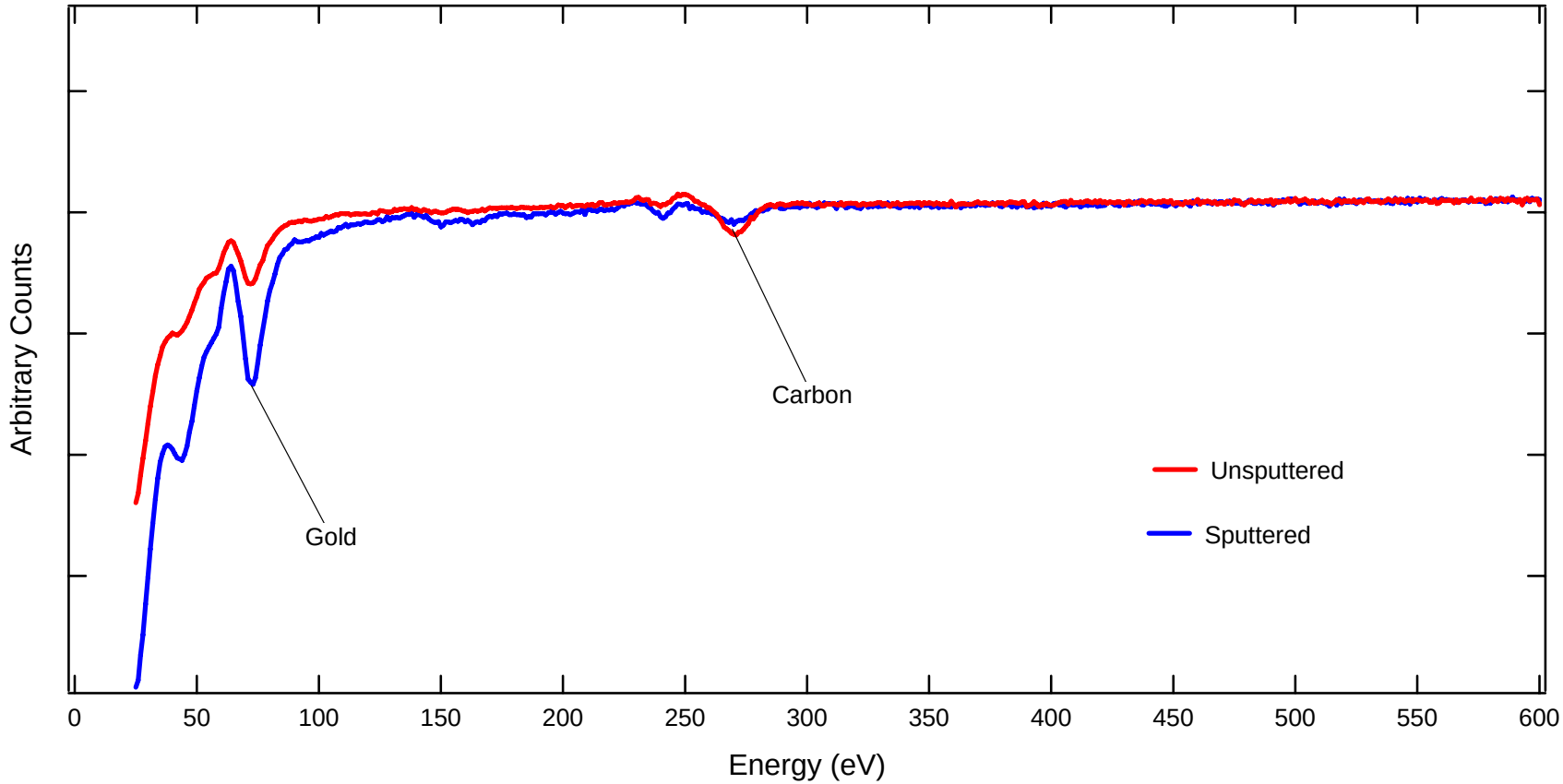

Figure 4-4 Auger Electron Spectra (AES) of polycrystalline Au. Samples before (red) and after (blue) Ar sputtering.

4.3 Surface preparation

Preparations of the sample surface are accomplished both before and after insertion of the sample into the chamber apparatus. The procedural steps involved have been studied extensively using various preparation techniques. Prior to this investigation, many samples were prepared for measurement [*Davies*, 1996, 1999] within the LittleBoy. In this investigation, only one sample was used that had been previously prepared and measured [*Davies*, 1999]. Sample "D" [Fig. 4-5] and its preparation procedures have been adopted to minimize the evolution of the sample [*Davies and Dennison*, 1997; *Dennison, Kite, Chang, and Davies*, 2000]. Predictable evolution of Sample "D" and its surface requires reliable preparation procedures involving a chemical cleaning (and flaming) of the sample surface before vacuum insertion, Argon sputtering the sample surface with 500 V ions at 1.5 μA beam current for ~3 hrs, and annealing the sample with the sample heater to 300 ^{o}C for times of ~20 hrs to 60 hrs. Evaluation of these preparation procedures is accomplished by measurement of the electron bombardment yields. Therefore, an overview of the conclusions given in the previous investigation [Davies, 1999] provide crucial information about the effects, which evaluate the preparation of the surface using the techniques of electron bombardment, sputtering, and annealing.

Measurements utilizing the tertiary return current detectors emphasize the total yield (σ), SE yield (δ), and BSE yield (η), by potentially biasing the detectors to the customary +50 volt demarcation. The yields are calculated from the ratio of the differences of the sample, I_S, and tertiary, I_r, currents biased to +50 V and 0 V and the beam current, I_B, shown in the following relations

$$\delta_{meas} = \frac{\left[I_{S(50)} - I_{r(50)}\right] - \left[I_{S(0)} - I_{r(0)}\right]}{I_B} \tag{4.1}$$

$$\eta_{meas} = \frac{I_B - I_{S(50)} + I_{r(50)}}{I_B} \tag{4.2}$$

Just prior to chamber insertion, a given sample was affixed to a primary sample blank (a 25 x 25-mm piece of rhodium-coated OFHC copper) with a small amount of silver paint—a conducting, UHV-compatible adhesive (LB III, p. 30w). The photograph of Au sample "D" is a consistently flat sample with the exception of some irregular depressions [Fig. 4-5], most evident in the lower corners. These depressions were not selected for electron bombardment.

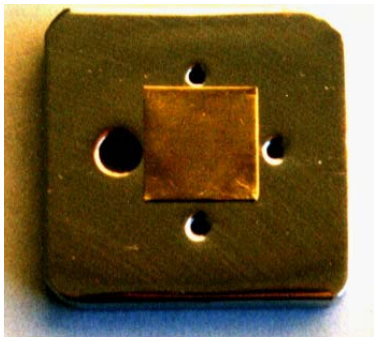

Figure 4-5 Au sample "D" mounted between four Faraday cups on a rhodium-coated blank.

To determine the effects of surface preparation on Au sample "D", Davies measured SE and BSE yield values [Fig. 4-6] using Eq. (4.1) and Eq. (4.2), which are tabulated in Table 4-1. Comparing these yield values, the effects of electron bombardment, sputtering, and annealing are evaluated. The eight key results useful in characterizing and preparing sample "D" are shown in the list below [*Davies, 1999*]. Preparation of the surface concluded that:

1. Gold samples were generally smooth at the micron level.

2. Argon sputtering resulted in surfaces contaminated with deeply embedded argon, affecting both δ and η determinations (D4, D6, D7, D8, and D11). Neon sputtering also produced consistent values for both δ and η (D9).

3. Surfaces that most closely resemble pure gold are sputtered, baked-out surfaces. A sputtered (or atmosphere-exposed) surface always drives δ and η in opposite directions (4.3(c)3). δ decreases and η increases, while σ remains constant (D3→D4 and D10→D11). Consistent with negative surface charging, the work function is changed by the removal (or adsorption) of physisorbed contaminants (4.3(d)3) resulting in a boosted kinetic energy of an emitted electron.

4. System bakeout anneal give rise to a maximum δ and a minimum η (D3).

5. Light electron beam bombardment and short-duration annealing result in small (~10% or less), but repeatable changes in δ and η (D1a, D5a, D6a, and D7a).

6. SEE and backscattering characteristics were generally uniform across the sample surfaces.

7. Systematic error in the SE and BSE yield determinations is in the range –6% to –20% for δ, and +15% to +51% for η (4.4(a)).

8. Light electron bombardment of a sputtered surface after an extended (~1 month) UHV exposure has no significant effect on either δ or η (D9).

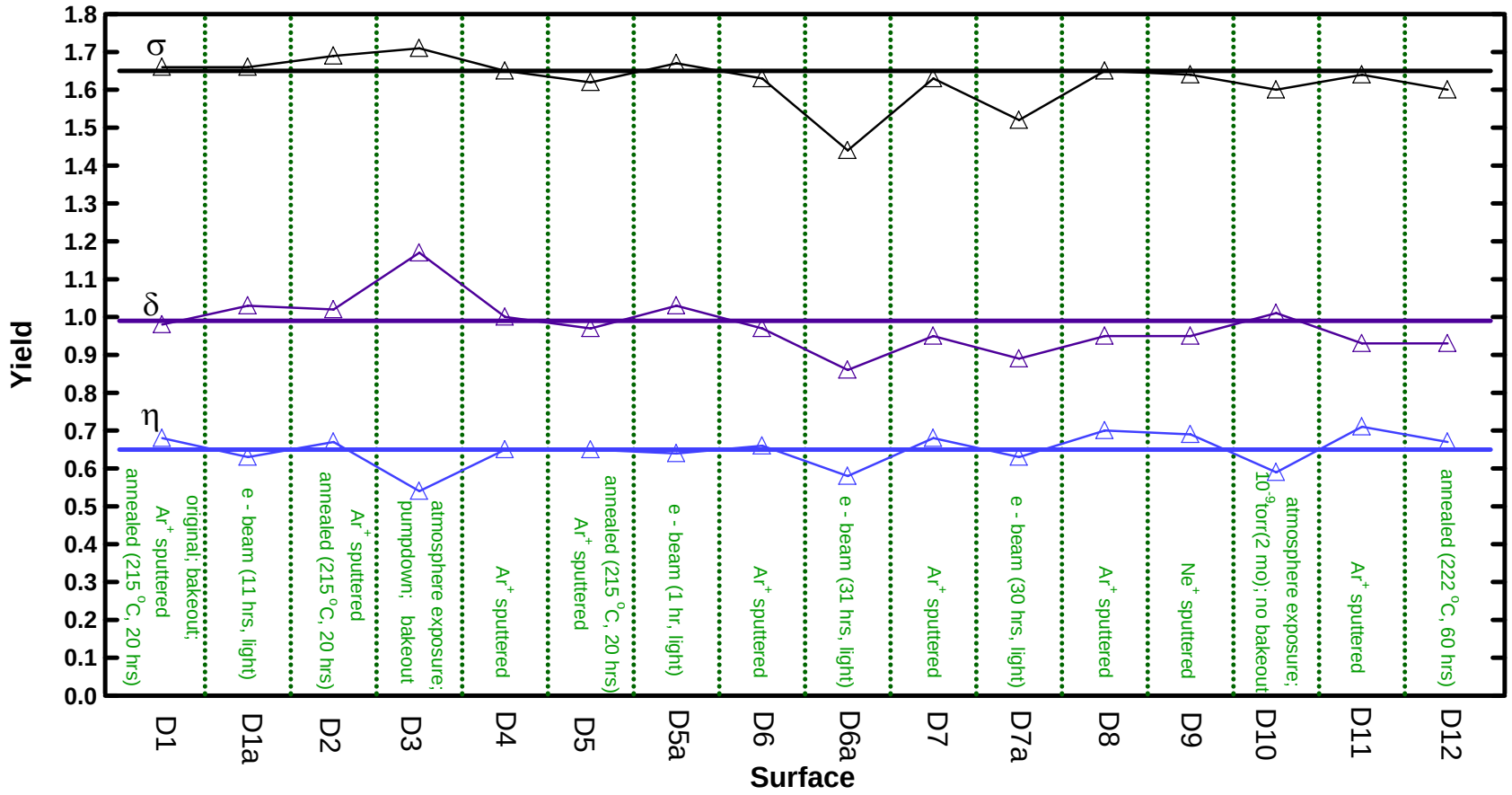

Figure 4-6 Total Yield, σ, SE Yield, δ, and BSE Yield, η, as functions of surface and location for sample D, respectively [*Davies, 1999*]. E_B = 1.5 keV. Error bars are considerably smaller than the measurement markers displayed [*Davies, 1999*]. Average trend for σ exclude D6a and D7a. Average trends for δ and η exclude D3, D6a, D7a, and D10.

Table 4.1 δ, η, and σ as a function of surface on sample "D". Surfaces exposed to some measure of extended electron beam bombardment are listed in green. Non-UHV surfaces are in blue. E_B = 1.5 keV. The average, standard deviation, standard deviation of the mean (SDOM) are also provided.

Surface	δ (±.01)	η (±.005)	σ (±.02)
D1	0.98	0.68	1.66
D1a	1.03	0.63	1.66
D2	1.02	0.67	1.69
D3	1.17	0.54	1.71
D4	1.00	0.65	1.65
D5	0.97	0.65	1.62
D5a	1.03	0.64	1.67
D6	0.97	0.66	1.63
D6a	0.86	0.58	1.44
D7	0.95	0.68	1.63
D7a	0.89	0.63	1.52
D8	0.95	0.70	1.65
D9	0.95	0.69	1.64
D10	1.01	0.59	1.60
D11	0.93	0.71	1.64
D12	0.93	0.67	1.60
average	0.99‡	0.65‡	1.65†
stdev	0.06‡	0.05‡	0.02†
SDOM	6 %‡	7 %‡	1 %†

† values are calculated excluding surfaces D6a and D7a.
‡ values are calculated excluding surfaces D3, D6a, D7a, and D10.

4.3.(a) Chemical Cleaning

To remove surface contaminants prior to vacuum insertion, the samples were chemically cleaned in consecutive baths of toluene (2-4 min), methylene chloride (2-4 min), acetone (5-7 min), isopropyl alcohol (2-4 min), methanol (3-5 min), distilled water (rinse), warm nitric acid (~30 min), and distilled water (~10 min) (LB III, p. 30w). Upon completion of this sequence of solvents, the samples were passed through an oxidizing flame and then, in order to minimize exposure of the surface to atmospheric contaminants, stored in distilled, de-ionized water until vacuum chamber insertion.

4.3.(b) Electron Bombardment

Beam currents were chosen in order to minimize the rate of beam-induced surface modifications. The well-known effect of carbon contamination through the process of electron-stimulated adsorption (ESA) [*Hillier*, 1948; *Davies and Dennison*, 1997; *Dennison, Kite, Chang, and Davies*, 2000] constantly modifies the surface and is highly dependent on beam current density and somewhat dependent on incident beam energy. The ESA of carbon did not occur at a problematic rate for beam-current densities $\leq \sim 10^{-4}$ A/cm^2. Changes in δ and η as a result of energetic electron bombardment were completely consistent with the known effects of ESA and ESD. Specifically, the dramatic drop in both δ and η with extended exposure to heavy electron bombardment is characteristic of the ESA of a thick layer of carbon (~ 200 Å). Off center beam locations increased δ because the incident beam angle became slightly non-zero due to the beam deflection angle. An alternative means of moving the beam location while holding the incident beam angle constant required moving the sample (and chamber apparatus) with micrometers.

4.3.(c) Sputtering

Evolution of the surface by adsorption (ESA) and desorption (ESD) of contamination is likely to occur in any UHV environment. *In situ* surface preparation using ion sputtering causes removal of adsorbates, but slightly degrades the sample by embedding ions deep within the surface. A significant change in δ as a result of sputtering is not surprising, as SEE is an extremely surface sensitive phenomenon; η, however, should not be particularly sensitive to changes in the first 50 Å or so of the sample surface. A significant change in η, therefore, may indicate sputter-induced effects occurring much deeper in the sample. The effects that energetic ions have on the surface are surface roughening, Argon embedding, and, equal and opposite changes in SE and BSE yields.

4.3.(c)1 Surface Roughening

The sputtering rates and durations used in this investigation were sufficient to remove, at most, ~100 Å from the surface causing a roughening of the surface. Sputter-induced surface modification can take the form of morphology changes, the embedding of contaminants—likely argon—deep into the surface, or a combination of the two. Morphologically, it is not uncommon for argon sputtering of gold to result in significant roughening of the surface at the micron level [*Barber et al*., 1973]. The SEM images suggest that a roughening by sputtering occurs. It appears, however, that the increased roughness was not so much *caused* by the sputtering, as uncovered by it. That is, the nature of the roughness—the parallel striations—would seem more plausibly a result of the sputtering, as uncovered by it. That is, the nature of the roughness—the parallel striations—would seem more plausibly a result of the sample fabrication (rolling, perhaps) than sputtering. Regardless, it is conceivable that the effect could be an overall reduction in δ, as is typical for rougher surfaces (though why η should be affected is unclear). Thus it would seem that the case for morphology-induced changes in δ and η is tenuous at best.

4.3.(c)2 Argon embedding

The contaminant layer is not the result of adsorption, but due to the migration of bulk contaminants within the sample to the surface—perhaps due to the bakeout, which is essentially a 72-hour, 150 °C anneal. But if this were the case, the contaminant level at 1000 Å should be no different from that at, say, 10,000 Å, and sputtering should have no effect on η. Since this line of reasoning would seem to rule out the removal of thick contaminant layers as an explanation for the sputter-induced elevation of η, sputter-induced surface modification is the only apparent explanation. Evidence supporting deep argon embedding as the mechanism underlying the sputter-induced change in η is stronger, though not entirely satisfying. Residual gas analyzer (RGA) measurements of the contaminant spectra during the lengthy, 300 ^{o}C sample anneals indicated the evolution of a considerable volume of argon from the sample, indicating argon had been embedded in the surface. Furthermore, it is observed that the influence of these anneals (and presumably the associated argon evolution from the sample surface) on δ and η was to push them in the directions of their pre-sputter values. It is noted, however, that if the observed changes are a result of

deep argon embedding, the effect is not particularly sensitive to species: measurements performed on surface D9, which was Ne^+ sputtered, revealed the same behavior. Thus, it would seem that the data presented here do not support an unequivocal solution to the mystery of increased BSE yield with sputtering: the removal of a thick layer of surface contamination can be ruled out, but evidence concerning morphology changes and argon embedding remains ambiguous. One additional clue, however, remains to be discussed.

4.3.(c)3 Equal and opposite changes in SE and BSE yields

It appears that while the numbers of SE's and BSE's are changing individually as a result of sputtering, the total number of electrons leaving the surface, $\delta+\eta$, is not changing (where it is again emphasized that these are the *defined* SE's and BSE's). Variations in the total yield, σ, is less than ±1%, except for two cases where σ decreased (D6a and D7a) due to long-term electron beam exposure. Changes in δ and η are really quite small, on the order of ±7% or less, except when exposed to atmosphere (D3 and D10) when contamination is most abundant. This suggests that the surface is charging negatively due to a change in work function while exposed to atmosphere. The change in work function further accelerates electrons as they are emitted from the surface with an increased kinetic energy effectively changing some of the SE's to BSE's resulting in an increased δ and a decreased η while σ remains constant. When exposed to atmosphere, contamination induces negative surface charging (D2 → D3 and D9 → D10). Likewise, sputtering alleviates practically all of the surface charging resulting in δ decreasing, η increasing, and σ remaining constant.

4.3.(d) Annealing

The procedural annealing provides three effects to the sample. Chemical reactions and changes in crystalline structure were not evident, however, the diffusion of bulk contaminants to the surface and the desorption of physisorbed surface contaminants occurred during the annealing process.

4.3.(d)1 No chemical reactions or changes in crystalline structure

The relatively low annealing temperatures used in this investigation (150 °C–300 °C) were not sufficient to induce chemical reactions at the sample surface (Greg Swain, personal communication, 1998), nor changes in crystalline structure (which generally require temperatures on the order of 80% of a materials melting temperature—about 720 K in the case of Au, whose melting temperature is ~900 K). The crystallite size is estimated at ~10nm based on scanning electron micrographs [*Davies, 1999, Fig. 4-3*]. Any suspected diffraction that may be observed in the spectra can be predicted using the Au powder diffraction pattern [Fig. 4-7] where the diffraction angle is plotted as a function of incident beam energy. Similar to X-ray diffraction, the electron wavelength as a function of voltage, V, is used with Bragg's law to determine the possibility of diffraction effects where the angle of diffraction is written as

$$\theta(V,d) = \tfrac{1}{2}\sin^{-1}\left(\frac{h}{2d(2m_e q_e V)^{1/2}}\right) \tag{4.3}$$

with Planck's constant, h, elementary charge, q_e, electron mass, m_e, and d-spacing, d. The allowable Miller indices for the nine lowest non-zero form factors for the fcc lattice are (111), (200), (200), (311), (222), (400), (331), (420), and (422). Using the Au lattice constant (a_o = 0.407 nm), the d-spacing is written as

$$d(h,k,l) = a_0(h^2 + k^2 + l^2)^{-0.5} \tag{4.4}$$

where the lower d/a_o ratios indicate the main diffractions and the higher d/a_o ratios indicate the weaker diffractions. After insertion of Eq. 4.4 into Eq 4.3, the intersections of form factor curves with the incident beam energies and emission angles used in this study can be located [Fig. 4-7, circles]. Analogous to X-ray powder pattern intensities, these electron diffraction peak intensities can be scaled by the square of the electron-to-X-ray form factor ratio. For crystallite sizes on the order of 10 nm or larger, diffraction peaks are estimated to have approximately 1 degree width based on the RD angular detection and the Scherrer formula for particle size broadening. The electron emission spectra at 100 eV may have significant contamination due to large amplitude diffraction peaks that occur within 1 degree of the 30°, 38°, 46°, 53° and 60° emission angles. With exception of the 14°, 17°, and 24° emission angles, there appears to be no

concern for diffraction caused by the polycrystalline surface (Appendix D) since the diffraction peaks are <10% of the most intense (111) peak.

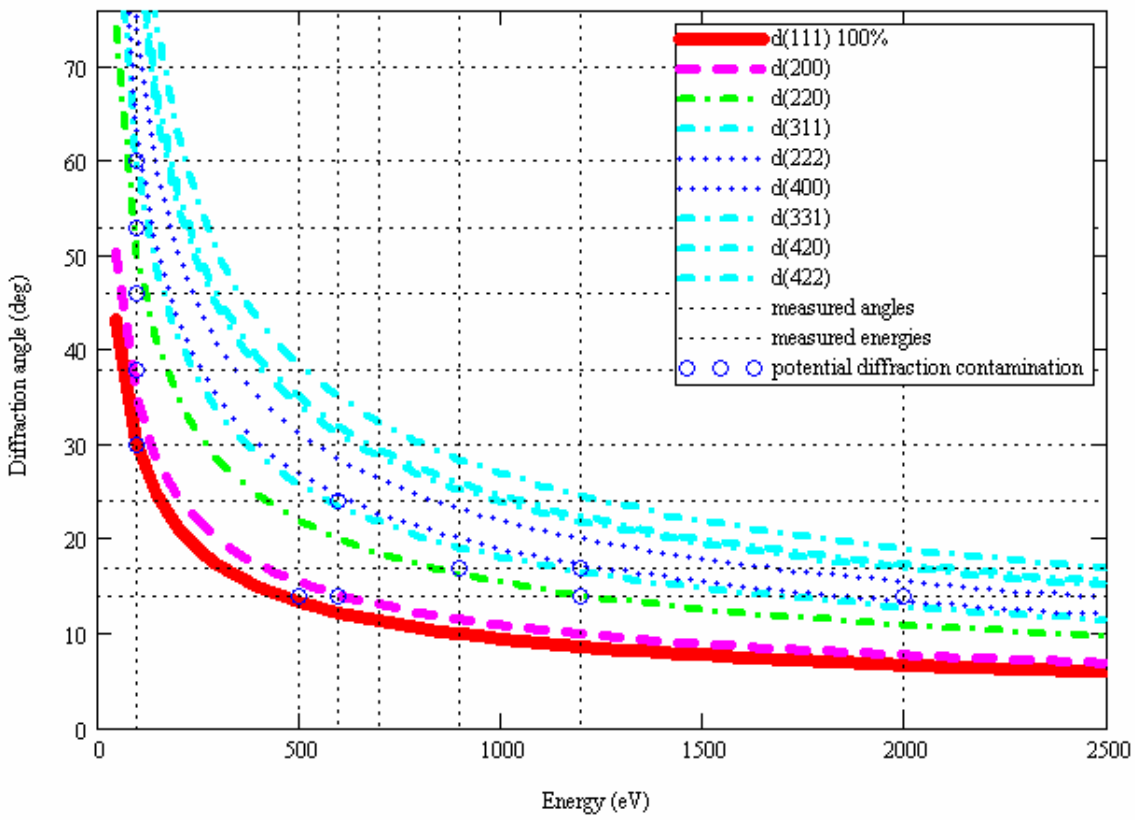

Figure 4- 7 Powder diffraction pattern taken from Bragg's law using Au lattice constant (a_o = 0.407 nm). Suspected diffraction may (circles) occur at 100 eV: (111) @ 30°, (220) @ 38°, (220) @ 46° and (220) @ 53°, and likely all larger coarse measured angles. Weaker suspected diffraction may also (circles) occur at 500 eV: (111) @ 14°, 600 eV: (200) @ 14°, and (311) @ 14°, 900 eV: (220) @ 17°, 1200 eV: (220) @ 14 ° and (311) @ 17°, and 2000 eV: (222) @ 14 °.

4.3.(d)2 Diffusion of bulk contaminants

Changes in δ and η as a result of sample heating were likely due to the diffusion of bulk contaminants to the surface, the evolution of these contaminants from the surface, and the desorption of physisorbed surface contaminants. The results of surfaces D2 and D3 suggest that the 150 °C, 72-hr anneal in association with the vacuum chamber bakeout was sufficient for the removal of any contaminant layer

formed as a result of atmosphere exposure during chamber insertion, and for the nearly complete evolution of any contaminant species embedded in the surface as a result of sputtering.

4.3.(d)3 Desorption of physisorbed surface contaminants

The immediate change (lowering) in δ resulting from even light electron bombardment following the 300 °C local anneals suggests a substantial presence of carbon on the sample surface following these anneals (where the ESA of carbon is responsible for the lower δ's). The carbon evolved into the UHV environment and adsorbed on the sample surface. RGA measurements of the existing contaminant species in the LittleBoy during these anneals revealed a substantially increased presence of physisorbed CO and CO_2, most likely coming from the sample heater. Furthermore, it was observed that extended exposure of the surface to vacuum (~1 month at ~$1x10^{-10}$ Torr) appeared to reduce the carbon presence on the sample surface, as evidenced by unchanging δ's over indefinite exposure to light electron bombardment. As addressed previously (4.3(c)3), the contamination induced negative surface charging results in equal amounts of increased δ and decreased η such that σ remains constant (D3 and D10). Sputtering cleans the major portion of surface contamination decreasing δ, and increasing η, while σ remains constant (D4 and D11). Finally, ESA cleans any remaining contamination resulting in a decrease of σ , δ , and η leading to the "best" yield values.

4.4 Previous Measurement Comparison

Based on the preceding discussion, it would seem that those surfaces, which had just undergone a bakeout are the closest to atomically clean gold (D3), while just-sputtered surfaces appear to be gold modified by embedded argon [4.3(c)2] (D1, D2, and D12). This hypothesis can be tested further by examining the results of previous investigators—specifically, those of *Thomas and Pattinson* [1970]. These measurements were chosen for comparison with the present work based on the comparability of the samples and the quality of the measurement apparatus and technique [*Thomas and Pattinson*, 1969, 1970]. Specifically, their samples were high purity, polycrystalline Au, vapor deposited *in situ*, measurements

performed under UHV and required only a few seconds to complete (giving high confidence that the samples were very close to atomically clean, though *in situ* surface characterization was not performed). Their yield results were $\delta(1500\text{ eV}) = 1.21 \pm 0.01$, $\eta(1500\text{ eV}) = 0.460 \pm 0.005$, and $\sigma(1500\text{ eV}) = 1.67 \pm 0.02$. On careful examination of the reported details of their apparatus and technique, it is reasonable that the SE and BSE yields for a clean Au surface should be comparable to their results. Introduced in Chap.1.4, measurements on identical sample material using the instrument (Fatman chamber) devoted to absolute SE and BSE yields are most likely better than Thomas and Pattinson or any others where surface quality of these measurements are validated with *in situ* surface analysis [Fig. 4-3]. Fatman chamber yields are $\delta(1500\text{ eV}) = 1.27 \pm 0.01$, $\eta(1500\text{ eV}) = 0.440 \pm 0.005$, and $\sigma(1500\text{ eV}) = 1.71 \pm 0.02$.

The total electron yield, σ, obtained by Thomas and Pattinson is in excellent agreement differing by less than 3% from the results obtained by Davies on sample "D" [Fig. 4-6]. However, the comparison also reveals significant disagreement among the SE and BSE yields; specifically, the δ's are 10–30% low, while the η's are 20–50% high. Comparison to our Fatman chamber results also reveals excellent agreement with σ, but 20% larger η, and 10% smaller δ.

Regarding physical differences between the samples, surface contamination and surface morphology (roughness) are potential sources of discrepancy between the δ's. In particular, it is easily conceivable that the surfaces of this work are "dirtier" than those of Thomas and Pattinson, and it is easy to imagine that the mechanically formed sample of the present investigation, while appearing relatively smooth, is rougher than the vapor deposited sample of Thomas and Pattinson. However, since the SE and BSE yields taken in our Fatman chamber compare in some regard better to Thomas and Pattinson the discrepancies are most likely due to systematic error in the method using the tertiary samples.

4.5 Systematic Error Using the Tertiary Samples

Equally biasing the two tertiary samples to +50 V prompts approximately half of the emitted SE's into the regions of the tertiary samples [Fig. 3-3]. Assuming that 50% is the maximum number of SE's collected by the tertiary samples, a calculation can be made to approximate the systematic error. In the following summary developed by Davies [*Davies, 1999*], $s(0)$, $s(50)$, $r(0)$, $r(50)_{true}$, $r(50)_{meas}$, *se,* and *bse*, and I_B are the sample currents at 0 V and +50 V, the return (tertiary sample) current at 0 V, the actual and measured return currents at +50 V, and the *se*, *bse*, and beam currents, respectively. We have

$$s(0) = I_{\mathrm{B}} - bse - se + r(0) \tag{4.5}$$

$$s(50) = I_{\mathrm{B}} - bse - \gamma \cdot se + r(50)_{true} \tag{4.6}$$

where γ is defined as the fraction of SE's collected by the tertiary samples, and $r(50)_{true}$ is given by $r(50)_{true} = r(50)_{meas} - \gamma \cdot se$. The "gamma factor", γ , ranges from $0 < \gamma < 0.5$, where $\gamma = 0$ leads to no systematic error, and $\gamma = 0.5$ leads to indefinable yields from the 50% maximum assumption above. Requiring that their sum remain constant, the definitive boundary between the *se* and *bse* currents may be addressed for systematic error. From (4.5) and (4.6), the expressions for the corrected *se* and *bse* currents becomes

$$se = (1-2\gamma)^{-1}\left[s(50) - r(50)_{meas} - s(0) + r(0)\right] \tag{4.7}$$

$$bse = I_{\mathrm{B}} - (1-2\gamma)^{-1}\left[s(50) - r(50)_{meas}\right] + \frac{2\gamma}{1-2\gamma}\left[s(0) - r(0)\right] \tag{4.8}$$

This sort of systematic error is a direct result of detector geometry so no dependence on E_b appears. Incorporation of the extra SE's collected by the tertiary samples (Eq. 4.5) effectively underestimates δ by a factor of $1-2\gamma$. The overestimation of η by a factor of $\left[s(0) - r(0)\right]$ in the last term of Eq. (4.8) is necessarily a direct consequence of requiring the se's and $r(50)_{meas}$ to differ by 2 γ in Eq (4.6).

4.5.(a) Estimating the Gamma Factor

Assuming the total yield is a constant, $\delta + \eta = \sigma$ and the backscattered yield, η, is always greater than zero, an additional restriction on the gamma factor can be found. If the effect of including γ is to increase δ, it must also be that η is *decreased*. Returning to Eq. (4.8), this means that the second term should be greater than the first. Imposing this constraint, along with the additional facts from Davies measurements, it is always the case that $\left[s(50) - r(50)_{meas}\right] < \left[s(0) - r(0)\right]$, leading to

$$\gamma \leq \frac{I_{\mathrm{B}} - \left[\mathrm{s}(50) - \mathrm{r}(50)_{\mathrm{meas}}\right]}{2I_{\mathrm{B}} - 2\left[\mathrm{s}(0) - \mathrm{r}(0)\right]} \tag{4.9}$$

Applying expression (4.9) to data set D3.01 (one of the data sets for surface D3) gives an ultimate upper bound on γ of approximately 16%. Based on Davies derivation of Eq. (4.9), this says γ *equals* 0.16 if $\eta = 0$, for an incident beam energy of E_B = 1.5 keV (the beam energy for data set D3.01). In order to estimate a more accurate value for γ, BSE yield values from *Thomas and Pattinson* [1970] ($\eta = 0.46$) and those of sample surface "D6" [*Davies, 1999*] were obtained at a readily tested beam energy (E_B = 1.5 keV). Applying T & P's value Eq. (4.6) results in

$$\eta = 0.46 = \frac{bse}{I_{\mathrm{B}}}$$

which implies

$$0.46 I_{\mathrm{B}} = \frac{I_{\mathrm{B}}(1 - 2\gamma) - \left[s(50) - r(50)_{meas}\right] + 2\gamma\left[s(0) - r(0)\right]}{1 - 2\gamma}$$

Solving for γ yield

$$\gamma = \frac{0.54 I_{\mathrm{B}} - \left[\mathrm{s}(50) - \mathrm{r}(50)_{\mathrm{meas}}\right]}{2(0.54 I_{\mathrm{B}}) - 2\left[\mathrm{s}(0) - \mathrm{r}(0)\right]} \tag{4.10}$$

Reviewing the sample "D" data, Davies found that surface D3 had the lowest value for the BSE yield ($\eta = 0.54$), while surface D8 had the highest value ($\eta = 0.70$). Using the data from these two surfaces, Davies estimates realistic upper and lower bounds on γ by applying Eq. (4.10). Results of the upper and lower bounds on the systematic errors in δ and η show the systematic error using the tertiary samples [Table 4-2].

Table 4.2 Using the tertiary samples provides a realistic estimate for the upper and lower error bounds. $E_B = 1.5$ keV.

Surface	γ	% error (δ)	% error (η)
D3	0.03	- 6	+ 15
D8	0.10	- 20	+ 51

The calculations made in determining the systematic error within the Fatman chamber are quite similar, where the results of numerical correction factors in δ and η are associated with the hemispherical retarding grid analyzer [Table 4-3].

Table 4.3 Summarization of empirically and numerically derived correction factors for total, SE, and BSE yields due to losses in detector apparatus. Values for the empirical total yield correction factor, determined at $E^{2\sigma}$, were consistent with the numerically derived value to within 3% [*Nickles, 2002 and Thomson, 2005, p.159*].

Electron Yield	Empirical Correction Factor	Numerical Correction Factor
Total Yield	1.15	1.18
SE Yield	Not Yet Determined	1.15
BSE Yield	Not Yet Determined	1.4

4.5.(b) δ and η as Functions of Beam Energy

Total, SE, and BSE yield measurements for a number of incident beam energies in the range 1–3 keV were accomplished by Davies on polycrystalline gold surfaces A0*i* and D9. Comparison of these results with those of previous investigators aids in assessing the accuracy of the present yield determinations and serves to further assess the reliability of the instrument and method employed in the current investigation.

Figure 4-8 depicts δ, η, and σ vs E_B for surfaces A0*i* and D9 [*Davies, 1999*]. Two sets of δ's and η's are presented for each surface: values as measured (*i.e.*, uncorrected for systematic error), and values corrected for the systematic error described in 4.5 (a). The corrected values are located midway between the upper and lower bounds determined by the systematic error estimates, while the error bars depict the upper and lower bounds themselves. Also presented in the figure are the results of three other investigators, *Thomas and Pattinson* [1970], *Holliday and Sternglass* [1957], and *Reimer* [1993], along with three semi-empirical models describing δ vs E_B. The shape of the δ vs E_B curves obtained for both surfaces in this investigation closely compare with those of Thomas and Pattinson. More specifically, δ's and η's for surface A0*i* (corrected for systematic error) are nearly identical with those of Thomas and Pattinson. For surface D9, η's are in excellent agreement with Thomas and Pattinson, but the δ's are ~12% low. For both surfaces, the total electron yield, σ, is ~5% lower than that of Thomas and Pattinson. These results indicate the expected trend of δ as a function of beam energy, and differences in magnitude can be attributed to surface contamination and systematic error in δ and η determinations.

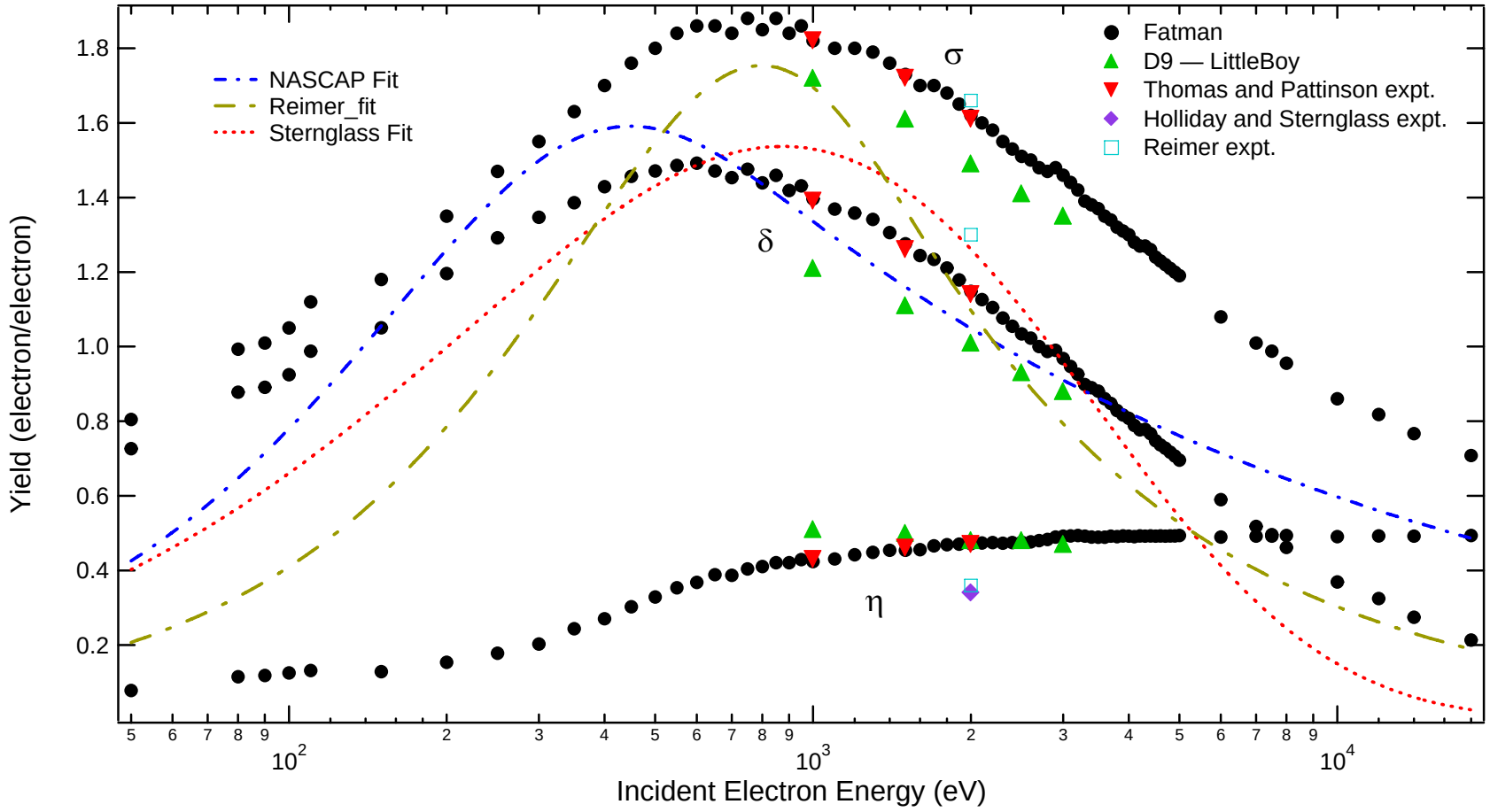

Figure 4-8 δ, η, and σ as functions of incident electron energy [*Clerc, 2005*]: comparison of surface D9 measurements [*Davies, 1999*] with previous experiment and empirical SEE models. Random errors for present experiment values are significantly smaller than the markers displayed. Experimental error for previous measurements were not reported by the authors.

4.5.(c) Comparison to Theory

The four models displayed in Fig. 4-8 are given by:

NASCAP: $$\delta(E) = 1.114\left(\frac{E_{\max}}{E}\right)^{1.35-1}\left\{1-\exp\left[-2.28\left(\frac{E}{E_{\max}}\right)^{1.35}\right]\right\}\cdot\delta_{\max} \tag{4.11}$$

Reimer: $$\delta(E) = 1.31\left(\frac{E_{\max}}{E}\right)^{1.8-1}\left\{1-\exp\left[-1.45\left(\frac{E}{E_{\max}}\right)^{1.8}\right]\right\}\cdot\delta_{\max} \tag{4.12}$$

Sternglass: $$\delta(E) = \frac{E}{E_{\max}}\cdot\exp\left[2-2\left(\frac{E}{E_{\max}}\right)^{0.5}\right]\cdot\delta_{\max} \tag{4.13}$$

where δ_{max} and E_{max} are 1.5 and 650 eV [Fig. 4-8], respectively, as taken from the CRC [1979]. These formulations correspond to two of the basic semi-empirical formulations described in [2.2]. Specifically, the NASCAP [*Young, 1956*] (Eq. 4.11) and Reimer [*Reimer, 1977*] (Eq. 4.12) models are based on a formulation by *Dionne* [1975] which assumes the constant-loss power law of Eq. (2.3), with n = 1.35 and n = 1.8, respectively. The Sternglass model [*Sternglass, 1950*] (Eq. 4.13), by contrast, is based on the Bethe relation of Eq. (2.2). Good agreement between the data of this investigation and the NASCAP model reaffirms the demonstrated success of this formulation for energies less than ~4 E_{max}, and the previously observed failure of the Sternglass formulations for energies less than ~8 E_{max}.

4.6 Conclusion

Investigations of the sample and its surface have led to comparisons of results from other investigations and demonstrated how methodic preparation has led to the ability to measure precise SEE scattering cross sections under well developed procedures and well defined boundary conditions. The sample and its surface have been characterized by several different techniques. The closely associated techniques used for characterization of the sample acquire electron bombardment yield information. The acquisition of total (σ), secondary (δ), and backscattered (η) absolute yields has been accomplished within two UHV systems on identical sample material.

The comparisons of yields using the tertiary sample technique (LittleBoy chamber) and the hemispherical retarding grid analyzer technique (Fatman chamber), were made to those in the literature, which used a vapor deposition technique. After accounting for the correction of systematic error and empirical and numerical correction factors, excellent agreement is observed in the absolute yields. Deviations of up to 20% for δ's and 51% for η's reasonably confirm that sample evolution is predictable and surface preparation must follow a rigorous order.

The following general observations are summarized [4.3] regarding δ and η pertaining to the preparation of the surface: (*i*) light electron beam bombardment and short-duration annealing result in small (~10% or less) but repeatable changes in δ and η; (*ii*) heavy electron beam bombardment and longer-duration annealing, such as a 72-hour system bakeout, induce larger (~20%–50%) changes in δ and η; and (*iii*) ion sputtering, regardless of the surface being sputtered (or sputtering species), produces consistent values for both δ and η. Pertaining to these observations, evidence to the following has been presented:

1. Ion sputtering results in a smooth gold surface, possibly contaminated with embedded argon to a depth of 500–1000 Å. Surface D3 is likely the best surface against which to compare the results of *Thomas and Pattinson* [1970] and Fatman UHV chamber [Clerc, 2005]; There is no sign of surface damage or of carbon or oxygen contamination;

2. Hotter annealing (~200–300 °C) initially contaminates the sample surface with physisorbed carbon as a result of evolving CO and CO_2 from the heater into the chamber atmosphere; the carbon eventually desorbs of its own accord if the sample is allowed to sit under UHV vacuum;
3. Light electron beam bombardment initially desorbs physisorbed contaminants and evolves embedded argon at the beam location through ESD; depending on the annealing history of the sample, noticeable ESD of carbon can be immediate, or may not occur at all (up to at least 45 hours of beam exposure);
4. The long-duration anneals (system bakeouts) desorb physisorbed surface contaminants and evolve embedded argon from the surfaces of previously sputtered samples; thus, these surfaces are the closest in this investigation to clean, polycrystalline gold.

CHAPTER 5

ANGLE- BEAM ENERGY- RESOLVED SPECTRAL MEASUREMENTS

A complete set of angle-energy-resolved yield measurements—*i.e.*, AR spectra—"represents the maximum amount of information that can be obtained for a given electron population leaving a material surface" [*Rösler and Brauer*, 1981a] (neglecting such properties as spin, etc.). Examples of AR spectra presented in this chapter are the most complete collection, to date, for a given population of electrons leaving a polycrystalline gold surface.

Referring to the notation development in section 3.3(b), the population of electrons are divided into four different groups or sub-populations according to their physical origin. The elastically scattered population, the quasi-elastic population , the BackScattered Electron (BSE) population originating from the primary incident electrons, and the Secondary Electron (SE) population, which originate from within just a few monolayers of the polycrystalline Au surface. A fifth special population of electrons (Auger electrons) is addressed in this chapter. Evidence confirms Auger electrons are present only in the higher beam energy spectra (E_b = 2 and 2.5 keV). For simplicity's sake each population will be discussed in separate sub—sections directly referring to the exaggerated AR spectrum [Fig. 3-37] for the various populations. The mathematical nomenclature and labels are defined in Table 3.3 to help bridge the analytical gap. The notation is directly mapped so that emphasis is placed on electron origin.

The BSE population is a broad group, which includes both the elastically scattered population and the plasmon population. The BSE population normally contains loss features. This holds true for the plasmon population. However, this does not hold true for the elastic population. Even though the elastic population is technically part of the BSE population, because the electrons originated from the primary incident electrons, there is no energy loss. The BSE peak is assumed to be comprised of an evident plasmon loss peak on the high energy side of the BSE peak. There is no evidence for any additional (lower energy) plasmon loss peaks in these spectra. Discussion of the BSE peak includes parts of the first plasmon loss peak (quasi—elastic) since a two order of magnitude difference in energy resolution is used to measure the larger BSE peak.

The AR data is taken and tabulated into groups of incident beam energy, E_b. Data set information is tabulated in Appendix E and contains LabBook reference information for specific E_b resolution spectra. Each E_b resolved spectral data group is further divided into varying voltage ranges, or resolutions of electron emission energy that are allowed by the capabilities of the tandem biasing supply (3.2(e)) of the rotatable detector (RD) and its floating ammeter. The summary of AR Energy spectral results is given in terms of energy resolutions [Table E.1]. Each of the four different energy resolutions (10 eV, 1 eV, 0.1 eV, and 0.01 eV) is limited to a specific energy measuring range. The two largest resolutions provide information about the coarser spectral features (SE and BSE populations), while the two smallest resolutions provide information about the finer spectral features (elastic and plasmon populations). The energy resolved spectral data group is finally divided into emission angle. The Beam Energy—resolved (E_bR) spectra presented in this chapter are shown for several emission angles depending on the angular resolution, likewise. An overview of the entire spectra from 0 Volts to the incident beam energy, E_b, is shown along with the pieces of spectra at higher resolution such as the Elastic, BSE, and SE peaks. The procedure of the derivative process includes details of the absolute yield error calculation in quadrature (3.2(i)).

As applicable, detailed descriptions of multiple resolutions are given followed by the extraction of key points, which mark the major peaks and valleys from each spectrum segment. A key point consists of an energy location (in eV) and a yield intensity (in $sr^{-1} * eV^{-1}$). The key points of interest are the Elastic peak, the first plasmon peak, the higher energy BSE peak, the low energy SE peak and the valleys separating these peaks.

An AER spectrum uniting the varying resolutions (Figs. E-14, E-32, E-51, E-68 and E-86) measured with E_b = 900 Volts and the specific emission angle of 14^o Counter—Clockwise is presented [Fig. 5-1] on a logarithmic scale and includes linear blowups of the SE and BSE peaks. The SE peak is fit with the Chung and Everhart model and the BSE peak is overlaid with an empirical exponential fit. These two fits intersect near 100 eV at an intensity of $1x10^{-4}$ $sr^{-1} * eV^{-1}$, approximately three orders of magnitude less than the SE peak (2 eV). Just as in Figure 1-2 (E_b = 1500 eV), the Chung and Everhart model (Eq. 2.7) justifies the lower energy shape at the peak, but falls off faster than the data between 50 eV and 150 eV.

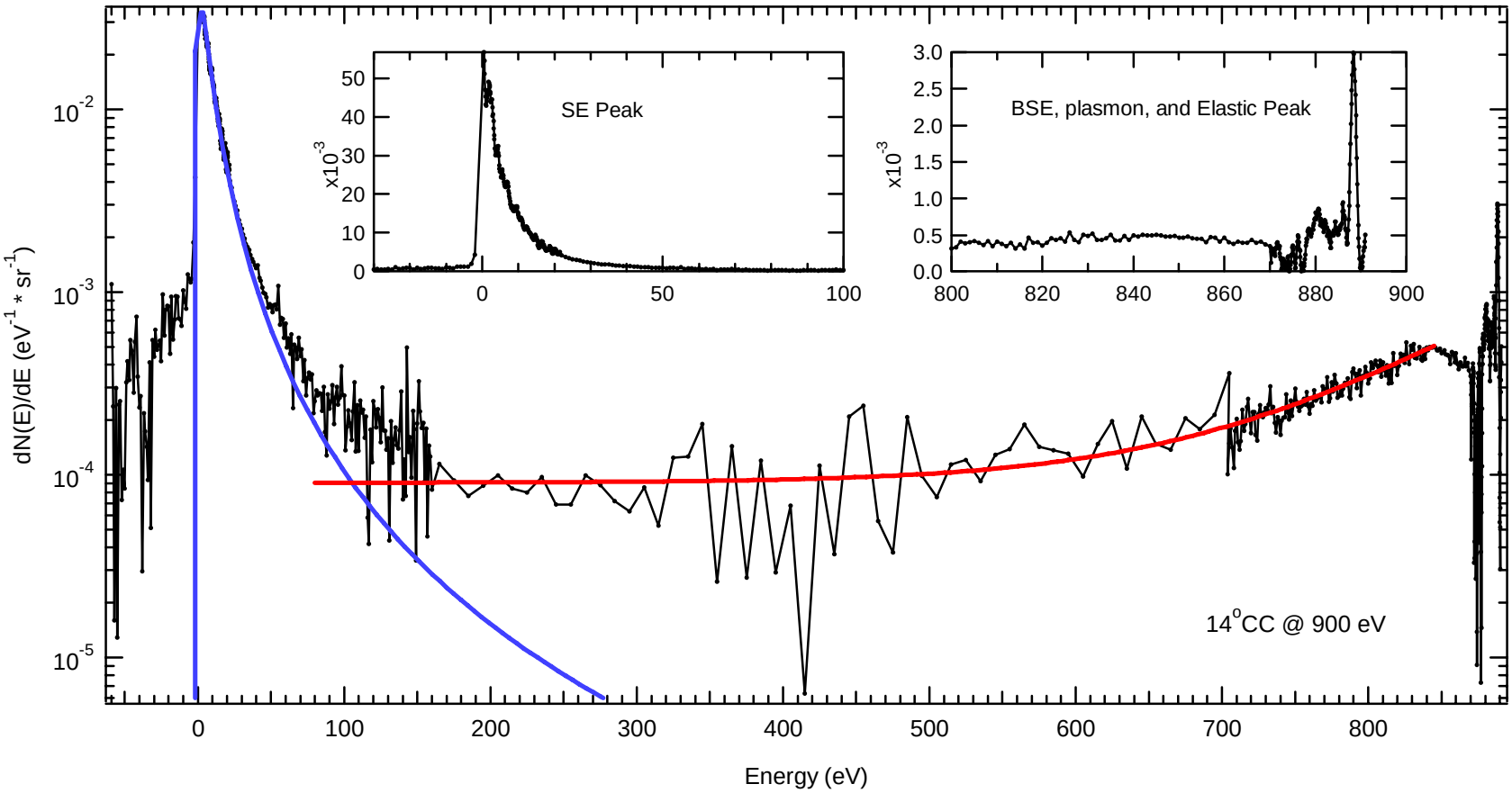

Figure 5-1 Total spectrum measured with E_b = 900 eV and emission angle of 14° Counter—Clockwise using 10 eV, 1 eV, and 0.1 eV Resolutions. The blowups show the 1 eV to 0.1 eV resolution spectra for the SE peak (left) and the BSE region (right) including plasmon and elastic peaks. Blue line is a Chung and Everhart Fit. Red line is an empirical exponential fit.

The Chung and Everhart fitting parameters for this spectra are within reason; the material-dependent k parameter is (161 ± 4) x 10^3, the work function ϕ = (7.3 ± 0.1) eV, E_F = (-9.7 ± 0.1) eV, and χ^2 = 0.002. The empirical exponential model of the quasi-elastic BSE peak has the form

$$\frac{dN}{dE} = \frac{dN(E_{\min})}{dE} + A\exp\left[\frac{E}{\tau}\right], \tag{5.1}$$

where the energy emission decay constant, τ = (95 ± 1) eV, dictates the rate at which the low energy BSE tail increases from the intensity at the local minimum, $\frac{dN(E_{\min})}{dE}$ = (90 ± 2) x 10^{-6} $eV^{-1}*sr^{-1}$, to the BSE peak. The amplitude, A = (24 ± 3) x 10^{-9} $eV^{-1}*sr^{-1}$, scales the emission and is most likely dependent on emission angle, α, (5.2(b)) via the Rutherford (Eq. 2.15) or Mott (Eq. 2.16) distribution models.

At times it is useful to examine the raw data directly from the retarding field analyzer. The raw, pre-differentiated data—that leads to the spectra for E_b = 900 eV and emission angle 14° CC in Fig. 5-1—are shown in Fig. 5-2. As discussed in Chapter 3.2(i), the process to get from the pre-differentiation data to AER spectra is to take a derivative specific to the resolution of the data. The integral of Fig. 5-1 is implemented [Fig. 5-2, black], along with the concatenated raw data from the data files listed in Table E-1, D3501, D3505, D3506, D3507, D3511, D3512, and D3513 (column 14° angle emission). This comparison confirms that the discontinuities in the raw data can be removed in the integrated data, so that absolute yields can be located and determined directly from the integrated spectra. The integral of the spectrum (Fig. 5-2, black line) is also used to calculate yield information. Referring to 3.2(i), only the error in the RDBias changes for differing resolutions and hence an appropriate smoothing approach is also verified.

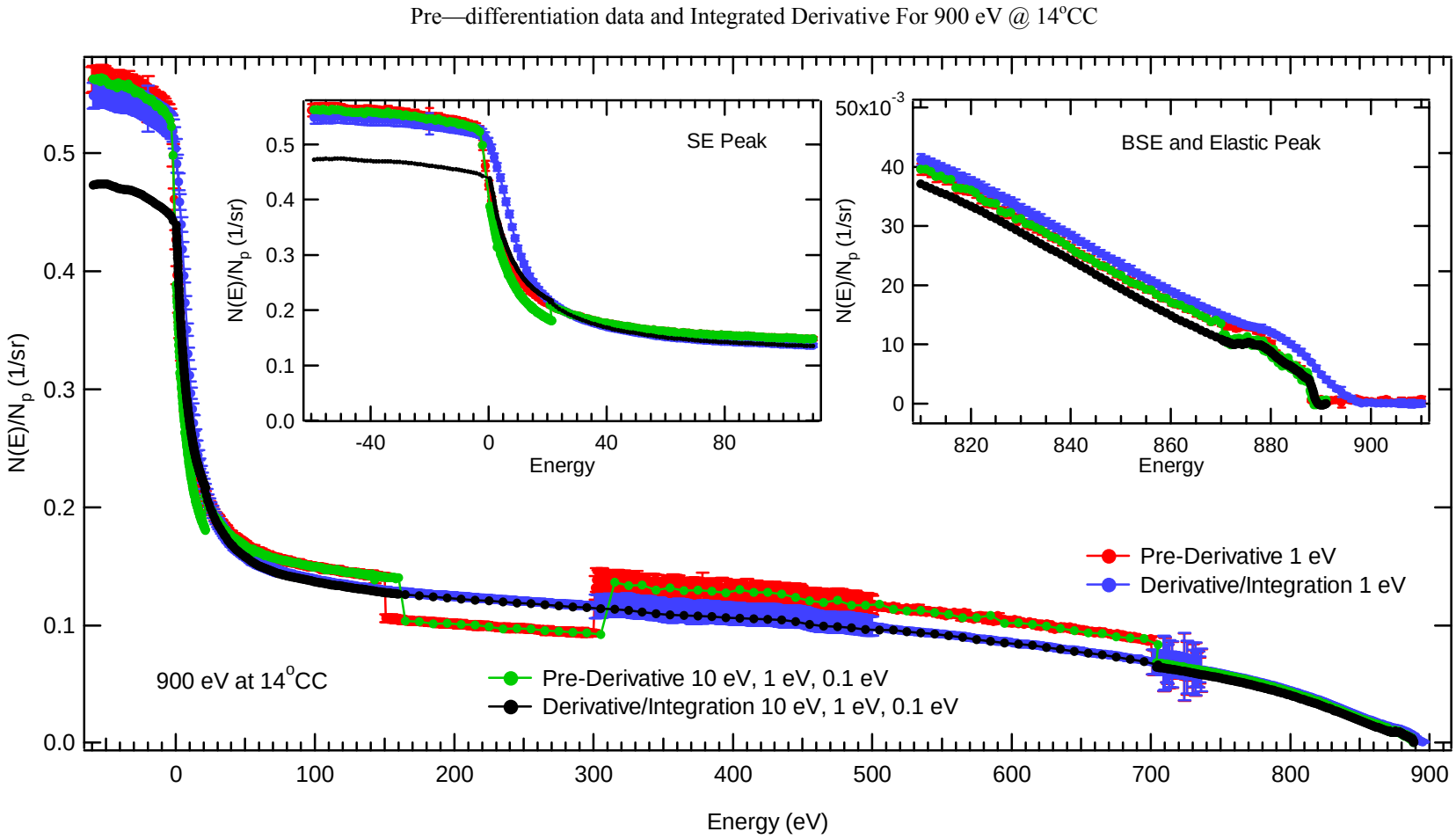

Figure 5-2 Pre—differentiated data using the 1 eV resolution (red) and using 10 eV, 1 eV, and 0.1 eV resolutions (green) at E_b = 900 eV and emission angle of 14° Counter—Clockwise. Also included are the integrated derivative for the 1 eV resolution (blue) and for the 10 eV, 1eV, and 0.1eV resolutions (black). The blowups show the 1 eV to 0.1 eV resolution transitions.

5.1 Elastic Peak Features

The elastic peak is a feature with an energy equal to the incident beam energy, E_b. The word elastic is defined as no energy loss. Since several collisions or scattering events make a population, the population is observed as a peak.

The elastic peak has characteristic features referred to in Fig. 3-37 and listed in Table 3.3. These peak features are (a) the peak position or energy, E_{el}, (b) the peak amplitude or intensity, $dN(\alpha,E_{el};E_b)/dE_e$, (c) the integrated intensity or yield, $\delta(\alpha,E_{el};E_b)$, and (d) the peak width. To view the elastic peak features in detail, pieces of spectra are magnified [Fig. 5-4] for several emission angles, α. By definition, a spectrum is the intensity given as a function of energy emission. The intensity is always a ratio of the current emitted to the current normally incident. Therefore, at E_{el}, $dN(\alpha,E_{el};E_b)/dE_e$ is a function of α and E_b.

The elastic peaks were all studied in two resolutions (1 eV and 0.1 eV). Each resolution required its own analysis technique including a unique smoothing number to make the spectra match properly when concatenated (Chap. 3.2(i)). All eight of the incident beam energy data sets were taken at 1 eV resolution. Six of the eight incident beam energy data sets were also taken at 0.1 eV resolution. When this was the case, the more resolved energy was provided. Concatenations of 0.1 eV resolution AR spectra [Fig. E-32] and 1 eV resolution AR spectra [Fig. E-51] are then smoothed. The 0.1 eV step size has been used to resolve the energies and intensities of the peaks. These resolution spectra (Fig. E-30 through Fig. E-35) span the energy range from ~20 eV below the incident beam energy, E_b, to a few eV above the beam energy for each respective E_b (E-5(c)). Note, analysis of the spectral characteristic includes both resolutions properly concatenated.

Each of these four characteristics may provide structural information. Structural information has been investigated in other studies; comparing structural information taken here with that of other studies is used to validate our data. Specifically, structure in the yield information found for both resolutions are compared against each other using emission angle as a range. The peak widths determined using the two resolutions are also compared directly.

It is important to recognize that spectra in this study are typically identified by beam energy rounded to the nearest 100 eV. For example, consider the upper right inset [Fig. 5-1] labeled as E_b equal to 900 eV. The intensity of the peak is about 4.6 x 10^{-3} 1/sr*1/eV and is precisely located at about 884 eV. The electron gun's beam energy was not set precisely to 900 eV, since the location of the elastic peak truly defines the primary electrons voltage, since the electron gun's voltmeter is only accurate to ±25 eV where 884 eV is well within the meters boundary. Once the E_b was set, it was not changed until the entire specrtral group for that E_b was taken. For book-keeping purposes, 0.1 eV resolution data are referred to with those voltage labels measured by direct comparison to the data (e.g., 95 eV, 490 eV, 880 eV, 1180 eV), and all lower resolution data referred to with the coarser labels (e.g., 100 eV, 500 eV, 900 eV, 1200 eV). This descrepancy in notation occurred since E_b was not determined precisely until the high energy elastic spectra was measured and recorded.

As described to earlier, spectral characteristics are derived from the spectra. However, yield characteristic are measured from the raw pre-differentiated data. The high-energy features of the pre-differentiated data [Fig. 5-2, upper right] for E_b = 900 eV and angle emission of 14^o CC are magnified [Fig. 5-3] to compare the derivative followed directly by an integration results using the 0.1 and 1 eV resolutions. The 0.1 eV step size is used to resolve the energy positions and yield intensities of the elastic peaks. The raw data [Fig. E-6] is referenced directly to several different data files. The raw data file, D3511 (see Table E-1), using 0.1 eV resolution is concatenated to the raw data file, D3505, using 1 eV resolution at an energy location of 870 eV. The raw data for the 1 eV resolution [Fig. E-6] is referenced directly to the raw data file and differentiated spectra are compared with various emission angles in Fig. E-51 and similarly compared with various other E_b's in Fig. E-57. The integrated areas of the elastic peaks measured using 0.1 eV and 1 eV resolution are further compared.

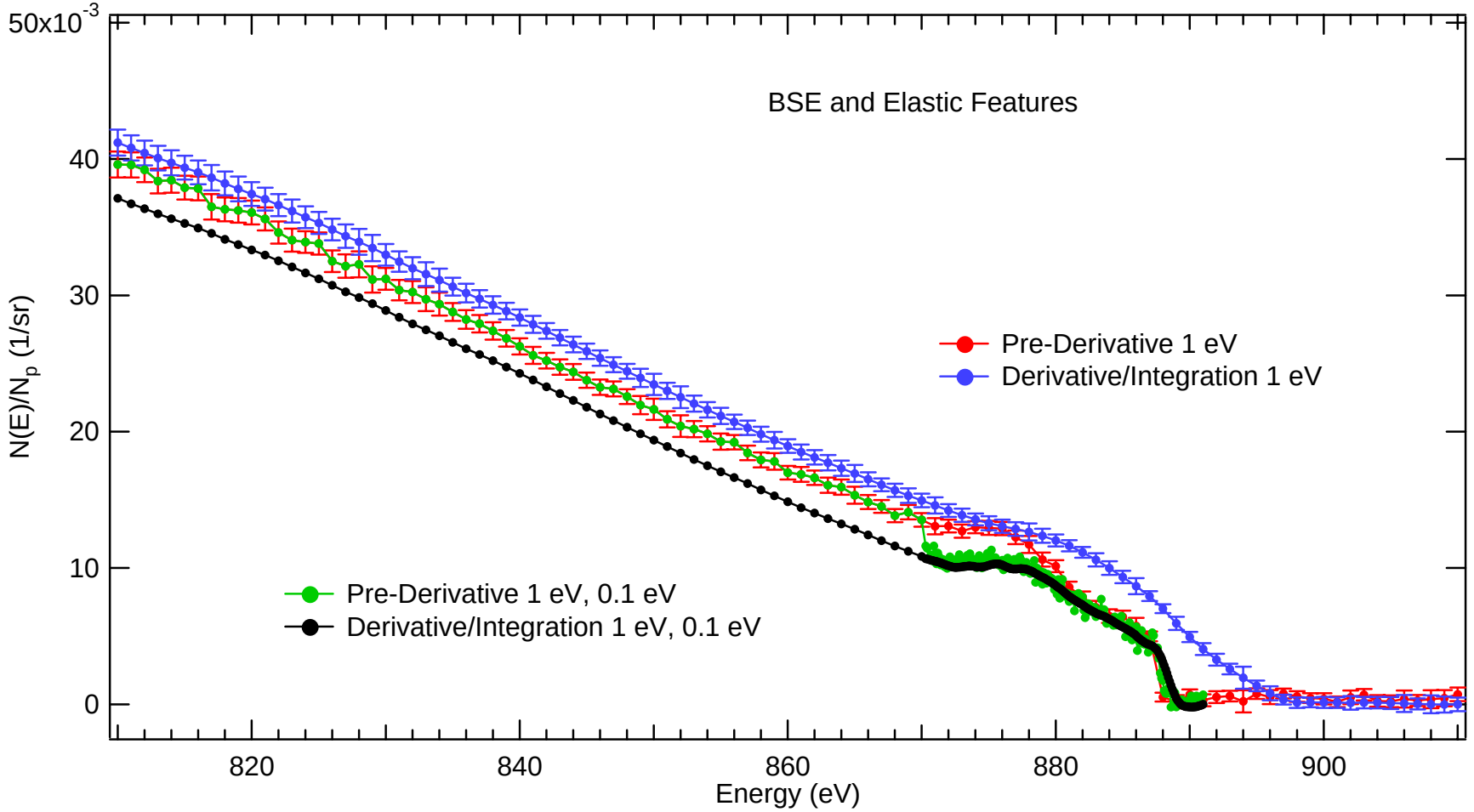

Figure 5-3 Pre-Derivative raw data (green and red) and integrated derivative (black and blue) at E_b = 900 eV and emission angle of 14° Counter—Clockwise. The 1 eV to 0.1 eV resolution transition (black and green) occurs at 870 eV. The elastic feature is positioned at ~884 eV.

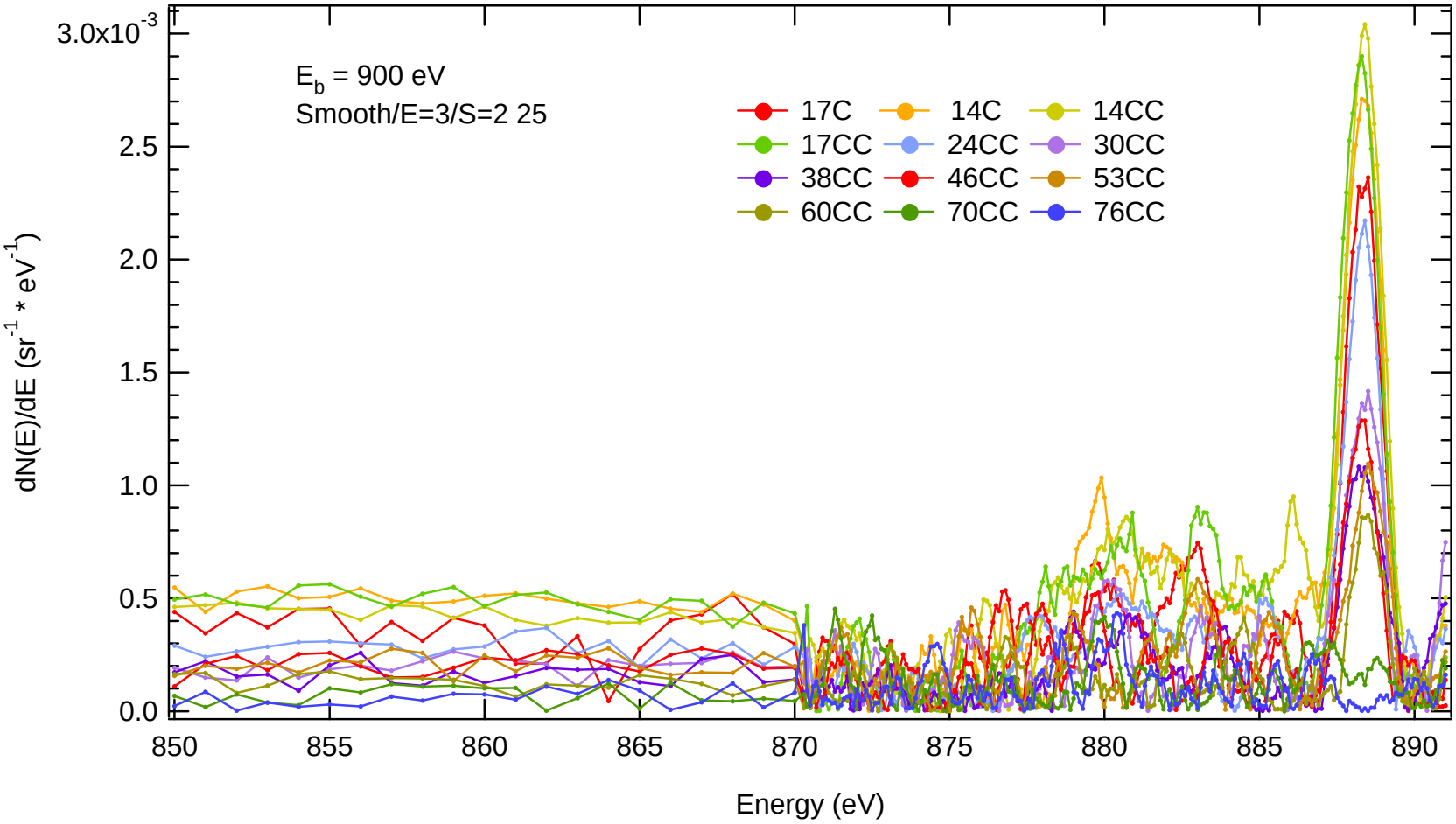

Figure 5-4 Elastic and plasmon peaks at 900 eV incident beam energy for several emission angles using the 0.1 eV and 1 eV resolutions.

5.1.(a) Elastic Peak Energy

Does the deviation of the elastic position from its respective beam energy depend on the beam energy or the emission angle? My guess is from thinking about it (transferring momentum to the crystal) that there is a dependence in emission angle b/C the problem becomes relative (it's a reference frame problem) but there is no reference with incident beam energy. There are 2 consequences, (1) the stray fields eminating the surface can be probed as deviations of the work function, (2) the same sorts of patterns (deviations from the stray fields eminating the surface) should be observable with the lowest energy emissions. So if the high energy elastic energies have a dependence on emission angle then the lowest should have a similar dependence. The differences in the highest and lowest would determine the angle dependence of the work function of the metal.

The energy position of the elastic peak is a characteristic that can be examined by investigating the relationship to incident beam energy. By measuring the deviations from the peak energy from its respective beam energy The deviations from sdkjlsdjflsj can then be compared to one another. In order to compare the elastic peak energy positions of different beam energies, the deviations from each respective Eb should be considered. The deviation of the elastic peak energy position, E_{el}, from the beam energy, E_b, is plotted against E_b [Fig. 5-5] and against emission angle [Fig. 5-6] using the 0.1 eV resolution. Values are tabulated (Table 5.1) and include the average and standard deviation over emission angle. It is important to note that the position of the elastic peak was not set precisely by the gun controller's front panel display but rather by an amount insisting that the elastic peak lie precisely on the origin. For example, the E_b = 900 eV @ 14° CC elastic peak is the same in both Figures 5-4 (above 870 eV). The elastic peak portion of these spectra are shown at 0.1 eV resolution though they have also been measured at the 1 eV resolution as shown in Fig. 5-2 and Fig. 5-3. Again emphasis is placed on the fact that the elastic peak was not exactly at 900 eV, but at 888 eV as shown in Fig. 5-4.

Variations in position (except at $\alpha \geq 70^{o}$) are <0.5 eV or from < 0.5% to < 0.01%. Indeed, the standard deviation is no greater than 0.5 eV (Table 5.1) and is greater than the average deviation. Further, the uncertainty of the energy is the same as the uncertainty in the resolution that the search routine uses, which is ±0.1 eV [see Fig. 5-4]. Taken together, these suggest that the deviations are simply random errors. One may note that Fig. 5-6 looks like it has some structure. Specifically, at 50^{o} CC emission angle, there are peaks for E_b = 900 eV and 1200 eV. These larger variations at high angle probably result from uncertainties due to low count rates in and near the peak.

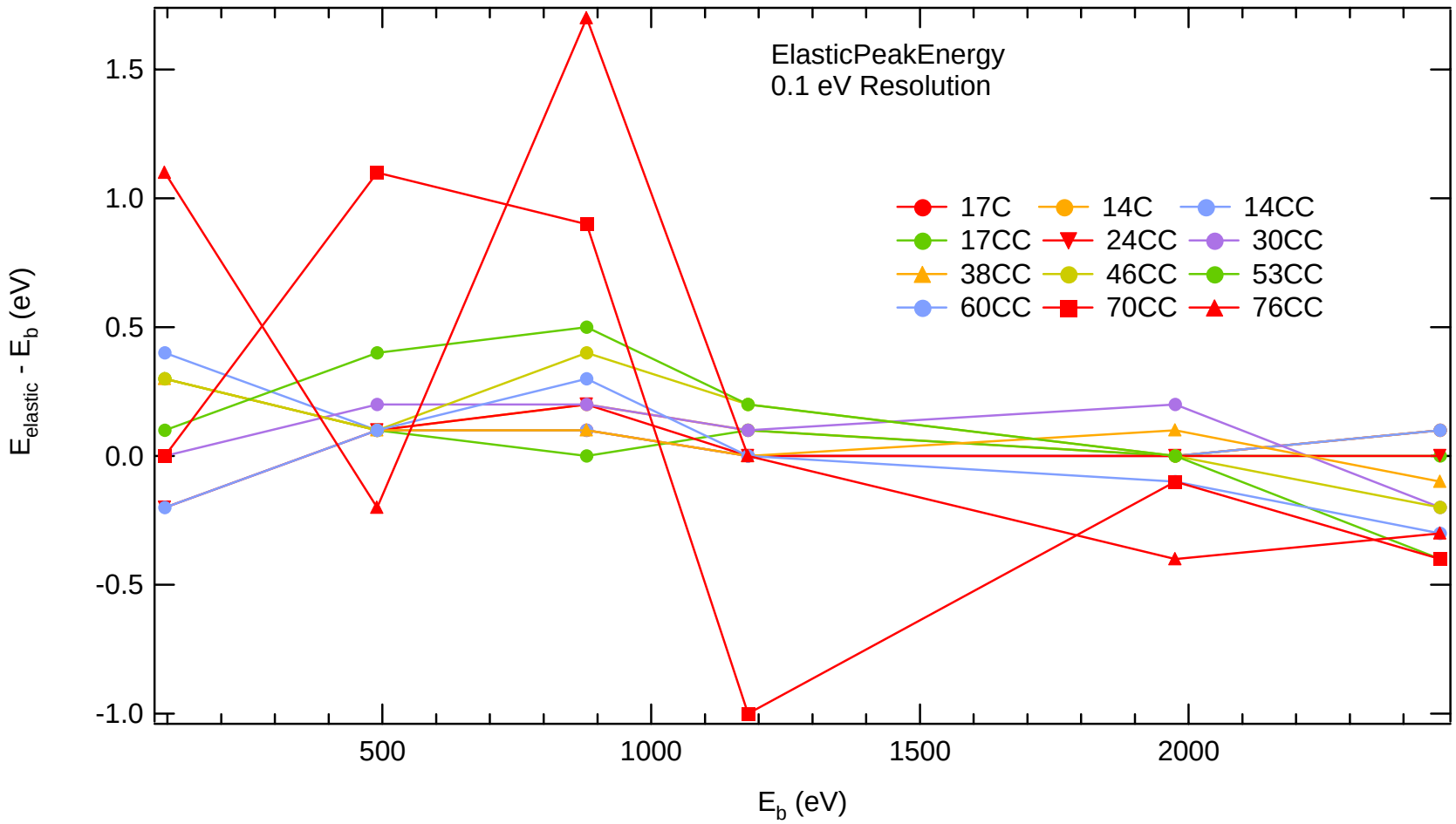

Figure 5-5 Angular resolved elastic peak energy measured at 0.1 eV resolution as a function of incident energy..

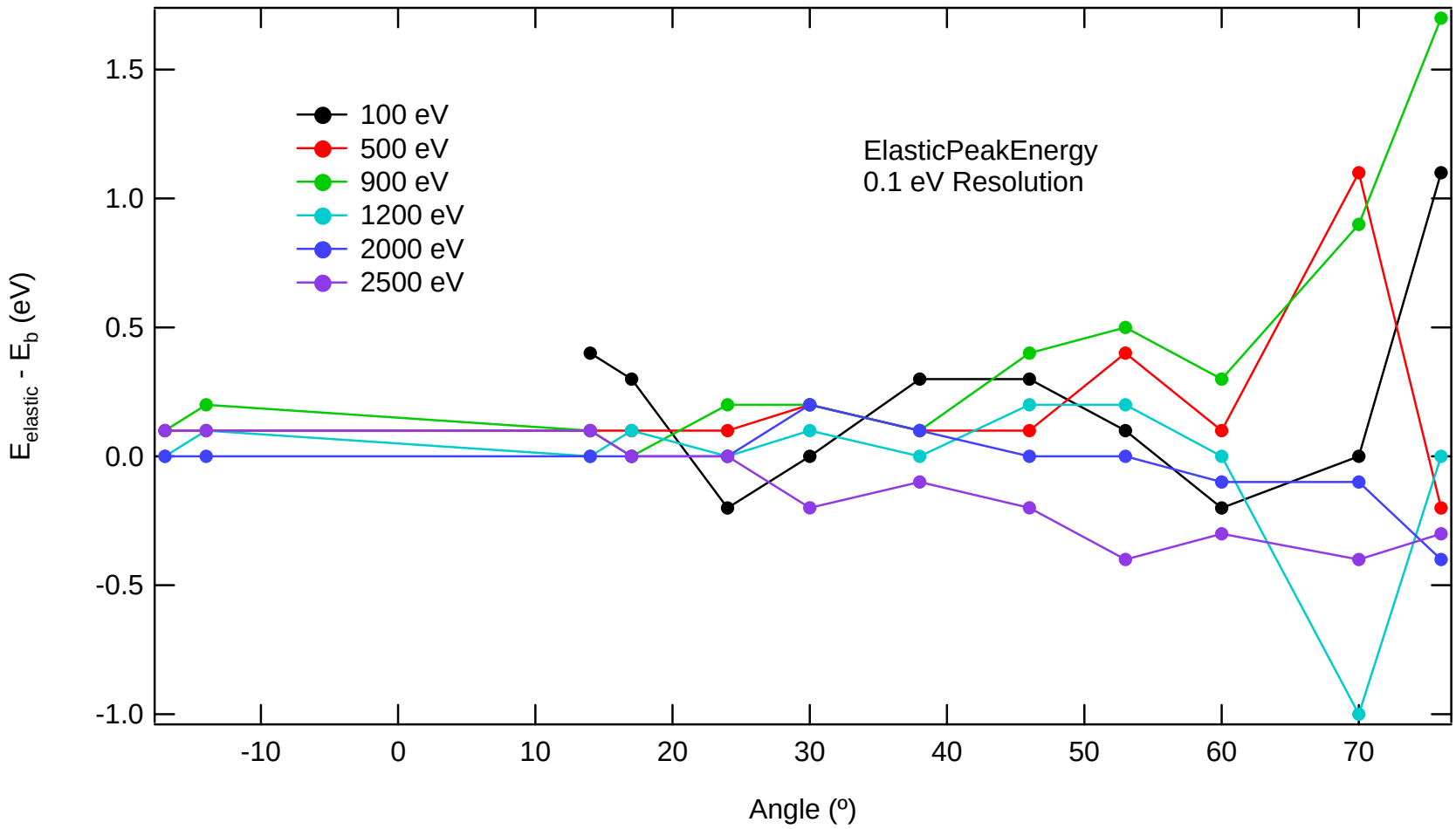

Figure 5-6 Beam Energy Resolved Elastic Peak Position at 0.1 eV resolution as a function of emission angle.

Table 5.1 Elastic Peak Energy. All 0.1 eV resolution peak energies are subtracted from the beam energy and have units of eV with an error of 0.5%.

Beam Energy	Emission Angle (^{o})													
	17C	14C	14CC	17CC	24CC	30CC	38CC	46CC	53CC	60CC	70CC	76CC	Ave	StDev
100 eV	*	*	0.4	0.3	-0.2	0	0.3	0.3	0.1	-0.2	0	1.1	0.2	0.4
500 eV	0.1	0.1	0.1	0.1	0.1	0.2	0.1	0.1	0.4	0.1	1.1	-0.2	0.2	0.3
600 eV	*	*	*	*	*	*	*	*	*	*	*	*	*	*
700 eV	*	*	*	*	*	*	*	*	*	*	*	*	*	*
900 eV	0.1	0.2	0.1	0.0	0.1	0.2	0.1	0.4	0.5	0.3	0.9	1.7	0.4	0.5
1200 eV	0.0	0.1	0.0	0.1	0.0	0.1	0.0	0.2	0.2	0.0	-1.0	0.0	0.0	0.3
2000 eV	0.0	0.0	0.0	0.0	0.0	0.2	0.1	0.0	0.0	-0.1	-0.1	-0.4	0.0	0.1
2500 eV	0.1	0.1	0.1	0.0	0.0	-0.2	-0.1	-0.2	-0.4	-0.3	-0.4	-0.3	-0.1	0.2
Ave	0.06	0.1	0.12	0.08	0.02	0.08	0.08	0.13	0.13	-0.3	0.08	0.32	0.1	0.12
StDev	0.05	0.07	0.15	0.12	0.13	0.16	0.13	0.22	0.32	0.22	0.79	0.87	0.27	

5.1.(b) Elastic Peak Intensity

The elastic peak intensity, $dN(\alpha,E_{el};E_b)/dE_e$, located at the elastic peak's energy position, E_{el}, is measured using the 1 eV and 0.1 eV resolution. The Elastic ER angular cross sections are also resolved in terms of emission angle [Fig. 5-8] and is the same data as that shown in Fig. 5-7 except the lines connecting the points are called Elastic AR intensities.

The intensity is plotted using the 0.1 eV resolution against E_b [Fig. 5-7, blue] for various emission angles and against emission angle [Fig. 5-8, green] for various E_b's. The tabulated values given in Table 5.2 are for the 0.1 eV resolution.

The intensity value of the E_b = 900 eV elastic peak for the 14^o Counter—Clockwise emission is written as $dN(\alpha = 14^o \text{ CC}, E_{el}; E_b = 900 \text{ eV})/dE_e = 3.755 \times 10^{-3}$ 1/sr*1/eV. The 0.1 eV resolution intensities are an order of magnitude higher than those of the 1 eV resolution intensities, but since the widths of the 1 eV resolution Elastic Peaks are an order of magnitude smaller. This is because the sliding derivative process is the same in both resolutions.

It is easy to see here [Fig. 5-7] that there is tendency for the intensity of the elastic peak to be a maximum of 4×10^{-3} 1/sr * 1/eV at E_b = 900 eV (emission angles less that 30^oCC) or 2×10^{-3} 1/sr * 1/eV at E_b = 500 eV (emission angles greater than 30^o CC) though it is not understood why the two Clockwise emission angles both maximize at E_b =1200 eV.

For comparison, the elastic peak intensities are resolved [Fig. 5-7] in terms of E_b. Even though the 1 eV resolution has been used to determine the peak intensity, the values are very comparable to those determined with 0.1 eV resolution. The term for this kind of plotted information is the cross section [Fig. 5-8]. The Elastic peak intensity measured at these discrete E_b values contain peaks at higher emission angles. For example, an additional peak near 40^o CC occurs at E_b = 500 eV and an additional peak near 50^oCC occurs at E_b = 900 eV and 1200 eV. This agrees with Rutherford's $\text{Sin}^4(\theta)$ cross section distribution.

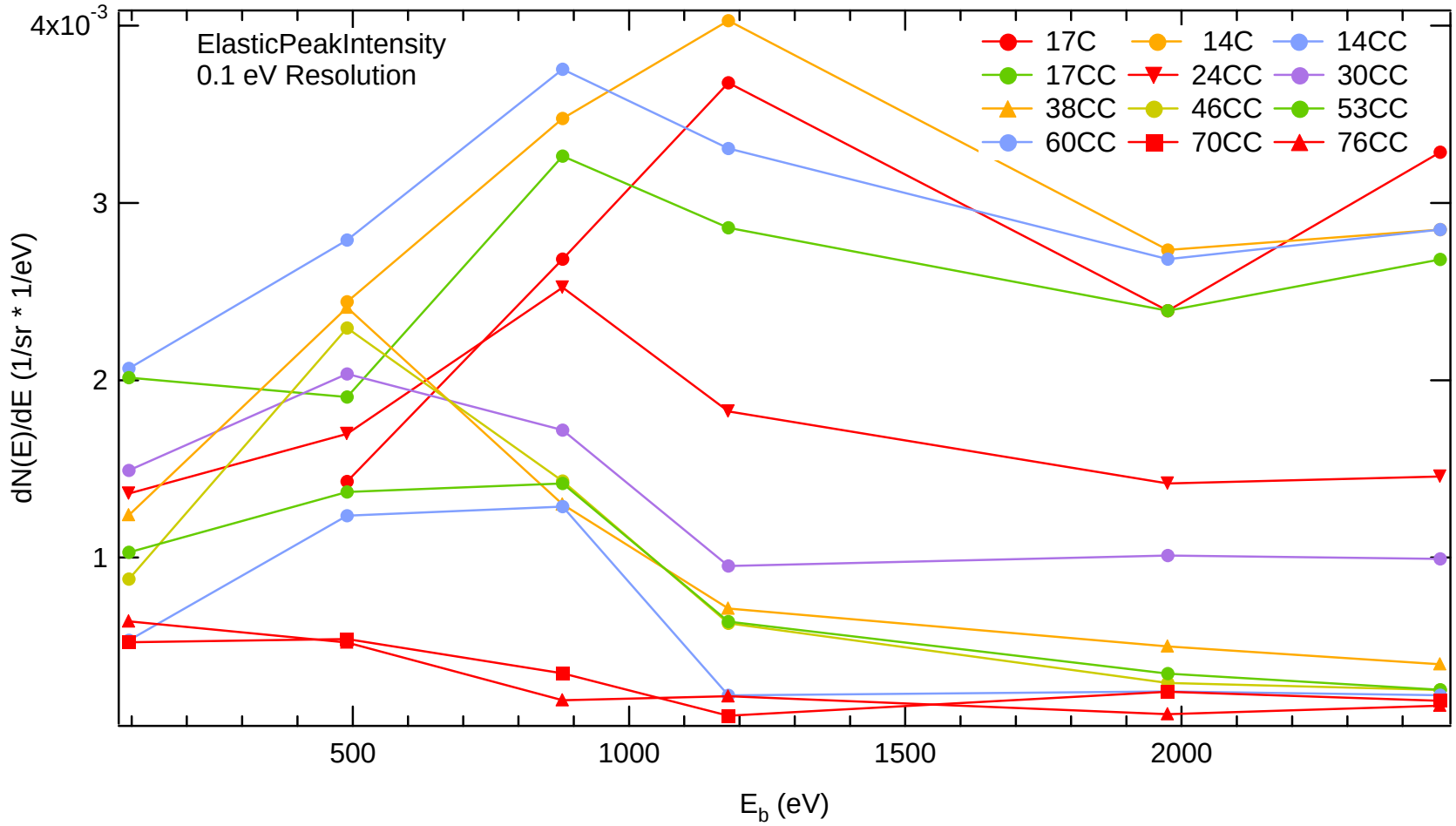

Figure 5-7 Elastic Peak Intensity versus incident beam energy measured using the 0.1 eV resolution spectra for selected emission angles.

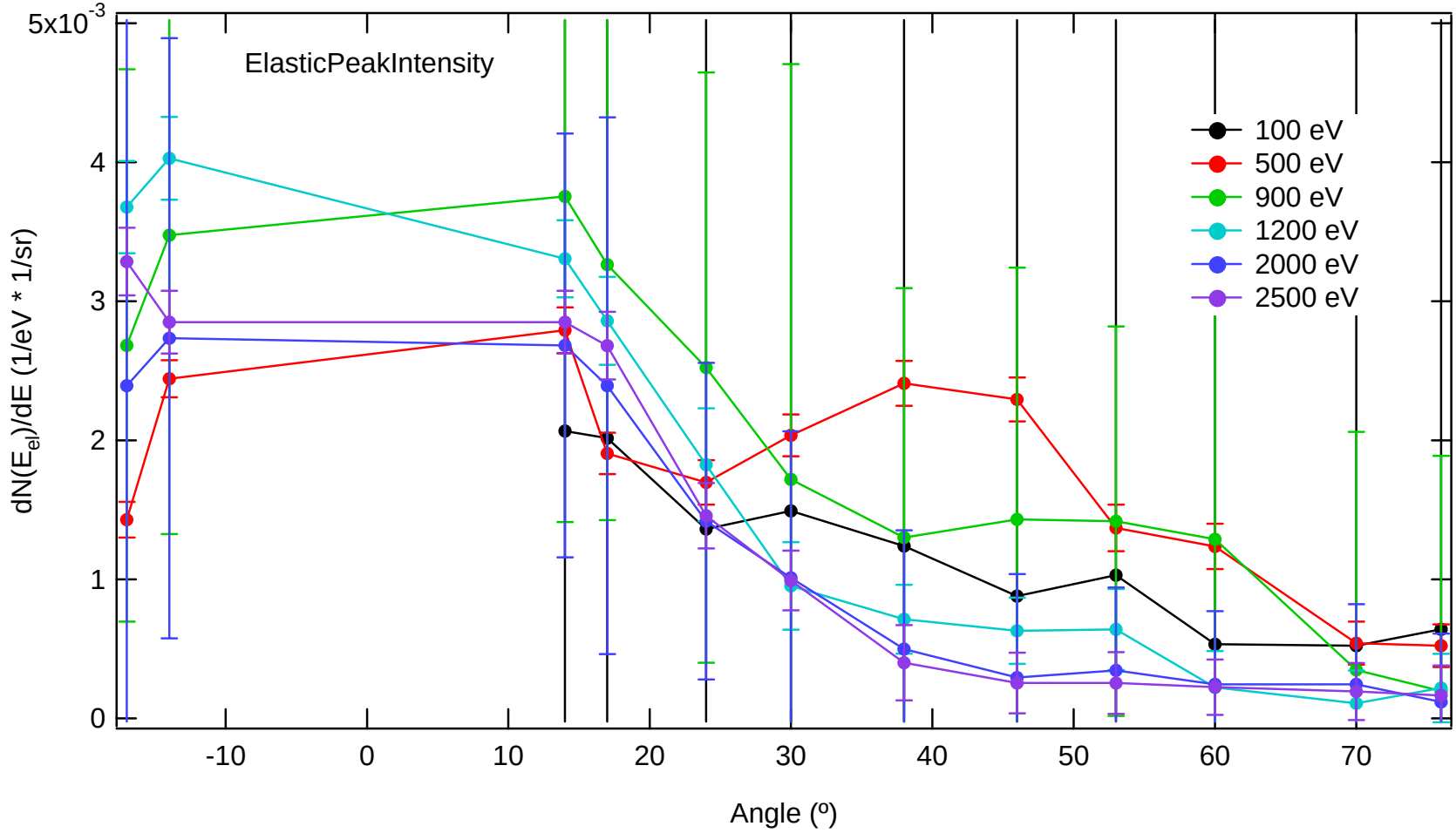

Figure 5-8 Elastic Peak Intensity versus emission angle measured using the 0.1 eV resolution spectra for selected incident beam energies.

Table 5.2 Elastic Peak Intensity. All 0.1 eV resolution yield intensities have units of (1/sr*1/eV) * 10^{-6} and an error of 5% (1/sr*1/eV).

Beam Energy	Emission Angle (^{o})											
	17C	14C	14CC	17CC	24CC	30CC	38CC	46CC	53CC	60CC	70CC	76CC
100 V	*	*	2294	2053	1432	1684	1294	1050	1066	578	602	665
500 eV	1428	2442	2791	1906	1698	2035	2410	2294	1370	1237	541	521
600 eV	*	*	*	*	*	*	*	*	*	*	*	*
700 eV	*	*	*	*	*	*	*	*	*	*	*	*
900 eV	2683	3476	3755	3264	2523	1719	1301	1431	1418	1287	347	196
1200 eV	3678	4028	3307	2860	1825	953	712	630	640	223	109	218
2000 eV	2392	2734	2683	2392	1418	1011	499	293	346	245	244	118
2500 eV	3286	2850	2850	2681	1457	993	399	254	254	224	192	165

5.1.(c) Shape Characteristics (FWHM)

Analysis of the shape of the elastic peak provides evidence about both instrumental resolution and fractional energy exchange of the elastic electrons. High resolution spectra (0.1 eV resolution) are shown Fig. 5-9 (same as Fig. E-38) and peak intensity values are tabulated in Table 5.2. The origin of each E_b resolved spectra is shifted by the respective incident electron beam energy, E_b, so that comparison of various E_b spectra can be accomplished. .

Additional even higher resolution spectra (0.01 eV resolution) taken over a range of emission angles at 1500 eV beam energy are shown in Fig. 5-? and Fig. 5-?. The spectra shown in Fig 5-9 demonstrate that the basic shape of the elastic peak does not change a great deal with beam energy.

Though the E_bR spectra @ 14°CC [Fig. 5-9] have been smoothed (Table 5.4), it its easy to see that the FWHM measures the least for E_b = 900 eV at approximately 1.1 eV and measures the greatest for E_b = 100 eV at approximately 1.9 eV. Intermediate values for E_b = 500 eV, 2000 eV, and 2500 eV are also shown. The Elastic Peak typically measures the thermal spread (or width) of the electron filament source addressed in Chapter 3.2(e).

These energy values are directly related to the Blackbody radiation using the $E = k_B T$ relation. The temperatures for the greatest and least FWHM span from 1000 K to 2000 K and are well within the limits of the electron gun filament though the spectra for E_b = 100 eV heavily degraded the filament. Pushing the limits of the electron gun's design required filament replacement and may require an alternate gun design for probing emission energies less then 100 eV.

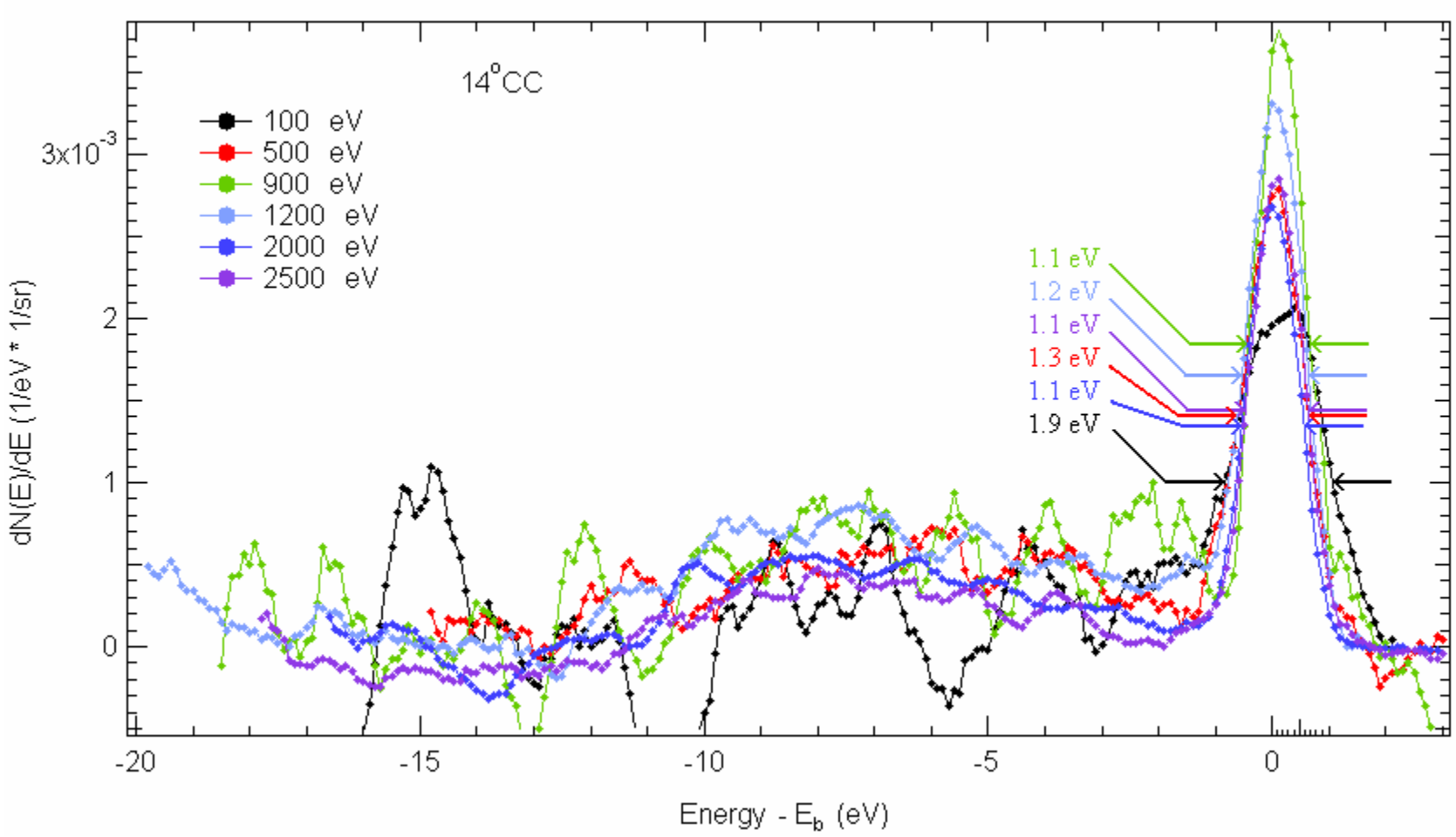

Figure 5-9 Beam Energy Resolved Elastic Peak Energy Spectra at 14° Counter-Clockwise emission for selected beam energies.

5.1.(d) Elastic Yield

The elastic peak yield, $\delta(\alpha,E_{el}; E_b)$, is determined to be the integrated intensity between the boundaries of the elastic peak. The extent of the peak is addressed in 5.1(a) with the spectra measured at 0.01 eV, 0.1 eV, and 1 eV resolutions. While the elastic yield can be calculated by integrating the electron emission spectrum $dN(\alpha, E_e, E_b)/dE_e$ over this energy range; a more direct approach, both experimentally and theoretically, is to calculate the elastic yield as the difference of the pre-differentiated data (see, e.g., Fig. 5-2) at the upper and lower energies of the elastic peak energy range. This is obvious since the pre-differentiated data is just the integral of dN/dE_e.

The plots of elastic peak yields versus emission angle show the same trends observed for the elastic peak intensity. The elastic yields as a function of emission angle, calculated using both the 0.1 eV and 1 eV resolution cross sections, are plotted [Fig. 5-10] and tabulated in Table 5.3. In general, the elastic yield decreases with increasing energy. The elastic yields of the incident beam energies 500 eV, 900 eV, and 1200 eV all behave qualitatively like Mott cross sections in their angular distributions. As with the elastic intensity, these yields contain a significant additional peak between 40^o CC and 50^o CC emission angle with a difference in increasing yield intensity of ~1 x 10^{-3} (1/sr) from approximately 10^o CC less emission angle. In fact, the trends are more evident since the integrated peak has a better signal-to-noise ratio than the elastic peak intensity alone. The possibility of diffraction effects exists in the E_b = 500 eV @ 40^o emission [Fig. 4-7] but not for the E_b = 900 eV or E_b = 1200 eV. The elastic yield calculated using the 1 eV resolution is compared with elastic yield calculated using the 0.1 eV resolution. The respective uncertainties [Fig. 5-11] are calculated in quadrature (Eq. 3.7) for the 0.1 eV and 1 eV resolution elastic yields. The uncertainties span from 5 x 10^{-6} to 1, but most of the values lay within one order of magnitude ranging from 10^{-3} to 10^{-2} 1/sr. This extensive span in uncertainties stresses the difficulty of any further comparisons of these resolutions in spectral data.

As an aside, note that the 0.01 eV resolution spectra [Fig. 3-18 and Table 3.1] have been fit to a Doniach and Sunjic theory (Eq. 2.17) for E_b = 1500 eV. However, these highest resolution yields are not

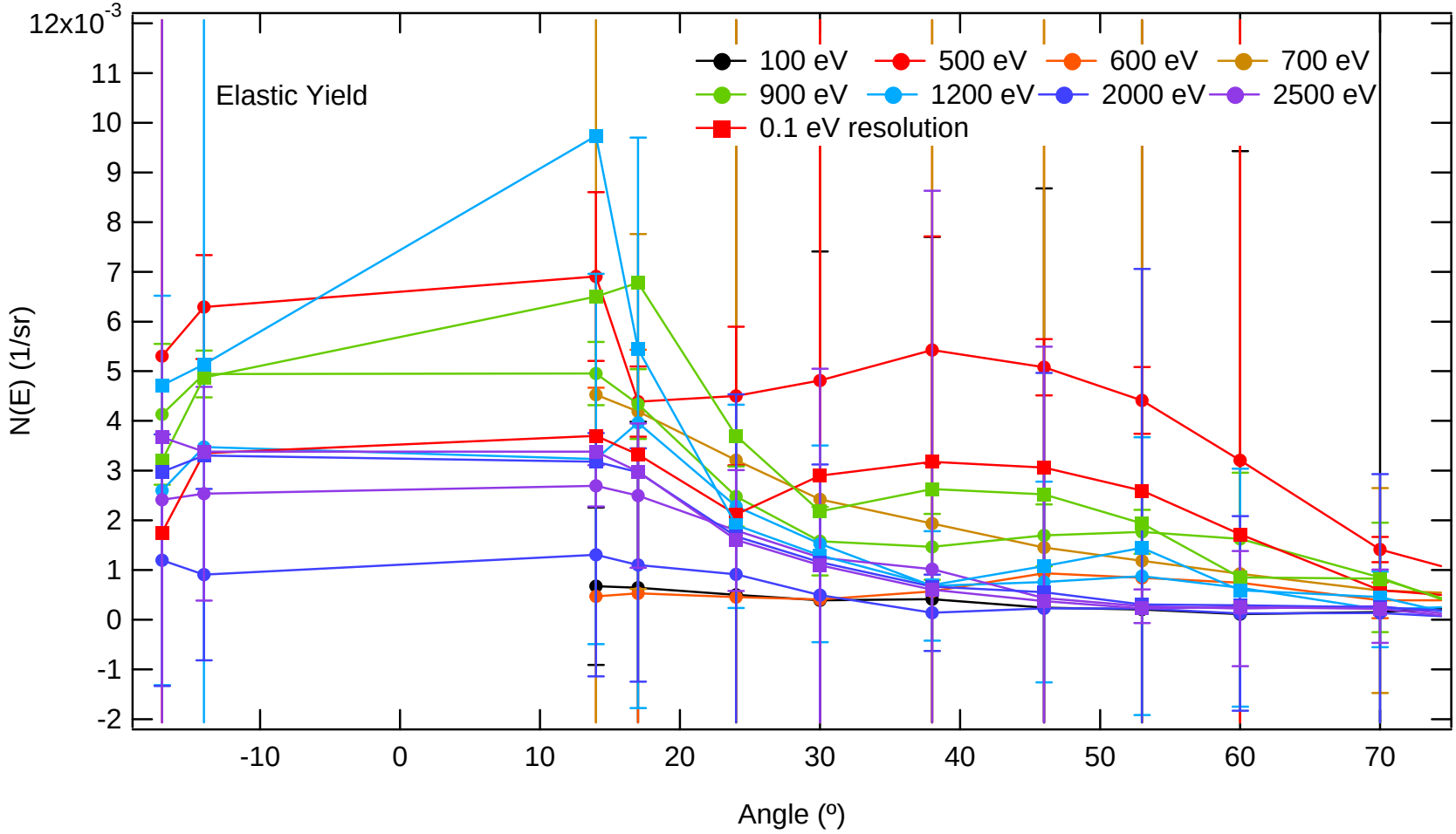

Figure 5-10 Elastic peak yield versus emission angle for several incident beam energies measured using 1 eV (circles) and 0.1 eV (squares) resolution.

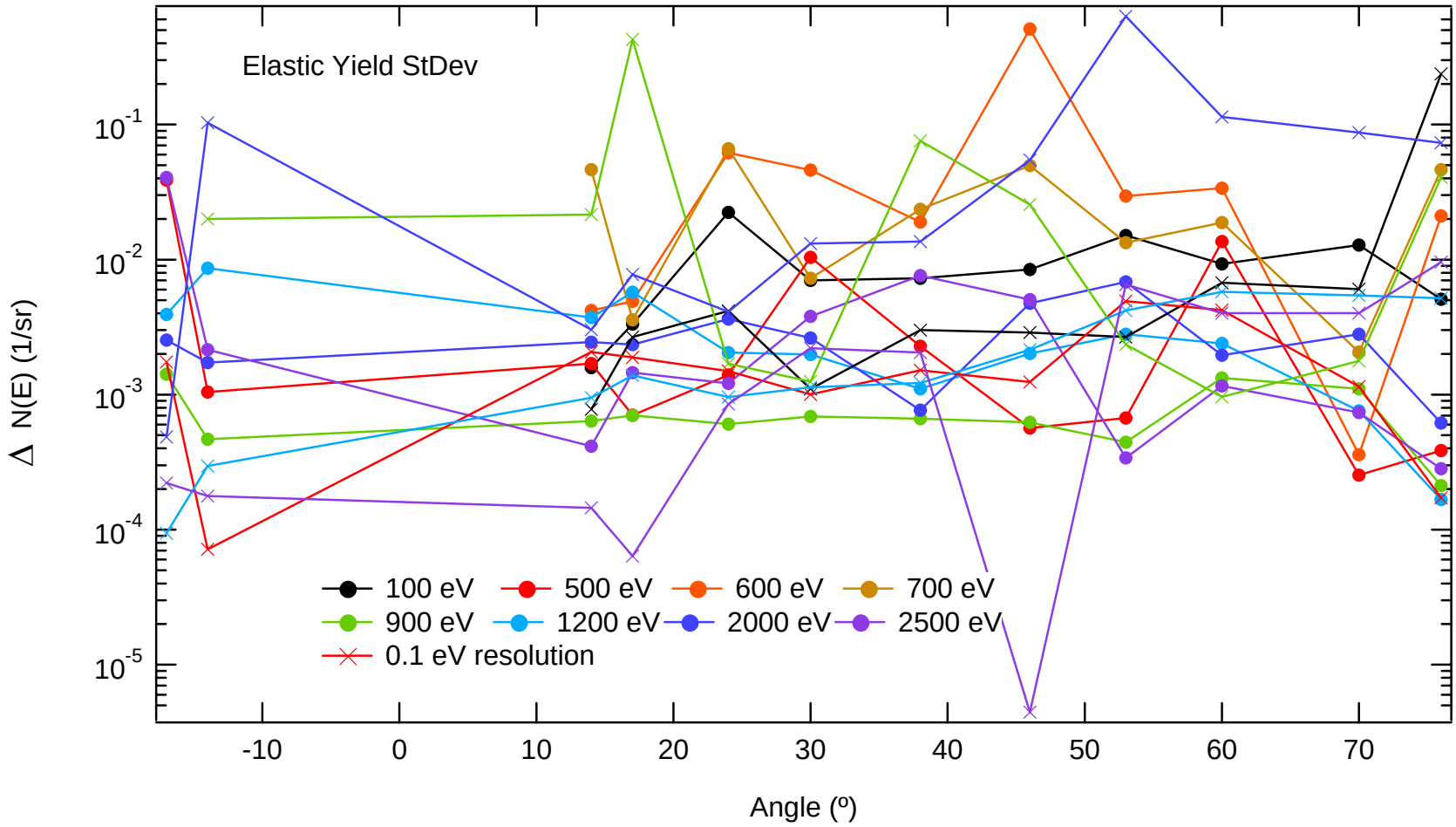

Figure 5-11 Uncertainties in elastic peak yield versus angle for several incident beam energies measured at 1 eV and 0.1 eV resolution. ΔN(E) are shown on a log scale with units of inverse steradians.

considered here, because of the RD's energy resolution (calculated geometrically), is greater than 0.01 eV step size. The geometrical energy resolution of the RD [Chap 3.2(e)] has been predicted to be 0.3 eV and measured to be 0.2 eV, so utilizing the 0.1 eV resolution data should be more than sufficient for calculating yields. In addition, the Doniach and Sunjic type fit is not used, since the RD's voltage bias supply is 20 to 30 times less than the RD's energy resolving power.

The 0.1 eV resolution spectra are chosen for a more thorough investigation. For all emission angles measured at an energy resolution of 0.1 eV, the elastic peak yield values are plotted against E_b [Fig. 5-12] and tabulated in Table 5.3. The elastic yield plotted as a function of E_b does not show any obvious trends as was found for the elastic peak intensity.

Even though the spectra have been calculated using the same sliding derivative method (Eq. (3.4)), the intensities of the 0.1 eV resolution data are an order of magnitude greater, and the FWHM's are an order of magnitude less than those of the 1 eV resolution data. The product of the intensity by the width exactly cancel this order of magnitude difference leading to comparable yields between resolutions.

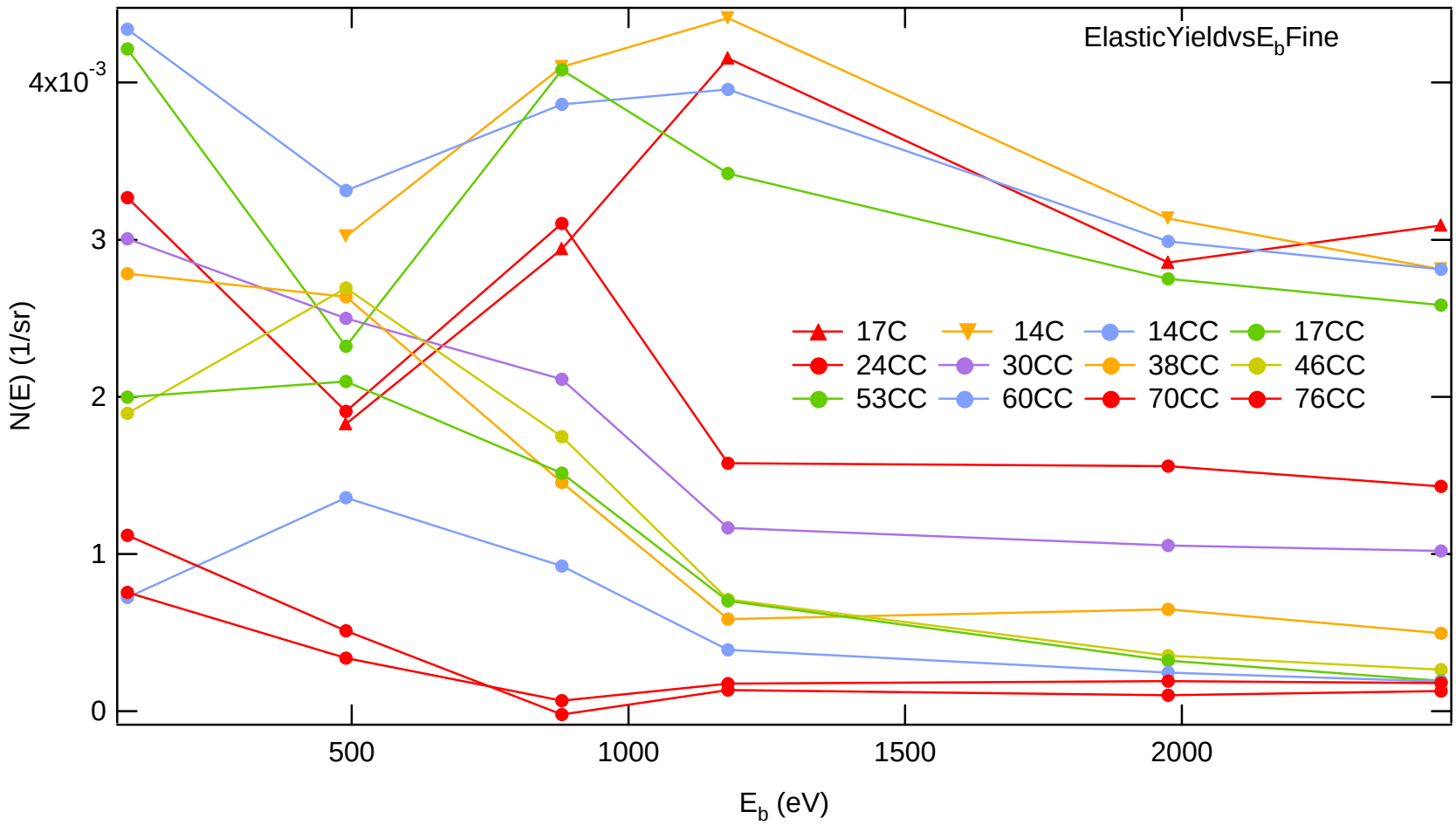

Figure 5-12 Elastic peak yield cross sections for several emission angles using the 0.1 eV resolution spectra.

Table 5.3 The elastic peak yield at 0.1 eV resolution given in units of 10^{-3} inverse steradians.

Emission Angle (^{o})	incident beam energy (eV)					
	100 eV	500 eV	900 eV	1200 eV	2000 eV	2500 eV
17C	*	1.8 ± 0.2	2.9 ± 41	4.2 ± 5	2.86 ± 73	3.09 ± 10
14C	*	3.0 ± 1.2	4.1 ± 2	4.4 ± 5	3.14 ± 87	2.81 ± 4
14CC	-0.33 ± 0.8	3.3 ± 4	3.9 ± 1	4.0 ± 6	2.99 ± 114	2.58 ± 4
17CC	0.34 ± 3	2.3 ± 5	4.1 ± 2	3.4 ± 4	2.75 ± 633	1.43 ± 7
24CC	0.36 ± 4	1.9 ± 1	3.1 ± 26	1.6 ± 2	1.56 ± 55	1.02 ± 0.005
30CC	0.09 ± 1	2.5 ± 2	2.1 ± 76	1.2 ± 1	1.05 ± 14	0.50 ± 2
38CC	0.30 ± 3	2.6 ± 1	1.45 ± 1	0.59 ± 1	0.65 ± 13	0.27 ± 2
46CC	0.20 ± 3	2.7 ± 1	1.75 ± 2	0.71 ± 0.9	0.35 ± 4	0.19 ± 0.8
53CC	0.10 ± 3	2.1 ± 1.9	1.52 ± 427	0.70 ± 1	0.32 ± 8	0.19 ± 0.06
60CC	0.11 ± 7	1.4 ± 2	0.92 ± 22	0.39 ± 0.9	0.25 ± 3	0.18 ± 0.1
70CC	0.13 ± 6	0.34 ± 0.07	0.07 ± 20	0.18 ± 0.3	0.19 ± 103	0.18 ± 0.2
76CC	0.44 ± 24	0.5 ± 2	-0.02 ± 0.001	0.14 ± 0.09	0.10 ± 0.5	0.13 ± 0.2

5.2 Plasmon Peak Features

The identification of the first quasi-elastic signature is exaggerated as the first bump below the elastic peak in Fig. 3-37. The characteristic features of the peak, defined in Table 3.3, are peak position energy, E_{pl}, intensity, $dN(\alpha,E_{pl};E_b)/dE_e$, integrated intensity or yield, $\delta(\alpha, E_{pl}; E_b)$, and peak width. This peak is somewhat broader than the elastic peak and is labeled the first plasmon peak. Since it is only identifiable using the 0.1 eV resolution, the optimum biasing capabilities of the instrument allow the energy emissions to span from the incident beam energy, E_b, to about 20 eV below E_b. A higher resolution plot of the high-energy portion of the spectra is given [Figs. 5-4 and 5-9] using the 0.1 eV resolution, The AR spectra are given in Appendix E [Fig. E-30 through Fig. E-35] and the same E_bR spectra [Fig. E-38 through Fig. E-47] are scaled with each respective displaced E_b for comparison. From these portions of spectra, two key points of interest are measured, tabulated, and compared. These points of interest lead to the characteristic features determining the energy, size, and, shape of the plasmon peak as well as the area underneath the peak or the plasmon yield. The comparative ratio to the elastic peak is presented in terms of intensity and yield.

5.2.(a) Plasmon Peak Energy

An automated programming search routine was used to locate the energy positions, E_{pl}, of the plasmon peak intensity at the various values of the parameters of the incident beam energy, E_b, and the emission angle, α. The first plasmon peak's energy results are plotted in Fig. 5-13 along with the average values at each energy (dashed lines) and tabulated in Table 5.4 with averages and standard deviations. The resulting values expressed as a deviation from E_b, vary from –1.3 eV to –9.4 eV. For example, the first plasmon peak energy for the E_b = 900 eV [Fig. 5-13, green] is an average of 4 eV below the elastic peak. At E_b = 1200 eV and 2500 eV, plasmon peaks are observed to be closer to 8 eV below E_b. The elastic peak measured energy position [Fig. 5-8] is found using the same energy resolution of 0.1 eV.

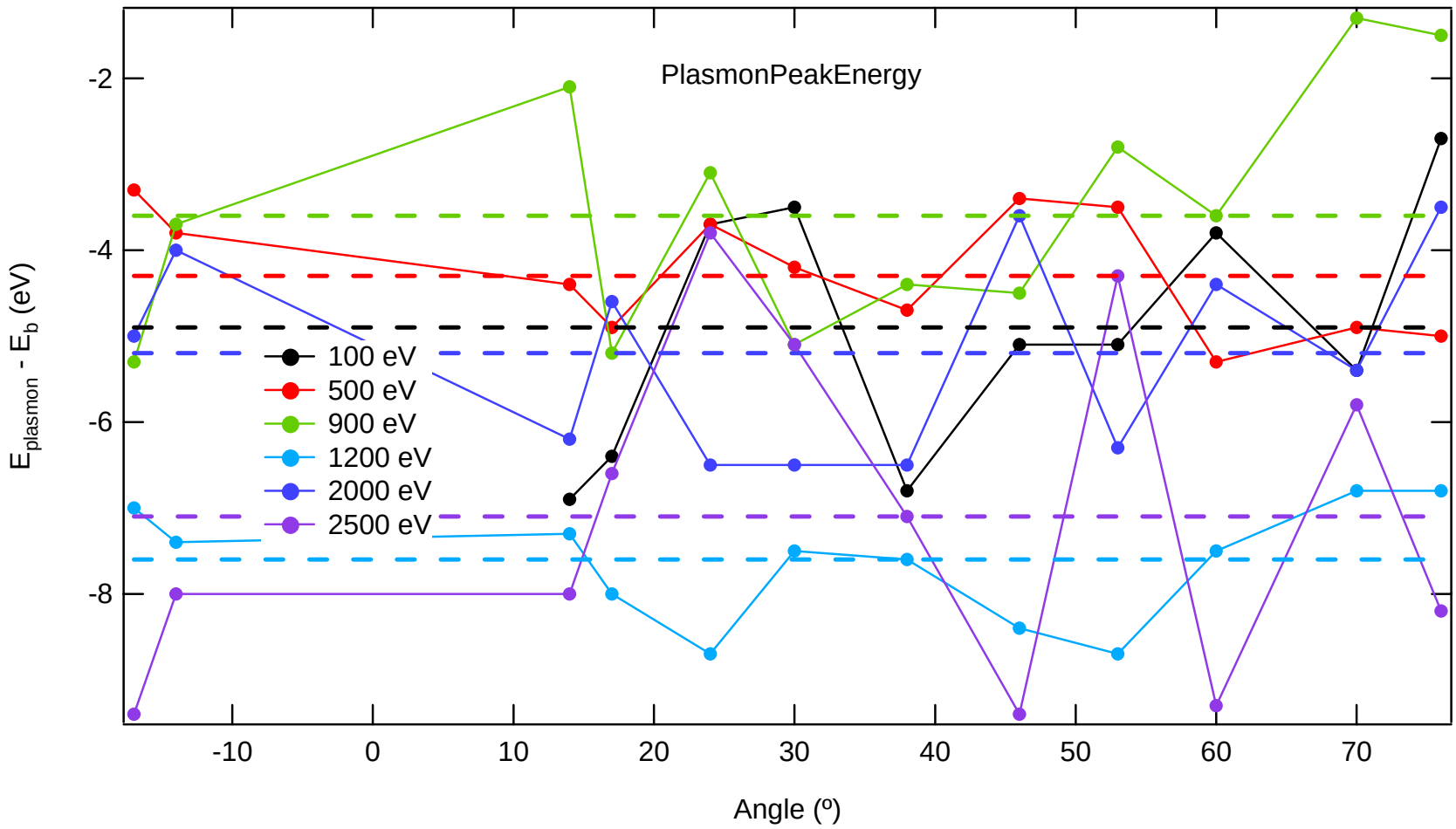

Figure 5-13 Plasmon peak energy is given in terms of its displacement from the incident beam energy. Averages over E_b are shown as superimposed dashed lines of the same color.

Table 5.4 Plasmon Peak Energy. All peak energy positions are subtracted from the beam energy and have units of eV with an error of 5%.

Beam Energy	Emission Angle (deg)													
	17C	14C	14CC	17CC	24CC	30CC	38CC	46CC	53CC	60CC	70CC	76CC	Ave	StDev
100 eV	*	*	-6.9	-6.4	-3.7	-3.5	-6.8	-5.1	-5.1	-3.8	-5.4	-2.7	-4.9	1.5
500 eV	-3.3	-3.8	-4.4	-4.9	-3.7	-4.2	-4.7	-3.4	-3.5	-5.3	-4.9	-5.0	-4.3	0.7
600 eV	*	*	*	*	*	*	*	*	*	*	*	*	*	*
700 eV	*	*	*	*	*	*	*	*	*	*	*	*	*	*
900 eV	-5.3	-3.7	-2.1	-5.2	-3.1	-5.1	-4.4	-4.5	-2.8	-3.6	-1.3	-1.5	-3.6	1.4
1200 eV	-7.0	-7.4	-7.3	-8.0	-8.7	-7.5	-7.6	-8.4	-8.7	-7.5	-6.8	-6.8	-7.6	0.7
2000 eV	-5.0	-4.0	-6.2	-4.6	-6.5	-6.5	-6.5	-3.6	-6.3	-4.4	-5.4	-3.5	-5.2	1.2
2500 eV	-9.4	-8.0	-8.0	-6.6	-3.8	-5.1	-7.1	-9.4	-4.3	-9.3	-5.8	-8.2	-7.1	2.0
													-5.5	1.3

* Spectra not measured using 0.1 eV resolution

The average elastic peak energy (Table 5.2) subtracted from the angle-averaged plasmon peak energy plotted as a function of emission angle [Fig. 5-13] demonstrates that there is no angular dependence of E_{pl}.

Also plotted [Fig. 5-14] is the plasmon peak deviation from E_b as a function of E_b for the selected emission angles. The angle-averaged plasmon peak energy deviation [Fig. 5-14, squares] is also provided in order to determine if there is any evidence for dependence on E_b. A linear trend [Fig. 5-14, dash] is fit to this average showing an increase in plasmon peak energy deviation with increasing E_b. All averages fall within a standard deviation of the line fit except for E_b = 900 eV and E_b = 1200 eV. In this case, the dependence on E_b is small and may be more easily understood by investigating the intensity of the plasmon peak.

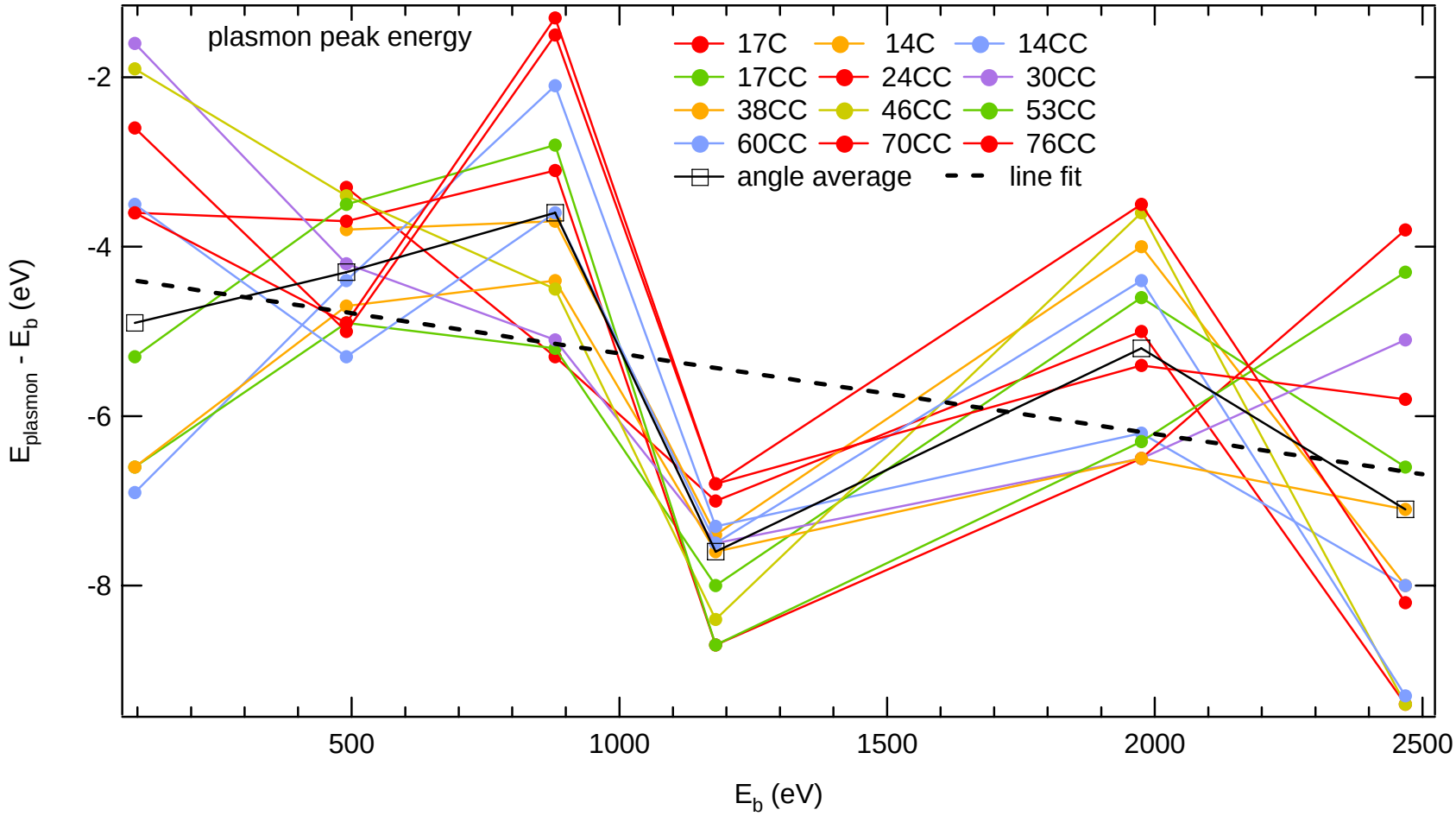

Figure 5-14 Plasmon peak energy versus incident beam energy for several emission angles. Angle averages (open squares) are also given and superimposed with a line fit (dashed). The line fit (dash) has coefficients of (–4 ± 1) eV intercept with slope of (–0.0009 ± 0.0007) and $\chi^2 = 9$.

5.2.(b) Plasmon Peak Intensity

The first plasmon peak intensities, $dN(\alpha, E_{pl}; E_b)/dE_e$, are shown [Fig. 5-15] and tabulated in Table 5.5. Trends in the intensities are clearly evident. They are greatest at lower emission angles and decrease with increasing emission angle. The intensities falls within the yield boundaries of 0 to 1.2 x 10^{-3} (eV^{-1} sr^{-1}) and contains a couple of anomalous minor peaks at 24° CC (100 eV and 500 eV) and 53° CC (900 eV and 1200 eV).

To determine the nature of the angular dependence of the plasmon peak intensity, the data are compared with three angular models, a Lambert cosine law, screened Rutherford scattering and screened Mott scattering. Fits to these models for E_b = 2500 eV data are shown in [Fig 5-15] for comparison. $dN(\alpha, E_{pl}; E_b = 2500\ eV)/dE_e$ is fit with a Lambert cosine (Eq. 2.8) law containing a single intensity parameter B written as

$$\frac{dN(\alpha, E_{pl})}{dE_e} = B\cos(\alpha) \tag{5.2}$$

For the E_b = 2500 eV case, B = (3.7 ± 0.4) x 10^{-4} eV^{-1} sr^{-1} with χ^2 = 1 x 10^{-7}, the measured intensity clearly falls off faster than this fit. A two parameter Rutherford scattering model (Eq. 2.15), having a screening factor β, and a constant, C, (a combination of, k, atomic number Z, and E), given as

$$\frac{dN(\alpha, E_{pl})}{dE_e} = \frac{C}{\left(1 + 2\beta - \cos\alpha\right)^2}, \tag{5.3}$$

is fit to the E_b = 2500 eV case for comparison. This fit, having β = (0.16 ± 0.04) and C = (6 ± 2) x 10^{-5} eV^{-1} sr^{-1}, is a factor of 3 better with χ^2 = 3 x 10^{-8}, but still does not capture the shape completely. A three parameter Mott (Eq. 2.16) cross section for a constant, C_1, the Mott cross section contribution, and constant, C_2, the Rutherford cross section contribution containing the screening factor β written in the form

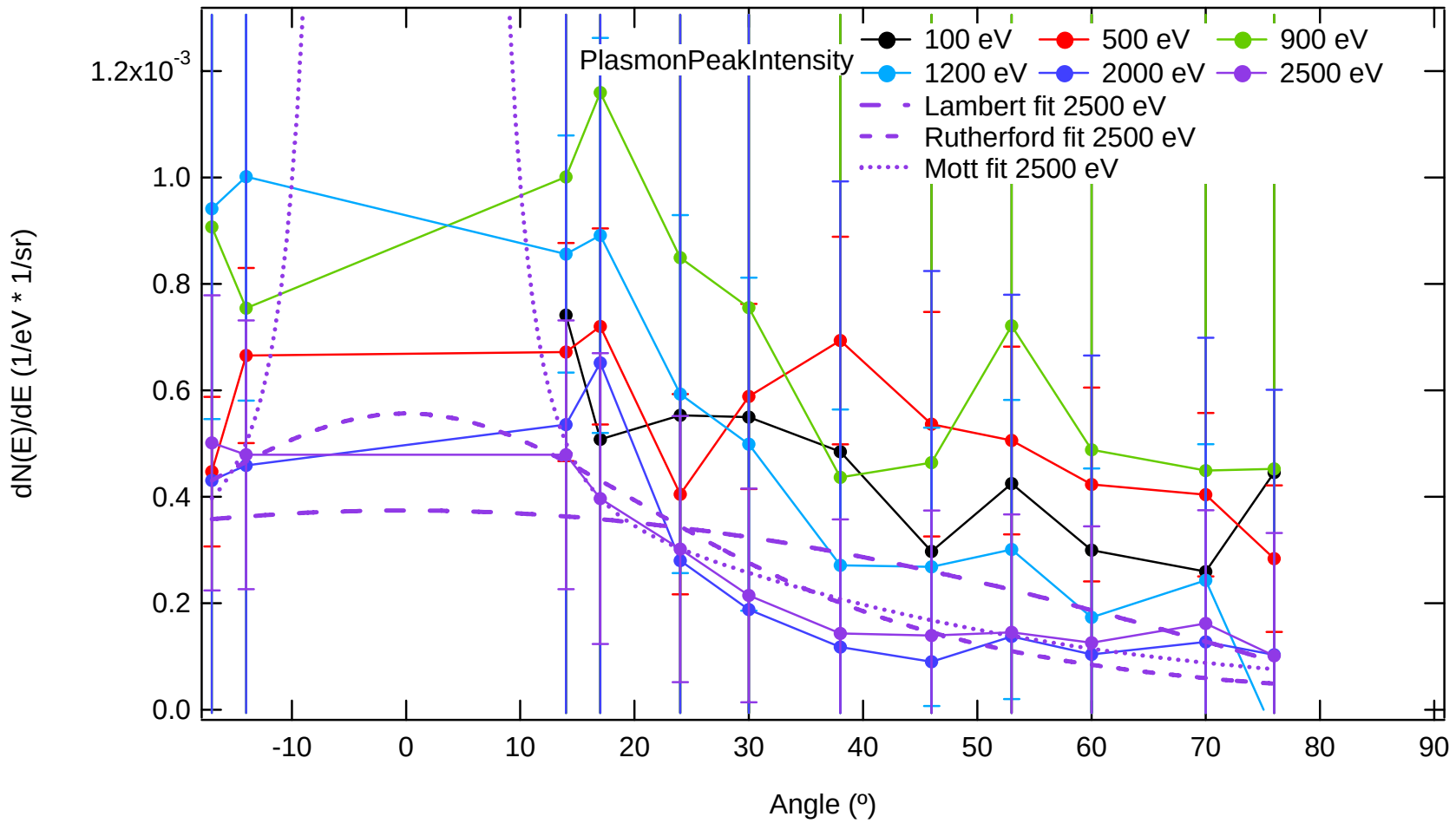

Figure 5-15 Plasmon peak intensity at the location of the first surface plasmon peak for several different beam energies. The Lambert cosine law, Rutherford trend, and Mott trend are fit to E_b = 2500 eV data. The Rutherford fit is qualitatively the best.

Table 5.5 Plasmon Peak Intensity. All peak intensities have units of (eV^{-1} sr^{-1}) * 10^{-6} and an error of 5% (eV^{-1} sr^{-1}).

Beam Energy	Emission Angle (^{o})											
	17C	14C	14CC	17CC	24CC	30CC	38CC	46CC	53CC	60CC	70CC	76CC
100 eV	*	*	742	508	553	550	485	297	425	300	260	446
500 eV	447	666	672	720	405	589	694	537	506	423	404	284
600 eV	*	*	*	*	*	*	*	*	*	*	*	*
700 eV	*	*	*	*	*	*	*	*	*	*	*	*
900 eV	907	755	1001	1160	849	756	437	465	722	488	449	453
1200 eV	941	1002	856	891	593	499	271	269	301	174	243	188
2000 eV	431	459	536	652	280	188	118	90	138	104	127	103
2500 eV	501	479	479	397	302	215	144	140	146	126	162	101

* not measured

$$\frac{dN(\alpha, E_{pl})}{dE_e} = \frac{C_1}{\sin^4(\alpha/2)} + \frac{C_2}{(1+2\beta-\cos\alpha)^2} \tag{5.4}$$

is also used to qualitatively determine the shape. The Mott fit, having $C_1 = (4 \pm 1) \times 10^{-8}$ eV^{-1} sr^{-1}, $C_2 = (1.5 \pm 0.9) \times 10^{-4}$ eV^{-1} sr^{-1}, and $\beta = (0.3 \pm 0.1)$ is slightly better with $\chi^2 = 2 \times 10^{-8}$, is slightly qualitatively better yet, but still falls off slower than the data. The Rutherford fit qualitatively captures the $E_b = 2500$ eV data best and seems to offer most ideal shape analysis for the rest of the incident beam energy data.

5.2.(c) High Energy Plasmon Peak Comparison

Data in Table 5.5 suggests that there is not a strong dependence of the plasmon peak intensity or E_b, as was concluded in section 5.1(b) for the elasic peak intensity. To determine if the beam energy dependence of these two peaks is similar we investigate the ratio of the first plasmon peak intensity to the elastic peak intensity. The 0.1 eV resolution plasmon peak intensities are shown divided by the 0.1 eV resolution elastic peak intensities [Fig. 5-7]. This ratio of intensities is plotted against E_b [Fig. 5-16] with a logarithmic scale. This ratio is found to be roughly constant, on the order of ~40%. Only 4 out of 70 data points are found to have ratio yield intensity values greater than 1.

There may be some indication that the ratio decreases with increasing E_b. If we ignore $\geq 70^o$ data (low peak intensities and poor peak determinations), then the ratio of ~0.50 at low E_b and ~0.20 at higher E_b, with a weak E_b dependence. A linear trend is included in Fig 5-16 to show the best qualitative determination of the weak E_b dependence. Given the lack of E_b dependence for the integrated plasmon peak found in section 5.2(c), it seems unlikely that there is a significant E_b dependence of the plasmon peak intensity.

5.2.(d) Plasmon Yield Calculation

In order to measure the plasmon yield, $\delta(\alpha, E_{pl}; E_b)$, one must first determine the boundaries of the plasmon peak. The high-energy boundary of the plasmon peak is dubbed the Elastic-Plasmon minimum

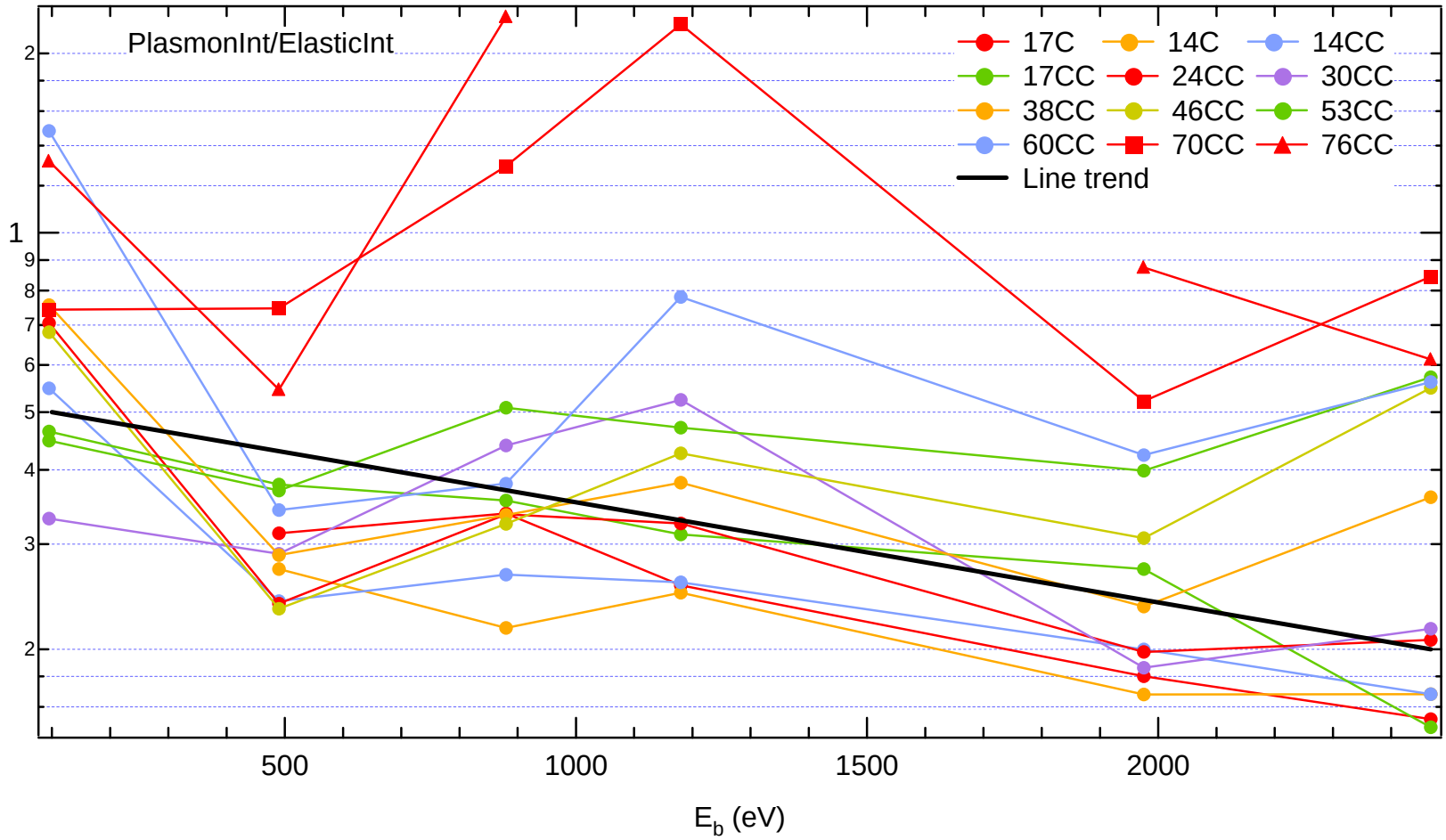

Figure 5-16 Ratio of intensity of the first plasmon peak to the elastic peak versus incident beam energy. The line trend decreases with increasing E_b.

transition, $E_{pl\text{-}el}$ [Fig. 3-37]. The energy positions and yield intensities of the Elastic-Plasmon minimum transition are addressed in 5.5(b) and are used to determine the yield of the first plasmon peak. For example, the plasmon yield can be calculated by integrating $dN(\alpha, E; E_b)/dE_e$ from the low-energy boundary feature [Fig. 5-1, right blowup, e.g. E = ~875 eV] of the plasmon peak to the high-energy boundary, $E_{pl\text{-}el}$, [Fig. 5-1, right blowup, e.g. $E_{pl\text{-}el}$ = ~883 eV]. Integration over the first plasmon peak is equivalent to subtracting the pre-differentiated data [Fig. 5-3, green] using the same energy boundaries (3.2(i)).

The emission angle dependence of the plasmon yield is similar to that observed for the plasmon peak intensity. The plasmon yield is plotted against emission angle [Fig. 5-17] for several incident beam energies using the 0.1 eV resolution data. The results of the plasmon peak yield cross section (E_bR Plasmon Yield) are tabulated, along with associated errors in Table 5.6. Yield values are greatest for small angle emissions and decrease for increasing angle emissions.

Though it is not understood why E_b = 1200 eV plasmon yield values are quantitatively largest (~3×10^{-3} 1/sr), it is clear that the distribution is Rutherford like at emission angles less than 30^o CC. The Rutherford fit (Eq. 5.2) having parameters $\beta = (0.07 \pm 0.01)$ and $C = (9 \pm 3) \times 10^{-5}$ sr^{-1}, and $\chi^2 = 6 \times 10^{-7}$, shows a good agreement within all but two data points within error. The exceptions show additional spikes in yield values for 100 eV and 500 eV near 38^o CC emission with approximate values of 1×10^{-3} 1/sr. The E_b = 2000 eV data has a peak with yield value of 1.3×10^{-3} sr^{-1} but the error bar gives large doubt to whether this is really legitimate. E_b = 500 eV and 2500 eV data has peaks of yield value 1×10^{-3} sr^{-1}.

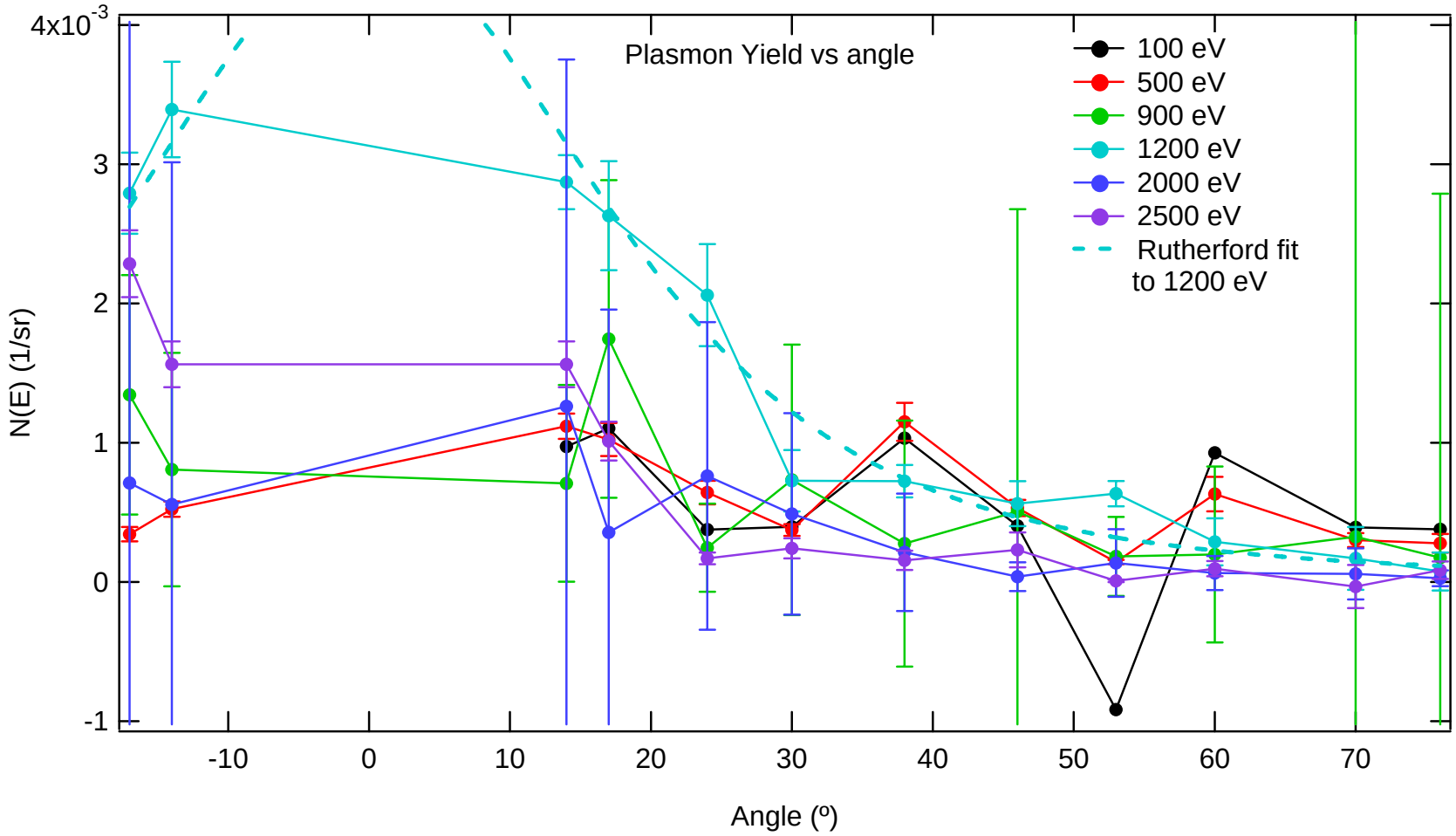

Figure 5-17 Plasmon Peak Yield versus emission angle for several incident beam energies. Error bars of the 100 eV data are not shown because they are too large and interfere with the other cross sections.

Table 5.6 The plasmon peak yield given in as x 10^{-3} 1/sr.

Emission Angle (^{o})	Incident Beam Energy (eV)					
	100 eV	500 eV	900 eV	1200 eV	2000 eV	2500 eV
17C	*	0.34 ± 0.051	1.3 ± 0.86	2.8 ± 0.29	0.71 ± 5.0	2.3 ± 0.24
14C	*	0.52 ± 0.054	0.81 ± 0.84	3.4 ± 0.34	0.56 ± 2.5	1.6 ± 0.17
14CC	-0.032 ± 0.30	1.1 ± 0.09	0.71 ± 0.71	2.9 ± 0.19	1.3 ± 2.5	1.6 ± 0.17
17CC	0.26 ± 2.8	1.0 ± 0.12	1.7 ± 1.1	2.6 ± 0.39	0.36 ± 1.6	1.0 ± 0.14
24CC	0.079 ± 1.2	0.64 ± 0.085	0.25 ± 0.32	2.1 ± 0.37	0.76 ± 1.1	0.17 ± 0.042
30CC	0.65 ± 7.2	0.37 ± 0.042	0.73 ± 0.97	0.73 ± 0.22	0.49 ± 0.72	0.24 ± 0.072
38CC	0.43 ± 4.8	1.1 ± 0.14	0.28 ± 0.88	0.72 ± 0.12	0.21 ± 0.42	0.16 ± 0.068
46CC	0.082 ± 0.86	0.53 ± 0.058	0.51 ± 2.2	0.56 ± 0.16	0.037 ± 0.10	0.23 ± 0.13
53CC	0.15 ± 3.6	0.14 ± 0.015	0.18 ± 0.28	0.63 ± 0.09	0.14 ± 0.24	0.0076 ± 0.0098
60CC	-1.4 ± 200.0	0.63 ± 0.12	0.20 ± 0.63	0.29 ± 0.17	0.065 ± 0.12	0.095 ± 0.055
70CC	-0.33 ± 24.0	0.30 ± 0.049	0.32 ± 4.0	0.17 ± 0.23	0.057 ± 0.18	-0.034 ± 0.16
76CC	-0.08 ± 3.7	0.28 ± 0.068	0.17 ± 2.6	0.074 ± 0.14	0.026 ± 0.057	0.085 ± 0.063

5.2.(e) Comparison of High Energy Yields

The ratio of the plasmon peak yield [Fig. 5-17] to the elastic peak yield [Fig. 5-12] is plotted against incident beam energy [Fig. 5-18]. Both yields are measured using the 0.1 eV resolution. The ratio is consistent at ~0.35; no energy dependence is evident. The spread in the plasmon yield values in Fig. 5-18 are less than the plasmon peak intensity in Fig. 5-14. This should be expected, given the higher signal-to-noise ratio for an integrated peak.

Notice that the E_b = 900 eV @ 17^{o}C is the largest value above 4. Some negative values do not show up on the plot because of the logarithmic scale, but most other values ratio between a 0.1 and 1. There are only four values greater than 1.

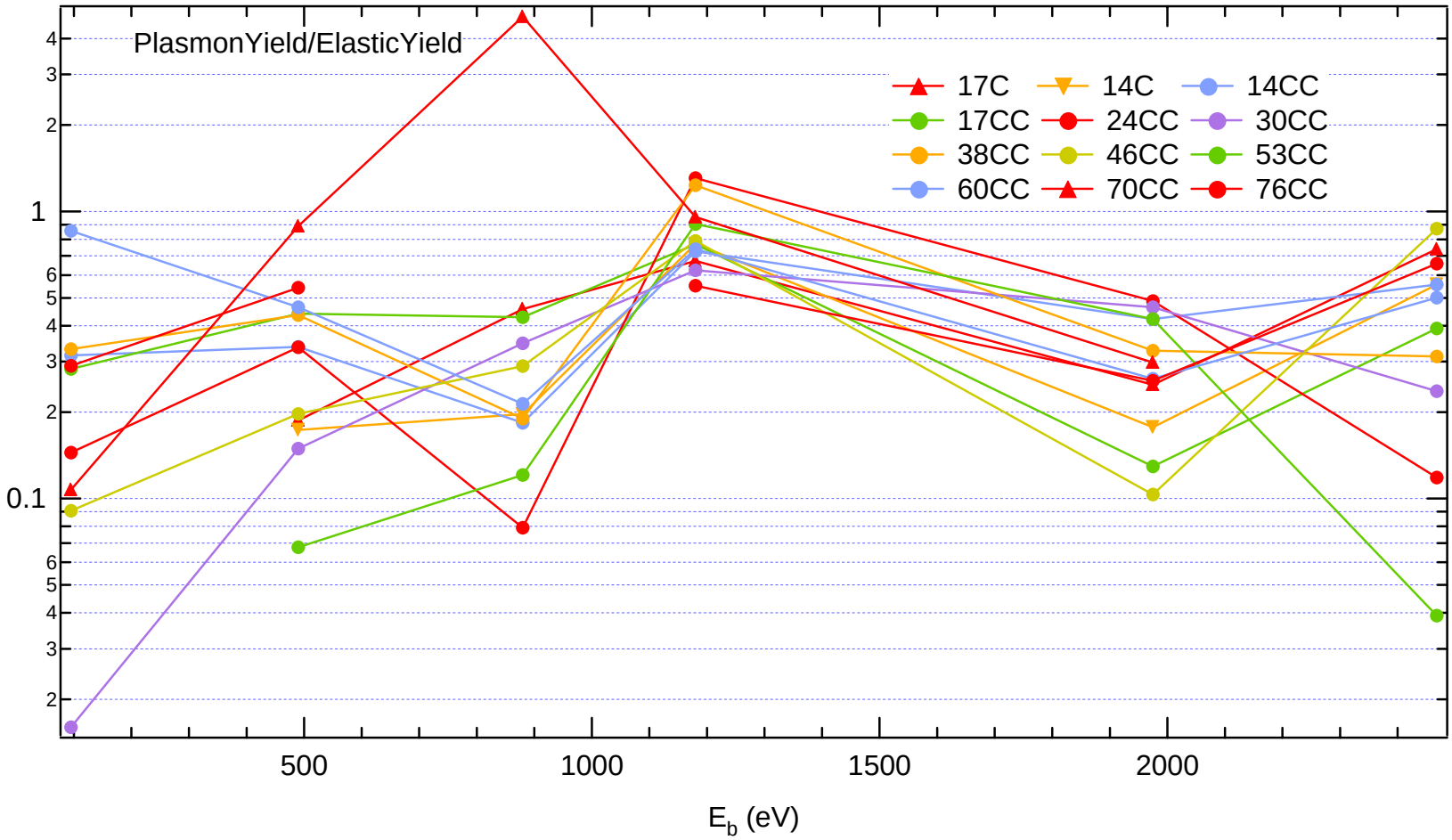

Figure 5-18 Ratio of the plasmon peak yield to the elastic peak yield versus the incident beam energy for various emission angles. There are only four values greater than 1. The ratio is consistent at ~0.35. No energy dependence evident.

5.3 Inelastic BSE Peak Region

The backscattered electron (BSE) region is comprised of electrons in a high end of the emission spectrum. The region extends from E_b down to an energy E_{min} (or, alternateld, to 50 eV). The high energy electrons are generally elastically or quasi-elastically backscattered electrons originating from the incident beam. The key features of the BSE region are shown in Fig. 3-37 schemattically. The BSE region includes the well defined narrow elastic peak (sec 5.1) and plasmon peak (sec. 5.2). It also includes a large broad peak below the plasmon peak, referred to as the BSE peak, that is discussed in this section. The characteristic features of the BSE peak, defined in Table 3.3, are energy, E_{BSE}, intensity, $dN(\alpha,E_{BSE};E_b)/dE_e$, yield, $\delta(\alpha, E_{BSE}; E_b)$, and width. The broad BSE peak is best seen in wide energy range plots, such as Fig. 5-46, Fig. 5-49, or Fig. 5-50. In addition, fine structure peaks have been identified in the BSE region; this is decussed in sec 5.3(d). Finially, the low energy boundary of the BSE region, at Emin, is discussed in detail in sec. 5.5(a).

Because the BSE region includes both the broad BSE peak and many narrow features such as the elastic, plasmon, or BSE fine structure peaks, it is necessary to examine both low and high resolution emission spectra data. A magnification of the high-energy portion of a composition resolution AER spectrum is given for an incident beam energy of 900 eV and emission angle of 14^o [Fig. 5-1, upper right]. The BSE peak has been best captured using the 1 eV resolution data where the energy emissions span from the incident beam energy, E_b, to ~200 eV below E_b. The E_bR spectra are given [Fig. E-48 through Fig. E-54] for the same selected E_b's as those measured in coarse energy resolution (10 eV). The 1 eV resolution provides the best measurements, with the least error, of the energy location, E_{BSE}, and intensity, $dN(E_{BSE})/dE$, of the peak. However, the 10 eV resolution provides the best yield determination of the BSE yield, σ, because the BSE population spans such a broad energy emission, ranging from approximately 0.4 E_b to E_b. As seen in section 5.5(a), the normalized AR spectra at 14^o CC emission [Fig. 5-49] shows that the BSE Peak for all E_b seems to be roughly located in the energy percentage of 85% ± 5% of E_b. For comparison to the selected emission angles, the AR spectra are also given [Fig. E-55 through Fig. E-66].

Presentation of the higher energy portions of spectra using the 0.1 eV and 1 eV resolutions [Fig. 5-4, linear axis] emphasize the fine peak features of the entire spectra [e.g., Fig. 5-50 at E_b = 900 eV], but fail to accentuate the "broadness" of the BSE peak requiring a coarser 10 eV resolution [Fig. 5-19, logarithmic axis]. From these logarithmically plotted concatenated portions of spectra, the energy positions, E_{BSE}, and yield intensities, $dN(E_{BSE})/dE$, of the BSE peak are measured, tabulated, and compared.

Comparison of the inelastic BSE yield intensity to that of the elastic yield intensity is also investigated. The energy positions of the BSE and SE peak delineation at both, E_{min}, (5.5) and the customary lower energy boundary (50 eV) are used to calculate the inelastic BSE yield, σ. The E_{min} calculated inelastic BSE yield is then contrasted with the customary inelastic BSE yield.

Important yield ratios to the elastic yield (5.1(d)) and to the total yield (5.8) are finally investigated to emphasize this section.

The ratios of the inelastic BSE yield to the elastic yield (5.1(d)) and to the total yield (5.8) are calculated, these are interpreted as the ratio of inelastic to elastic BSE and the fraction of the total yield due to inelastic BSE, respectively.

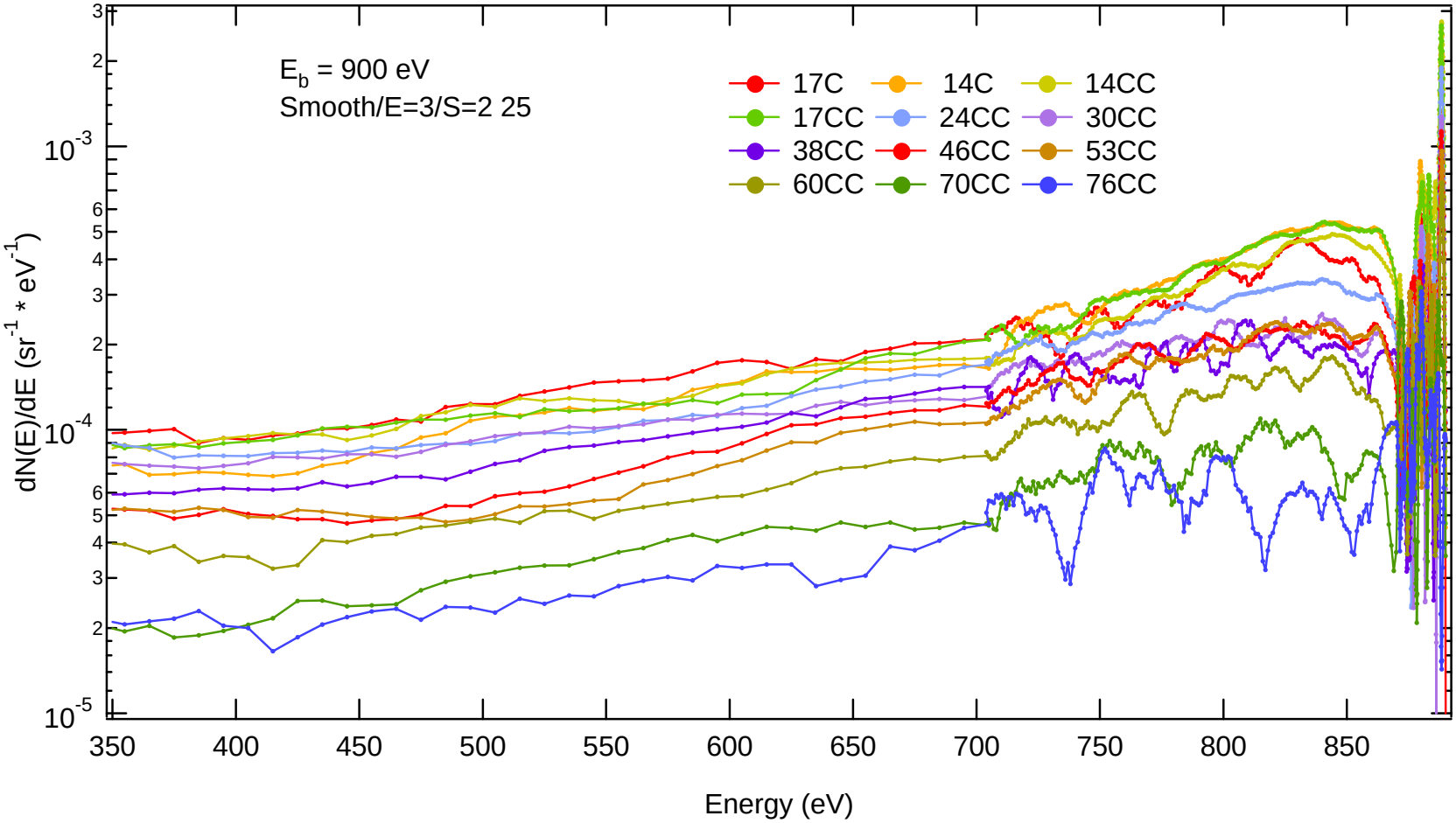

Figure 5-19 BSE AR spectra taken at an incident beam energy of 900 eV and several emission angles. Note the Y-axis log scale.

5.3.(a) BSE Peak Features

A programming search routine was used to locate the broad BSE peak's energy positions and intensities. Since these features are best measured with the 1 eV resolution data, energy normalized spectra of the BSE population are first provided for various incident beam energies [Fig. 5-20]. The energy range is normalized in the same manor as the full spectra using the coarse 10 eV resolution [Fig. 5-49] to emphasize the BSE peak's energy position. The yield of the BSE Peak was calculated using the 10 eV resolution data because only the 10 eV resolution was used to measure the lower energy boundary of the BSE peak at either E_{min} or 50 eV.

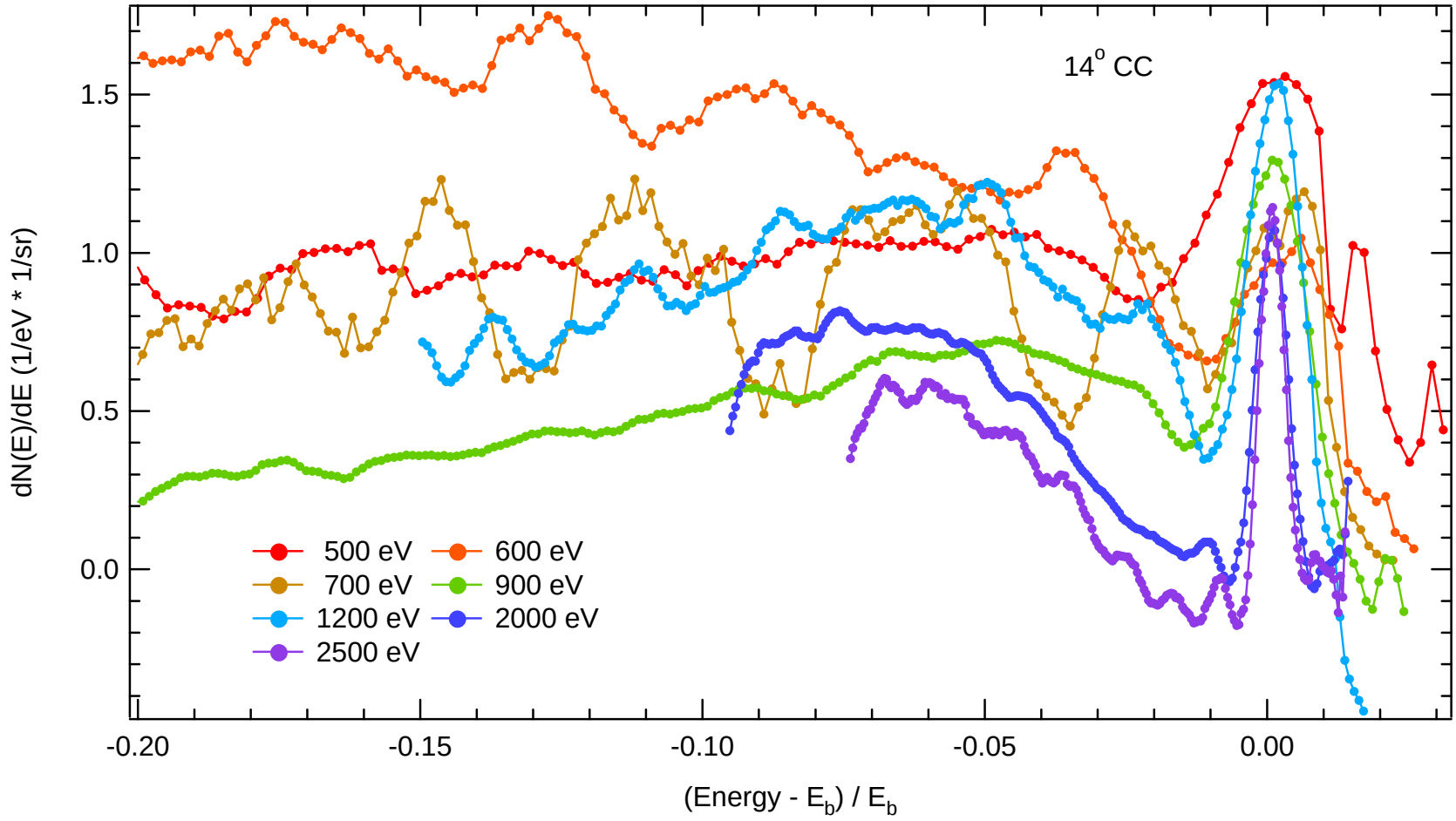

Figure 5-20 Normalized BSE AR energy spectra measured with 1 eV resolution at 14° Counter-Clockwise emission for selected beam energies.

5.3.(a)1 BSE Peak Energy

The actual BSE energy positions are tabulated [Table 5.7], along with the average and standard deviation calculated over a range of emission angles. For example, $E_{BSE}(E_b = 900\ eV)$ averages over 12 emission angles to be (833 ± 16) eV. Based on these average and standard deviation calculations, there is no angular dependence for the BSE peak energy. To further test the angular dependence, the BSE peak energy, E_{BSE}, is plotted [Fig. 5-21] as the energy deviation from the incident beam energy ($E_{BSEpeak} - E_b$) as a function of emission angle so that various incident beam energies, E_b, can be compared. Again, the plots in Fig. 5-21 do not suggest there is any angular dependence for the BSE peak energy. Maybe it is worth plotting the $E_b = 500$ eV BSE spectra for all angles. Its in the Appendix E. Go Look from 470 eV to 366 eV. There is an apparent trend in Fig. 5-7 for the $E_b = 500$ eV BSE energy position. However, the reason for any structure in the BSE energy position is unclear.

Based on the angle-averaged deviations of E_{BSE} from E_b listed in Table 5-7, there appears to be an increase in the deviation with E_b. The fractional deviation $(E_b - E_{BSE})/ E_b$ is roughly constant at ~12%, suggesting that the deviation is linearly proportional to E_b. It should be noted that there is substaintial variation in the fractional deviation, so that confidence in this linear trend is not high.

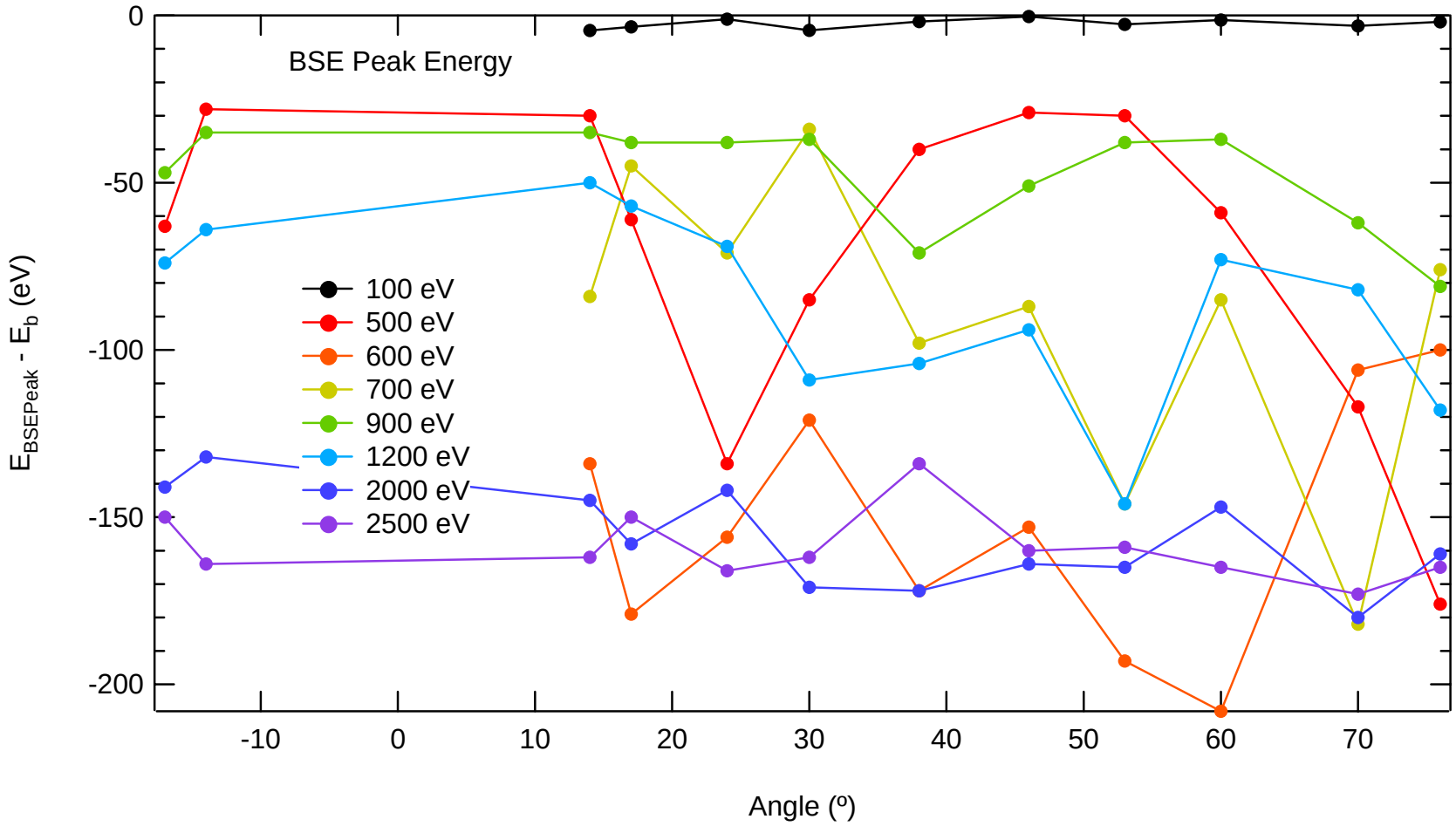

Figure 5-21 BSE peak energy using the fine 1eV resolution (0.1 eV resolution for 100 eV).

Table 5.7 BSE Peak Energy.

Beam Energy	Emission Angle (deg)															
	17C	14C	14CC	17CC	24CC	30CC	38CC	46CC	53CC	60CC	70CC	76CC	Ave	StDev	E_b-Ave	$\frac{E_b\text{-Ave}}{E_b}$ %
500 eV	437	472	470	439	366	415	460	471	470	441	383	324	429	48	71	14.2
600 eV	*	*	466	421	444	479	428	447	407	392	494	500	448	37	152	25.4
700 eV	*	*	616	655	629	666	602	613	554	615	518	624	609	44	91	13.0
900 eV	833	845	845	842	842	843	809	829	842	843	818	799	833	16	68	7.5
1200 eV	1106	1116	1130	1123	1111	1071	1076	1086	1034	1107	1098	1062	1093	28	107	8.9
2000 eV	1834	1843	1830	1817	1833	1804	1803	1811	1810	1828	1795	1814	1819	15	182	9.1
2500 eV	2318	2304	2306	2318	2302	2306	2440	2308	2309	2303	2295	2377	2324	42	176	7.0

All 1 eV resolution yield intensities have units of eV and an error of 5% (1/sr*1/eV).

5.3.(a)2 BSE Peak Intensity

The BSE peak intensity, $dN(\alpha, E_{BSE}; E_b)/dE_e$, is the ratio emitted electrons to those incident [Fig. 5-22] measured at the BSE peak's energy position, E_{BSE}. For example, for E_b = 900 eV @ 14° CC angle emission, [Fig. 5-19, yellow], the yield intensity at the BSE peak is ~589 x 10^{-6} (1/eV * 1/sr), though without the smoothing, the tabulated [Table 5.9] value is 589 ± 24 x 10^{-6} (1/eV * 1/sr).

The plots in Fig. 5-22 clearly show a stron dependence of the BSE peak intensity on emission angle. The intensities measure the greatest value for low angle emission and the least values for high angle emission. The BSE peak intensity is modeled with the two parameter Rutherford trend (Eq. 5.2) where the screening, β, and amplitude, C, parameters are given in Table 5.8. It should be noted that the curves in Fig. 5-22 for E_b = 100 eV, 500 eV, and 600 eV show a more subtle additional emission angle dependence that contain a smaller local intensity peak at higher emission angle. The additional peak intensity for E_b = 100 eV and 600 eV occurs at 60° CC, but for E_b = 500 eV, the emissions intensify near 40° CC degrees. These trends are not well understood.

Table 5.8 BSE Peak Intensity Rutherford fit coefficients.

Beam Energy	β	C (x 10^{-4} sr^{-1} eV^{-1})	χ^2 (x 10^{-9})
100 eV	1.1 ± 0.6	6.8 ± 7	8
500 eV	0.6 ± 0.1	4.1 ± 1	5
600 eV	5 ± 15	95 ± 513	7
700 eV	0.17 ± 0.02	0.4 ± 0.06	1
900 eV	0.25 ± 0.05	1 ± 0.5	30
1200 eV	0.18 ± 0.03	0.9 ± 0.2	20
2000 eV	0.08 ± 0.01	0.2± 0.04	7
2500 eV	0.2 ± 0.02	0.2 ± 0.05	0.5

The BSE peak intensity also shows clear evidence of a dependence on Eb. Analysis of the values in Table 5.9 shows that E_b = 900 eV and E_b = 1200 eV have the overall greatest intensities at the BSE peak's position. In general, the BSE peak intensity at all emission angles is peaked between 900 eV and 1200 eV, near dmax, and falls off substantially at lower and higher energies. At high energies up to 2500 eV, the BSE peak intensity falls by a factor of ~5 at all emission angles. At larger energies down to 500 eV the BSE peak intensity falls off a similar amount but the trends are not nearly as consistant. The fall off in the BSE peak intensity is ……

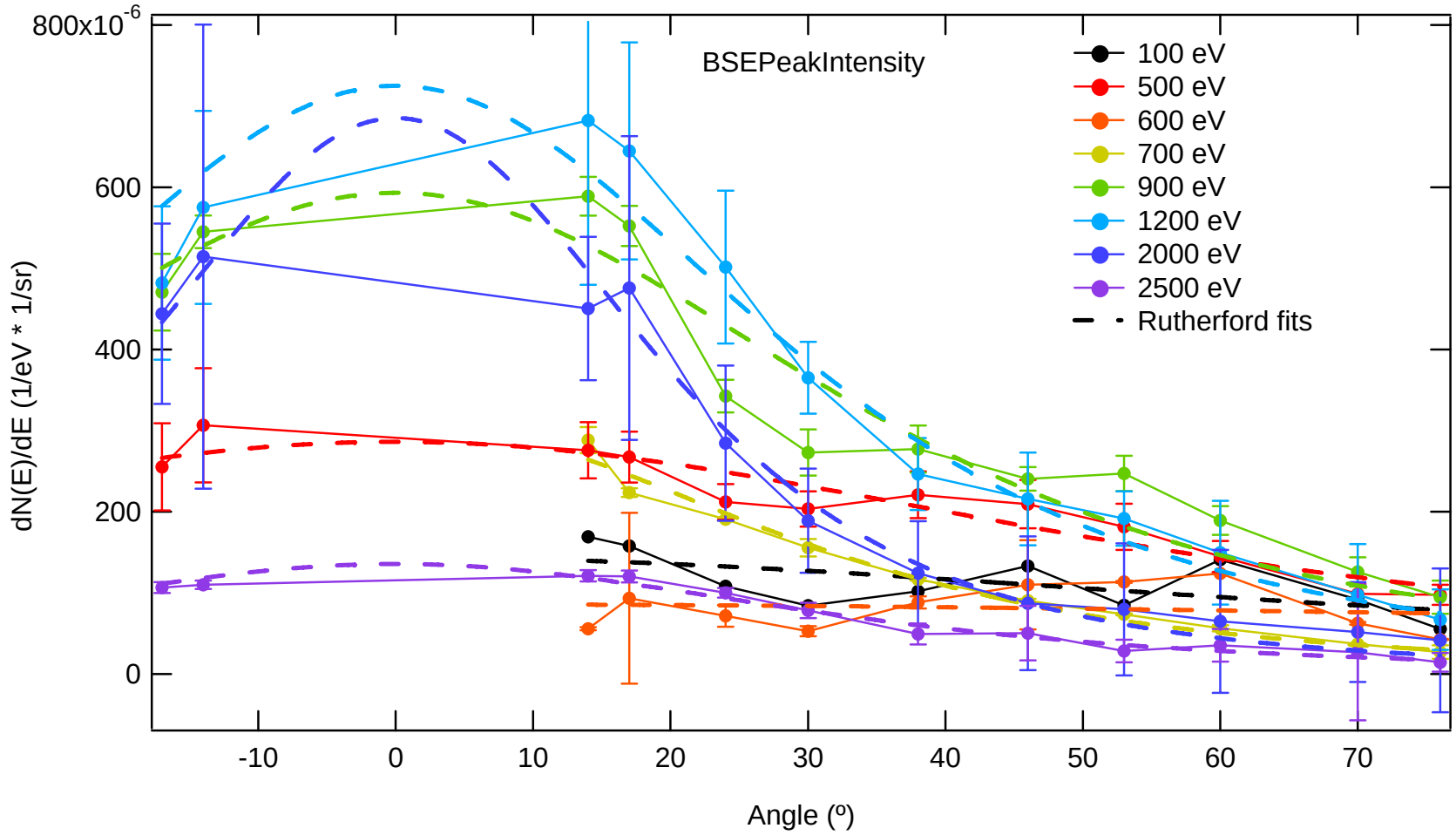

Figure 5-22 BSE peak intensity at the peak's position using the 1 eV resolution (0.1 eV resolution for 100 eV).

Table 5.9 BSE Peak Intensity.

Beam Energy	Emission Angle (°)											
	17C	14C	14CC	17CC	24CC	30CC	38CC	46CC	53CC	60CC	70CC	76CC
500 eV	255 ± 54	307 ± 71	276 ± 35	267 ± 31	212 ± 22	203 ± 22	221 ± 29	209 ± 30	182 ± 29	145 ± 19	99 ± 12	98 ± 12
600 eV	*	*	56 ± 2	94 ± 105	72 ± 14	53 ± 6	88 ± 7	110 ± 55	113 ± 1	124 ± 0.7	63 ± 2	43 ± 0.6
700 eV	*	*	288 ± 16	224 ± 5	191 ± 2	156 ± 11	117 ± 1	91 ± 2	74 ± 1	56 ± 4	37 ± 1	27 ± 8
900 eV	471 ± 47	545 ± 20	589 ± 24	552 ± 25	343 ± 20	273 ± 29	277 ± 29	241 ± 15	247 ± 21	189 ± 18	126 ± 18	95 ± 21
1200 eV	482 ± 95	575 ± 119	682 ± 203	645 ± 134	502 ± 94	365 ± 44	246 ± 44	216 ± 57	192 ± 34	149 ± 64	98 ± 63	67 ± 37
2000 eV	444 ± 111	514 ± 286	450 ± 88	476 ± 187	285 ± 96	189 ± 64	124 ± 64	87 ± 82	80 ± 82	65 ± 88	52 ± 61	42 ± 89
2500 eV	107 ± 7	110 ± 5	121 ± 7	120 ± 7	100 ± 6	78 ± 9	49 ± 13	50 ± 34	28 ± 14	35 ± 23	27 ± 84	14 ± 12

All 1 eV resolution yield intensities have units of (1/sr*1/eV) * 10^{-6} and are given with error of the same units.

5.3.(b) High Energy Inelastic BSE Peak Comparison

A comparison is made of the intensities of the two largest BSE features, the elastic peak and the BSE peak, in hopes of identifying trends. The intensities of the elastic peak [Fig. 5-8] and the inelastic BSE peak [Fig. 5-22] have been discussed (5.1.(b) and 5.4.(a)2) in some detail. As discussed at the beginning of sec. 5.3, elastic scattering is a result of the primary electrons scattering back and eventually becoming emitted from the sample. This classifies the elastically scattered population as part of the BSE population. However, it is useful to classify the elastic and inelastic BSE peaks as separate sub-populations so that their intensities can be compared, even though they are measured with two different energy resolutions (0.1 eV and 10 eV, respectively).

The ratios of the intensities of the BSE peak to the elastic peak are given as a function of emission angle [Fig. 5-23] for several incident beam energies. The primary observation is that the ratio values are about 0.5 for normal incidence and increase to values greater than unity for increasing emission angle. This shows that the BSE intensity does not fall off as fast as the elastic peak intensity, with increasing emission angle. A second observation is that the E_b = 600 eV ratio is a lot greater than the other incident beam energy values; this suggests that there may be an error in the 600 eV data that is most likely due to a calibration error. This discrepancy is evident in several subsequent plots.

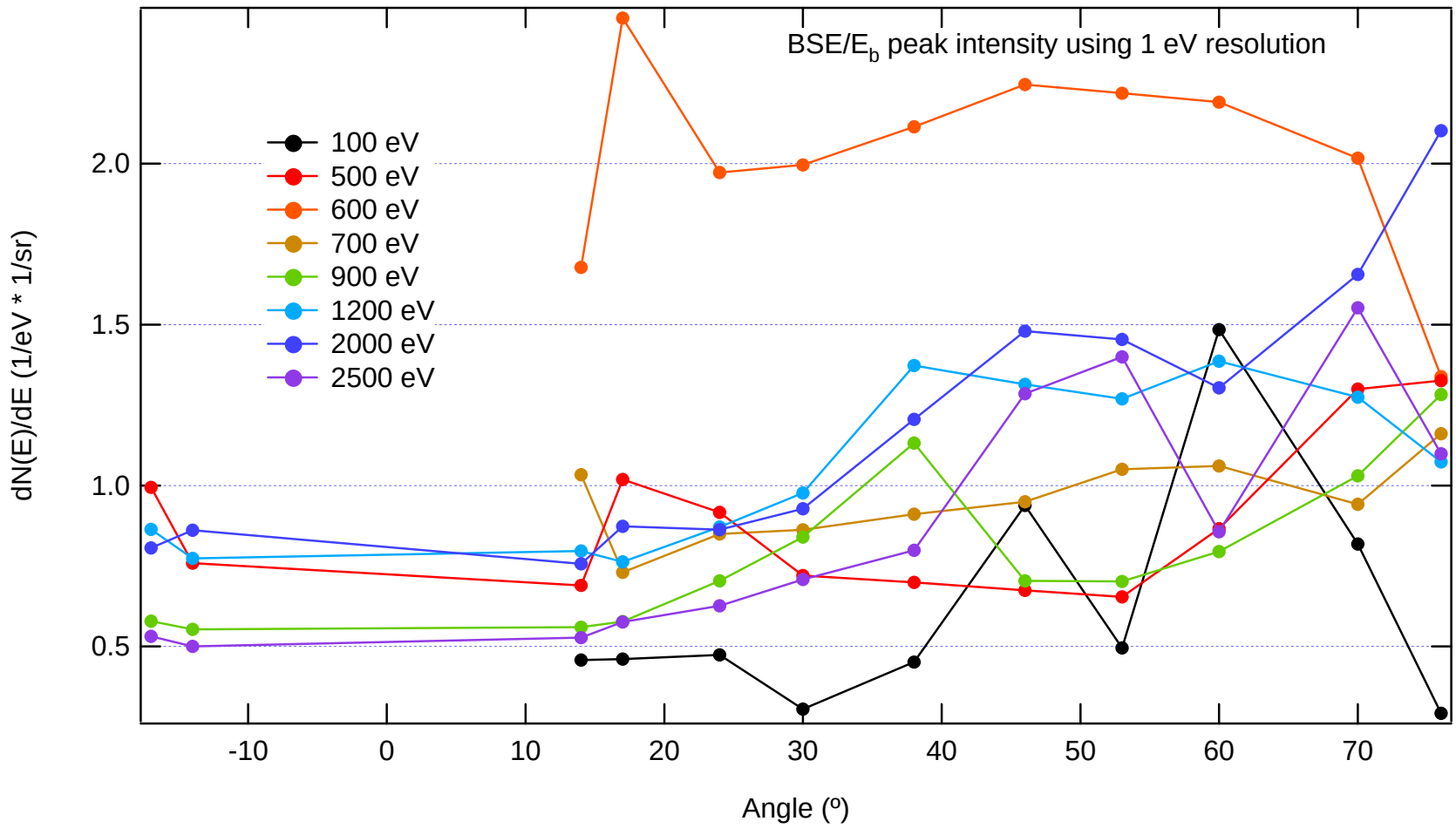

Figure 5-23 BSE peak to elastic peak intensity ratio for selected beam energies using the 1 eV resolution (0.1 eV resolution for 100 eV).

5.3.(c) Inelastic BSE Yield

The inelastic BSE yield, $\eta_{ER}(\alpha, E_{BSE}; E_b)$, is the population of high energy electrons originating from the primary incident beam and includes quasi-elastic (plasmon) and elastically scattered electrons. The inelastic BSE yield is calculated by measuring the area underneath the BSE peak [Fig. 3-37] between two energy boundaries such as E_{min} and E_{el}. Thus, the BSE yield as calculated in this section is only the scattering from inelastically backscattered electrons. Note that this differs from the standard definition of the backscattered yield $\eta(E_b)$, which includes energies from E_{min} (or 50 eV) up to E_b and contributions from both elastically and inelastically backscattered electrons. Note also that the plasmon peak is included in the inelastic BSE yield.

Choosing the two integration boundaries is important because different energy resolutions contribute to the composite BSE yield in different energy ranges of the spectrum. For example, the high energy portion of E_b = 900 eV spectra [Fig. 5-19] show that most of the BSE yield contribution comes from the 10 eV and 1 eV resolution data between 350 eV and 850 eV and very little contribution comes from the quasi-elastic and elastic features [Fig. 5-4] resolved using the 0.1 eV resolution data. This being the case, the inelastic BSE yield is calculated using the 10 eV resolution using the high energy boundary E_{el} even though this resolution is too large to measure quasi-elastic and elastic features.

The lower energy boundaries of 50 eV (customary delineation) and E_{min} eV (improved delineation) are compared and contrasted in terms of α and E_b. The improved inelastic BSE yield is then is compared to other yields such as the elastic yield calculated using the 0.1 eV resolution. Finally, the angle integrated inelastic BSE yield, $\eta_F(E_{BSE}; E_b)$, is addressed for the two different lower energy boundaries and compared to the BSE yields measured within the Fatman chamber using an angle-integrated hemispherical grid retarding field analyzer.

5.3.(c)1 Customary Boundary

Using the customary 50 eV demarcation boundary, the inelasticBSE yield values, $\eta_{ER}(\alpha, E_{BSE}; E_b)$, are calculated and shown plotted against emission angle [Fig. 5-24] and against E_b [Fig. 5-25]. The $BSE_{50\text{-}Eb}$ yield values are tabulated in Table 5.11. Values here are from 0.335 to 0.015 1/sr. The BSE yield has been measured using the 10 eV resolution spectra. The high energy tail of the BSE peak spectra is measured at 1 eV resolution, but was not used to calculate the BSE yield because it was not measured at the low energy tail of the BSE Peak.

Figure 5-24 shows a well defined dependence of the $BSE_{50\text{-}Eb}$ yields with emission angle. This yield decreases with increasing angle, as did the inelastic BSE peak intensity. However, the angular dependence at lower energies is best modeled with a Lambert law similar to the SE behavior and at higher energies is best modeled with a Rutherford or Mott function……. For E_b = 500 eV @ 1 eV, 700 eV, 900 eV, 1200 eV, 2000 eV, and 2500 eV the inelastic BSE yields are modeled with the two parameter Rutherford trend (Eq. 5.3) where the screening, b, and amplitude, C, parameters are given in Table 5.10. For the 100 eV, 500 eV @ 10 eV, and 600 eV, the Lambert cosine law (Eq. 5.2) is used with amplitude parameter, B. The χ^2 values are also provided.

Table 5.10 BSE Peak Yield (50 eV to E_b eV) Rutherford fit coefficients.

incident beam energy	beta	B (sr^{-1})	C (x 10^{-4} sr^{-1})	χ^2
100 eV	NA	0.02 ± 0.003	NA	0.0003
500 eV @ 10 eV	NA	0.10 ± 0.002	NA	0.0001
500 eV @ 1 eV	0.38 ± 0.04		0.06 ± 0.01	0.0003
600 eV	NA	0.07 ± 0.002	NA	0.0001
700 eV	0.33 ± 0.05		0.07 ± 0.02	0.0009
900 eV	0.30 ± 0.03		0.07 ± 0.01	0.0009
1200 eV	0.27 ± 0.02		0.07 ± 0.009	0.0008
2000 eV	0.23 ± 0.01		0.05 ± 0.004	0.0003
2500 eV	0.32 ± 0.03		0.05 ± 0.008	0.0004

A trend is clearly prominent for the BSE yield plotted against E_b in Fig. 5-25. The maximum is located between E_b = 1200 eV and E_b = 2000 eV across all emission angles. The inelastic BSE yield decreases with increasing energy by a factor of ~2 at 2500 eV beam energy. The inelastic BSE also decreases with decreasing energy to ~1/8 of its peak value. The anomalous behavior at E_b = 600 eV, mentiond first in sec. 5.3(d), is also observed here. This Eb dependence is similar to that seen for the elastic peak intensity. The inelastic BSE yield is found to fall of approximately proportional to the empirical term $-(E_b - 1500\ eV)^2$.

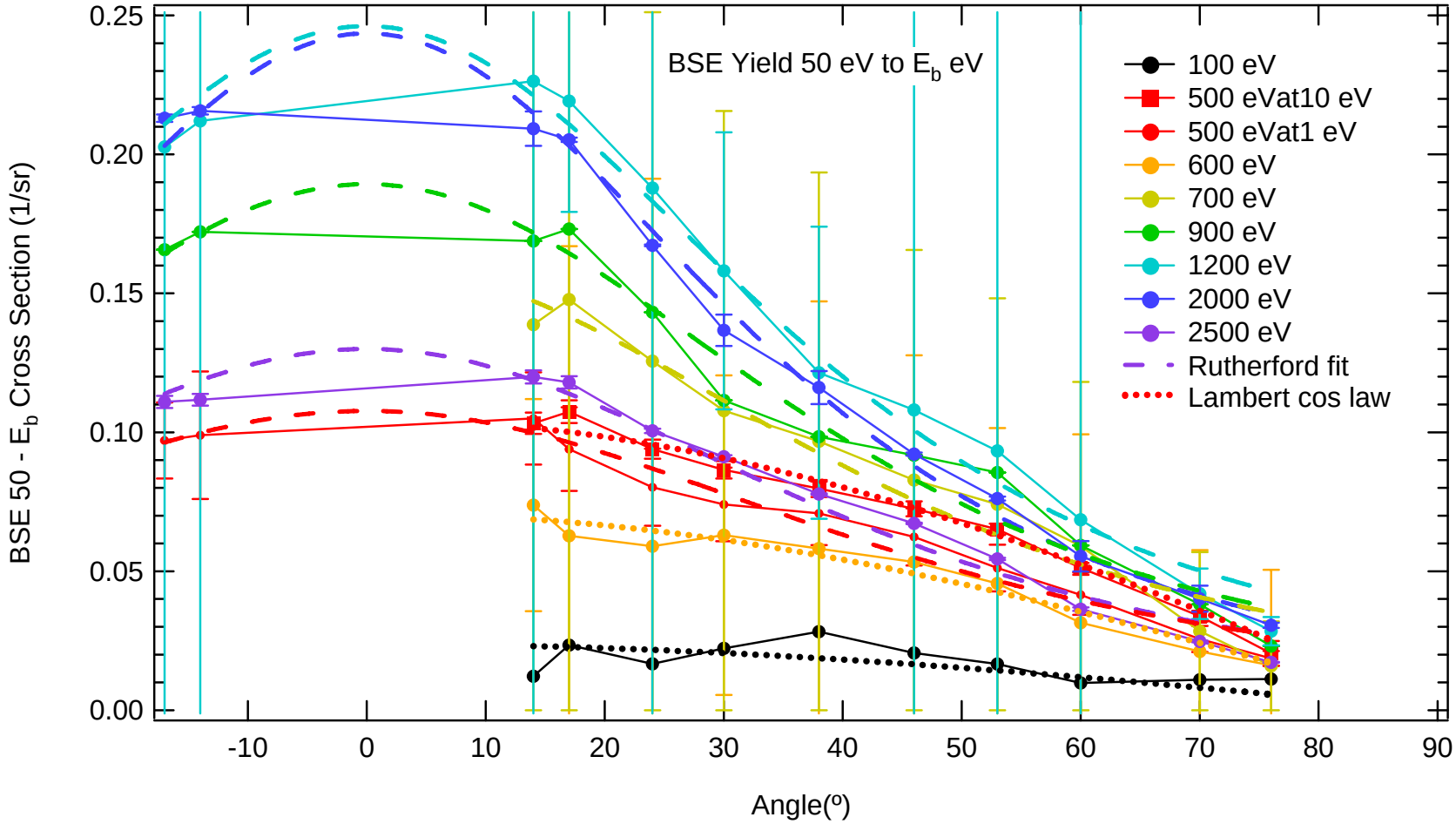

Figure 5-24 Back Scattered Electron using 50 eV – E_b eV cross section versus emission angle for several selected beam energies. E_b = 500 eV @ 1 eV, 700 eV, 900 eV, 1200 eV, 2000 eV, and 2500 eV the BSE peak yields are modeled with the two parameter Rutherford theory (dash) and E_b = 100 eV, 500 eV @ 10 eV, and 600 eV, the Lambert cosine law (dots).

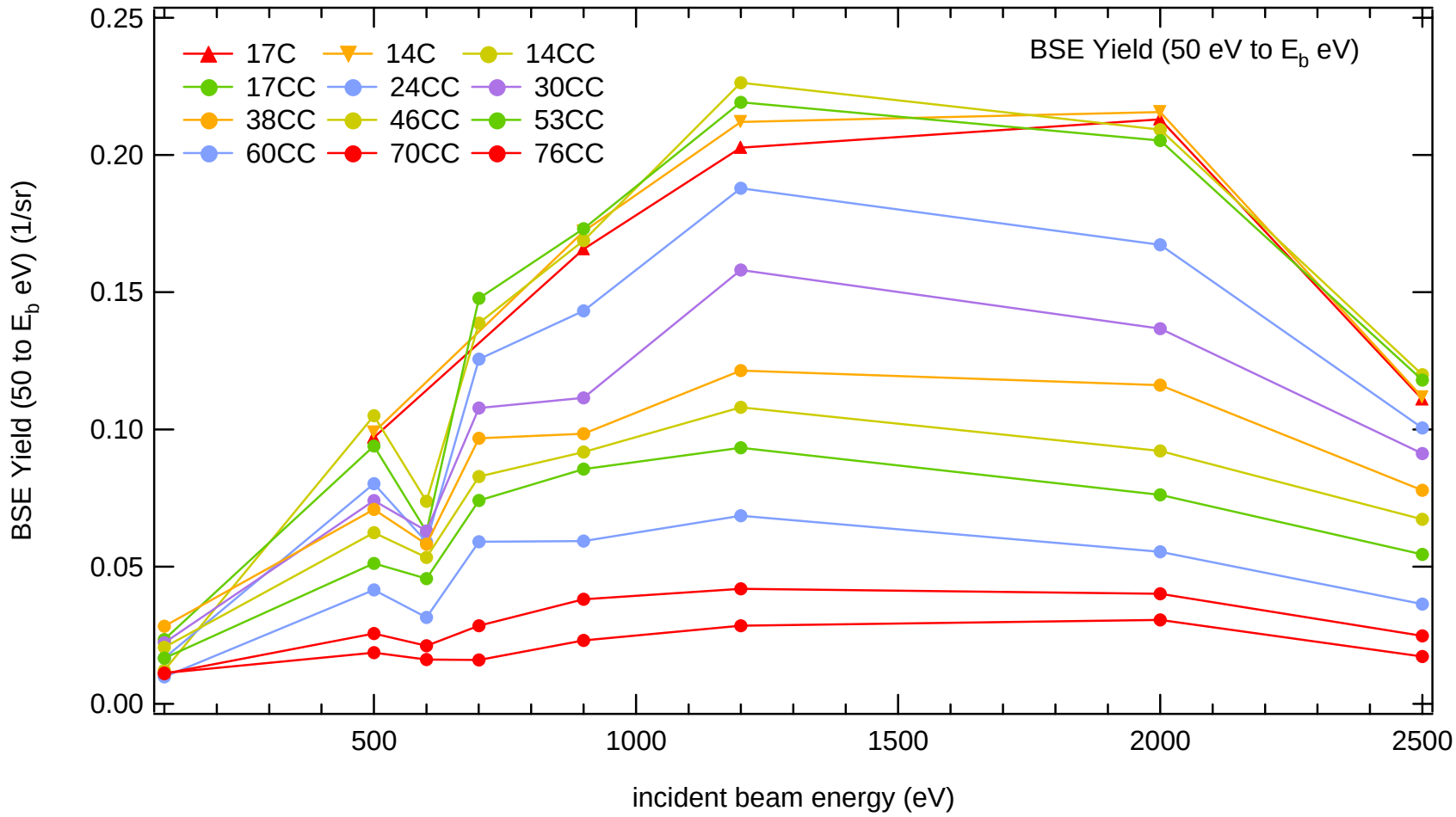

Figure 5-25 BSE AR distributions versus incident beam energy for selected beam energies in the 50-E_b eV range.

Table 5.11 The BSE Yield (50 - E_b) given in units of inverse steradians.

Emission Angle (°)	Incident Beam Energy (eV)							
	100	500	600	700	900	1200	2000	2500
17C	*	0.019 ± 0.001	*	*	0.166 ± 0.025	0.203 ± 0.5	0.213 ± 0.1	0.111 ± 0.05
14C	*	0.026 ± 0.02	*	*	0.172 ± 0.0004	0.212 ± 0.5	0.216 ± 0.2	0.112 ± 0.009
14CC	0.012 ± 0.1	0.042 ± 0.01	0.074 ± 0.04	0.139 ± 0.1	0.169 ± 0.001	0.226 ± 2	0.209 ± 0.4	0.120 ± 0.003
17CC	0.023 ± 0.1	0.051 ± 0.003	0.063 ± 0.1	0.148 ± 0.04	0.173 ± 0.002	0.219 ± 0.1	0.205 ± 0.5	0.118 ± 0.02
24CC	0.017 ± 0.2	0.062 ± 0.01	0.059 ± 0.1	0.126 ± 0.16	0.143 ± 0.004	0.188 ± 0.7	0.167 ± 0.4	0.101 ± 0.8
30CC	0.022 ± 0.3	0.071 ± 0.009	0.063 ± 0.06	0.108 ± 0.03	0.111 ± 0.005	0.158 ± 0.06	0.137 ± 0.02	0.091 ± 0.003
38CC	0.028 ± 0.4	0.074 ± 0.002	0.058 ± 0.09	0.097 ± 0.08	0.098 ± 0.007	0.122 ± 0.01	0.116 ± 0.09	0.078 ± 0.007
46CC	0.021 ± 0.7	0.080 ± 0.01	0.053 ± 0.07	0.083 ± 0.15	0.092 ± 0.001	0.108 ± 0.1	0.092 ± 0.1	0.067 ± 0.01
53CC	0.017 ± 0.015	0.094 ± 0.003	0.046 ± 0.06	0.074 ± 0.06	0.086 ± 0.0004	0.093 ± 0.03	0.076 ± 0.09	0.054 ± 0.02
60CC	0.010 ± 0.9	0.105 ± 0.007	0.032 ± 0.07	0.059 ± 0.1	0.059 ± 0.0002	0.069 ± 0.1	0.055 ± 0.2	0.036 ± 0.02
70CC	0.011 ± 0.007	0.099 ± 0.004	0.021 ± 0.04	0.028 ± 0.03	0.038 ± 0.01	0.042 ± 0.02	0.040 ± 0.04	0.025 ± 0.002
76CC	0.011 ±0.06	0.097 ± 0.02	0.016 ± 0.03	0.016 ± 0.06	0.023 ± 0.002	0.028 ± 0.04	0.031 ± 0.3	0.017 ± 0.004

5.3.(c)2 E_{min} Boundary

Using the E_{min} demarcation boundary to separate SE from BSE electrons, the inelastic BSE yield values, $\eta_{ER}(\alpha, E_{BSE}; E_b)$, are calculated and shown plotted against emission angle [Fig. 5-26] and against E_b [Fig. 5-27] with actual values tabulated in the Table 5.13. The energy boundary value used in this section is the location of the minimum separating the SE and BSE peaks, E_{min}. These yields are substantially less than those calculated using the 50 eV boundary, and are found to exhibit some what different Eb and emission angle trends. A detailed discussion of the lower boundary of the BSE distribution at Emin is found in sec. 5.5(a). The number of electrons in the disputed energy region from 50 eV to Emin are studied in section (5.9).

Figure 5-26 shows a well-defined dependence of BSEEmintoEb on emission angle, very similar to that observed in section 5.3(a)1 for BSE50-Eb. In tis case how ever, the Rutherford model provides the best fit to the data over the full range of beam energies. The inelastic BSE yields plotted against emission angle are modeled with the two parameter Rutherford theory (Eq. 5.3) where the screening, β, and amplitude, C, parameters are given in Table 5.12. This is taken to mean that the majority of electrons from Emin to Eel are BSE electrons originating from the incident beam, which are found to follow the Rutherford model for the angular dependence of elastically scattered BSE.

Table 5.12 BSE Peak Yield (E_{min} eV to E_b eV) Rutherford fit coefficients.

Beam Energy	β	C (x 10^{-4} sr^{-1})	χ^2
100 eV	3 ± 10	0.25 ± 1.8	0.0004
500 eV	0.41 ± 0.08	0.04 ± 0.01	0.0003
600 eV	0.62 ± 0.13	0.08 ± 0.03	0.0002
700 eV	0.31 ± 0.1	0.03 ± 0.02	0.001
900 eV	0.32 ± 0.05	0.05 ± 0.01	0.001
1200 eV	0.25 ± 0.02	0.05 ± 0.008	0.0008
2000 eV	0.18 ± 0.02	0.02 ± 0.003	0.0005
2500 eV	0.42 ± 0.06	0.04 ± 0.01	0.0002

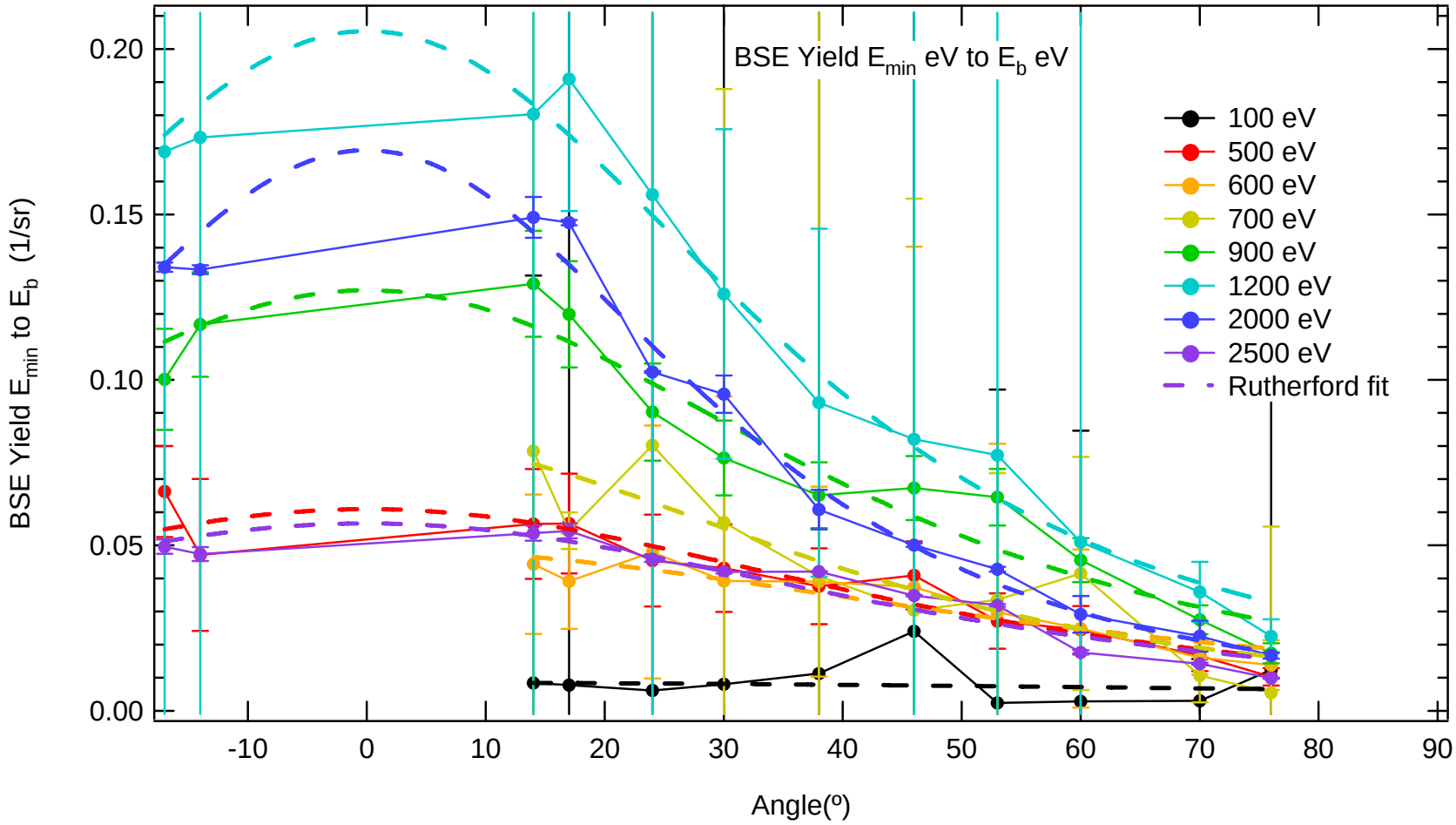

Figure 5-26 BSE yield E_{min} eV – E_b eV angular distributions for selected beam energies in the E_{min} - E_b eV range. The BSE peak yields are modeled with the two parameter Rutherford theory (dash).

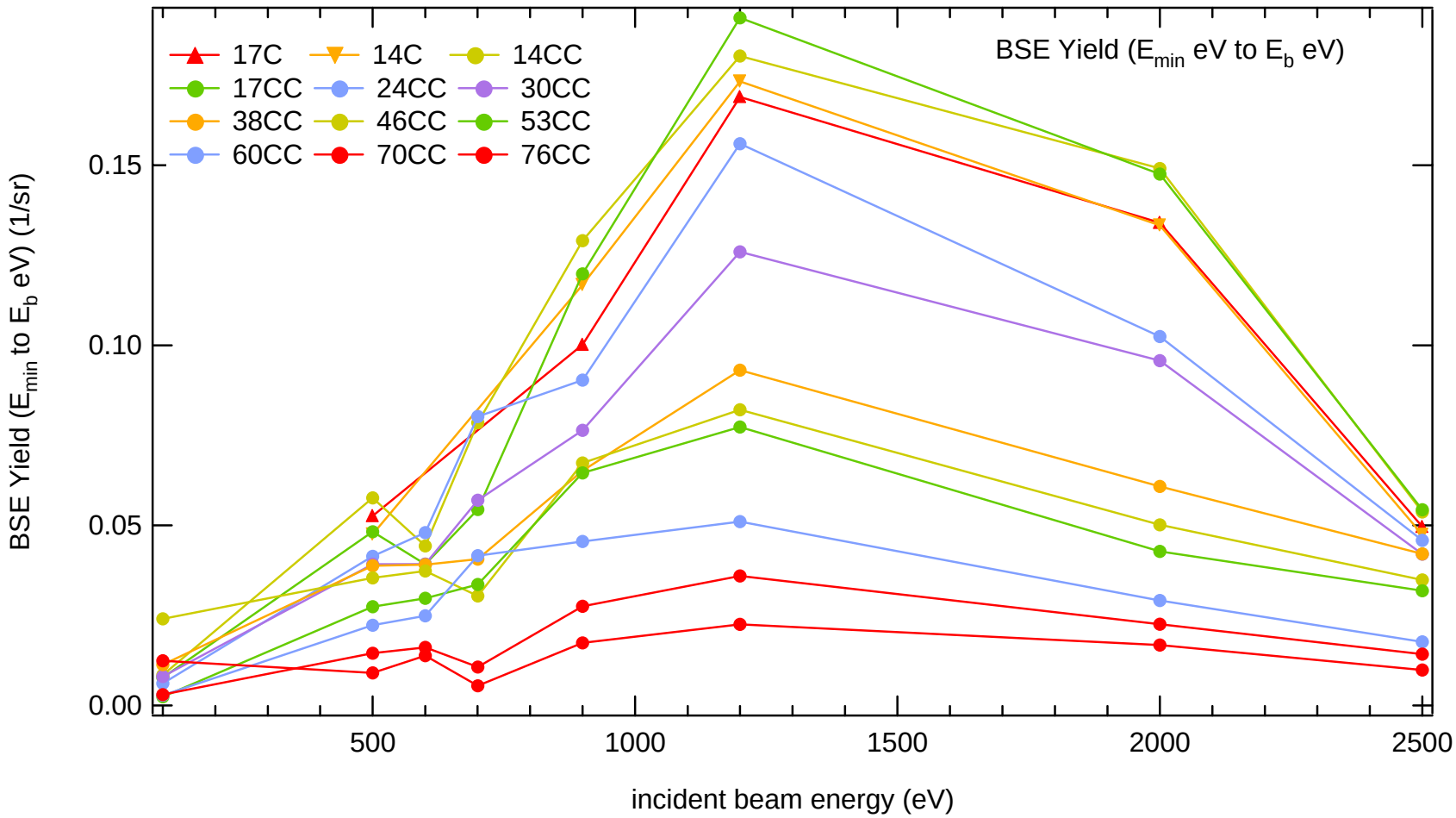

Figure 5-27 BSE AR distributions versus incident beam energy for selected beam energies in the E_{min} - E_b eV range.

Table 5.13 The BSE Yield (E_{min} - E_b) given in units of inverse steradians.

Emission Angle (°)	Incident Beam Energy (eV)							
	100	500	600	700	900	1200	2000	2500
17C	*	0.01 ± 0.001	*	*	0.100 ± 0.1	0.169 ± 0.9	0.134 ± 1	0.050 ± 0.8
14C	*	0.017 ± 0.02	*	*	0.12 ± 0.04	0.173 ± 0.6	0.133 ± 0.3	0.047 ± 0.2
14CC	0.008 ± 0.1	0.025 ± 0.01	0.044 ± 0.02	0.063 ± 0.1	0.13 ± 0.03	0.180 ± 1	0.149 ± 0.4	0.054 ± 0.1
17CC	0.008 ± 0.3	0.027 ± 0.003	0.039 ± 0.02	0.052 ± 0.02	0.12 ± 0.03	0.191 ± 0.07	0.148 ± 0.8	0.054 ± 0.4
24CC	0.006 ± 0.4	0.041 ± 0.01	0.048 ± 0.06	0.079 ± 0.7	0.09 ± 0.02	0.156 ± 0.5	0.102 ± 1	0.046 ± 11
30CC	0.008 ± 0.4	0.038 ± 0.009	0.039 ± 0.06	0.045 ± 0.03	0.08 ± 0.03	0.126 ± 0.05	0.096 ± 1	0.042 ± 0.09
38CC	0.011 ± 0.9	0.043 ± 0.002	0.039 ± 0.03	0.052 ± 0.2	0.07 ± 0.05	0.093 ± 0.006	0.061 ± 0.03	0.039 ± 0.3
46CC	0.024 ± 0.4	0.045 ± 0.01	0.037 ± 0.1	0.045 ± 0.3	0.07 ± 0.03	0.082 ± 4	0.050 ± 0.3	0.035 ± 2
53CC	0.002 ± 0.1	0.057 ± 0.003	0.03 ± 0.06	0.027 ± 0.2	0.06 ± 0.01	0.077 ± 0.001	0.043 ± 0.7	0.029 ± 0.9
60CC	0.003 ± 0.08	0.056 ± 0.007	0.025 ± 0.04	0.019 ± 0.1	0.05 ± 0.06	0.051 ± 0.5	0.029 ± 0.2	0.020 ± 0.5
70CC	0.003 ± 0.01	0.047 ± 0.004	0.016 ± 0.01	0.012 ± 0.08	0.03 ± 0.1	0.036 ± 0.2	0.023 ± 0.03	0.014 ± 0.09
76CC	0.012 ± 0.1	0.066 ± 0.02	0.014 ±0.003	0.007 ± 0.2	0.02 ± 0.04	0.023 ± 0.7	0.017 ± 0.3	0.010 ± 0.3

The larger the error bar, the more dependence of E_b on emission angle. The E_b = 1200 eV data shows very little angular dependence, hence small error bar and at E_b = 2500 eV there is a substantial angular dependence, hence large error bar due to AES contribution of E_{min}. The most significant difference is that now, $\eta_{ER}(\alpha, E_{BSE}; E_b = 1200\ eV)$ is the maximum yield measuring 0.19 sr^{-1} for low angle and 0.02 sr^{-1} for high angle scattering. This maximum is nearer to the E_{max} measured with the hemispherical grid analyzer in the Fatman chamber at ~750 eV (see Fig. 4-8). Notice also that $\eta_{ER}(\alpha, E_{BSE}; E_b = 2000\ eV)$ is greater than $\eta_{ER}(\alpha, E_{BSE}; E_b = 2500\ eV)$. In addition, the anomalous effect observed at $\eta_{ER}(\alpha, E_{BSE}; E_b = 600\ eV)$ is less than yields using 50 eV.

Noticeably different BSE yields emerge using the boundaries 50 eV to E_b rather than E_{min} to E_b. All of these distributions have the placement of energy where the counts are a minimum. An affect was made to the difference distribution. Specifically, the difference in energy boundaries for E_b = 500 eV and 600 eV is 200 eV, for E_b = 900 eV and 1200 eV is 350 eV, for E_b = 2000 eV is 850 eV, and for E_b = 2500 eV is 1150 volts. These differing boundaries lead to a greater yield distribution for E_b = 1200 eV than E_b = 2000 eV. There is also a subtle increase in yield for the E_b = 900 eV data where the yield at 45° CC is greater than that of 38 ° CC. The yields when finding the area under the spectra from E_{min} to E_b are all less than the yields when finding the area under the spectra from 50- E_b.

Although this BSE yield calculation gives a good idea of the trend and shape, it will not be presented here.

5.3.(c)3 Ratio of Elastic Yield to BSE Yield

This section compares the ratio of the elastic yield based on 0.1 eV resolution data [Fig. 5-12] to the inelastic BSE yield [Fig. 5-27] (based on 10 eV resolution data) plotted against E_b on a logarithmic scale [Fig. 5-28]. The plot shows 1/E law fall off towards high beam energy. This ratio is the number of elastically backscattered electrons to the number of inelastically backscattered electrons, because the BSE yield as calculated in this section exclude the elastic yield. Recall the Rutherford (Eq. 2.15a), screened Rutherford (Eq. 2.15b) and Mott (Eq. 2.16) all are proportional to E^{-2} (at least to first order). Also

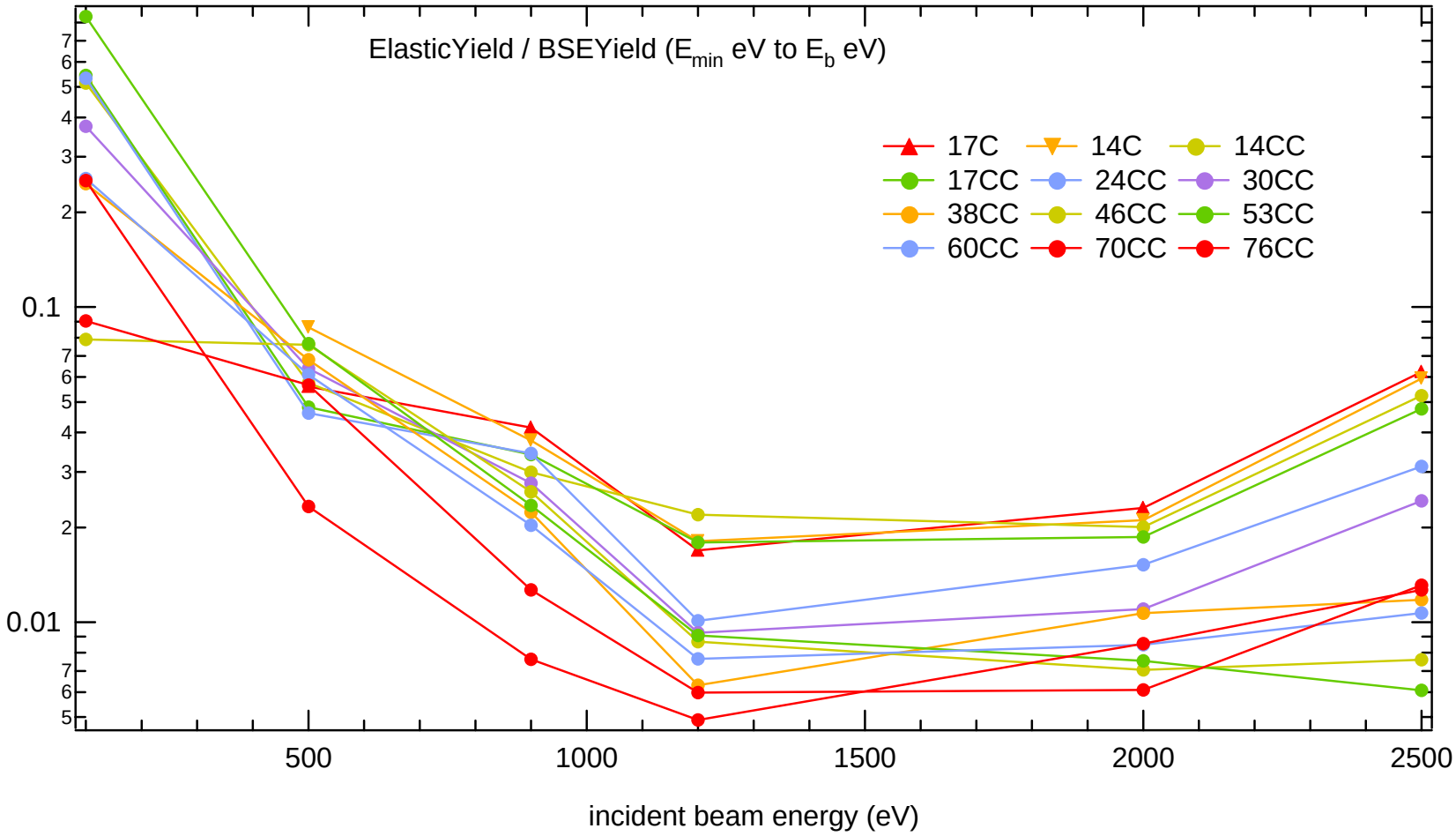

Figure 5-28 Ratio of elastic yield to BSE yield (E_{min} – E_b eV).

electron is an electron that has been scattered back no matter where (depth) it was produced as long as it was measured with an energy greater than E_{min}. The elastic yield is ~70% to ~0.5% of BSE. This means that not many BSE make it out unscathed. Low energy elastic electrons are more likely to make it out unscathed than higher energy elastic electrons. This must be due to larger solid angle of getting out for low energy than high energy, even though λ_{inel} is increasing with increasing E_b. Perhaps λ_{el} and λ_{inel} have different E_b dependence.

5.3.(c)4 Ratio of BSE Yield to Total Yield

The fraction of the total yield attributed to inelastically backscattered incident electrons as a function of beam energy is calculated as the ratio of the inelastic backscattered yield to the total yield. The total yield as a function of Eb for various emission angles is calculated in sec. 5.6 and plotted in Fig. 5-60. The inelastic BSE yield as a function of Eb for various emission angles (calculated using Emin as the lower energy limit to the BSE population) is shown in Fig. 5-27.

This ratio is plotted in Fig. 5-29 for various emission angles. The ratio varies fro ~5% to ~35%, but most values are near the mean ratio of ~20%. The plots suggest there may be a weak maximum near 1500 eV.

Using the Total Yield against E_b [Fig. 5-60] provided in a further section (5.6), it is useful to calculate the ratio of the BSE yield [Fig. 5-27] to the Total Yield. The yield ratio is calculated using the E_{min} value as the delineation of the BSE population. This ratio is shown plotted against the incident beam energy [Fig. 5-29] for several emission angles. The ratio shows inelastic collisions peak at ~1500 eV. Same trend is evident in Fig. 5-28.

This is yet another example of ability to measure absolute yields can allow for the comparison of one type of electron (inelastic backscattered PE) with another (all electrons). For instance, this BSE to Total yield ratio is the fraction of PE that have undergone an inelastic collision (or collisions) and made it out.

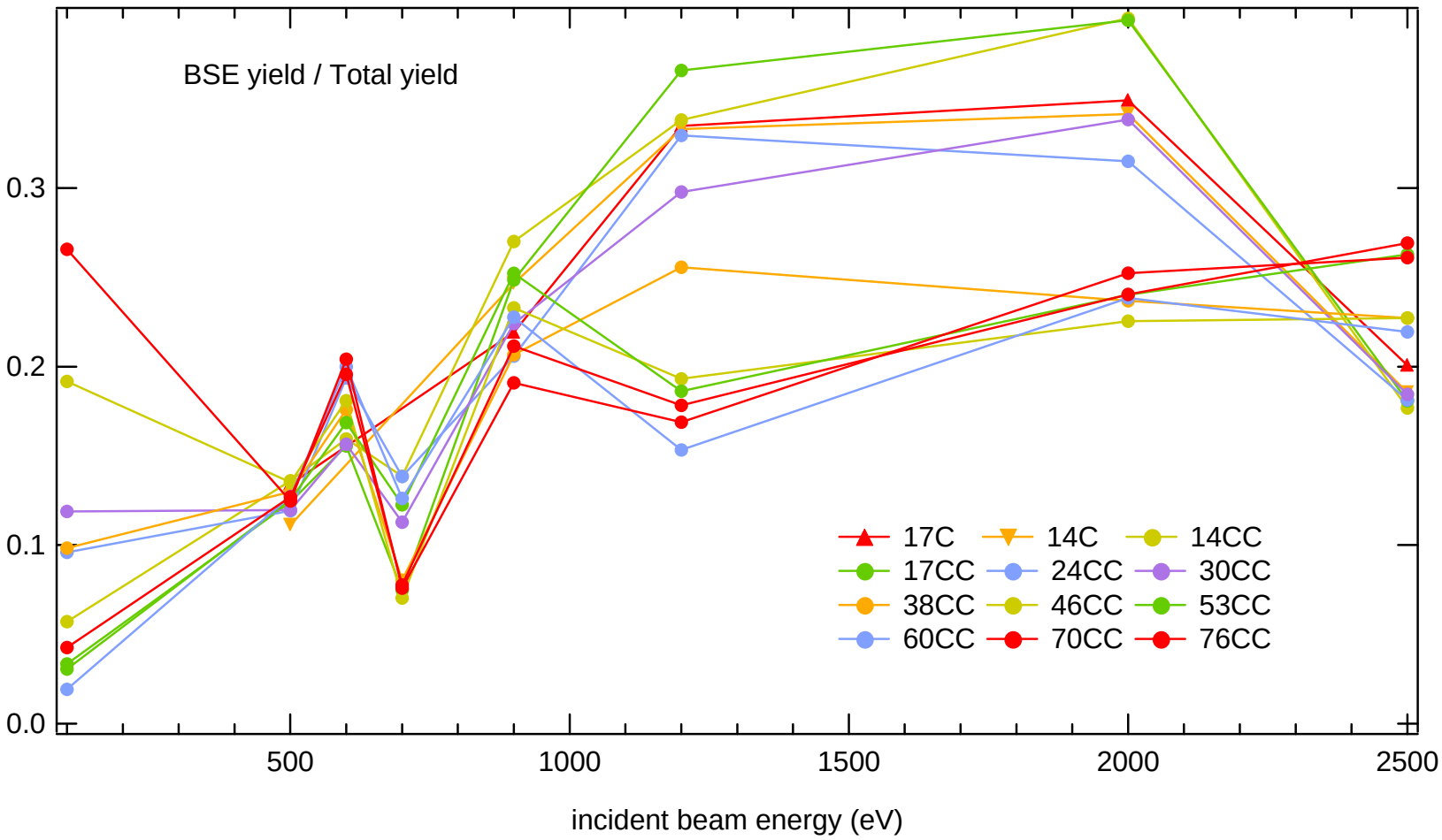

Figure 5-29 The ratio of BSE Yield, calculated using E_{min}, to the Total yield.

5.3.(c)5 Angle Integrated Comparisons

The angular cross sections presented for several incident beam energies have been resolved at coarse and fine angle emission (E_b = 900 eV). Numerical integration of these angular cross sections provides the backscattered yield for all angles from 0° to 90° emission. The integration of the Rutherford fit, used to model $\eta_c(\alpha)$ and $\eta_f(\alpha)$, is calculated for each E_b. After integration of the Rutherford fit, these results are compared to BSE yields fit to 50 eV data and E_{min} data.

Comparison of the angle integrated BSE yield, $\eta_c(E_b)$, to that taken with the FatMan chamber [Fig. 5-30] shows that values reasonably agree considering the coarseness (angle) of the data. Though using 50 eV [Fig. 5-25] instead of E_{min} [Fig. 5-27] as the lower energy boundary for yield calculation, Eq. (3.16), make little observable difference, quite a bit of difference is observed after integration over angle, Eq. (3.18). Percent differences range from 7% (E_b = 1200 eV) to 28% (E_b = 600 eV) with an overall average of 16% difference and standard deviation of the 6%.

Note that E_{min} yield is consistently less than 50 eV yield (and Fatman yield except at 1200 eV). The difference in the BSE yields at each E_b calculated using E_{min} and 50 eV are quantified in Chap. (5.9). Incorrectly labeled BSE (that are really SE)

The integral of (Eq. 5.3) is

$$N(\alpha, E_{pl}) = \frac{C\tan(\frac{\alpha}{2})}{4\beta(1+\beta)\left(\tan(\frac{\alpha}{2})^2 + \beta + \beta\tan(\frac{\alpha}{2})^2\right)} + \frac{CM}{4\beta} + \frac{CM}{2} \qquad (5.5)$$

$$M = \frac{\arctan\left[\frac{(1+\beta)}{\sqrt{\beta+\beta^2}}\tan(\frac{\alpha}{2})\right]}{(1+\beta)\sqrt{\beta+\beta^2}}$$

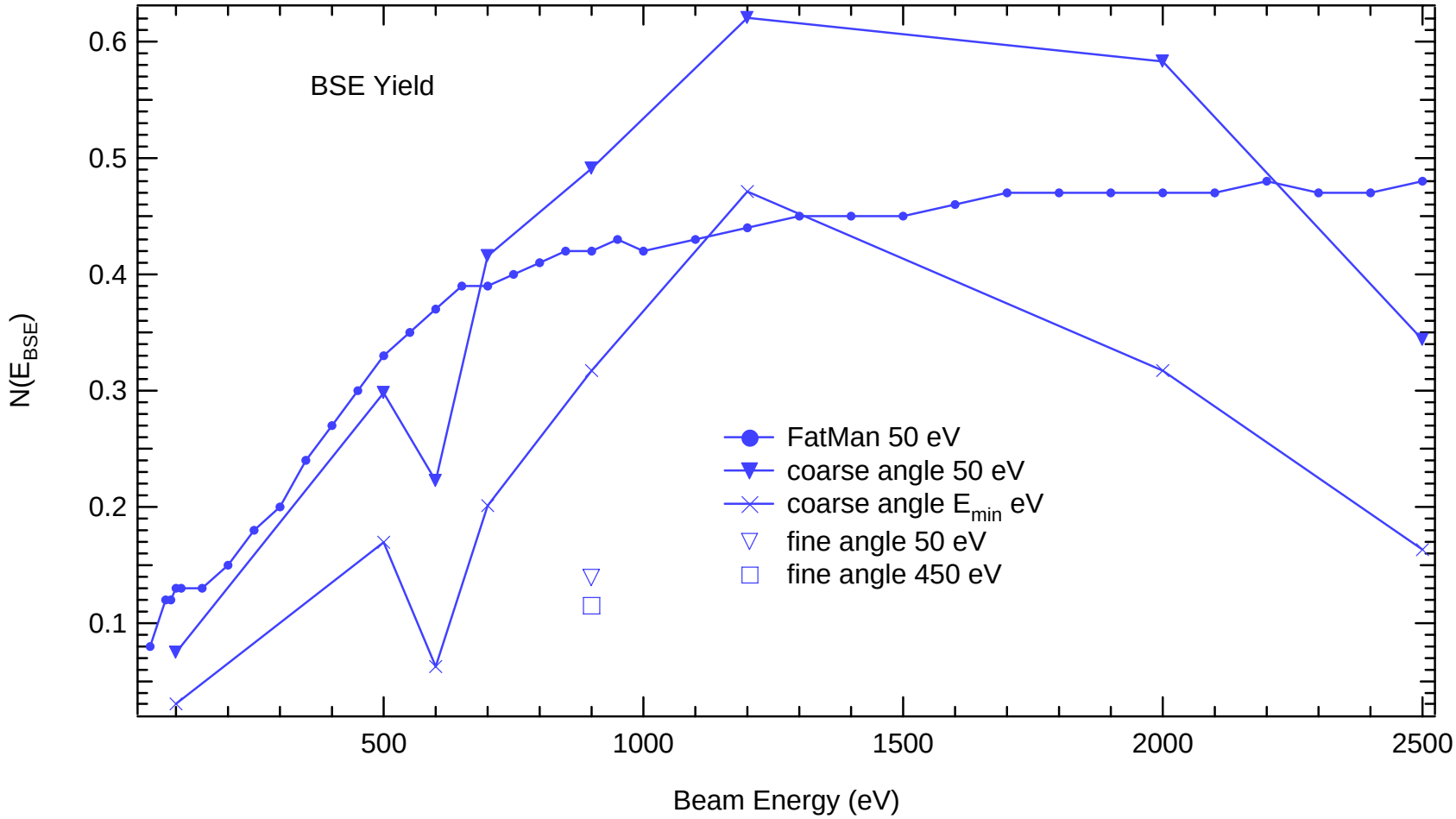

Figure 5-30 BSE Yield integrated over angle using Eq. (5.5) and calculated with boundaries of E_{min} eV – E_b eV and 50 eV – E_b eV. The integrated fine angle yields for E_b = 900 eV using 50 eV and 450 eV are also included. BSE yields (Fatman chamber) measured using 50eV – E_b eV are shown for comparison [*Clerc et. al., 2005*].

5.3.(d) Angle Resolved BSE Yield Distributions

The SE yield, $\eta_f(\alpha; E_b)$, has been measured using a fine angular resolution at E_b = 900 eV [Fig. 5-31]. Again these finer angle resolution distributions (cross sections) primarily diagnosed the RD angle automation capabilities where the RD was biased to only two other non-grounded voltages (50 eV and 450 eV).

The Rutherford (Eq. 5.3) type fit and the Mott (Eq. 5.4) type fit have been used to model the distributions. The coefficients for the Rutherford fits for the 50 eV boundary data are $\beta = (0.37 \pm 0.04)$ and $C = (0.038 \pm 2) \times 10^{-5}$ eV^{-1} sr^{-1}, with $\chi^2 = 9 \times 10^{-3}$. The coefficients for the Rutherford fits for the 450 eV (E_{min}) boundary data are $\beta = (0.30 \pm 0.04)$ and $C = (0.022 \pm 2) \times 10^{-5}$ eV^{-1} sr^{-1}, with $\chi^2 = 6 \times 10^{-3}$.

The three coefficients for the Mott cross section for the 50 eV boundary data are $C_1 = (1 \pm 0.1) \times 10^{-6}$ eV^{-1} sr^{-1}, $C_2 = (38 \pm 3) \times 10^{-3}$ eV^{-1} sr^{-1}, and $\beta = (0.37 \pm 0.01)$ with $\chi^2 = 3 \times 10^{-3}$. For the 450 eV boundary, the coefficients are $C_1 = (1 \pm 0.1) \times 10^{-6}$ eV^{-1} sr^{-1}, $C_2 = (21 \pm 1) \times 10^{-3}$ eV^{-1} sr^{-1}, and $\beta = (0.29 \pm 0.01)$ with $\chi^2 = 1 \times 10^{-3}$.

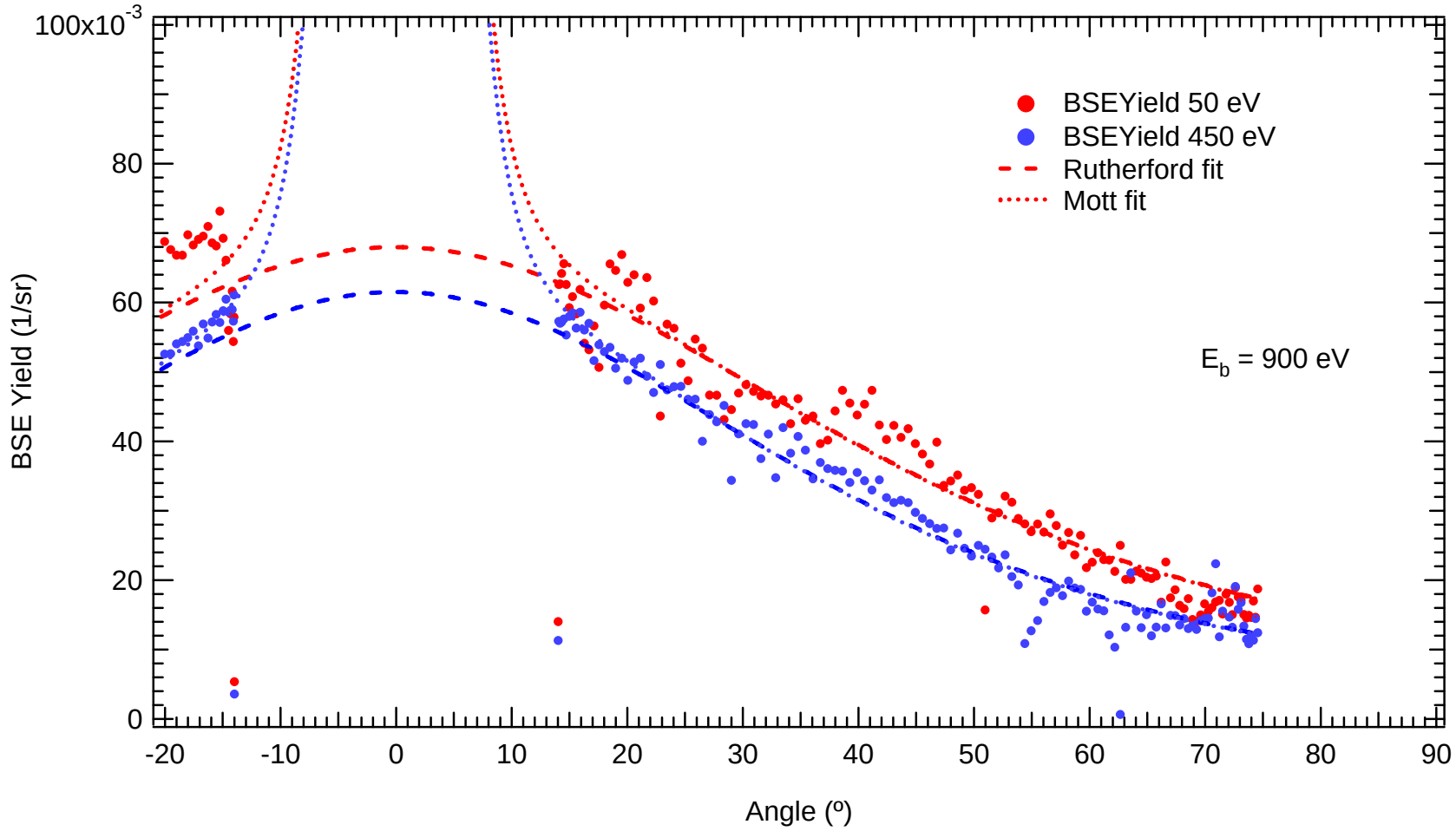

Figure 5-31 Angular resolved BSE yield using RD bias of 50 eV and 450 eV (E_{min}) for 900 eV incident beam energy. Rutherford (dash) and Mott (dot) fits are included.

5.3.(e) BSE Fine Structure

There is limited evidence in our data for fine structure peaks in the inelastic BSE spectra, particularly in the region near the BSE peak. These small peaks are believed to result from single and multiple inelastic collisions of the backscattered primary electrons. The possible scattering mechanisms include bulk and surface plasmon creation, core level excitations, interband transitions and combinations of these [Leiro, 1983].

Similar fine structure loss features have been measured for Au using a variety of techniques including high resolution electron energy loss spectroscopy (HREELS) [Fenno, 1998], [Werner, 1994; 2001], X-ray photo emission spectroscopy (XPS) [Leiro, 1983] and optical measurements of the dielectric function [Daniels, 1970; Wehenkel, 1975]. Careful analysis of such spectra can determine the relative differential probability for various energy loss mechanisms in the energy loss process. It is also possible to separate the bulk and surface components of these processes and to determine the inelastic mean free path from the shape of the spectra. However, this endeavor is complicated by the complex, often noisy spectra. The need for deconvolution of instrumentation effects is appearant due to the large number of peaks associated with various combinations of the quanta of different energy loss mechanisms. In general, the intensities of these peaks are small compared to say Ag. To date, there have not been definitive loss mechanisms assigned to all of the observed peaks, although individual authors have made some progress in this regard. Both incident energy and emission angle dependence of various peaks have been noted in the literature [Leiro, 1993; Daniels, 1970; Werner 1999; Werner, 2001].

An informal study of the HREELS spectra of polycrystalline Au was conducted by Fenno, and was reported by Davies [1999, Fig. 6-12]. The spectra [Fig. 5-32] were taken using an Auger spectrometer (VG model 31-F) equipped with a high resolution electrostatic hemispherical analyzer. Pass energies of 1.0 keV and 2.5 keV were used, similar to the beam energies used in this dissertation. Data from the different spectra compared nicely. Energy loss peaks were observed at -2.8 eV, -5.9 eV, -8.9 eV, -15.9 eV, -24.7 eV, and -33.0 ev, relative to the elastic peak [Fenno, 1998].

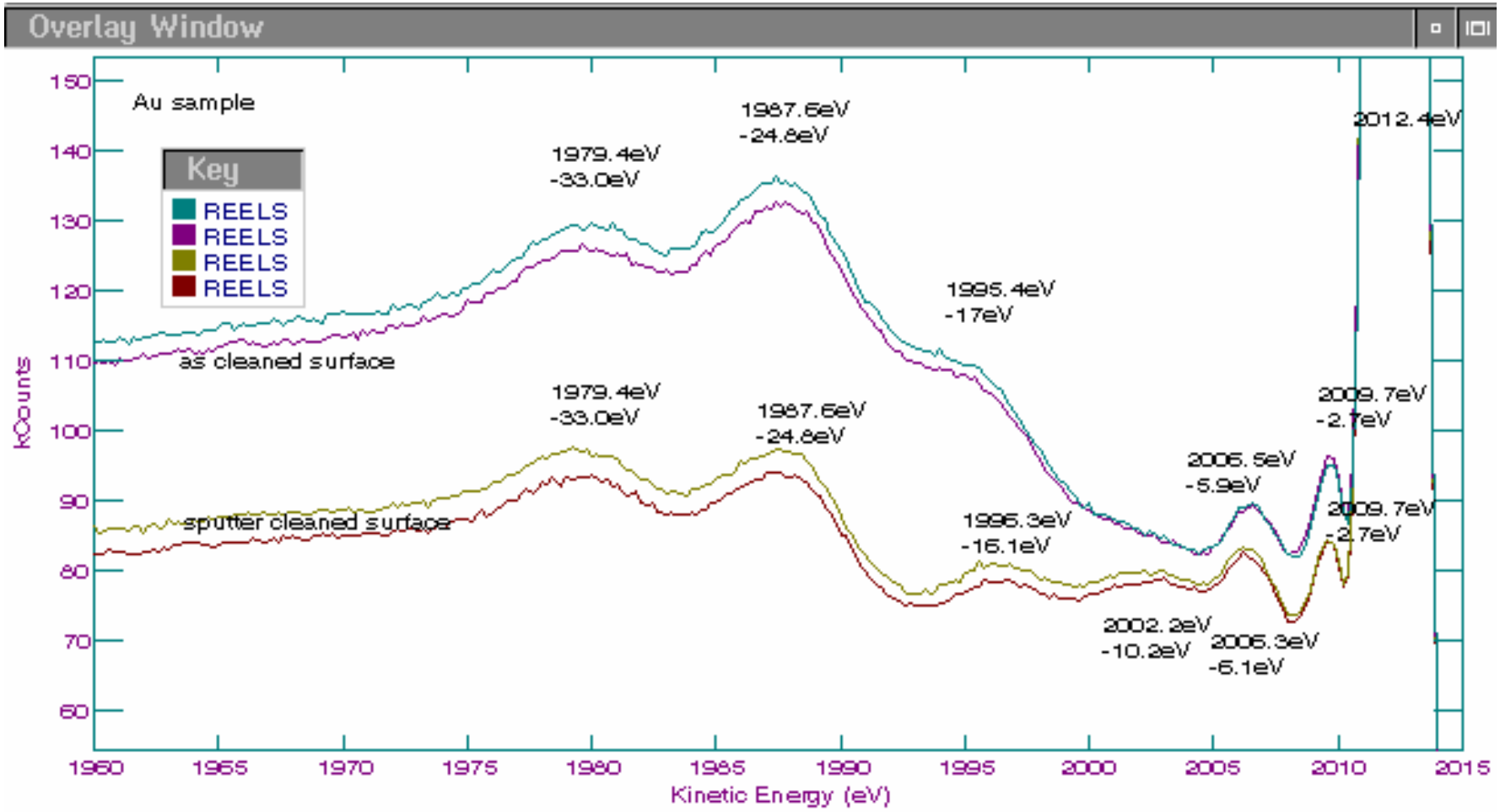

Figure 5-32 Reflected electron energy loss (REELS) spectra for sample A, performed for ultrasonically cleaned surface (upper curves) and sputtered surfaces (lower curves). E_B = 2012 eV.

Rather than present an exhaustive study of this fine structure, we present only some example spectra showing that such features are present in the data. Careful analysis of this aspect is left to future investigators. It is difficult to identify the peak positions and intensities in our spectra, and how these change with E_b and emission angle because of the signal-to-noise ratio for these weak peaks. Because these are relatively low intensity, narrow peaks in the midst of other larger peaks, it is even difficult to know where to look and at what energy to resolve.

Careful scrutiny of Fig. 5-19 and Fig. 5-20 show evidence of fine structure. Both graphs plot intensity versus emission energy and focus on the region below the inelastic BSE peak. Figure 5-19 shows data for E_b = 900 eV at various energies plotted directly against beam energy, emphasizing the angular dependence of the fine structure. Figure 5-20 shows data at 14^o CC emission energy loss, emphasizing the E_b dependence of the fine structure. Figure 5-33 show the same data in Fig. 5-19, after it has been smoothed. The fine structure appear more visable after smoothing; guides to the eye [Fig. 5-33] suggesting angular dispersion of some of the fine structure have been added to the graph.

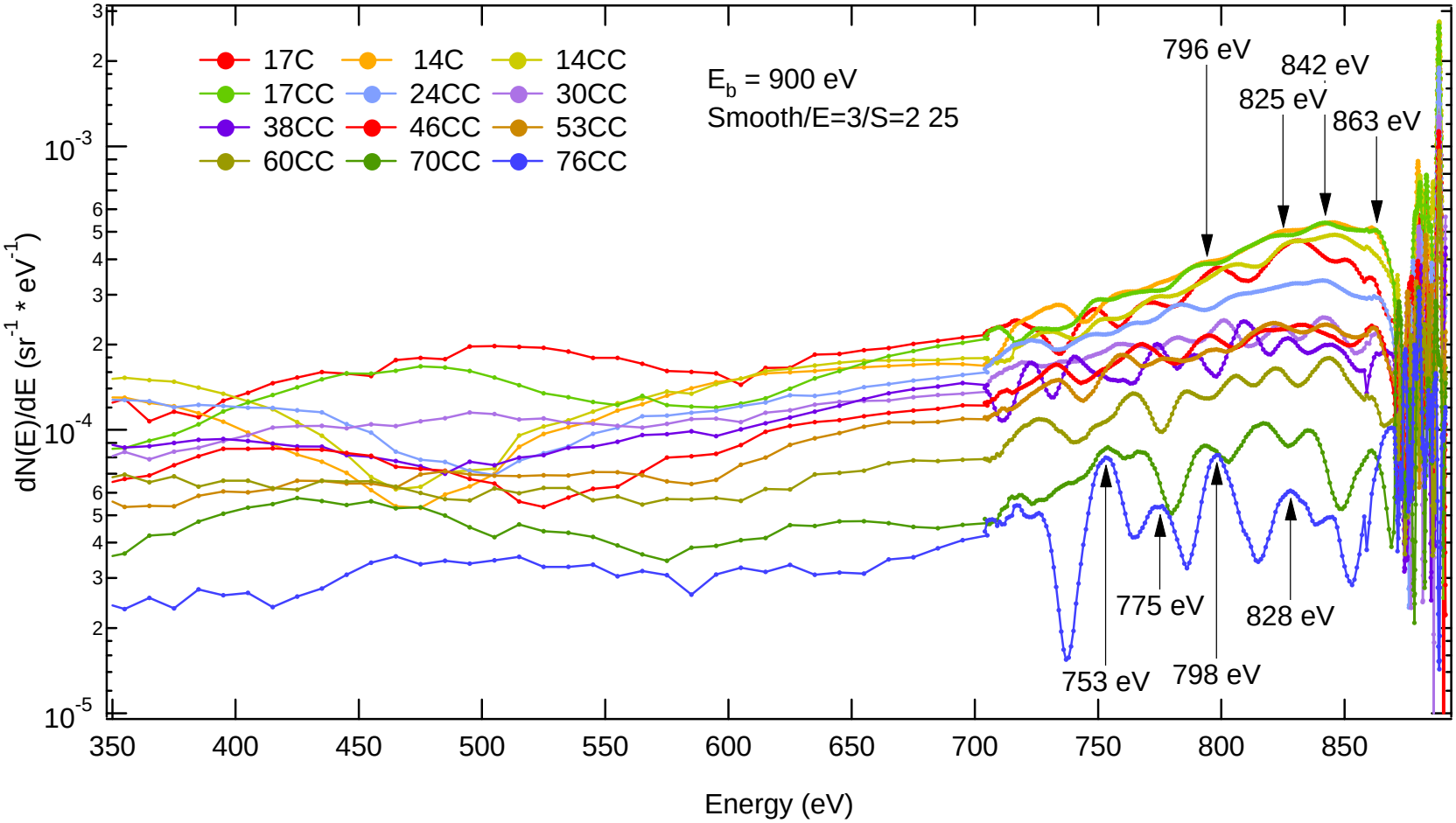

Figure 5-33 BSE AR spectra taken at an incident beam energy of 900 eV and several emission angles. Similar to Fig. 5-19, these spectra have undergone an additional smooth

5.4 SE Peak

Despite the many uses of secondary electrons, progress towards understanding the mechanisms of production and transport occurs by measurement of the angle— energy— resolved emission spectra. Defining a secondary electron in terms of its mechanism character, using energy and angular bounds, provides insight to the inner workings of the scattering medium. The characteristic features of the SE peak, defined in Table 3.3, are energy, E_{SE}, intensity, $dN(\alpha,E_{SE};E_b)/dE_e$, yield, $\delta(\alpha, E_{SE}; E_b)$, and width.

The spectra resolved at E_b = 900 eV [Fig. 5-34] are concatenations of E_bR spectra [Fig. E-68] using the 1 eV RD bias resolution and E_bR spectra [Fig. E-86] using the 0.1 eV RD bias resolution. This concatenation occurs at 20 eV. In addition, these spectra include the E_bR spectra [Fig. E-14] using the coarse 10 eV RD bias resolution from 160 eV to 450 eV in which case, the spectra at higher back scattered energies [Fig. 5-19] continue to complete the spectra [Fig. 5-50].

For comparison to the selected emission angles, the AR spectra are given for 0.1 eV resolution [Fig. E-88 through Fig. E-99], for 1 eV resolution [Fig. E-72 through Fig. E-83], and for the coarse 10 eV resolution [Fig. E-18 through Fig. E-29]. The SE peaks features are addressed in terms of the energy position of the peak and its yield intensity. Normalized SE peaks also provide information about the width of the SE peak with respect to emission angle and energy resolution. The integrated yields are calculated with the customary 50 eV demarcation and the E_{min} eV energies. The integrated yields are then compared with the higher energy backscattered and total yields. This section concludes with comparisons to the most current theory and cross section results.

5.4.(a) SE Peak Features

First is the SE Peak Position. Second is the SE Peak Intensity. Third there is the shape or width. The shape of the AR SE spectra (without smoothing) is now shown normalized FWHM (10 eV resolution spectra). Then come the SE yields calculated using customary features and a better delineation, E_{min}, discussed in 5.3. Then comparisons of the SE yield using the E_{min} delineation to the Total Yield.

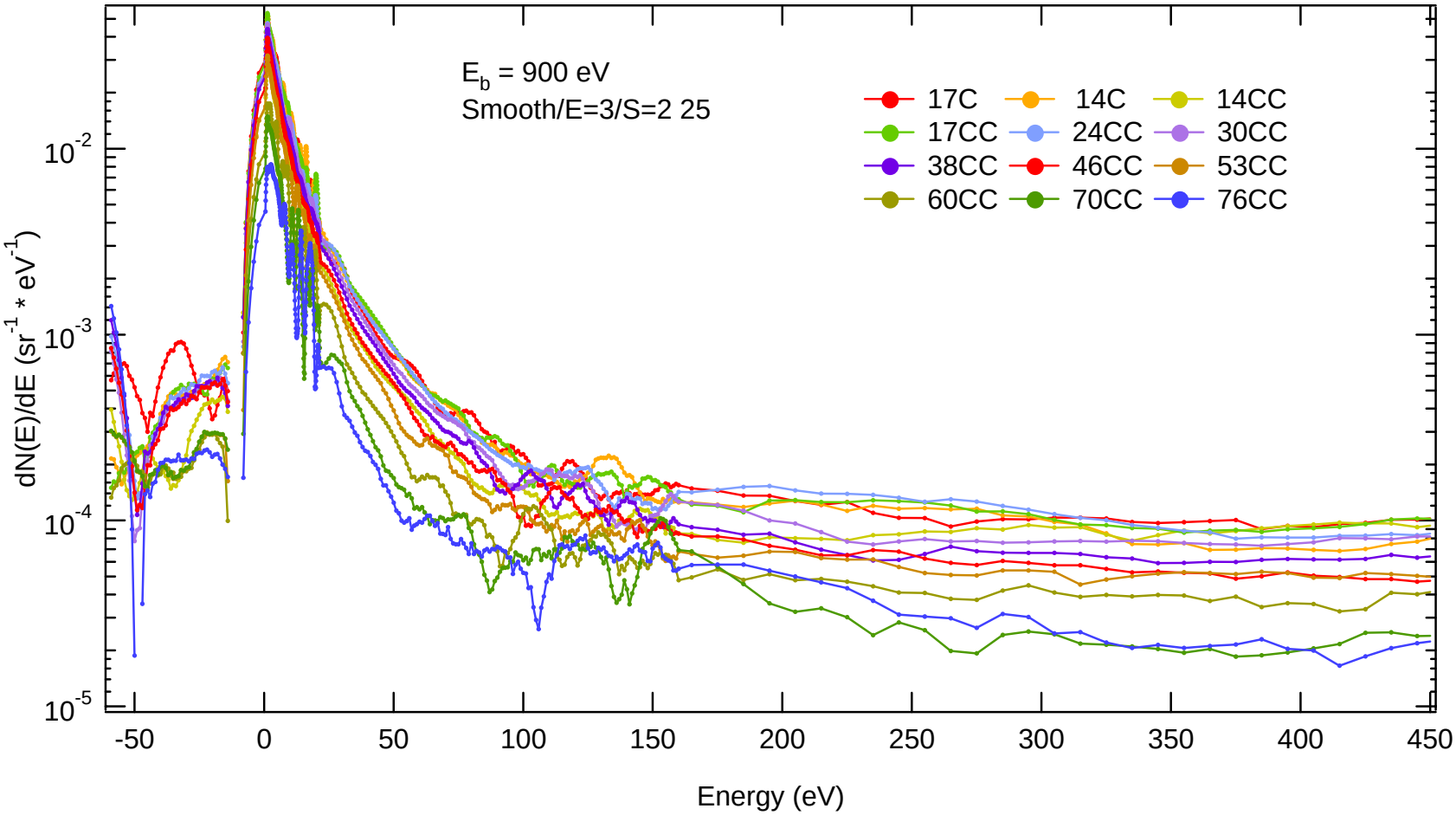

Figure 5-34 SE peak at 900 eV incident beam energy for selected emission angles.

5.4.(a)1 SE Peak Energy

The energy position of the SE peak, E_{SE}, is presented in terms of 0.1 eV and 1 eV resolutions. It is important to realize that all values are positive voltages. The values are tabulated in Table 5.14 along with average and standard deviations over angle. The SE peak energy position measured at 1 eV resolution [Fig. 5-35] results in averages ± 0.5 eV. The energy position values measured using the 0.1 eV (Fine) resolution include precisions to the tenth of an eV.

The averages of 2.0 ± 0.5 eV, 2.1 ± 0.6 eV, and 2.2 ± 0.9 eV are all within reason.

It is interesting to note that the SE peak energy positions increase with increasing emission angle though the standard deviation value 0.5 eV is the smallest of the measured 0.1 eV resolution values at E_b's 100 eV through 2500 eV.

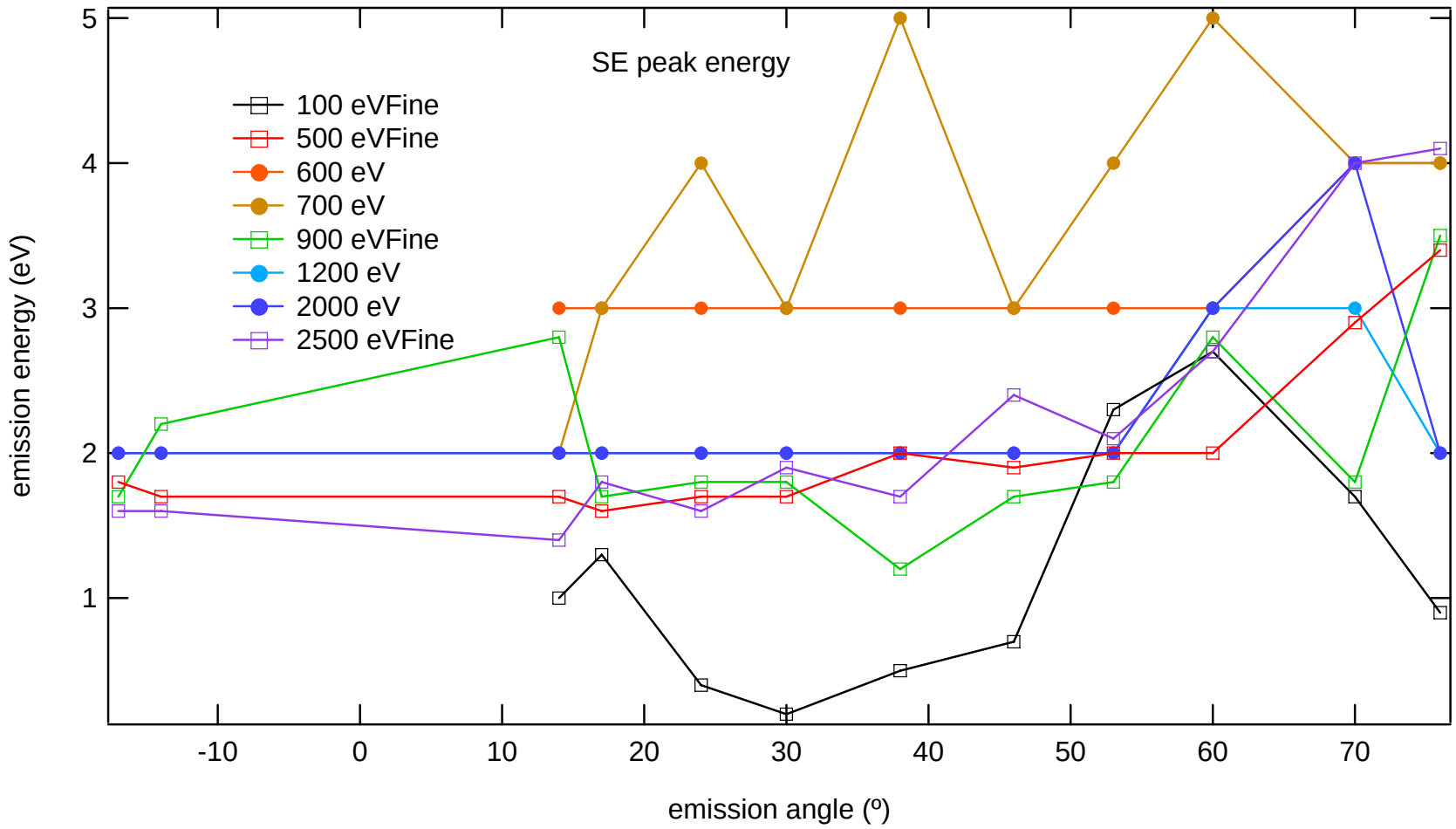

Figure 5-35 SE peak energy using the 1 eV (closed circles) and 0.1 eV (open squares) resolutions.

Table 5.14 The SE Peak Energy. All energy positions have units of eV and an error of 1 eV for 600 eV, 700 eV, 1200 eV, and 2000 eV and an error of 0.1 eV for 100 eV, 500 eV, 900 eV, and 2500 eV.

Beam Energy	Emission Angle (^{o})													
	17C	14C	14CC	17CC	24CC	30CC	38CC	46CC	53CC	60CC	70CC	76CC	Ave	StDev
100 eV	*	*	1.0	1.3	0.4	0.2	0.5	0.7	2.3	2.7	1.7	0.9	1.2	0.8
500 eV	3.4	2.9	2.0	2.0	1.9	2.0	1.7	1.7	1.6	1.7	1.7	1.8	2.0	0.5
600 eV	*	*	3	3	3	3	3	3	3	3	4	4	3.2	0.4
700 eV	*	*	2	3	4	3	5	3	4	5	4	4	3.7	0.9
900 eV	1.7	2.2	2.8	1.7	1.8	1.8	1.2	1.7	1.8	2.8	1.8	3.5	2.1	0.6
1200 eV	3	3	3	3	3	3	3	3	3	3	2	3	2.9	0.3
2000 eV	3	3	3	3	3	3	3	3	3	3	4	5	3.3	0.6
2500 eV	1.6	1.6	1.4	1.8	1.6	1.9	1.7	2.4	2.1	2.7	4.0	4.1	2.2	0.9

5.4.(a)2 SE Peak Intensity

The intensity of the SE peak, $dN(\alpha,E_{SE};E_b)/dE_e$, contributes an important surface characteristic of the scattering material. The occurrence of such high yield intensities at such low emission energies signifies the existence of production mechanism information. Two energy resolutions are again combined (1 eV and 0.1 eV) to give precise detail about the SE peak's intensity and error at the energy location of the peak (5.4.(a)1). The results are given in terms of emission angle [Fig. 5-36] and incident beam energy, E_b [Fig. 5-38]. The A E_b resolved distribution (cross section) is shown with a logarithmic vertical scale [Fig. 5-37] to contrast the 1 eV (circles) and 0.1 eV (squares) resolutions. This resolution mixing is accomplished for diagnostic confirmation but qualitative analysis shows that the intensity falls off with increasing angle. When viewed logarithmically, the Lambert law (Eq. 5.2) falls off slower than the E_b = 2500 eV data for both resolutions. The SE peak intensity measured using the 1 eV and 0.1 eV resolutions [Fig. 5-34] measures upwards of 25 x 10^{-3} 1/eV*1/sr and taper off toward values of 1 to 7 x 10^{-3} 1/eV*1/sr for larger emission angles. Average values for each E_b are also given.

High energy elastic and BSE emission spectra always follow low energy SE emission spectra measurements due to the low energy effects of ESA contamination on the sample surface (Table E-1). The values are tabulated in Table 5.15 and include amplitude fit coefficients, B, for the Lambert law.

$$\frac{dN(E_{SE})}{dE_e} = B\cos(\alpha) \tag{5.2}$$

The amplitude coefficients for the fine resolution Lambert law (not tabulated) are B = (0.038 ± 0.008) eV^{-1} sr^{-1}, (0.0327 ± 0.0007) eV^{-1} sr^{-1}, and (0.008 ± 0.002) eV^{-1} sr^{-1} with χ^2 = 0.005, 0.00004, 0.0005 for E_b = 500 eV, 900 eV, and 2500 eV, respectively. These fits look like those of Davies [Fig. 2-4] for the 2 to 5 eV cross sections. The anomalous behavior observed in the E_b = 1200 eV data peaked at 53° CC emission angle is not understood.

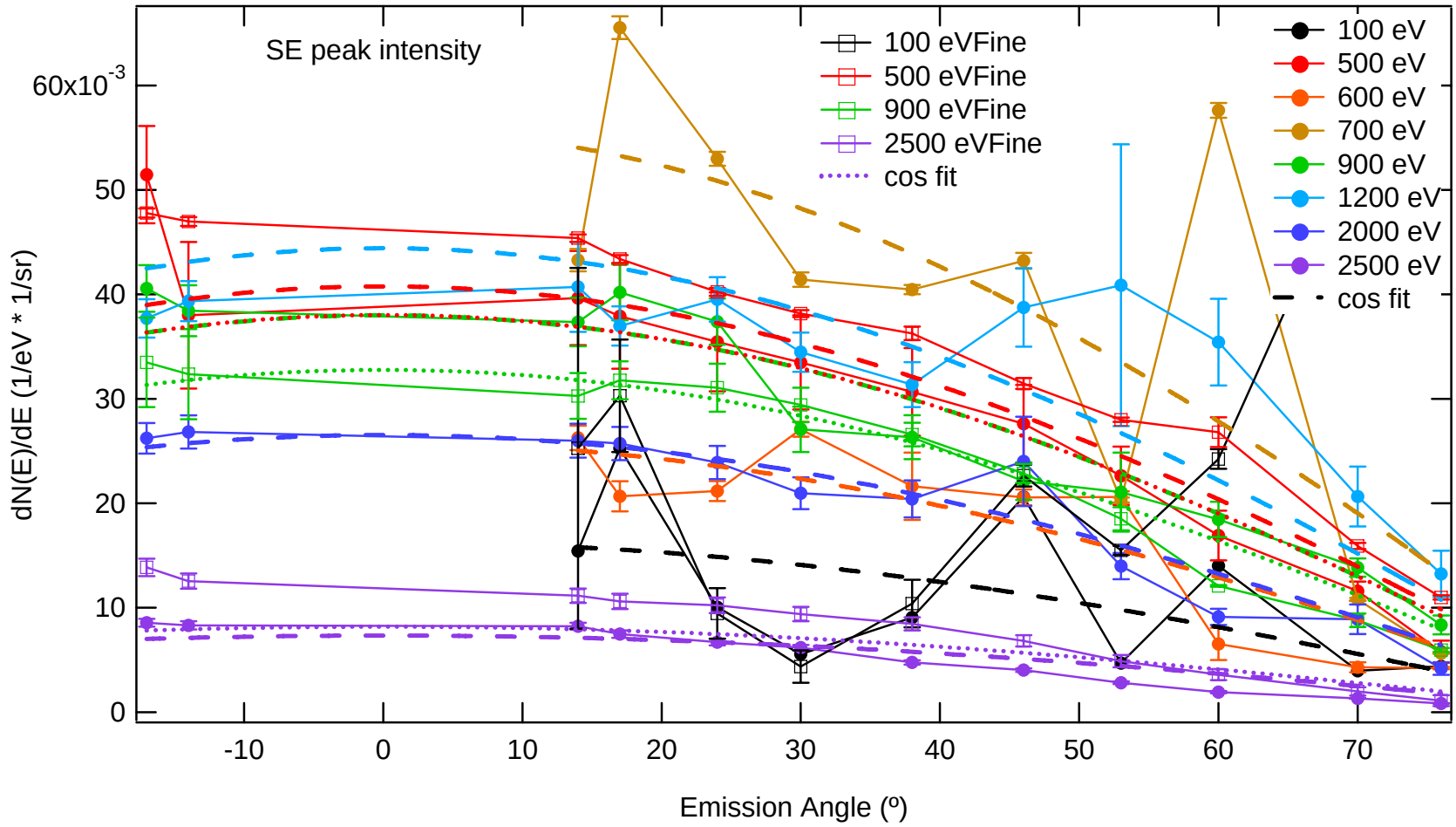

Figure 5-36 The SE peak intensity using the 1 eV (circles) and 0.1 eV (squares) resolutions.

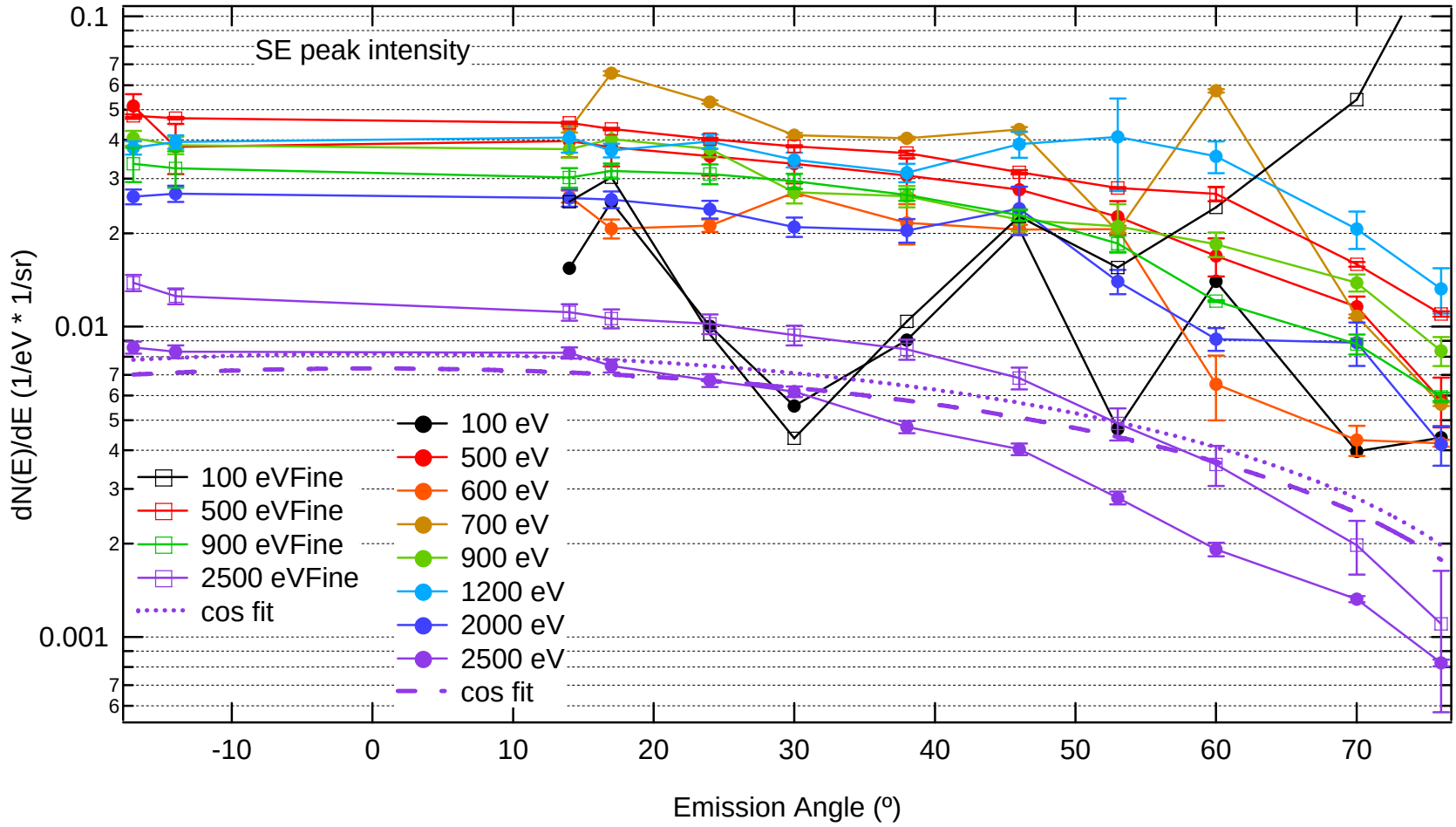

Figure 5-37 The SE peak intensity on a logarithmic scale using the 1 eV (circles) and 0.1 eV (squares) resolutions.

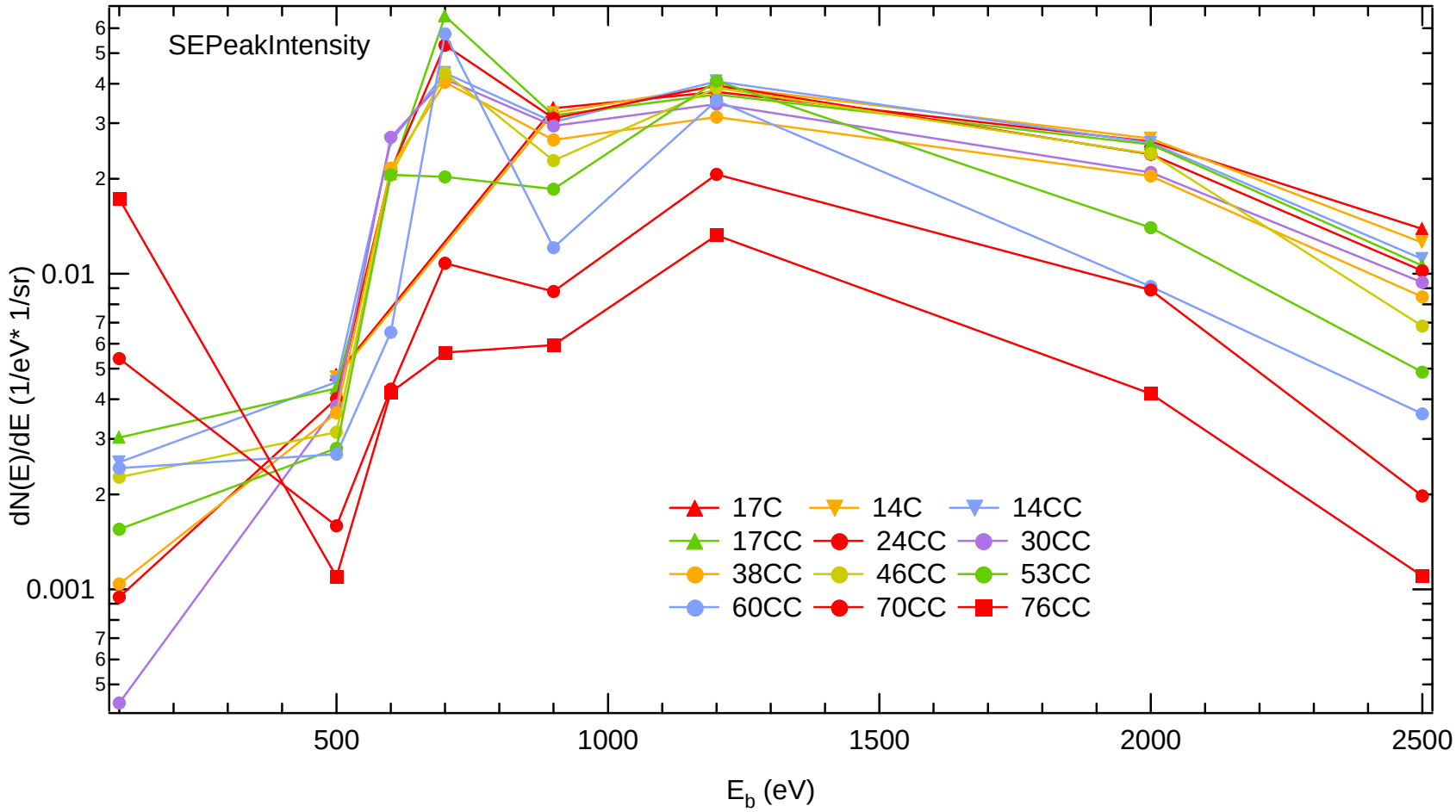

Figure 5-38 The SE peak intensity on a logarithmic vertical scale using the 1 eV (600 eV, 700 eV, 1200 eV, and 2000 eV) and 0.1 eV (100 eV, 500 eV, 900 eV, and 2500 eV) resolutions.

Table 5.15 The SE Peak Intensity. All yield intensities have units of (1/sr*1/eV) * 10^{-3} and include error in units of (1/sr*1/eV) * 10^{-3}.

Emission Angle (^{o})	Incident Beam Energy (eV)							
	100 eV	500 eV	600 eV	700 eV	900 eV	1200 eV	2000 eV	2500 eV
17C	*	4.8 ± 0.4	*	*	33 ± 4	38± 2	24 ± 1	13.9 ± 0.8
14C	*	4.7 ± 0.4	*	*	32 ± 4	39 ± 2	24 ± 1	12.6 ± 0.7
14CC	2.5 ± 17	4.5 ± 0.4	26 ± 1	43 ± 1	30 ± 2	38 ± 2	23 ± 1	11.1 ± 0.7
17CC	3.0 ± 5	4.3 ± 0.4	21 ± 1	66 ± 1	32 ± 2	37 ± 1	23 ± 1	10.6 ± 0.7
24CC	0.9 ± 2	4.0 ± 0.4	21 ± 1	53 ± 0.7	31 ± 2	37 ± 2	22 ± 1	10.2 ± 0.7
30CC	0.4 ± 2	3.8 ± 0.3	27 ± 1	41 ± 0.7	29± 2	32 ± 2	20 ± 1	9.4 ± 0.7
38CC	1.0 ± 2	3.6 ± 0.6	22 ± 3	40± 0.4	27 ± 1	30 ± 2	19 ± 2	8.5 ± 0.6
46CC	2.3 ± 1	3.1 ± 0.5	21 ± 0.8	43 ± 0.7	23 ± 0.9	37 ± 3	18 ± 2	6.8 ± 0.5
53CC	1.6 ± 0.4	2.8± 0.2	21 ± 0.5	20 ± 0.2	19 ± 1	40 ± 12	14 ± 1	4.9 ± 0.6
60CC	2.4 ± 0.9	2.7 ± 1	7 ± 2	58 ± 0.7	12.1 ± 0.1	32 ± 4	8.5 ± 0.8	3.6 ± 0.5
70CC	5.4 ± 3	1.6 ± 0.3	4.3 ± 0.5	11± 0.1	8.8 ± 0.7	20± 3	7.2 ± 1	2.0± 0.4
76CC	17.3 ± 1	1.1 ± 0.2	4.2 ±0.1	5.6 ± 0.1	5.9 ± 0.2	13 ± 2	3.4 ± 0.4	1.1 ± 0.5
B	0.016 ± 0.003	0.041 ± 0.002	0.026 ± 0.002	0.056 ± 0.006	0.038 ± 0.001	0.044 ± 0.003	0.027 ± 0.001	0.007 ± 0.001
χ^2	0.0004	0.0002	0.0001	0.002	0.0001	0.0006	0.00006	0.00007

5.4.(a)3 Normalized SE Peak (FWHM)

The E_b resolved SE spectra for E_b = 2500 eV are provided for closer examination of the shape while normalized. The SE spectra using the 0.1 eV resolution [Fig. 5-39] are provided in two concatenated, located at 0 to 2 eV, sets of Bertan Voltage settings. Verification of the zero reading on the negative energy side of the spectra has been made since absolute spectra are measured. The normalization process uses the zero reading to remove the background noise accountable by the contribution of scattered charge from the inner walls of the Aquadag coated shield (Chamber Apparatus) and the possible SE's produced within the Aquadag coated rotatable detector.

The full width at half maximum (FWHM) varies from 4 eV to 5 eV. This is not an appreciable amount.

The position of the peak moves to higher values as the scattering angle is increased. Compare normalized SE spectra especially E_b = 2500 eV to say that the work function changes with respect to emission angle. It only changes by about ½ Volt.

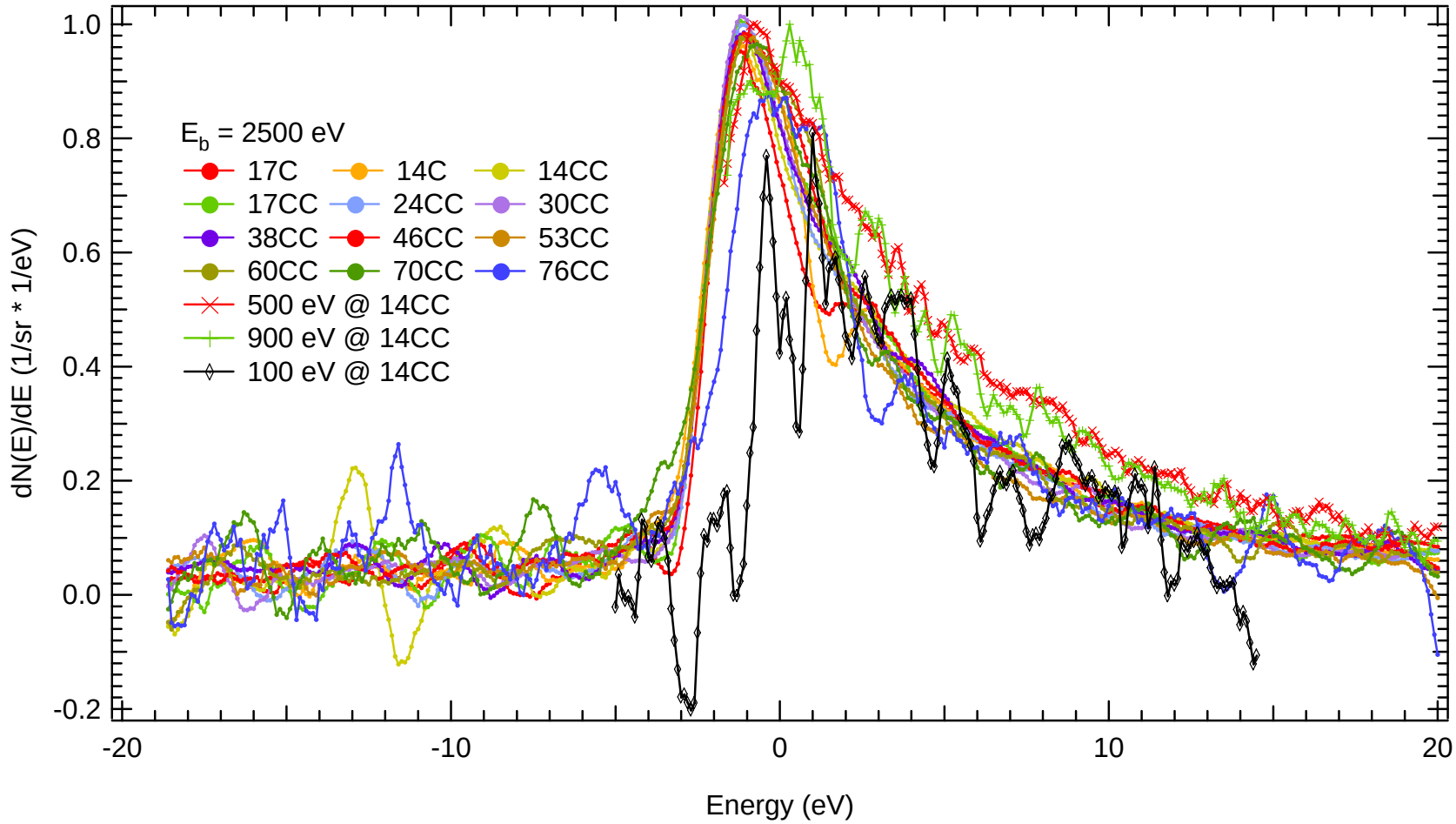

Figure 5-39 Normalized SE peak measured at 2500 eV incident beam energy using the 0.1 eV resolution for selected emission angles.

5.4.(b) SE Yield

The fine resolution spectra of the SE Peak have also been resolved at 0.1 eV. Though the Elastic peak has been resolved at the finest 0.01 eV resolution [Chap. 3], the finest energy resolution spectra of the SE peak are resolved at 0.1 eV. $\delta_{ER}(\alpha, E_{SE}; E_b)$

5.4.(b)1 Customary Boundary

Customarily, the 50 eV boundary has been used to calculate the SE yield, $\delta_{ER}(\alpha, E_{SE}; E_b)$. (Table 5.16). The results are given in terms of emission angle [Fig. 5-40] and incident beam energy, E_b [Fig. 5-41]. This conventional calculation is used here primarily to compare with other data taken at Utah State University. The fits are Lambert cosine law (Eq. 5.2) so that the $\delta(\alpha=0)$ can be easily compared in 5.4(b)5. The Fatman vacuum chamber provides E_b resolved data taken on polycrystalline Au.

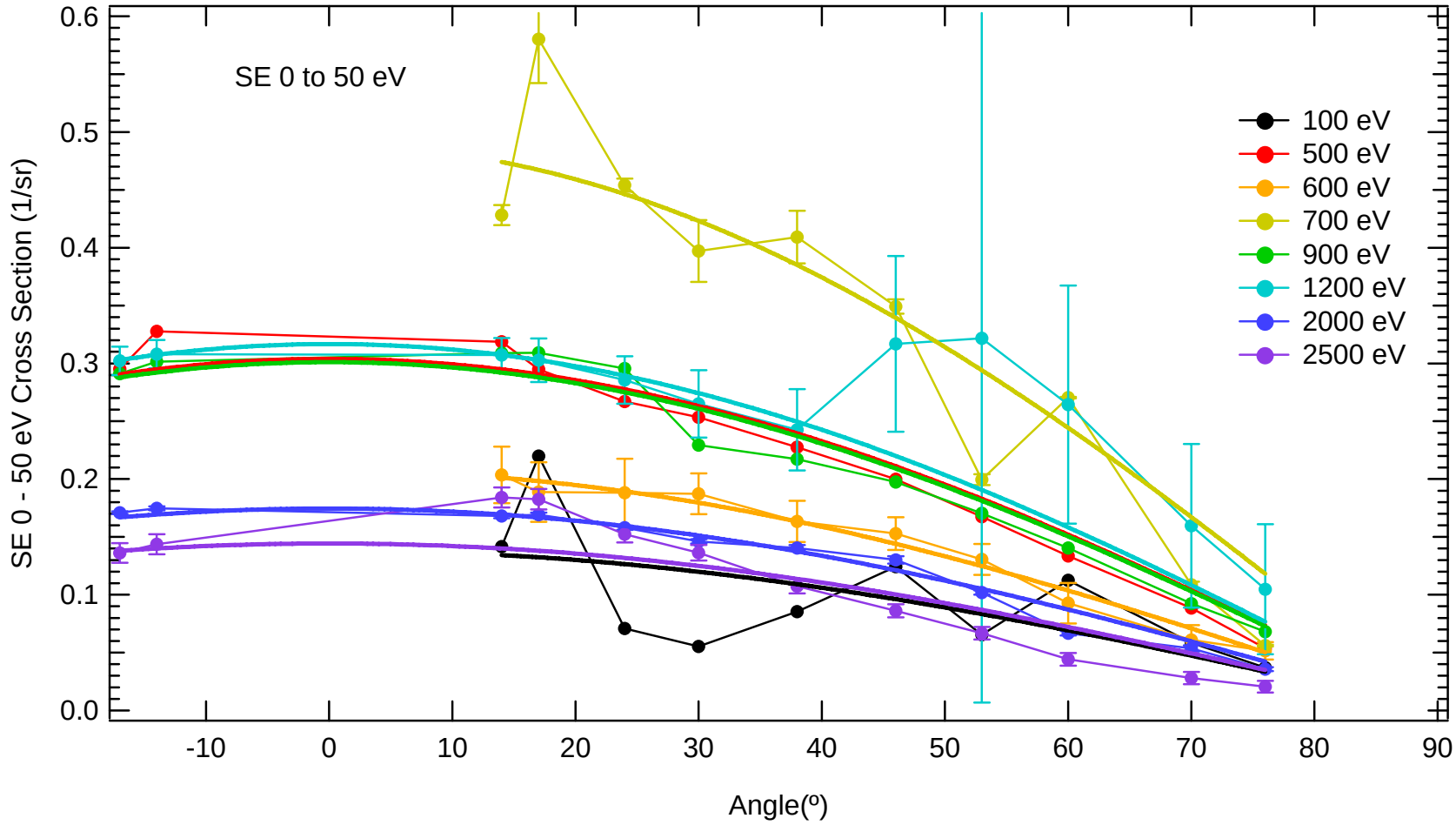

Figure 5-40 Secondary Electron angular distributions for selected beam energies in the 0 - 50 eV range using the 10 eV resolution.

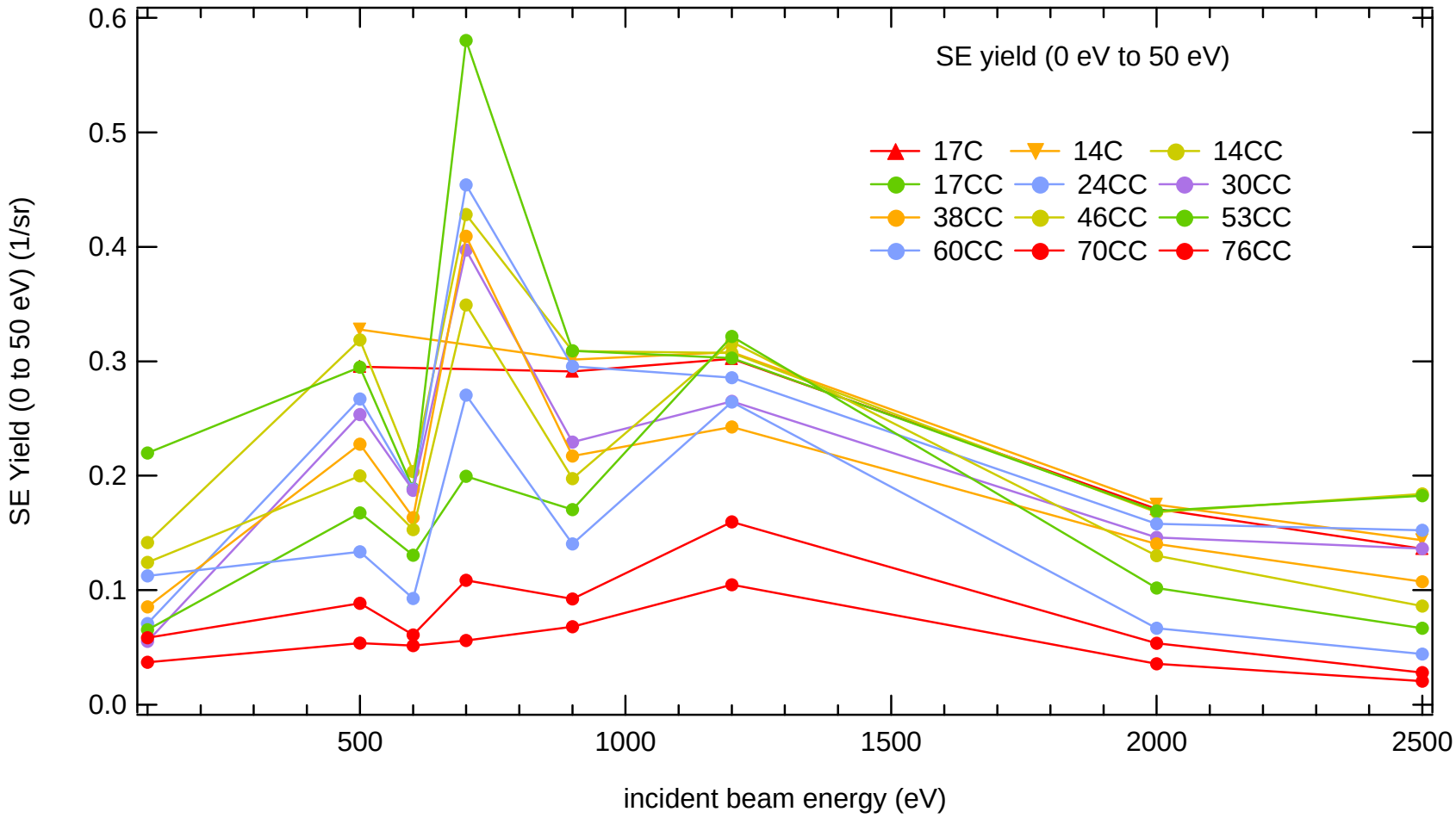

Figure 5-41 SE AR distributions for selected incident beam energies in the 0 - 50 eV range.

Table 5.16 The SE Peak Yield (0 – 50 eV) given in units of inverse steradians * 10^{-3}.

Emission Angle (°)	Incident Beam Energy (eV)							
	100	500	600	700	900	1200	2000	2500
17C	*	295 ± 14	*	*	291 ± 2	302 ± 30	171 ± 1	136 ± 2
14C	*	328 ± 23	*	*	301 ± 2	308 ± 30	175 ± 1	145 ± 2
14CC	142 ± 234	319 ± 17	204 ± 24	428 ± 36	309 ± 2	307 ± 30	168 ± 6	184 ± 2
17CC	220 ± 317	295 ± 15	189 ± 26	580 ± 95	309 ± 2	303 ± 40	169 ± 0.8	183 ± 2
24CC	71 ± 154	267 ± 14	188 ± 29	454 ± 3	296 ± 2	286 ± 30	158 ± 0.3	152 ± 0.8
30CC	55 ± 136	254 ± 13	187 ± 18	397 ± 47	229 ± 2	265 ± 50	146 ± 6	136 ± 0.5
38CC	85 ± 166	227 ± 12	163 ± 18	409 ± 80	217 ± 2	243 ± 53	141 ± 6	107 ± 0.2
46CC	124 ± 188	200 ± 10	153 ± 14	349 ± 55	197 ± 2	317 ± 163	130 ± 0.5	86 ± 0.2
53CC	65 ± 104	168 ± 8	131 ± 13	200 ± 14	170 ± 2	322 ± 371	102 ± 0.7	67± 0.4
60CC	113 ± 129	134 ± 7	93 ± 17	270 ± 27	141 ± 2	264 ± 224	67 ± 6	44 ± 0.7
70CC	58 ± 74	89 ± 5	61 ± 13	109 ± 19	92.3 ± 2	160 ± 9	54 ± 5	28 ± 0.3
76CC	37 ± 74	54 ± 3	51 ± 7	56 ± 1	68.0 ± 2	105 ± 5	36 ± 0.9	20 ± 0.2

5.4.(b)2 E_{min} Boundary

Now, the more sensible delineation, E_{min}, is used as the higher energy boundary to calculate the yield of the SE peak. Shown in section 5.3, the local minimum, E_{min}, separating the SE and BSE peaks is a better boundary because the intensity of the spectra continues to decrease for emission energy values greater than the customary 50 eV.

The difference of the SE angular distribution and the BSE angular distribution is the small amount of miscounted charge between 50 eV and E_{min} eV. Again, the result using the bounds 0 to 50 eV is noticeably different from the result using 0 to E_{min}.

Using the E_{min} eV demarcation, the SE yield, $\delta_{ER}(\alpha, E_{SE}; E_b)$, is shown against angle [Fig. 5-42] and against E_b [Fig. 5-43]. The SE yield values are tabulated in Table 5.17. So, though the E_bR BSE peak definitely shifted to a lower incident beam energy value, the E_bR SE yield showed no energy shift.

Notice that the E_b = 1200 eV also has the higher angle bump in it.

The Big Deal here is that the Red (E_b = 500 eV) is now less that the orange (E_b = 600 eV) [Fig. 5-41]. Where in Fig. 5-39 the Red (500 eV) is greater than the orange (600 eV). There must be an error in the 100 eV because it also drastically changes to a lower value. The reason for this is unknown.

The difference between the two SE distributions should also be shown and is within the error bar of the instrument. The E_b = 900 eV is only greater than the E_b = 1200 eV on a few angles. The E_b = 600 eV yield is less than the E_b = 500 eV yield for all angles.

It is important to note here that $E_b = 0$ eV has been used as the upper bound of integration. The energy boundaries extend a bit further into the positive or ionic measurement part of the spectrum. This doesn't by any means limit the instrument's ability to detect positive ions with the Faraday Cup's structure [Fig. 3-5]. Never-the-less the true zero of this floating ambient background is somewhere between the vacuum energy level and the gold sample. A future correction would be to look through every tertiary current starting with those taken with the LittleBoy in the symmetrical configuration. This may help to determine the effect of the Aquadag coating applied to the inner-shield. Temperature changes (1/40 th eV) are still low priority because of the relatively high Incident Electron Beam energies.

Now the SE yield is calculated using the E_{min} value.

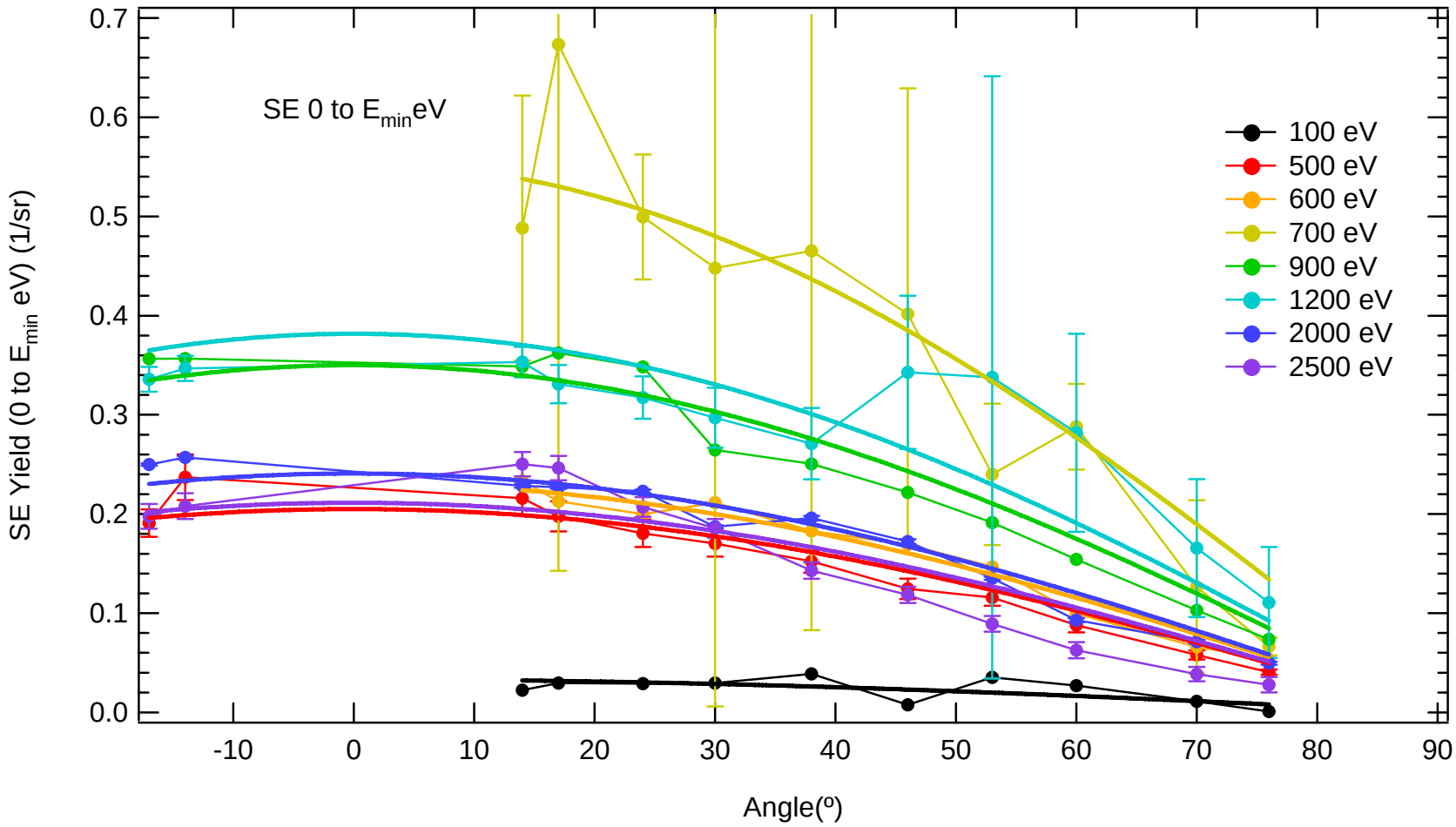

Figure 5-42 SE AR distributions for selected incident beam energies in the 0 - E_{min} eV range.

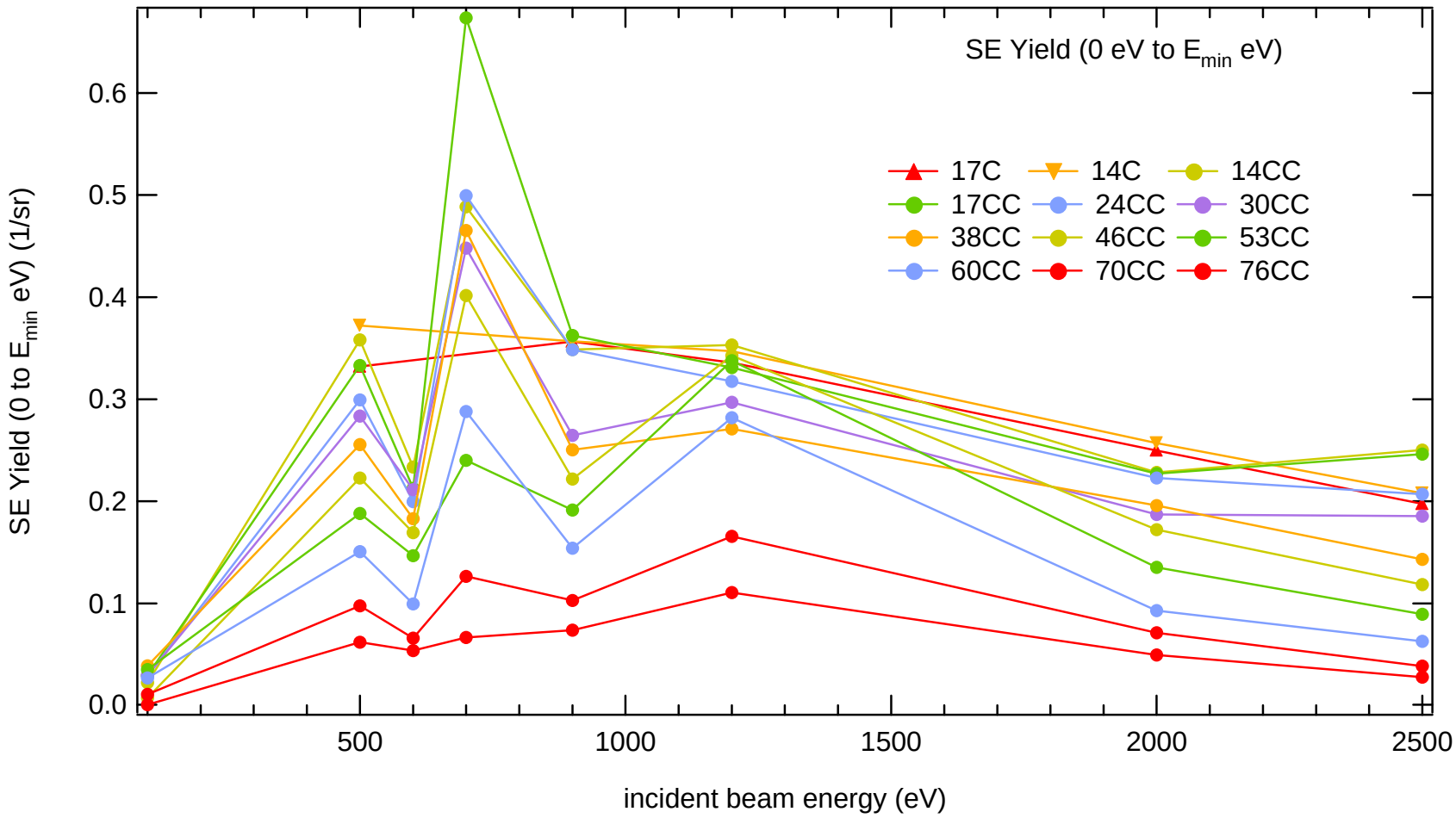

Figure 5-43 SE AR distributions for selected incident beam energies in the 0 - E_{min} eV range.

Table 5.17 The SE Peak Yield (0 eV to E_{min} eV) given in units of inverse steradians * 10^{-3}.

Emission Angle (°)	Incident Beam Energy (eV)							
	100	500	600	700	900	1200	2000	2500
17C	*	191 ± 49	*	*	357 ± 2	336 ± 13	250 ± 1	198 ± 13
14C	*	237 ± 107	*	*	357 ± 2	347 ± 13	257 ± 2	208 ± 13
14CC	22 ± 5	216 ± 64	234 ± 2	488 ± 134	349 ± 2	353 ± 15	228 ± 2	250 ± 12
17CC	30 ± 5	198 ± 59	213 ± 2	674 ± 531	362 ± 2	331 ± 19	227 ± 2	246 ± 12
24CC	29 ± 5	181 ± 55	200 ± 2	499 ± 63	348 ± 2	318 ± 21	223 ± 2	207 ± 1
30CC	30 ± 5	170 ± 51	212 ± 2	448 ± 442	265 ± 2	297 ± 30	187 ± 2	186 ± 1
38CC	39 ± 5	152 ± 46	183 ± 2	465 ± 382	250 ± 2	271 ± 36	196 ± 2	143 ± 0.8
46CC	8 ± 5	125 ± 38	169 ± 2	402 ± 227	222 ± 2	343 ± 77	172 ± 3	119 ± 0.8
53CC	35 ± 5	116 ± 37	147 ± 2	240 ± 71	191 ± 2	338 ± 304	135 ± 2	89 ± 0.8
60CC	27 ± 5	88 ± 30	100 ± 2	288 ± 43	154 ± 2	282 ± 100	93 ± 2	63 ± 0.8
70CC	11 ± 5	58 ± 23	66 ± 2	126 ± 87	103 ± 2	166 ± 70	71 ± 1.8	39 ± 0.7
76CC	1 ± 5	41 ± 19	54 ± 2	67 ± 9	74 ± 2	111 ± 56	50 ± 1.6	28 ± 0.8

5.4.(b)3 Ratio of SE Yield to Total Yield

Like 5.3(c)4, the ratio of the BSE yield to the Total yield [Fig. 5-68], the ratio of the SE yield to the Total Yield is provided [Fig. 5-44] against E_b for several emission angles. The first fact to notice is that all ratio values lie between 0.5 and 1. The second fact to notice is that this ratio value seems to be smallest somewhere near E_b = 2000 eV. This is logical because the BSE yield to Total yield ratio shows E_b = 2000 eV to have the greatest ratio value. This is with a slight exception of the same two emission angles (14^o CC and 60^o CC) in both ratios.

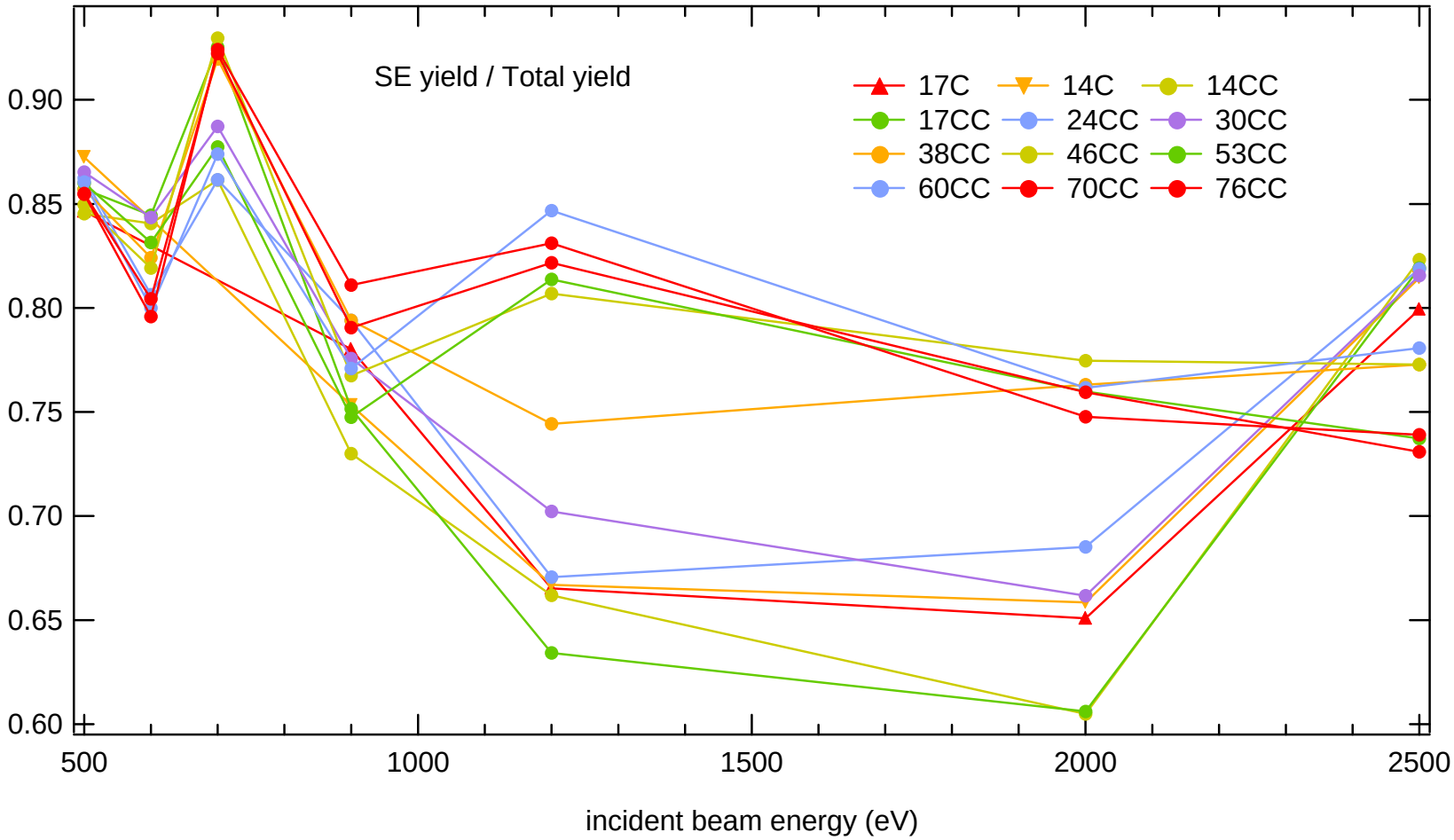

Figure 5-44 The ratio of the SE yield, calculated using E_{min}, to the total yield. The 10 eV resolution is used exclusively.

5.4.(b)4 Finer Resolution SE Yields

The SE Yield calculated using the 1 eV resolution is now compared with the SE Yield calculated using the 0.1 eV resolution. These data are not very comparable because the 0.1 eV resolution spectra is measured to the maximum energy boundary of 20 eV. Neither the 1 eV resolution nor the 0.1 eV resolution are measured to the E_{min} demarcation (except for E_b = 100 eV, but is not very dependable anyway due to the electron gun filament degradation). Therefore, no further SE Yields are calculated. The SE yield measured using the 1 eV resolution to the historic demarcation of 50 eV [Fig. 5-42] compares qualitatively well with the SE yield calculated using the 10 eV resolution with the conventional 50 eV [Fig. 5-37] and with the newly developed E_{min} eV [Fig. 5-39] upper integration boundaries. All SE yields are fit relatively well with the Lambert cosine law except for the E_b = 1200 eV.

Of considerable importance is that the SE Yield emission, calculated using the 0.1 eV resolution from 0 eV to 20 eV [Fig. 5-43], is almost near isotropic (cosine like), but there are small deviations from the cosine law such as E_b = 900 eV and E_b = 2500 eV.

At the 1 eV resolution, the boundaries of integration are the SE_{max} position and 50 eV and maybe shouldn't be here because it wrecks the E_{min} idea. These boundaries should possibly be disregarded because it compromises the E_{min} theory.

The Lambert cosine law gives $\delta(0)$ values of (8 values for 1 eV) and (3 values for 0.1 eV).

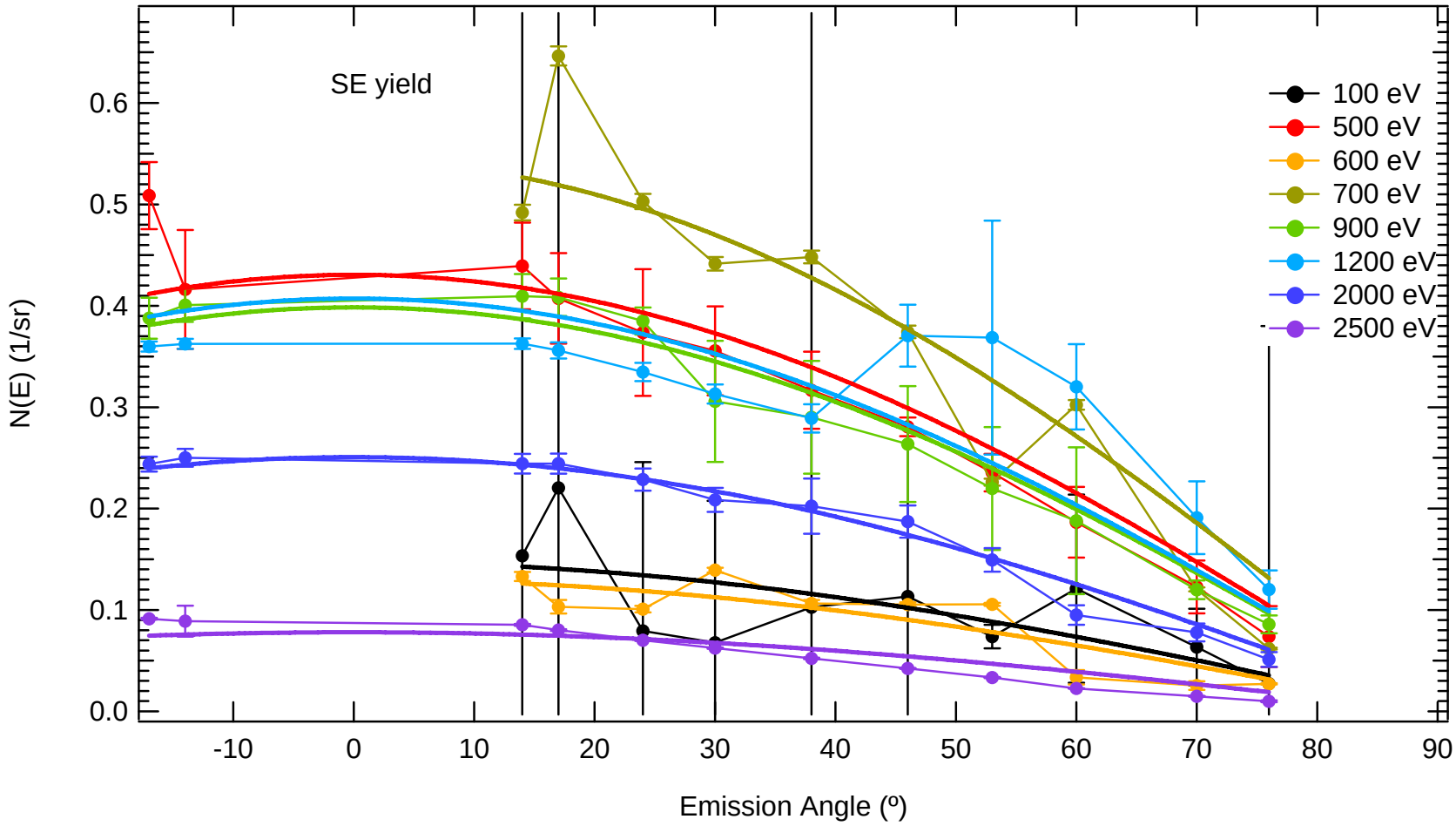

Figure 5-45 SE AR distributions for selected incident beam energies in the 0 - 50 eV range using the 1 eV resolution.

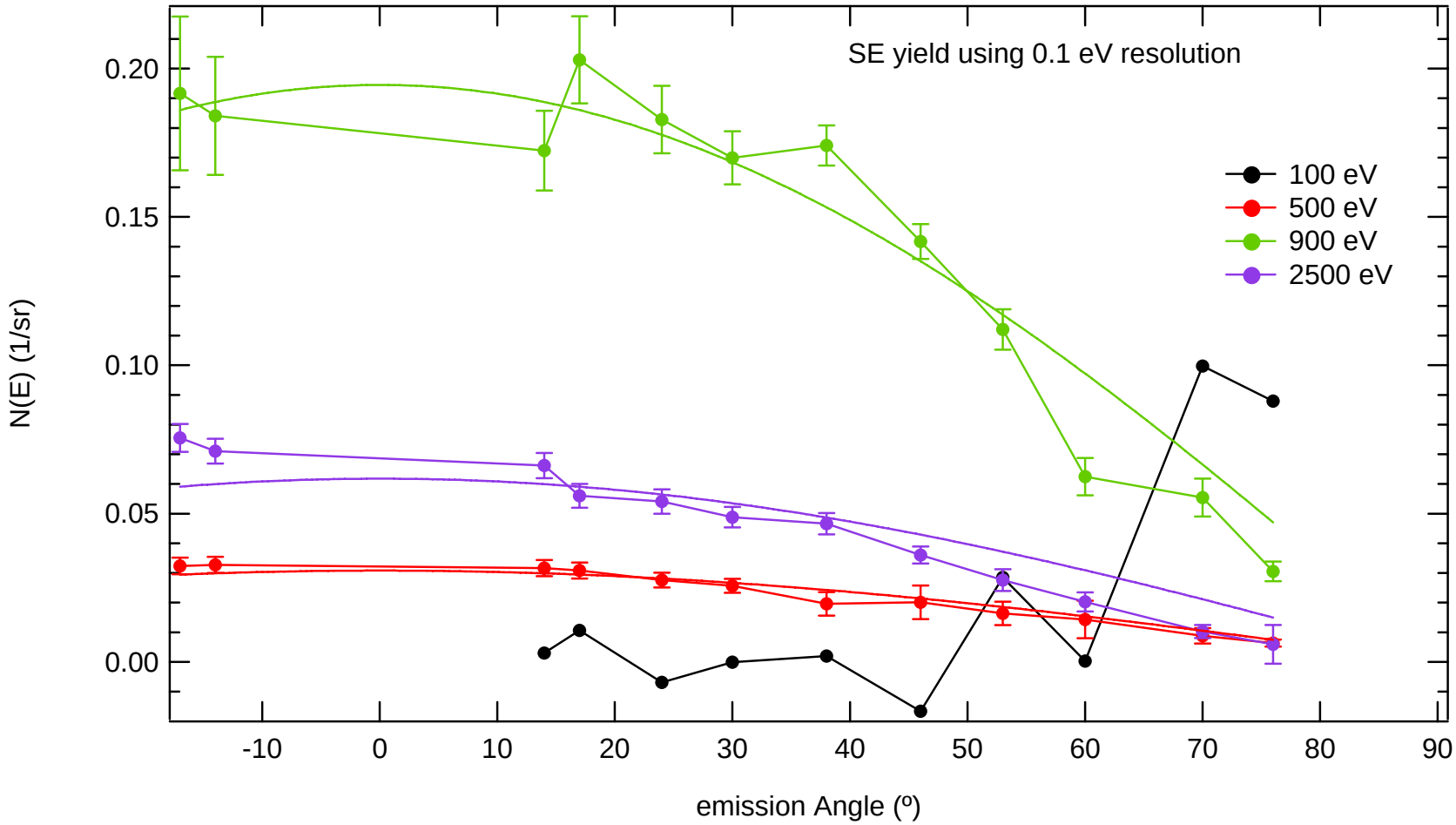

Figure 5-46 SE yield calculated using the fine 0.1 eV resolution. The boundaries of integration are the SEmaxPosition and 20 eV.

5.4.(b)5 Angle Integrated Comparisons

The SE yield angular cross sections presented for several incident beam energies have been resolved at coarse and fine angle emission (E_b = 900 eV). The coarse angular resolutions for all energiy resolutions are also compared to each other as well as to other yield data taken with the Fatman chamber on identical sample material. Just as in section 5.3.(c)5, the numerical integration of these SE angular cross sections provides the SE yield for all angles from 0^o to 90^o emission. The integration of the Lambert cosine law, used to model $\delta_c(\alpha)$ and $\delta_f(\alpha)$, is calculated for each E_b. The results are compared to SE yields calculated using the customary boundary of 50 eV and E_{min} E_b eV data. The emission angle is integrated by isotropically fitting the SE Yield vs. angle plots.

[Fig. 5-45]

General trends are consistent for four LittleBoy sets and agree pretty well with Fatman results. Comparison of the angle integrated SE yield measured using the hemispherical retarding field analyzer (Fatman chamber) technique [Fig. 1-3 and Fig. 4-8] to the angle integrated is provided for several energy resolutions. The SE yields measured using the 10 eV resolutions are calculated with the upper integration boundaries of 50 eV [Fig. 5-44, larger circles] (5.4(b)1) and E_{min} eV (x's) (5.4(b)2). Using the 1 eV resolution, only the 50 eV upper boundary [Fig. 5-44, triangles] has been measured (5.4(b)4), which compares better with 50 eV using 10 eV resolution at lower E_b and compares better with E_{min} eV using 10 eV resolution at higher E_b. The SE yield using the 0.1 eV resolution was only measured to 20 eV (5.4(b)4) for E_b = 500 eV, 900 eV, and 2500 eV [Fig. 5-44, open circles] and measures the smallest yield, but is provided for completeness.

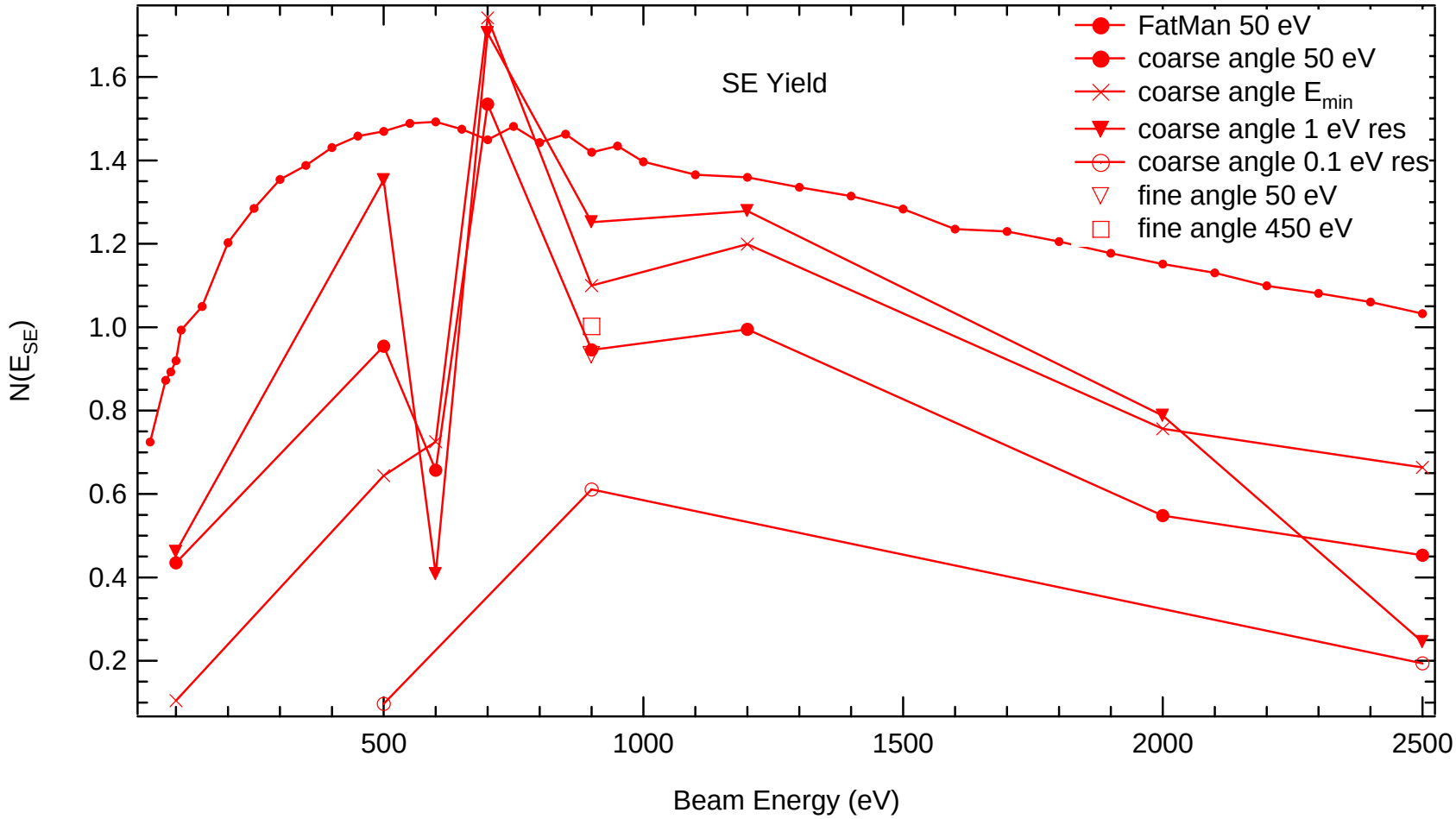

Figure 5-47 SE Yield comparisons integrated over angle (isotropically) and calculated with boundaries of 0eV – E_{min} eV and 0eV – 50 eV. . The integrated fine angle yields for E_b = 900 eV using 50 eV and 450 eV are also included. SE yields (Fatman chamber) measured using 0eV – 50 eV are shown for comparison [*Clerc et. al., 2005*].

5.4.(c) Angle Resolved SE Yield Distributions

Like section 5.7,

The SE yield, $\delta_C(\alpha; E_b)$, has been measured using a fine angular resolution at $E_b = 900$ eV. Again these finer angle resolution distributions (cross sections) primarily diagnosed the RD angle automation capabilities where the RD was biased to only two other non-grounded voltages (50 eV and 450 eV). After subtracting each of these distributions from the RDbias = 0 eV [Fig. 5-61], the AR $E_b = 900$ eV SE yield [Fig. 5-45] can be compared to the theoretical isotropic emission.

The important thing to notice here is that trends are provided by the theoretical results of Rosler and Brauer on the graph. Though they are simulated for aluminum, they provide some sort of qualitative trend for other metals. From their work, the core electron excitations are provided for 50 eV and 200 eV emissions, electron-plasmon energy exchange at 20 eV and 26 eV energy emissions, and dynamic screened electron production for 20 eV and 200 eV energy emission are given for comparison.

The E_b resolved angular distribution, cross section, for the SE yield is shown using fine angle resolution.

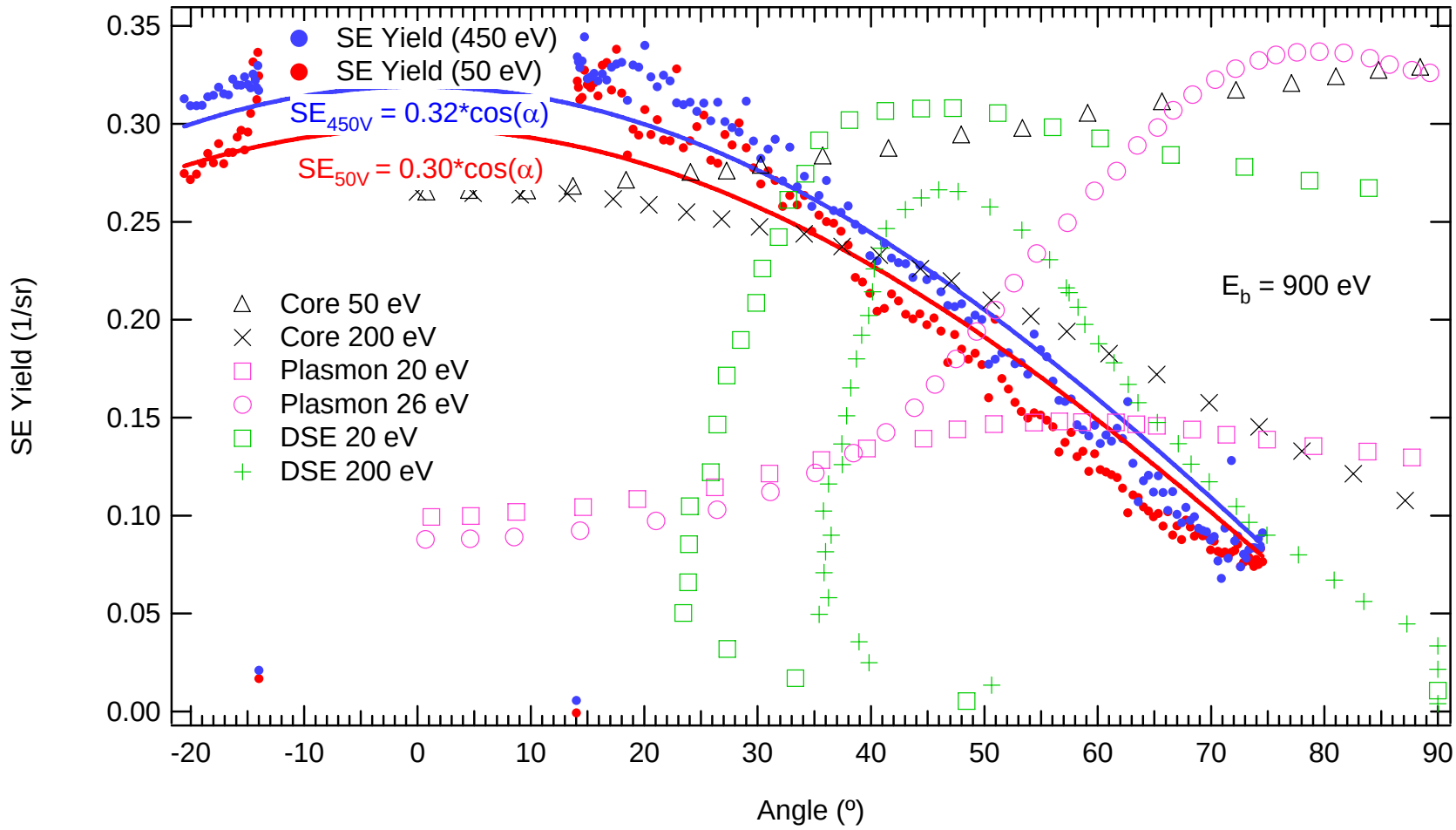

Figure 5-48 The SE yield cross section resolved at fine emission angle.

5.4.(d) Auger Peaks

The evidence of a specific kind of secondary electron emission activity, called Auger electron emission, is under investigation. The characteristic features of an auger peak, defined in Table 3.3, is energy, E_{AES}, and intensity, $dN(\alpha,E_{AES};E_b)/dE_e$. This is curious and deserves a closer look at the E_b = 2500 eV @ 14°CC coarse resolution spectra [Fig. 5-49, purple]. There is no reason to believe that any angular dependence on the energy location of the local minimum, E_{min}, exists. The argument for weak angle dependence of E_{min} is that the SE part falls of near cosine-like, while the elastic is Mott-like (not sure what quasi-elastic (plasmon) angle dependence is). Since they have different angle dependence, one can get an effect where the E_{min} is slightly angle dependent.

In order to emphasize the possibility of negative yields, $dN(\alpha, E_{min}; E_b = 2500 \text{ eV})/dE_e < 0$, [Fig. 5-53 and Fig. 5-54] and concurrently addressing the very wide ranges of E_{min} positions, the E_b— AR distributions are shown [Fig. 5-46] for E_b = 2500 eV (10 eV resolution) where clearly angular dependence on E_{min} is evident.

E_{min} is plotted against angle to show that there is a small dependence with angle not as easily seen in Figure 5-51. The dependence on angle is probably due to the Auger peaks, which are very dependent on emission angle. The spectrum at E_b = 2000 eV and 2500 eV are seemingly the only incident energies with an angular dependence.

This is shown for E_b = 2000 eV and 2500 eV by providing the second derivative, $d^2N(\alpha, E_{min}; E_b)/dE_e^2$ of the E_b— AR distributions for E_b = 2500 eV [Fig. 5-47] and E_b = 2000 eV [Fig. 5-48] with respect to emission energy. The signature Au peaks located at 1720 eV, 2020 eV, and 2110 eV compare very well with those measured in the literature (JR's red Auger book). The peaks of ~2300 eV and ~2450 eV are direct result of the quasi-elastic BSE peak.

The presentation of E_{min}/ E_b vs E_b [Fig. 5-51] is now a means of determining the amount of overlap that the SE and BSE tails begin to overlap each-other. Another way to have angle dependence of E_{min} for higher E_b would be as follows. AER peaks are at fixed E measured from E = 0 (not E_b). At higher

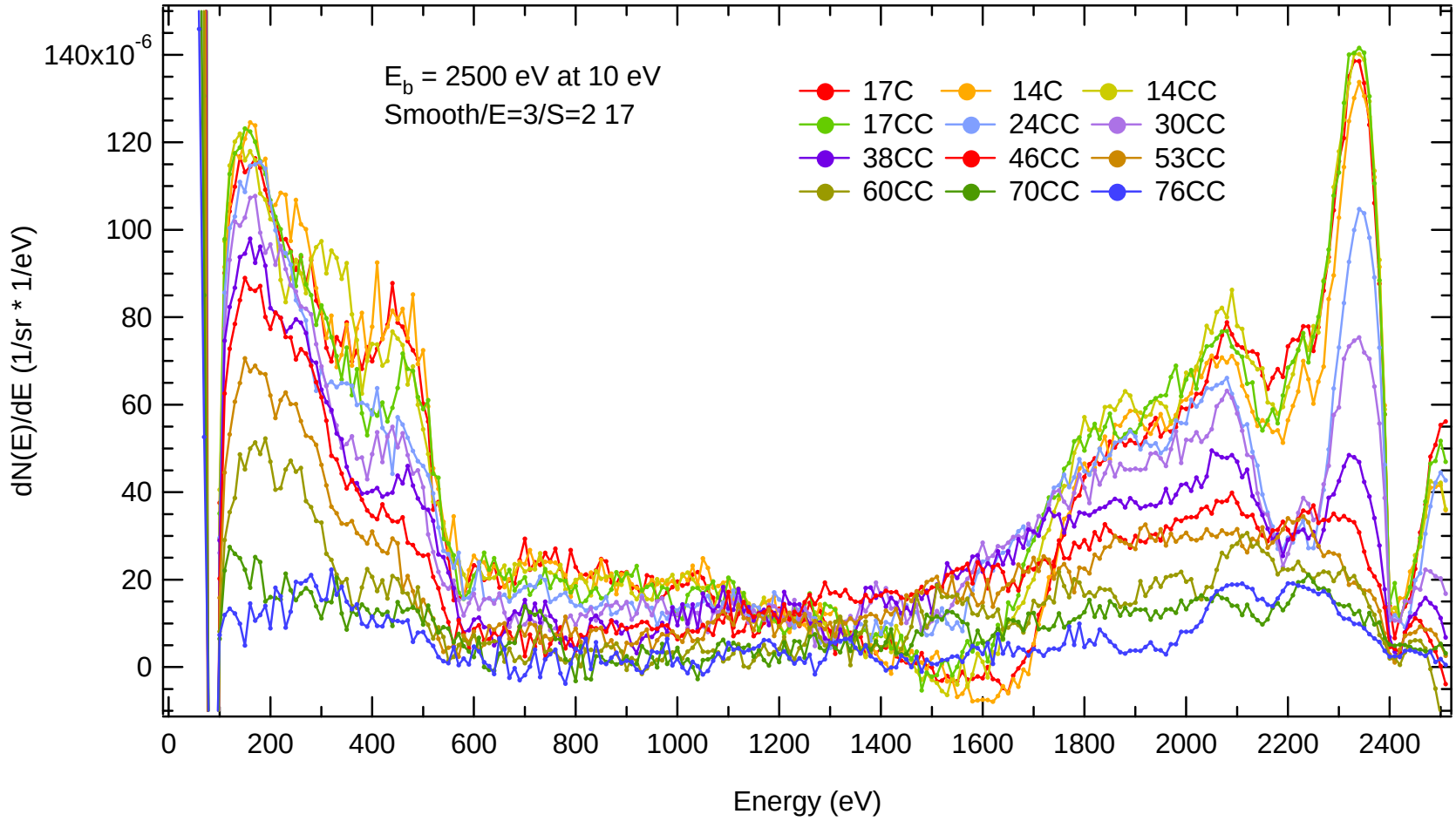

Figure 5-49 AR spectra for E_b = 2500 eV and for emission angles of 17 degrees Clockwise to 76 degrees Counter—Clockwise.

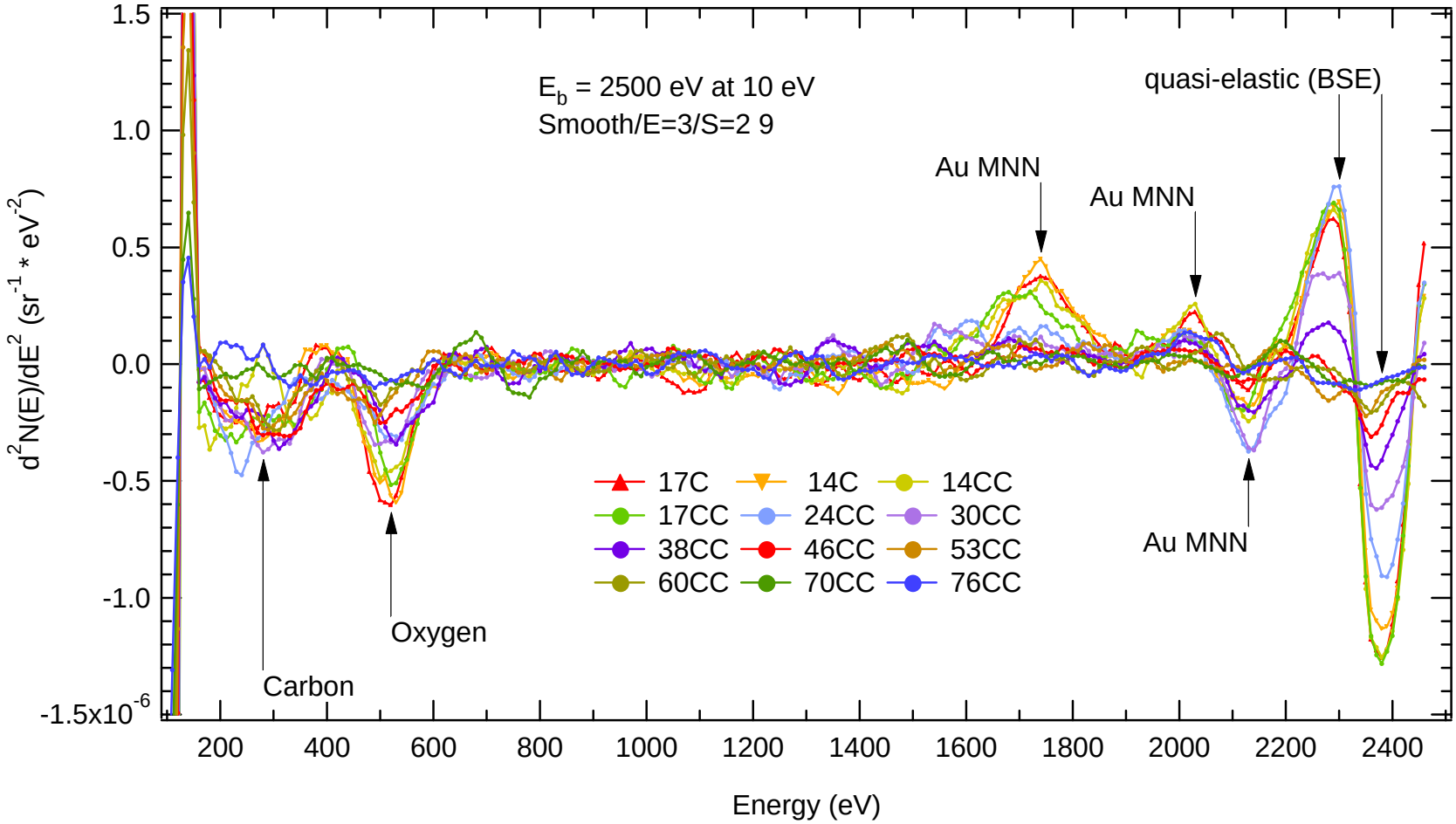

Figure 5-50 Auger spectra for E_b = 2500 eV given at emission angles of 17° Clockwise to 76° Counter—Clockwise.

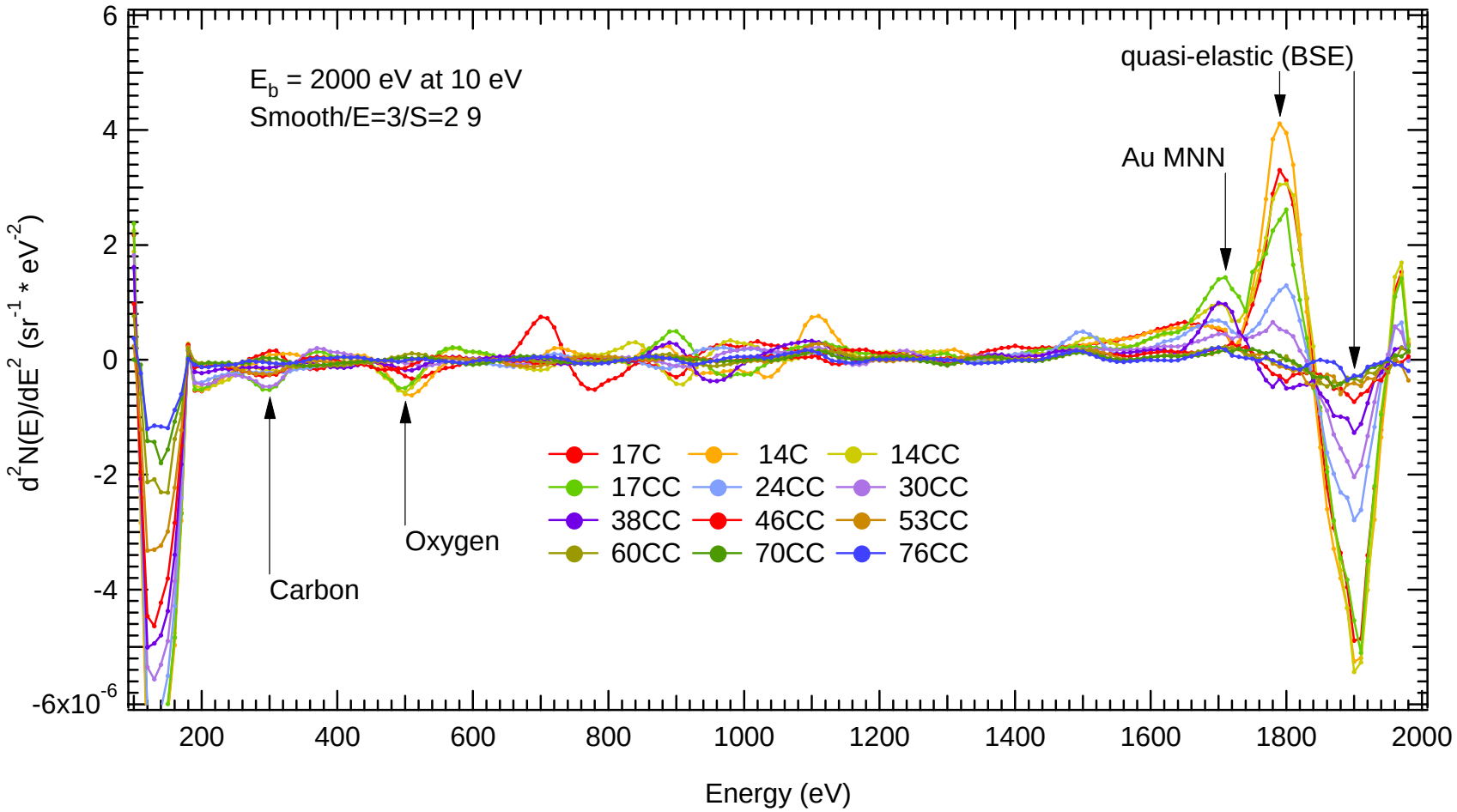

Figure 5-51 Auger spectra for E_b = 2000 eV given at emission angles of 17° Clockwise to 76° Counter—Clockwise.

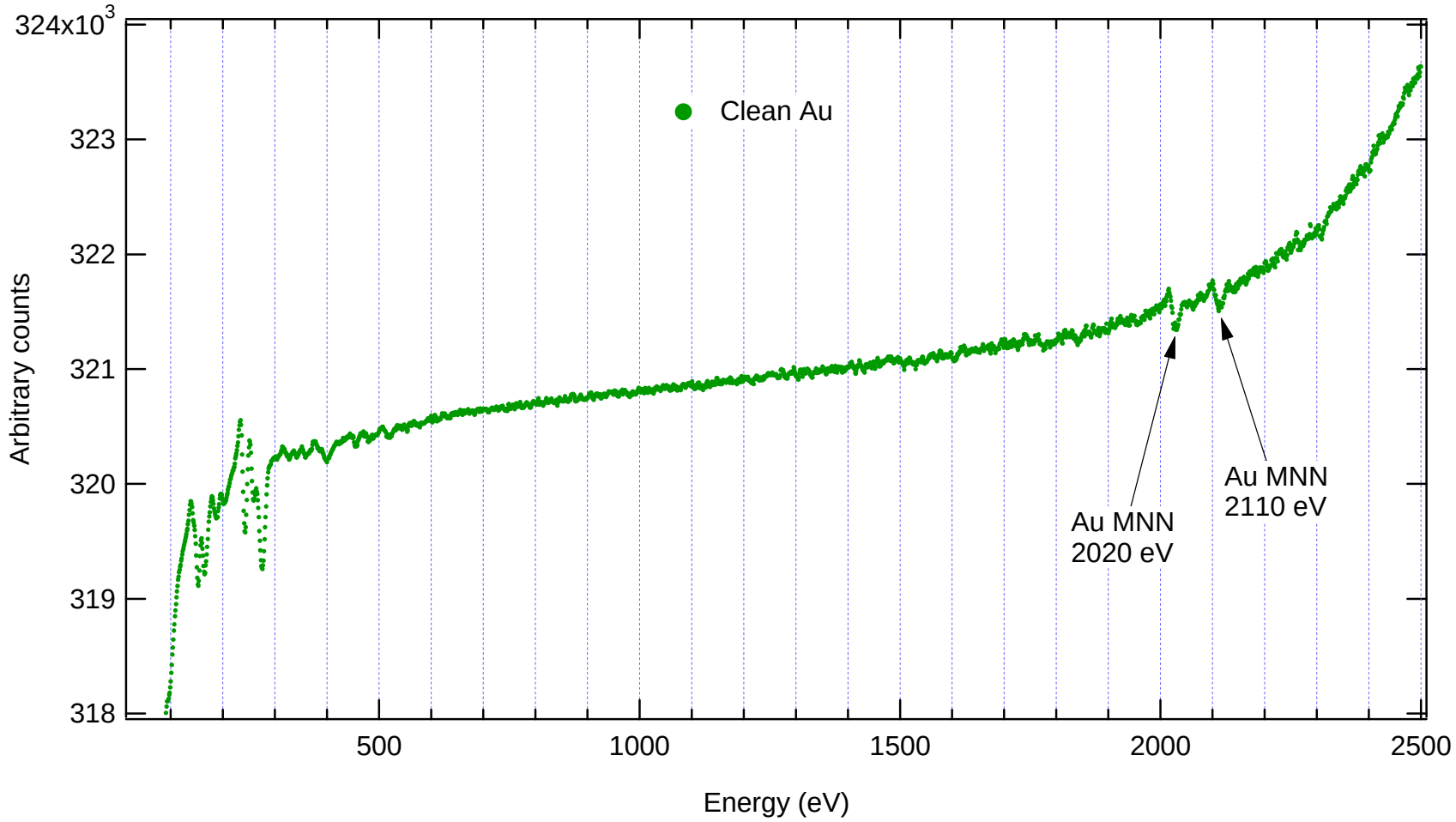

Figure 5-52 Auger spectra for E_b = 2000 eV using the cylindrical mirror analyzer [Fatman chamber].

E_b, the AES peaks may be found near E_{min} (E_b) while at lower E_b, the AES are not near E_{min}. Thus, there is a (false) dependence of E_{min} on E_b (and also angle since AES peaks have different and dependence than SE, elastic, or quasi-elastic.

Any trend may lead to important energy exchange mechanism such as Auger electron interactions. This is easiest to determine by observation of the error bar (standard deviation). The largest error bars occur at large E_b's (2500 eV and 2000 eV), and the smallest E_b, 100 eV. The average of the ratio is tabulated on the right along with the standard deviation (Table 5.18). A linear fit shows an almost zero slope at 40% [Fig. 5-52] concluding that E_{min} does not change significantly for the incident beam energies measured.

Therefore, the highest and lowest energy we have fewer multiple scatters that "wash out" the pronounced angular dependence of the individual production mechanisms. Interpretation of these extra features as evidence for production mechanism information content in energy— angular— electron emission spectra.

The second derivative shows several broad peaks. For the E_b = 2500 eV [Fig. 5-50], two predominant peaks at 1740 eV and 2020 eV present themselves as Auger signatures. The possible Auger peak located at 2110 eV is negative and may indicate that a reverse Auger process is occurring. The probability of a reverse process is much more likely to occur at higher energies because the doubly ionized atom becoming singly ionized would most easily happen outside the shielded core, closeset to the valence band. This is not well understood. Since these peaks are not dependent on E_b, they must be evident in other spectra at the same energies. For the E_b = 2000 eV [Fig. 5-51], the 1740 eV peak exists but is much larger in intensity.

Comparing intensities of these peaks as functions of emission angle [Fig. 5-52] shows that the 1740 eV Auger peak from the E_b = 2000 eV is larger than that of the E_b = 2500 eV. This may be due to a larger BSE background which is #% larger than the E_b = 2500 eV. Notice also that the 2020 eV Auger peak has the least intensities.

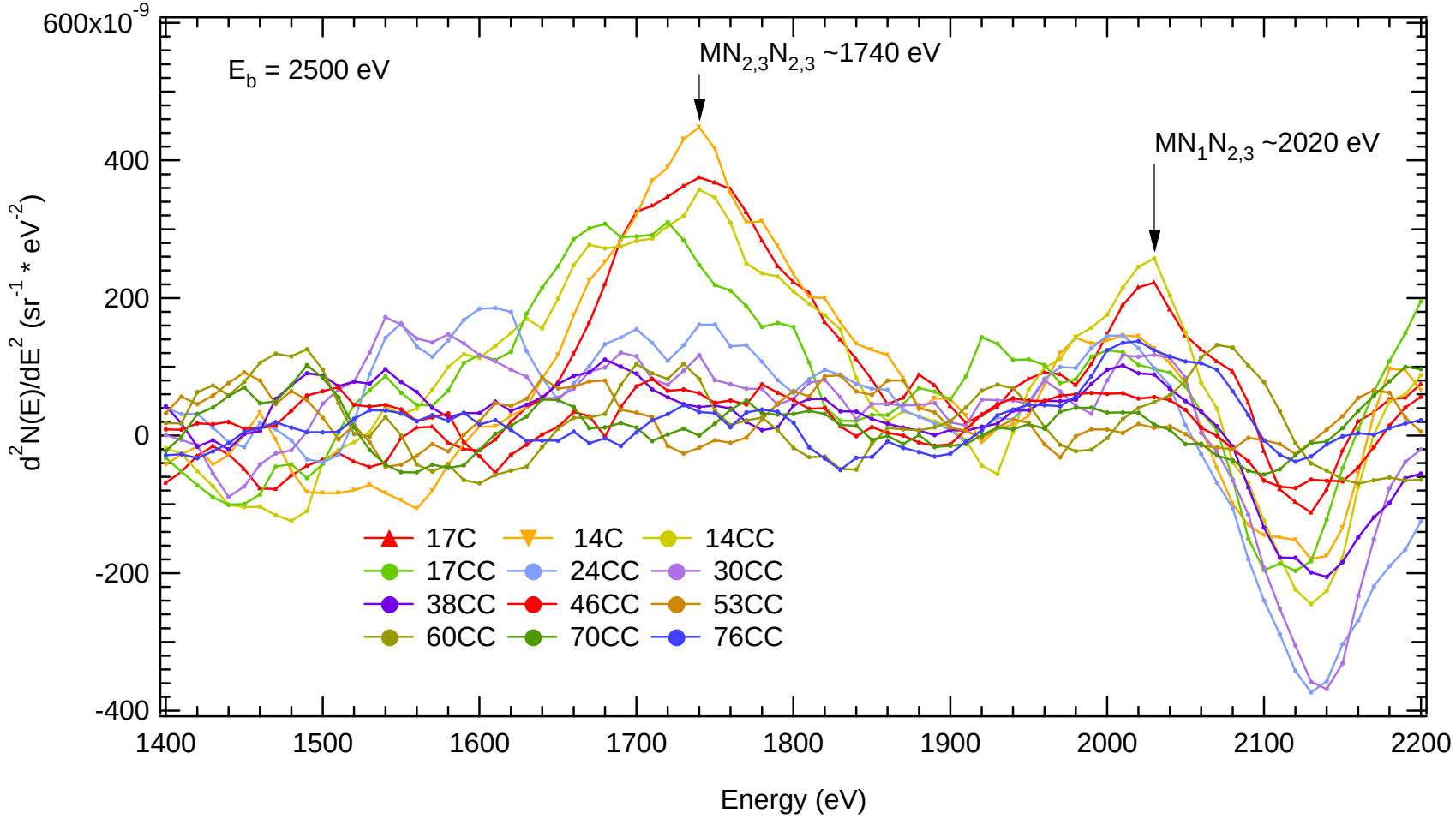

Figure 5-53 Auger (derivative) spectra for E_b = 2000 eV given at emission angles of 17° Clockwise to 76° Counter—Clockwise.

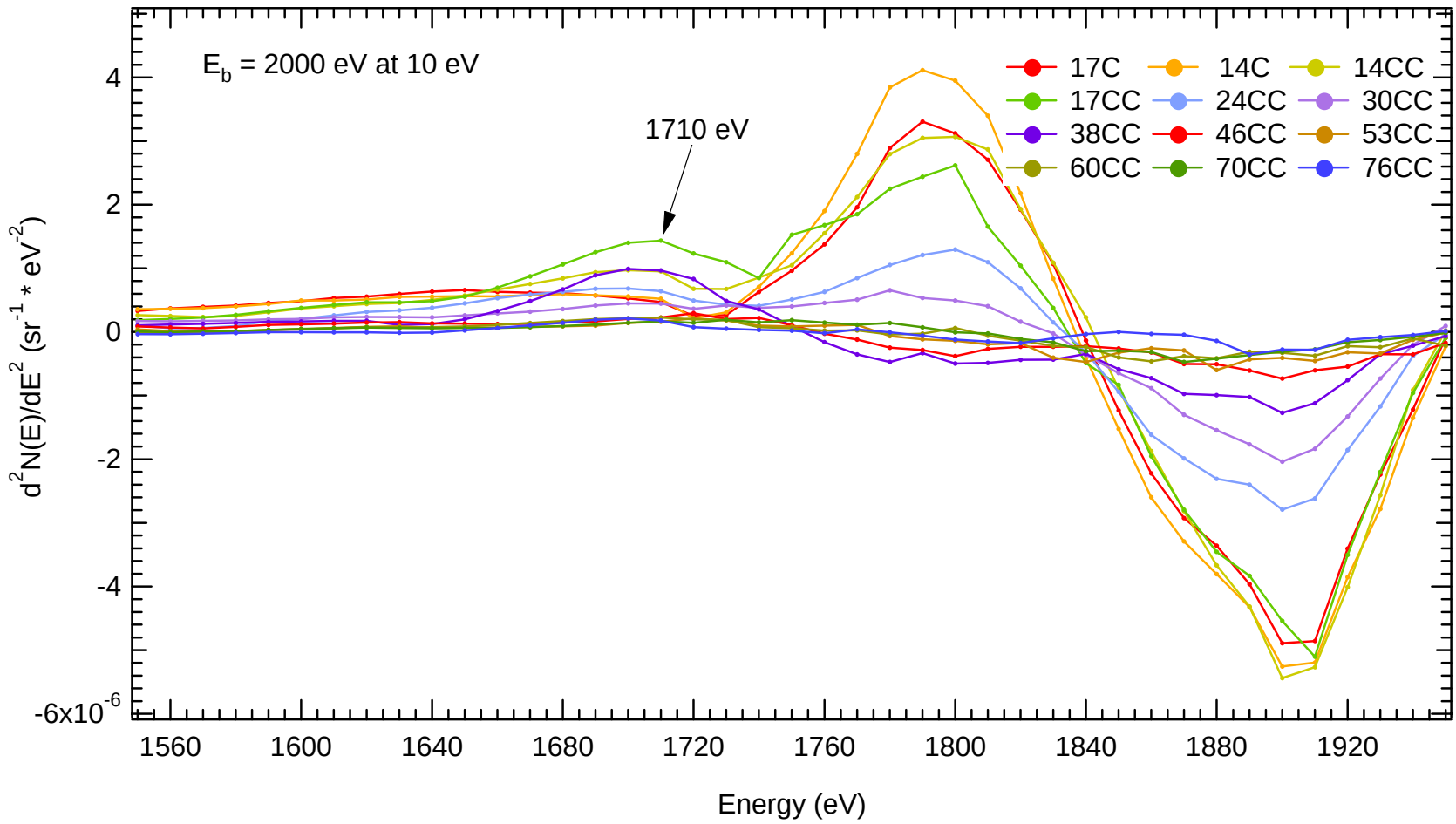

Figure 5-54 Auger (derivative) spectra for E_b = 2000 eV given at emission angles of 17° Clockwise to 76° Counter—Clockwise.

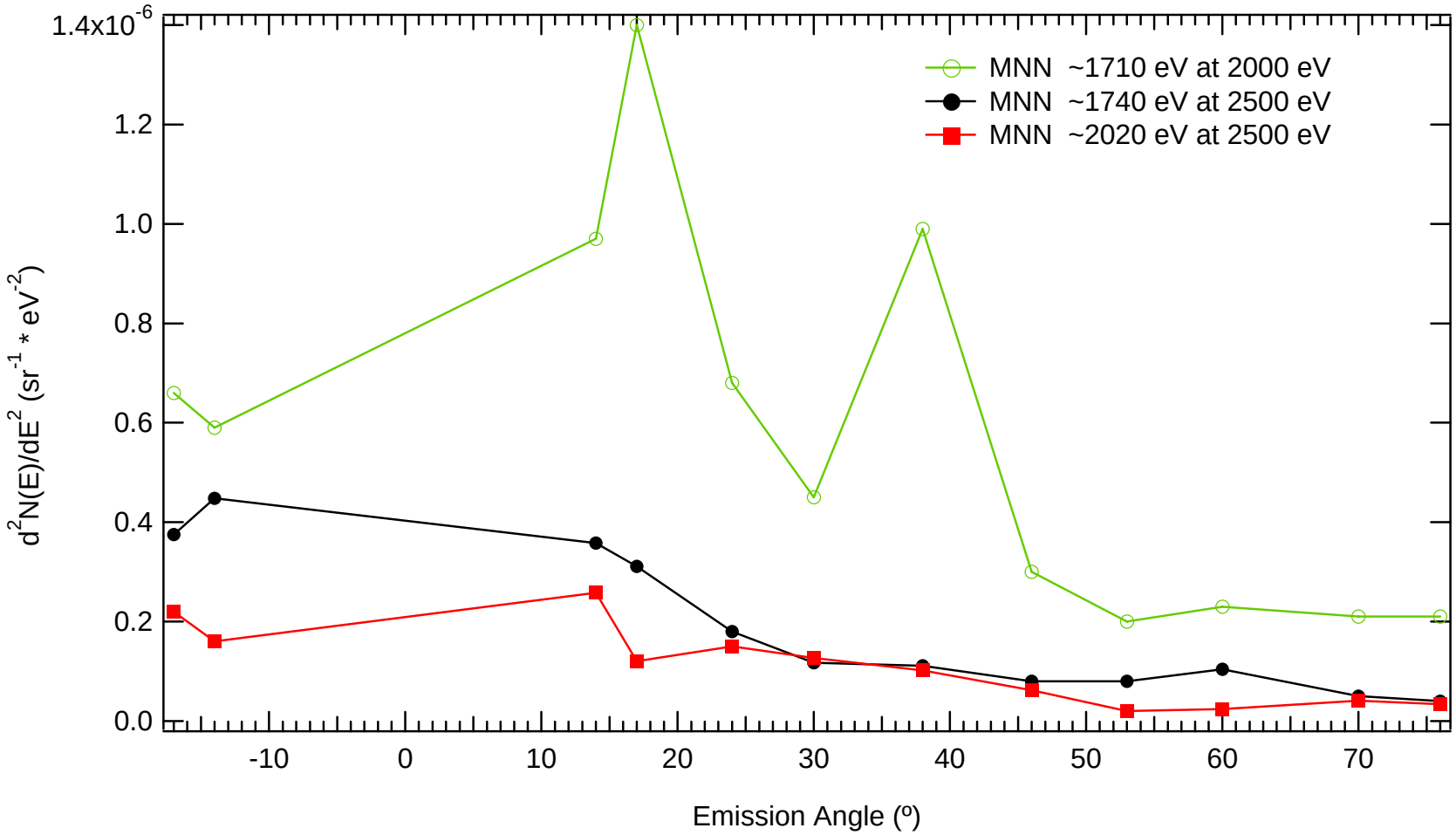

Figure 5-55 Intensities of the Auger peaks at 1740 eV (closed circle) and 2020 eV (closed square) for E_b = 2000 eV and peaks at 1710 eV for E_b = 2500 eV (open circles) as a function of emission angle.

5.5 Transitions

A transition from one peak to another in a spectrum possesses an intensity minimum. The energy location of the minimum is where two tails of each peak intersect one another as they fall off in opposite directions. An example of this is clearly shown in Fig. 1-2 and Fig. 5-1 where the tails of the SE and BSE fit cross one another near the minimum, E_{min}. The transition can be compared to other transitions within a spectrum and can ultimately be used to fit both peaks. The location of the transition energy is found by using a simple search routine programmed to compare successive intensities and store the energy position where the intensity is minimized.

There are three transitions studied, one for each energy resolution. The BSE-SE transition using the 10 eV, the elastic-BSE transition using the 1 eV resolution, and the elastic-plasmon transition using the 0.1 eV resolution are studied in terms of energy location and intensity.

5.5.(a) BSE and SE Peak Delineation (E_{min} Features)

The dividing boundary separating the BSE and SE peaks, the delineation, is now under investigation. Since it is possible for a secondary electron to have a very high emission energy (greater than say 50 eV) even though the creation of such an SE originated from very near the surface, a more detailed view of the maximum energy an SE can have is in question. The total AR—E_b normalized spectra presented in [Fig. E-18 through Fig. E-29] are given [Fig. 5-49] for each of the coarsely resolved RD angle positions. The term total emphasizes that the x-axis range includes the entire possible emission energies given as a ratio to each spectrum's beam energy, E_b. The total E_b resolved spectra presented for E_b = 900 eV are chosen from a selection of various other measured E_b [Fig. E-10 through Fig. E-17]. This cross section of spectra with its angularly resolved counterparts [Fig. 5-1] has been smoothed with the SG algorithm by 25 data points [Fig. 5-50].

All spectra are shown at a resolution of 10 eV with the exception of the E_b = 100 eV data, which is given at a resolution of 1 eV. Viewing the AR spectra in this way provides a comparison of the yield minimum located between the high energy BSE peak and the low energy SE peak.

The selected incident beam energies are 100 eV, 500 eV, 600 eV, 700 eV, 900 eV, 1200 eV, 2000 eV, and 2500 eV and the yields are given in units of $eV^{-1} * sr^{-1}$ on the y-axis and in units of eV on the x-axis. Using these spectra, the minimum yield, E_{min}, features are investigated in terms of their location between the BSE and SE peaks.

This shared yield minimum is used to fit each peak with its own corresponding functional trend. Theoretically, in the process of fitting a peak feature, the tail of the peak is also fitted. Therefore, the SE peak's tail, which extends through to the BSE peak, can be modeled separately using the local minimum yield intensity and the BSE's tail fit in the same manner. Therefore, the dependence of the position of E_{min} and its associated yield intensity, $N(E_{min})$, are investigated in terms of variables E_b and emission angle.

The total E_b normalized spectra, [Fig. 5-49], show that some intensity values, $dN(\alpha = 14^o$ CC, E_{min} ; E_b = 100 eV, E_b = 2500 eV)/dE_e, measure negative yield emission. Due to the electron gun's physical design, the E_b =100 eV data occurred using the highest electron beam currents leading to less dependable results as expected. However, there may be significant information from E_b = 100 eV data if there is a high beam current to surface plasmon correlation which may provide possible diffraction effects [Fig. 4-7] discussed in 4.3(d)1. Discuss this a bit further.

However, this is not always the case. For example, computer located values showed high StDev/Ave percentage at E_b = 900 eV, but on close examination of Fig. 5-1 (E_b = 900 eV @ 14^{o}CC), the E_{min} position is more likely at 250 eV rather than the computer found 420 eV. This changes the StDev/Ave percentage from 21% to 24%. So, even-though the percentage became greater, there is still no evidence of a trend dependence on emission angle.

Since the StDev is upwards of 30% of the average, a verification by eye is briefly accomplished. For example, Fig 5-1 shows the EAR spectra for E_b = 900 eV @ 14°CC where E_{min} is technically searched by computer to be 420 eV, but is actually more like 250 eV (Table 5.16, red).

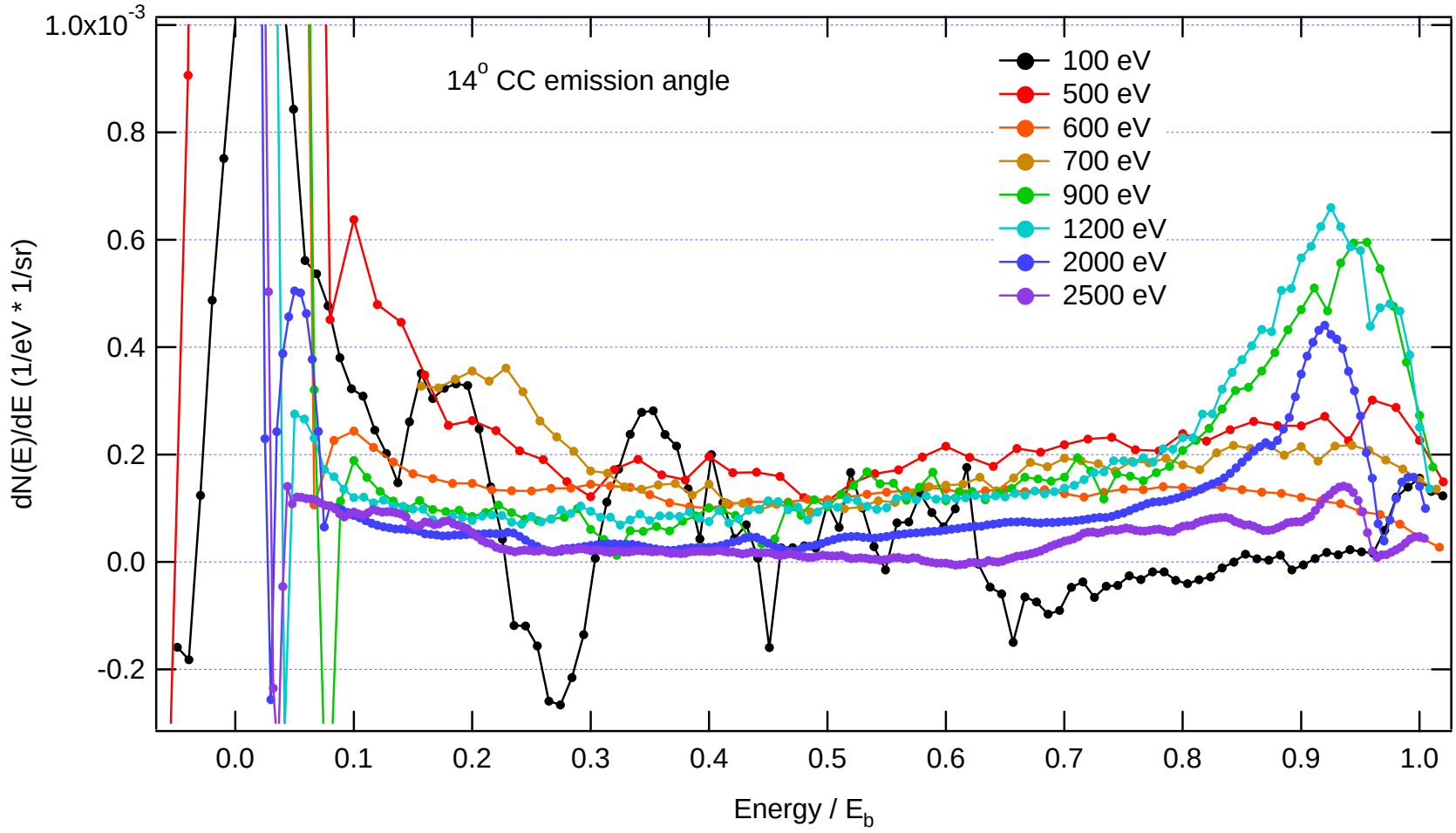

Figure 5-56 Normalized AR energy spectra at 14° Counter-Clockwise angle of emission for selected beam energies. The minimum energy separating the low and high energy peaks is roughly constant at ~45% of E_b.

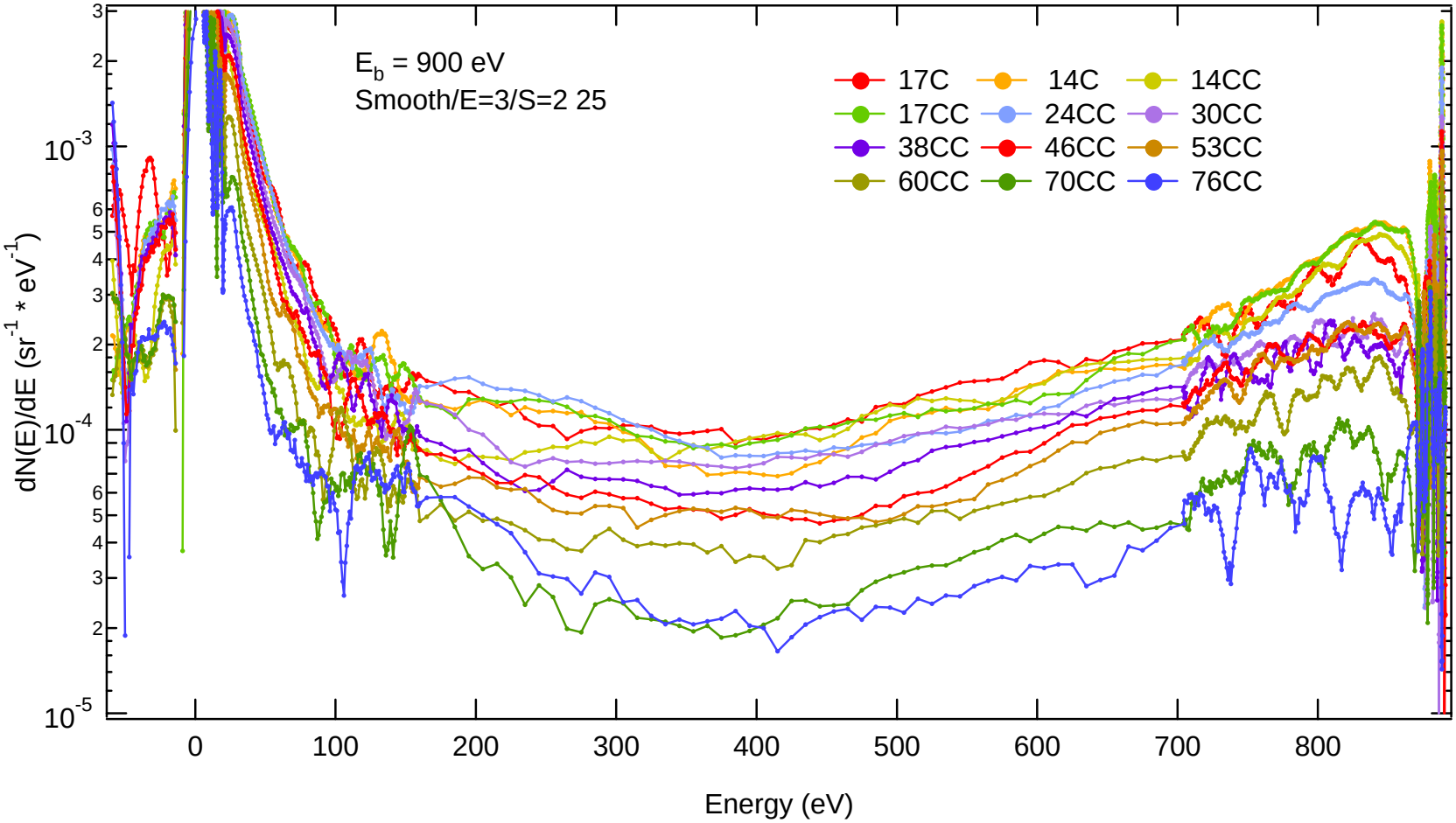

Figure 5-57 Normalized E_bR energy spectra for 900 eV and several selected emission angles. The minimum separating high and low energy peaks is constant at ~35%. No angle dependence is evident.

5.5.(a)1 E_{min} Energy Position

The total AR—E_b normalized spectra for angle emission of 14° Counter—Clockwise [Fig. 5-49] shows that each spectrum contains a local minimum, E_{min}, separating the SE peak and the BSE peak. A first good guess for E_{min} (or E / E_b) is 45% of E_b because the tails are expected to fall off at the same rate. In this case, there is reason to believe that angular dependence on the energy location of the local minimum, E_{min}, exists, however examination of the E_b = 900 eV, AR spectra [Fig. 5-50] shows that E_{min} occurs at about 35% to 40% of E_b.

Unlike Fig. 5-49 (shown linearly), the logarithmic plot of Fig. 5-50 clearly shows that the energy position of E_{min} separating the SE and BSE peaks exists and demands investigation. There is debate over whether useful information can be gathered by the assumption that an E_{min} will always exist for all possible E_b. For the E_b's measured in this study, dependencies on the E_b and emission angle variables are now discussed. There are trends in the energy position of E_{min}. In order to examine broad functional trends in the spectral data it is important to first locate the boundaries of the trends. There are three boundaries in each spectra, 0, E_{min}, and E_b. 0 and E_b are defined and E_{min} must be located between 0 and E_b. Each spectrum contains a local minimum, E_{min}, separating the SE peak and BSE peak.

The energy position of the local minima, E_{min}, between the SE and BSE peaks is tabulated in Table 5.18 and the average and standard deviation over emission angles are also listed. The percentages of the average and standard deviation to the beam energy are provided as well as the percentage of the StDev to the average. These locations are relatively constant up to 2000 eV. Using computer generated values, one can analyze the data and see if there is a trend or noise. One has a trend if, on average, each successive value changes in the same direction or in a similar fashion as the last value. One notices noise if, on average, each successive value changes in the opposite directions (i.e. E_b = 600 eV) as the last value. The ratio E_{min}/E_b of the location is plotted [Fig. 5-51] as a percentage for several E_b against the emission angle for use in determining any possible trends. The average of the ratio is tabulated on the right Table 5.18

along with the standard deviation. Examining the percentage of the StDev to the average suggests a speculation to any trend. The higher the percentage, the more likely there is to be a trend.

5.5.(a)1a E_{min} Dependence on E_b

The average percent of E_{min} / E_b is plotted as a function of E_b [Fig. 5-52]. Four trend lines are fit to the data at four orders of E_b dependence. Provided as a percentage of E_b, this accounts to E_b^{-1}, E_b^{o}, E_b^{1}, and E_b^{2} for customary, constant, linear, and parabolic type dependencies, respectively. The best fit line falls below 50 %, is better than the historical arbitrary 50 eV, but is worse than the parabolic fit [Fig. 5-52]. There is only observable dependence of the local minimum position on emission angle in the E_b = 2500 eV spectra [Fig. 5-51, purple line]. The critical thing to notice about the standard deviation of E_{min}/ E_b at E_b = 1200 eV is that it is the smallest at 7% and at E_b = 2500 eV the value is the largest at 15%.

Table 5.18 Local Minimum Energy Location (eV) Between the SE and BSE Peaks. All energy locations have an error of 5 eV with the exception of E_b = 100 eV which has an error of 0.5 eV. The average, standard deviation, and percent of StDev/Ave % are also listed. Values in parentheses are percentages of the beam energy.

Beam Energy	Emission Angle (°)														
	17C	14C	14CC	17CC	24CC	30CC	38CC	46CC	53CC	60CC	70CC	76CC	Ave	StDev	StDev/ Ave %
100 eV	*	*	82	85	87	85	88	89	83	95	87	94	87.5 (88%)	4.3 (4%)	4.9
500 eV	260	320	260	200	170	140	220	190	290	200	170	230	221 (44%)	53.3 (11%)	24.2
600 eV	*	*	240	230	120	230	220	190	230	170	170	100	190 (32%)	49.4 (8%)	26.0
700 eV	*	*	340	360	220	380	250	240	320	340	350	360	316 (45%)	57.4 (8%)	18.2
900 eV	520	390	250	340	380	300	320	280	380	520	320	310	359 (40%)	85.9 (10%)	23.9
1200 eV	210	320	390	230	290	300	350	280	130	270	130	280	265 (22%)	79.1 (7%)	29.9
2000 eV	930	1070	540	530	910	340	1010	740	740	1020	830	960	802 (40%)	230 (12%)	28.6
2500 eV	1650	1590	1520	1490	1290	1300	920	750	890	930	830	780	1162 (46%)	344 (14%)	29.6

Note: The values in red are determined by eye from Fig. 5-1.

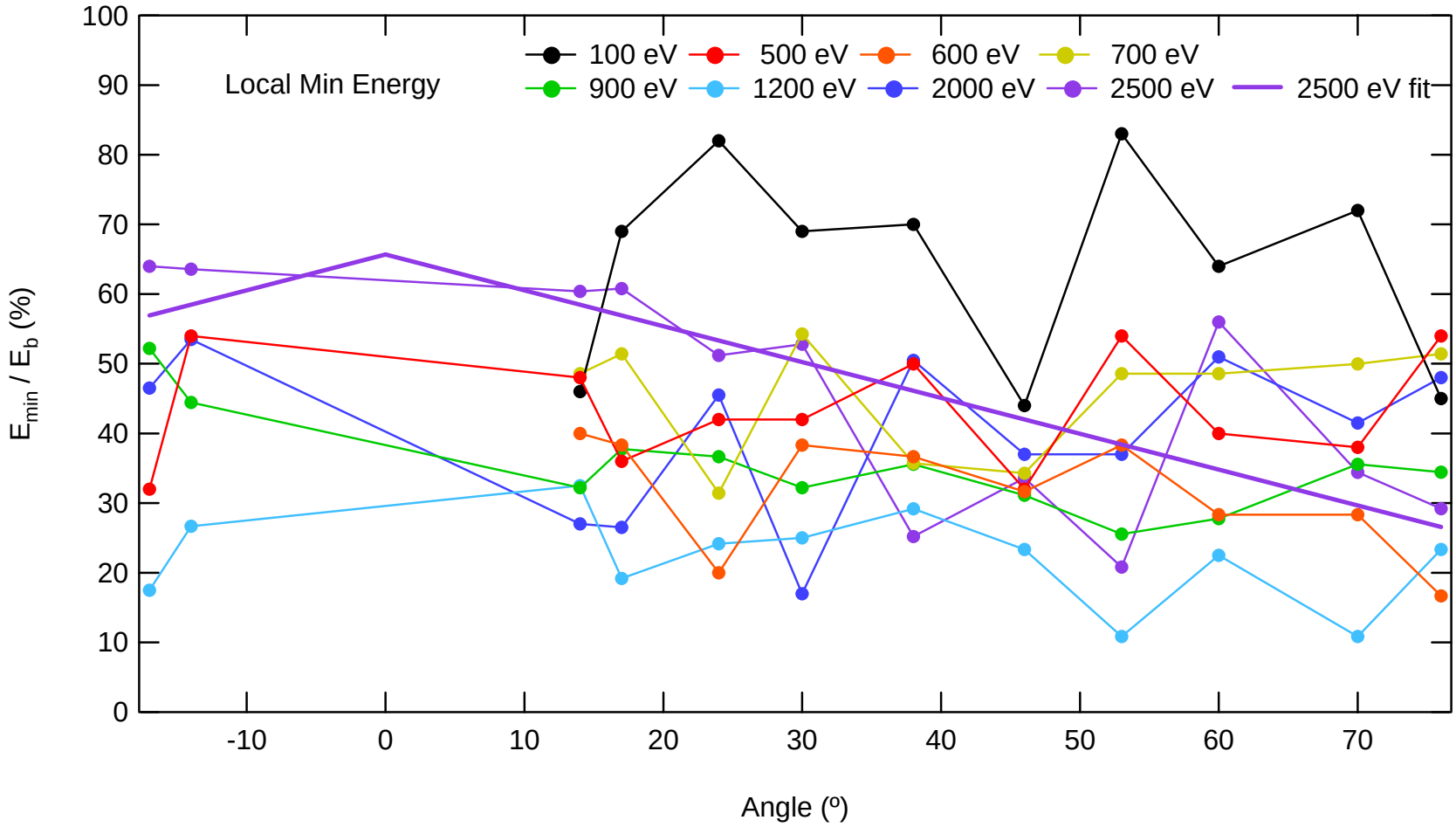

Figure 5-58 The local minimum energy position in terms of the percentage of E_b plotted against emission angle for several E_b. The line fit for E_b = 2500 eV has a slope of –0.515 and $E_{min}/E_b(a = 0)$ = 65.7 %.

Emphasis is placed on the very large 15% (probably due to Auger effects) and is addressed in 5.4(d). The average of the ratio is tabulated on the right along with the standard deviation Table 5.18.

Four fits to E_{min} / E_b % as a function of emission angle are shown. The zero parameter historical arbitrary 50 eV (light dash) has the worst χ^2. The single parameter constant % (dotted), shown as E_{min} / E_b % = a, has no dependence on E_b and has a χ^2 of blank. The two parameter linear fit (bold), written as E_{min} / E_b % = a + b * E_b, falls below 50 %, is better than the both the zero parameter and the constant 40%. The three parabolic fit (bold dash), written as E_{min} / E_b % = a + b * E_b + c * E_b^2 has the best fit. These coefficients are tabulated in Table 5.19. Line and parabolic fits both show better confidence than the historic constant 50 eV delineation. The parameters are listed in the table below. The linear fit shows an almost zero slope at 40%, which concludes that E_{min} does not change significantly for the incident beam energies measured. Constant %, linear and parabolic all fit data adequately. Improvements to linear or parabolic fit may not justify added compliration. This is addressed by calculating reduced χ^2 for 3 fits.

Table 5.19 Fit coefficients for E_{min}.

	zero (% E_b)	const (%) a	linear (% / E_b) b	squared (% / E_b^2) c	χ^2
	50 eV / E_b	NA	NA	NA	Blank
		40	NA	NA	Blank
		41.3 + 6	-0.005 + 0.006	NA	10.5
		68.5 + 12	-0.06 + 0.02	2.1e-5 + 0.8e-5	3.4

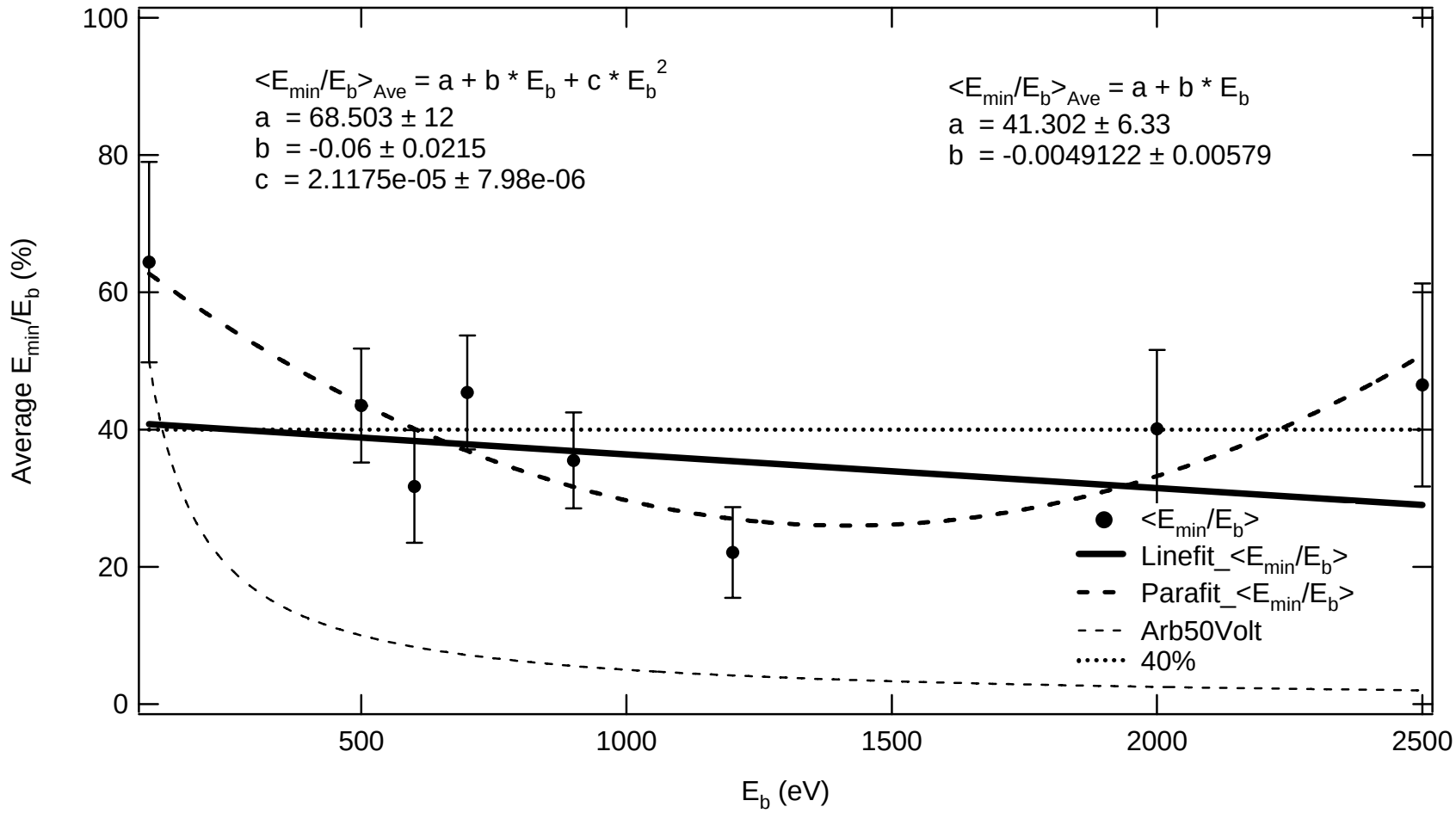

Figure 5-59 The average ratio of E_{min} to E_b versus E_b. The error bars represent the standard deviation of the average ratio over all angles. Fits to the data are the arbitrary 50 eV (light dash), linear with no slope (dotted), linear with slope (bold), and parabolic (bold dash). The best fit line falls below 50 %, is better than the historical arbitrary 50 eV, but is worse than the parabolic fit.

5.5.(a)1b E_{min} Dependence on Emission Angle

As seen in Figure 5-52, the angular dependence is contained within the error bar. As the size of the error bar increases, the chances are much greater that an angular dependence exists. Review of the percentage of the standard deviation to the average of the E_{min} position over emission angle (right column of Table 5.18) shows that the greatest values of ~30% are observed for beam energies of 1200 eV, 2000 eV, and 2500 eV. This suggests that an angular dependence may exist, but the trend of such a dependence [Fig. 5-51, purple line] is not clearly evident. Now talk about purple line.

As long as 40% = StDev/Average is a decent guideline to look for a dependency of E_{min} on emission angle, a completely different energy exchange mechanism, such as Auger, may offer the proper trend.

5.5.(a)2 $dN(E_{min})/dE$ Yield Intensity

The yield intensity at the local minimum decreases with increasing emission angle.

Referring back to Fig. 5-49 (E_b = 2500 eV, purple), and noticing that the yield intensity is less than zero at the local minimum, E_{min}, the EAR yield intensities, $dN(E_{min})/dE_e$, are plotted [Fig. 5-53] and fitted with a Lambert cosine law. The yield intensities are tabulated in Table 5.20 along with the single isotropic amplitude fitting parameter, B (Eq. 5.2). All of the yield values are positive except the E_b = 2500 eV, which can be used to fix the calibration curves needed to provide absolute measurement. Two $dN(E_{min})/dE_e$ values measured at E_b = 900 eV (70^o CC and 76^o CC) are also negative. In addition, $dN(E_{min})/dE_e$, shows the near isotropic fall off towards zero yield values for greater E_b with the exception addressed in the next section.

The scaling of $dN(E_{min})/dE_e$ with the total integrated yield, σ, can be tested by calculating the ratio.

The main dependence is in the Lambert law.

The dependence on angle is probably due to the Auger peaks, which are very dependent on emission angle. The spectrum at E_b = 2500 eV is the only one with an angular dependent E_{min}.

To show that the yield value for E_b = 900 eV compared to E_b = 1200 eV is an additional dependence on E_b not shown in the last sub-section (5.5(a)1a).

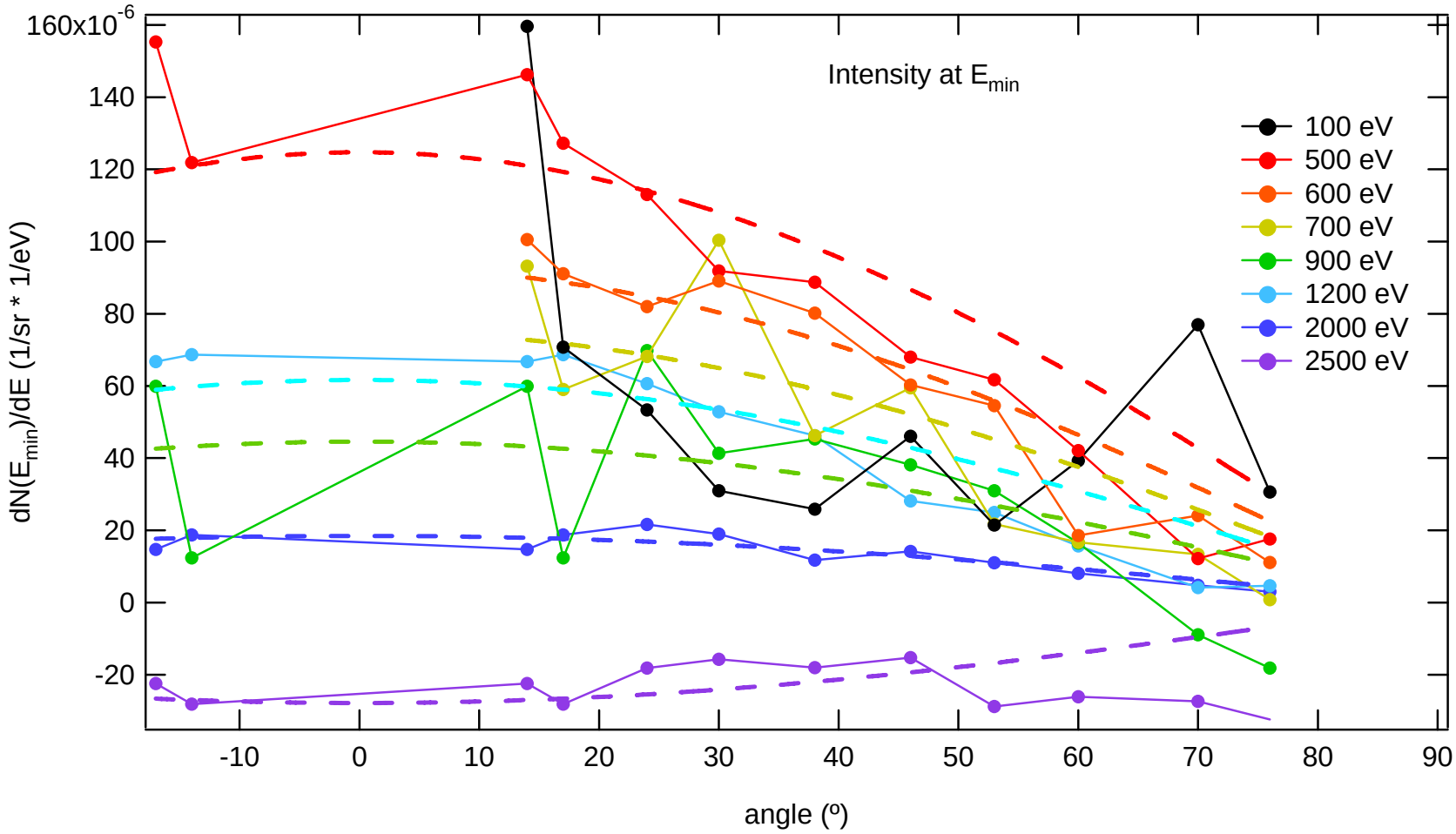

Figure 5-60 Yield intensity, $dN(E_{min})/dE_e$, at the local minimum, E_{min}, located between the SE and BSE peak as a function of emission angle. 100 eV data is given divided by 10.

Table 5.20 Yield Intensity at Local Minimum Energy Location Between the SE and BSE Peaks. All yield intensities have units of (1/sr*1/eV) * 10^{-6} and an error of 5% (1/sr*1/eV). Isotropic yield intensity fitting parameter B is determined by using $dN(E_{min})/dE = B * \cos(\alpha)$.

Beam Energy	Emission Angle (deg)													
	17C	14C	14CC	17CC	24CC	30CC	38CC	46CC	53CC	60CC	70CC	76CC	$B(10^{-6})$	$B/\delta_{Emin}(10^{-6})$
100 eV	*	*	1596	708	533	310	258	460	215	393	770	306	782	23697
500 eV	155	121	146	127	113	92	89	68	62	42	12	18	125.7	613
600 eV	*	*	101	91	82	89	80	60	55	19	24	11	92.7	403
700 eV	*	*	93	59	68	100	46	59	22	17	13	1	75.0	135
900 eV	60	12	60	12	70	41	45	38	31	16	-9	-18	44.7	128
1200 eV	67	69	67	69	61	53	46	28	25	16	4	5	61.7	162
2000 eV	15	19	15	19	22	19	12	14	11	8	5	3	18.5	77
2500 eV	-22	-28	-22	-28	-18	-16	-18	-15	-29	-26	-27	-32	-27.8	-132

Percentages of the energy location of the minimum, E_{min} (located between the SE and BSE peaks), are given for several E_b versus emission angle [Fig. 5-59]. First given is the yield of the minimum energy, E_{min}, separating the SE and BSE peaks. Close examination of [Fig. 5-60] shows that the intensity at E_{min} for E_b = 2500 eV is negative. Investigation of the size of the error bar plotted as the average of the ratio to E_b [Fig. 5-49], and noticing that the percentage emission is relatively small at 30% [Fig. 5-50] for large emission angles and large, near 65%, for the small emission just near normal incidence.

The E_{min} intensity vs. emission angle [Fig. 5-60] shows one more thing not easily seen in section 5.4(d), an additional dependence on E_b. Notice how the B fitting parameter at 900 eV is less than the B fitting parameter at 1200 eV (Table 5.20, right columns).

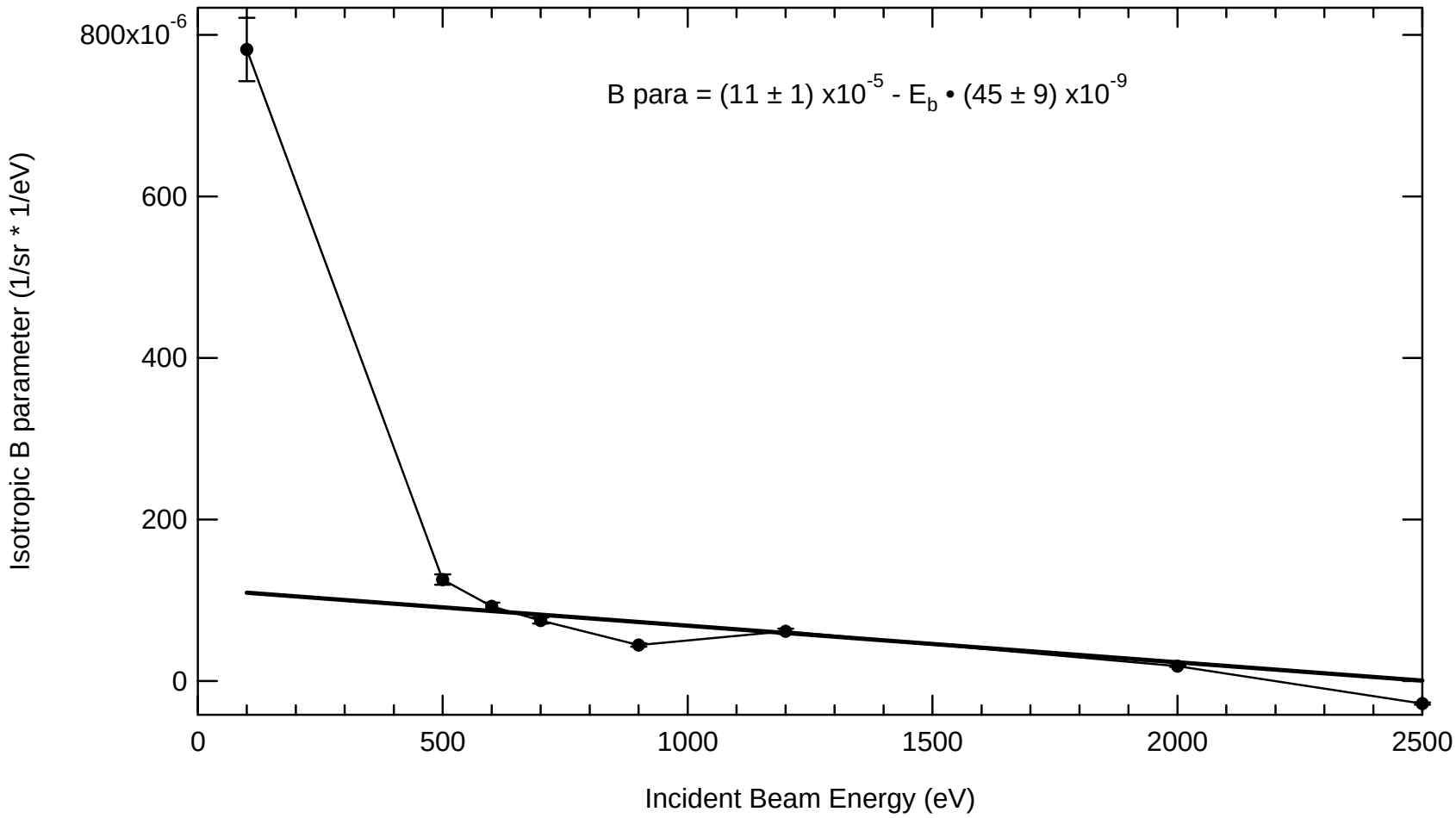

Figure 5-61 Isotropic fitting parameter, B, vs incident beam energy using $dN(E_{min})/dE = B * \cos(\alpha)$. The linear fit does not include the 100 eV data.

5.5.(b) Elastic-Plasmon Minimum Transition

First, the Elastic-Plasmon minimum boundary using the 0.1 eV resolution is different than the Elastic-BSE minimum boundary using 1 eV resolution. But for discussion sake, lets compare the boundaries anyway. Fig. 5-64 shows the Elastic-BSE boundary minimum position, which is (at most) 3 eV from the elastic peak.

Specifically, the energy positions and yield intensities of the Elastic—Plasmon boundary minimum, which separates the Elastic peak from the next lower energy peak (the first Plasmon peak) is studied. The characteristic features of a transition, defined in Table 3.3, are energy, $E_{trasition}$, and intensity, $dN(\alpha,E_{trasition};E_b)/dE_e$,.

The minimum between the Elastic peak and the Plasmon peak, Elastic—Plasmon boundary minimum, is now addressed. The energy positions and yield intensities of the Elastic—Plasmon boundary minimum are located with a programming search routine.

5.5.(b)1 Elastic-Plasmon Energy

Elastic-Plasmon minimum energy position [Fig. 5-62] is presented as the difference in energy from the elastic peak energy.

The statistics of the minimum are given for five incident beam energies. The average shown in the second to last column in Table 5.21 is used as the high energy boundary to calculate the Plasmon peak's yield. Since the only low energy boundary of the first plasmon peak is not well known, the next minimum value located near double the energy position of the maximum (~7 eV) with an error of a couple of Volts is used to calculate the first Plasmon peak's yield. This is feasible as long as this plasmon peak is symmetric in shape. To test for a symmetric peak shape, determine the amounts of energy between the peak and the low and high energy minimums on either side of the peak. For E_b = 900 eV, [Fig. 5-4] the average plasmon

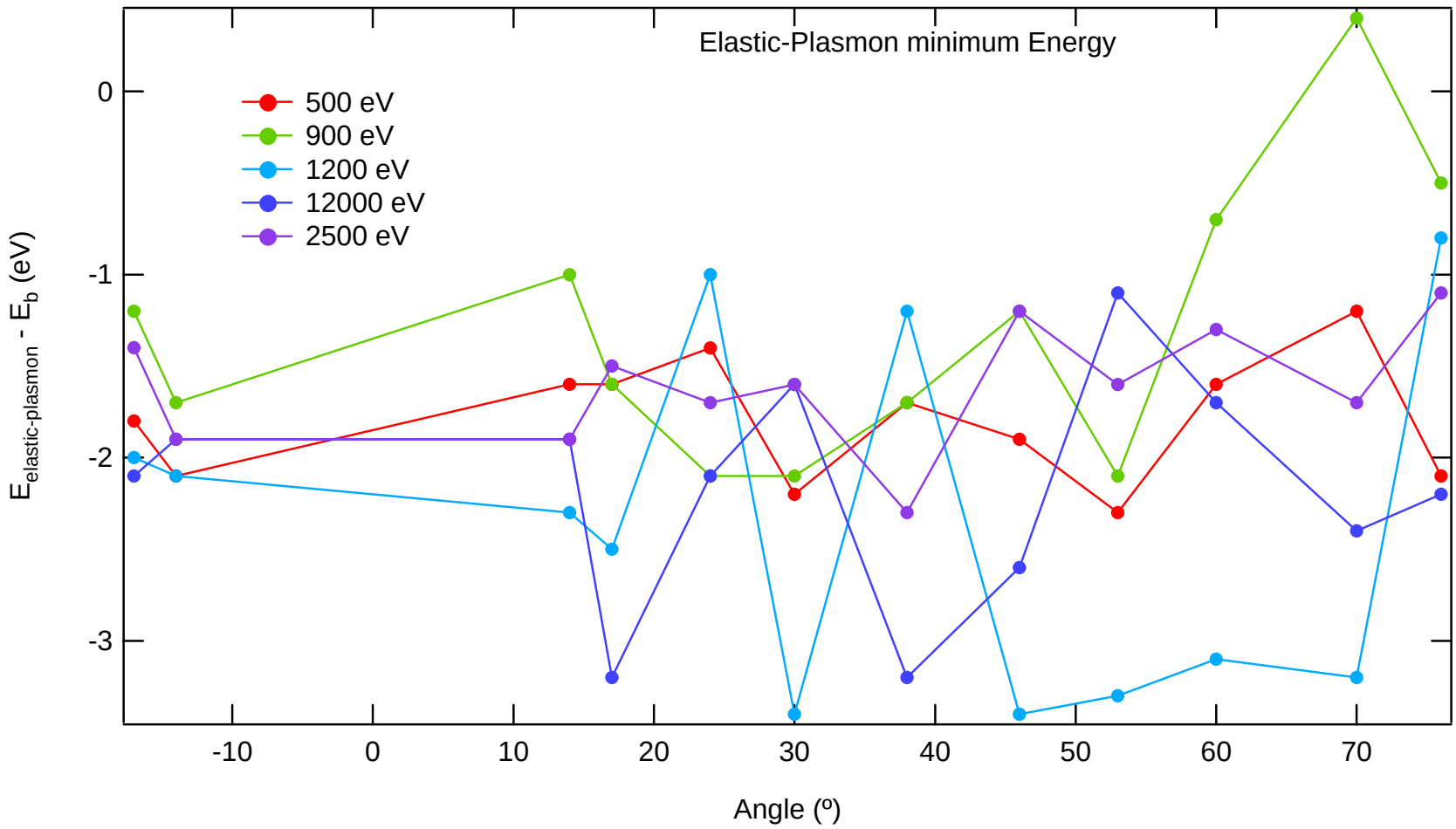

Figure 5-62 Elastic—Plasmon boundary minimum transition energy using the 0.1 eV resolution.

Table 5.21 Elastic-Plasmon Boundary Minimum Transition Energy. All 0.1 eV resolution minimum positions are subtracted from the beam energy and have units of eV with an error of 5%.

Beam Energy	Emission Angle (deg)													
	17C	14C	14CC	17CC	24CC	30CC	38CC	46CC	53CC	60CC	70CC	76CC	Ave	StDev
100V	*	*	*	*	*	*	*	*	*	*	*	*	*	*
500V	-1.8	-2.1	-1.6	-1.6	-1.4	-2.2	-1.7	-1.9	-2.3	-1.6	-1.2	-2.1	-1.8	0.3
600V	*	*	*	*	*	*	*	*	*	*	*	*	*	*
700V	*	*	*	*	*	*	*	*	*	*	*	*	*	*
900V	-1.2	-1.7	-1.0	-1.6	-2.1	-2.1	-1.7	-1.2	-2.1	-0.7	0.4	-0.5	-1.3	0.8
1200V	-2.0	-2.1	-2.3	-2.5	-1.0	-3.4	-1.2	-3.4	-3.3	-3.1	-3.2	-0.8	-2.4	1.0
2000V	-2.1	-1.9	-1.9	-3.2	-2.1	-1.6	-3.2	-2.6	-1.1	-1.7	-2.4	-2.2	-2.2	0.6
2500V	-1.4	-1.9	-1.9	-1.5	-1.7	-1.6	-2.3	-1.2	-1.6	-1.3	-1.7	-1.1	-1.6	0.3

peak max is located at 888.2 eV (Table 5.4) + 0.4 eV (Table 5.2, Ave) – 3.6 eV (Table 5.5, Ave) = 885 eV. The low energy minimum defining the plasmon peak seems to occur at roughly 874 eV [Fig. 5-4]. + 0.2 eV (Table 5.2) and the elastic—plasmon minimum is an average of 888.2 – 1.3 eV, then 886.9 – 884.4 = 2.5 eV, and 884.4 – 874 = 10 eV. However, symmetry is not the case because 2.5 eV is only a forth of 10 eV.

5.5.(b)2 Elastic-Plasmon Intensity

Elastic—Plasmon boundary minimum intensity is measured at the position of the minimum position using 0.1 eV Resolution.

This value spans from 1.3 eV below the elastic peak to 2.4 Volts below the elastic peak. For example, the intensity for the E_b = 900 eV shown in green [Fig. 5-56] is a positive value [Table 5.22] 3 out of 12 angles, however, the standard deviation is large and an average value of -55×10^{-6} 1/sr * 1/eV will be used to concatenate the 0.1 eV and 1 eV resolution data together. This is legitimate because the Plasmon peak is most likely material dependant and no surface changes occur such as contamination or reconstruction.

This is really trouble because I have to find the minimum energy lower bound of the plasmon peak.

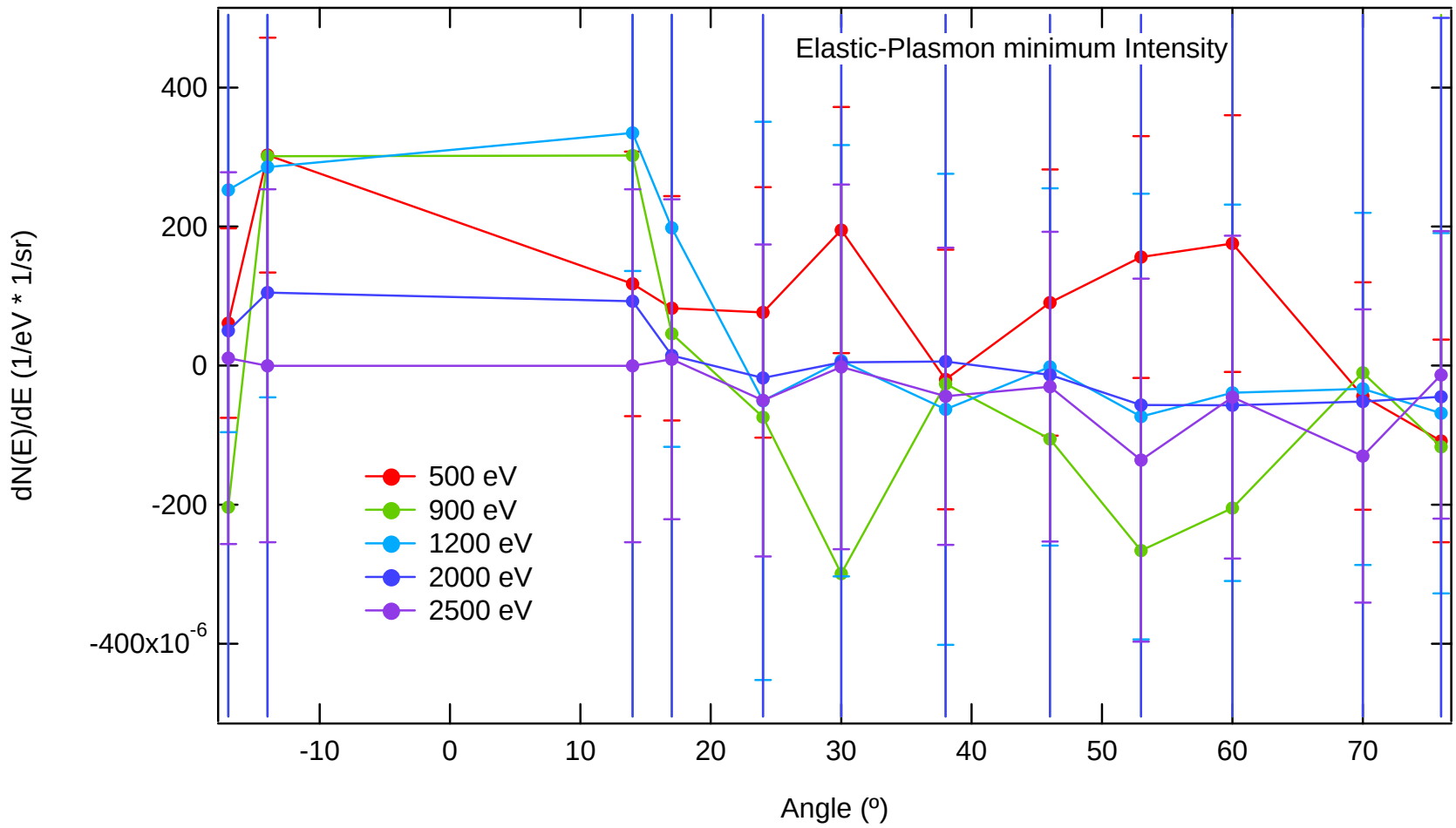

Figure 5-63 Elastic—Plasmon boundary minimum transition intensity using the 0.1 eV resolution spectra.

Table 5.22 Elastic-Plasmon Boundary Minimum Transition Intensity. All 0.1 eV resolution yield intensities have units of (1/sr*1/eV) * 10^{-6} and an error of 5% (1/sr*1/eV).

Beam	Emission Angle (^{o})													
Energy	17C	14C	14CC	17CC	24CC	30CC	38CC	46CC	53CC	60CC	70CC	76CC	Ave	StDev
100 eV	*	*	-309	-577	-475	-114	-403	-303	-265	-297	-683	-440	-489	265
500 eV	61	303	118	83	77	195	-20	91	156	176	-44	-108	91	112
600 eV	*	*	*	*	*	*	*	*	*	*	*	*	*	*
700 eV	*	*	*	*	*	*	*	*	*	*	*	*	*	*
900 eV	-204	301	302	46	-74	-300	-26	-105	-266	-205	-10	-117	-55	196
1200 eV	253	286	335	198	-51	7	-63	-2	-73	-39	-34	-68	63	156
2000 eV	50	105	93	15	-18	5	6	-13	-57	-57	-52	-45	3	56
2500 eV	11	0	0	9	-50	-2	-44	-30	-136	-45	-130	-13	-36	50

5.5.(c) Elastic-BSE Minimum Transition

As with determining the Plasmon Peak yield, it is important to find the high energy boundary of the BSE peak using the Elastic-BSE minimum boundary energy [Fig. 3-37]. The transition between the elastic peak and the BSE peak is investigated in terms of the energy position and the intensity at the energy position. The only minute difference here is that the data taken at 1 eV resolution is used to determine the BSE yield instead of the 0.1 eV resolution. Hence, the features of the quasi-elastic region are not observed in these spectra.

5.5.(c)1 Elastic-BSE Energy

The Elastic—BSE minimum transition energy position is a lot larger having maximum values at most 20 eV from the Elastic peak. Referring back to the Normalized BSE AR Energy Spectra [Fig. 5-20], this position, $-0.01*E_b$, has no apparent dependence on E_b. But if minimum is ~1% of E_b, then it is proportional to E_b and does have a dependence. The Elastic-BSE minimum energy shown against emission angle [Fig. 5-64] are subtracted from the elastic peak energy position. The tabulated values of the Elastic-BSE minimum energy Table 5.23 include averages and standard deviations. The average of the Elastic-BSE minimum energy transition is subtracted from the average elastic peak energy position of 102.5 eV, 494.4 eV, 594.4 eV, 694.4 eV, 888.2 eV, 1189.5 eV, 1981.3 eV, and 2475.5 eV, respectively. A line trend is fit to this average [Fig. 5-65] with a zero slope (-11.6 eV below the incident beam energy). This fit does not include the E_b = 100 eV data because there is no observed BSE peak.

There is little if any angle dependence. Varies with E_b, but not sure what the dependence is.

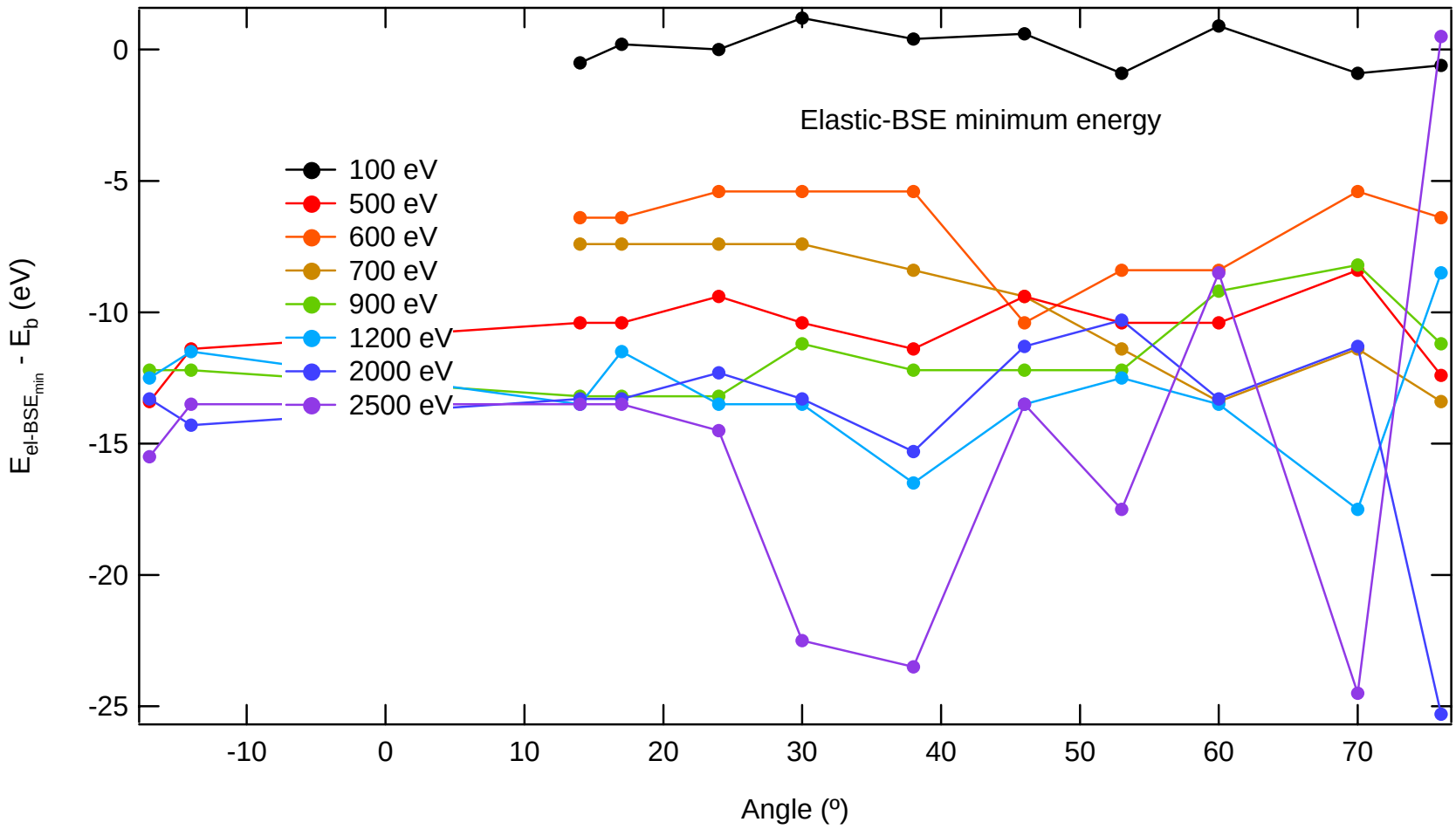

Figure 5-64 Elastic—BSE boundary minimum transition energy using the 1 eV resolution spectra.

Table 5.23 Elastic-BSE Boundary Minimum Transition Energy. All 1 eV resolution yield intensities have units of eV and an error of 5% eV.

Beam Energy	Emission Angle (^{o})													
	17C	14C	14CC	17CC	24CC	30CC	38CC	46CC	53CC	60CC	70CC	76CC	Ave	StDev
100 eV	*	*	97.5	98.5	101	95.6	95.7	101.6	99.8	95.5	98.7	96.7	98	2.2
500 eV	481	483	484	484	485	484	483	485	484	484	486	482	484	1.4
600 eV	*	*	588	588	589	589	589	584	586	586	589	588	588	1.7
700 eV	*	*	687	687	687	687	686	685	683	681	683	681	685	2.5
900 eV	876	876	875	875	875	877	976	876	876	879	880	877	877	1.6
1200 eV	1177	1178	1176	1178	1176	1176	1173	1176	1177	1176	1172	1181	1176	2.3
2000 eV	1968	1967	1968	1968	1969	1968	1966	1970	1971	1968	1970	1956	1967	3.9
2500 eV	2460	2462	2462	2462	2461	2453	2452	2462	2458	2467	2451	2476	2461	6.9

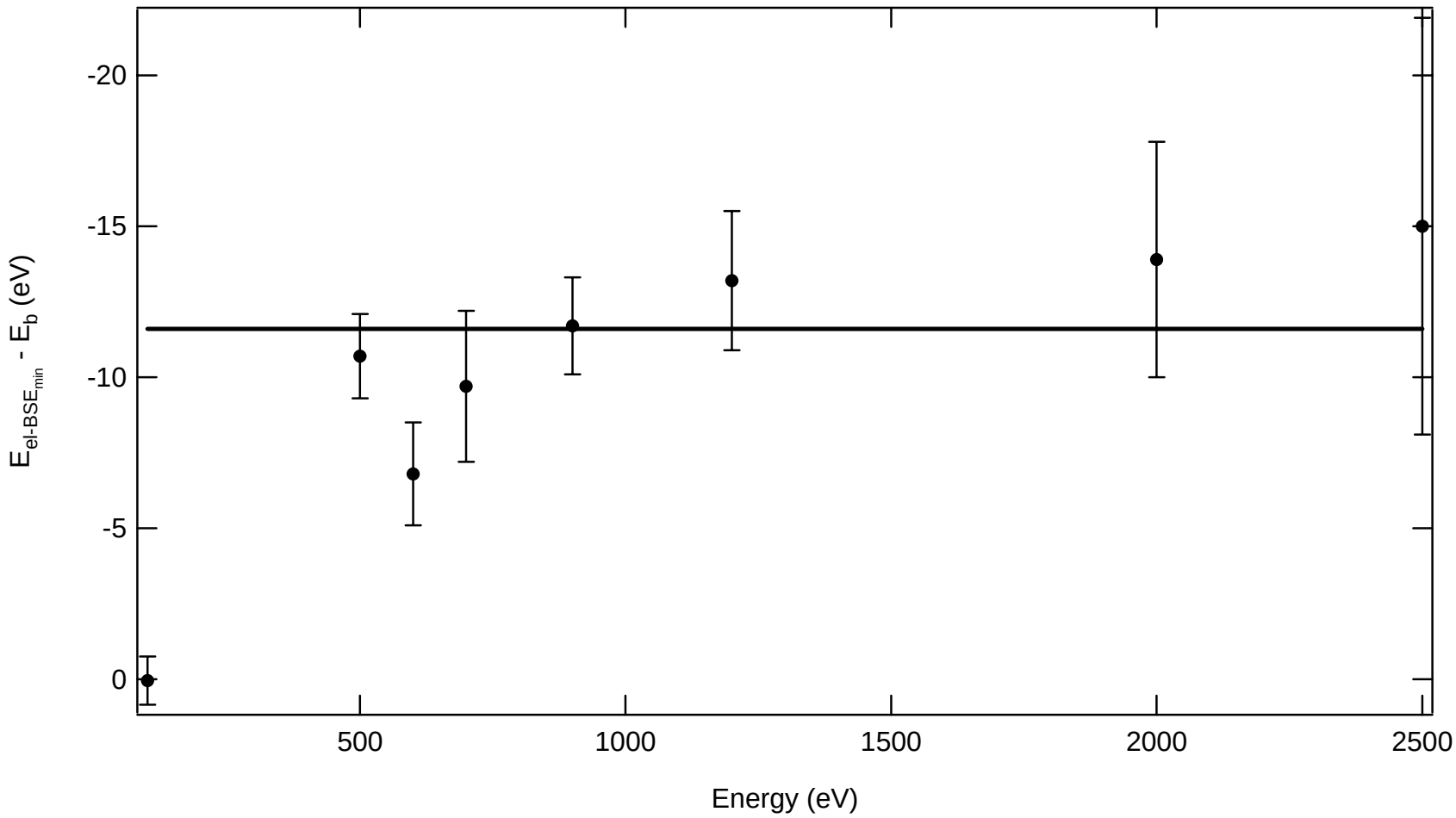

Figure 5-65 The average of the Elastic—BSE boundary minimum transition energy with the standard deviation as the error bar. The line fit is the average and does not include the E_b = 100 eV data.

5.5.(c)2 Elastic-BSE Intensity

The intensities of the Elastic-BSE minimum boundary [Fig. 5-65] measured using the 1 eV resolution can be easily compared with those of the elastic-plasmon boundary minimum [Fig. 5-66] measured using the 0.1 eV resolution. The maximum yield values are 0.3 x 10^{-3} 1/eV*1/sr for E_b = 900 eV and 1200 eV. The maximum values for the latter are 0.3x10^{-3} 1/eV*1/sr for E_b = 900 eV and 0.2x10^{-3} 1/eV*1/sr for E_b = 500 eV and 1200 eV. The dependence on emission angle appears to be Rutherford like.

Be aware that the Elastic—BSE minimum boundary intensity is less than zero for E_b = 100 eV, 2000 eV, and 2500 eV. This is most likely evidence for Auger activity. Notice that the intensity [Fig. 5-59] for most emission angles have the greatest values at low emission angles and taper towards zero for high emission angles just as in the BSE peak intensity. The intensity values are tabulated in Table 5.24.

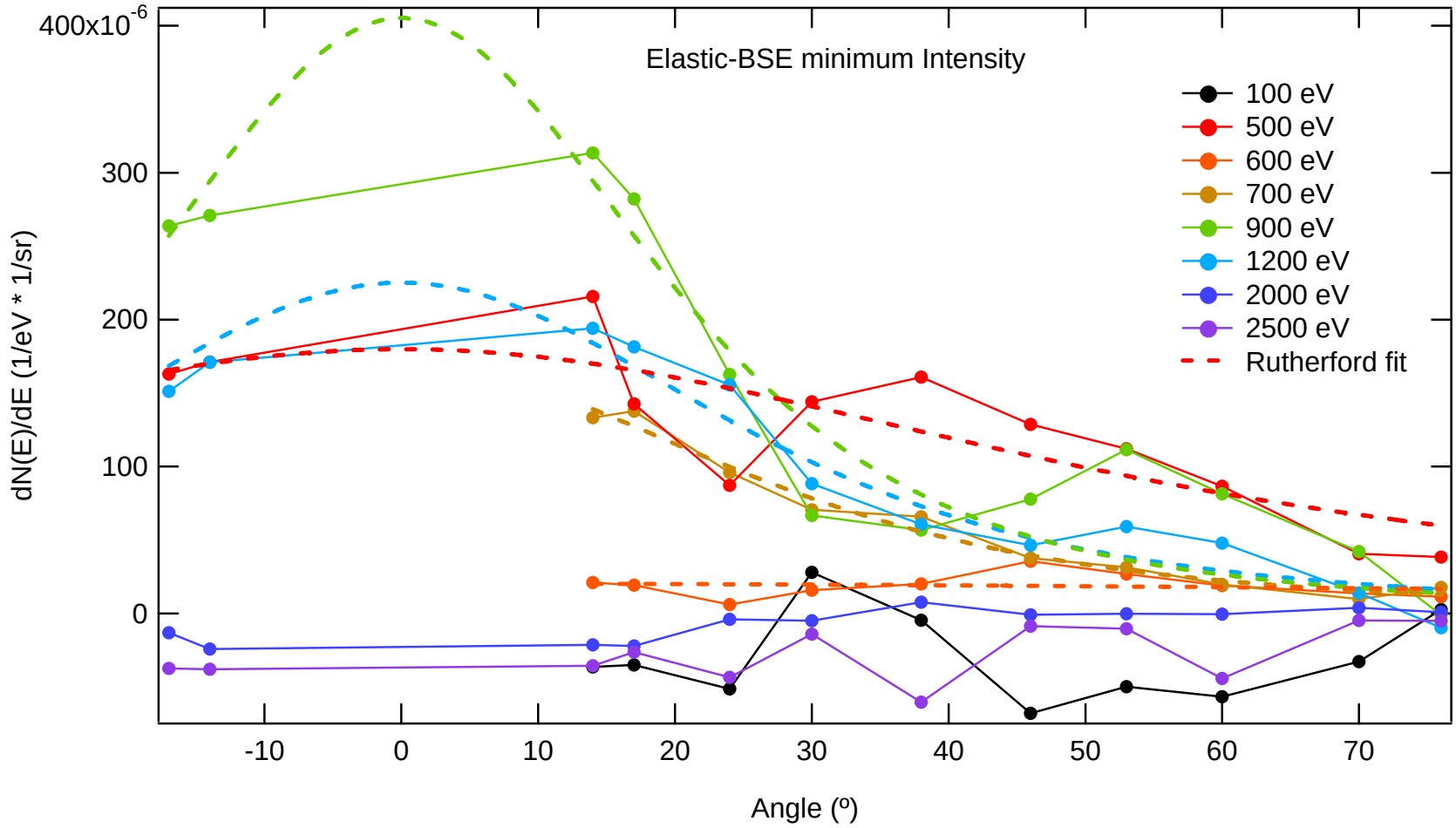

Figure 5-66 Elastic—BSE boundary minimum transition intensity of the fine 1 eV resolution. Fit are to the Rutherford model (dash).

Table 5.24 Elastic-BSE Boundary Minimum Transition Intensity. All 1 eV resolution yield intensities have units of (1/sr*1/eV)*10^{-6} and an error of 5% (1/sr*1/eV).

Beam Energy	Emission Angle (^{o})														
	17C	14C	14CC	17CC	24CC	30CC	38CC	46CC	53CC	60CC	70CC	76CC	beta	C (10^{-6} $eV^{-1}sr^{-1}$)	χ^2
100 eV	*	*	-78	-121	-51.4	-50.4	-31.7	-68	-128	-150	-54.7	-111	*	*	*
500 eV	163	171	216	143	87.2	144	161	129	112	86.6	40.6	38.4	0.5 ± 0.2	200 ± 100	1e-8
600 eV	*	*	20.9	19.3	6	15.8	20.2	35.5	26.8	19	13.5	11.3	3 ± 9	1000 ± 5000	6e-10
700 eV	*	*	133	138	96	70.5	65.8	37.6	31.4	19.6	9.7	17.8	0.14 ± 0.02	10 ± 2	4e-10
900 eV	264	271	313	282	163	67	57	78	111	81.3	-22.2	-1.1	0.09 ± 0.03	12 ± 6	2e-8
1200 eV	151	171	194	181	155	88.4	61	46	59	48	-21.5	-10	0.14 ± 0.03	18 ± 6	3e-9
2000 eV	-13.1	-24.2	-21.5	-22.2	-4.1	-5	5.5	-1	-5.1	-3	-3.9	0.1	*	*	*
2500 eV	-37.4	-38	-35.6	-26.3	-43.5	-14.5	-70	-14.8	-18	-44.2	-10.7	-8.3	*	*	*

5.6 Incident Beam Energy Resolved Total Yield

The area measured underneath the E_bR spectra (at each coarse angle setting), over the entire range of the spectra (0 eV to E_b eV) provides the total E_bR yield, $\sigma_C(\alpha; E_b)$, or cross section. It is important to give the total yield because all partial yields such as the elastic, plasmon, BSE and SE yields contribute to the total yield. In this case, an Auger electron factor plays a part in contributing to the total yield [Fig. 3-37].

For example, the E_b = 900 eV @ 14° CC spectrum, Fig. 5-1, the total E_bR angular distributions are given by Eq. 3.16 where the upper bound of integration is E_b.

This integrated area, for each E_b, provides the total E_bR Yield and is "read off" of the pre—differentiated data [Fig. 5-2, black], E_b = 900 eV @ 14° CC E(0 eV) = 0.47 sr^{-1} with reference given in appendix E [Fig. E-2 through Fig. E-9].

The process of using the pre—differentiated data [Fig. 5-2, black], amounts to following the prescribed procedure given in 3.2(i) to concatenate the spectral pieces together. In doing so, through the Simpson's rule (Eq. 3.6), the error is calculated in quadrature by Eq. (3.7).

The total yield is measured for the selected incident beam energies of 500 eV, 600 eV, 700 eV, 900 eV, 1200 eV, 2000 eV, and 2500 eV using the spectra measured at 10 eV resolution (100 eV @ 0.1 eV resolution).

Total yields are given as a function of emission angle [Fig. 5-67] where, as expected, smaller emission angles have larger total yields. The Lambert law (Eq. 5.2) having amplitude parameter, *B*, is fit to the total yield vs. emission angle for several E_b.

The total yield values and their associated errors are tabulated in Table 5.25 and include error bars calculated in quadrature. Also included are the amplitude fitting parameter for the Lambert law with associated χ^2 and the other fit (Eq. 5.2) with it's associated χ^2. Since the measurements are absolute, the

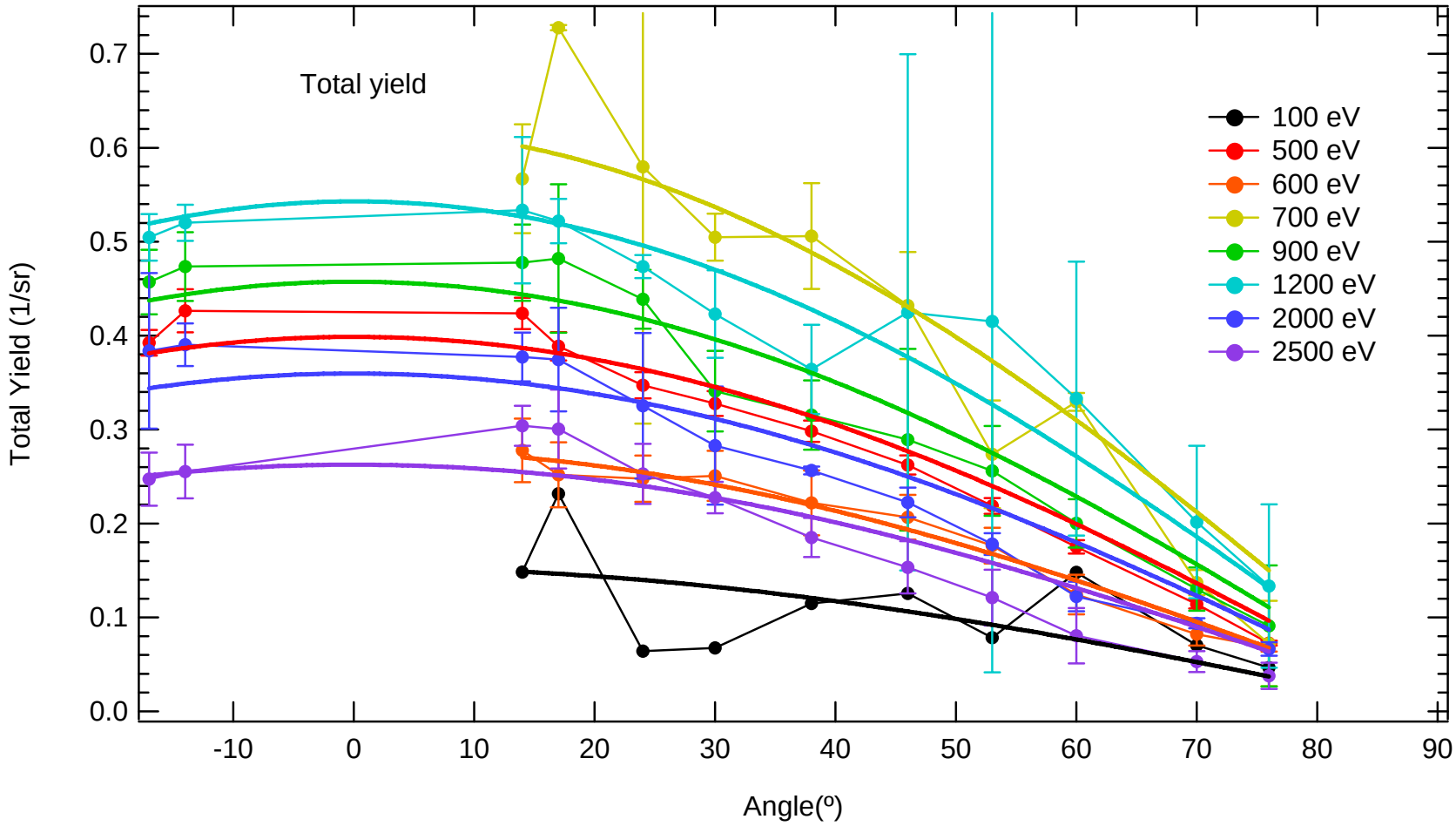

Figure 5-67 Total yield distributions (versus emission angle) given in units of inverse steradians for selected incident beam energies.

Table 5.25 The Incident Beam Energy Resolved Total Yield given in units of inverse steradians.

Emission Angle (^{o})	Incident Beam Energy (eV)								σ_{max} (sr^{-1})	E_{max} (eV)	χ^2
	100	500	600	700	900	1200	2000	2500			
17C	*	0.072 ± 0.003	*	*	0.46 ± 0.03	0.51 ± 0.03	0.38 ± 0.08	0.25 ± 0.03	0.49	977	0.005
14C	*	0.114 ± 0.005	*	*	0.47 ± 0.04	0.52 ± 0.02	0.39 ± 0.02	0.26 ± 0.03	0.51	940	0.005
14CC	0.148	0.175 ± 0.007	0.28 ± 0.03	0.57 ± 0.06	0.48 ± 0.04	0.53 ± 0.08	0.38 ± 0.03	0.30 ± 0.02	0.51	1031	0.04
17CC	0.232	0.219 ± 0.008	0.25 ± 0.04	0.728 ± 0.003	0.48 ± 0.08	0.52 ± 0.02	0.38 ± 0.06	0.30 ± 0.04	0.53	965	0.1
24CC	0.064	0.26 ± 0.01	0.25 ± 0.03	0.6 ± 0.3	0.44 ± 0.03	0.47 ± 0.01	0.33 ± 0.08	0.25 ± 0.03	0.46	1002	0.05
30CC	0.068	0.30 ± 0.01	0.25 ± 0.03	0.51 ± 0.03	0.34 ± 0.04	0.42 ± 0.05	0.28 ± 0.06	0.23 ± 0.02	0.40	971	0.03
38CC	0.115	0.33 ± 0.01	0.22 ± 0.04	0.51 ± 0.06	0.32 ± 0.04	0.36 ± 0.05	0.257 ± 0.004	0.19 ± 0.02	0.37	892	0.04
46CC	0.125	0.35 ± 0.01	0.21 ± 0.02	0.43 ± 0.06	0.29 ± 0.09	0.4 ± 0.3	0.22 ± 0.02	0.15 ± 0.03	0.35	946	0.04
53CC	0.078	0.39 ± 0.02	0.18 ± 0.02	0.27 ± 0.06	0.26 ± 0.05	0.42 ± 0.4	0.18 ± 0.01	0.12 ± 0.03	0.29	1026	0.03
60CC	0.148	0.42 ± 0.02	0.12 ± 0.02	0.329 ± 0.009	0.20 ± 0.03	0.33 ± 0.1	0.12 ± 0.02	0.08 ± 0.03	0.24	886	0.05
70CC	0.070	0.43 ± 0.02	0.08 ± 0.01	0.14 ± 0.01	0.13 ± 0.02	0.20 ± 0.08	0.094 ± 0.005	0.05 ± 0.01	0.14	993	0.09
76CC	0.047	0.39 ± 0.01	0.07 ± 0.01	0.07 ± 0.05	0.09 ± 0.06	0.13 ± 0.09	0.066 ± 0.007	0.04 ± 0.01	0.09	1037	0.03
B (sr^{-1})	0.15	0.399	0.279	0.62	0.46	0.54	0.36	0.26			
χ^2	0.02	0.006	0.001	0.04	0.01	0.02	0.01	0.01			

100 eV error bars (not included) are 2 – 3 times larger than respective yield.

yields provided here are not normalized to any other work in the literature. Large errors for 100 eV data are due to low count rate and unstable electron gun.

It is duly noted that all of the yields increase as the angle decreases except for the 1200 eV distribution where all the error bars are calculated in quadrature. The solo exception is for the E_b = 1200 eV curve that shows as anomalous increase in total yield at 46° to 53° degrees. Notice also that E_b = 700 eV has the greatest total yields from 14° CC to 46° CC and E_b = 1200 eV has the greatest total yields from 53° CC to 76° CC. E_b = 2500 eV has the least total yields. Total yields are also given as a function of E_b [Fig. 5-68] and fit with the Variable N (3.S) model (n = 1.41) where the $\sigma_{max,}$ $E_{max,}$ and χ^2 are tabulated in Table 5.25.

Curves all seem to have consistent shape. Sketch two possible curves for 17° CC data; red assumes 700 eV is anomalously high and black assumes 600 eV and 900 eV are anomalously low. Both look like standard $\sigma(E_o)$ yield curves. The black curve with a peak at ~700 eV is closer to the Fatman yield curves.

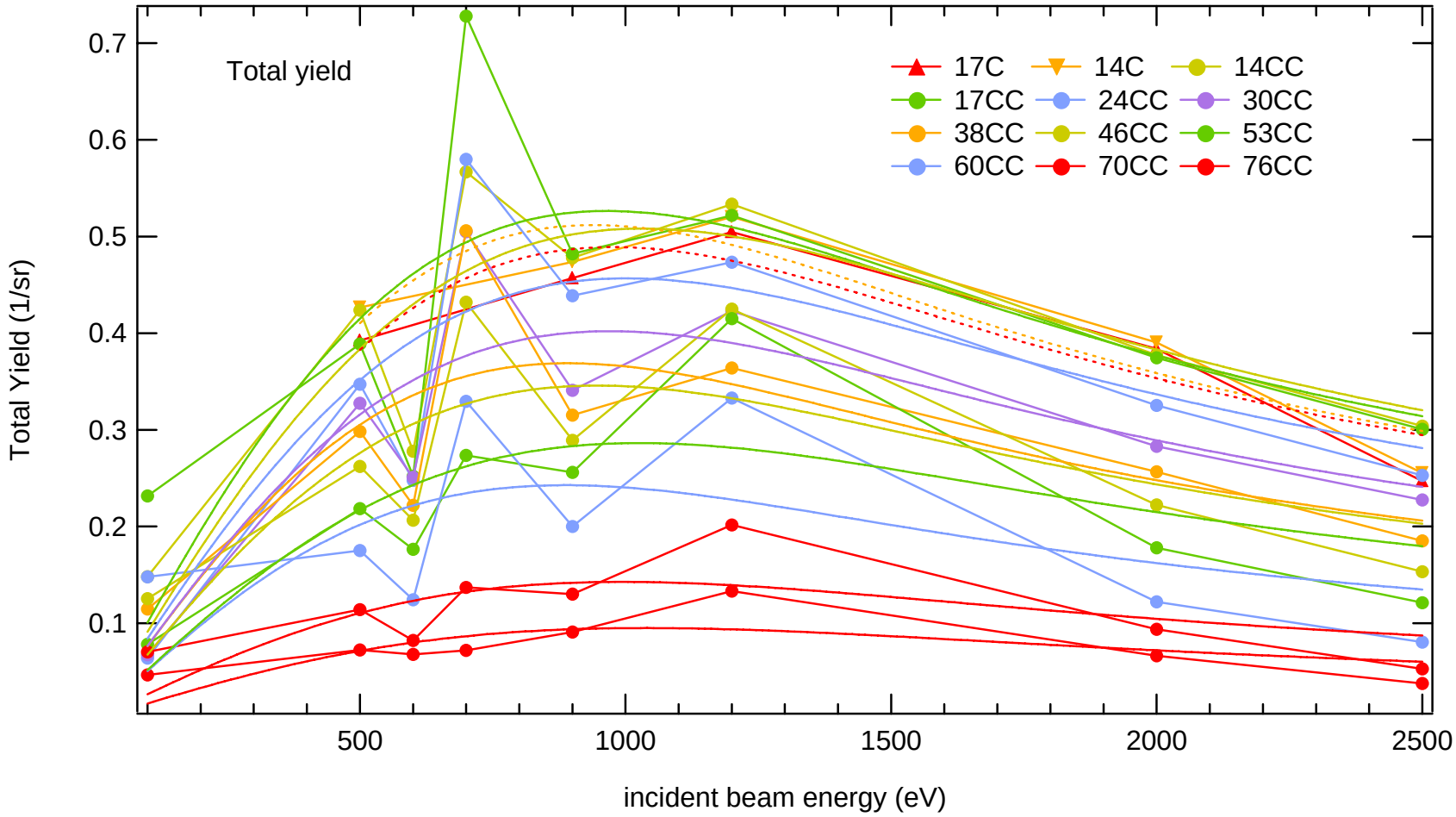

Figure 5-68 Total Yield versus incident beam energy given in units of inverse steradians for the twelve selected angles. VariableN fits (n = 1.41) are provided for Clockwise (dot) and Counter-Clockwise (solid) emission angles.

5.7 Angle Resolved Total Yield Distributions

In addition to measuring the Total yield using coarse, $\sigma_C(\alpha; E_b)$, angular resolution, much finer E_b - Angular resolutions, $\sigma_f(\alpha; E_b)$, have been measured. Used primarily as a diagnostic tool to assess the automation capabilities of the rotatable detector (RD) cable (3.2(a)), the detailed distributions (cross sections) of polycrystalline Au are provide for several different E_b. The fine AR distributions are given [Fig. 5-69] for several E_b. For these measurements, the RD is biased to 0 V. The Rutherford model is used to fit each of the distributions. The units are given in inverse steradians, so integration of the Rutherford model Eq. (5.3) provides a unit-less total yield just as in the coarse angular resolution fits.

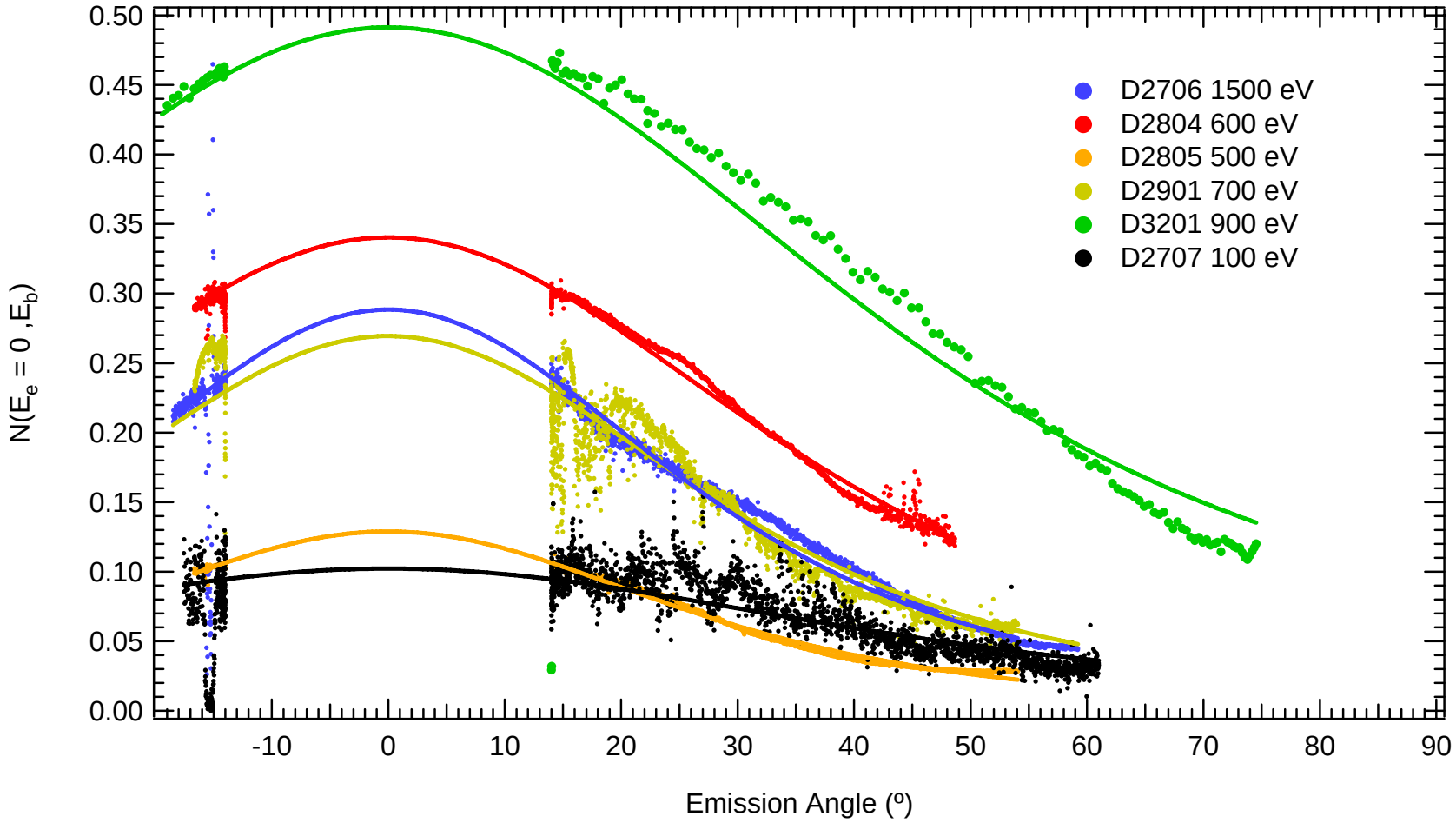

Figure 5-69 AR Total yield distribution for E_b = 100 eV, 500 eV, 600 eV, 700 eV, 900 eV, and 1500 eV measured in the non-symmetric angle configuration.

5.8 Angle Integrated Total Yields

The angular cross sections for several incident beam energies, E_b, for both coarse, $\sigma_C(\alpha; E_b)$, and fine, $\sigma_C(\alpha; E_b)$, angular resolutions have been presented. Numerical integration of these angular cross sections provides the total yield for all angles from 0^o to 90^o emission. The integration of the Rutherford fits to $\sigma_f(\alpha; E_b)$ is calculated for each E_b. These results are compared to data taken using a hemispherical grid detector on identical sample material.

These integrated emissions are now comparable to those taken in the FatMan chamber [Fig. 5-70]. The E_bR total yield versus emission angle [Fig. 5-67] are now compared to the fine angular resolved total yield results [Fig. 5-69] by integration the Rutherford fit. The fitting parameter is plotted against E_b for the coarse angle resolution [Fig. 5-70,triangles] and the fine angle resolution [Fig. 5-70,, plus symbols]. The total yield results measured in the FatMan chamber [*Clerc et. al., 2005*] are provided for comparison [Fig. 5-70, dots].

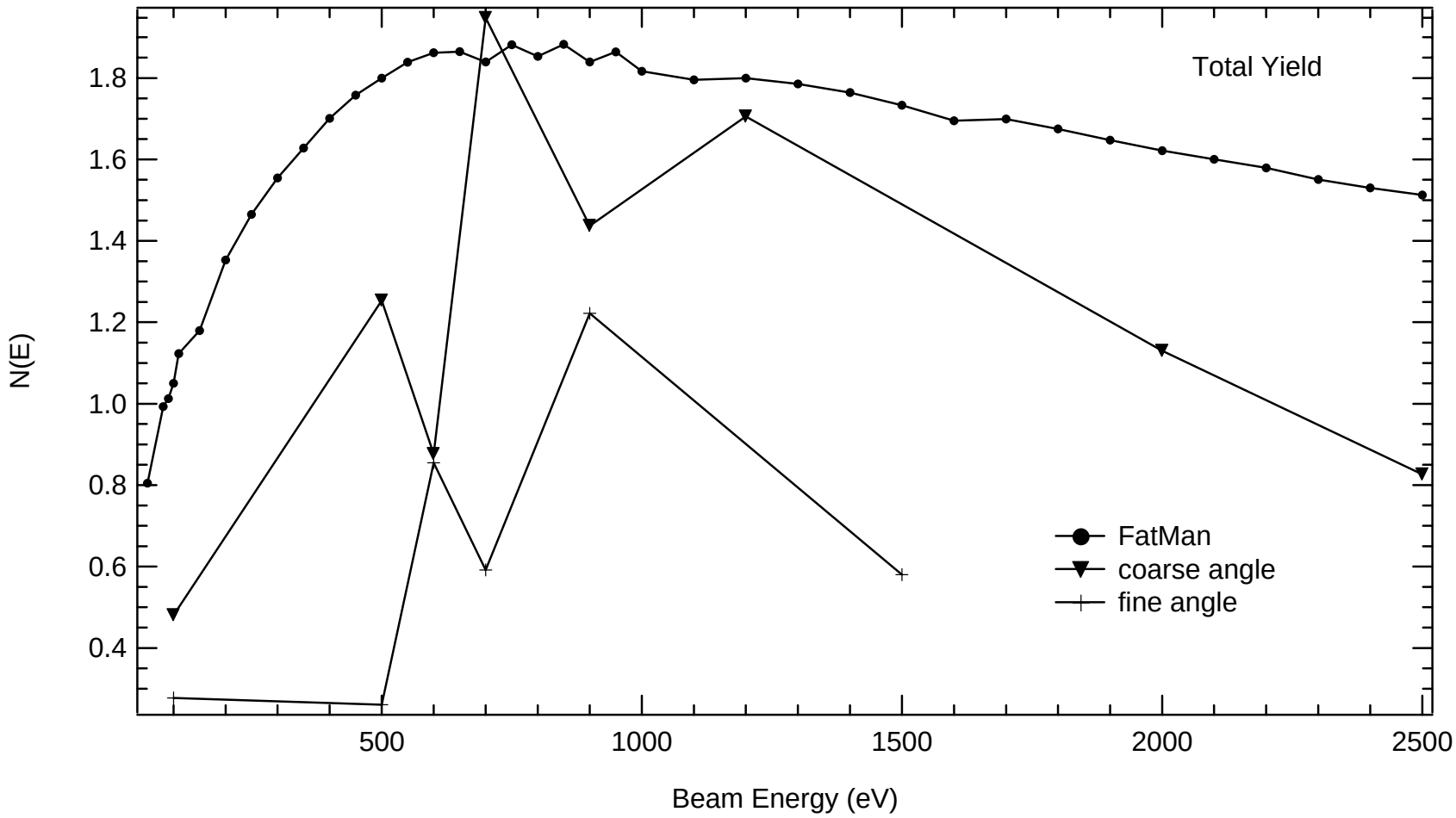

Figure 5-70 Total yield integrated over angle (isotropically). Total yield measured within the Fatman chamber [*Clerc et. al., 2005*] is shown for comparison.

5.9 Overcounted SE's, Undercounted BSE's

The last thing to give here is a plot of what is over—counted when calculating the SE and BSE yields using the 50 eV demarcation and E_{min}. The maximum yield is the same as the difference of to yields, (Y_{0to50}-Y_{50toEb}) minus ($Y_{0toEmin}$-$Y_{EmintoEb}$). This is basically summed up as the yield between 50 eV and E_{min} eV plotted against angle [Fig. 5-71] for several incident beam energies. The actual values for the $Yield_{50\text{-}Emin}$ are tabulated in Table 5.26.

The Yield miscounted between SE's and BSE's is substantial at maximum of 0.1 (10%). It is amazing that such a small difference can affect the SE Yield as in the E_b = 500 eV and 600 eV case and affect the BSE Yield as in the shift of the maximum peak from E_b = 2000 eV towards 1200 eV.

The 10 eV resolution of the BSE yield includes the small high energy features of the elastic and plasmon peaks.

Since these small yields are only maybe Elastic = 0.004, plasmon = 0.001 to 0.003, they account for only 3% to 20% of the BSE yield.

However, as indicated before, this is enough yield to shift the maximum BSE yield 100's of eV lower [Fig. 5-24 and Fig. 5-26]

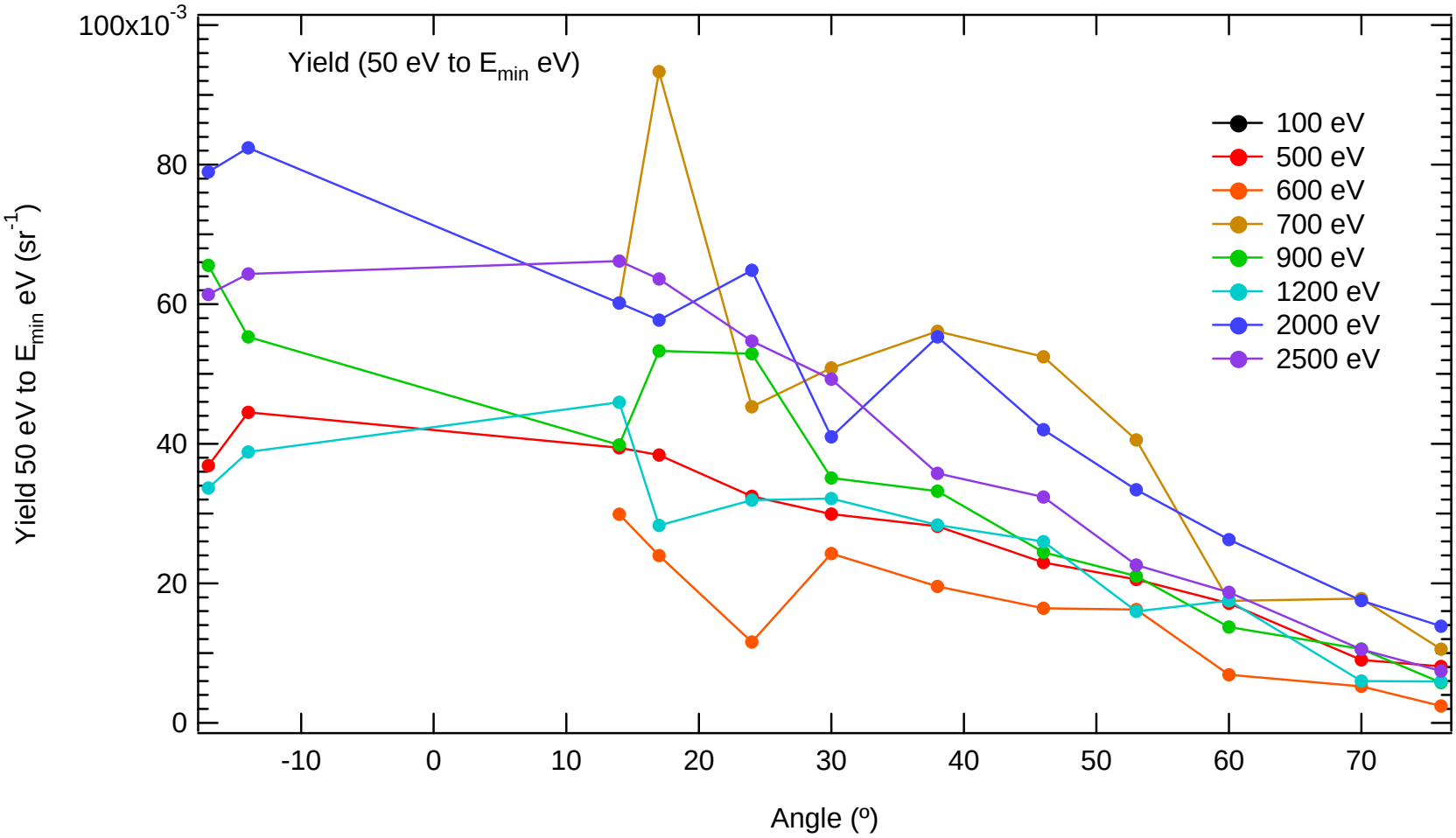

Figure 5-71 Yield 50 eV – E_{min}.

Table 5.26 The Yield for 50 eV - E_{min} eV given in units of inverse steradians. 100 eV error bars (not included) are 2 – 3 times larger than respective yield.

Emission Angle (deg)	Incident Beam Energy (eV)							
	100 eV	500 eV	600 eV	700 eV	900 eV	1200 eV	2000 eV	2500 eV
17C	*	0.072 ± 0.003	*	*	0.457 ± 0.034	0.505 ± 0.025	0.384 ± 0.083	0.247 ± 0.028
14C	*	0.114 ± 0.005	*	*	0.474 ± 0.037	0.520 ± 0.019	0.390 ± 0.023	0.255 ± 0.028
14CC	0.148	0.175 ± 0.007	0.278 ± 0.034	0.567 ± 0.058	0.478 ± 0.041	0.533 ± 0.078	0.377 ± 0.026	0.304 ± 0.021
17CC	0.232	0.219 ± 0.008	0.252 ± 0.035	0.728 ± 0.003	0.482 ± 0.079	0.522 ± 0.024	0.375 ± 0.055	0.301 ± 0.042
24CC	0.064	0.262 ± 0.010	0.248 ± 0.025	0.580 ± 0.274	0.439 ± 0.031	0.473 ± 0.012	0.325 ± 0.078	0.253 ± 0.032
30CC	0.068	0.298 ± 0.011	0.251 ± 0.027	0.505 ± 0.025	0.341 ± 0.043	0.423 ± 0.047	0.283 ± 0.063	0.228 ± 0.017
38CC	0.115	0.328 ± 0.013	0.222 ± 0.035	0.506 ± 0.056	0.315 ± 0.037	0.364 ± 0.048	0.257 ± 0.004	0.185 ± 0.021
46CC	0.125	0.347 ± 0.014	0.207 ± 0.024	0.432 ± 0.057	0.289 ± 0.097	0.425 ± 0.275	0.222 ± 0.016	0.153 ± 0.028
53CC	0.078	0.389 ± 0.015	0.176 ± 0.019	0.274 ± 0.057	0.256 ± 0.048	0.415 ± 0.374	0.178 ± 0.012	0.121 ± 0.030
60CC	0.148	0.424 ± 0.017	0.124 ± 0.021	0.329 ± 0.009	0.200 ± 0.026	0.333 ± 0.146	0.122 ± 0.016	0.080 ± 0.029
70CC	0.070	0.427 ± 0.023	0.082 ± 0.012	0.137 ± 0.013	0.130 ± 0.023	0.202 ± 0.081	0.094 ± 0.005	0.053 ± 0.011
76CC	0.047	0.392 ± 0.014	0.068 ± 0.004	0.072 ± 0.046	0.091 ± 0.064	0.133 ± 0.087	0.066 ± 0.007	0.038 ± 0.014

5.10 Conclusion

The energy positions and yield intensities the peak and valley features have been investigated using three different energy resolutions (0.1 eV, 1 eV, and 10 eV). The organization of the peak and valley features [Fig. 3-37] demonstrate the useful energy (and angular) resolving "power" of the charge detection instrument. The size of the energy spanning electron population of each specific feature is best observed by a similar size energy resolution. Since the elastic and plasmon populations have narrow peak features, utilization of the highest energy resolution powers of 10^{-2} eV (Chap. 3.2(e)) and 10^{-1} eV are used to most precisely probe, describe, and diagnose feature characteristics. The exponential zero power (10^{0} eV) is used to further compare and contrast the elastic peak. The plasmon features were measured with the 10^{0} eV resolution, however the plasmon peak was not observed. In the process of analyzing the much broader SE and BSE populations, using the coarser 10 eV resolution, an additional population was discovered (Auger).

Data obtained by varying the energy resolutions of the RD bias allow detailed comparisons of spectral measurements as well as extractions of key points from these spectra. For all features, the peak (or minimum) energy position is located with a simple programming search routine. The yield intensity at the energy position is also recorded and tabulated. The most important results listed below follow the subsection structure of this chapter according to the origin of the electron at the moment of production. The higher energy emitted electrons originating from those primarily incident are addressed first followed by those originating from the sample surface.

Though the standard deviation of the elastic peak energy position (5.1(a)) over emission angle was no greater than the thermal spread of the source, 0.6 eV, it seems as if there is a small dependence on emission angle perhaps caused by uniform electric field emanating from the surface. The elastic peak intensity (5.1(b)) shows qualitative structure similar to Rutherford's model. The FWHM of the elastic peak (5.1(c)) relate directly to black body radiation of the electron gun filament. In addition, evidence is shown

that measurement of the 100 eV data severely heat degraded the gun filament. The elastic peak yields (5.1(d)) are very comparable for the 1 eV and 0.1 eV resolutions.

The first plasmon peak is located (5.2(a)) an average energy position of 5.5 eV below the elastic peak. There is no observed dependence of the energy position of the first plasmon peak. The first plasmon peak intensity (5.2(b) and 5.2(c)) is clearly dependent on emission angle. Neither the Rutherford nor the Mott cross section models describe the dependence though the Mott cross section appears to be qualitatively better than the Rutherford (or Lambert) models. The dependence is best observed as a ratio to the elastic peak intensity where the largest emission angles approach and surpass unity and the smallest emission angles ratio values between 0.1 and 0.5. The plasmon yield (5.2(d)) seems to have a dependence on emission angle where particular interest is devoted towards the largest yields at E_b = 1200 eV. The ratio of the plasmon yield to the elastic yield. (5.2(e)) shows no clear dependence on either E_b or emission angle though all angle averaged ratios result between 10% and 80%.

The BSE peak's energy position (5.3(a)1) looks as though some structure exists against emission angle (e.g. E_b = 500 eV and 900 eV), though the reason for this is not clear. The BSE peak's intensity (5.3(a)2) is dependent on emission angle where the two parameter Rutherford fits are provided to explain the intensity quite well. E_b = 1200 eV is observed to have the greatest intensities for 17° C to 30° CC while E_b = 900 eV is observed to have the greatest intensities for 38° CC to 76° CC. Intensities for E_b = 500 eV are greater than intensities for E_b = 600 eV. The reasoning behind these last two observations is not well understood. The ratio of the BSE peak intensity to elastic peak intensity (5.3(b)) shows that with respect to emission angle, the BSE intensity does not fall off as fast as the elastic peak intensity. The anomalous values for the E_b = 600 eV do not compare with the other E_b and are not well understood.

The BSE yield maximum values shifts from E_b ~ 1500 eV using the customary boundary (50 eV) (5.3(c)1) towards E_b = 1200 eV using E_{min} as a boundary (5.3(c)2). The ratio of the elastic yield (measured using 0.1 eV resolution) to the BSE yield (measured using the 10 eV resolution) calculated using E_{min} (5.3(c)3), is a minimum at E_b ~ 1500 eV. The ratio of the BSE yield to the total yield ratio (5.3(c)4) always

measure less than 40%. Angle integrated BSE yields (5.3(c)5) are calculated using the customary boundary (50 eV) and E_{min}. These yields compare fairly well with those using the hemispherical retarding field analyzer technique (Fatman chamber) where only the customary boundary is used.

The SE peak's energy position (5.4(a)1) appears to have no angular dependence using 10 eV resolution, but does show a small angular dependence using the 0.1 eV resolution.

The SE peak intensity (5.4(a)2) are compared using the 0.1 eV and 1 eV resolutions (log). The 100 eV and 500 eV intensities are off by an order of magnitude for these two different resolutions. The FWHM of the SE peak (5.4(a)3) (E_b = 2500 eV) measures 4.5 eV to 5.4 eV with increasing emission angle. As E_b increases, the FWHM decreases linearly from 7 eV to 4.5 eV. The SE yield values (5.4(b)) are calculated using the customary boundary (50 eV) (5.4(b)1) and using the E_{min} boundary (5.4(b)2). The ratio of the SE yield to the total yield (5.4(b)3) vary in range from 60% (E_b = 2000 eV) to 95% (E_b = 700 eV). These ratios, when added to the BSE yield to the total yield ratios, equal 1. Finer resolution yields (5.4(b)4) are provided using the 1 eV and 0.1 eV resolutions to energies 50 eV and 20 eV, respectively. Though the shapes of the peaks provide qualitative information, only the integrated yield of the former compares well to the SE yield using the 10 eV resolution. Angle integrated SE yields (5.4(b)5) are comparable to those taken with the Fatman chamber on identical sample material. The fine angle resolved SE yield distributions (5.4(c)) are measured for E_b = 900 eV and are compared with the theoretical cross sections predicted for three different production mechanisms using aluminum. Though the materials are different, these are the only (easiest) theoretical calculations in the literature. The electron-core production mechanism (200 eV on Al) appears to look most like the Au data.

The Auger peaks (5.4(d)) present in the data are comparable to other sources. A closer look at the Auger signatures suggest that E_{min}'s angular dependence for E_b = 2500 eV occurs as a direct effect of the Auger energy exchange mechanism.

The transition energies (5.5) between the SE and BSE peaks, E_{min}, between the elastic and plasmon peaks, $E_{el\text{-}pl}$, and between the elastic and BSE peaks, $E_{el\text{-}BSE}$, are investigated. There ia a

dependence of E_{min} on E_b (5.5(a)1a). The dependence does not seem to be a simple (linear) one, but rather, more complex (parabola) when observed as a ratio of E_{min} to E_b. Probing for dependence of E_{min} on emission angle (5.5(a)1b) suggests the "turning on" of a completely different energy exchange mechanism (Auger process) having very prominent signature for E_b's >= 1200 eV. The dependence of the intensity of $dN(E_{min})/dE$ on E_b (5.5(a)2) is shown by fitting the isotropic parameter, $B\pi(\theta = 0)$ of $dN(E_{min})/dE$ vs. emission angle on E_b. The trend of E_b's dependence on $dN(E_{min})/dE$'s isotropic parameter is not entirely clear, but linearly decreases with increasing E_b. Elastic—plasmon (5.5(b)1) and Elastic—BSE (5.5(c)1) transition energies show questionable, if any, dependence on either emission angle or E_b, but their intensities (5.5(b)2 and 5.5(c)2) both depict clear dependence on emission angle.

The E_b R Total yield (5.6) using the coarse angular resolution show that E_b = 700 eV has the greatest total yields from 14° CC to 46° CC and E_b = 1200 eV has the greatest total yields from 53° CC to 76° CC. AR total yield (5.7) using the finest angular resolutions show that E_b = 900 eV has the greatest total yields. The angle integrated total yields (5.8) are very comparable to those measured in the Fatman chamber. The coarse angle integrated total yields (5.6) are all larger than the fine angle integrated total yields (5.7). Though both of these lie in the ballpark, the reason for the discrepancy it is not well understood.

The most relevant result in this study involves the determination of an emitted electron in terms of it origin. The production mechanism of a detected electron is not well described by its energy though a better distinguishing characteristic is made than one used habitually. The overcounted SE's and undercounted BSE's (5.9) using the customary 50 eV demarcation is clearly shown by comparison to the counts using the transition between the SE and BSE peaks, E_{min}.

CHAPTER 6

Discussion and Conclusion

This study set out to determine which electrons could be measured with a rotatable retarding field analyzer Faraday Cup detector (RD) that is capable of energy- and angle- resolved (EAR) measurements. Diagnostic information has been used to determine the quality of the data taken after implementing current instrument updates. While comparing diagnostic data before and after current updates of the instrument, it has been discovered that absolute spectral measurement and corresponding extracted secondary electron (SE), backscattered electron (BSE), plasmon, and elastic yields are now quite similar to those of other experiments [Fatman chamber]. Production mechanism information is present through observations of various scattering mechanisms (diffraction, elastic, plasmon, core level, Auger, etc.). The global nature of the data set and the ability to compare relative importance of these mechanisms from absolute nature of data is emphasized. The data then can be compared to other finer resolution data (e.g., REELS, AES, diffraction, Fatman, SE/BSE) and current quantum mechanical theory [*Rösler and Brauer, 1981*, *Granachad and Cailler, 1985*].

Using eight beam energies ranging from 100 eV to 2500 eV, spectra have been resolved at 12 different emission angles ranging from 17^{o} Clockwise to 76^{o} Counter—Clockwise and at 4 different orders of magnitude of (RD) voltage resolutions ranging from 10^{-2} eV to 10^{1} eV on clean, annealed, and sputtered polycrystalline gold. A summary of results, recommendations for further research, and concluding remarks are provided in this chapter.

6.1 Summary of Results

There have been several recommendations regarding the instrument and method given by a previous researcher [Davies, 1999] that were completed (followed up) and evaluated in this study. The evaluation of the specific newly improved characteristics of the instrument and the method performance are

listed in the next section. A summary of the most current angle- and energy- resolved (AER) results is then given to aid/support the validation of these instrument improvement and method.

6.1(a) Evaluation of the Performance of the Instrument and Method

The RD design has proven extremely effective, with an energy resolution that is much more than adequate for the intended purpose of measuring both broad and fine peak features of electrons emitted from a surface. The following instrument and method improvements are listed and referenced.

1. The presence of ambient electric fields within the chamber apparatus (CA) have been minimized with a colloidal graphite Aquadag coating. Testing of the instrument in a symmetrical arrangement (3.2.(f)) has shown that deviations in spectral measurements occur only at energies less than the SE peak energy (<2 eV).

2. The new technique of decrementing the RD bias (and ammeter) at decreasing voltages has further improved the spectral measurements by increased stabilization of the RD circuit (3.2.(f)).

3. Accurate absolute yield measurements are now possible due to increased signal-to-noise ratios, improved beam stability, and the new ability to monitor and measure the primary electron beam emission current (3.2.(d)).

4. A complete structure of acquisition and analysis programming tools using IGOR and LabVIEW has been developed and used to extract relevant information leading to trends in both broad (Auger and SE/BSE delineations) and finer energy (non-isotropic SE yield cross section) emissions (3.2.(b)).

5. New elastic peak measurements have been made using the finest (0.01 eV) of emission energy resolutions configured with a tandem RD biasing supply technique (3.2.(e)).

6. Auger electron peaks have been observed to provide *in situ* surface characterization using the RD (5.4(d)). Carbon and oxygen signatures are monitored (<1 monolayer) and compared to the cylindrical mirror analyzer (Fatman) technique on identical sample material (4.2(c) and (5.4(d)).

7. The angular resolution of the RD has been increased (0.35^{o}) by the implementation of a new stepper motor and automated controller. Thus, descriptive information regarding possible angular diffraction can be measured to high angular resolution (3.2.(a)).

Complete details of the instrumentation modifications, validation tools, and upgrade effectiveness are provided in Chapter 3.

6.1(b) Summary of Direct and Extracted Results

Acquisition of a representative set of simultaneous angle- and energy- resolved (AER) SE and BSE measurements is by far the most important achievement of this investigation. The data were used to construct AR spectra and E_bR angular distributions, which were in turn examined through extraction of key features (peaks and minimums) of dominant electron populations. Concurrently, the analysis of extracted results to date are the following:

1. Evidence strongly suggesting that SE's dominate the population of emitted electrons through energies significantly greater than 50 eV, with a strong dependence of the SE to BSE delineation, E_{min}, on incident beam energy, E_b. There is a diminishing shift in BSE yield's peak energy by hundreds of Volts (5.4(b) and 5.3(c)).

2. New indications that specific SE (and BSE) production mechanisms dominate at various incident beam energies, E_b [5.4 and 5.5] which do not support the (isotropic SE yield) predictions of the most current quantum mechanical theories [*Rösler and Brauer, 1981*, *Granachad and Cailler, 1985*].

3. Evidence supports the presence of Auger (5.4(d)), plasmon loss (5.2), and core level electron emission features. Preliminary data of E_b and angle dependence of these peaks was addressed. Observations of plasmon losses and core level excitations were also present, similar to REELS peaks observed in previous studies.

6.1(b)1 Overview of Measured Results

Three parameters, emission energy, E_e, incident energy, E_b, and emission angle, α, are varied during this investigation. All extracted statistics are provided in terms of energy spectra, E_e, the incident beam energy, E_b, and the emission angle, α. These two latter parameters provide A- E_b resolved and E_b- A resolved information that were discussed in terms of E_e spectral features [Fig. 3-37] in Chap. 5. They were specifically investigated for variances in intensity (peaks and minimum transitions) with respect to E_b and

α, which were summarized in Table 3.3. Emphasis is placed on the global nature of these resolved features establishing the immense size of the AER database.

To condense the information of this immense AER database, the investigated features have been summarized in Table 6.1, organized according to the physics of their production mechanism. The organization of these features, emphasizes the E_b and α dependence (vertical columns) of the predominant production related region (horizontal rows). References to tables and figures are provided for fast reference. Each peak and transition feature contains information about the peak (or minimum) energy location and peak (or minimum) intensity. The first three major rows (elastic, first plasmon, and BSE) correspond to features originating from the primary electron. The next two rows (SE and Auger) correspond to electrons originating from the surface of the sample. Total yields are combinations or integrations over E_b or α; coarse and fine angle resolved yields allow for comparisons to measurements using other instruments. The undercounted SE's and overcounted BSE's row demonstrates that the definition of electron origin (primarily or sample produced) can be quantitatively discussed. Lastly, the transitions (minimum features) between the peak features, given in the last three rows (E_{min}, $E_{el\text{-}pl}$, and, $E_{el\text{-}BSE}$), provide additional quantitative information useful for discussing electron origins in terms of production mechanism. Angle integrated yield intensities are provided for peak features (SE, BSE, and Total) in the last column to demonstrate the instruments angular resolving power.

This data set has the ability to compare relative importance of the theoretically predicted production mechanisms from the absolute nature of the data. The most relevant E_b and emission angle results (column's 3 and 4) are now addressed according to the physics of their origin.

Table 6.1 Summary of experimental AER data from polycrystalline Au.

Region	Item		Beam Energy		Emission Angle		Angle Integrated
	Energy	Symbol	Dependence	Reference	Dependence	Reference	
Elastic Peak	Peak energy	E_{el}	$E_{el} = E_b$ ($\pm$ 0.3eV)	Fig. 5-5, Table 5.1	None	Fig. 5-6, Table5.1	
	Peak Intensity	$dN(E_{el})/dE_e$	None	Fig. 5-7, Table 5.2	Mott(Eq5.4)	Fig. 5-8, Table 5-2	
	Integrated Intensity	σ_{el}	None	Fig. 5-12, Table 5.3	Mott(Eq5.4)	Fig. 5-10, Table 5.3	
	FWHM		Low energy HWHM increases ~80% with E_b	Fig. 5-9	None	Fig. 3-18, Table 3.1	
First Plasmon Peak	Peak energy	E_{pl}	Peak separation increases with increasing E_b, approx. linearly. $(E_b - E_{pl}) = 4$ eV - $9x10^{-4} E_b$	Fig. 5-14, Table 5.4	None	Fig. 5-13, Table 5.4	
	Peak Intensity	$dN(E_{pl})/dE_e$	None	Fig. 5-16, Table 5.5	Rutherford(Eq5.3)or Mott(Eq.5.4)	Fig. 5-15, Table 5.5	
	Integrated Intensity	σ_{pl}	None	Fig. 5-18 σ_{pl}/σ_{el}	Rutherford(Eq5.3) or Mott(Eq.5.4)	Fig. 5-17, Table 5.6	
Inelastic BSE Region	Peak energy	E_{BSE}	$(E_b - E_{BSE})/E_b$~12% with deviation roughly linearly proportional to E_b	Table 5.7	None	Fig. 5-21, Table 5.7	
	Peak Intensity	$dN(E_{BSE})/dE_e$	Falls off ~ $-(E_b - 1000\text{ eV})^2$	Table 5.9	<Rutherford(Eq5.3) Table 5.8	Fig. 5-22, Table 5.9 Fig. 5-23 (ratio)	
	Integrated Intensity	η_{BSE} (50 eV to E_b)	Falls off ~ $-(E_b - 1500\text{ eV})^2$	Fig. 5-25, Table 5.11	<Rutherford(Eq5.3) Table 5.10	Fig. 5-24, Table 5.11	Fig. 5-31
		η_{BSE} (E_{min} to E_b)	Falls off ~ $-(E_b - 1200\text{ eV})^2$	Fig. 5-27, Table 5.13 Fig. 5-28 (ratio) Fig. 5-29 (ratio)	Rutherford(Eq5.3) Table 5.12	Fig. 5-26, Table 5.13	Fig. 5-30
	Fine Structure	--	varies	Sec. 5.3(d) Fig. 5-32	varies	Sec. 5.3(d)	

SE Region	Peak energy	E_{SE}				Fig. 5-35, Table 5.14	
	Peak Intensity	$dN(E_{SE})/dE_e$		Fig. 5-38, Table 5.15	Lambert(Eq5.2)	Fig. 5-36, Fig. 5-37, Table 5.15	
	Integrated Intensity	δ_{SE} (0 to 50 eV)	Variable N	Fig. 5-41, Table 5.16	Lambert(Eq5.2)	Fig. 5-40, Table 5.16 Fig. 5-45, Fig. 5-46	Fig. 5-47
		δ_{SE} (0 to E_{min} eV)	Variable N	Fig. 5-43, Table 5.17 Fig. 5-44 (ratio)	Lambert(Eq5.2)	Fig. 5-42, Table 5-17 Fig. 5-48	
	FWHM		None	Fig. 5-36	None	Fig. 5-36	
AES Peaks	Peak energy	E_{AES}	None	None	None		
	Peak Intensity	$d^2N(E_{AES})/dE_e^2$	Not well understood		Lambert(Eq5.2)	Fig. 5-55	
Total Yields	E_bR Total Yields	$\sigma_c(\alpha; E_b)$ $\sigma_f(\alpha; E_b)$	Variable N	Fig. 5-68, Table 5.25	Lambert(Eq5.2)	Fig. 5-67, Table 5.25	Fig. 5-70
	AR Total Yields				Rutherford(Eq5.3)	Fig. 5-69	
Undercounted SE's and Overcounted BSE's Region		(50 eV to E_{min})				Fig. 5-71, Table 5.26	
E_{min} Minimum	minimum energy	E_{min}	Linear or parabolic Table 5.19	Fig. 5-59, Table 5.18	Linear due to Auger, else none	Fig. 5-58, Table 5.18	
	minimum intensity	$dN(E_{min})/dE_e$		Fig. 5-61, Table 5.20	Lambert(Eq5.2)	Fig. 5-60, Table 5.20	
$E_{el\text{-}pl}$ Minimum	minimum energy	$E_{el\text{-}pl}$	None	Table 5.21	None	Fig. 5-62, Table 5.21	
	minimum intensity	$dN(E_{el\text{-}pl})/dE_e$		Table 5.22	Rutherford(Eq5.3)	Fig. 5-63, Table 5.22	
$E_{el\text{-}BSE}$ Minimum	minimum energy	$E_{el\text{-}BSE}$	Not well understood	Fig. 5-65 Table 5.23	None	Fig. 5-64, Table 5.23	
	minimum intensity	$dN(E_{el\text{-}BSE})/dE_e$		Table 5.24	Rutherford(Eq5.3)	Fig. 5-66, Table 5.24	

6.1(b)2 (E_b, Angle) Results

Each feature (peak and transition) was presented in measurements of energy and intensity as variables of incident beam energy, E_b, and emission angle, α. Since there are many measured results, only the most significant result from each electron population feature will be addressed. Following the overview in the previous section, these results are explained according to electron origin. Therefore, primary electron origin is explained first then surface electron origin is explained followed by the combination (Total yield) and separation using transition minimums.

The elastic feature gives information that assists in determining the resolution of the instrument. The width of the elastic peak determines the thermal spread of the electron gun source. Using gaussian statistics, the standard deviation of the peak is a measure of the resolution of the instrument. Measurement of the gaussian peak width (HWHM) averages 0.35 eV (3.2(e)) using the 0.01 eV RD resolution and 0.6 eV (5.1(c)) using the 0.1 eV RD resolution. The elastic peak intensity and elastic yield show qualitative Rutherford angle dependence, but no evident E_b dependence.

The first plasmon peak, with an energy separation below the elastic peak ($E_b - E_{pl}$), increases ~linearly with E_b, is typically ~13 eV wide, and show no E_b dependence. The intensities and yields range from 5% (larger E_b) to 50% (smaller E_b) of the corresponding elastic intensities and yields, follow Mott angular intensities and yield distributions, and show no E_b dependence. Coincidentally, the plasmon peak energy for E_b = 1200 eV averages the largest separation (7.6 eV) below the elastic peak while also measuring the largest plasmon yield values in this study.

The BSE peak position and yield are not random, there is structure. Only the elastic portion of the BSE peak is observed for E_b = 100 eV spectra due to the minimum of the inelastic mean free path occurring at 100 eV [Fig. 2-1]. The energy position of the BSE yield (calculated using 50 eV) is larger than the energy position of the BSE yield (calculated using E_{min} eV). When the BSE yield is calculated using E_{min}, the energy position of the BSE yield shifts to lower energies. The BSE Yield comparing the customary

demarcation to the E_{min} demarcation has a shifted maximum from an energy of about 2000 eV (using 50 eV) towards 1200 eV (using E_{min} eV), which indicates that the BSE yield does not just increase with increasing E_b, but contains structure. This is evidence for the presence of the second cross over which overcomes the BSE yield at E_b = 2000 eV [Fig. 5-18] rather than at E_b = 1200 eV [Fig. 5-20]. In the E_{min} case, the BSE yield is always less than the SE yield. A most notable result is seen in the BSE yield. Notice that the E_b = 1200 eV beam energy increase in total yield at 46 and 53 degrees. Notice also that E_b = 1200 eV has the greatest yields and that E_b = 2500 eV generally has the least yields.

The SE region shows several important results. The intensity of the SE peak, located at 2 eV (using 0.1 RD resolution) falls off almost isotropically as a function of emission angle. The angle integrated SE yield, as a function of E_b, calculated using E_{min} has positive energy shift in E_b compared to that of the SE yield calculated using 50 eV. As a result, the 2nd crossover, where δ=1, shifts higher by tens of Volts. The angular dependence of SE yield also varies slightly from isotropic emission. This is further summarized in section 6.1(b)3 using fine angle resolution. Other deviations from the Lambert law are observed. For example, the anomalous behavior observed at large angle emission for E_b = 1200 eV shown as a larger portion of emitted SE is intriguing, but not well understood.

Auger peaks are observed for Au MNN transitions in E_b = 2000 eV and E_b = 2500 eV spectra. Though the dependence of the intensity of the spectral derivative shows Lambert law dependence on emission angle, the dependence on E_b is not well understood due to lack of data.

Total yields are resolved $\sigma(E_b; \alpha)$ and investigated for dependencies on E_b and emission angle. The area underneath the E_bR spectra (at each angle) over the entire range of the spectra (0 eV to E_b eV) provides the total E_bR angular distributions. When plotted against emission angle, there is dependence on emission angle having anomalies in the E_b = 700 eV, 900 eV, and 1200 eV distributions. These anomalies are also present in the E_bA resolved SE yields. They are not caused by diffraction or Auger effects and are not well understood.

Under-counted SE's and over-counted BSE's. In order to more precisely investigate the production mechanisms of the SE's emitted from polycrystalline Au, the local minimum, E_{min}, separating the SE and BSE peaks has been measured and used to calculated yields. The SE (δ) and BSE (η) yields show that SE's are typically *under-counted and that BSE's are over-counted* by comparison to a traditional arbitrary 50 eV demarcation boundary.

E_{min}, the local minimum demarcation is dependant on E_b and emission angle. The dependence of E_{min} on E_b is initial observed to be parabolic. The dependence of $d(E_{min})/dE$ on angle has a negative slope probably because of the Au Auger signatures observed in the E_b = 2000 eV and E_b = 2500 eV spectra. After accounting for Auger signatures at E_b = 2500 eV and inelastic mean free path minimum [Fig. 2-1] at E_b = 100 eV, the dependence of E_{min} on E_b is observed to be linear. What is known is that, at low E_b, the shifting of E_{min} is an artifact of diffraction and at high E_b, the shifting of E_{min} is an artifact of Auger effects.

$E_{el\text{-}pl}$, the transition (minimum) between the elastic and plasmon peaks (0.1 eV RD resolution) occurs at the average of about 1.9 eV below the elastic peak. The energy shows no dependence on either E_b or emission angle. The intensity shows qualitative evidence of Rutherford dependence on emission angle.

$E_{el\text{-}BSE}$, the transition (minimum) between the elastic and BSE peaks (1 eV RD resolution) show possible dependence on E_b. Though the dependence of energy on E_b is not well understood, evidence suggests that there is no dependence of energy emission angle. The intensity of this transition shows Rutherford dependence on emission angle.

6.1(b)3 Fine Angular Cross Section Results

Perhaps the most useful tool for gathering scattering information from the sample is the ability to highly resolve the angularly emitted electrons which provide (E_e', E_b') distribution cross sections. The finest angle resolved measurements have been made to test the isotropic (cosine like) behavior of secondary electron emission. Initial measurements were used to determine the angular resolution of the instrument. Though those measurements were scarce, data has been gathered to provide insightful physics.

The distributions of the total yield (Chap. 5.7) are most abundant and have been fit with a Rutherford model to show that many deviations are present. For example, the total yield, $\sigma_f(E_b = 500\ eV)$, has a minor disturbance above the fit at ~25^o and below the fit at ~40^o. These deviations are not well understood, but what is known is that they cannot be explained by angular diffraction scattering. The two major components of the total yield are the BSE yield (Chap. 5.3.(c)) [Fig. 5-31] and SE yield (Chap. 5.4.(d)) [Fig. 5-46]. These yields have been measured with direct bias of the RD at 50 eV and E_{min} eV for entire distribution scans $\eta_f(E_b = 900\ eV)$ and then subtracted from $\sigma_f(E_b = 900\ eV)$ to produce $\delta_f(E_b = 900$ eV). Residuals from the deviations in the SE yield can then be understood by production mechanism cross sections.

The integration of the fine angular distributions leads to yields that are less than those of the integration of the coarser angle resolved distribution [Fig. 5-67]. Though the reason for this is not well understood, it is apparent that the shape of the distribution is more important than the integrated yield value.

Speculation of over-counting of the transmission parameter in the transport mechanism to model the SE's should account for deviations in this emission pattern. These cross section distributions show production mechanism information which may be observable by the theorists after they reduce the elastic propagator in their simulation.

Additional data needs to be taken using the finest angle resolution. The most useful data for determining deviations of SE emission from the Lambert cosine law are those of the finest angle resolution.

6.2 Recommendations for Further Research

Further research in secondary electron emission (SEE) using energy- angle- resolved (EAR) absolute measurements is addressed to guide the researcher on pathways most likely to produce useful results. A summary of recommendations for direction toward useful studies is divided into instrument modifications, theoretical modeling, and experimental research. Though the instrument, in its current state, does not need modifications to accomplish further experimental research, implementation of the most basic upgrades would most likely be beneficial.

6.2(a) Instrument Modifications

After evaluation of the effectiveness of the modifications already made to the existing apparatus (see Sec. III.A.), one additional major modification should be considered. A new sample holder with a spherical shaped design may significantly improve the apparatus.

Evidence suggests that a substantial portion of the electric field problems noted in the AR measurements, as well as the large systematic error in the total yield measurements, is a result of poor sample arrangement. Improving the electron emission environment will provide a more accurate AER spectral measurement. Specifically, removing the primary sample from the large sample holder currently being used, removing the present sample heater and thermocouple, and eliminating the tertiary samples altogether should minimize stray fields and improve the area of vacuum where electron trajectories lie along straight paths. While the loss of annealing capability is not preferable, ion sputtering should maintain the ability to produce a clean surface. Ideally, the new design should include a scheme for annealing the sample as well as measuring its temperature. This could be accomplished by use of non-contact electron bombardment heating and IR pyrometer temperature measurements. Regarding the tertiary samples, ancillary measurements indicate that the return current to the primary sample, even under conditions of positive bias, is not as significant as once thought [LBIII, p. 81y]—eliminating the need for the tertiary samples. Finally, reorienting the sample vertically and mounting the electron gun and RD in the horizontal plane will allow for all AR measurements to be made for a single azimuthal angle.

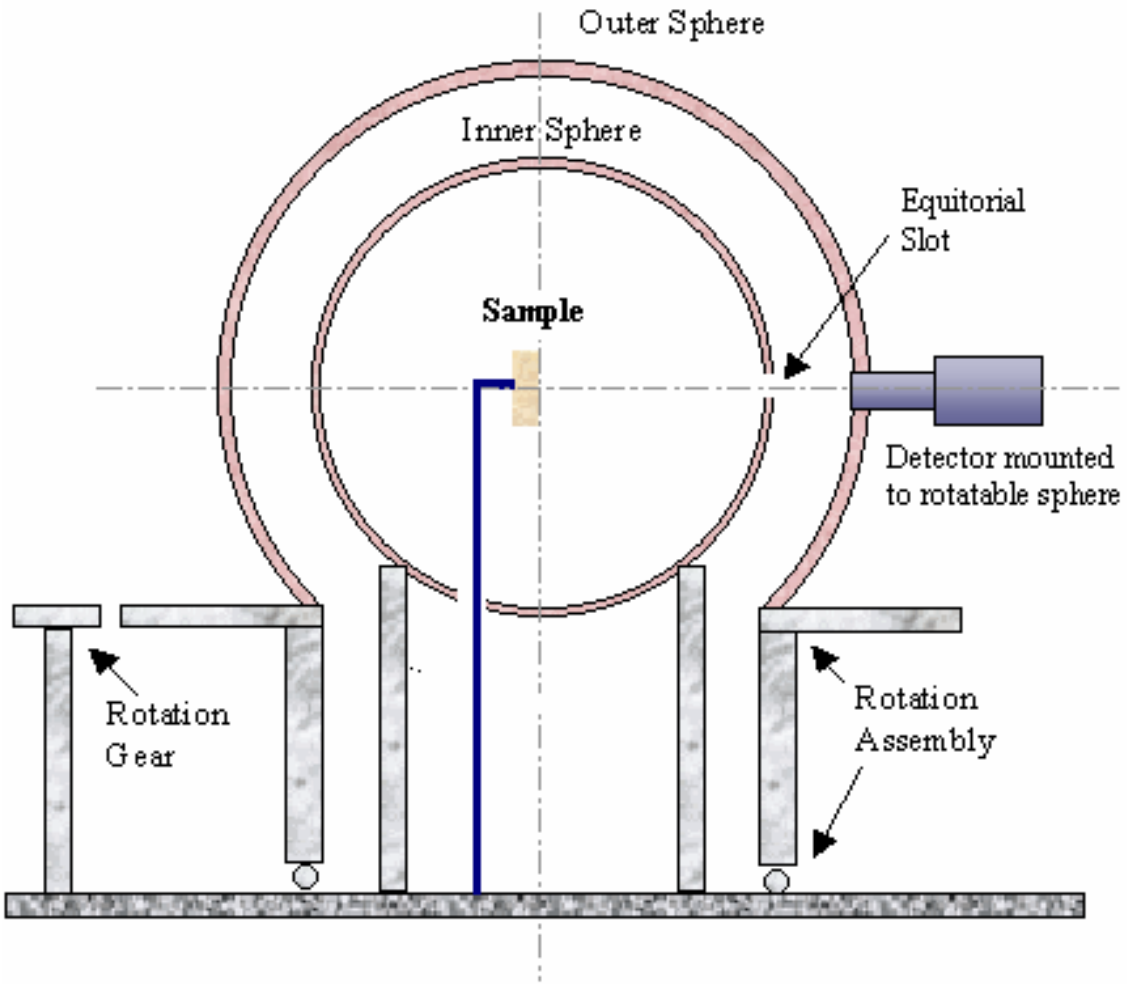

Figure 6-1 Schematic depicting double-sphere design for measurement of angle-resolved SE spectra. [*Davies, 1999, p. 173*]

A new spherical design of the sample stage similar to that of Jonker [1951] should be implemented [Fig. 6-1]. In the Jonker design, the sample is located at the center of two concentric conducting spheres. The inner sphere and sample are held at ground, creating a field free region inside the inner sphere, while the outer sphere and attached detector rotate in the horizontal plane about the sample. The outer sphere can be biased as desired, and the resulting electrostatic field in the region between the two spheres is ideally radial. Each sphere has a slot running about the equator—to allow for the escape of SE's and BSE's in the case of the inner sphere, and to allow primary beam access to the sample in the case of the outer sphere. The interior of both spheres is coated with colloidal graphite (Aquadag) to prevent surface charging, reduce tertiary SE production, and provide for a uniform work function. Total yield determination with this scheme may be possible through some sort of biasing scheme for the sample and inner sphere.

Several variations of the double sphere design are also possible. First, one could likely eliminate the inner sphere altogether without serious affect: it is the field-free aspect of the design that is most important, and removing the inner sphere while grounding the outer sphere preserves this quality. Replacing the spheres with cylinders (single or double) is a second option, and such a design may prove easier to fabricate [*Reimer, 1977*].

As presented here, the single or double sphere (or cylinder) design leaves a number of important details un-addressed. Beam current measurement, total yield determination, ion beam access for sputtering, and sample heating are a few examples of additional considerations. This will require an additional overhaul of the apparatus.

A number of more minor suggestions that could improve the instrument are listed below. These are considerably easier to implement.

1. The quality of the electron beam current monitor can be improved to enhance the signal-to-noise ratio of the yield measurement. There is some sort of "weird" cross talk causing noise in the detector signal [Fig. 3-12]. Improving the beam current signal will increase the signal-

to-noise ratio. Alleviating the prominent noise should improve the analysis technique so that a number less than L=220, in Eq. 3.12, further minimizes the drift of the $V_{controller}$ signal. Ideally, this number should be L = 1. Floating the electron gun beam current monitor to the electron beam energy will probably further stabilize the circuit by the elimination of ground loops. This modification will require an additional isolation amplifier to bring the $V_{controller}$ output signal to ground for input to the data acquisition card (DAQ2000) and may require complete removal of the front panel display analog ammeter (and circuit). At this time, it would probably be easiest to also modify the front panel display of the gun controller by installation of the new digital voltmeter.

2. The beam current monitor can be improved with another modification. Further AER measurements may be improved by feedback of the ion pump output signal into the $V_{controller}$ signal via an operational amplifier. This modification most likely will require floating the ion pump signal to the incident beam energy. However, a new fused filament circuit should probably be added in succession with the operational amplifier to protect the filament from current surges due to vacuum chamber outgassing. Diagnostics of this circuit can be monitored with the existing Tertiary samples. The Ion pump/electron beam feedback circuit should be compared to the RD current circuit because they are both floating at different voltages. Letting L go to unity in Eq. 3.6c (e.g., $\langle I_s/I_b \rangle_{L=1} * I_{RD}/I_s$ is calculated at every data point), would no longer require sample current monitoring. This would ultimately eliminate any need for grounding the sample. Additional complications may arise with charging of the sample.
3. The reliability and accuracy of the angular motion control can be improved. The RD cable that transfers rotational motion from outside the chamber apparatus (CA) to inside the CA is prone to damage. When damaged, a “flopping” of the RD angular setting makes the angular resolved data appear to have bumps [Fig. D-1] at every revolution of the RD cable. The RD

cable makes a 90^{o} flex from the chamber feedthrough to the apparatus bottom plate. The newly installed steppermotor revolves the RD cable with more than enough torsional torque. The RD cable can become torsionally damaged when the RD is forcibly stopped by a support post that holds the chamber apparatus together (3.1(c)). In order to prohibit further damage, software could be included to provide limits to the RD motion. LabVIEW software has already been used to record each change in position of the steppermotor in the file "RDangle.txt". The locations of the support posts could be included in the software or a separate triggering limit switch within the chamber could be arranged to stop the steppermotor when contact is made with a post. The LabVIEW program DetermineZeroAngle.pxp (C-2(c)) is very useful because it is able to resolve the RD setting at the finest angular resolution of $1/20^{th\ o}$, however, the Tick Multiplier can easily cause the steppermotor to cause further damage to the RD cable. Note: A new replacement for the damaged cable requires a complete removal of the CA.

4. Automated data acquisition can be improved by complete control of the beam detector bias. The enhancement may also eliminate the present difficulty from discontinuities in the RD signal baseline which require the need for the differentiation/integration step in the data processing. The Bertan Voltage supply is not yet automated and is hence the weakest link in computer controlled data acquisition. It could be automated possibly, except that it floats above the Keithley, because the Keithley needs to be grounded in order to be GPIB controlled. The possibility of introducing an additional ground loop problem via GPIB control of the Bertan is not known. Diagnosing a possible problem by measurement of the jitter, the ripple, or signal-to-noise ratio of the floating Bertan is also not clear. Our easy way to do this is with an optoisolated GPIB interface, now commercially available. Alternately, the Bertan could be programmed with 0 – 10 V analog signal from a high resolution (16-bit) DAC card, that has been isolated from ground using an isolation amplifier or an optoisolator.

5. Installation of a new or improved electron gun potentially will offer many improvements to the system. It may extend the incident energy range, provide more precise yields by having a more stable beam current, improve the energy resolution by reducing the incident beam thermal spread, or minimize sample contamination by allowing stable operation at lower beam currents. For lower incident beam energy measurements (<100 eV) a new electron gun design will be required. In order to obtain low emission currents on the order of nanoamperes, a different cathode—anode and electronic circuit design will be needed to efficiently and effectively produce low energy incident electrons without severe degradation to the filament. Recognition of the largest FWHM of the elastic peak (Chapter 5.1) for the lowest incident beam energy, E_b = 100 eV, indicates that the filament degraded due to such high filament current. Installation of a Lanthanum hexaboride (LaB_6) filament would reduce the thermal spread in the incident electron beam (now larger than the detector energy resolution). LaB_6 cathodes provide higher current densities that operate at a much lower temperature due to a lower operational work function and greater emissivity than tungsten. This will primarily extend the incident energy range, but will also stabilize the emitted beam current providing higher precision spectral measurements and improve the EAR instrument resolution by reducing the incident beam thermal spread.
6. The installation of a new high resolution Faraday cup detector will most probably improve the resolution of the EAR spectral data [Fig. 6-2]. This smaller detector has already been designed and constructed [*Ford, 2000*] to incorporate the shield as a second aperture. Installation can take place without the implementing the spherical design. The energy resolution of the detector has been calculated from geometry alone to be 0.05%. Using

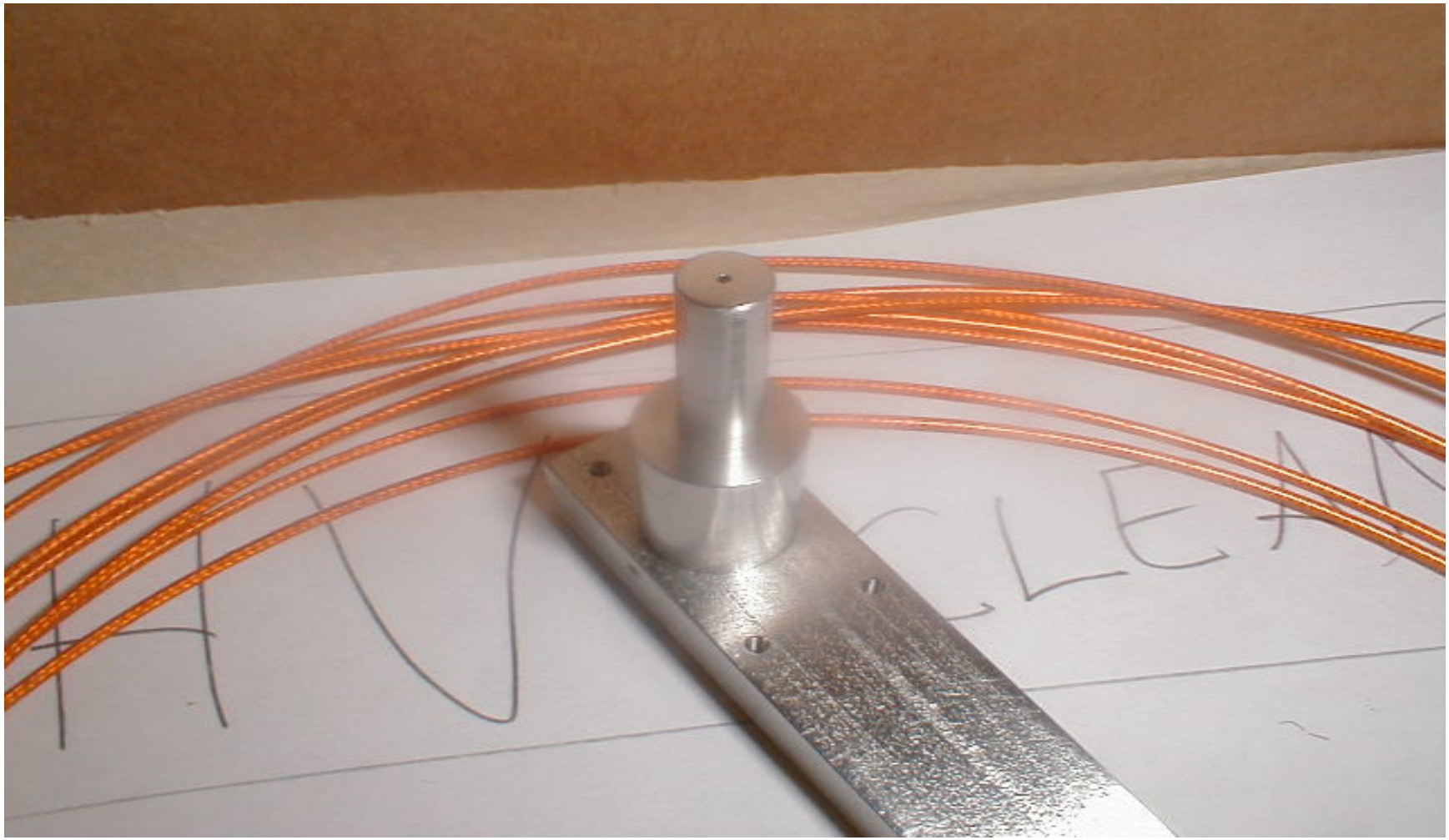

Figure 6-2 High resolution faraday cup charged particle spectrometer [*Ford, 2000*].

electron trajectory simulation software (SIMION), the energy of the detector is estimated to be better than 0.1%.

7. Incorporating a vapor deposition device [*Thomas and Pattinson, 1970*] would enhance the instruments capability to measure other materials. Sample materials that gather contamination quickly (e.g., Na) or vaporize (e.g., Sn) under UHV need *in situ* preparation capabilities.
8. Additional improvements that might also be considered include a separate sample characterization scheme (e.g., AES) would increase the quality of the EAR spectra. Including a cylindrical mirror analyzer is impractical due to special constraints, but since evidence of Auger signatures (5.4(d)) are confirmed, one might consider some sort of lock-in scheme for the RD signal (or sample signal) like that used for most conventional AES detection systems.
9. Installation of a faster DAC card and implementing a LabVIEW upgrade will increase count rates and enhance the ability to make new measurements (Appendix C) required by additional monitored signal channels.

Provide lists of these modifications in order of ease to do and in order that I would suggest they should most profitably be done. Which ones are mandatory to proceed to tasks outlined in 6.2(c).

6.2(b) Theoretical Modeling

After a few minor instrumentation improvements, such as fixing the bent RD cable and upgrading the tandem RD biasing supply, it seems evident that the absolute spectral measurements could be tested against the most current quantum mechanical theory involving the three step process of production, transmission, and emission of a secondary electron from a simply defined polycrystalline metal. The electronic properties change at the region of the phase boundary between the vacuum and the solid phase of the material making it possible to extract the production mechanism properties of the solid via emission properties of the vacuum. The proposed quantum transitions, based on energy excitation and decay, link

the electric dispersion relations (e.g., dielectric function) to the specific material under observation. Following this material dependent logic, it is essential to approximate the electric properties of the material. The appropriate approximations used for the Au dielectric function are (i) the Thomas-Fermi model, (ii) the random phase approximation (RPA), (iii) and an unscreened interaction. For high energies (E_b > 100 eV), scattering due to screening is "taken over" by scattering due to plasmon interaction because of the larger frequency argument in the dielectric function [*Rösler and Brauer, 1981b*].

Determination of the amounts of each of the three predominant production mechanisms (excitation of valence electrons, core electrons, and plasmon decay) is accomplished by propagating each mechanism to the surface (transport) using the Boltzmann transport equation and/or Monte Carlo techniques and comparing to the E_bAR distributions provided in this study. Following this model structure, comparisons to possibly both Boltzmann and Monte Carlo type simulations should initially be made with the finest angular resolved distributions presented in this study. Building each type of simulation involves mathematically understand the energy exchange propagators (exciton and plasmon) and the inelastic production mechanisms. It may be beneficial to incorporate each of the scattering equations from Rösler and Brauer individually into a Monte Carlo simulation just as Rösler and Brauer did by evolving by Boltzmann transport equation and independent mean free path equations. Each production mechanism could then be simulated separately, using respective cross section information and comparing with the fine angular distributions. Deviations from isotropic emissions should be clearly recognized.

Comparison to the Monte Carlo simulation where the mean free path is replaced by randomly choosing solid angles from cross sections taken from Rösler and Brauer would lead to the amount of over emphasis simulated by their elastic mean free path. Ultimately, the transmission of a scattering event would not depend on the mechanism by which it was produced there-by equating the definition of an emitted electron with that of a produced electron.

In addition to the fine angle distributions, the coarse angle distributions can be qualitatively used for comparing to simulations. Choosing to compare with the SE yield distributions of E_b = 500 eV, 900

eV, and 1200 eV emphasizes the greatest deviations from isotropic in the E_bAR data. Comparisons with the coarse angular distributions follow directly as with comparisons to the fine angular resolution.

At this point, it may be necessary to adjust the AER data set slightly with the factor L (Eq. 3.6(c)) by subtraction of major harmonics in coincidence of [Fig. 3-12] by those in $\langle I_s/I_b \rangle_{L=1}$, using the Fourier transforms of their error [Fig. 3-39] (Eq. 3.12(C)).

6.2(c) Experimental Research

A number of possible experimental studies present themselves as the most immediate and most logical next steps. These are presented here in the order that I suggest they be studied.

I suggest a comparative study of the Ag AER spectra with Au results presented in this thesis as a way to test the relative affects of the core electron production mechanism on SEE. This explains my favor as the next step and why it should be a relatively "clean" experiment focusing mostly on core level effects.

A complementary set of AER cross section measurements at a range of incident energies for polycrystalline Ag should be measured. The prominent candidates (Al, Ag and Cu) are challenging in that they acquire chemisorbed contaminants on the surface. Depending on whether the chemisorbed oxide that forms on the surface is more tightly bound or is more conductive (Cu) than another candidate should additionally diagnose *in situ* cleaning (annealing) procedures. Ag is chosen for the comparative study as it is very similar to Au in structure, lattice constant, binding energy, band structure [*Ashcroft, 1976, p. 305*], "second crossover" ($E(\delta=1)$), E_{max}, and corresponding maximum SE yield, but lacks a full f-shell as found in Au. Comparing the cross sections of these two metals with one another should provide information about the core electron production mechanism. Since Au and Ag both lack one electron from having an outer full d-shell, the excitation by decay of plasmons (mainly due to interband transitions near the surface) will have approximately similar plasmon damping and excitation functions [*Citrin, 1978*]. In addition, the core electron production mechanism can be isolated from the transport mechanism since the inelastic mean

free path as a function of electron energy for electrons traversing Au and Ag are approximately the same [*Lindau, 1974*].

Acquisition of AER measurements for polycrystalline aluminum. Data for additional materials should be acquired for comparison with gold, and since specific, detailed theoretical calculations have been made for SEE from aluminum (*e.g.*, *Rösler and Brauer* [*1981b*] and *Ganachaud and Cailler* [*1979b*]), aluminum seems the logical choice for the next material investigated. The largest hindrance with Al is the chemisorbed contaminant, Al_2O_3, which forms largely as a result of electron stimulated adsorption. Once data for Al have been acquired, detailed comparison with the theories of *Rösler and Brauer* [1981a, 1981b], *Jablonski* [1991], *Jablonski et al.* [1993, 1989], *Gryzínski* [1965], and *Michaud and Sanche* [1984] should be attempted. Such analysis will involve examination of fine structure in the SE peak and quasi-elastic cross section, as well as an attempt to account for the observed ER angular behavior over the entire range of emission energies. The spectra are not fit here because the feedback parameters are not known. The only parameter worth using to adjust the factor L in Eq. (3.12c) is by using the parameter of the $V_{controller}$ versus the I_b (sample FC) parameter because of the weird jitter [Fig. 3-12].

Acquisition of high RD resolution spectra for plasmon energy losses. Fine structure due to plasmon excitations—referred to as energy loss peaks—are well-documented features found near the elastic peak [*Reimer*, 1993]. Fine structure attributed to plasmon decay has been observed in integrated SE spectra, near the SE peak, for polycrystalline Au (5.2). The first plasmon peak is observed using the 0.1 eV resolution as a non-symmetric shape. Since the low energy boundary of the peak is not well defined, no fits were provided. Observations of both E_b and angle dependence of these peaks needs to be more carefully investigated. Using the 0.01 eV resolution, spectra could be measured to the lower energy boundary to deduce the E_b and angle dependence of the plasmon linewidths and intensities. The analysis technique would most likely involve de-convolution of the incident electron beam spread (elastic peak).

The ability to compare amounts of various mechanisms due to absolute nature of measurements is evident. The understanding of these signatures in the data for elementary electron excitations or "single

scattering events" will help determine the extent to which the amount of randomization has been made in the Monte Carlo simulations. This is accomplished by measuring ratios of intensities to the elastic peak.

Angular resolution in the Auger signatures would provide additional information not available using the Fatman chamber [*Kite, 2006*]. Similar studies can be done with broad peaks such as those found in the MNN Au Auger peaks.

Contamination studies. As thicker and thicker contaminant layers are deposited, SE and BSE production is affected at greater and greater depths within the surface. Examining the AR yields of various energy populations—obtained from AR spectra—as a function of contamination depth may prove beneficial for understanding details of SE and BSE transport. These are follow-up studies to the previous studies of $C/Al_2O_3/Al$ [*Davies, 1996*] and C/Au [*Chang et. al., 2000*].

Au Negative sample biasing. Since SE's originate within the sample, SE energies—as measured by the detector—are affected by sample bias, while BSE energies are not [*Thomson, 2005*]. Examining spectra taken under varying conditions of negative sample bias, therefore, may prove useful in identifying true secondaries, complementing the AER data. Though Fatman data are not angle resolved, preliminary measurements taken in the Fatman chamber have demonstrated this technique [*Abbott,2006, and Dennison, 2006*].

Thus, it is strongly recommended that additional means of organizing and displaying the extensive AER data set presented in this study be actively explored. One example that immediately comes to mind is looking at normalized AR spectra, analogous to the normalized angular distributions of Chap. 5.

6.3 Concluding Remarks

This investigation began approximately seven years ago with the initial goal of acquiring AER SE measurements for conductors, for the somewhat vague reason that there did not seem to be any such measurements in the literature. Throughout the data acquisition process, and even much of the analysis, focus remained primarily on the low-energy (< 50 eV) population. Eventually, however, it was realized that the data were rich with new information throughout the entire range of energies investigated. Detailed analysis has been accomplished for some of the data—much of it pertaining to instrument evaluation. Analysis for much more of the data has been accomplished to varying degrees—some only just begun. It may seem that much of the analysis presented is incomplete, and that is correct. Nevertheless, such analysis has been included in the hope of stimulating further work. Physics is an incremental process, and the acquisition of such a large, rich, and painstakingly analyzed data set appears to be a big increment.

References

Appelt, G., Fine structure measurements in the energy angular distribution of secondary electrons from a (110) face of copper, *Phys. Stat. Sol., 27*, 657-669, 1968.

Austin, L., and H. Starke, Uber die reflexion der kathodenstrahlen und eine damit verbundene neue erscheinung secundärer emission, *Ann. Physic, 9*, 271-293, 1902.

Barber, K.J., F.C. Frank, M. Moss, J.W. Steeds, and I.S.T. Tsong, Prediction of ion-bombarded surface topographies using Frank's kinematic theory of crystal dissolution, *J. Mat. Sci., 8*, 1030-1040, 1973.

Baroody, E.M., A theory of secondary electron emission from metals, *Phys. Rev., 78, 6*, 780-787, 1950.

Barut, A.O., The mechanism of secondary electron emission, *Phys. Rev., 93, 5*, 981-984, 1954.

Bennett, A.J., and L.M. Roth, Effect of primary-electron diffusion on secondary-electron emission, *Phys. Rev. B, 5, 11*, 4309-4324, 1972.

Bishop, H.E., Electron scattering in thick targets, *Brit. J. Appl. Phys., 18*, 703-715, 1967.

Bruining, H., *Secondary electron emission*, 178 pp., McGraw-Hill, New York, NY, 1954.

Bunney, R.E., Secondary electron emission, *Tech. Rep. NASA CR 54366*, 94pp., NASA Lewis Research Center, Cleveland, OH, 1965.

Chang, W.Y., N. Nickles, R.E. Davies, and J.R. Dennison, Utah State University ground-based test facility for study of electronic properties of spacecraft materials, *Proceedings of the Sixth International Spacecraft Charging Conference*, edited by D. Cooke, Boston, MA (in press), 1999.

Chung, M.S., and T.E. Everhart, Simple calculation of energy distribution of low-energy secondary electrons emitted from metals under electron bombardment, *J. Appl. Phys, 45*, 2, 707-709, 1974.

Citrin, P.H., G.K. Wertheim, and Y. Baer, Core-level binding energy and density of states from the surface atoms of gold, *Phys. Rev. Letters, 41, 20*, 1425-1428, 1978.

Clerc, S., John R. Dennison, Ryan Hoffmann, Johnathan Abbott, On the Computation of Secondary Electron Emission Models, received December 1, 2005.

Cosslett, V.E., and R.N. Thomas, Multiple scattering of 5-30 keV electrons in evaporated metal films II: Range-energy relations, *Brit. J. Appl. Phys., 15*, 1283-1300, 1964.

CRC, *Handbook of Chemistry and Physics, 59th edit.*, edited by R.C. Weast, p. E-349, CRC Press, Boca Raton, FL, 1979.

Daniels, J., Festenburg, C., Raether, C., and Zeppenfield, K., "Tracts in Modern Physics," Vol. 54 (Berlin; Springer) p.77.

Darlínski, A., Measurements of angular distribution of the backscattered electrons in the energy range of 5-30 keV, *Phys. stat. sol. (a), 63*, 663-668, 1981.

Davies, R.E., Measurement of Angle-Resolved Secondary Electron Spectra, Doctoral Dissertation, Dept. of Physics, Utah State Univ., Logan, UT, 1999.

Davies, R.E., and J.R. Dennison, Evolution of secondary electron emission characteristics of spacecraft surfaces, *J. Spacecraft Rockets, 34, 4*, 571-574, 1997.

Davies, R.E., An instrument for experimental secondary electron emission investigations, with application to the spacecraft charging problem, M.S. Thesis, 220 pp., May, 1996.

Dekker, A.J., Secondary electron emission, Solid *State Phys., 6*, 251-311, 1958.

Dekker, A.J., and A. van der Ziel, Theory of the production of secondary electrons in solids, *Phys. Rev., 86, 5*, 755-760, 1952.

Dionne, G.F., Origin of secondary-electron-emission yield-curve parameters, *J. Appl. Phys., 46, 8*, 3347-3351, 1975.

Dionne, G.F., Effects of secondary electron scattering on secondary emission yield curves, *J. Appl. Phys., 44, 12*, 5361-5364, 1973.

Drescher, H., L. Reimer, and H. Seidel, Backscattering and secondary electron emission of 10-100 keV electrons and correlations to scanning electron microscopy, *Z. f. Angew. Physik, 29, 6*, 331-336, 1970.

Doniach, S., and Sunjic, M., *Journal of Phys., Solid State Phys., 3*, 285, 1970.

Everhart, T.E., N. Saeki, R. Shimizu, and T. Koshikawa, Measurement of structure in the energy distribution of slow secondary electrons from aluminum, *J. Appl. Phys., 47, 7*, 2941-2945, 1976.

Farnsworth, H.E., Electronic bombardment of metal surfaces, *Phys. Rev., 25*, 41-57, 1925.

Fenno, Charlotte A., Seagate Technologies, Longmont Co., private communication, 1998.

Fröhlich, H., Theorie der sekundärelektronenemission aus metallen, *Ann. der Phys., 5, 13*, 229-248, 1932.

Ganachaud, J.P., and M. Cailler, A monte-carlo calculation of the secondary electron emission of normal metals I. The model, *Surf. Sci., 83*, 498-518, 1979.

Ganachaud, J.P., and M. Cailler, A monte-carlo calculation of the secondary electron emission of normal metals II. Results for aluminum, *Surf. Sci., 83*, 519-530, 1979.

Gérard, P., J.L. Balladore, H. Pinna, A. Ouabbou, and J.P. Martinez, Systéme de mesure de l'énergie d'électrons rétrodiffusés en fonction de l'angle d'émission, *J. Phys. III France, 2*, 1015-1027, 1992.

Gruzin, P.L., Y.V. Petrikin, and A.M. Rodin, Measureing spectral angular distributions of backscattered electrons, *Sov. J. At. Energ., 33*, 779-781, 1972.

Gryzínski, M., Classical theory of atomic collisions. I. Theory of inelastic collisions, *Phys. Rev., 138, 2A*, A336-A358, 1965.

Hölzl, J., and F.K. Schulte, Work Function of Metals, in *Solid Surface Physics, Vol. 85*, pp. 1-150, Springer-Verlag, New York, 1979

Henrich, V.E., Role of bulk and surface plasmons in the emission of slow secondary electrons: Polycrystalline aluminum, *Phys. Rev. B, 7, 8*, 3512-35-19, 1973.

Hillier, J., On the investigation of specimen contamination in the electron microscope, J. Appl. Phys., 19, 226-230, 1948.

Hohn, F.J., M. Kindt, H. Niedrig, and B. Stuth, Electron backscattering by thin top layers on bulk materials, *Optik, 46*, 491-500, 1976.

Holliday, J.E., and E.J. Sternglass, Backscattering of 5-20 keV electrons from insulators and metals, *J. Appl. Phys., 28, 10*, 1189-1193, 1957.

Jablonski, A., C. Jansson, and S. Tougaard, Elastic electron backscattering from surfaces: Prediction of maximum intensity, *Phys. Rev. B, 47, 12*, 7420-7430, 1993.

Jablonski, A., Elastic electron backscatteing from gold," *Phys. Rev. B, 43, 10*, 7546-7554, 1991.

Jablonski, A., J. Kraaer, and S. Tougaard, Elastic electron backscattering from surfaces, *Phys. Rev. B, 39, 1*, 61-71, 1993.

Jahrreiss, H., and W. Oppel, Angular distributions of secondary electrons originating from thin films of different metals in re-emission and transmission, *J. Vac. Sci. Tech., 9, 1*, 173-176.

Jonker, J.L.H., The angular distribution of the secondary electrons of nickel, *Philips Res. Rep. 6*, 372-387, 1951.

Joy, D.C, A model for calculating secondary and backscattered electron yields, *J. Micro., 147*, 51-64, 1987

Kanter, H., Energy dissipation and secondary electron emission in solids, *Phys. Rev., 121, 3*, 677-681, 1961.

Kanter, H., Zur Rückstreuung von Elektronen im Energiebereich von 10 bis 100 keV, *Ann. Phys., 6, 20*, 144-166, 1957.

Kittel, C., *Introduction to Solid State Physics*, p. 560, John Wiley & Sons, Inc., New York, 1996.

Kollath, R., Sekundärelektronen-emission fester körper bei bestrahlung mit electronen, in *Encyclopedia of Physics, Vol. 21*, Springer, Berlin, 1956.

Krane, K.J., Dispersion and damping of volume plasmons in polycrystalline aluminum and indium, *J. Phys. F: Metal Phys., 8, 10*, 2133-2137, 1978.

Lerio J., Minni E., and Suoninen E., "Study of plasmon structure in XPS spectra of silver and gold," *J. Phys. F: Metal Phys. 13*, 215-221, 1983.

Lye, R.B., and A.J. Dekker, Theory of secondary emission, *Phys. Rev., 107, 44*, 977-981, 1957.

Massoumi, G.R., W.N. Lennard, H.H. Jorch, and P.J. Schultz, Backscattering of 35 keV electrons from thick targets, *AIP Conf. Proc*., 39-43, 1990.

McKay, K.G., Secondary electron emission, in *Advances in Electronics*, edited by L. Marton, pp. 65-130, Academic Press, New York, NY, 1948.

Meyer-Arendt, J.R., *Introduction to Classical and Modern Optics* (2 ed.), p. 383, Prentice-Hall, Englewood Cliffs, New Jersey, 1984

Michaud, M., and L. Sanche, Interaction of low-energy electrons(1-30 eV) with condensed molecules: I. Multiple scattering theory, *Phys. Rev. B, 30, 10,* 6067-6077, 1984.

Neubert, G., and S. Rogaschewski, Backscattering coefficient measurements of 15 to 60 keV electrons for solids at various angles of incidence, *phys. stat. sol. (a),* 59, 35, 35-41, 1980.

Nickles, N., R.E. Davies, and J.R. Dennison, Application of secondary electron energy and angular distributions to spacecraft charging, *Proceedings of the Sixth International Spacecraft Charging Conference*, edited by D. Cooke, Boston, MA (in press), 1999.

Niedrig, H., Electron backscattering from thin films, *J. Appl. Phys., 53, 4*, R15-R9, 1982.

Ono, S., and K. Kanaya, The energy dependence of secondary emission based on the range-energy retardation power formula, *J. Phys. D: Appl. Phys*., 12, 619-632, 1979.

Oppel, W., and H. Jahreiss, Angular distribution measurements of secondary electrons from thin self supporting Al and Au films, *Z. Physik, 252*, 107-117, 1972.

Peeters, F., E.R. Puckrin, and A.J. Slavin, Angular dependence of the secondary electron emission crystal current: Effects of surface modification, J. Vac. Sci. Technol.: A8, 797-799, 1989.

Powell, B.D., and D.P. Woodruff, Plasmon effects in electron energy loss and gain spectra in aluminum, *Surf. Sci., 33*, 437-444, 1972.

Powell, C.J., and A. Jablonski, *NIST Electron Inelastic-Mean-Free-Path Database* – Version 1.1, National Institute of Standards and Technology, Gaithersburg, MD (2000).

Pillon, J., D. Roptin, and M. Cailler, Secondary electron emission from aluminum, *Surf. Sci., 59,* 741-748, 1976.

Quinn, J.J., Range of excited electrons in metals, *Phys. Rev., 126*, 1453, 1962.

Ramsier, R.D., and J.T. Yates, Jr., Electron-stimulated desorption: Principles and applications, *Surf. Sci. Rep., 12,* 243-378, 1990.

Reimer, L., *Image Formation in low-voltage scanning electron microscopy*, 144 pp., SPIE, Bellingham, WA, 1993.

Reimer, L., and D. Stelter, FORTRAN 77 Monte-Carlo program for minicomputers using Mott cross-sections, *Scanning, 8*, 265-277, 1986.

Reimer, L., *Scanning Electron Microscopy*, p. 17, Springer-Verlag, Berlin, 1982.

Reimer, L., and Drescher, H., Secondary elecron emission of 10-100 keV electrons from transparent films of Al and Au, *J. Phys. D, Appl. Phys*., 10, 805-815, 1977.

Rester, D.H., and J.H. Derrickson, Electron backscatter measurements for perpendicular and non-perpendicular incidence at 1.0 MeV bombarding energy, *Nucl. Instr. Meth., 86*, 261-267, 1970.

Rösler, M., and W. Brauer, Theory of secondary electron emission I. General theory for nearly-free-electron metals, *Phys. Stat. Sol. (b), 104,* 161 161-175, 1981a.

Rösler, M., and W. Brauer, Theory of secondary electron emission II. Application to aluminum, *Phys. Stat. Sol. (b), 104*, 575-587, 1981b.

Sakurai, J.J., *Modern Quantum Mechanics*, p.388, Addison Wesley, Reading, MA, 1985.

Schou, J., Secondary electron emission from solids by electron and proton bombardment, *Scanning Microscopy, 2, 2*, 607-632, 1988.

Smith, T., Auger electron spectroscopy and ion sputter profiles of oxides on aluminum, *Surf. Sci., 55, 601-624*, 1976.

Sternglass, E.J., Theory of secondary electron emission by high-speed ions, *Phys. Rev., 108, 1*, 1-12, 1957.

Sternglass, E.J., Backscattering of kilovolt electrons from solids, *Phys. Rev., 95*, 2, 345-358, 1954.

Sternglass, E.J., Secondary electron emission and atomic shell structure, *Phys. Rev., 80*, 925-926, 1950.

Suszcynsky, D.M., and J.E. Borovsky, Modified Sternglass theory for the emission of secondary electrons by fast-electron impact, *Phys. Rev. A, 45, 9*, 6424-6428, 1992.

Tesar and Eckertora, The dependence of the angular distribution of backscatteed electrons on the atomic number of the target, *Czech. J. Phys., B23*, 867-870, 1973.

Thomas, S. and E.B. Pattinson, Range of electrons and contribution of back-scattered electrons in secondary production in aluminum, *J. Phys. D, 3*, 349–357, 1970.

Thomas, S. and E.B. Pattinson, Automatic measurement of secondary electron emission characteristics of TaC, TiC and ZrC, *Brit. J. Appl. Phys. (J. Phys. D), ser. 2, 2* 1539–1547, 1969.

Thomson, C. D., Measurement of the Secondary Electron Emission Properties of Insulators, Doctoral Dissertation, Dept. of Physics, Utah State Univ., Logan, UT, 2005.

Tsutsumi, K., Suzuki, T., Nagasawa, Y., Effective Methods to Prevent Charging in Auger Electron Spectroscopy, JEOL EPMA Surface Analysis Group, Application and Research Center, 2006.

van der Ziel, A., A modified theory of production of secondary electrons in solids, *Phys. Rev., 92, 1*, 35-39, 1953.

van Oostrom, A., *Some aspects of auger microanalysis*, Surf. Sci., 89, 615-634, 1979.

Wehenkel, C., Ph. D. Thesis, Universite P of M Curie, Paris, 1975.

Werner, W. S. M., and Hayek, M., "Influence of the Elastic Scattering Cross Section on Angle Resolved Reflection Electron Energy Loss Spectra of Polycrystalline Al, Ni, Pt, and Au," *Surf. Interf. Anal., 22* (1994)79.

Werner, W. S. M., Smekal, W., and St-ri, H., "Angular Distribution of the Surface Excitation Probability for Medium Energy Electrons Backscattered from a Polycrystalline Au Surface," *Surf. Interf. Analysis 31*(2001)475.

Werner, W. S. M., "Obtaining quantitative information on surface excitations from reflection electron energy loss spectra (REELS)," *Surf. Interf. Anal. 35*(2003)347

Woolridge, D.E., Theory of secondary emission, *Phys. Rev. 56*, 563-578, 1939.

Young, J.R., Penetration of electrons in aluminum oxide films, *Phys. Rev.*, *103, 2*, 292-293, 1956.

Young, J.R., Penetration of electrons and ions in aluminum, *J. Appl. Phys., 27, 1*, 1-4, 1956.

APPENDIX A

VARIAN ELECTRON GUN SOURCE

The electron source comes from a tungsten ribbon filament which when heated, emits electrons through thermionic emission. The anodes attract and collimate the electrons by way of a large bias. A front view [Fig. A-1] and 45^{o} view [Fig. A-2] of the electron gun [Varian model 981-2125] show the many components used to test, diagnose, and tune the source of hot electrons used to make the beam. The correct voltage and current range settings for this type of anode filament are tuned and monitored with the electron gun controller [Varian model 981-0246]. The manual for this custom made controller, housed in the laboratory, has been updated numerously over the past 30 years to date. All of the modifications are listed in Table A-1. The electrical diagnostics providing information about the source continue to improve as upgrades are made to the gun controller. Necessary upgrades are specifically addressed in Chap. 3, section 2 as modifications to the apparatus. Presented here is specific information related to the generation of the source and its associated beam characteristics.

The gun controller contains both a source of electrons as well as monitors used to tune, regulate, and characterize their accelerated beam. The source is made of a high voltage supply, a current supply, and a filament current stabilizing feedback loop. The beam is electrically monitored with a voltmeter and two ammeters, respectively. The beam is also diagnosed with the help of a Faraday cup (mounted in the sample block) and an additional ammeter, which measures current flowing to the sample block. Moving the beam across the Faraday cup while measuring the current provides beam profiles used to characterize the beam shape. Coax voltage output cables from an independent beam voltage source [Hewlett Packard model 6516A] are fed directly into the Varian electron gun controller case. Voltages are delivered to the stabilizing feedback loop, the current supply, and the filament (cathode).

A-1. Current Supply

The Lambda current supply (Lambda model LM225) provides current to the filament. The voltage inputs across the current supply are variably controlled from zero to seven volts and translate to

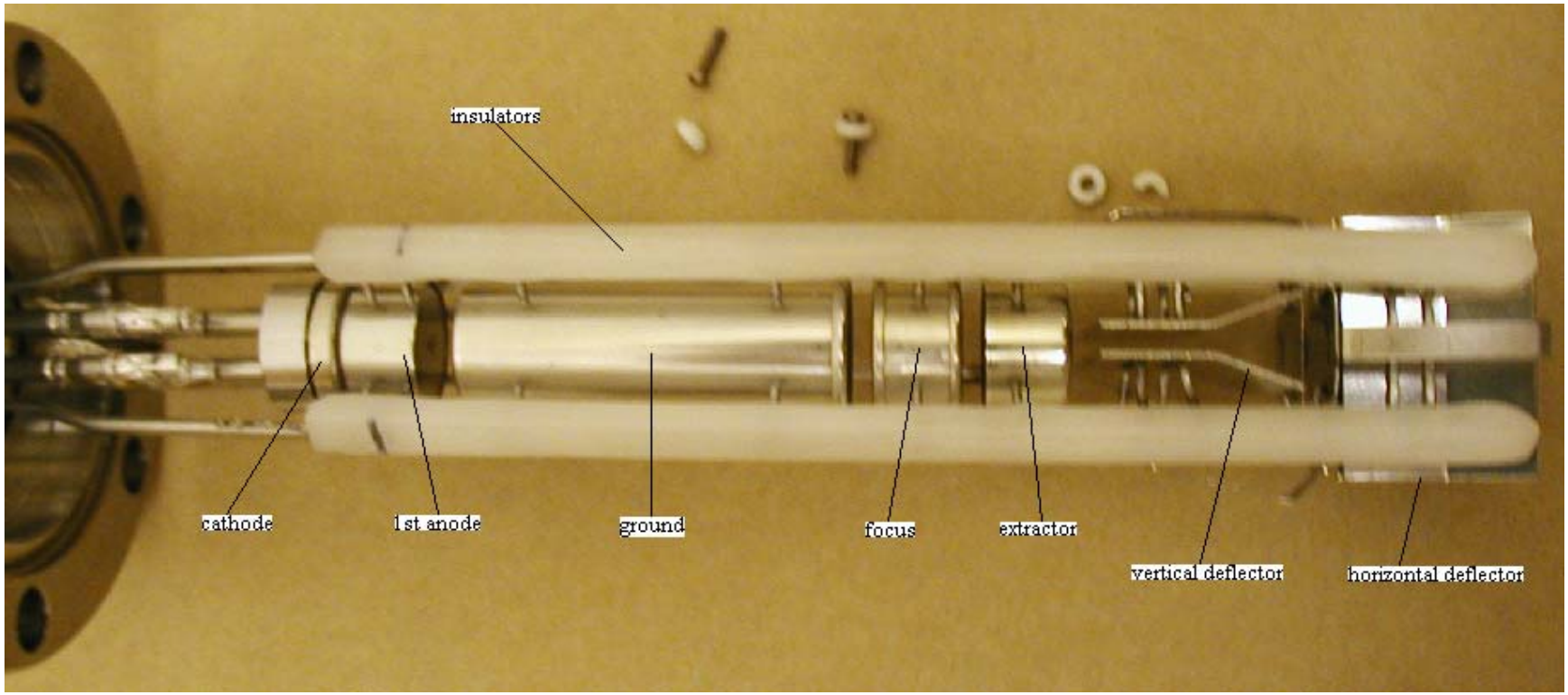

Figure A-1 Varian Electron gun consists of a cathode filament, anodes, and long white insulators used to isolate from a grounding shield (not shown). From left to right, the main components are the cathode, 1st anode, focus, extractor, vertical, and horizontal deflectors.

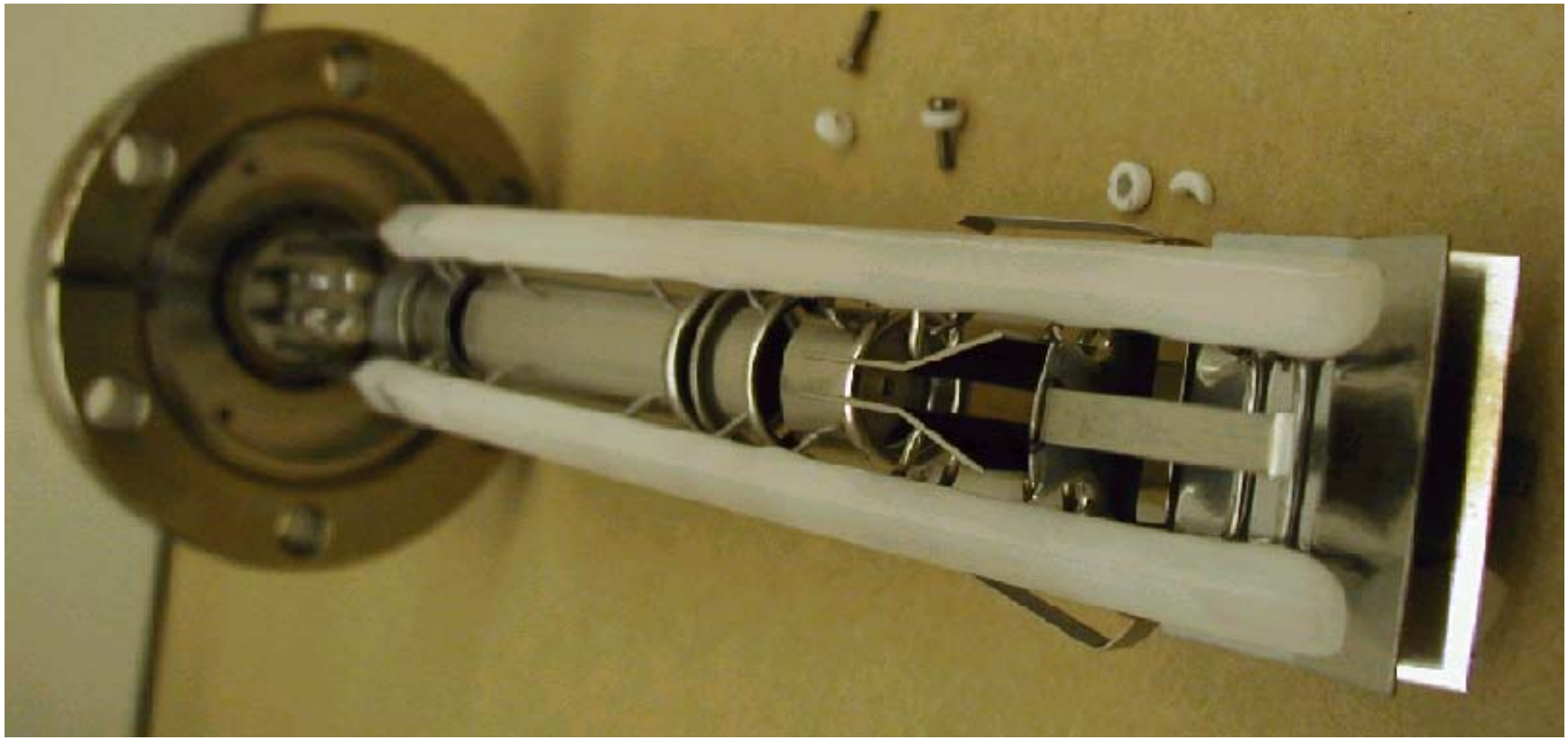

Figure A-2 The 45^{o} view of the Varian Electron Gun shows details the extractor and vertical and horizontal deflectors.

Table A-1. Modifications to the Varian Electron Gun Controller

1. 06-25-97 Replaced emission control pot (5k) with 1M ohm pot.
2. 06-25-97 Replaced resister R15 (470ohm) with 510k ohm resister.
3. 06-25-97 Added 1Mohm resister in series with 1M ohm pot for emission control.
4. 07-25-97 Replaced 1Mohm resister with 0.5M ohm resister in series with emission control pot. Currently, then the emission control is variable for 0.5 – 1.5M ohm producing a beam current for 0 – 0.9 μAmps.
5. 08-15-97 Replaced R15 (510k ohm) with 470k ohm due to heat damage.
6. 08-19-97 Replaced R16 (100k ohm) with 200k ohm (1/2 watt).
7. 08-19-97 Replaced R15 ½ watt 470k ohm with 1 watt 470k ohm.
8. 09-10-97 Added 50k ohm, 10 watt resister in between R26 (focus pot) and R5 to improve focus.
9. 09-10-97 Removed 470k resistor in series with 1M ohm emission pot.
10. 09-09-97 Replaced 741 op amp with Raytheon OP-07T op amp.
11. 1999 Blew Voltage supply and removed it.
12. 07-25-99 Tapped emission current with new op amp (across R21). Two new holes in back for Ib output.
13. 07-26-99 Replaced R25 1M ohm pot with 300k ohm precision 10 turn pot.
14. 07-01-00 Added R7 (47k ohm) between yellow ground and $-V_o$-12 (op amp pin #4).
15. 07-01-00 Added CR10 (5.1V – 4733) between yellow and orange grounds.
16. 07-01-00 Added jumper wire * (see card).
17. 07-05-00 Removed R13 and replace with jumper.
18. 07-05-00 Replaced OP-07 with OP177F.
19. 07-09-00 Added extractor circuit to back (pin 7 = -Vo +12). R4 = 2.2k ohm (3 turn pot). R30 = 25k ohm. C11 = 20μF (100V).
20. 07-09-00 Replaced CR6 (2.4V) with 3.3V (4728).
21. 07-09-00 Replaced CR9 (6.8V) with 6.2V (4735).
22. 03-30-01 Added 47k ohm across R25 (300k ohm 10 turn pot).
23. 03-30-01 Reversed the polarity for the extractor circuit by removing wire from pin #7 = $-V_o$+12 and attaching to pin #0 = $-V_o$-12. (reversed C11 polarity).
24. 03-30-01 Replaced CR10 with 5.6V (4734)
25. 01-27-03 Replaced CR9 with 6.2V (4735)

filament currents from ~1 mA to ~1 μA, respectively. The current supply (Lambda LM225) is floating at the beam voltage in series with the 2.0 Ω filament. An auxiliary rectifier provides power to the bias supply of the current supply, which controls both a voltage amplifier and an error amplifier. A separate rectifier provides power for the drivers and the series regulator (LM225 schematic in manual).

A-2. Filament current stabilizing feedback loop

The filament current is stabilized with a feedback loop that floats at the beam voltage, V_b. The circuit providing this current stability includes an operational amplifier (Op Amp) and several other diodes, resistors, and capacitors. This circuit board includes rectifiers that power the Op Amp with ±12V. The front of the circuit board [Fig. A-3] has two different numbering schemes. The numbers 0 through 7 (with stars) are designated for wire numberings inside the gun controller [Varian gun manual]. The numbers 1 through 6 are the labeled zener diodes with the additional zener diode located on the back of the circuit board [Fig. A-4]. The circuit board can be easily removed from its designated slot for testing and replacement of electrical components. The notch allows the circuit board to be inserted in only one way. Characteristics of the electron source change most rapidly over the life-time of the zener diodes. To diagnose degradation of these zener diodes for use in source characterization, a list of their respective resistance measurements is included in Table A-2.

The configuration of the electronic components providing stable current to the filament [Fig. A-5] is known as a precision power voltage source (Horowitz and Hill, p. 385). In this configuration, current traverses from the floating ground (HP 6516A) to the current supply (LM-225) and filament along various possible different paths. Referring to Fig. A-5, the current traveling through the filament is adjusted by controlling the difference of the current inputs of the Op Amp. This is ultimately accomplished by tuning the amount of current flow through the 300kΩ (10 turn) variable resistor. As the resistance is lowered, there is less current flow through R15 or R12 resulting in an increasing filament current. Increasing the variable resistance results in more current flow through R15 or R12 resulting in a decrease of filament current. The operational amplifier, which stabilizes the filament current, has two input currents with voltages rectified by a 6.8V zener diode (CR9) on the non-inverting (+) input and a 2.4V zener diode (CR6)

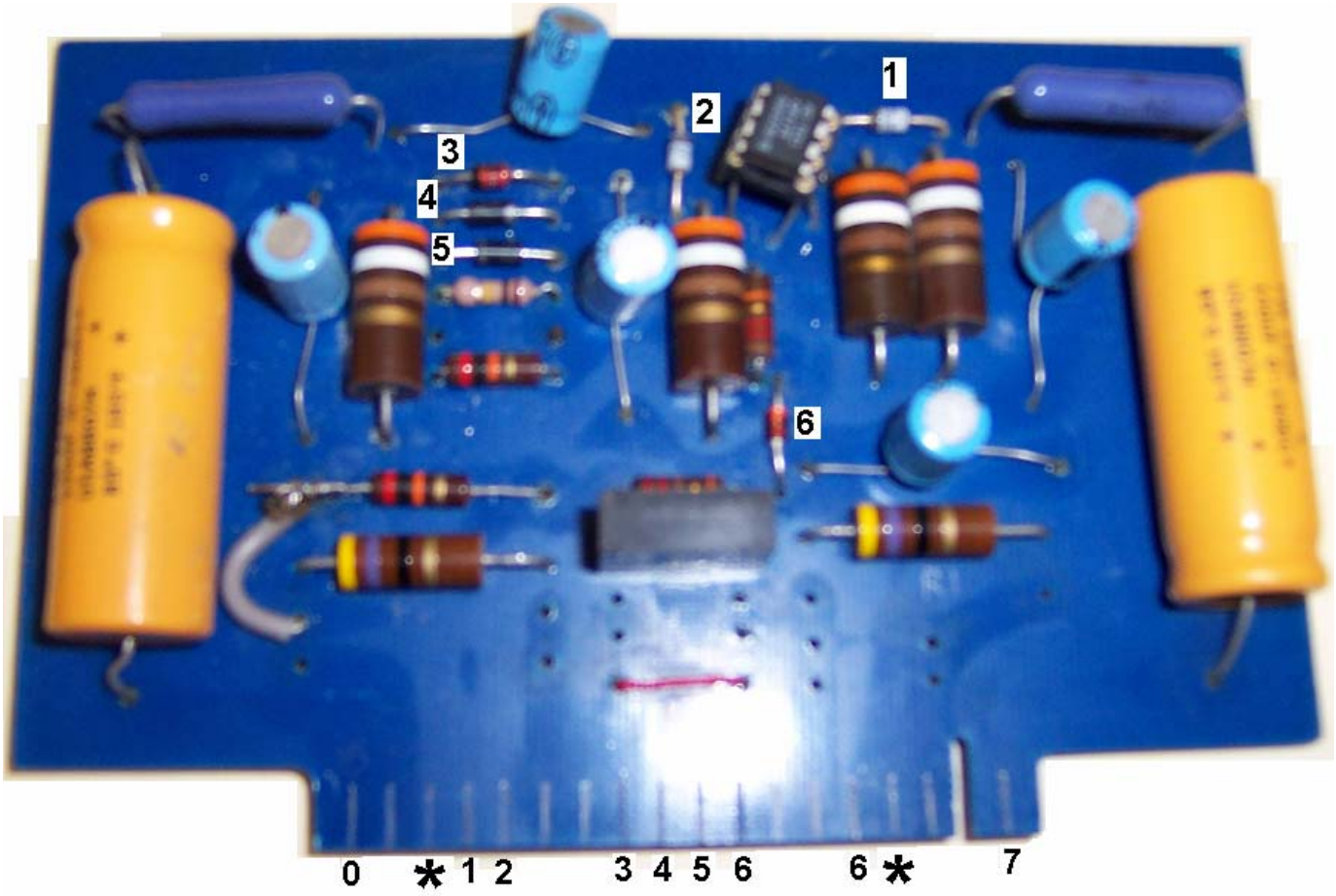

Figure A-3 Front of the Varian electron gun stabilizing current feedback loop. The top numbers list the zener diodes. The bottom numbers correspond to labeled wires in the electron gun controller. The two stars indicate a jumper wire.

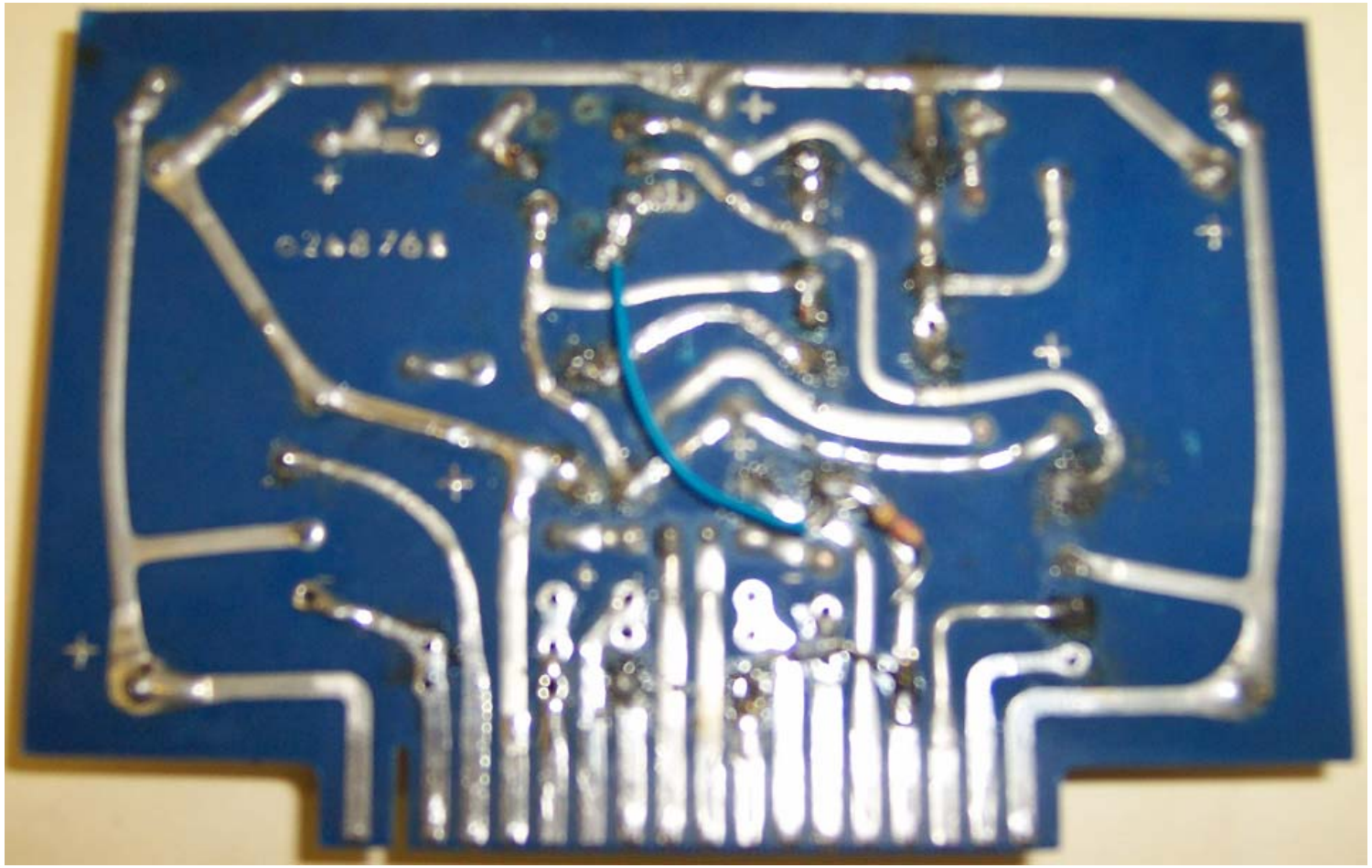

Figure A-4 Back of the Varian electron gun stabilizing current feedback circuit board. The seventh diode is shown in gray just below the resistor.

Table A-2. Zener Diode Resistance Measurements. All zener units are in ohms. The last column is the Varian gun controller front panel dial reading with maximum of 1000 (ten turns).

Date	Back Zener	Zener 1	Zener 2	Zener 3	Zener 4	Zener 5	Zener 6	CurrentDial
	627.9	647	654	652	504	507	634	932
	641	664	668	663	520	523	646	938
	626.8	644	652	652	504	508	634	937
	623.8	644	651	647	500	502	631	937
	623.7	652	653	650	501	505	632	941
	642	673	667	662	520	522	645	952
3/8/2003	642.3	666	667	663	521	523	646	950
3/29/2003	631	648	655	651	506	509	635	948
3/30/2003	626	648	652	648	504	508	634	946
4/12/2003	628	650	656	652	506	509	635	940
4/24/2003	629	650	655	652	505	508	636	941

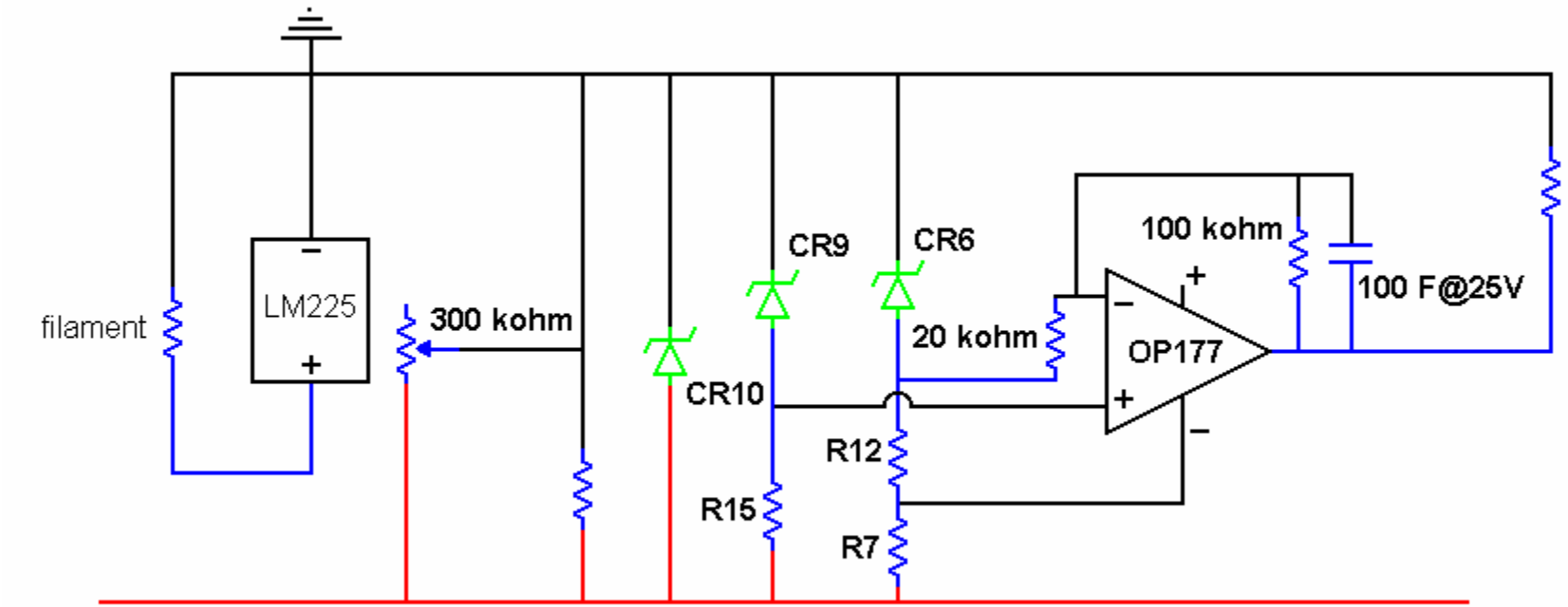

Figure A-5 Precision power voltage source used by the Varian Electron gun controller to stabilize the filament current. High ground is red and low ground is black.

on the inverting (-) input. The 20kΩ parallel resistor ensures that the non-inverting input current is always greater than the inverting input. Filtered circuit current is fed back through the inverting (-) input of the operational amplifier causing any alternating current to be nullified. This circuit arrangement allows precise control of the current supply. Note: R7 is a safety resistor used to protect the Op Amp and other surrounding electrical equipment from damage.

A-3. Current Monitor

The design of this current monitor by Bill Fletcher of Design Analysis Associates Inc., doubly amplifies the current and outputs a voltage and is know as a Precision Resistor Complement. Provided here is the additional information [Fig. A-6] omitted from the electron gun controller box shown in Figure 3-5. The current is monitored across the 19kΩ resistor and filter capacitor. All 1kΩ, 10kΩ, 100kΩ, and 1MΩ resistors are ceramic, high temperature invariant resistors. The double amplification using the 2277 Burr Brown packed chip takes advantage of the ultra low noise by feedback through the inverting (-) inputs, yet contains a "shadow" noise signal [Fig. 3-12, black] not diagnosed. The output voltage of this Precision Resistor Complement monitors the difference between the anode currents and the cathode current. Alignment of the electron source into the Faraday cup, located on the sample's right [Fig. 3-1], shows a directly proportional relationship between the anode-cathode difference, $V_{controller}$, and the beam current, I_{beam}, measured at the sample (3.4(b)). Every $V_{controller}$- I_{beam} calibration curve [Fig. 3-38] is generated by varying the filament current [Fig. A-5, 300kΩ variable resister], and then consolidating the $V_{controller}$ and I_{beam} results for each respective incident electron beam energy. Varying any of the other anodes (e.g., focus, extractor, and deflectors) which are electrically combined with the first anode also alters the $V_{controller}$- I_{beam} calibration curve. Though interesting, the effects of the focus anode on the beam current have not been addressed. The deflector anodes are set at zero deflection and are not used so that the $V_{controller}$- I_{beam} calibration curve will be as accurate as possible. This ultimately minimizes the error in the AER absolute measurement.

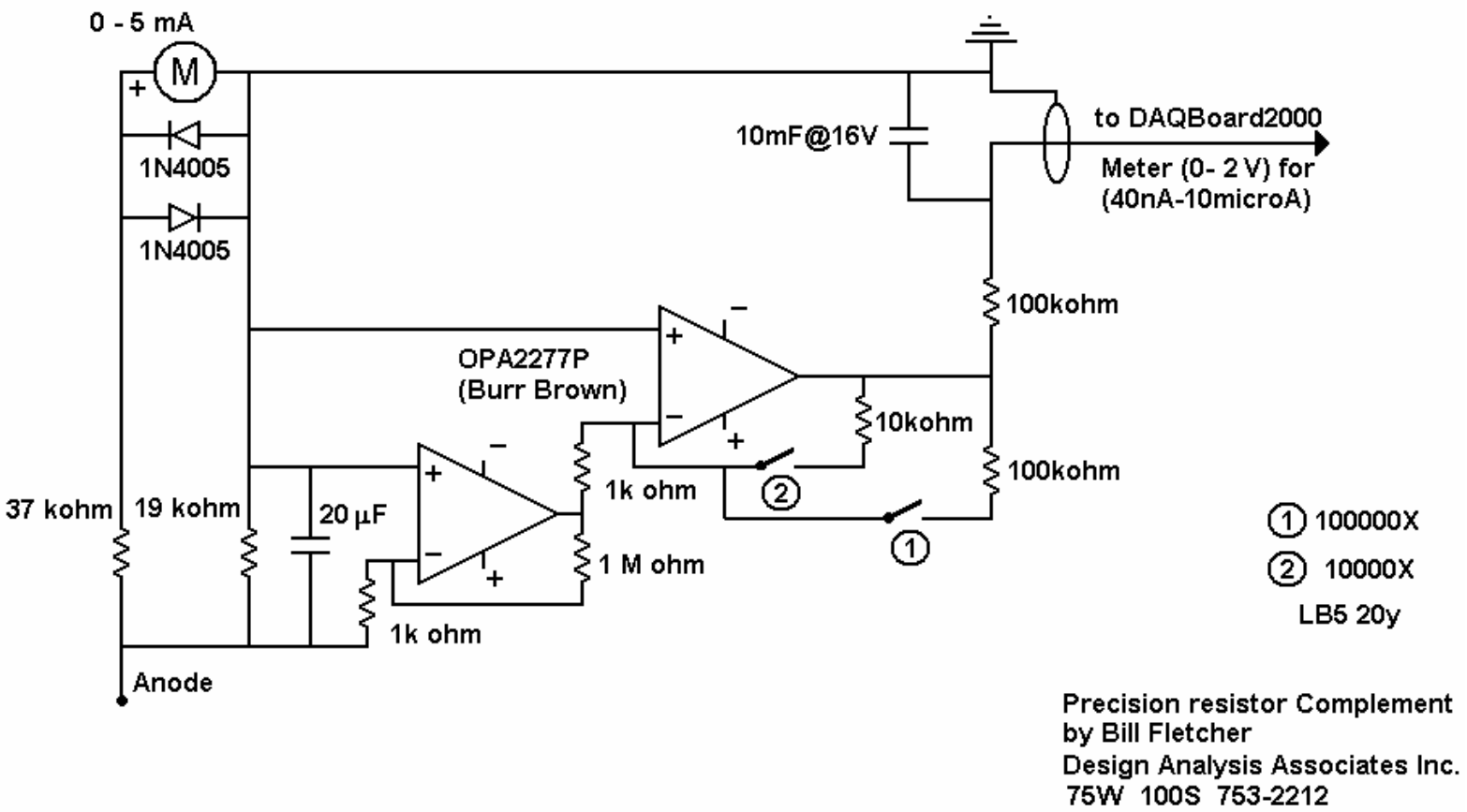

Figure A-6 Precision resistor complement shows to amplifiers in series, which output a voltage from 0 to 2 volts.

A-4. Beam Profiles

Determination of the beam current density is accomplished by moving the Faraday cup with the X-axis micrometer across the beam while measuring I_{beam}. The beam profiles for 1000 eV [Fig. A-7] and 2000 eV [Fig. A-8] are shown for two different extractor settings. The extractor has been set for a maximum Faraday cup current and a minimum Faraday cup current.

To determine the beam shape and density, a de-convolution of the beam profiles must occur. The beamspot size at target distance typically measures a FWHM of 1.5 mm in diameter. The de-convolution of this spread gives an electron beam density of 1.5 nA/mm^2 for all four curves.

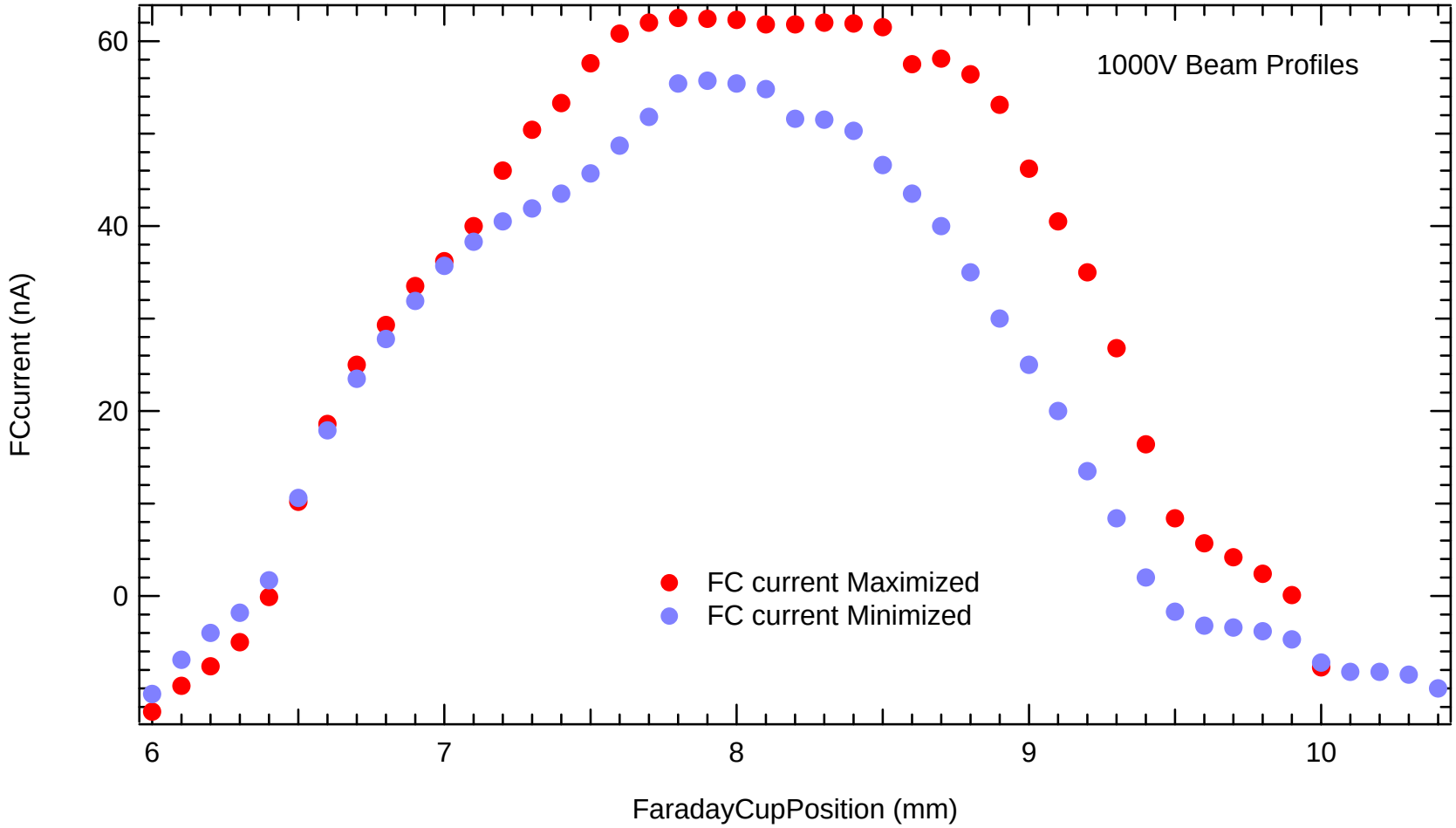

Figure A-7 Beam profiles for electron beam energy of 1000 eV for two different extractor settings.

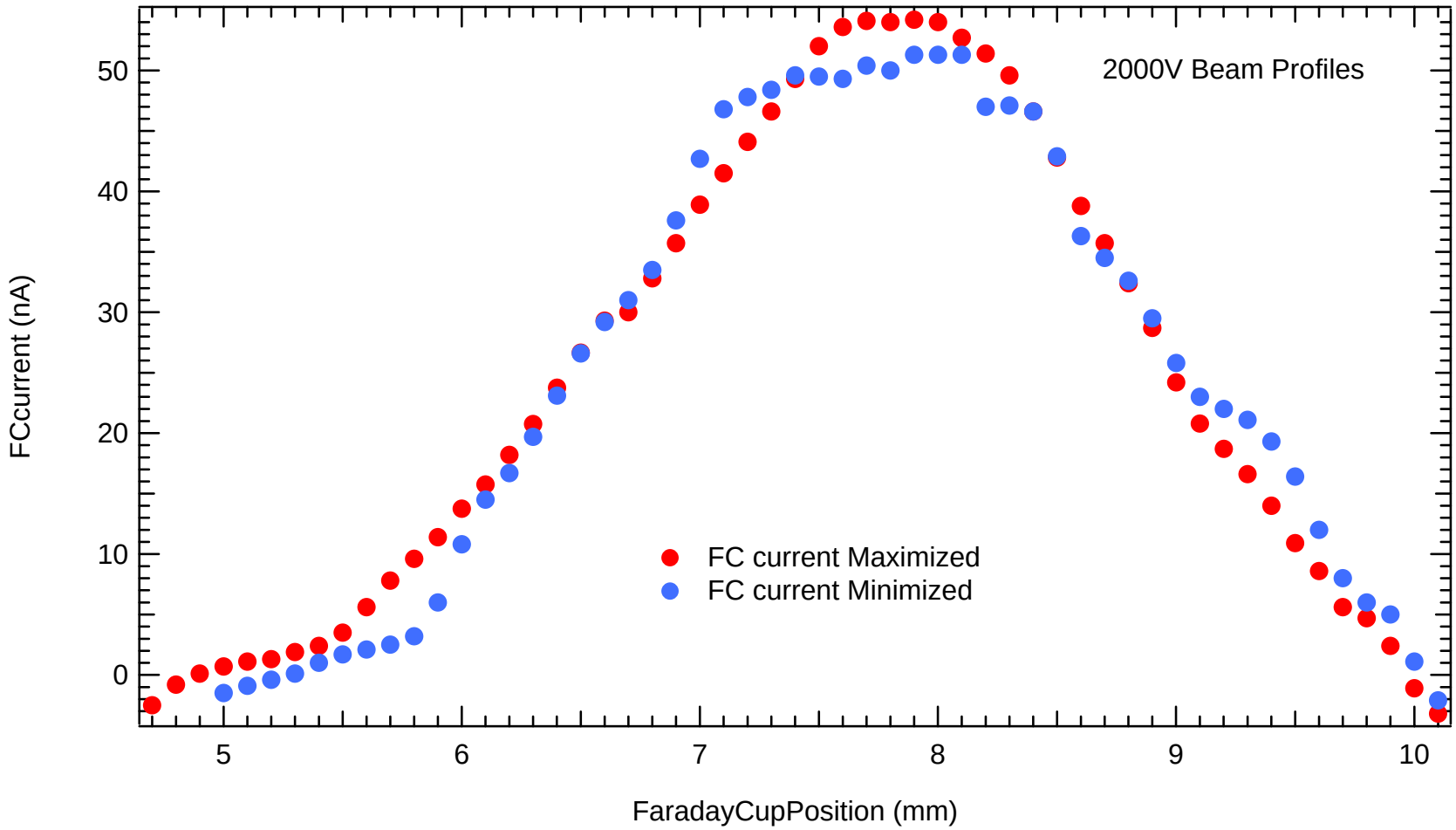

Figure A-8 Beam profiles for electron beam energy of 2000 eV for two different extractor settings.

APPENDIX B

STEPPER MOTOR CONTROLLER

Angular movement of the rotatable detector (RD) is an essential constituent of the angular-energy-resolving (AER) LittleBoy apparatus. The angular motion of the RD is ultimately controlled by a stepper motor, which has been specifically designed for automatically taking AER data. Presented here are the specifics of how the RD is controlled and manipulated. Operation occurs through several chain-like sequences. The components of operation are a gear conversion, a flexible RD cable, a UHV feedthrough bearing, a stepper motor, and a stepper motor controller. The stepper motor controller under LabVIEW control activates the stepper motor, which causes the rotation of the cable.

B-1. The RD Gear Conversion

The RD is mounted directly onto the big gear [Fig. B-1]. The big gear is situated on a bearing capable of rotating independently from the fixed bottom plate. As contact is made with the little gear, a rotation conversion occurs. A 12 to 1 RD gear ratio conversion (scaling down) provides improved angular precision of the RD placement (see 3.2(a)). The small gear rests in a long hollow aluminum shaft, which is pressed to fit into a small rectangular plate mounted to the bottom plate. The small gear is connected to a collet by means of two set screws.

B-2. The RD Cable and UHV Feedthrough Bearing

The RD cable is used to change axes of rotation from the horizontal to vertical. Both ends of the RD cable are attached to collets by means of mounting screws. One end of the RD cable is connected to the small gear [Fig. B-1] along a vertical rotating axis, and the other is connected to a UHV feedthrough bearing along a horizontal axis. The UHV feedthrough bearing [model #] is capable of sustaining a low 1 x 10^{-11} torr. The feedthrough bearing is mounted to the RD cable feedthrough port just below the signal, heater, and thermo-couple feedthrough port [Fig. B-2].

RD Gear Conversion

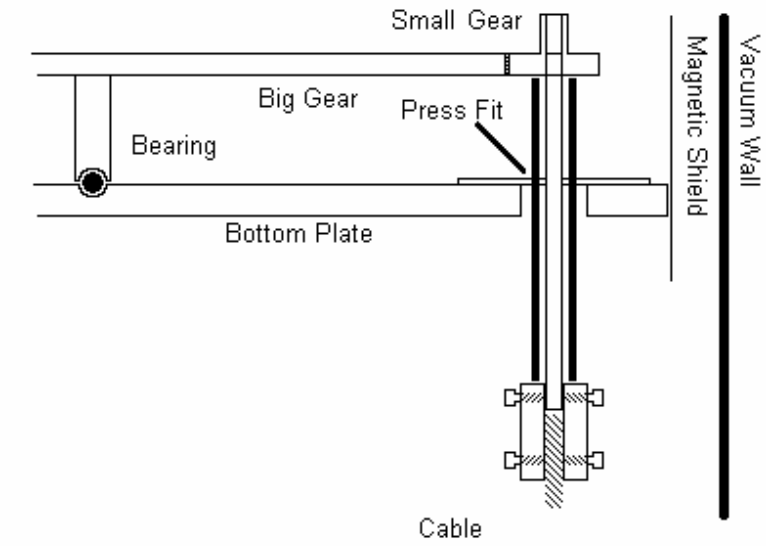

Figure B-1 The RD gear rests on a bearing (side view) and is driven by the small gear, which is attached to the cable. The small gear shaft is pressed to fit into a small plate, which is fixed to the bottom plate.

LittleBoy Apparatus Feedthrough Ports

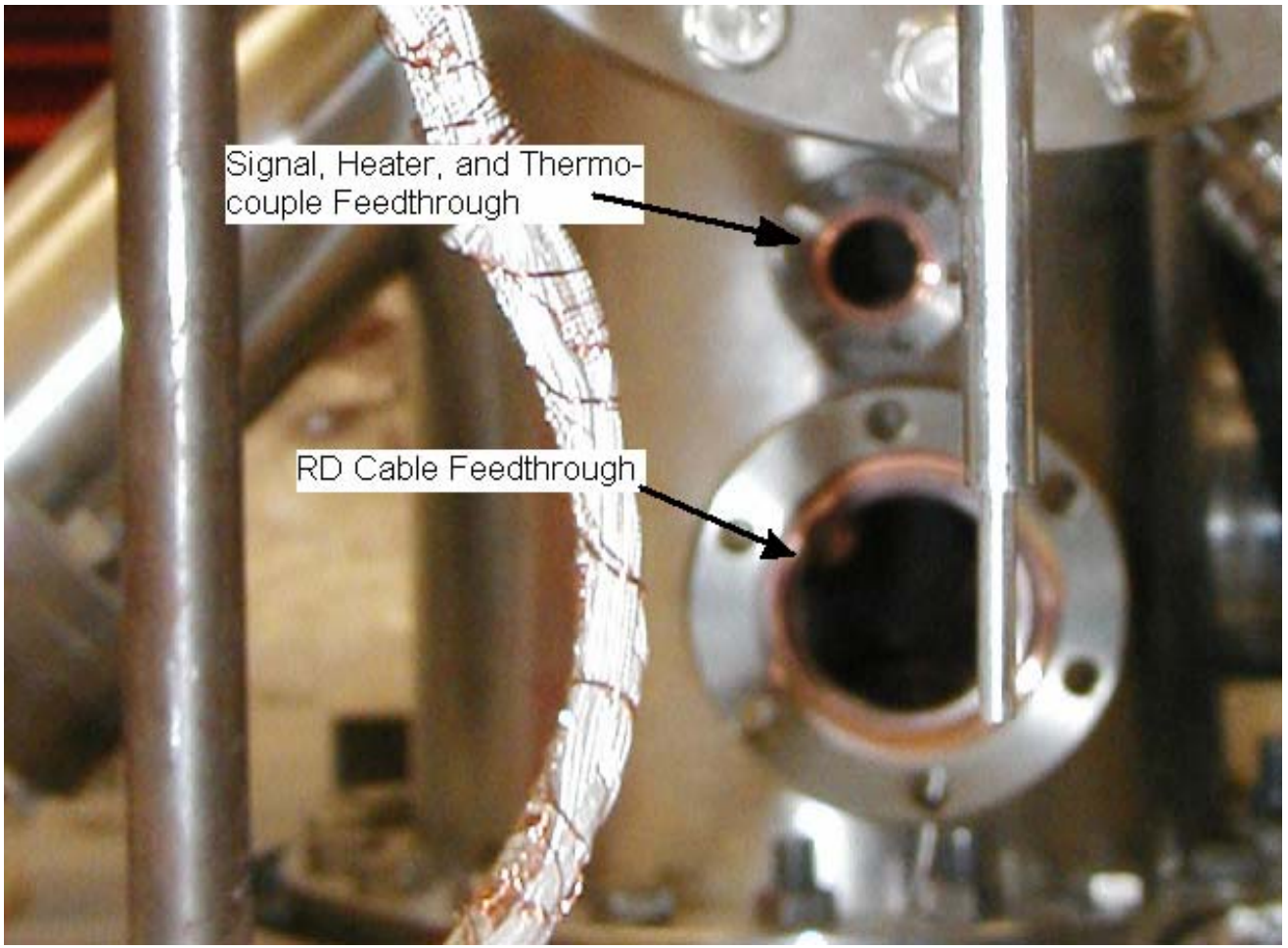

Figure B-2 Feedthrough ports for the signal, heater, and thermocouple (on top) and the RD cable.

B-3. The Stepper Motor

The stepper motor is a standard Slo-Sync model number M061-FD-6110 [Fig. B-3]. The solenoids provide angular movement of $1/400^{th}$ of a full revolution per magnetic pulse. The measuring device, attached to the turning dial of the UHV feedthrough, can be turned by hand or by the connected stepper motor. The stepper motor is connected to a baffle to correct for axle misalignment correction, and the baffle is connected to the UHV feedthrough bearing. Each are connected with one set screw.

B-4. The Stepper Motor Controller

The stepper motor controller (AMSI model number 8003-DM) controls the stepper motor through direct connection. The electrical schematic of the stepper motor controller is shown [Fig. B-3]. The power LED is activated when the power supply is plugged in. The Clock LED is activated for each pulse of the stepper motor. The LabVIEW software controls the stepper motor controller through a 25 pin parallel printer port. LabVIEW programs can be seen in appendix C. The right side of the controller schematic shows four direct connections to the LabVIEW software. The H/F (half step/full step) is directly connected to the EN (enable), both constantly HI, so that the controller is always enabled and always takes half steps. LabVIEW controls enable through pin 8 of the 25 pin connector. The direction (DIR) of motion is controlled through pin 3, and the clock (CLK) is controlled through pin 2 of the 25 pin connector.

Stepper Motor and Controller Schematic

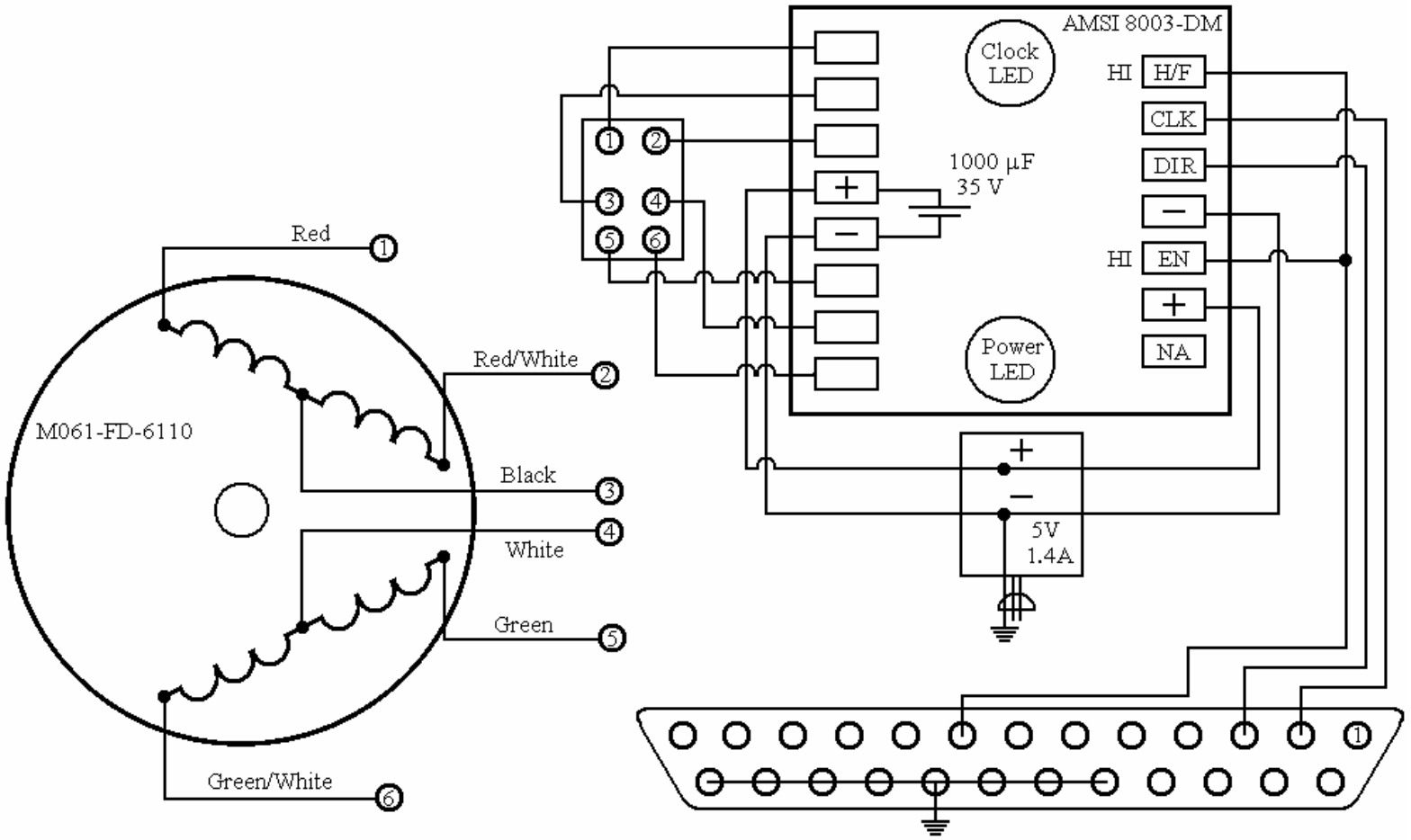

Figure B-3 The stepper motor with wiring diagram on left and the stepper motor controller schematic on right. The numbers 1 through 6 connect.

APPENDIX C

LabVIEW PROGRAMS

There are several LabVIEW programs custom developed specifically for the LittleBoy instrument. All of these programs are configured to utilize outputs from the computer and take input from specified devices via PCI computer card, GPIB, parallel port, and RS232 connections. The corresponding specified devices are the DaqBoard2000 (National Instruments), the Keithley 237 voltage supply, the stepper motor controller, and the ARGA quadrupole mass spectrometer. Various combinations of these devices are controlled with LabVIEW for different purposes. Each LabVIEW VI program is explained in detail and a summary is provided in Table C-1.

C-1 Stepper Motor Programs

There are two programs used to move the stepper motor. Both programs use the 25 pin parallel port address 378 as output to the stepper motor controller [appendix A] and work independently of any other devices. All computer screen displays dealing with the stepper motor are shown in blue.

C-1.(a) Steppermotor.vi

The steppermotor.vi moves the stepper motor 400 steps in the “Number of Steps” box and shows the real-time movement in the “Steps Completed” box [Fig. C-1]. . There is a toggle switch option for clockwise or counter-clockwise movement. The time between steps is initialized at 2 milliseconds so that accuracy is kept when running this as a subVI. The VI will work with a millisecond time increment if run as a subVI, but not accurately due to overhead time.

C-1.(b) Motor1.vi

Motor1.vi LabVIEW program moves the stepper motor a finite number of ticks with the maximum of 2160 (from support post to support post) shown in the “Number of Steps” box [Fig. C-2]. . The real-

Table C-1 LabVIEW Programs

*.vi Program	DAQBoard					Keithley237				Stepper Motor	ARGA	Save to file
	Channels	Scan Count	Scan (Hz) Frequency	Total Scans	Graphs	Bertan Bias(V)	compliance†	Multiplier	Adder			
StepperMotor										X		
Motor1										X		X
DaqBoard	1-4,6	10000	1.00E+04	30000	1							
EARSpectraDaq2000	1,2,3	1000	1.00E+03	30000	0							X
EARSpectraDaq2001	1,2,6	1000	5.00E+04	1000	1 RD/S	0	3,8,10,0.00001	0.1	0			X
EARSpectraDaqTert	1,2,4,6	1000	5.00E+04	1000	1 RD/S	500	3,8,10,0.00001	0.1	0			X
MonitorPressure	1,2,4,6	1000	5.00E+04	1000	4	0	3,8,10,0.00001	0	0			X
SEpeak	1-4,6	3000	5.00E+04	220	1 RD/S	0	3,8,10,0.00001	1	-110	X		X
SEpeakfine	1-4,6	3000	5.00E+04	220	1 RD/S	9	2,8,10,0.00001	0.1	-11	X		X
BSEpeak1V	1-4,6	3000	5.00E+04	220	1 RD/S	1100	3,8,10,0.00001	1	-110	X		X
BSEpeakfine	1-4,6	3000	5.00E+04	220	1 RD/S	1180	2,8,10,0.00001	0.1	-11	X		X
MidEnergy10V	1-4,6	10000	5.00E+04	22	1 RD/S	1000	3,8,10,0.00001	10	-110	X		X
MidEnergy1V	1-4,6	3000	5.00E+04	220	1 RD/S	2400	3,8,10,0.00001	1	-110	X		X
DetermineZeroAngle	1-4,6	10000	4.00E+04	313	1 RD/S	0	2,8,10,0.00001	0	0	X		X
ARGAchart											X	X
ARGAcycle											X	

† The four numbers are used by the KTH 237 Basic Config VI [Fig. C-10] and are labeled Source Range, Compliance Measurement range, Volt Compliance and Current Compliance, respectively. See the Keithley 237 manual for further details.

StepperMotor LabVIEW Program

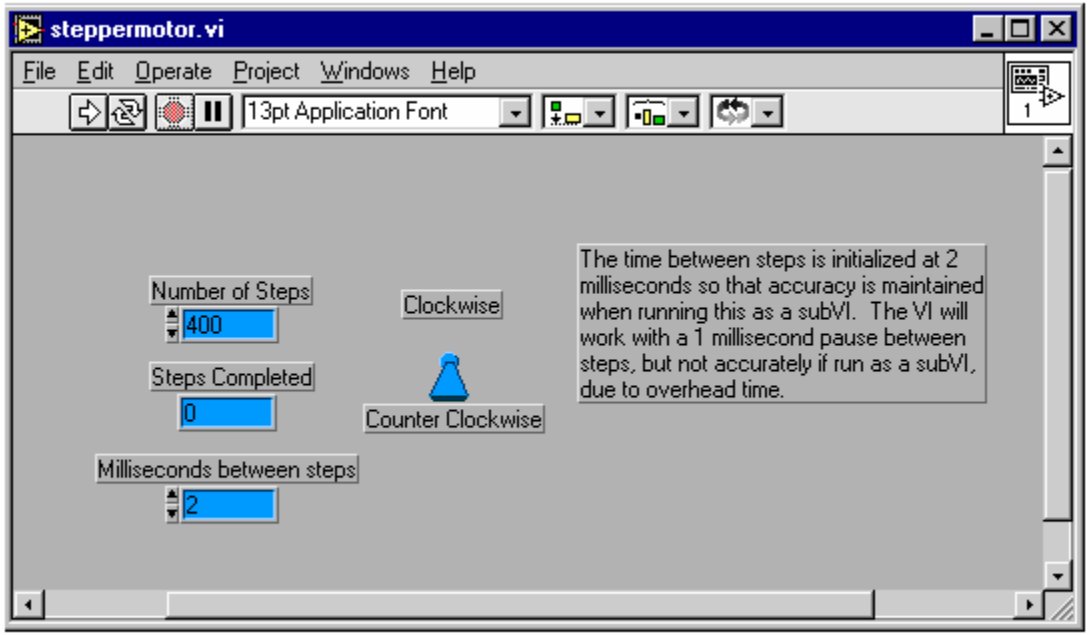

Figure C-1 StepperMotor LabVIEW program front panel moves the stepper motor a finite number of ticks at the maximum rate possible.

Motor1 LabVIEW Program

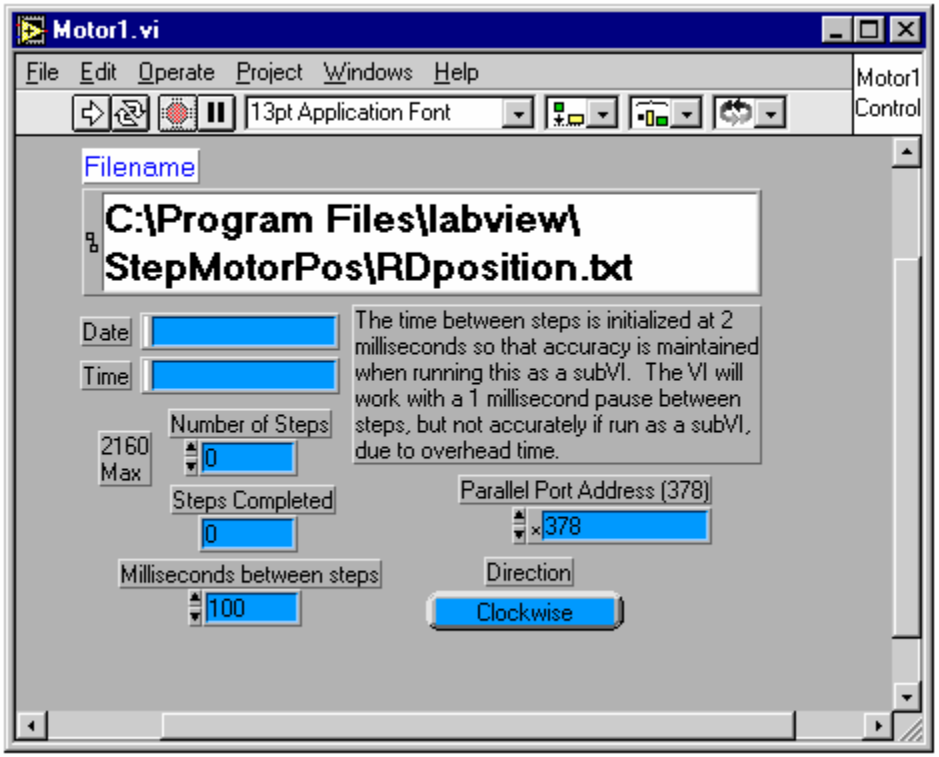

Figure C-2 Motor1 LabVIEW program front panel moves the stepper motor a finite number of ticks at a rate of 100 ms/step and records the angle move to file along with the current date and time.

time movement is shown in the “Steps Completed” box. After the move and prior to the end of the program, a record is made of the move as an amendment to the designated file C:\ProgramFiles\labview\StepMotorPos\Rdposition.txt. The date and time of the move is also recorded to the same file shown in the “Date” and “Time” boxes below the filename. There is a push button option for clockwise or counter-clockwise movement. The time between steps is initialized at 100 milliseconds. For further LabVIEW programs, which use the Motor1 VI as a sub VI, a wiring diagram is given [Fig. C-3]. This diagram shows how input is given to the RDstep, how the angle move is stored to file (pink), and how iteration takes place for further stored angle settings (outer film strip).

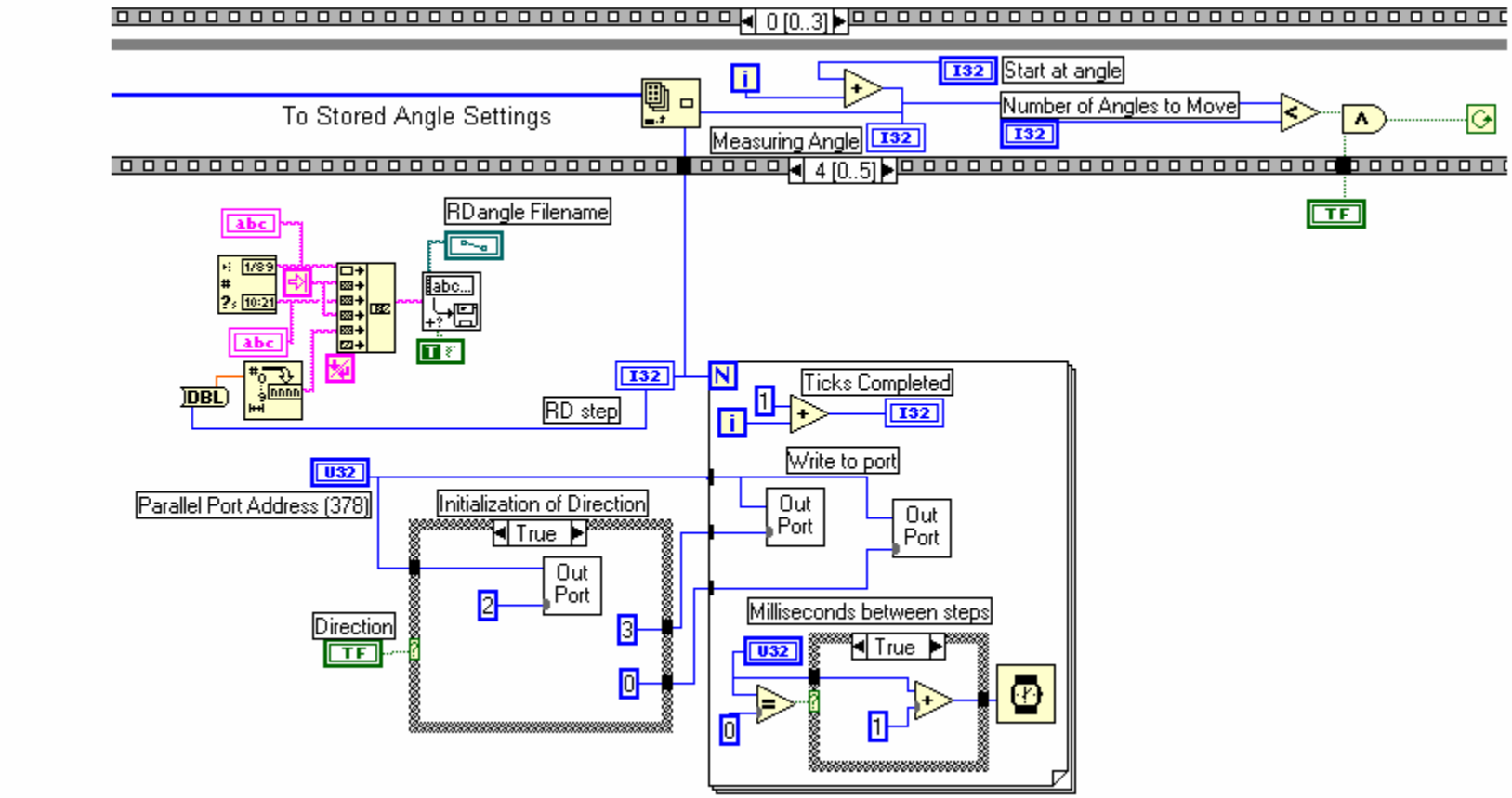

Figure C-3 Angular movement LabVIEW wiring diagram for controlling multiple angular movement of the rotatable detector via parallel port. File storage is in pink.

C-2 DaqBoard2000 Programs

There are several LabVIEW programs that take input from the DaqBoard2000 via a National Instruments PCI card. Use of GPIB as an interface for controlling the Keithley 237 and the parallel port for controlling the stepper motor have been incorporated as subVI's. The programs are divided into DAQBoard2000 channel monitoring programs for diagnostic purposes, energy resolved spectral measurement programs for data acquisition of AER spectra, and high angle resolved measurement programs for utilizing the highest angular resolution possible. Due to the complexity of the programs, computer screen display color coding of subVI's is used to make user interface more user friendly. The configurations of the DAQBoard2000 are shown in orange, gathered data from the DAQBoard2000 are shown in green, compliance setting configurations for the Keithley 237 are shown in pink with voltages and voltage step sizes shown in red, and stepper motor settings are shown in blue.

C-2.(a) DaqBoard2000 Channel Monitoring Programs

Five LabVIEW programs are used to take input from the DaqBoard2000 via a National Instruments PCI card for LittleBoy diagnostic and monitoring purposes. Two of these programs, DaqBoard.vi and EARspectraDAQ2000.vi solely use the DAQBoard2000. The other three programs, EARspectraDAQ2001.vi, EARspectraDAQTert.vi, and MonitorPressure.vi, permit control of the Keithley 237 for biasing the rotatable detector.

C-2.(a) i DaqBoard.vi

The DaqBoard program is used strictly for monitoring the DAQBoard2000 while the LittleBoy is warming up [Fig. C-4]. The scan count is set to 30,000 so that deviations in the six signals can be seen in real time. This is the best way to find and fix annoying antennas and ground-loop signals. This program records no data to file.

C-2.(a) ii EARspectraDAQ2000.vi

The EARspectraDAQ2000 program is used to test the maximum data taking rate for three input channels [Fig. C-5]. With 30,000 total scans per VI iteration, the maximum actual rate for taking data is 50 kHz. A graphing interface is not included because the data taking rate becomes diminished. The designated storage area for the data is C:\Program Files\Labview\EARspectra\data\HighHzTest.txt. A comment section for storing additional information is also provided. The wiring diagram for the DAQBoard2000 [Fig. C-6] shows how channels are configured and monitored from the DAQ*Basic module (up to five). The mean and standard deviation are calculated and stored to file (top right).

C-2.(a) iii EARspectraDAQ2001.vi

The EARspectraDAQ2001 program unites the DaqBoard and EARspectraDAQ2000 programs as well as the capability to bias the RD with the Keithley 237 via GPIB control [Fig. C-7]. The source range, compliance measure range, and compliance (shown in pink) can be set to enhance the signal-to-noise ratio of the output voltage to the RD. The table in the lower right is a guide for the source range setting [Fig. C-7]. The graph provides the ratio of the RD current to the Sample current at the expense of a much slower data taking rate (1 kHz). Designated storage of the data to a test file along with any comments is also capable. The wiring diagram for the configuration of the KTH237 BASIC CONFIG, iteration of the RD bias, and storage of the RD bias is depicted [Fig. C-10].

C-2.(a) iv EARspectraDAQTert.vi

Two improvements to the EARspectraDAQ2001 program are the addition of a tertiary channel and the ability to reset the RD bias after data taking is done. The EARspectraDAQTert program [Fig. C-8] is helpful for safety reasons. Since the Bertan voltage supply floats on top of the Keithley237, it is useful to be able to end the program with the Bertan at ground. Designated storage of the data to a test file along with any comments is also possible.

C-2.(a) v MonitorPressure.vi

This program is used to monitor and record four channels of the DAQBoard2000 while biasing the RD to a spectrum of voltages [Fig. C-9]. The program is very useful for monitoring pressure changes in the LittleBoy while RD bias changes and output from the vacuum ion pump into channel #3 of the DAQBoard is trivial. Every $V_{controller}$-I_{beam} current calibration curve is generated with the MonitorPressure.vi LabVIEW program (3.4(b)). The curve is generated, by running the program for varying filament current settings, and then consolidating the results. Every record is stored to the predetermined file C:\Program Files\labview\EARspectra\data\PreD****_#.txt where **** is the surface number and # is the filament current setting. Storage of any comments to the data is also possible (not shown).

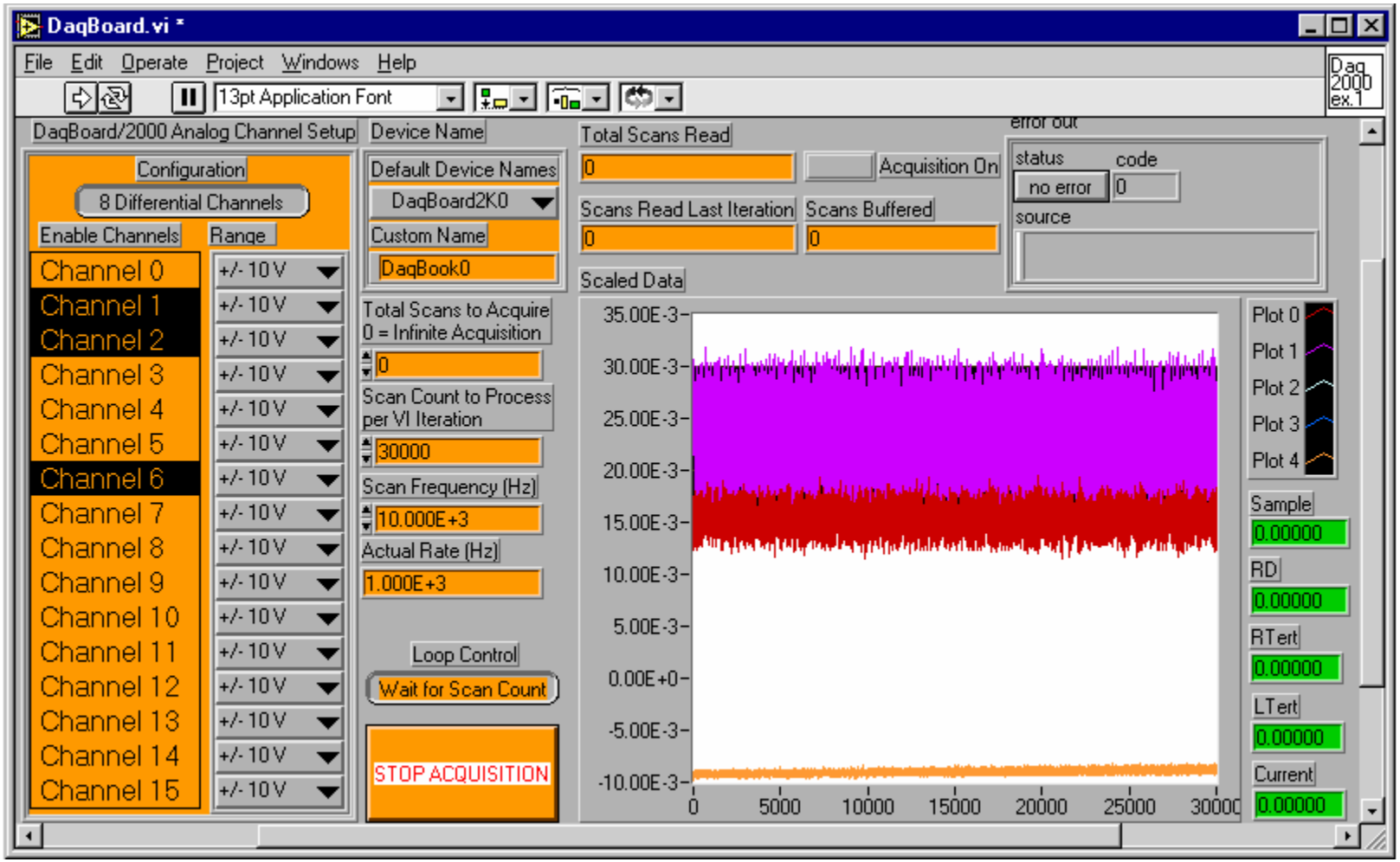

Figure C-4 The DaqBoard LabVIEW program monitors up to five channels with 30,000 counts per iteration that outputs to graph and average number (in green).

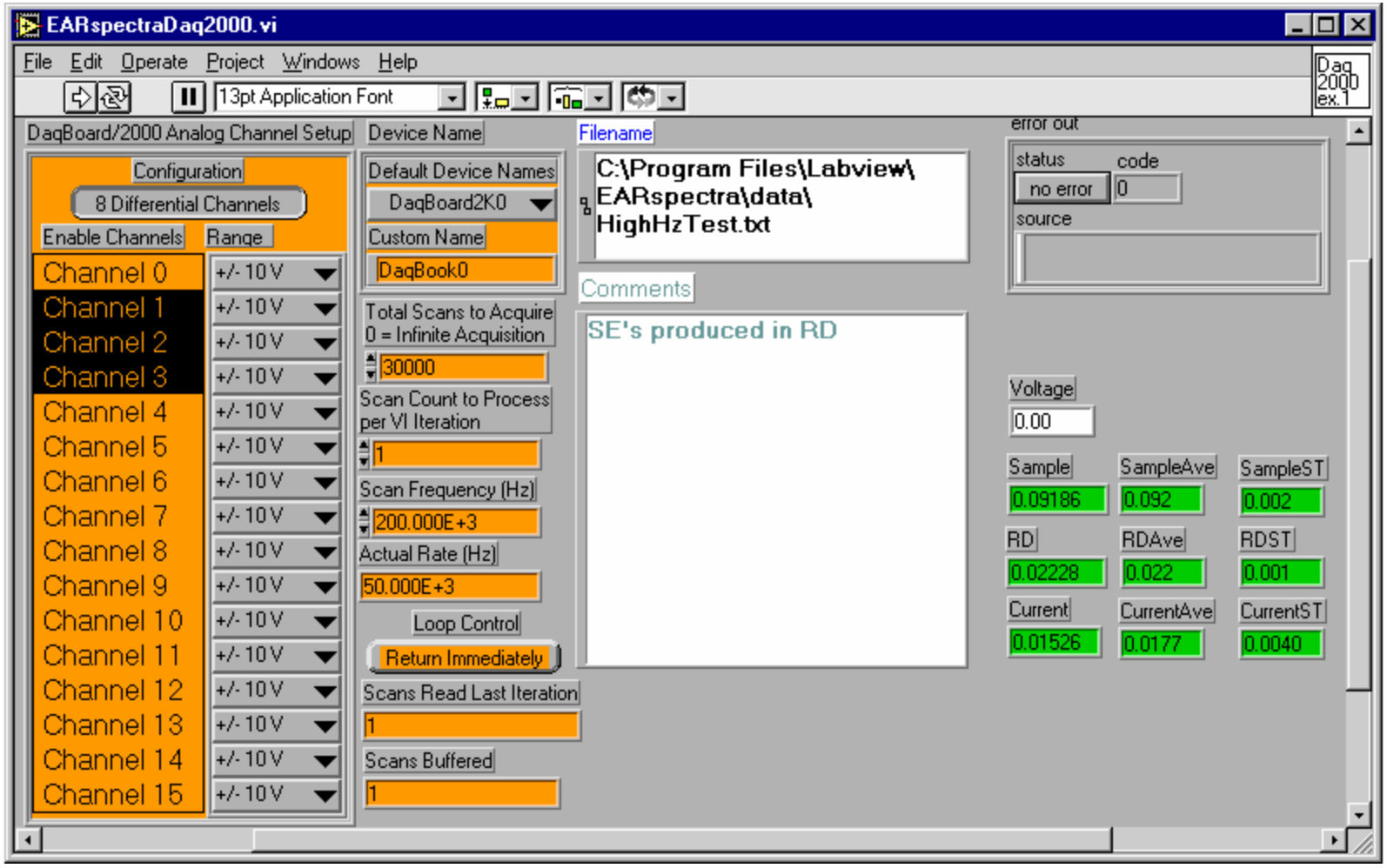

Figure C-5 EARspectraDAQ2000 LabVIEW program monitors three channels at the maximum data acquisition rate of 50 kHz.

DAQBoard2000 Monitoring LabVIEW Wiring Diagram

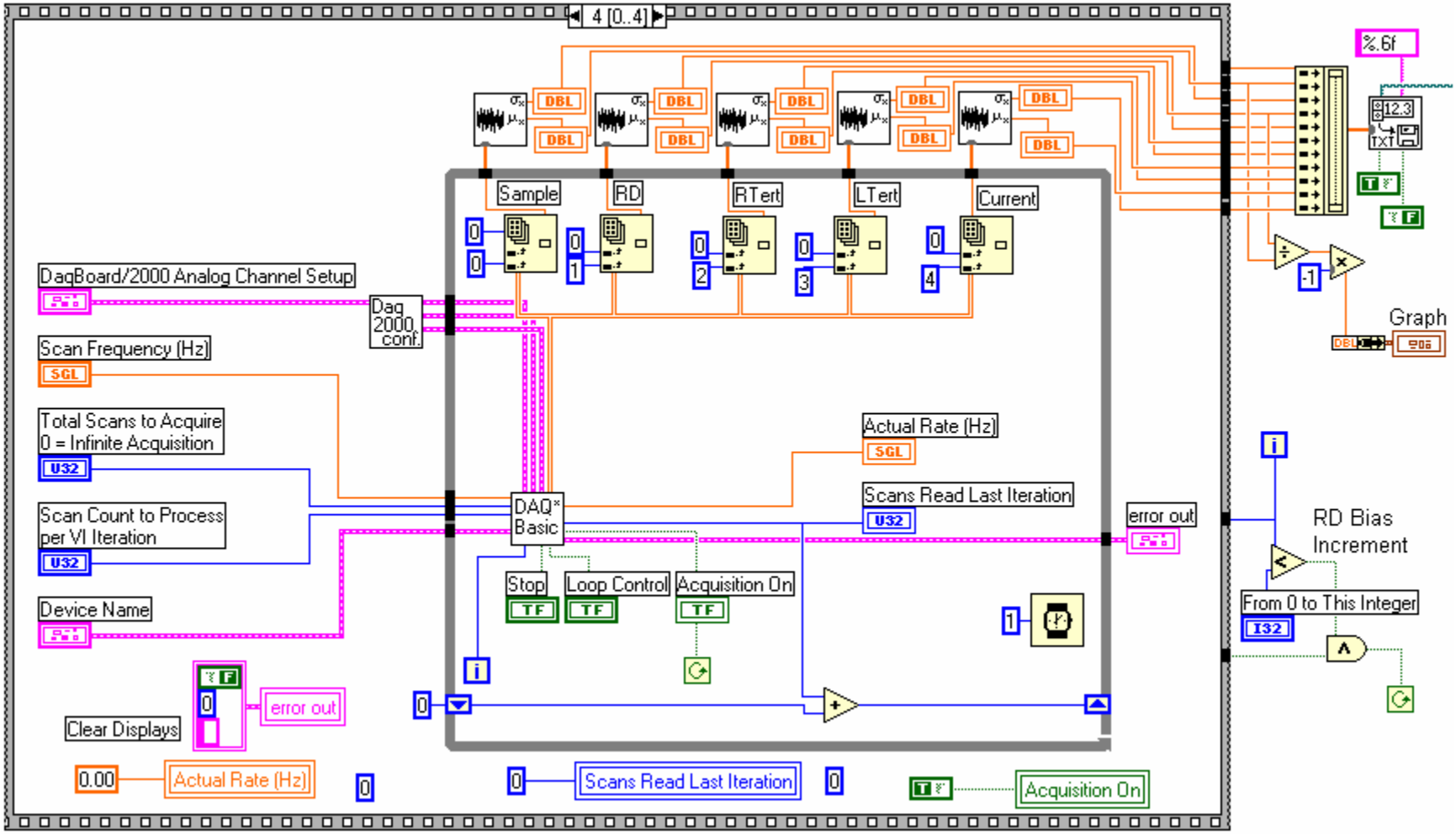

Figure C-6 DAQBoard2000 Monitoring LabVIEW wiring diagram.

EARspectraDAQ2001 LabVIEW Program

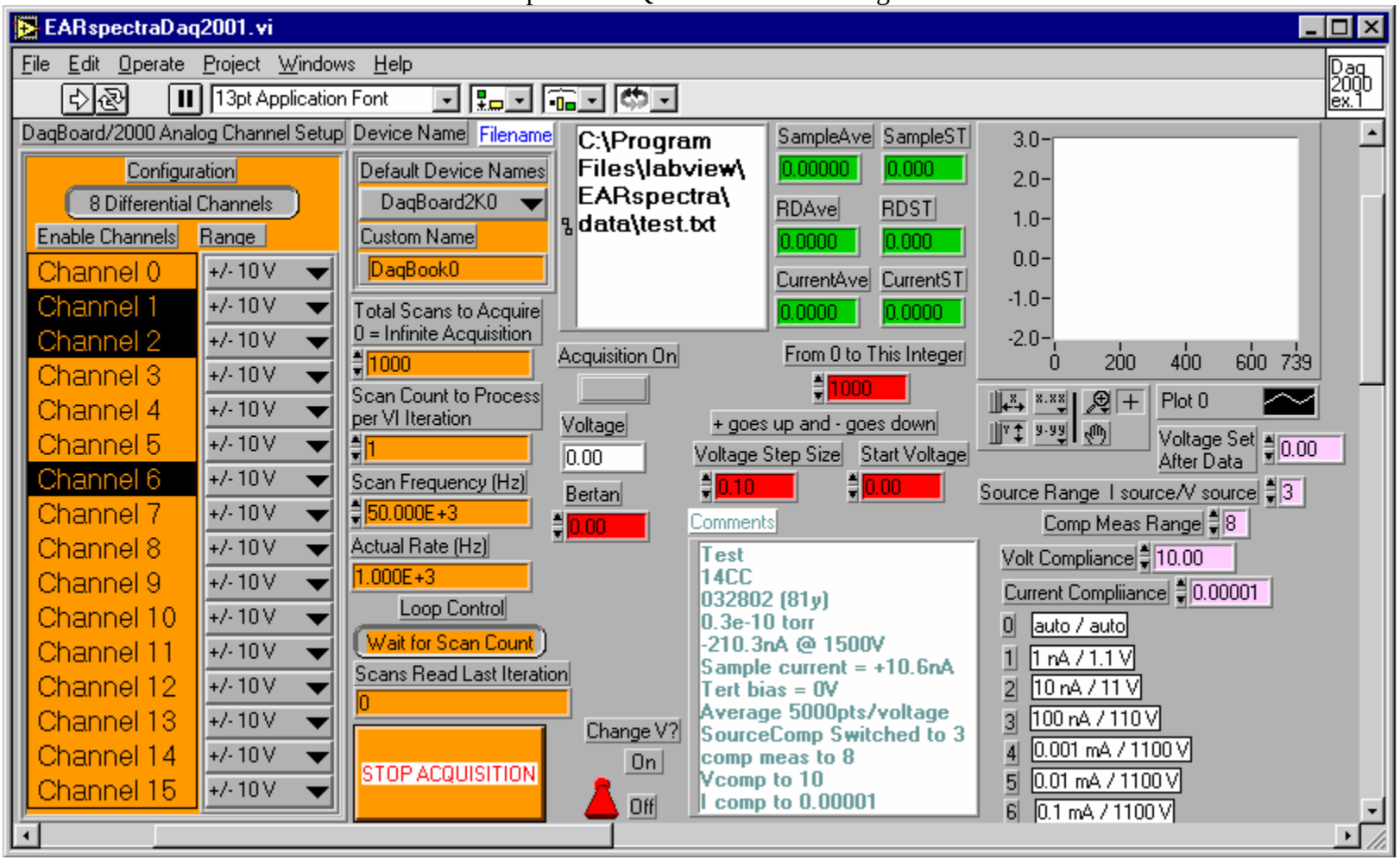

Figure C-7 EARspectraDAQ2001 LabVIEW program records three channels from the DAQBoard2000. The Bertan has been set to 0 volts.

EARspectraDAQTert LabVIEW Program

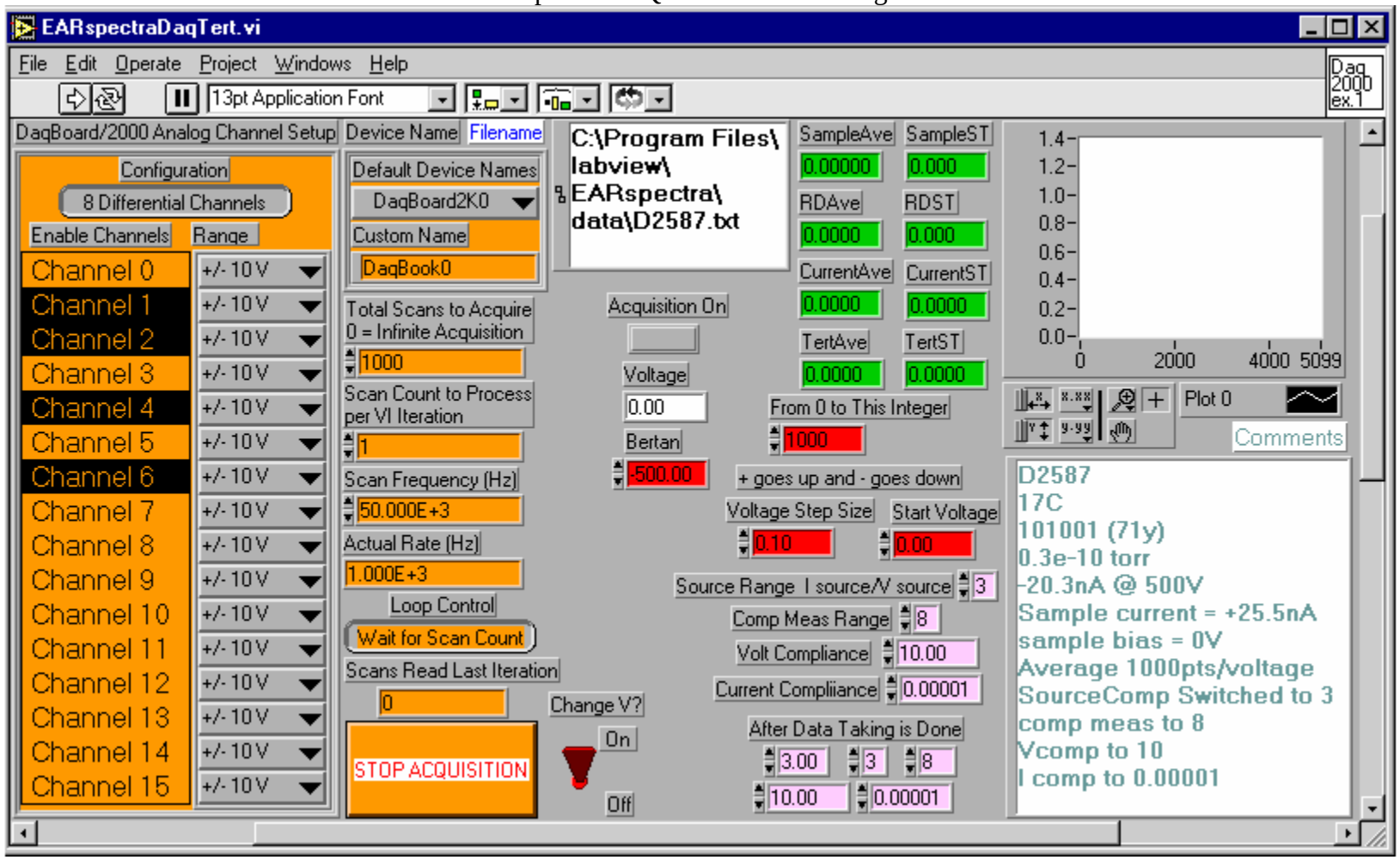

Figure C-8 EARspectraDAQTert LabVIEW program records four channels from the DAQBoard2000. The Bertan has been set to 500 volts.

MonitorPressure LabVIEW Program

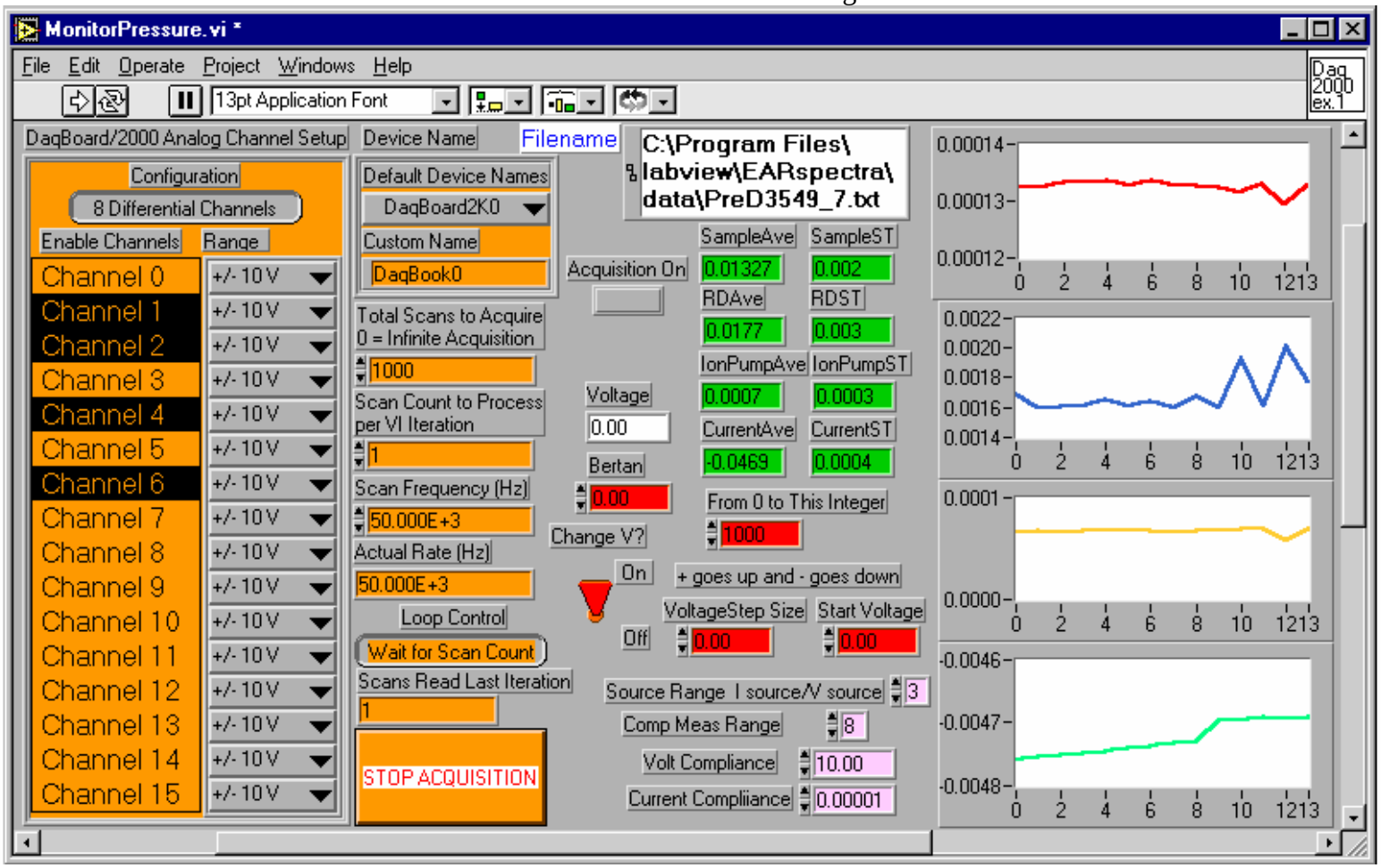

Figure C-9 MonitorPressure LabVIEW program records four channels from the DAQBoard2000. RD bias has been set to 0 volts.

Keithly237 Initialization LabVIEW Wiring Diagram

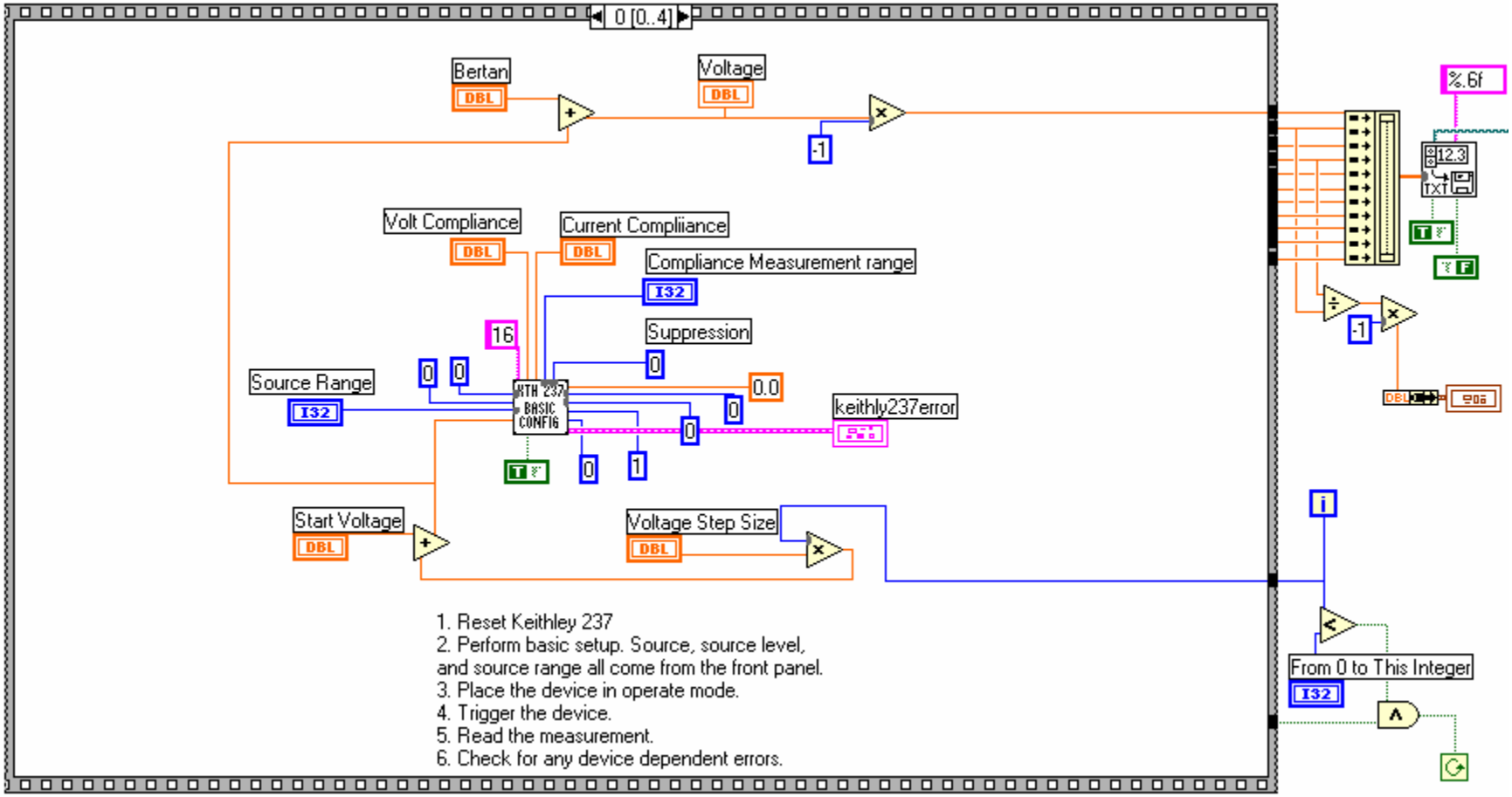

Figure C-10 Keithley237 Initialization LabVIEW wiring diagram.

C-2.(b) Energy Resolved Spectral Measurement Programs

There are six LabVIEW programs used to measure energy resolved spectra. Each is used for a specific energy range and resolution. All the programs use the same DAQBoard2000 configuration, DAQBoard2000 initialization (shown in orange), and data output to both the computer screen (shown in green) and recorded file (comments section not shown). Manipulation of the stepper motor is the same for every program and starts at a given angle shown in the "Start at angle" box (0-11). The three columns on the right show the nth angle number, the emission angle, and the tick mark shown on the stepper motor wheel. The stopping angle is the addition of the "Start at angle" box and the "Number of Angles to Move" box. For every nth move box, the number of stepper motor ticks has been calculated to move to each successive emission angle. For the duration of RD angle movement, the Keithley 237 is reset to its initial RD bias value (shown in pink). Though programs have been run to take spectra with increasing emission angle (counter-clockwise movement), all of these programs are used explicitly with decreasing emission angle (clockwise movement) to minimize backlash error.

C-2.(b) i High Energy Resolution

There are two LabVIEW programs used to take spectra at a high energy resolution. The SEpeakfine.vi and BSEpeakfine.vi programs both take spectra at 0.1 eV resolution in a 22 eV range [Fig. C-11 and Fig. C-12]. In order to accomplish this with the Keithley 237, the I source/V source in the "Source Range" must be set to 10nA/11V (2). The difference between the two programs is the initial RDbias Bertan setting. The Bertan setting for the SEpeakfine program is set to 9 volts in order to completely measure the SEpeak rise edge. The Bertan setting for the BSEpeakfine program is typically set to E_b-9 volts to completely capture the Elastic peak on the high energy side. In this case, E_b was set to 1189 volts and the Bertan was set to 1180 volts.

C-2.(b) ii Medium Energy Resolution

There are three LabVIEW programs used to take spectra at medium energy resolution. The SEpeak.vi, BSEpeak1V.vi, and MidEnergy1V.vi programs take spectra at 1 eV resolution in a 220 eV range [Fig. C-13, Fig. C-14, and Fig. C-15]. The Bertan setting for the SEpeak program is set to 0 volts in order to completely measure the SEpeak rise edge. Often times the Bertan is completely disconnected while using this program. The Bertan setting for the BSEpeak1V program is typically set to E_b-100 volts so that the Elastic peak can be measured along with features of the backscatter peak. In this case, E_b was set to 1189 eV. The Bertan setting for the Midenergy1V program is set to E_b-100 volts for the same reason. In this case, E_b was set to 2500 eV.

C-2.(b) iii Low Energy Resolution

There is one LabVIEW program used to take spectra at low energy resolution. The MidEnergy10V.vi program takes spectra at 10 eV resolution in a 220 eV range [Fig. C-16]. The scan count is 3.3 times larger than the other energy resolved spectral measurement programs, but the program as a whole takes ¼ the run time due to the decreased energy resolution. In other words, the total number of scans is ten times less than the previous energy resolution programs [Table C-1].

SEpeakfine LabVIEW Program

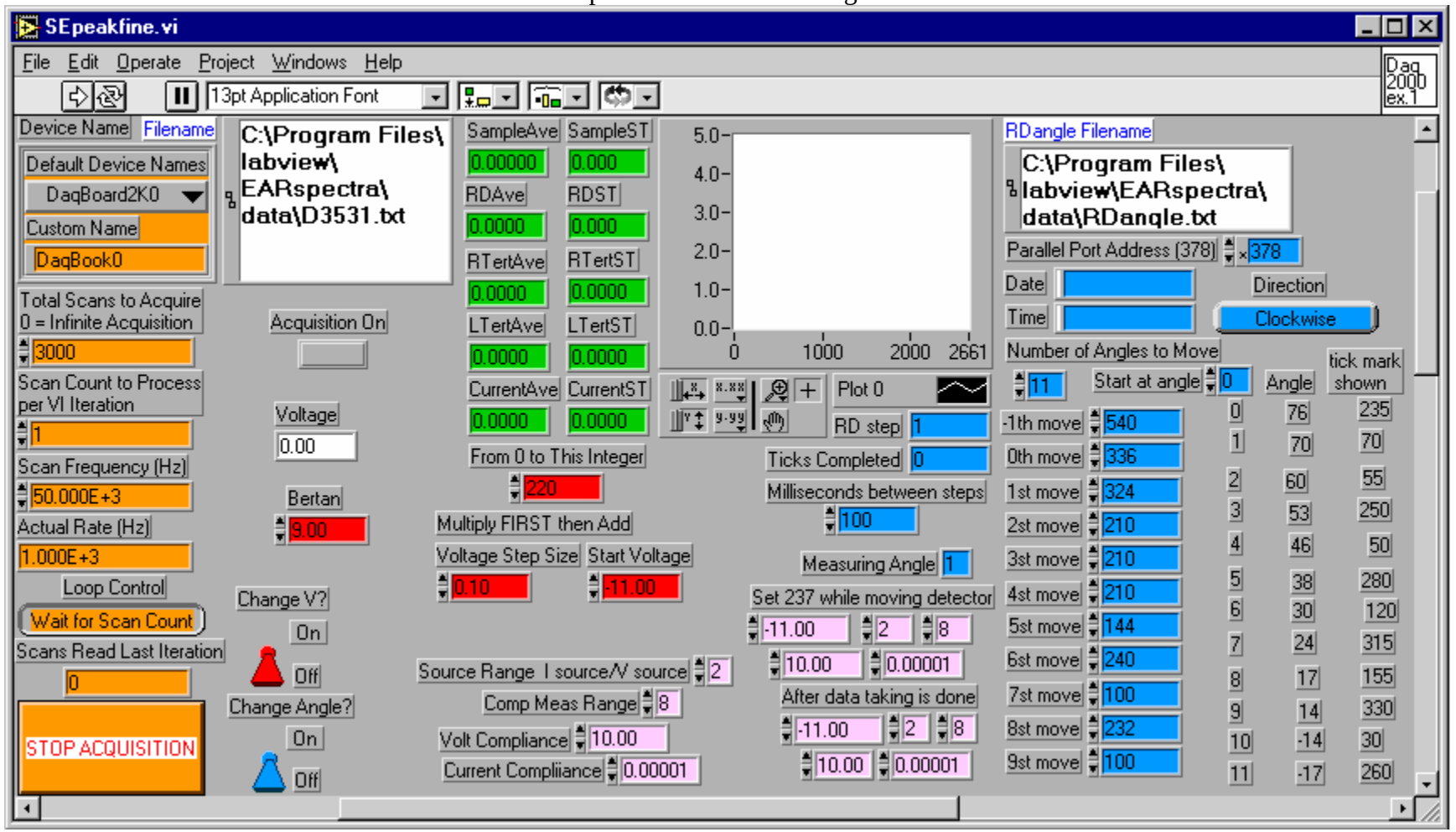

Figure C-11 SEpeakfine LabVIEW program takes twelve angle spectra at 0.1 eV energy resolution with the Bertan set at 9 volts.

BSEpeakfine LabVIEW Program

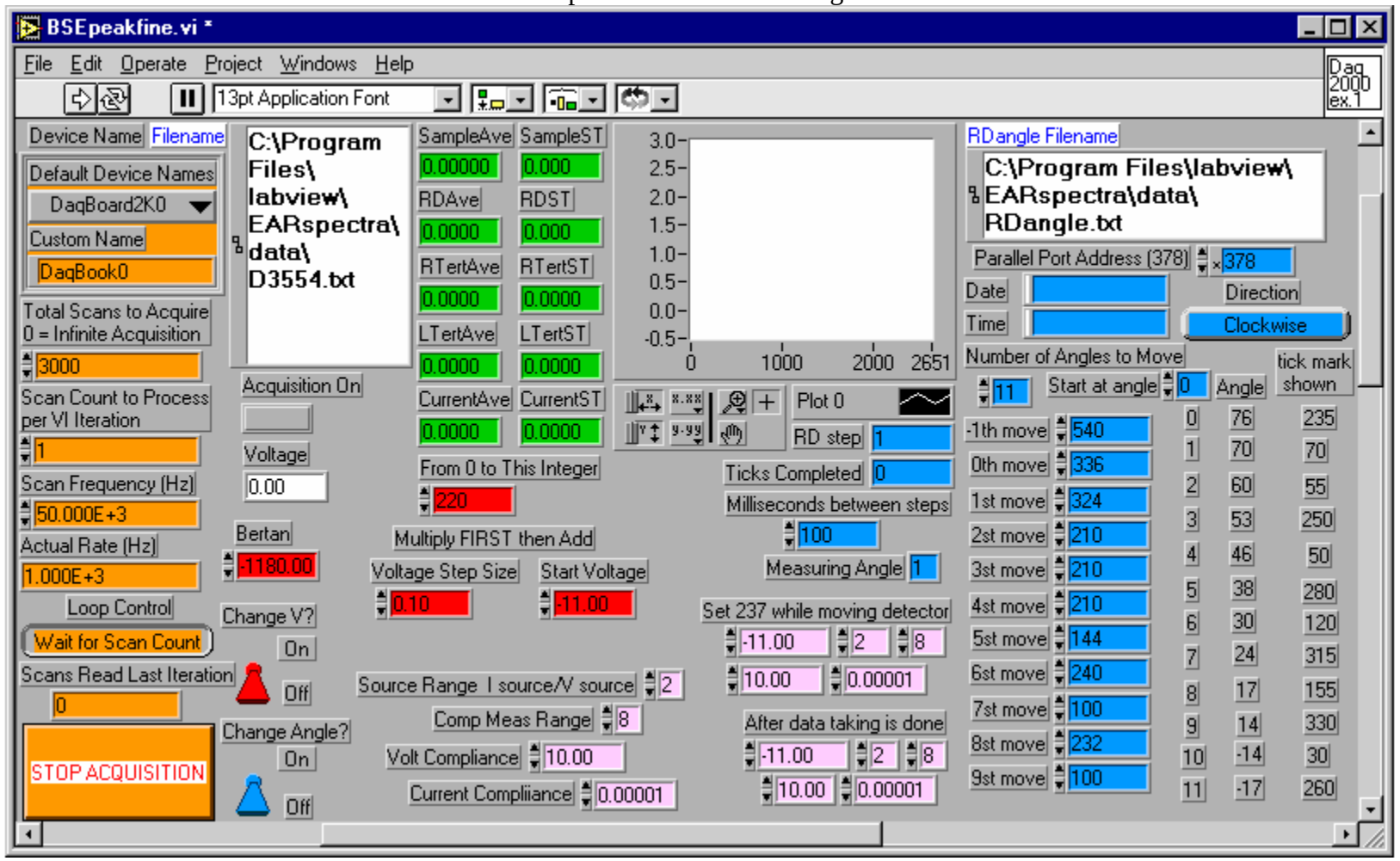

Figure C-12 BSEpeakfine LabVIEW program takes twelve angle spectra at 0.1 eV energy resolution with the Bertan set at 1180 volts.

SEpeak LabVIEW Program

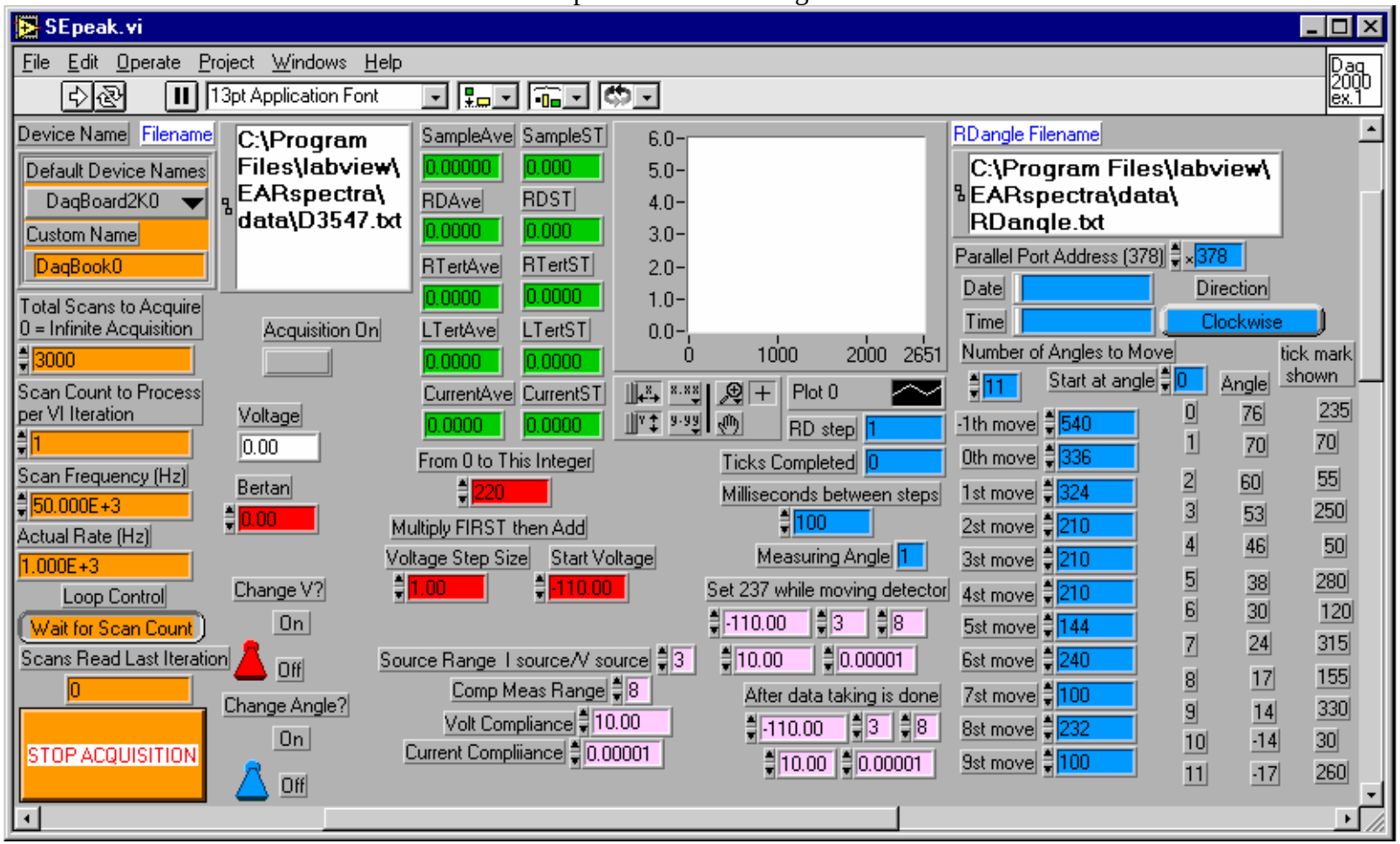

Figure C-13 SEpeak LabVIEW program takes twelve angle spectra at 0.1 eV energy resolution with the Bertan set at 0 volts

BSEpeak1V LabVIEW Program

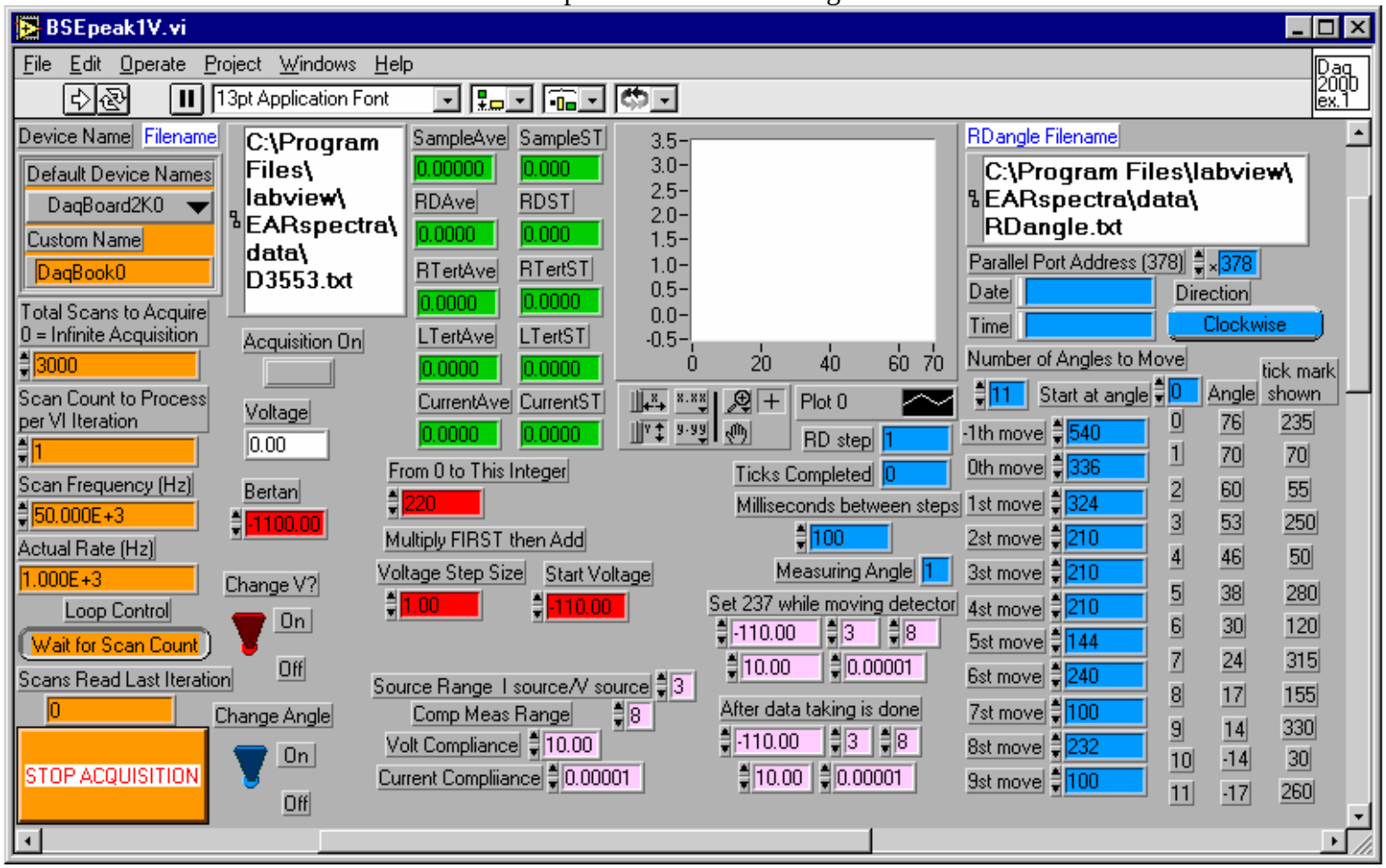

Figure C-14 BSEpeak1V LabVIEW program takes twelve angle spectra at 1 eV energy resolution with the Bertan set at 1100 volts.

MidEnergy1V LabVIEW Program

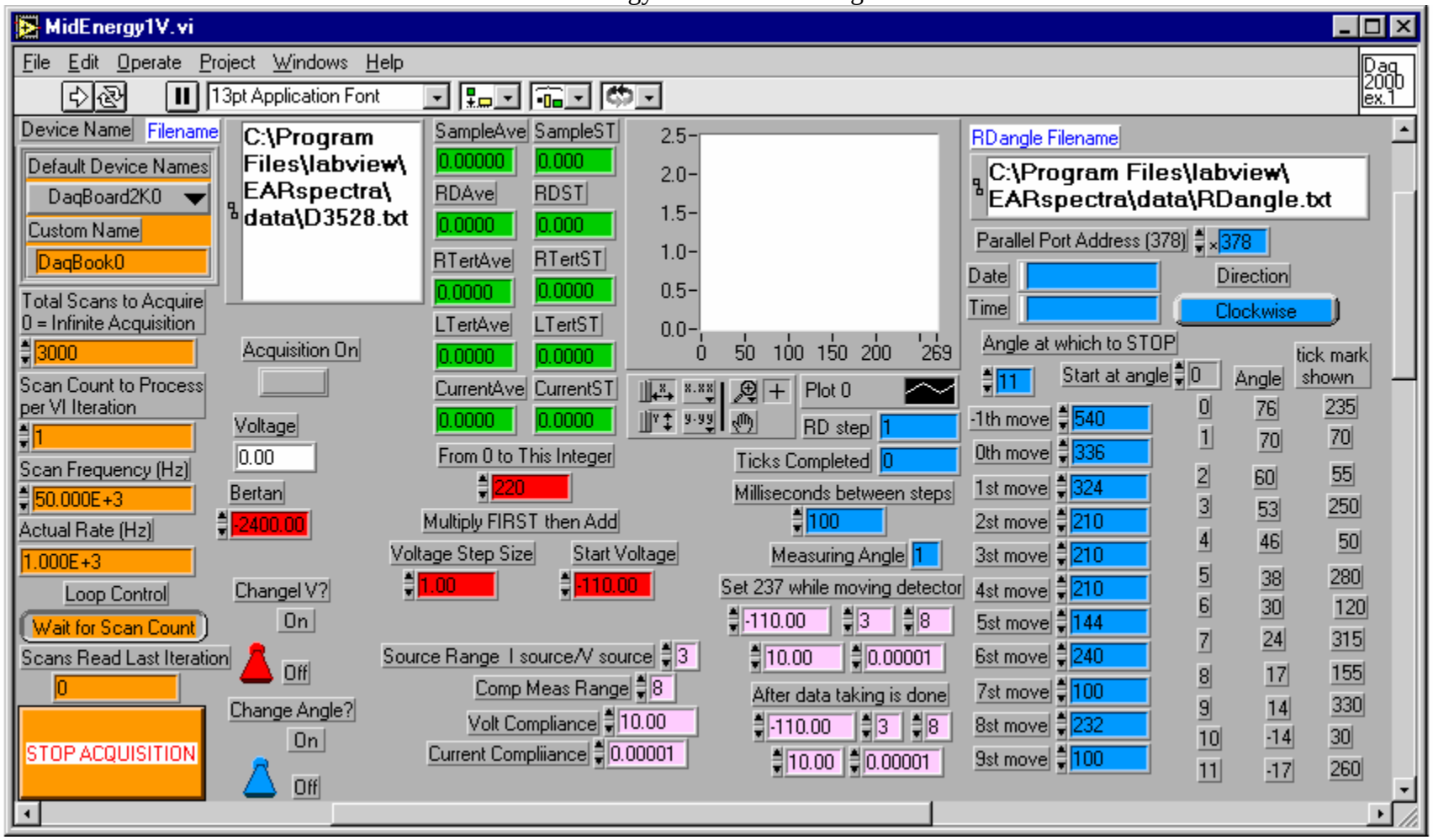

Figure C-15 MidEnergy1V LabVIEW program takes twelve angle spectra at 1 eV energy resolution with the Bertan set at 2400 volts.

MidEnergy10V LabVIEW Program

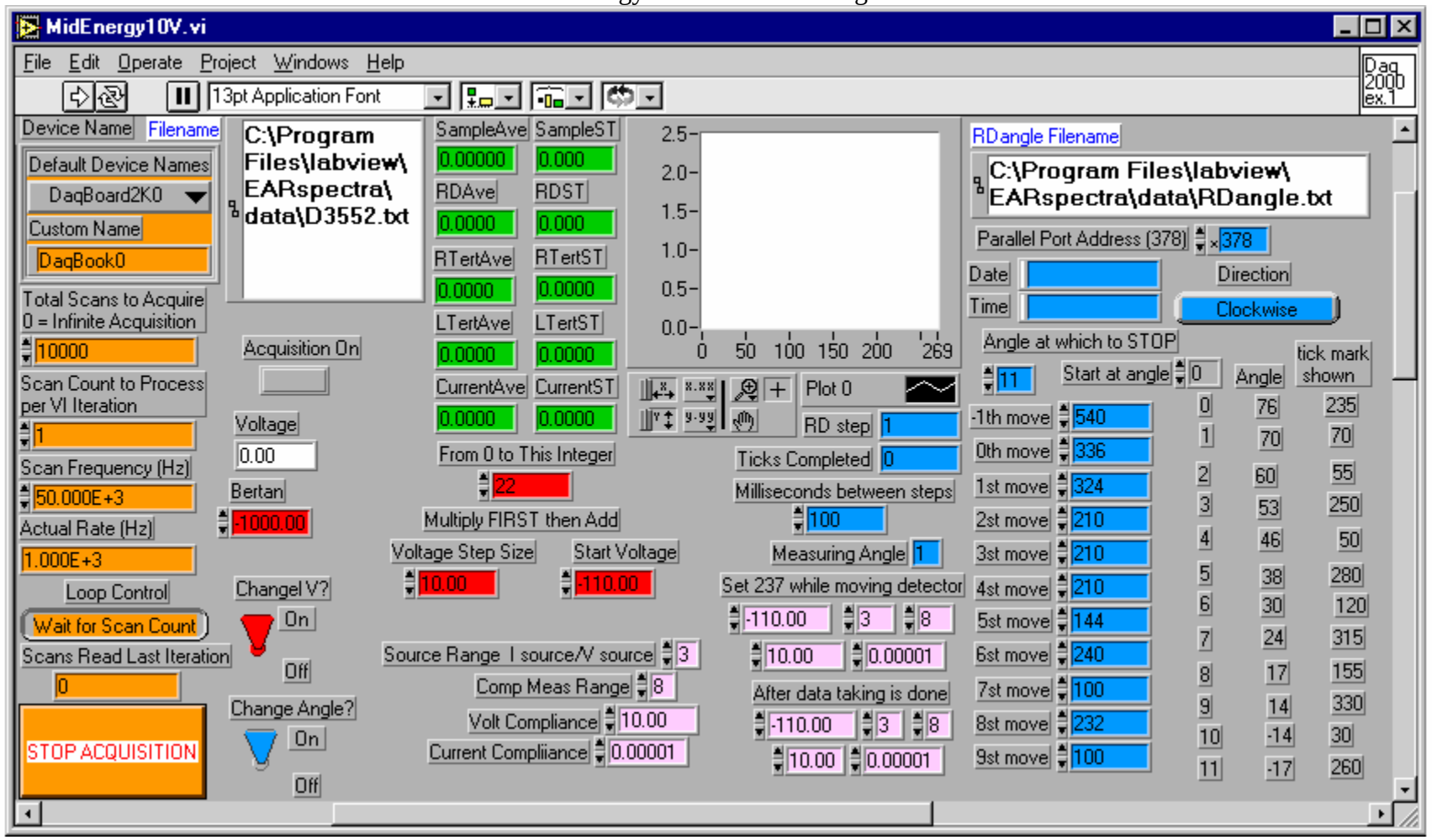

Figure C-16 MidEnergy10V LabVIEW program takes twelve angle spectra at 10 eV energy resolution with the Bertan set at 1000 volts.

C-2.(c) Angle Resolved Spectral Measurement Programs

The only LabVIEW program written to measure angle resolved spectra to fine resolution is the DetermineZeroAngle program [Fig. C-17]. The RD bias is set to a constant voltage while the RD angle is varied from 17^{o} clockwise emission to 76^{o} counter-clockwise emission at a resolution of ½ degree shown in the "Tick Multiplier" box. One tick is equal to 1/20th of a degree emission angle. The DetermineZeroAngle program has been used to measure the precision and accuracy of the RD angle position. It has also been used to assess damage to the RD cable, which transfers rotational motion from the stepper motor to the small gear (appendix D)

DetermineZeroAngle LabVIEW Program

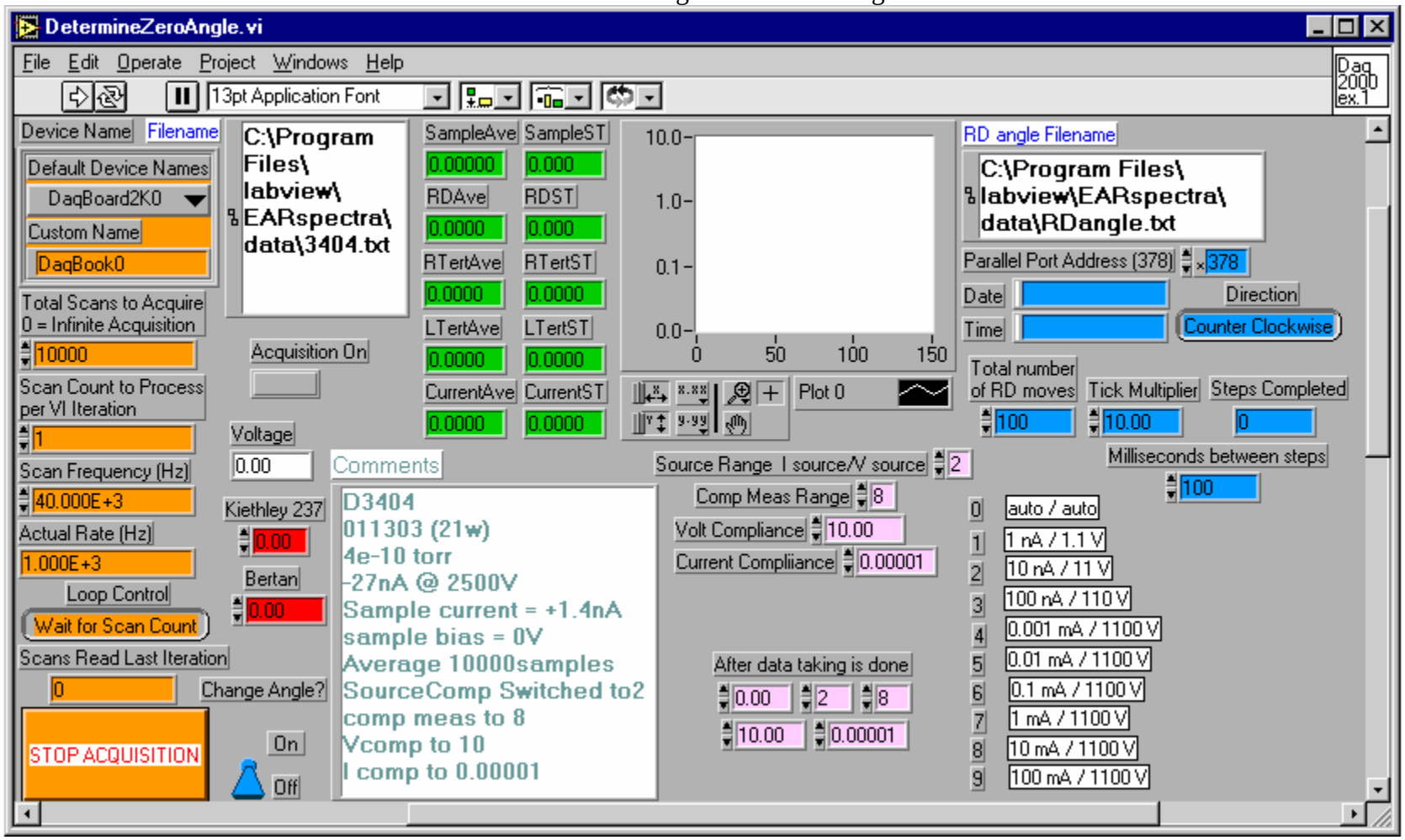

Figure C-17 DetermineZeroAngle LabVIEW program takes a spectrum at a constant RD bias and changes the RD angle at a fine resolution.

C-3 ARGA Programs

There are two LabVIEW programs which use RS232 to control and measure pressures from the ARGA quadrupole mass spectrometer. They are both similar in structure to configure the ARGA device [Fig. C-18 and Fig. C-19, purple]. Each program makes the ARGA continue in its mode even after the program is finished. Early termination of the program gives no information of the termination to the ARGA and therefore many changes in the "strings to write" [Fig. C-18 and Fig. C-19, yellow] allow for re-setting the device. For instance, a program will terminate with the ARGA in remote mode (RM;0:) and local mode (LO:) will need to be instructed in order to gain control of the front keypad. Many times the ARGA has trouble accepting a remote mode command. Sometimes a clean start of the ARGA is needed to let LabVIEW know that its OK to send a string, but even then, up to five repetitious RM commands were needed for computer control.

C-3.(a) ARGAchart.vi

The first LabVIEW program reads the partial pressure spectrum from mass 1 to 40 amu and charts the result to the computer screen [Fig. C-18]. The result is also saved to a file. The program may need to be run a couple of times to completely empty the buffer so that the mass and pressure show correctly in the two white rectangles. Requesting finite byte strings with delay times between are needed for LabView to correctly store the information as it comes in through the RS232 interface (shown in pink).

C-3.(b) ARGAcycle.vi

The second LabVIEW program reads partial pressures from preprogrammed masses (12 total) and charts them to the computer screen [Fig. C-19]. Requesting finite byte strings with delay times between are needed for LabVIEW to correctly store the information as it comes in through the RS232 interface (shown in pink). The program repeats for thirty iterations (shown in green).

ARGAchart LabVIEW Program

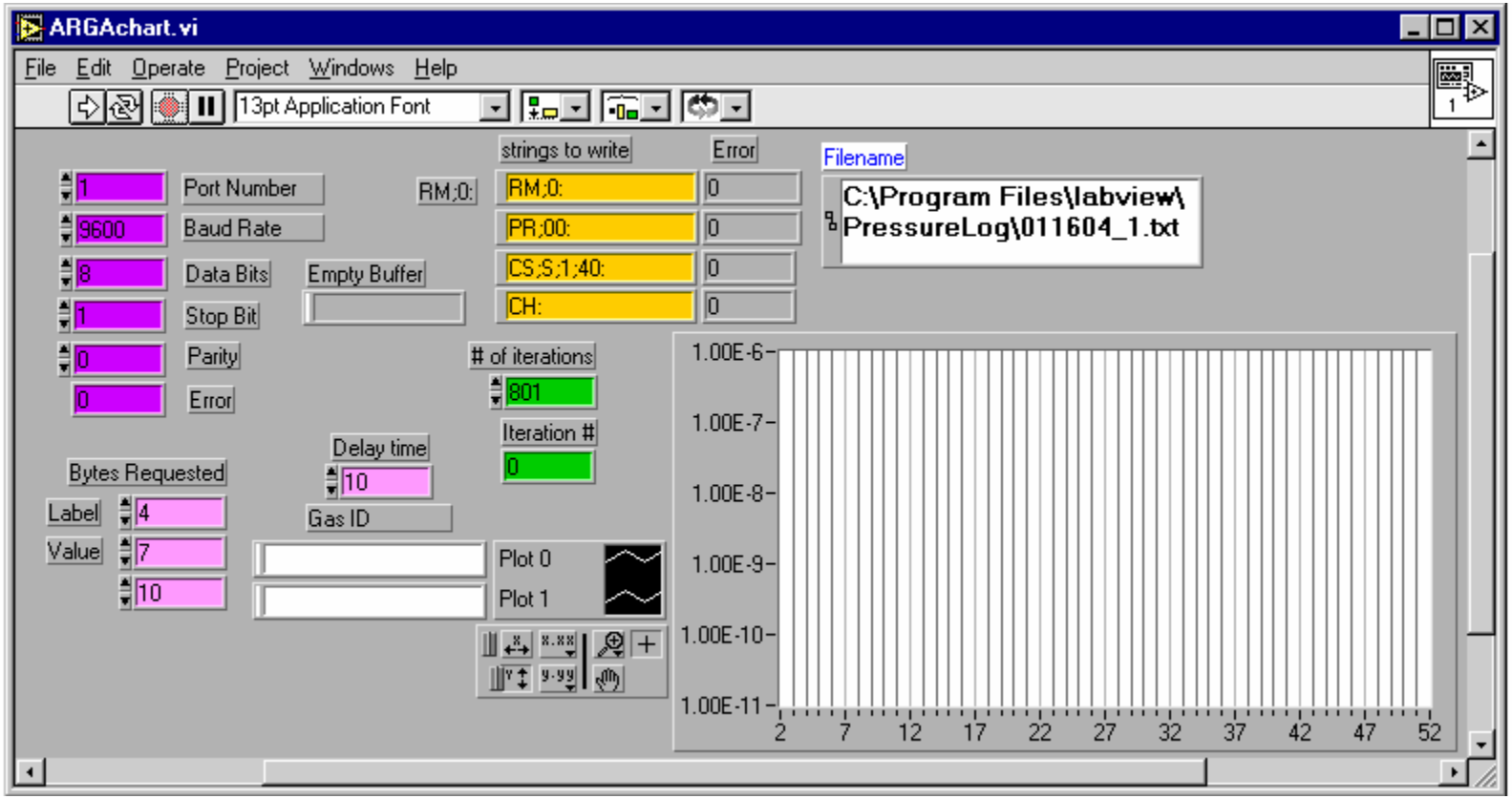

Figure C-18 ARGAchart LabVIEW program reads, plots, and records the partial pressure spectrum.

ARGAcycle LabVIEW Program

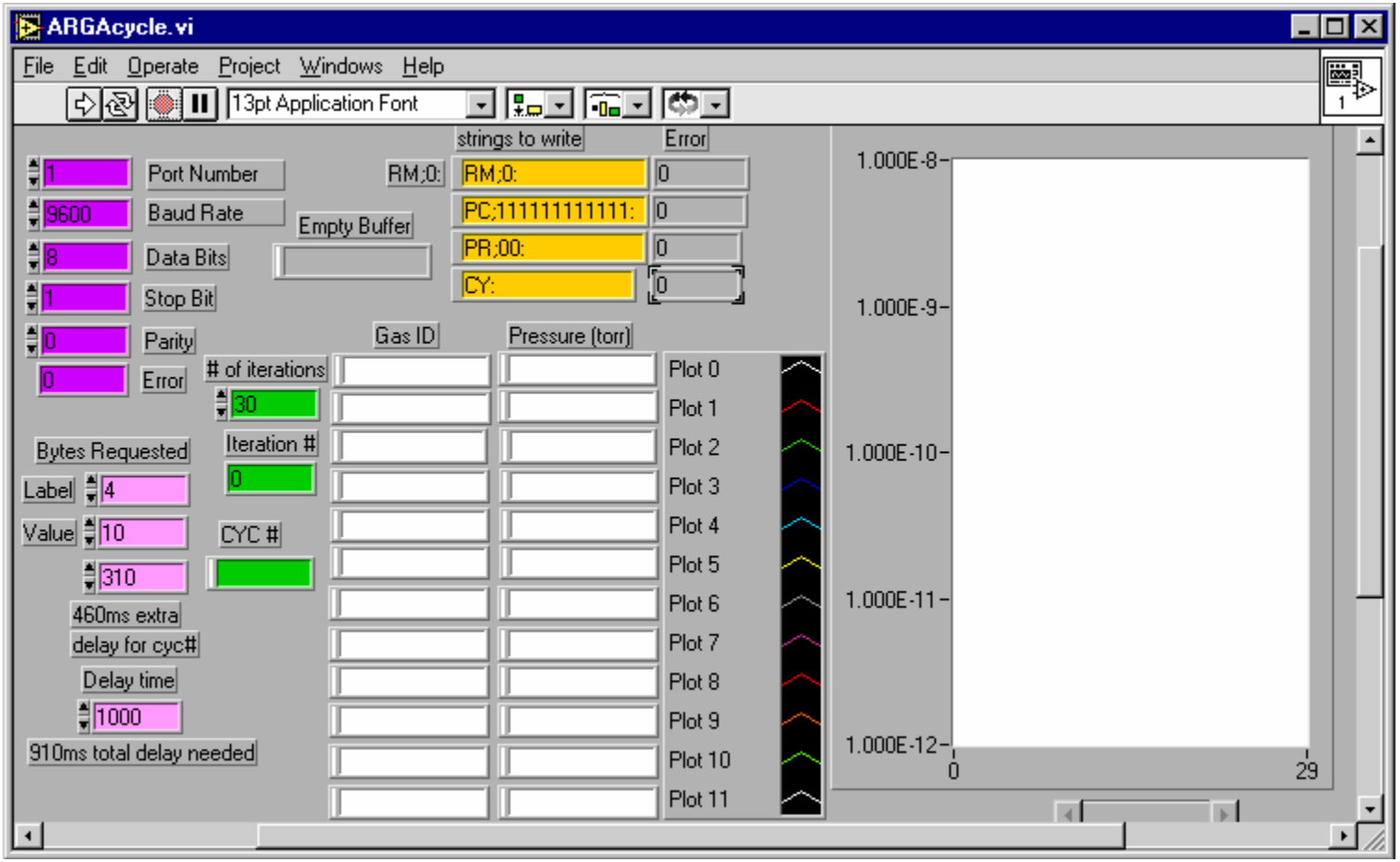

Figure C-19 ARGAchart LabVIEW program reads and plots residual gasses with their corresponding partial pressures.

APPENDIX D

ENERGY-RESOLVED ANGULAR DIAGNOSTIC MEASUREMENTS

A test was conducted to measure the ER angular distribution capabilities at the highest angular resolution of the LittleBoy. Stepping the newly installed steppermotor by its smallest possible step, ~1/20 degree (sections 3.2e, 3.1c, appendix A), accomplishes this task regardless of RD resolution. This is possible with the newly installed stepper-motor and controller. For time sake, only the total, $\sigma(\alpha,0,E_b)$, and SE yield, $\delta(\alpha,E'_{50V,450v},E'_b)$, were measured so that the highest angular resolution could help diagnose any symmetry problems in the chamber. Investigations conducted in the symmetrical configuration led to one additional instrumentation modification. Post investigations following a re-arrangement to the non-symmetrical configuration concluded that no further modification needed to be made.

D-1. Previous Investigations

A LabVIEW program (C-2(c)) was written to take advantage of the highest angular resolution of the newly installed steppermotor and controller (appendix B). An angle-resolved distribution, $\delta(\alpha,E'_e,E'_b)$, was measured by LabVIEW in the symmetric angular configuration [Fig. 3-8] with incident beam energy of 1500 eV [Fig. D-1]. These angular distributions are for clockwise and counter-clockwise movement of the RD biased at 0 eV. The maximum I_{RD}/I_{Sample} ratio is normalized to the solid angle ($3.66\text{x}10^{-5}$ sr^{-1}) and is a maximum of ~0.125 sr^{-1} and a minimum is ~ 0.077 sr^{-1}. Angular analysis included determining and comparing the angular locations of the repeatedly occurring peaks. The differences of the peak's locations were almost constant. For example, the difference in the RD angle positions for the Clockwise data are 11.1^o, 11.5^o, 12.0^o, and 11.1^o suggesting that the angle placement of the RD is not properly aligned by the steppermotor. Since these differences correspond angularly to one turn of the small gear [Fig. B-1], the misalignment must be caused by something between the steppermotor and the small gear. From this information, the piece that transfers rotational motion from the steppermotor to the small gear, was most likely defective. The torsionally bend RD cable has been replaced (3.2(a)).

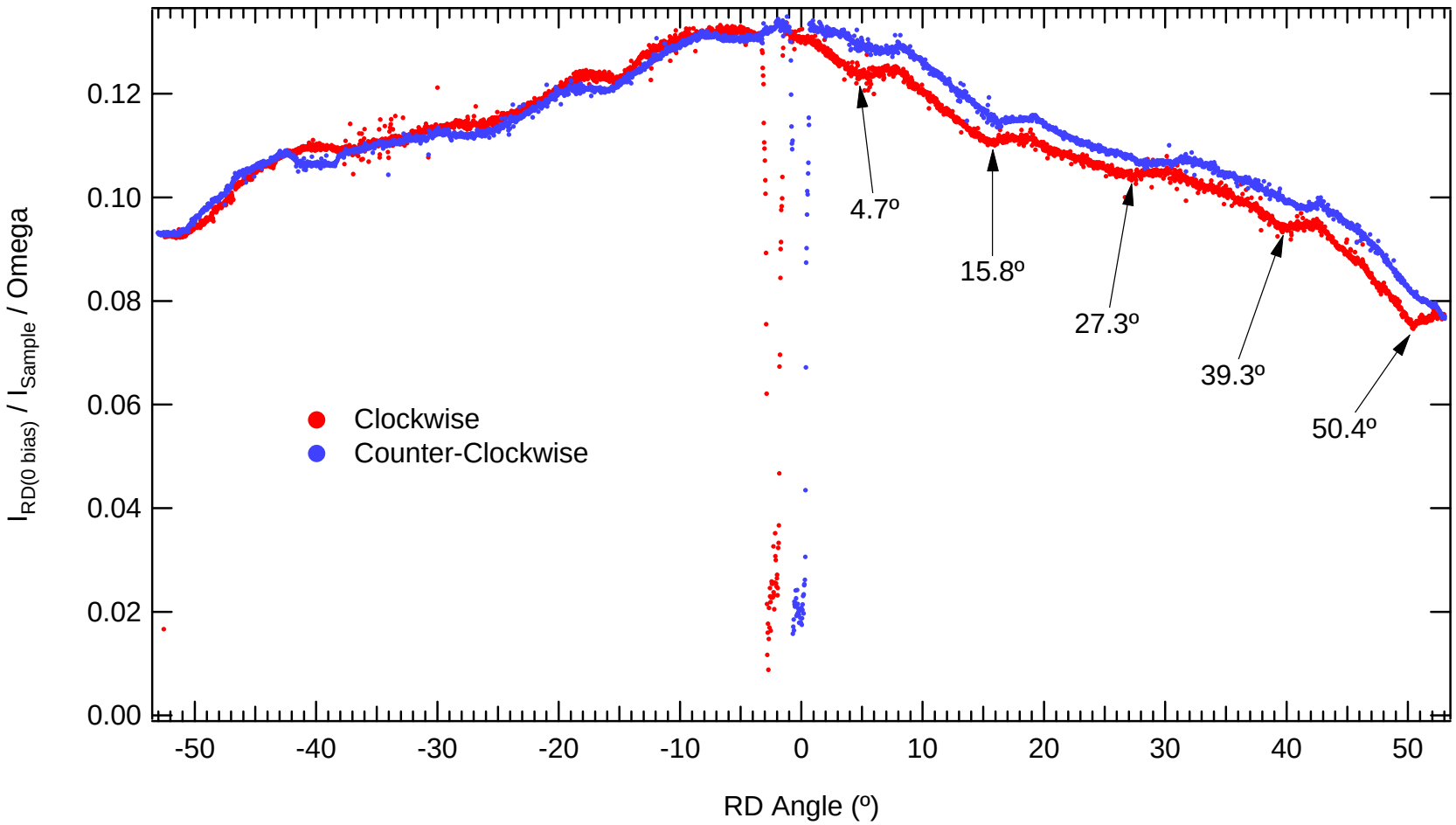

Figure D-1 Energy resolved angular distribution taken in the symmetric configuration at E_b = 1500 eV for the Clockwise (red) and Counter-Clockwise (blue) RD angle motion. The difference in the RD angle positions for the Clockwise data are 11.1°, 11.5°, 12.0°, and 11.1°, respectively.

Further investigation shows that the cable has slack, which is shown by a shift of the beam blockage location caused by the RD support post. Blockage of the beam has changed by approximately 2.5 degrees for Clockwise movement to Counter-Clockwise movement.

D-2. The two tertiary detectors

The detectors which stand also monitored for symmetry and for magnitude [Fig. D-2]. The ratio of the tertiary current to the sample current is typically ~10%.

And for sure look at [Fig. D-3]. And the RD current is typically 1-2% of the tertiary current, so the RD current is typically ~0.01% of the sample current.

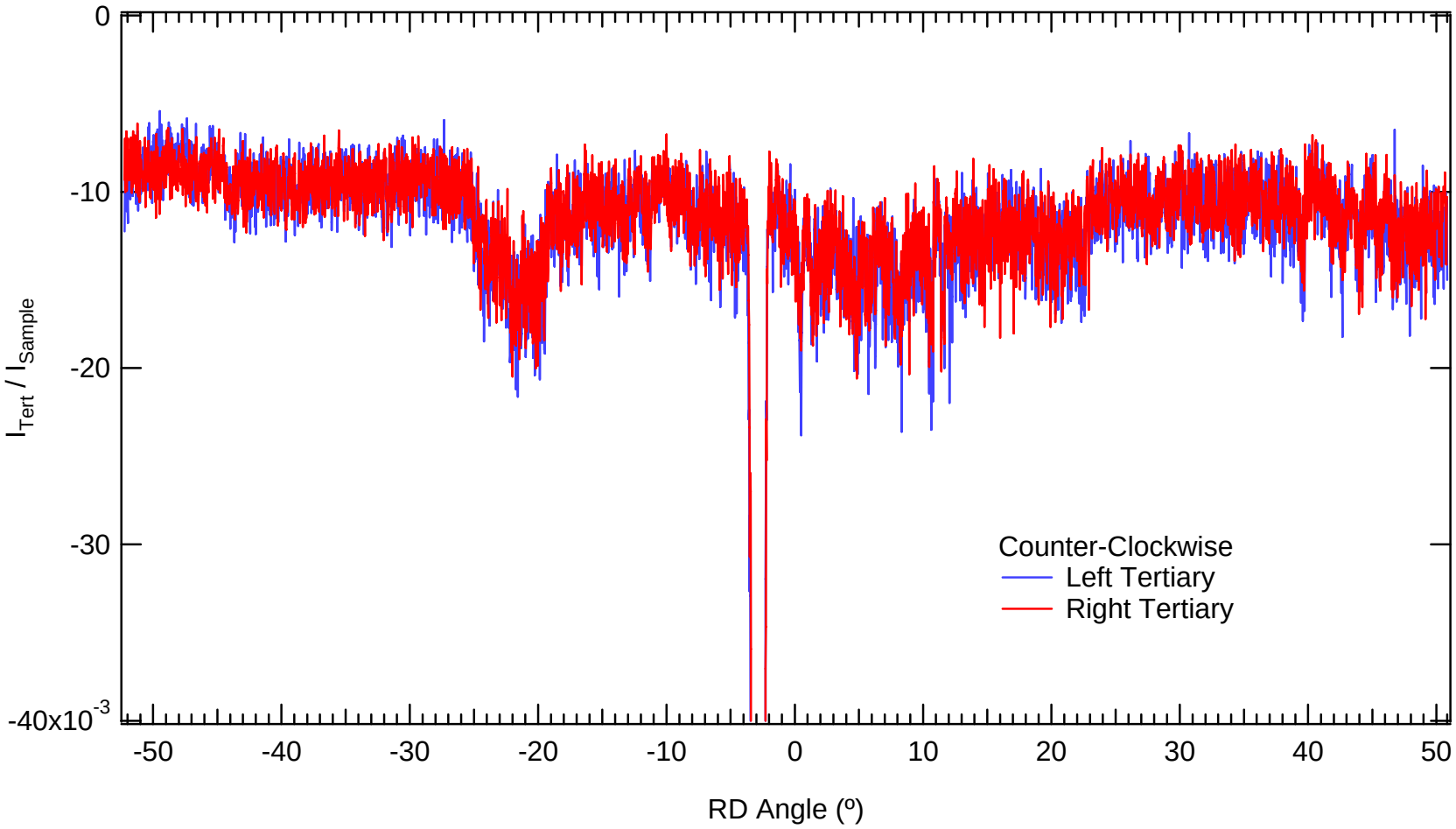

Figure D-2 This is the ratio of the Tertiary currents to the Sample current.

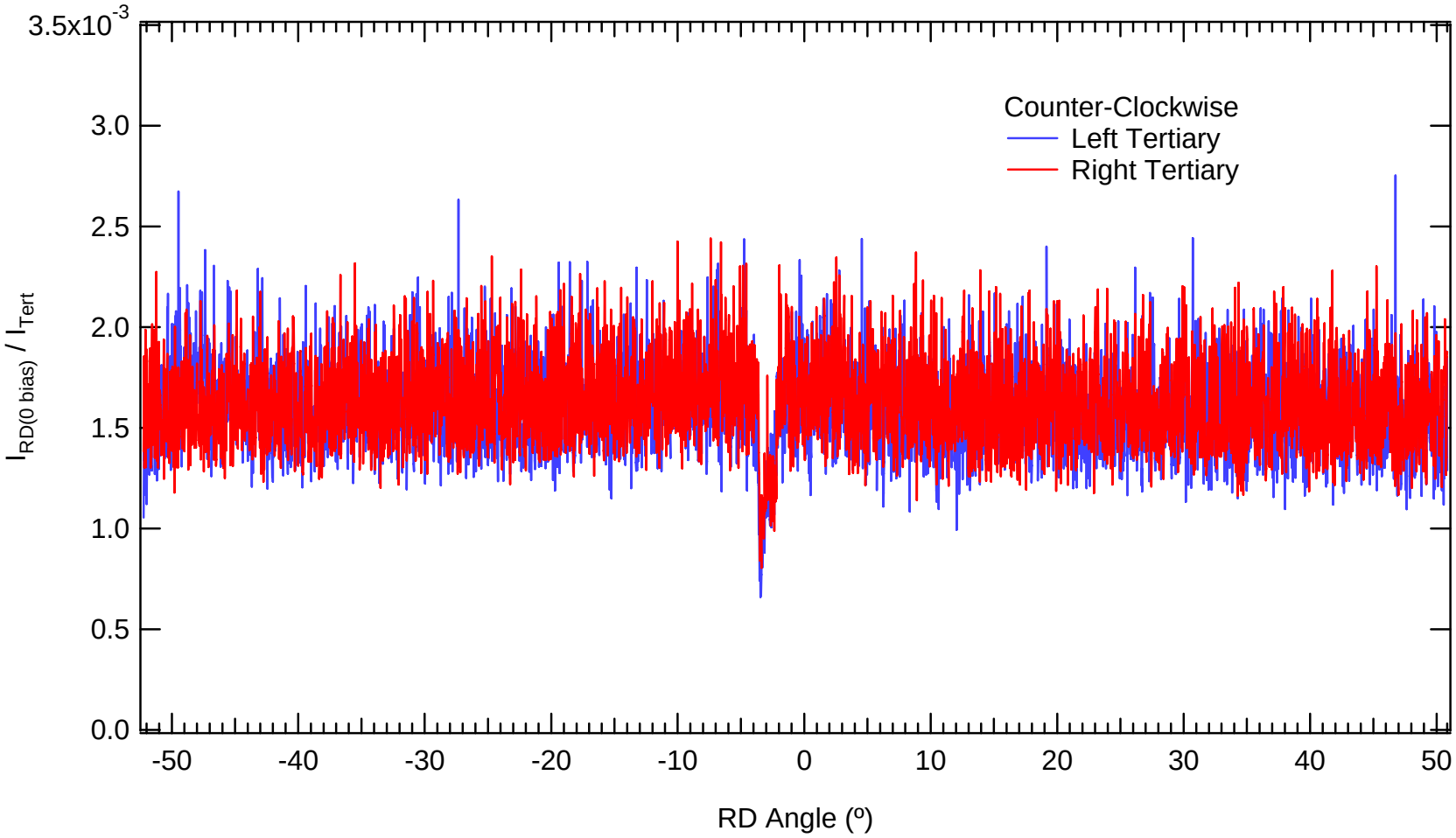

Figure D-3 This is the ratio of the RD to the Tertiary currents.

D-3. Post Investigations

After a diagnosis of the Right-Left symmetry of the RD signal, the LittleBoy chamber was re-configured in the non-symmetrical configuration.

Non-symmetrical configuration was re-configured concurrently as the RD cable was replaced.

The angular resolved distributions in the non-symmetrical configuration were measured for four different beam energies [Fig. D-4]. The distribution was subsequently measured with LabVIEW using the non-symmetrical configuration with other beam energies [Fig. D-4]. Notice that the peaks are no longer present. And don't forget about the Yield you calculated [Fig. D-5]. Unlike the Total Yields shown in Fig. D-4, the Fine angle—resolution SE cross section has been calculated for the E_b = 900 Volts using boundaries of 50 Volts and 450 Volts.

Above SE Emission peak ~2.5eV to 10eV the left-right agreement is ≤4%!! Given typical change in N max vs θ, this corresponds to ≤ ? degree uncertainty

Down to low energies (~0.5eV to 2.5eV), the left-right agreement is ≤8%.

Above ~10eV %diff is ≤8-10%. This is a reflection of much lower count rates at higher emission energy.

Note to Jason: Check to see if tertiary measurements for this data were taken. If so, then plot them.

Rob moved the beam into the Faraday Cup, measured the beam current, then moved the beam back to the sample and then made a spectrum measurement. Then he changed the angle and moved the beam back into the Faraday Cup, measured the beam current, and then moved the beam to the sample and made another spectrum measurement and then he changed the angle. He repeated that process 12 times for 12 different angles. A circuit, with a voltage output from the gun controller, which was directly proportionally to the beam current, was built. For every different energy, the calibration between the output voltage and the beam current was measured by using the Faraday cup. The beam was then moved on to the surface and 12 spectral measurements were taken, one for each angle, while measuring this voltage output. Throughout the measurement process, there was noise in the voltage signal, which was not remedied. For each portion of spectra, of each different angle, a different beam energy associated

calibration curve was used to calculate the beam current, which, though noisy, was averaged over large pieces of the spectra and at each angle, to make absolute spectral measurements.

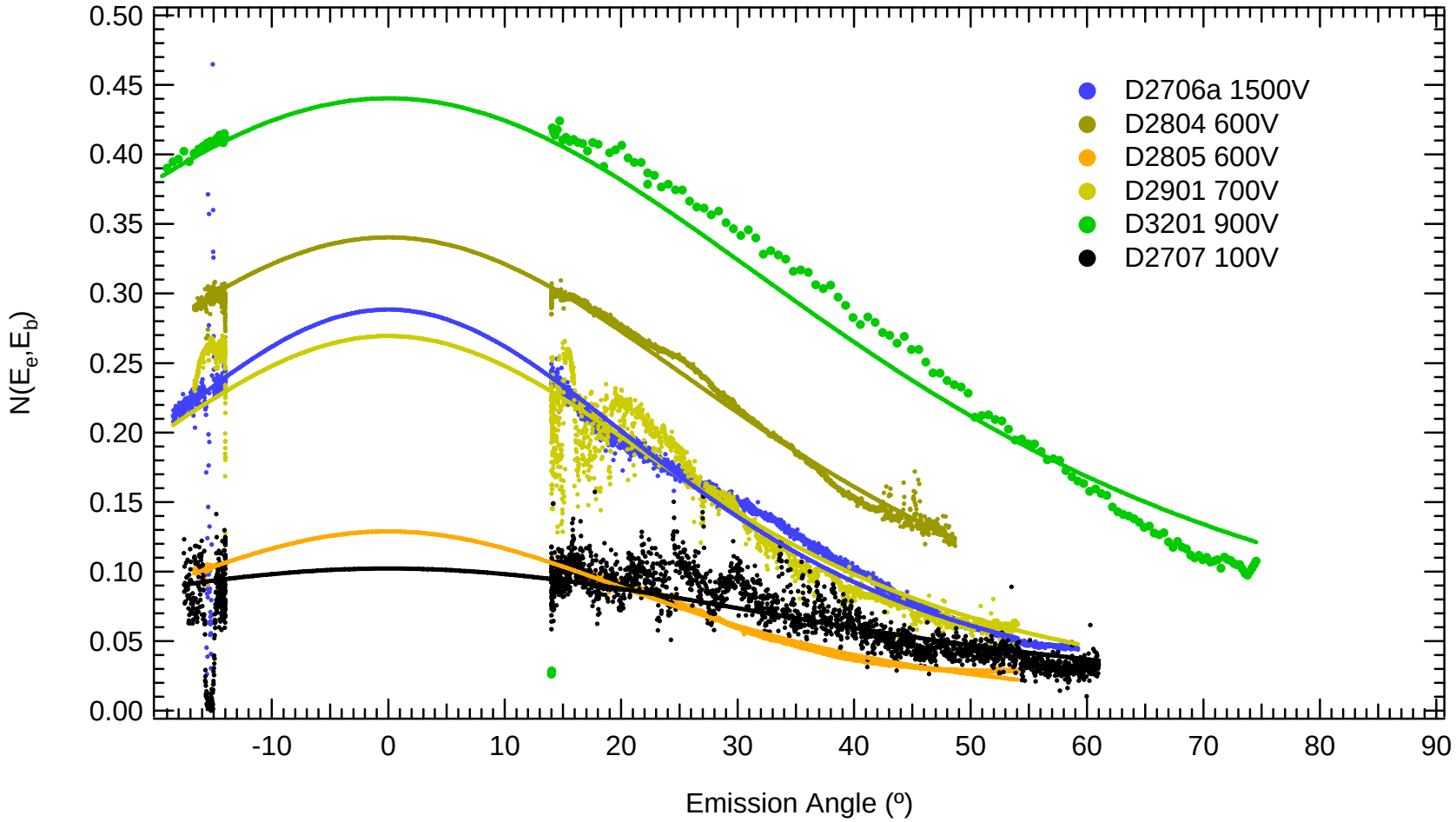

Figure D-4 Angular resolved total yield distribution for E_b = 100 eV, 600 eV, 700 eV, 900 eV, and 1500 eV measured in the non-symmetric angle configuration.

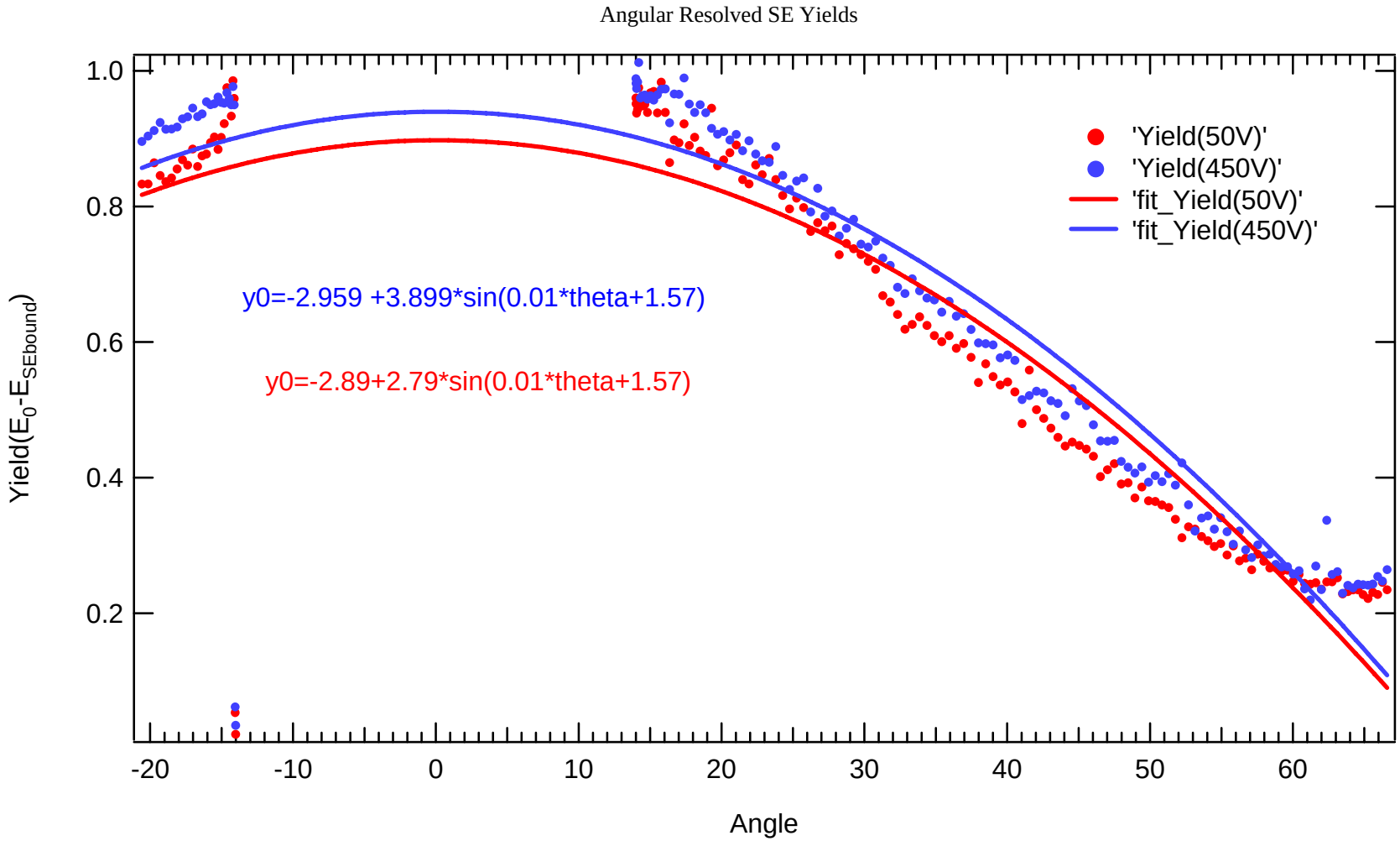

Figure D-5 Classical SE Yields for 50V boundary and 450V boundary. The beam energy is 900V.

APPENDIX E

ANGLE- ENERGY-RESOLVED DATA SUMMARY

The primary reason for providing a summary of the AER data is to emphasize the resolving capabilities of the instrument. A complete archive of the massive amount of data will be used compare to the most recent quantum mechanical theories. The three varied parameter values are the emission energy, E_e, the emission angle, α, and the incident beam energy, E_b. Each parameter has its own independent resolution and is used as a variable incremented over the RD bias energy ranges, E_e, then over emission angle ranges, α, and finally over beam energy ranges, E_b, respectively. For comparison, the high resolution emission angle distributions are given in Appendix D. The summary is ordered in a different manor than the spectral results shown in chapters 5 because the "weakest link", in terms of automation, occurs with the RD bias energy parameter, E_e. Construction of the spectra as E_e spans from 0 eV to E_b takes place during analysis. Before showing the AER summary, the environmental conditions are given along with the labeling scheme. The details of the environmental conditions and labeling scheme are given to assist in condensing the immense amount of spectral data provided.

E-1 Environmental Conditions

It is important that the UHV environmental conditions within the LittleBoy chamber be provided along with the AER data summary. The characteristics of the SEE phenomena can change depending on the environmental parameters addressed within the theory. The parameters most closely related to this investigation are the chamber pressure and the chamber temperature. The temperatures in this investigation are (300 ± 2) K (room temp.) monitored with the sample thermocouple (Chap 3.1(c). and Fig. B-2).

The least important of these is the chamber temperature because other phenomena become more important such as superconductivity (very low temperatures) and local phase changes (very high temperatures) between the solid—liquid interface in the Au sample attributed to the electron beam probe.

The total chamber pressure typically measures < 1 x 10^{-10} Torr. However, the operating pressure is upwards of an order of magnitude higher depending slightly on the electron beam energy due to the overall spray of charge from the sample [Fig. 1-3] and the electron beam current due to surface contamination. A LabVIEW program, MonitorPressure.pxp [Fig. 3-9], has been written and used (3.4(c)) to monitor the ion pump pressure. Random variations from fist raps (~0.1 s duration) to the LittleBoy table are shown [Fig. E-1]. The strong correlation with the RD current shows the fine sensitivity of the Littleboy while stabilized with rubber stopper feet. The physical vibrations, with intervals of approximately 7 sec, are pressure equalized and current stabilized. The significance of the uninterrupted controller voltage, $V_{controller}$, shows that there exists no immediate physical correlation between small pressure changes (2 to 7 x 10^{-9} Torr) and electron beam current. The result of the RD current and chamber pressure equalizing on approximately the same time scale (5 to 10 s) shows that physical vibration affects the amount of electron spray within the instrument. The ion pump pressure typically averages ~1x10^{-9} Torr during spectral measurement.

The partial pressures (ARGA quad—mass spectrometer) are useful for diagnosing electron stimulated adsorption (ESA) contamination (4.3(c) and 4.3(d)) and is minimized when the incident electron beam current density is minimized. The incident electron beam current density typically varies from ~5x10^{-6} A/cm^2 to 1x10^{-5} A/cm^2 (Appendix B, beamspot graph) over a 1.5 mm beamspot. A LabVIEW program has been written to measure the partial pressures (Appendix C) but has not been tested because of the mis—calibration of the recently repaired ARGA head ramping voltage regulator.

Theory (and limited experimental exidence-including Sternglass) suggests that SE/BSE yield for conductors are not strongly temperature dependent (unlike semiconductors and insulators that have modest

temperature dependence due to electron/hole creation across bandgap). Further, <=1% temperature variation is small, so variations in yields with temperature can be neglected. There might be a temperature effect in the beam current amplifier circuit or the electrometers, but this is likely small.

What causes variation in gun control current? I guess point is that Ibeam does not change with rap, but RD and pressure do. Could the signal spike in pressure and RD be simply current spikes in the sensitive current measurement for the pressure sensor and RD detector due to tribostatic induced currents in their cabling? Given that RD current spikes are >100uA (that's very large compared to typical pA signals), I think I'd be surprised if it is tribostatic.

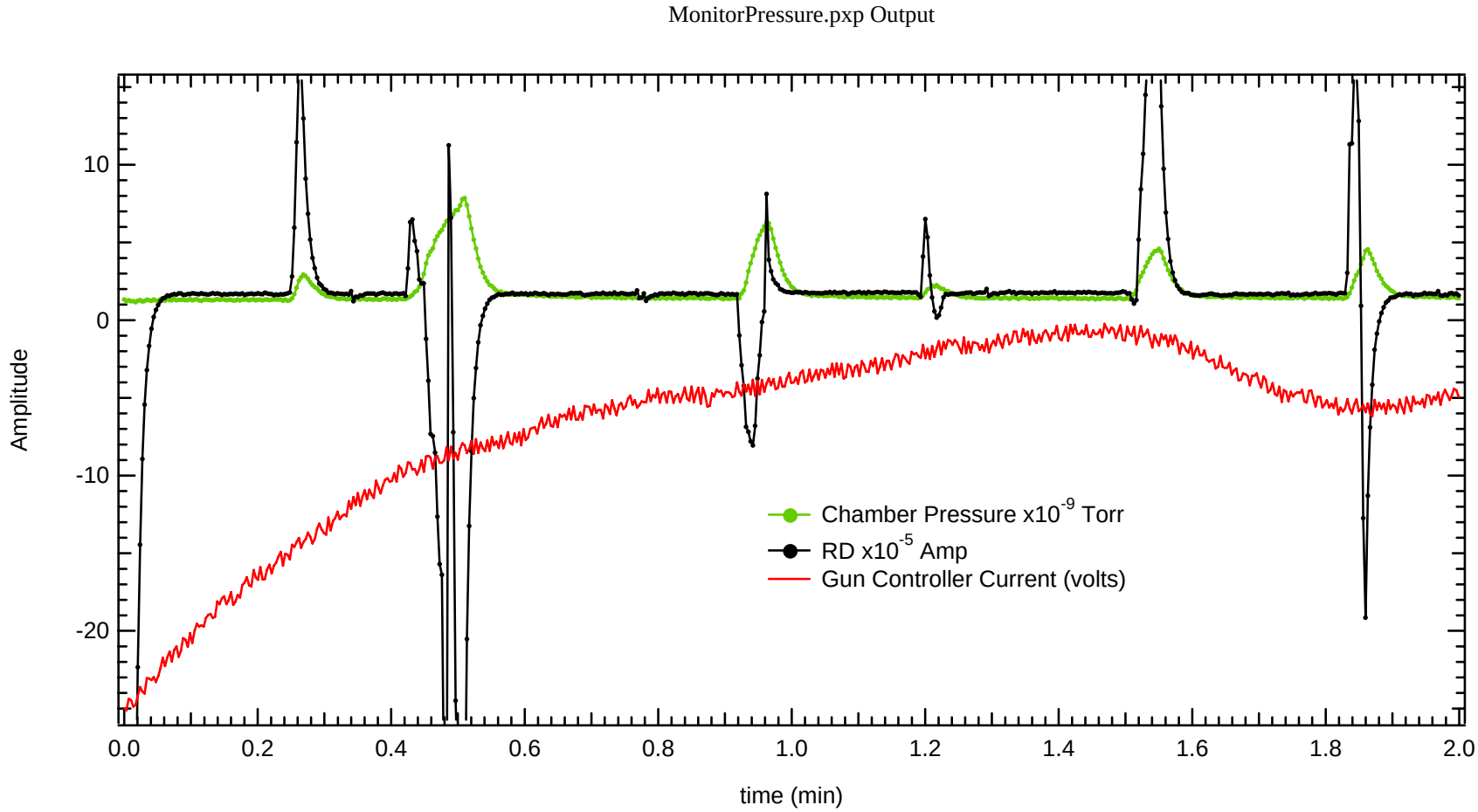

Figure E-1 Comparison of Chamber Pressure (ion pump), Rotatable Detector Current and electron gun controller current detected as a voltage, $V_{controller}$. The duration of each rap to the LittleBoy was ~0.1 s. The gun controller voltage was not affected during these raps.

E-2 Labeling Scheme

The labeling scheme for data files has been adopted from Davies [*Davies, 1999*]. The filename labeling the spectral data is a combination of the sample label, the surface label, and an incremental number. The sample label consists of one alphabetic character. The surface label consists of the first two-digit number following the letter label. The spectral data label consists of a second two-digit number distinguishing an uninterrupted measurement.

E-3 Spectral Data Summary for Polycrystalline Au Sample "D"

Since the Bertan RD biasing supply is the only parameter not automated by the LabVIEW software, it is used as the range in Chapters 5 and 6. In this way, the energy data is concatenated together to provide entire spectra for various beam energies and emission angles, respectively. The data analysis algorithm (3.2(i)) assists in ordering, extracting, and providing integrated yield information.

Table E-1 is an AER summary of eight different beam energies, given on the left, along with the Labbook cross reference. Note that the data of 500 eV elastic spectrum was taken with the LittleBoy in the symmetrical configuration [Fig 3-8] where the steppermotor had not yet been installed. The RD angles that have an X mark have been selected for analysis in Chapter 5. The positive RD angles are those in the Counter-Clockwise direction (looking down) and the negative RD angles are those in the Clockwise direction. In addition to the Bertan voltage, shown on the right, the incremental step voltage is given in the column labeled volt step. The spectral data filename is given under the sample surface label.

Table E-1 Angle- Energy- Resolved Data Summary for Incident Beam Energies of 100 eV, 500 eV, 600 eV, 900 eV, 1200 eV, 2000 eV, and 2500 eV.

Beam / Lab Energy/Book /reference	Sample Surface	RD Angle (^{o})												Bertan(V) Voltage	Volt(V) Step
		-17	-14	14	17	24	30	38	46	53	60	70	76		
100 eV	D2708					X	X	X	X	X		X	X	5.045	0.1
LB580w	D2709			X	X									5.05	0.1
	D2710			X	X			X	X	X	X	X	X	14.97	0.1
	D2711				X	X	X	X	X	X	X	X		35.03	0.1
	D2712			X	X	X	X	X	X	X	X	X	X	54.94	0.1
	D2713			X	X	X	X	X						74.95	0.1
	D2714								X	X	X	X	X	74.95	0.1
	D2715			X	X	X	X	X	X	X	X	X	X	95	0.1
	D2716										X			5	0.1
	D2717												X	35	0.1
	D2720					X	X							15	0.1
500 eV	D3301			X	X	X	X	X	X	X	X	X	X	400	1
LB615y	D3302			X	X	X	X	X	X	X	X	X	X	250	1
	D3303			X	X	X	X	X	X	X	X	X	X	50	1
	D3304			X	X	X	X	X	X	X	X	X	X	400	10
LB616y	D3305			X	X	X	X	X	X	X	X	X	X	250	10
	D3306			X	X	X	X	X	X	X	X	X	X	50	10
	D3307	X												400	1
	D3308	X												250	1
	D3309	X												50	1
	D3310		X											400	1
	D3311		X											250	1
	D3312		X											50	1
	D3313	X	X	X	X	X	X	X	X	X	X	X	X	490	0.1
	D3401	X	X	X	X	X	X	X	X	X	X	X	X	9	0.1

		-53	-46	-38	-30	-24	-17	17	24	30	38	46	53		
500 eVelastic	D2573							X							0.01
	D2574								X						0.01
	D2575										X				0.01
	D2576											X			0.01
	D2577												X		0.01
	D2578									X					0.01
	D2579	X													0.01
	D2580		X												0.01
	D2581			X											0.01
	D2582				X										0.01
	D2583					X									0.01
	D2584						X								0.01

Table E-1 (cont.)

Beam / Lab Energy/Book reference	Sample Surface	RD Angle (°) 14	17	24	30	38	46	53	60	70	76	Bertan(V) Voltage	Volt(V) Step
600 eV	D2801	X	X	X	X	X	X	X	X	X	X	500	1
LB583w	D2802	X	X	X	X	X	X	X	X	X	X	300	1
	D2803	X	X	X	X	X	X	X	X	X	X	100	1
	D2806				X	X	X	X	X	X	X	300	1
		14	17	24	30	38	46	53	60	70	76		
700 eV	D2902	X	X	X	X	X	X	X	X	X	X	600	1
LB588w	D2903	X	X	X	X	X	X	X	X			400	1
	D2904	X	X	X	X	X	X	X	X			200	1
	D2905	X	X	X	X	X	X	X	X	X	X	100	1
	D2906	X	X	X	X	X	X	X				300	1
		76	70	60	53	46	38	30	24	17	14	-14	-17		
900 eV	D3501	X	X	X	X	X	X	X	X	X	X	X	X	9	0.1
LB623w															
	D3504	X	X											50	1
	D3505	X	X	X	X	X	X	X	X	X	X	X	X	800	1
	D3506	X	X	X	X	X	X	X	X	X	X	X	X	600	1
	D3507									X	X		X	400	1
	D3508	X	X	X	X	X	X							200	1
	D3509	X	X	X	X	X	X	X	X					400	1
	D3510							X						200	1
	D3511	X	X	X	X	X	X	X	X	X	X	X	X	880	0.1
	D3512								X	X	X	X	X	200	1
	D3513								X	X	X	X	X	50	1
1200 eV	D3547	X	X	X	X	X	X	X	X	X	X	X	X	0	1
LB629w	D3548	X	X	X	X	X	X	X	X	X	X	X	X	200	1
	D3549	X	X	X	X	X	X	X	X	X	X	X	X	400	10
	D3550	X	X	X	X	X	X	X	X	X	X	X	X	600	10
	D3551	X	X	X	X	X	X	X	X	X	X	X	X	800	10
	D3552	X	X	X	X	X	X	X	X	X	X	X	X	1000	10
	D3553	X	X	X	X	X	X	X	X	X	X	X	X	1100	1
	D3554	X	X	X	X	X	X	X	X	X	X	X	X	1180	0.1

Table E-1 (cont.)

Beam / Lab Energy/Book reference	Sample Surface	RD Angle (°)												Bertan(V) Voltage	Volt(V) step
		-17	-14	14	17	24	30	38	46	53	60	70	76		
2500 eV	D3402	X	X	X	X	X	X	X	X	X	X	X	X	9	0.1
111hrs	D3403	X							X	X			X	50	1
LB624y		76	70	60	53	46	38	30	24	17	14	-14	-17		
	D3514													100	10
	D3515	X	X	X	X	X	X	X	X	X	X	X	X	200	10
	D3516	X	X	X	X	X	X	X	X	X	X	X	X	400	10
	D3517	X	X	X	X	X	X	X	X	X	X	X	X	600	10
	D3518	X	X	X	X	X	X	X	X	X	X	X	X	800	10
	D3519													800	10
	D3520	X	X	X	X	X	X	X	X	X	X	X	X	1000	10
	D3521	X	X	X	X	X	X	X	X	X	X	X	X	1200	10
	D3522	X	X	X	X	X	X	X	X	X	X	X	X	1400	10
	D3523	X	X	X	X	X	X	X	X	X	X	X	X	1600	10
	D3524	X	X	X	X	X	X	X	X	X	X	X	X	1800	10
	D3525	X	X	X	X	X	X	X	X	X	X	X	X	2000	10
	D3526	X	X	X	X	X	X	X	X	X	X	X	X	2200	10
	D3527													2400	10
	D3528	X	X	X	X	X	X	X	X	X	X	X	X	2400	1
	D3529	X	X	X	X	X	X	X	X	X	X	X	X	0	1
	D3530	X	X	X	X	X	X	X	X	X	X	X	X	2468	0.1
	D3531	X	X	X	X	X	X	X	X	X	X	X	X	8.68	0.1
		76	70	60	53	46	38	30	24	17	14	-14	-17		
2000 eV	D3532	X	X	X	X	X	X	X	X	X	X	X	X	0	1
LB627w	D3533	X	X	X	X	X	X	X	X	X	X	X	X	100	1
	D3535	X	X	X	X	X	X	X	X	X	X	X	X	200	10
	D3536	X	X	X	X	X	X	X	X	X	X	X	X	400	10
	D3537	X	X	X	X	X	X	X	X	X	X	X	X	600	10
	D3538	X	X	X	X	X	X	X	X	X	X	X	X	800	10
	D3539	X	X	X	X	X	X	X	X	X	X	X	X	1000	10
	D3540													1200	10
	D3541	X	X	X	X	X	X	X	X	X	X	X	X	1400	10
	D3542	X	X	X	X	X	X	X	X	X	X	X	X	1600	10
	D3543	X	X	X	X	X	X	X	X	X	X	X	X	1800	10
	D3544	X	X	X	X	X	X	X	X	X	X	X	X	1900	1
	D3545	X	X	X	X	X	X	X	X	X	X	X	X	1975	0.1
	D3546	X	X	X	X	X	X	X	X	X	X	X	X	1200	10

E-4 Pre—Differentiated Data Polycrystalline Au Sample “D”

These next six graphs are not pre—differentiated (raw data), rather, they are the integrated result of the differentiated raw data, which have been concatenated together to remove discontinuities. Each graph contains its own Incident Beam energy, $E_{b,}$ and all emission angles measured. It is useful to note that no smoothing has been done.

The E_b = 100 eV graph [Fig. E-2] utilizes the data summarized in the last section. The data files D2708 through D2720 have been taken at 0.1 eV resolution, then averaged over every ten points, differentiated, then integrated so that no discontinuities remain. A linear domain axis is given in units of inverse steradians.

For the remaining E_b graphs [Figs. E-3 through E-9], three different resolutions, 0.1 eV, 1 eV, and 10 eV are concatenated together by integrating the differentiated data. The higher resolution data is reserved for the lowest (near 0 eV) and highest (near E_b eV) emission energy range limits, and the lower resolution data is reserved for the wide range existing between these emission energy range limits. A logarithmic domain axis is given in units of inverse steradians.

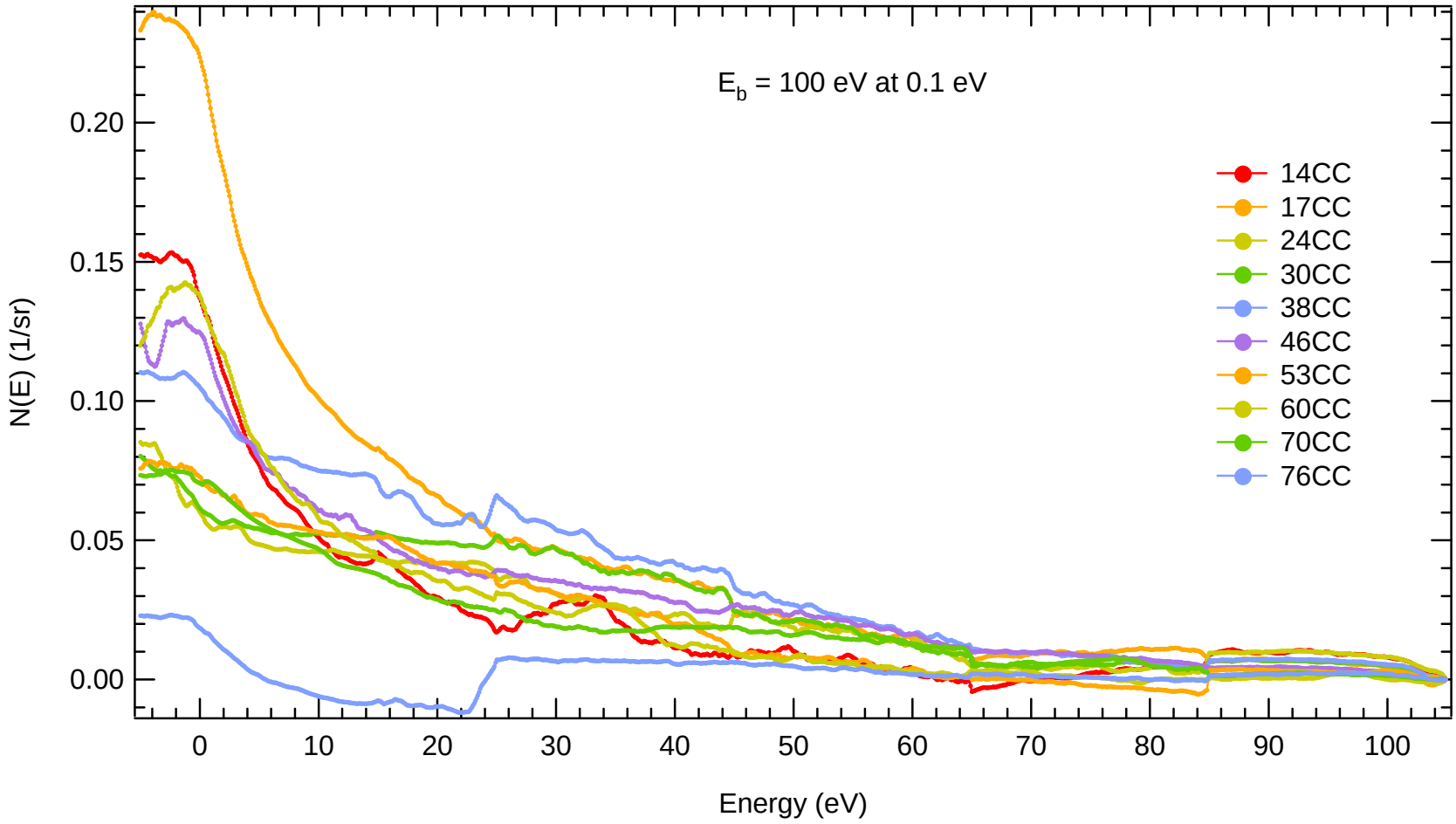

Figure E-2 N_{out}/N_{in} * $<S/I_b>_{200}$ at E_b = 100 eV with all six ranges concatenated given in units of inverse steradians.

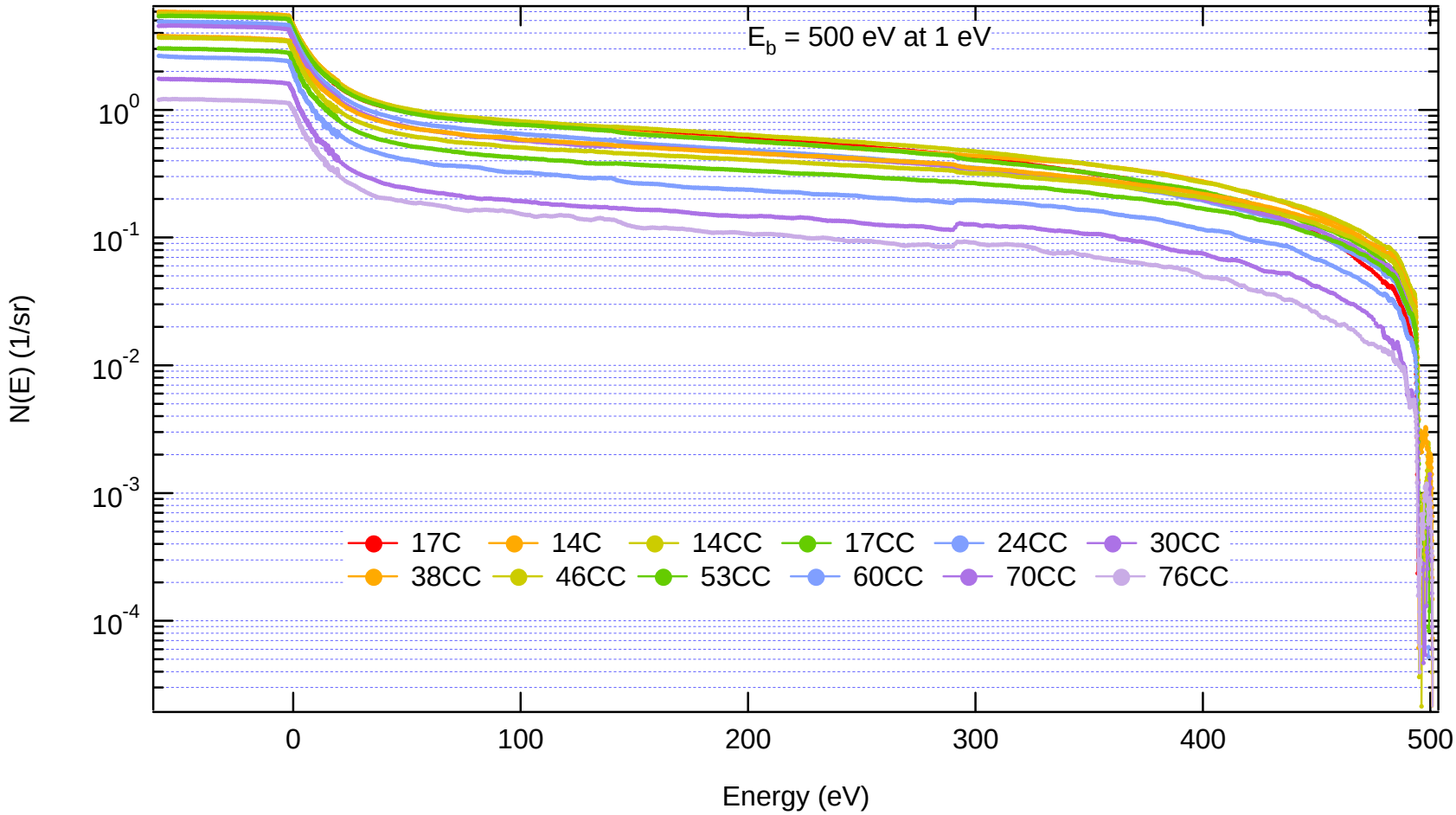

Figure E-3 N_{out}/N_{in} * $<S/I_b>_{220}$ at E_b = 500 eV with all five ranges concatenated given in units of inverse steradians.

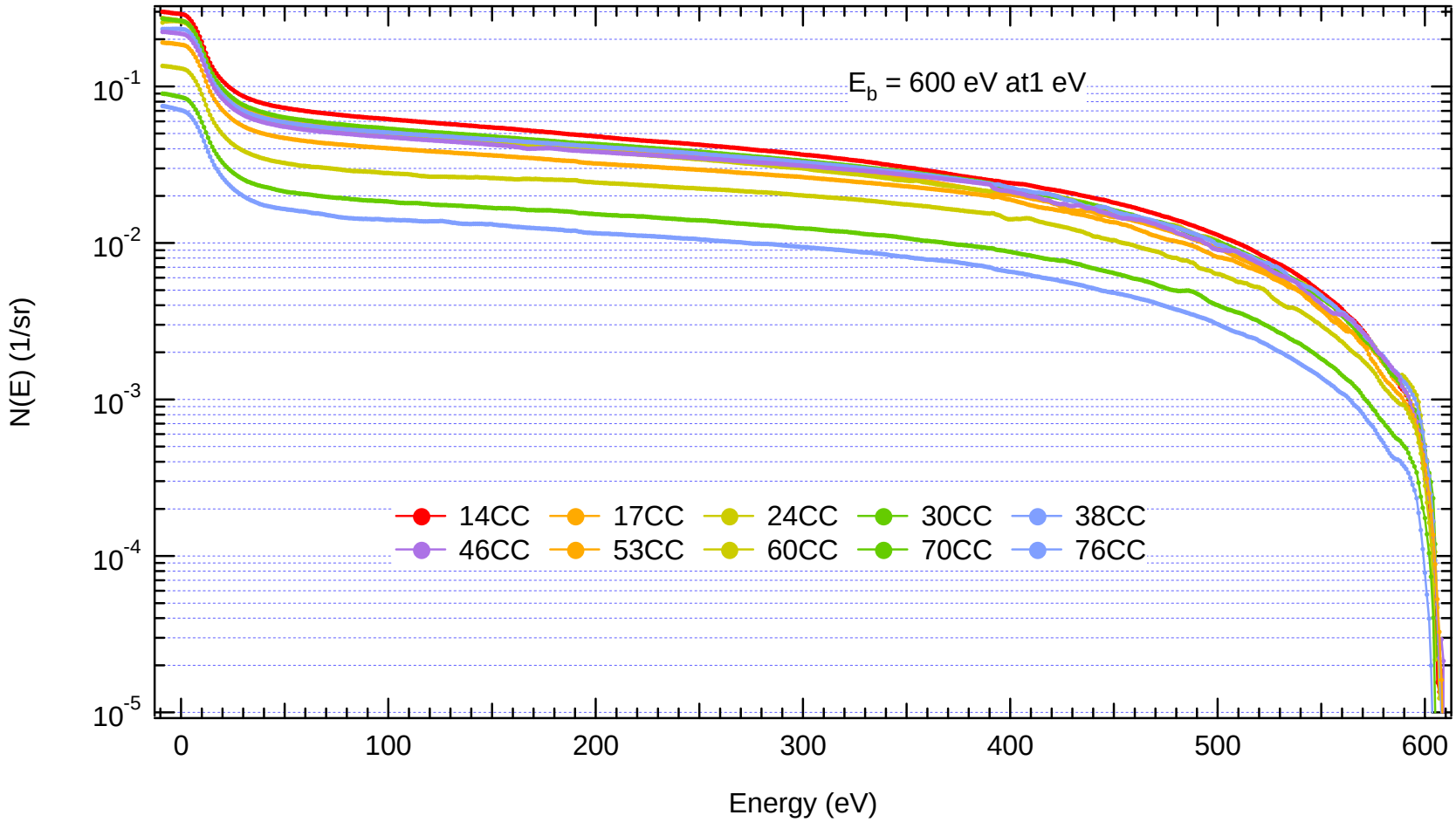

Figure E-4 N_{out}/N_{in} * $<S/I_b>_{220}$ at E_b = 600 eV with all three ranges concatenated given in units of inverse steradians.

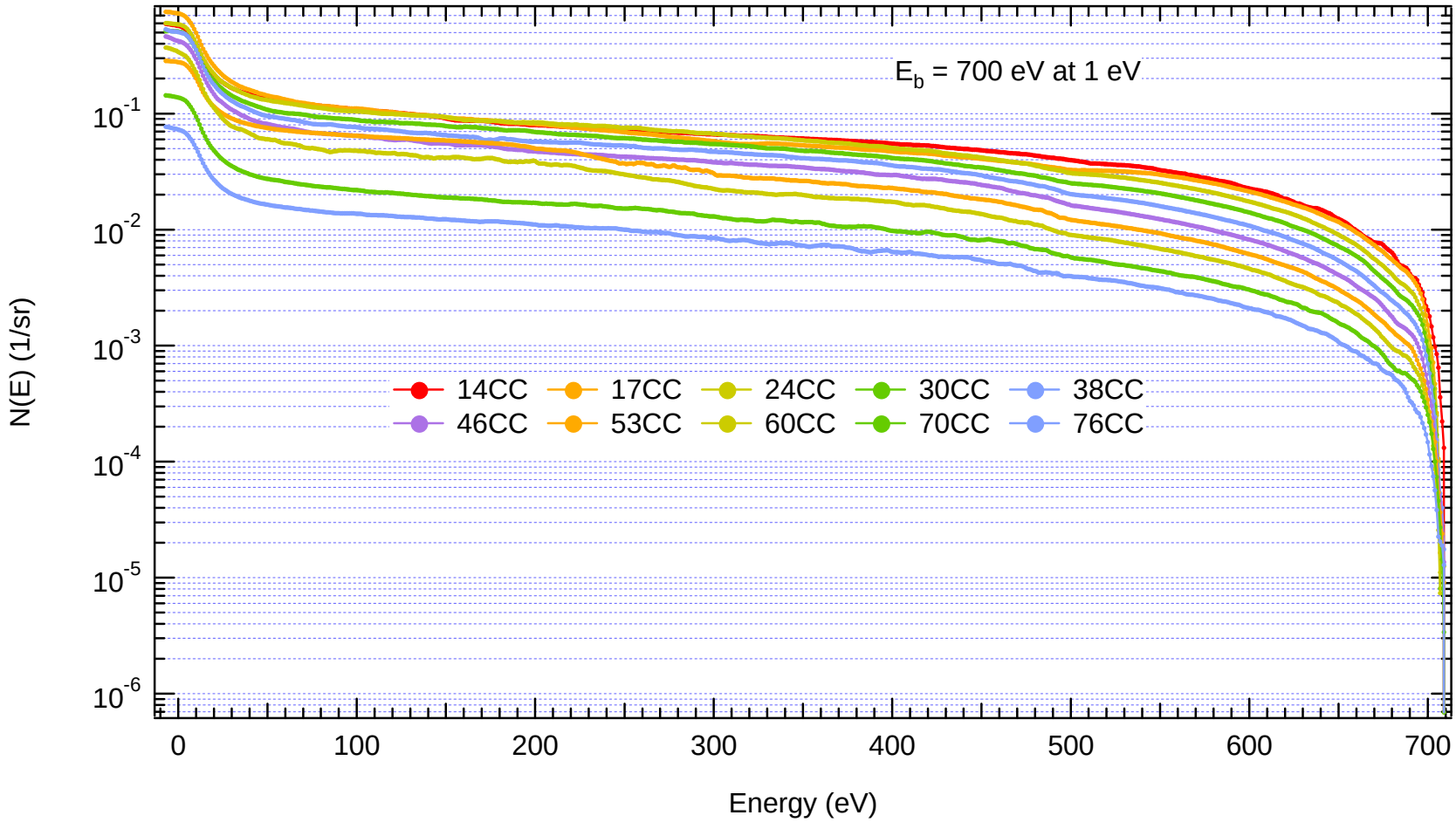

Figure E-5 N_{out}/N_{in} * $<S/I_b>_{220}$ at E_b = 700 eV with all five ranges concatenated given in units of inverse steradians.

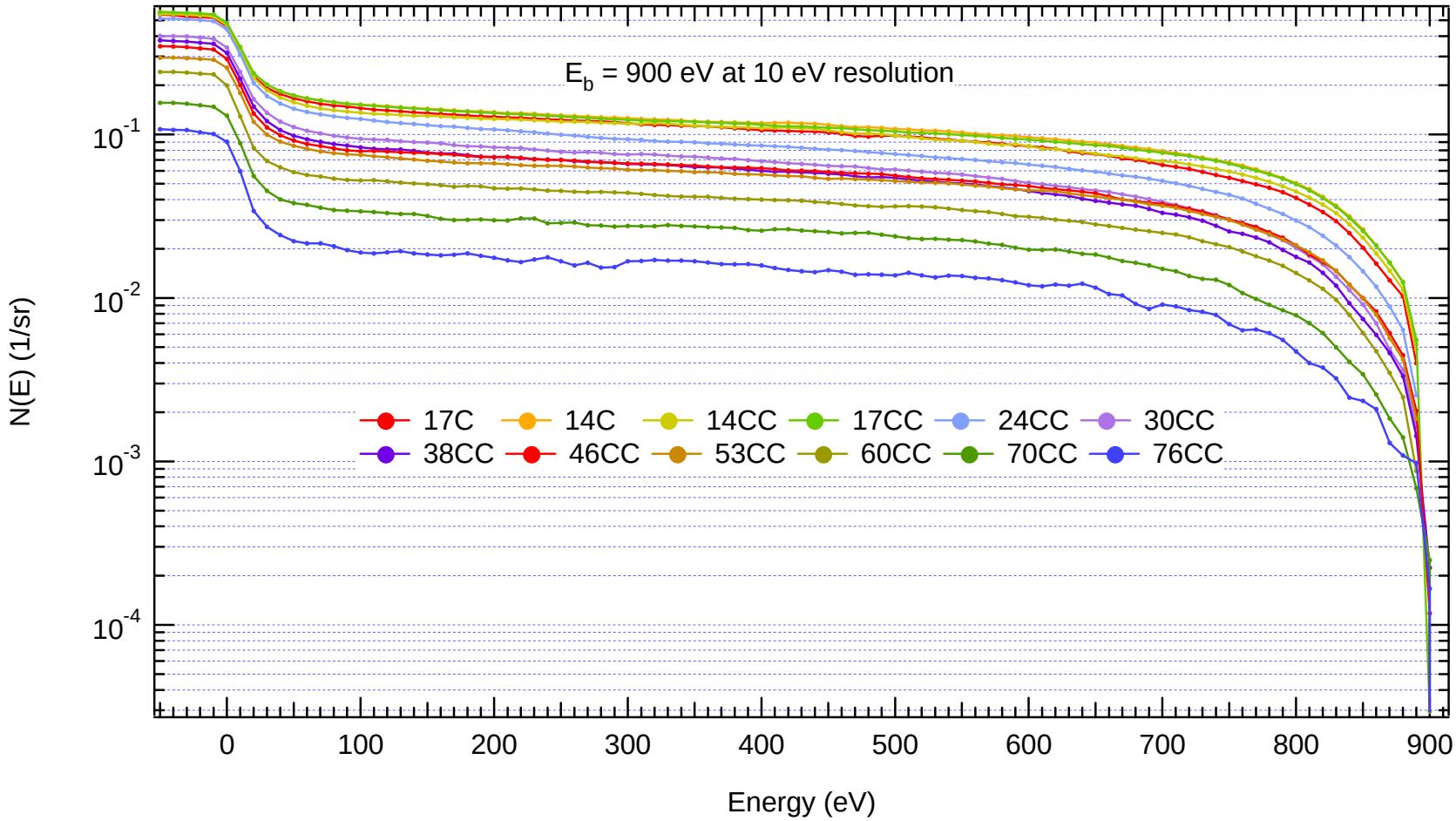

Figure E-6 N_{out}/N_{in} * $<S/I_b>_{220}$ at E_b = 900 eV with all seven ranges concatenated given in units of inverse steradians.

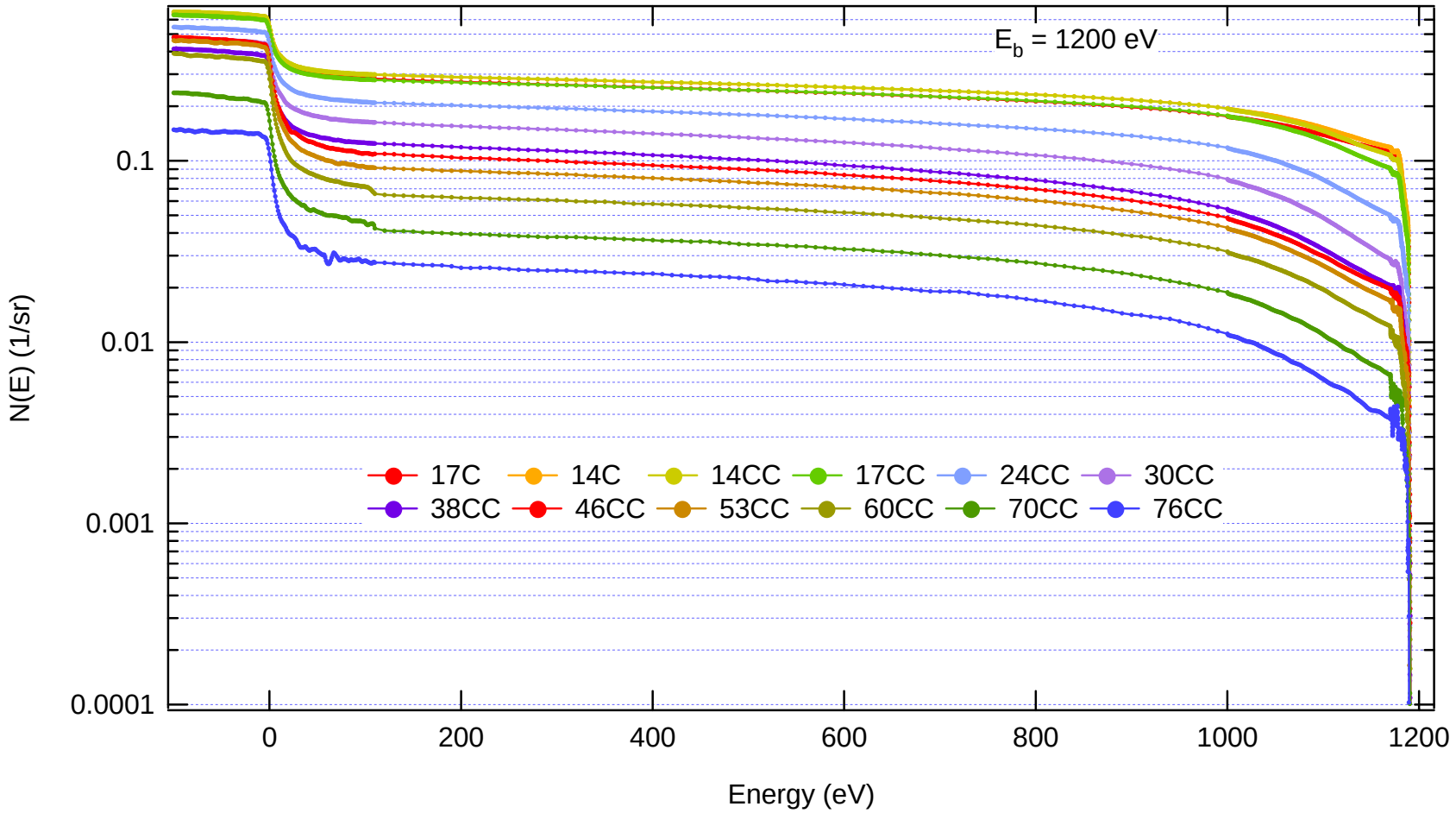

Figure E-7 N_{out}/N_{in} * $<S/I_b>_{220}$ at E_b = 1200 eV with all eight ranges concatenated given in units of inverse steradians.

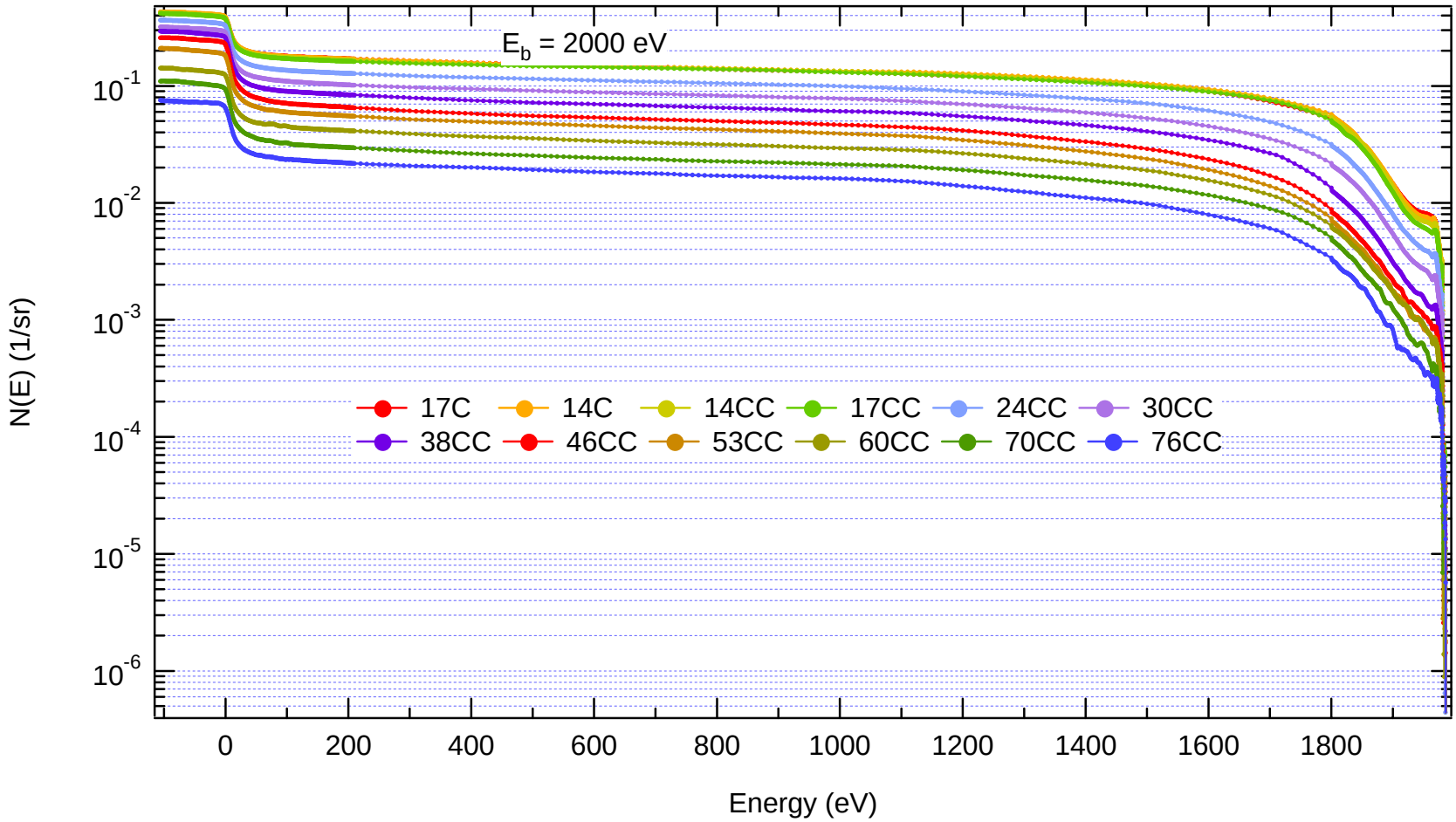

Figure E-8 N_{out}/N_{in} * $<S/I_b>_{220}$ at E_b = 2000 eV with all thirteen ranges concatenated given in units of inverse steradians.

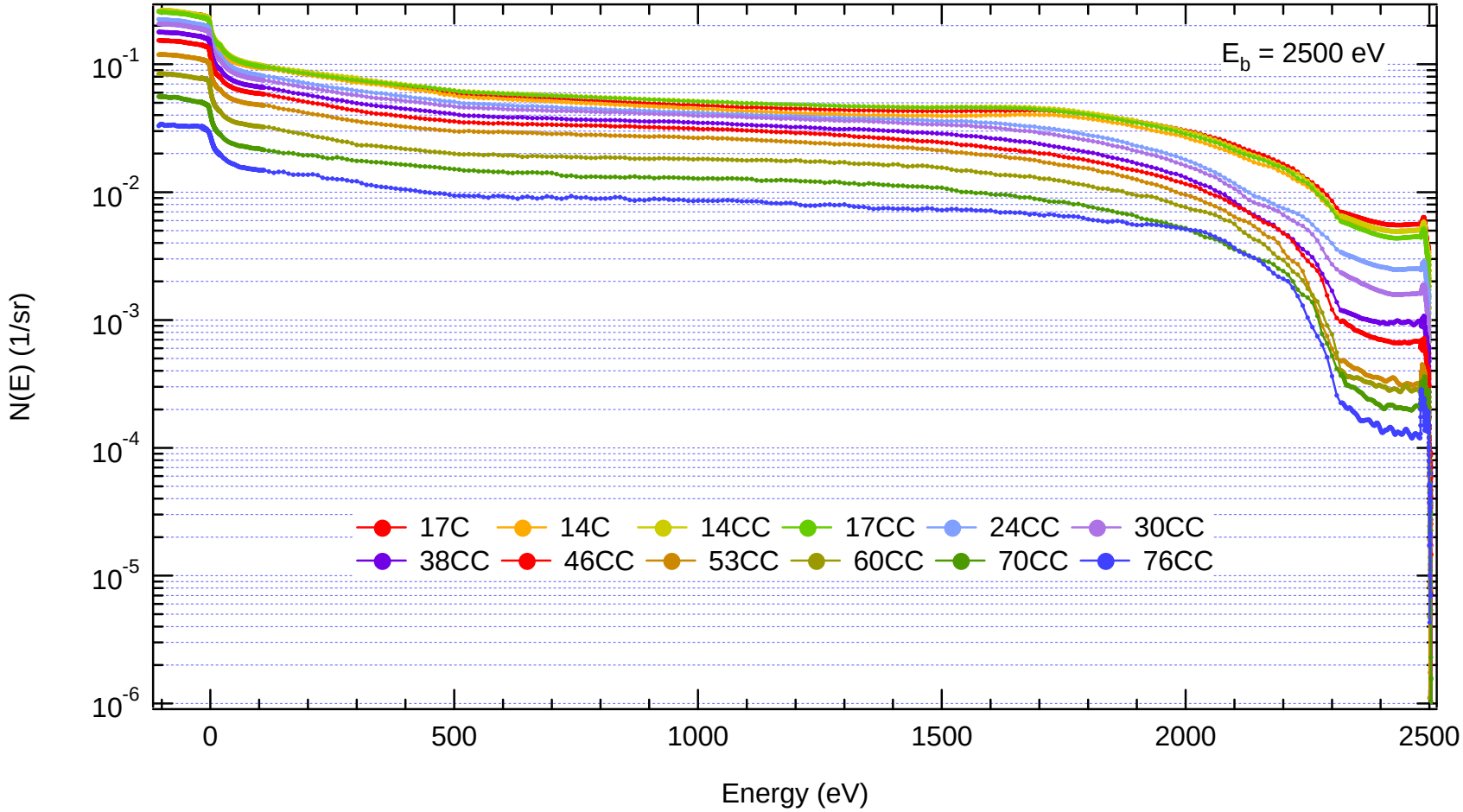

Figure E-9 N_{out}/N_{in} * $<S/I_b>_{220}$ at E_b = 2500 eV with all eighteen ranges concatenated given in units of inverse steradians.

E-5 Spectral Data Polycrystalline Au Sample "D"

The beam energy, E_b, resolved spectra measurements presented in this chapter emerge from the same data as those resolved by angle. New insight is gained by comparing different incident electron beam energy, E_b, spectra on the same graph. Maintaining the emission angle leads to information of key features that depend on E_b. The E_b resolved spectra are shown as they have been taken with the instrument resolved by emission energy first, then emission angle, and finally incident beam energy. However, the AR spectra are also given here to clarify the importance of differing energy resolutions. The spectra including mixed resolutions [Fig. 1-2 and Fig. 5-1] have been taken at different times, then concatenated together. The logarithmic yield scale is given to emphasize that absolute yields with units of inverse steradian times inverse electron volt (1/sr * 1/eV) are calculated through a derivative. Since the mixed resolution spectra look rather complicated, the E_b—resolved spectra will be again given in terms of similar resolutions.

The E_b—Resolved spectra presented in this chapter are shown for several emission angles. Twelve E_b—resolved spectra are given, one for each emission angle, to show interesting trends that will be used in Chapter 5. Each selected emission angle (17 degrees Clockwise through 76 degrees Counter-Clockwise) contains yields for selected E_b given in domain units of $eV^{-1} * sr^{-1}$ on the y-axis.

An overview of the entire spectra from 0 eV to the incident beam energy, E_b, is shown along with the pieces of spectra at higher resolution such as the Elastic, BSE, and SE peaks. For the coarse 10 eV resolution, the normalized energy in terms of percentage of E_b is given on the x-axis. For higher energy emissions using the 1 eV and 0.1 eV resolutions, the origins have been shifted so that several E_b's can be compared with one another. The coarse resolution spectra are given first followed by the higher energy finer resolutions, then the low energy finer resolutions, and then a summary is given followed by a discussion.

E-5(A) Coarse Resolution Spectra (E_b Resolved)

The AR energy spectra presented in Figs. E-10 through E-17 are shown for several selected incident beam energies, E_b. The selected incident beam energies are 100V, 500V, 600V, 700V, 900V, 1200V, 2000V, and 2500V and the yields are given in units of $eV^{-1} * sr^{-1}$ on the y-axis and in units of eV on the x-axis. These spectra are derived from the raw data measured in section E-3 at a coarse energy resolution of 10 eV. The only exception is that the E_b = 100 eV was taken at 0.1 eV resolution and the derivative was calculated at every 1 eV as referred to in the last section.

This was done in order to determine the minimum location (and intensity) existing between the high energy BSE peak and the low energy SE peak. Since each spectrum contains a local minimum separating these peaks, the concatenation of equivalent ranges of 10 eV resolutions assures that the minimum can be located with a simple search routine. This shared yield minimum is used to fit each peak with its own corresponding functional trend. In this way, the SE peak's tail, which extends through to the BSE peak can be modeled separately using this local minimum yield.

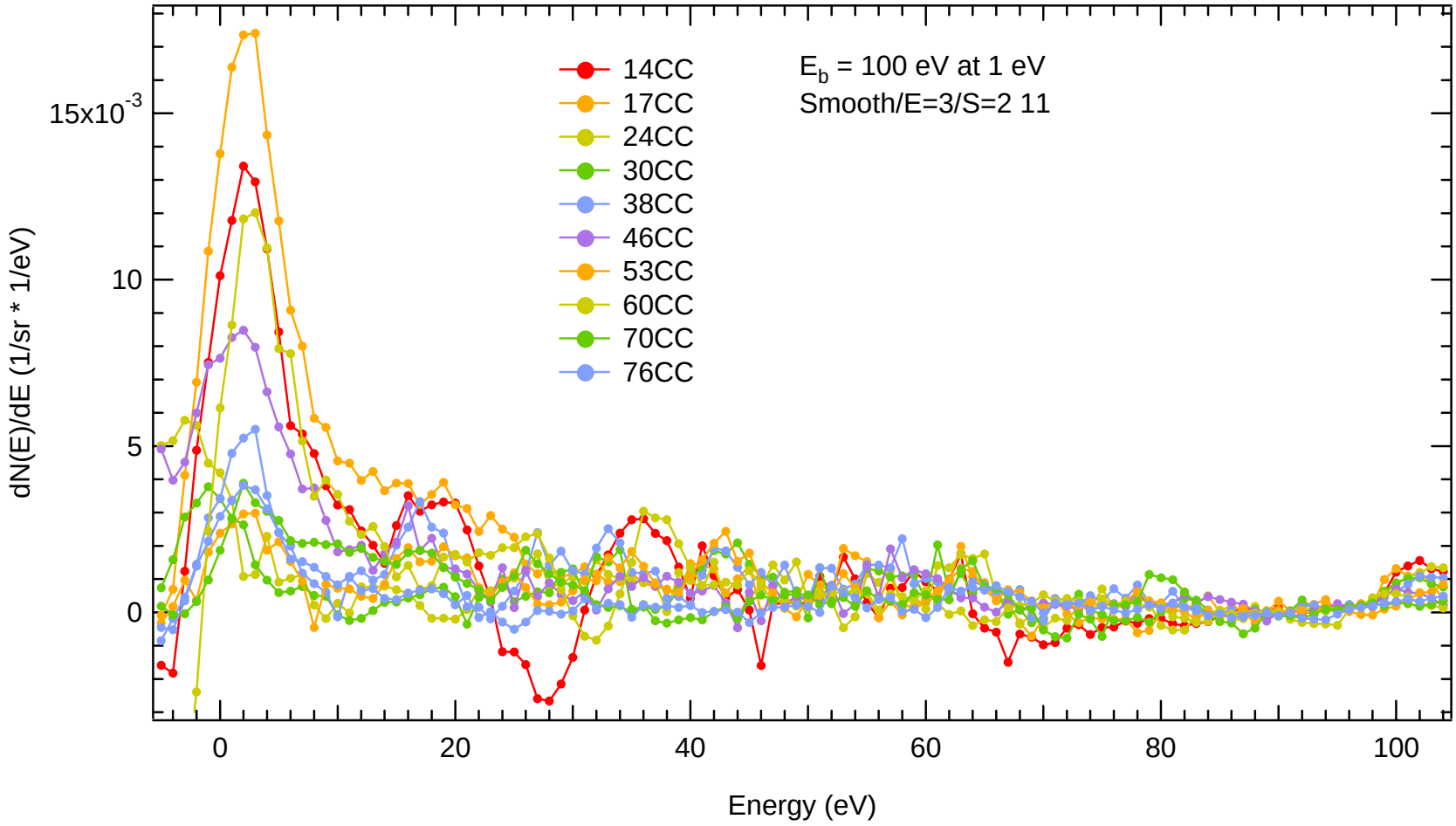

Figure E-10 AR spectra for E_b = 100 eV resolved at 1 eV for emission angles of 14^o Counter-Clockwise to 76^o Counter-Clockwise.

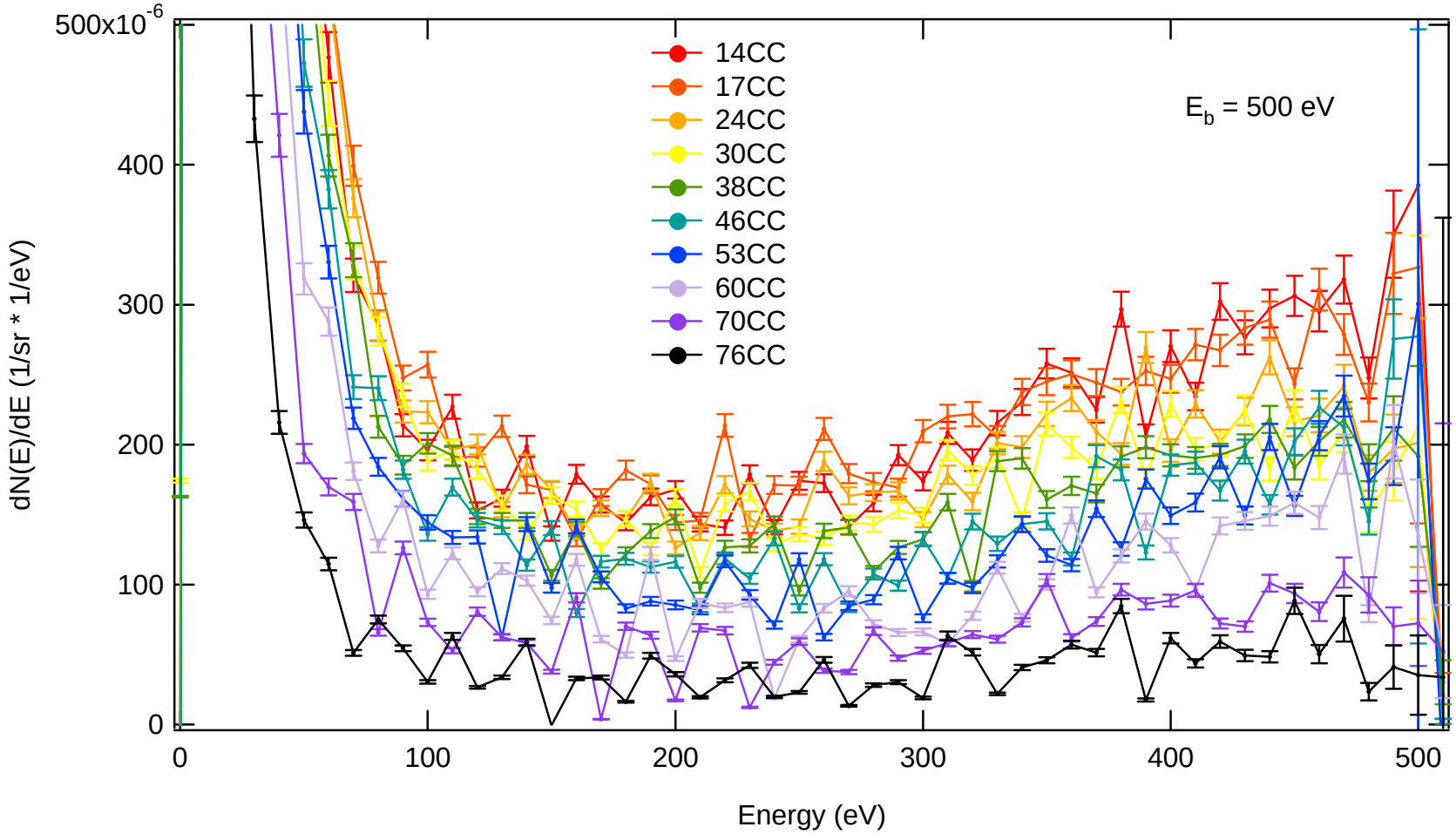

Figure E-11 AR spectra for E_b = 500 eV and for emission angles of 14 ^{o} counterclockwise to 76 ^{o} counterclockwise. No Smooth.

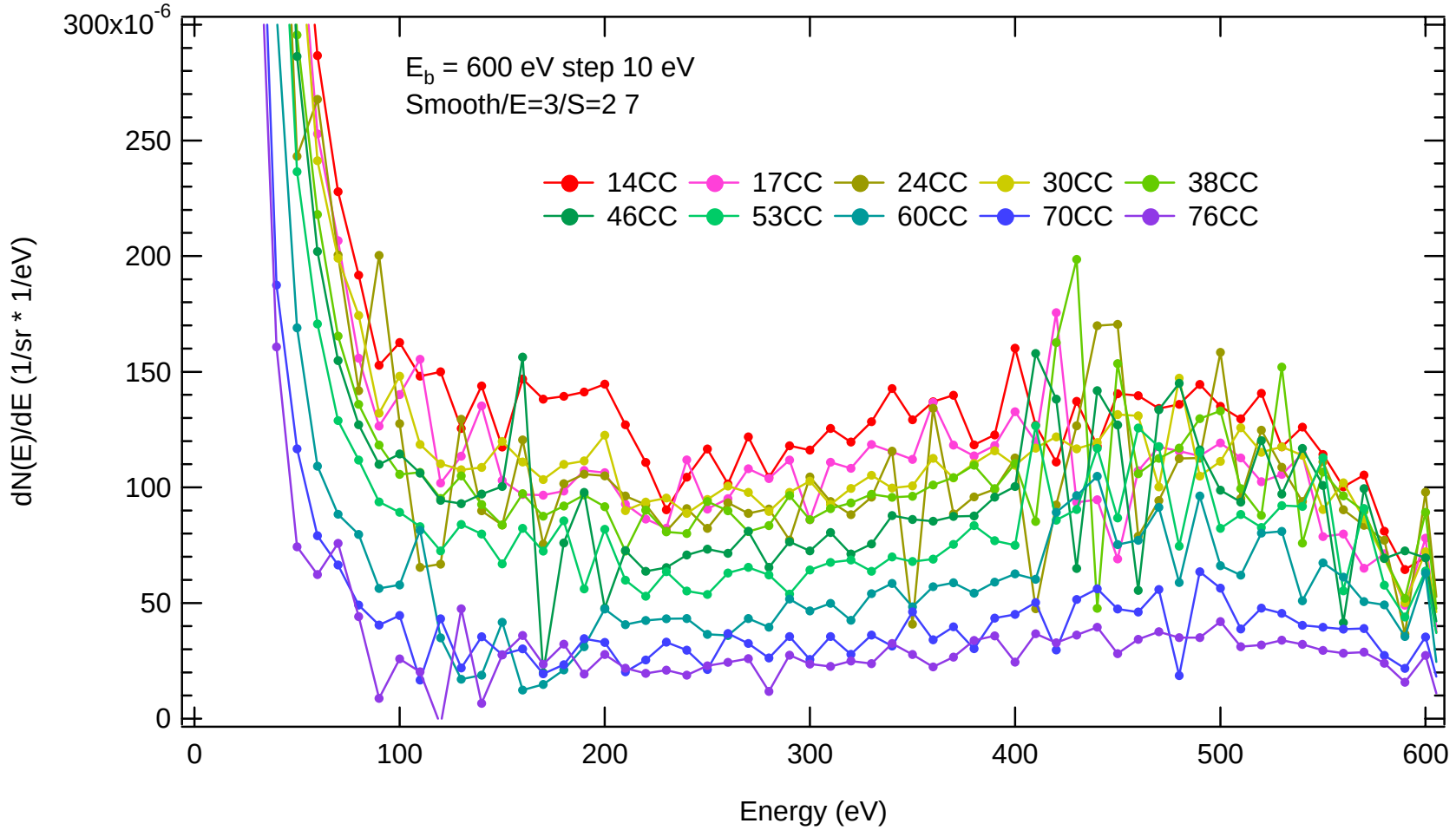

Figure E-12 AR spectra for E_b = 600 eV and for emission angles of 14 ^{o} counterclockwise to 76 ^{o} counterclockwise.

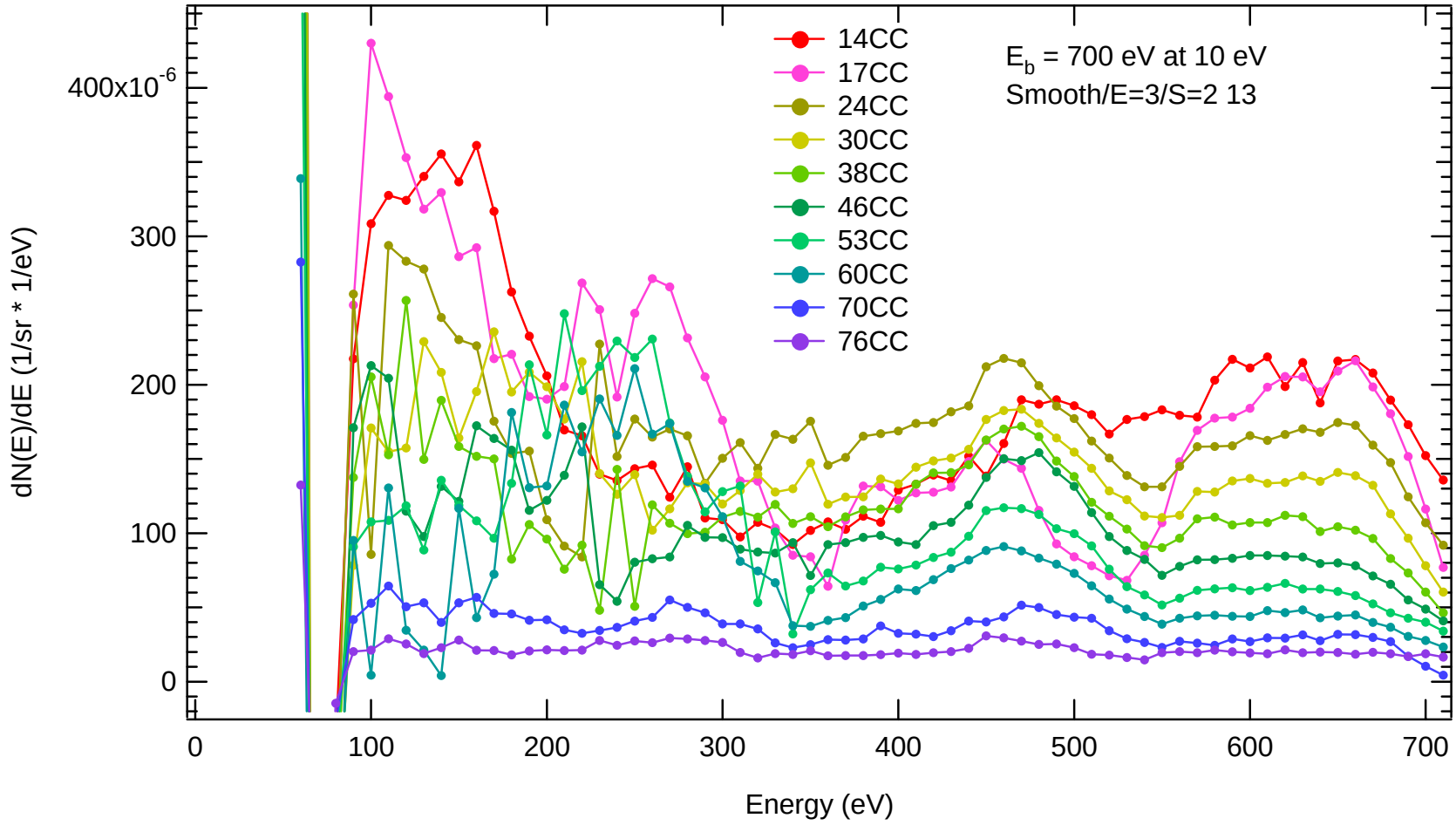

Figure E-13 AR spectra for E_b = 700 eV and for emission angles of 14 ^{o} counterclockwise to 76 ^{o} counterclockwise.

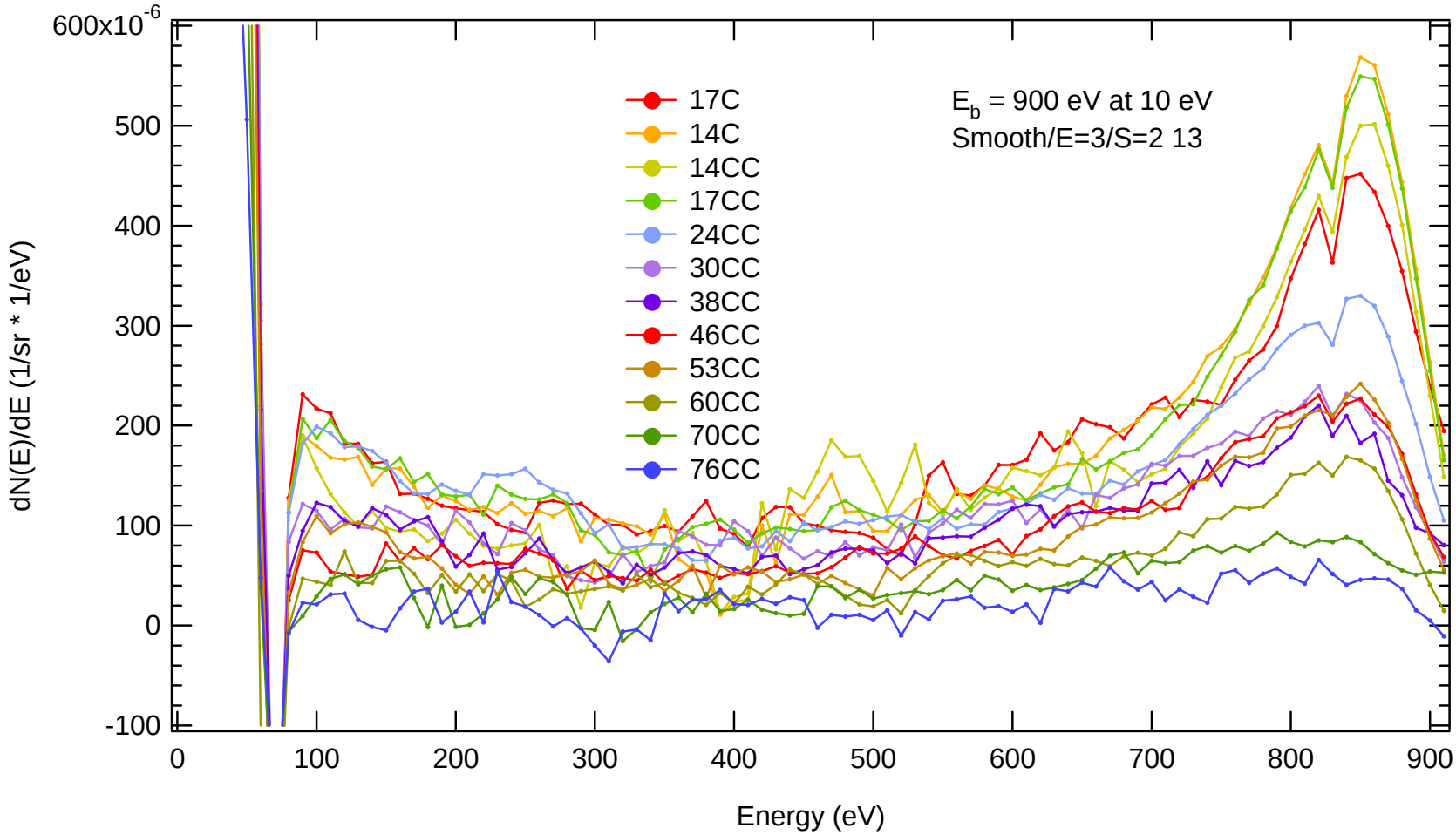

Figure E-14 AR spectra for E_b = 900 eV and for emission angles of 17 ^{o} clockwise to 76 ^{o} counterclockwise.

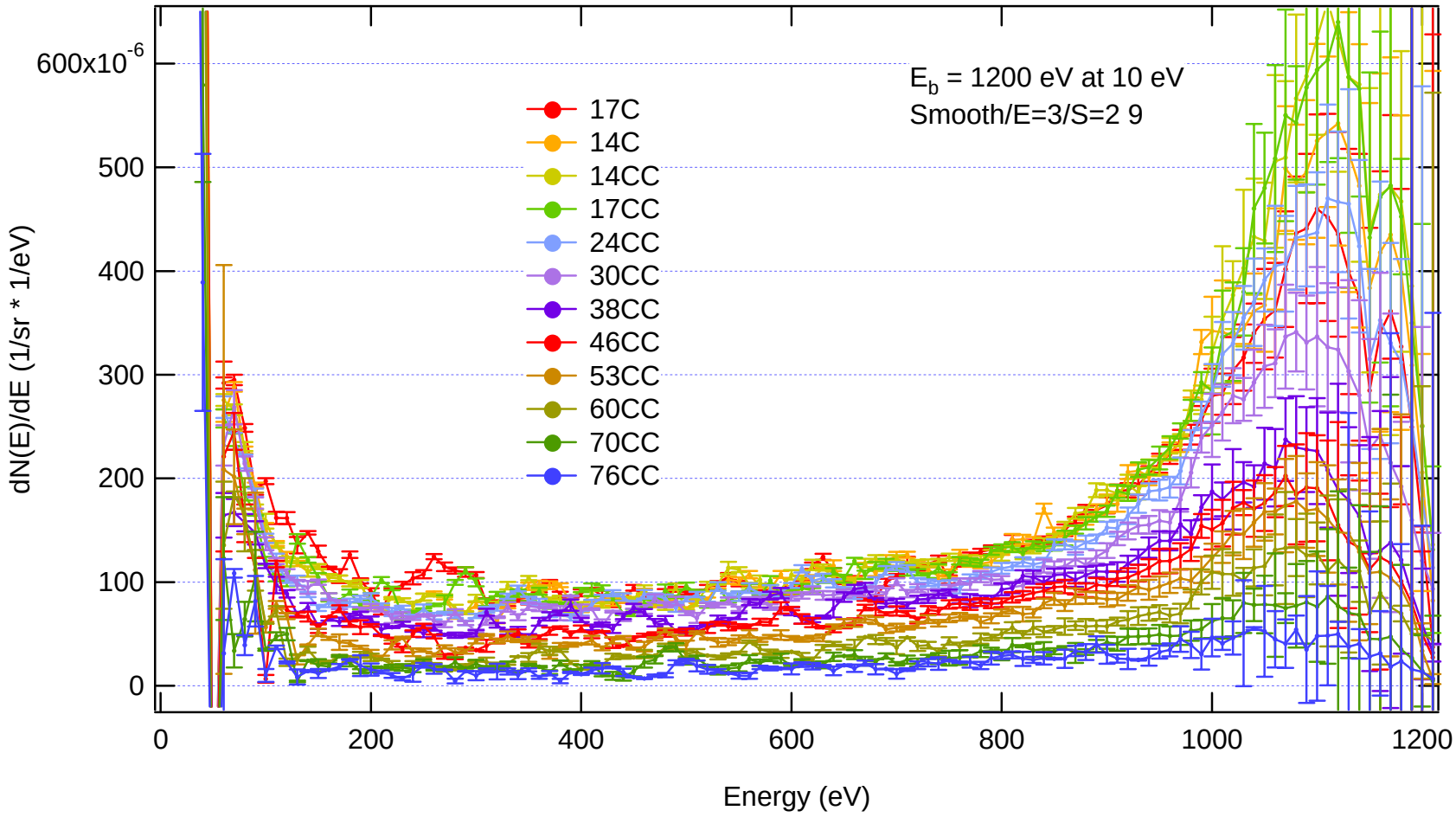

Figure E-15 AR spectra for E_b = 1200 eV and for emission angles of 17 ^{o} clockwise to 76 ^{o} counterclockwise.

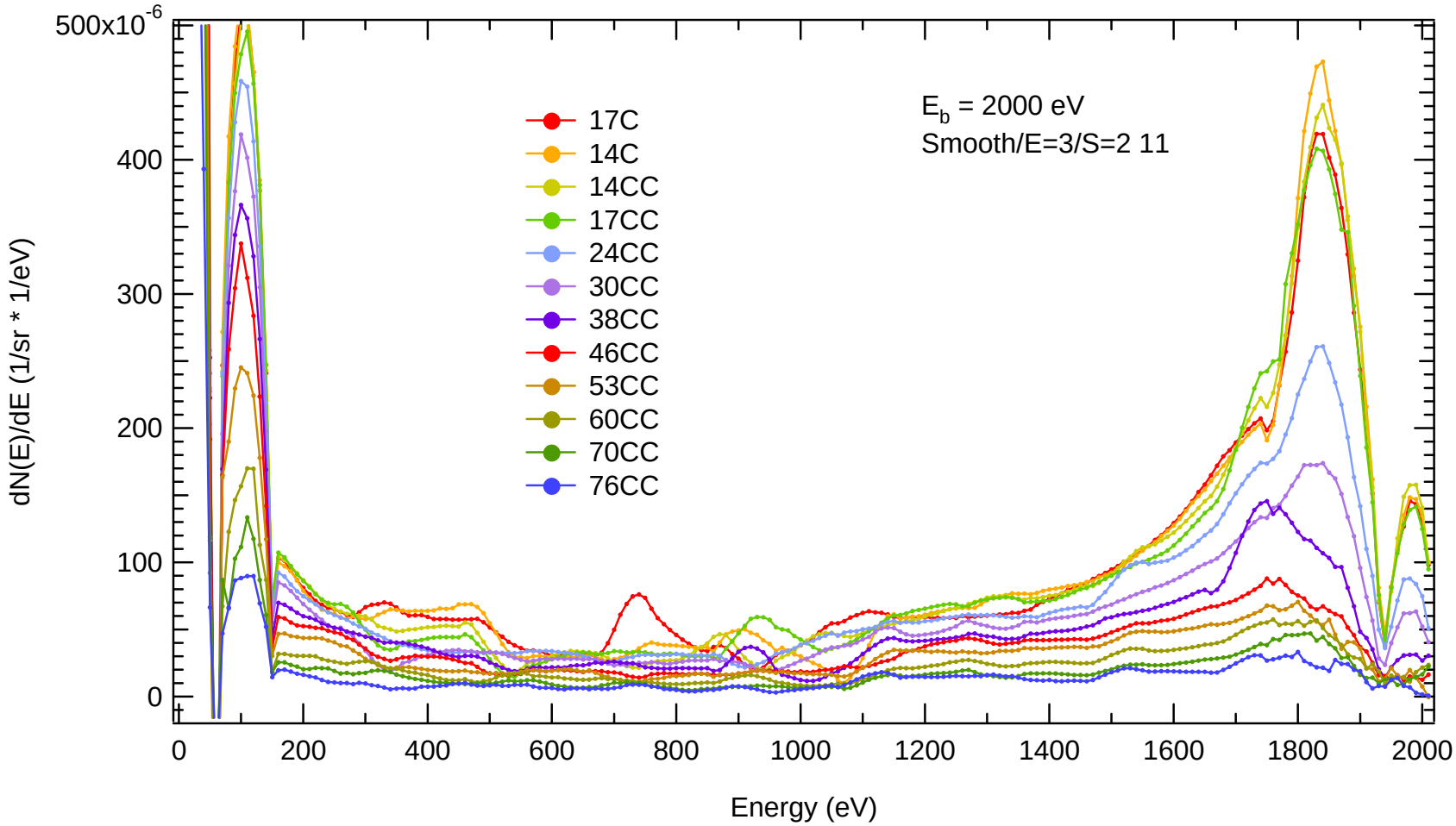

Figure E-16 AR spectra for E_b = 2000 eV and for emission angles of 17 ^{o} clockwise to 76 ^{o} counterclockwise.

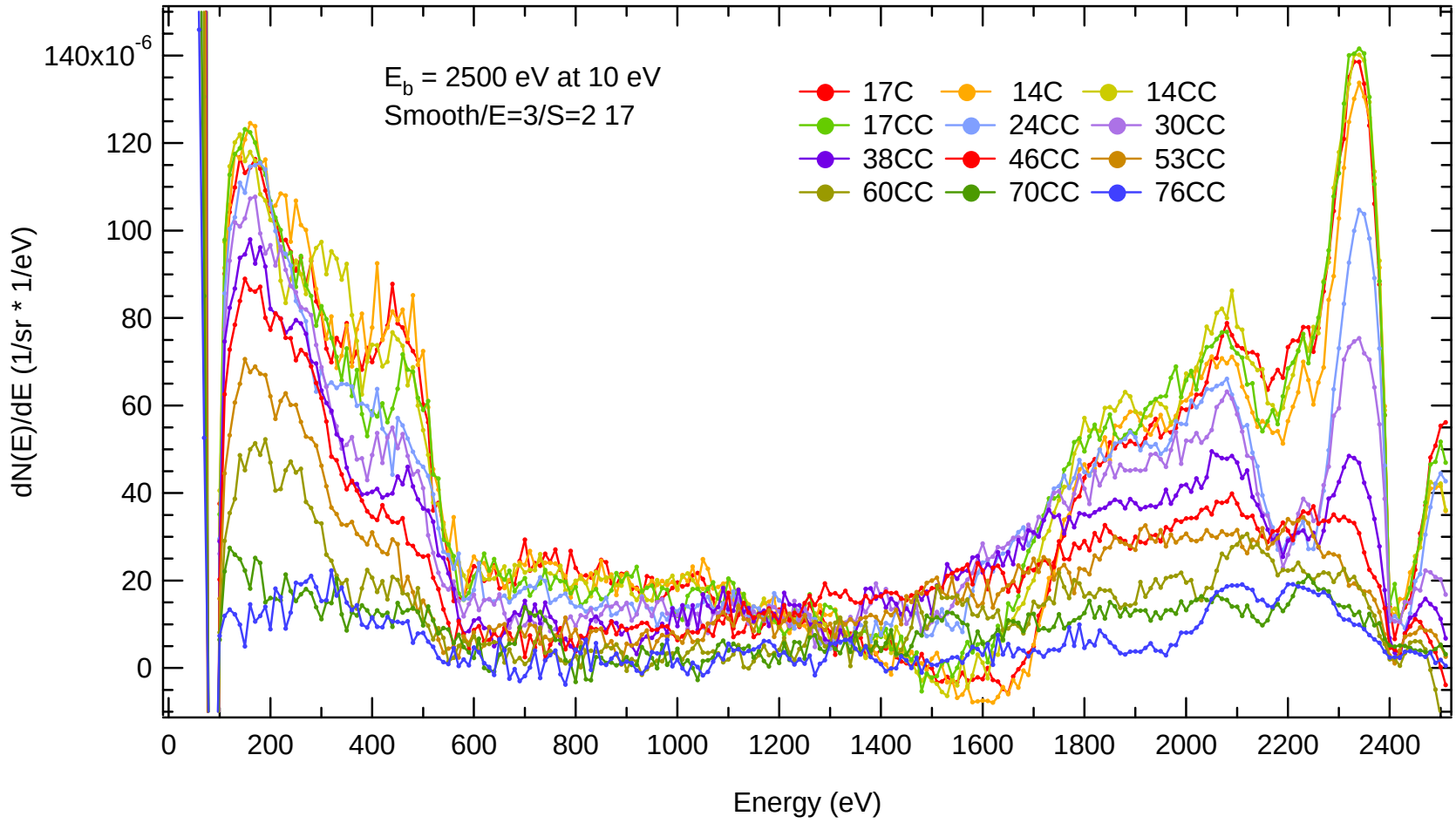

Figure E-17 AR spectra for E_b = 2500 eV and for emission angles of 17 ^{o} clockwise to 76 ^{o} counterclockwise.

E-5(B) Coarse Resolution Spectra (Angle Resolved – E_b normalized)

The total E_b normalized spectra presented in Figure E-18 through Figure E-29 are given for each of the RD angle positions. The term total emphasizes that the x-axis range includes the entire possible emission energies given as a ratio to each spectrum's beam energy, E_b.

All spectra are shown at a resolution of 10 eV with the excerption of the E_b = 100 eV data, which is given at a resolution of 1 eV referred to in the previous section. Viewing the AR spectra in this way provides a comparison of the yield minimum position and intensity located between the high energy BSE peak and the low energy SE peak. These are the same exact spectra presented in section E-5(A) where they have been re—grouped in terms of their emission angle, hence AR, rather than their incident beam energy.

It is important here to note that the smoothing number, after differentiation, is not the same for each spectra shown at the same emission angle. The SG smoothing numbers are presented in the following table.

Eb	ipf name	SGsmooth
100		2 11
500		
600		
700	Concat700at10V	2 13
900	Concat900secondCoarse	//2 13
1200	Concat1200coarse	2 9
2000	Concat2000coarse	2 11
2500	Concat2500secondCoarse	2 17/4 7

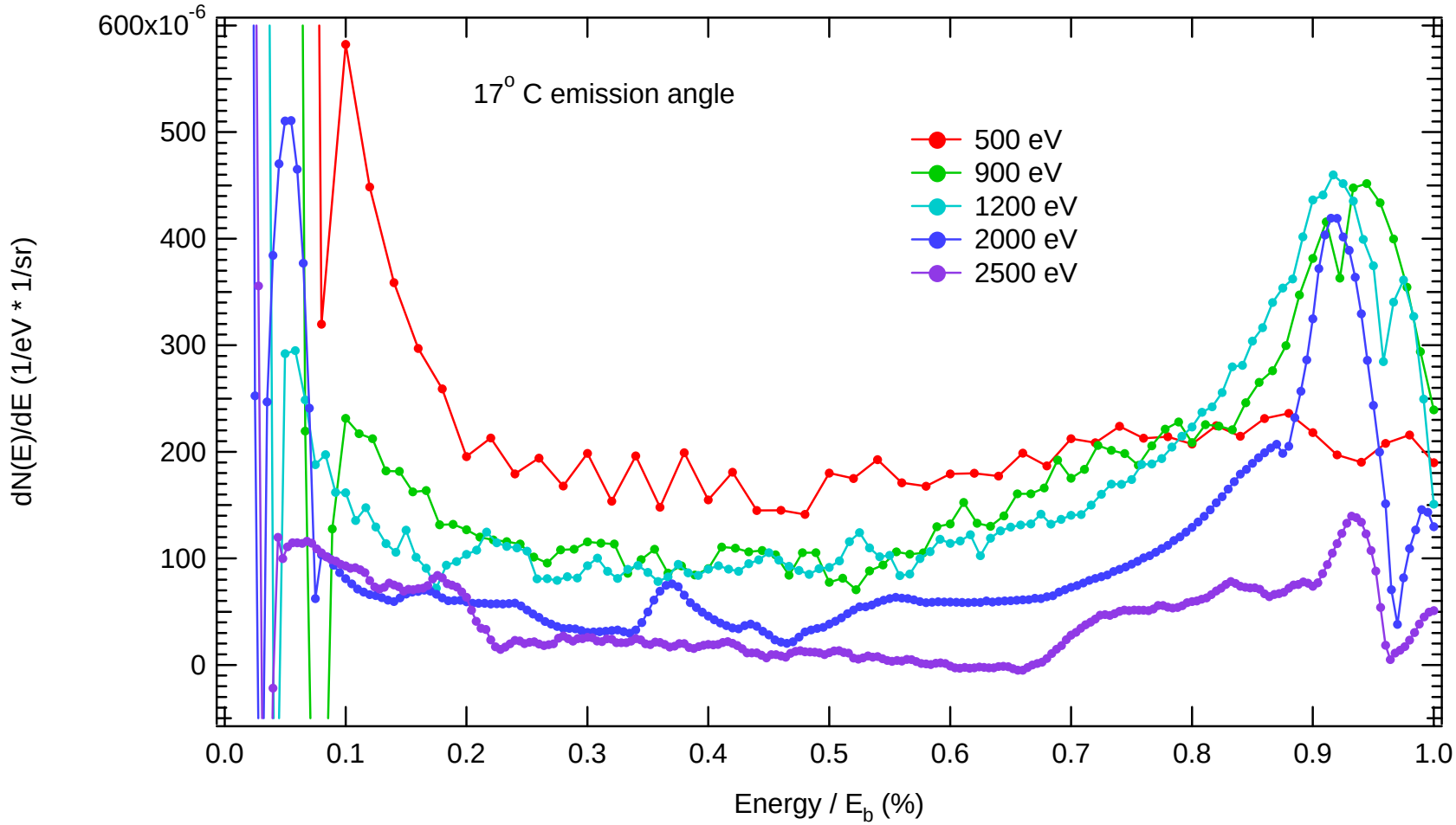

Figure E-18 Normalized AR Energy Spectra at 17° Clockwise emission for selected beam energies.

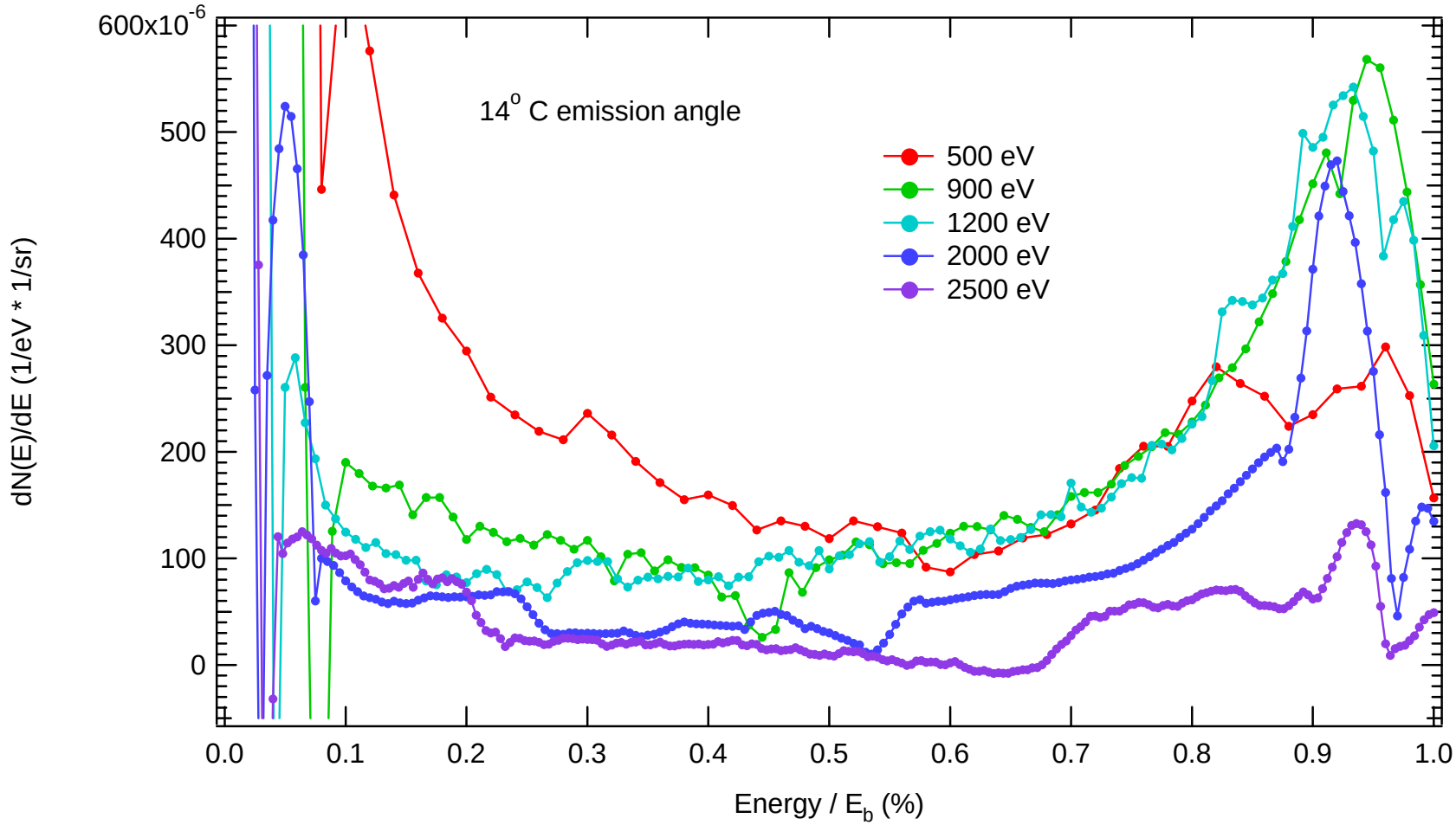

Figure E-19 Normalized AR Energy Spectra at 14° Clockwise emission for selected beam energies.

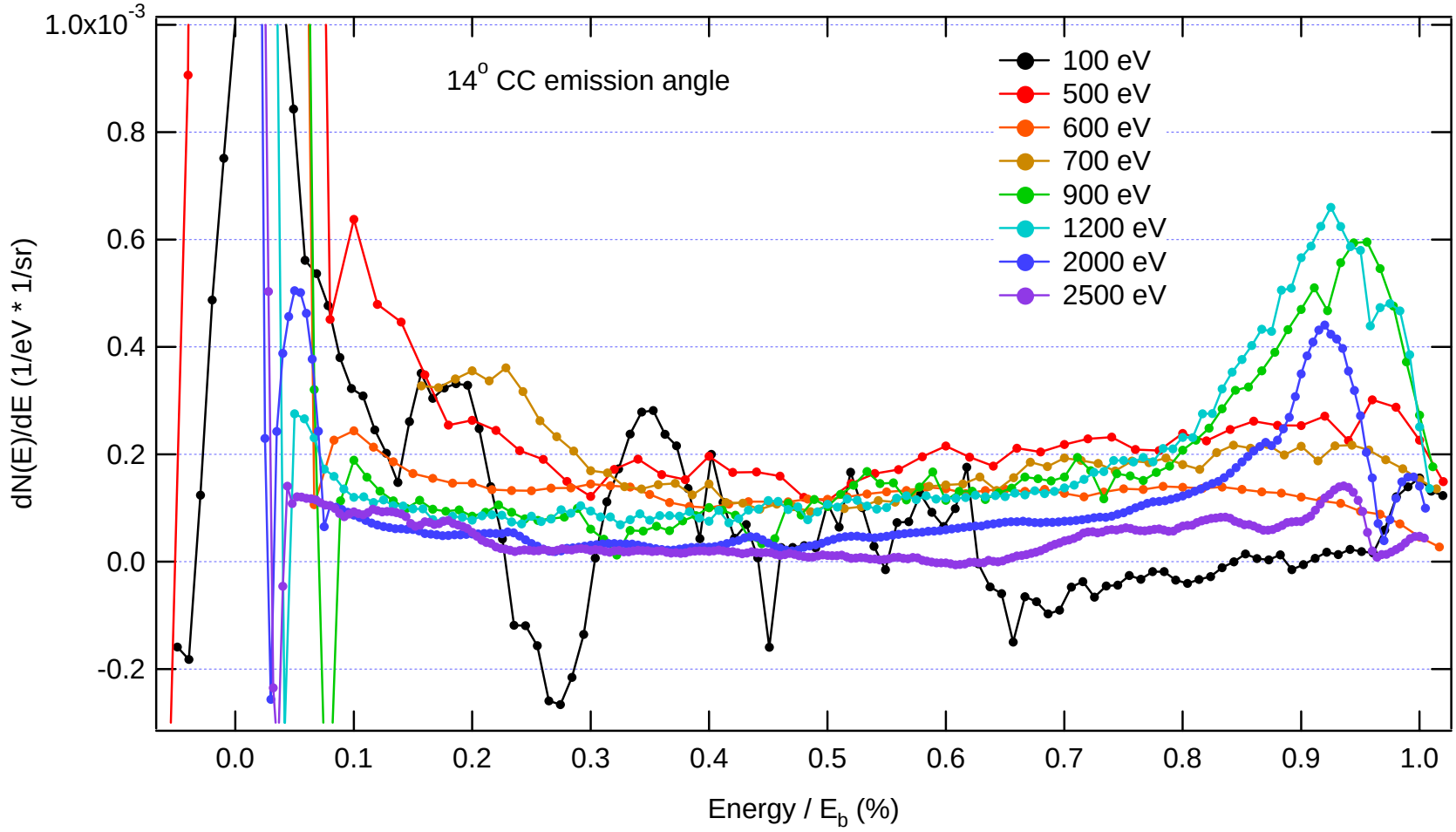

Figure E-20 Normalized AR Energy Spectra at 14° Counter-Clockwise emission for selected beam energies.

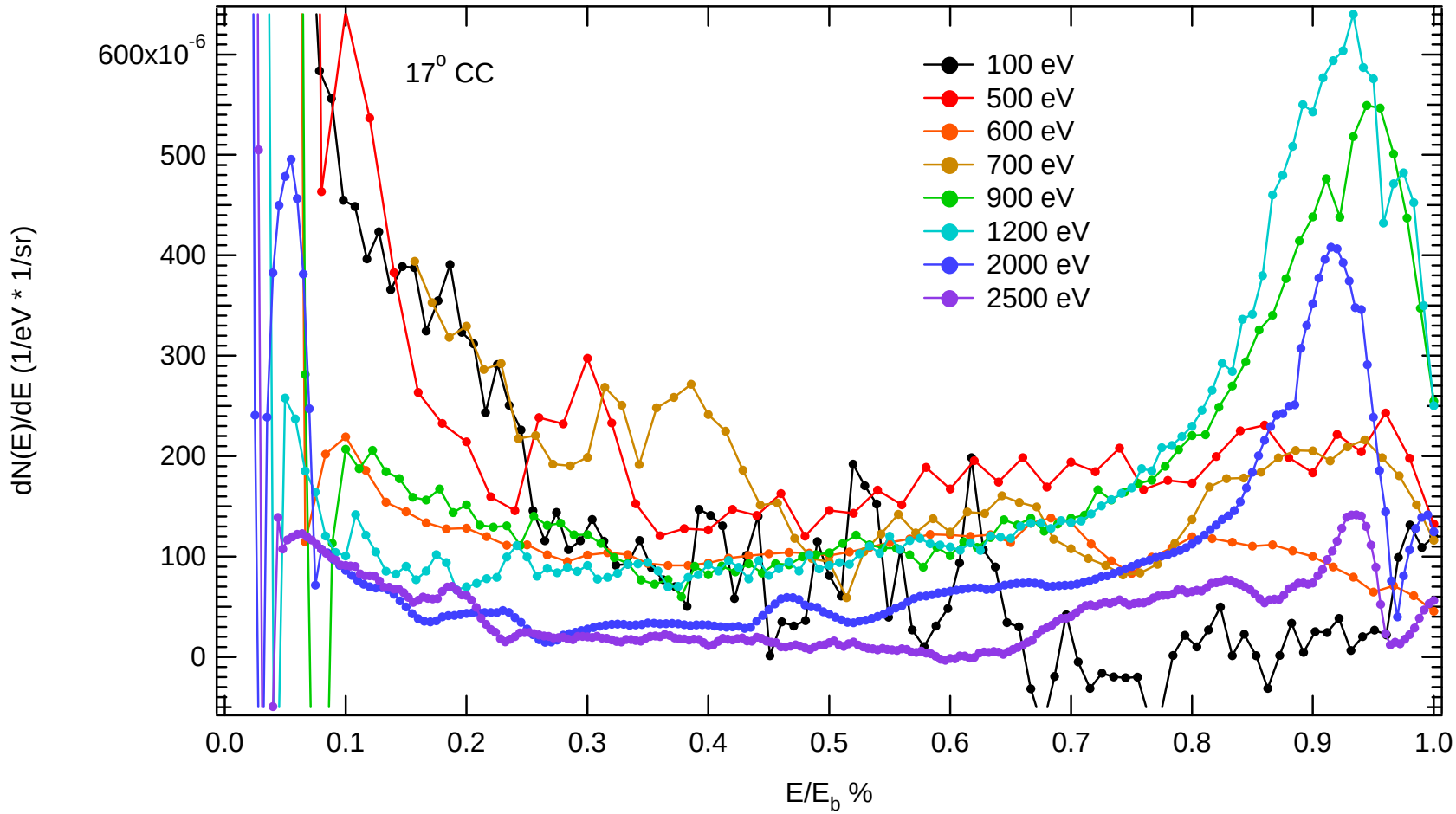

Figure E-21 Normalized AR Energy Spectra at 17^{o} Counter-Clockwise emission for selected beam energies.

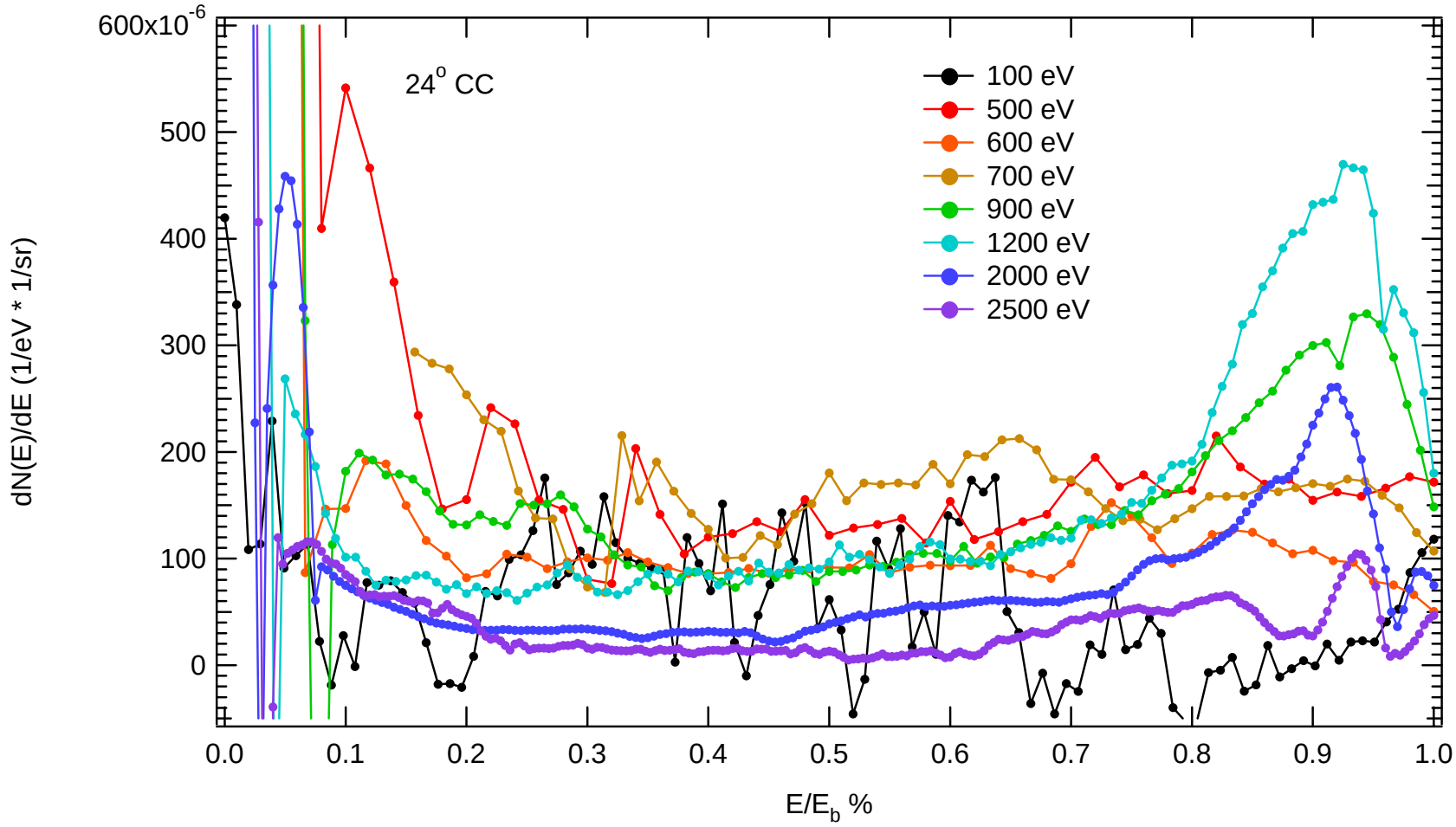

Figure E-22 Normalized AR Energy Spectra at 24^{o} Counter-Clockwise emission for selected beam energies.

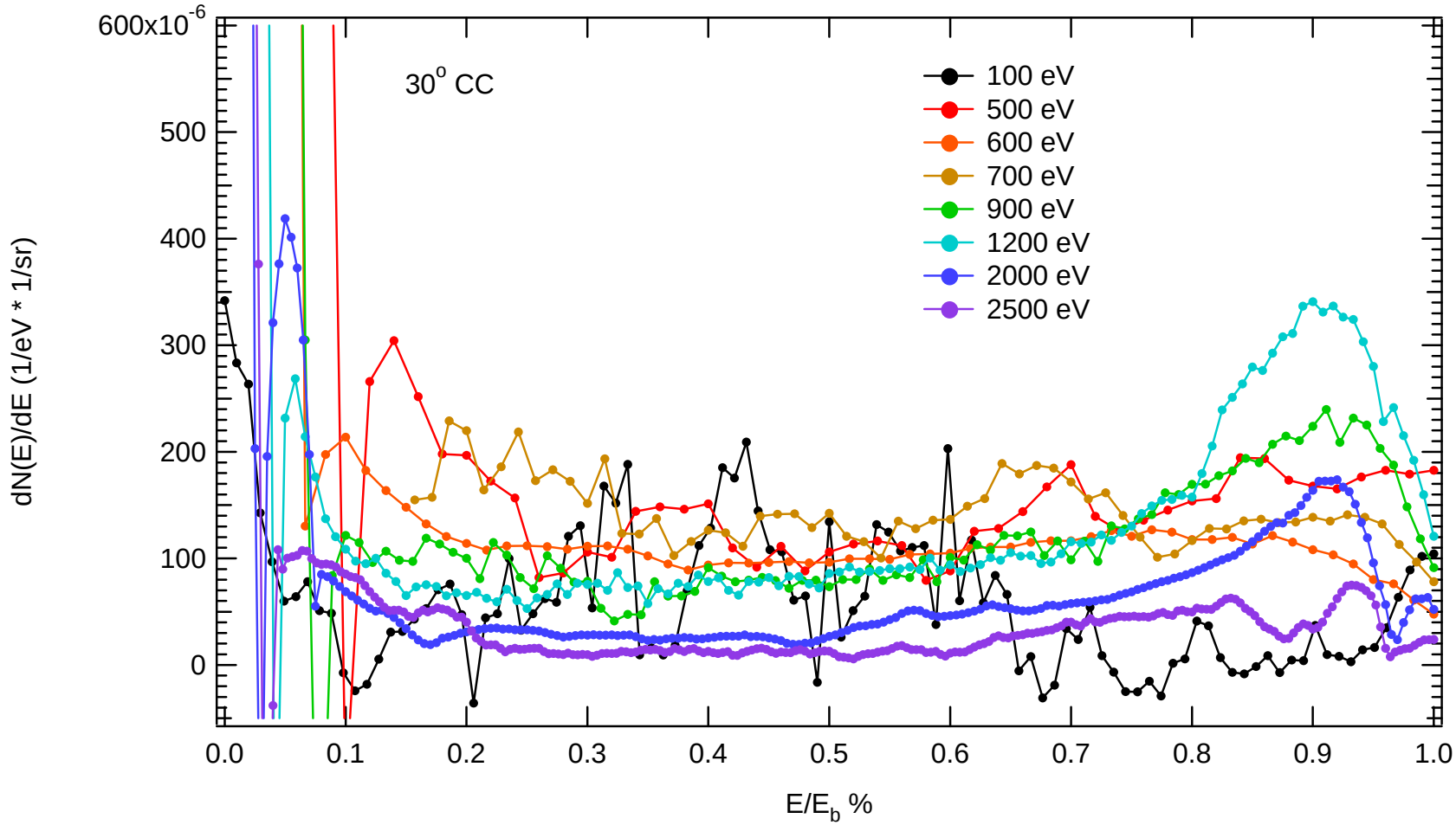

Figure E-23 Normalized AR Energy Spectra at 30° Counter-Clockwise emission for selected beam energies.

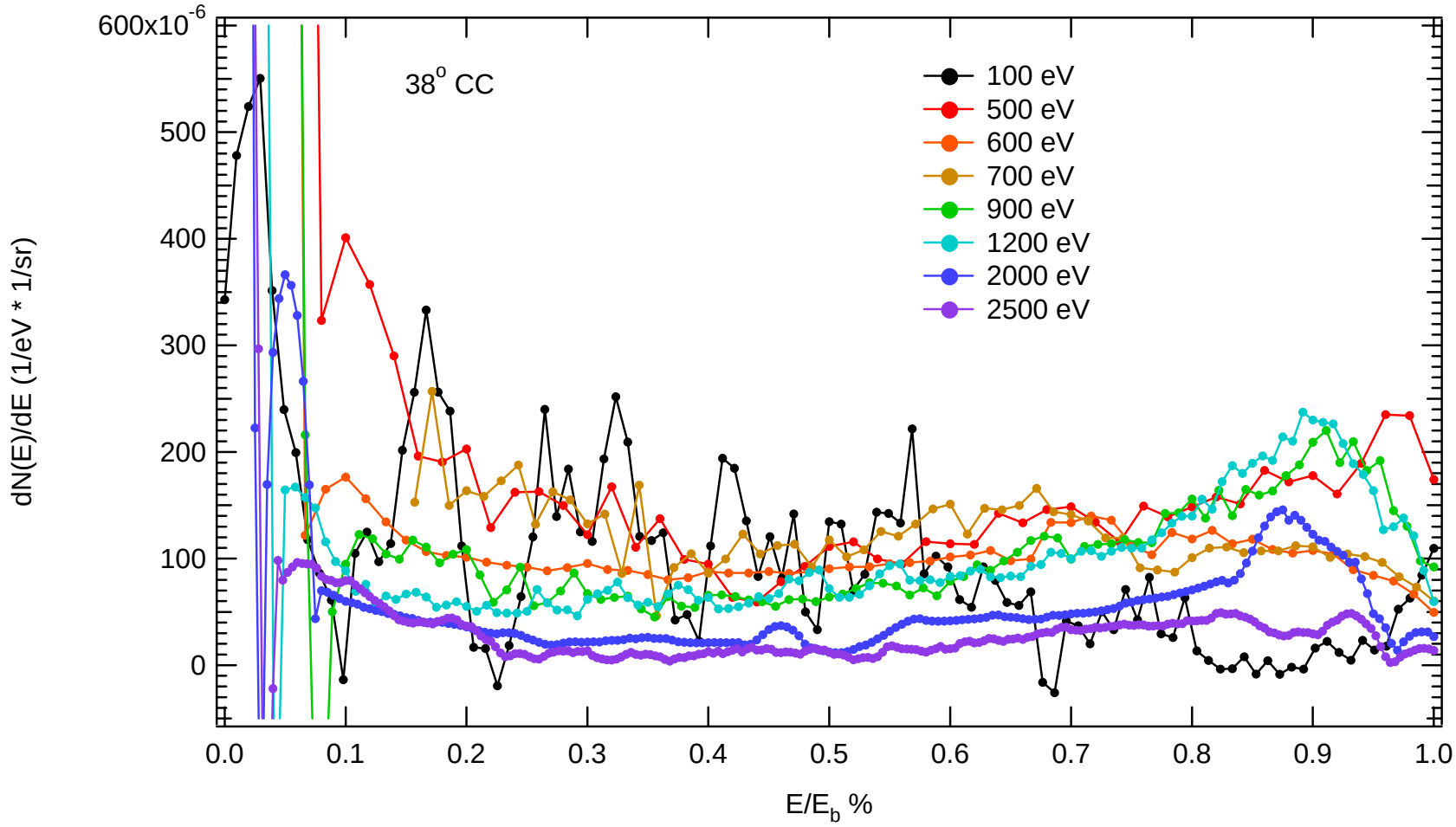

Figure E-24 Normalized AR Energy Spectra at 38° Counter-Clockwise emission for selected beam energies.

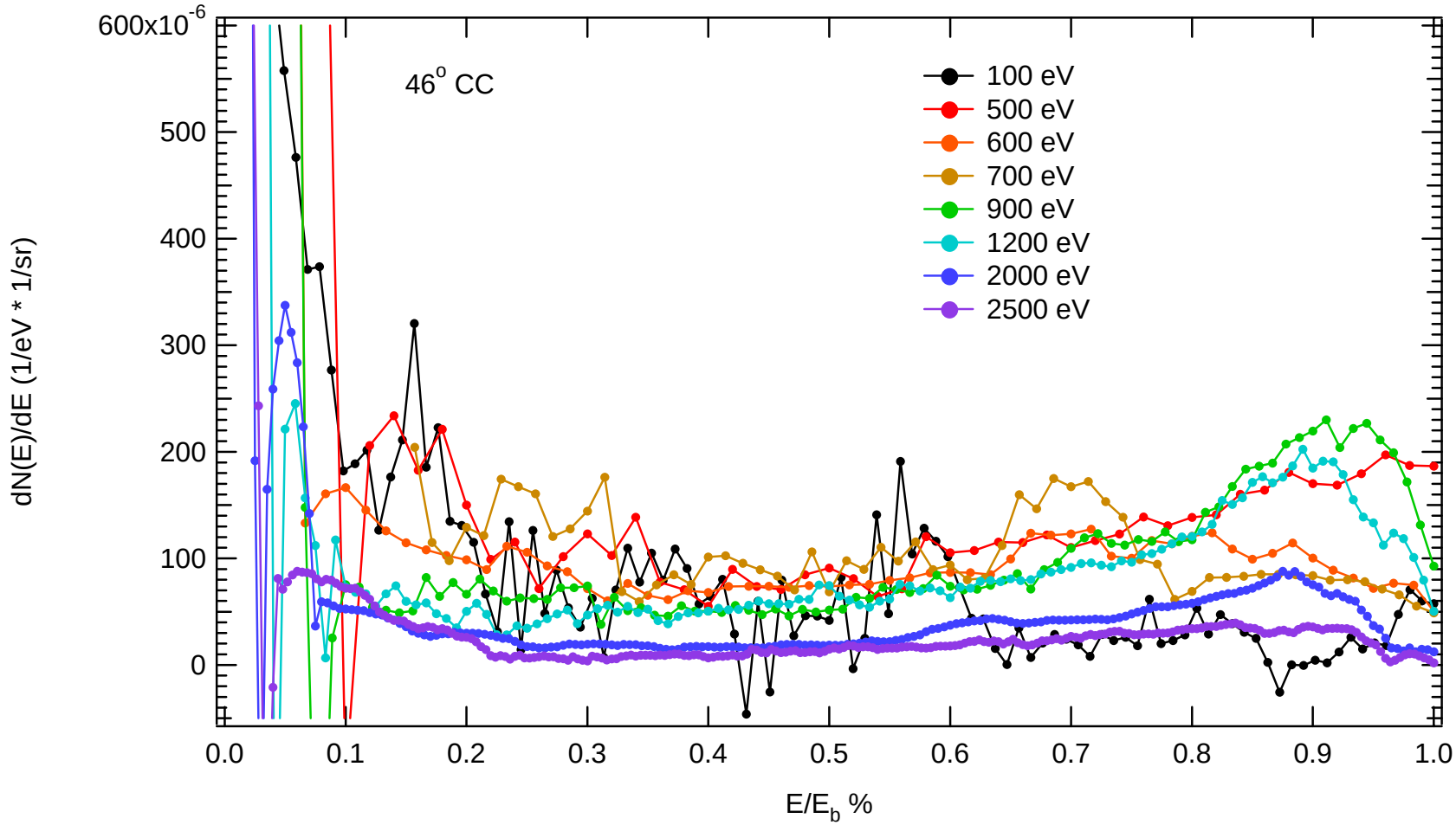

Figure E-25 Normalized AR Energy Spectra at 46° Counter-Clockwise emission for selected beam energies.

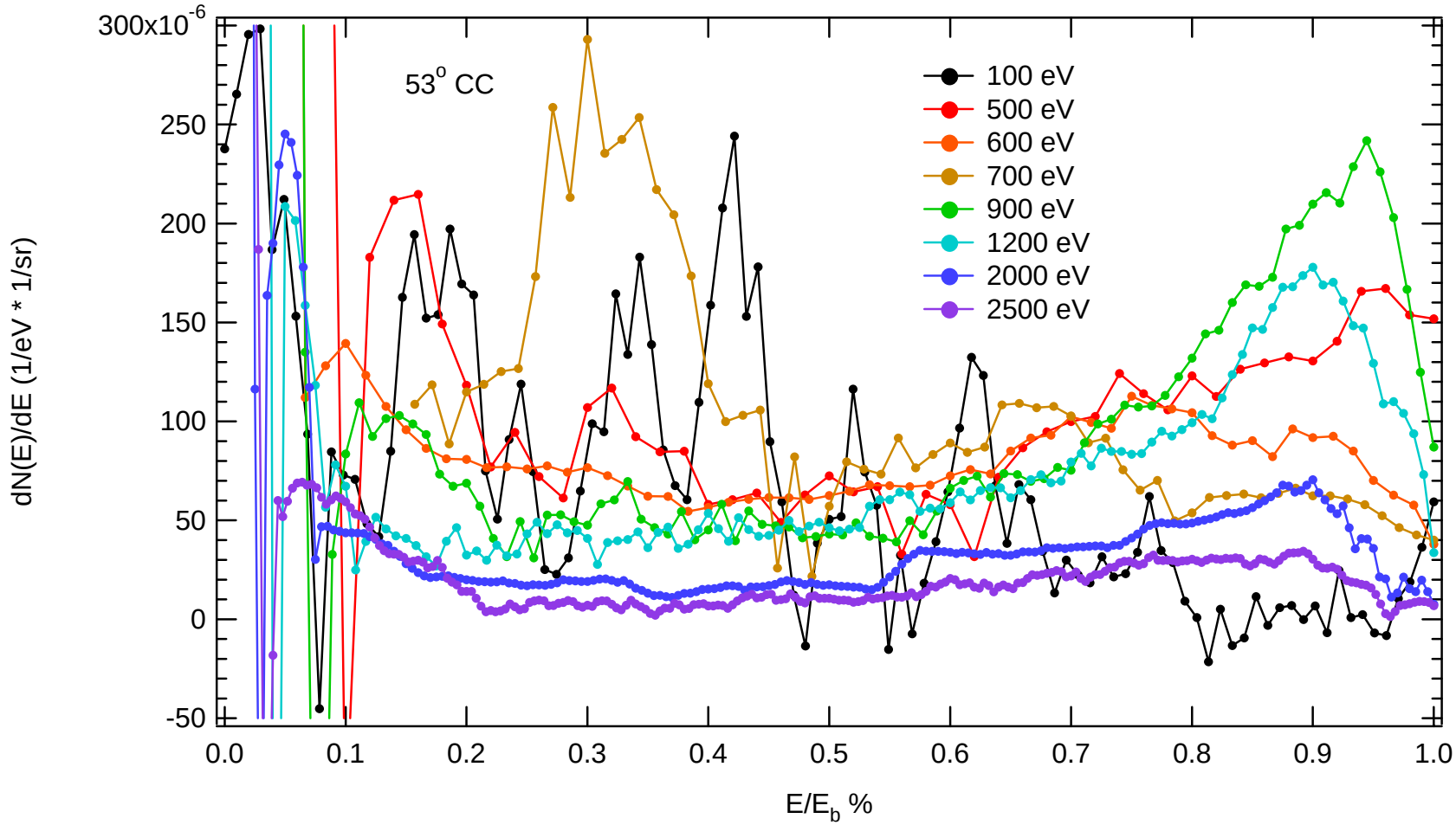

Figure E-26 Normalized AR Energy Spectra at 53° Counter-Clockwise emission for selected beam energies.

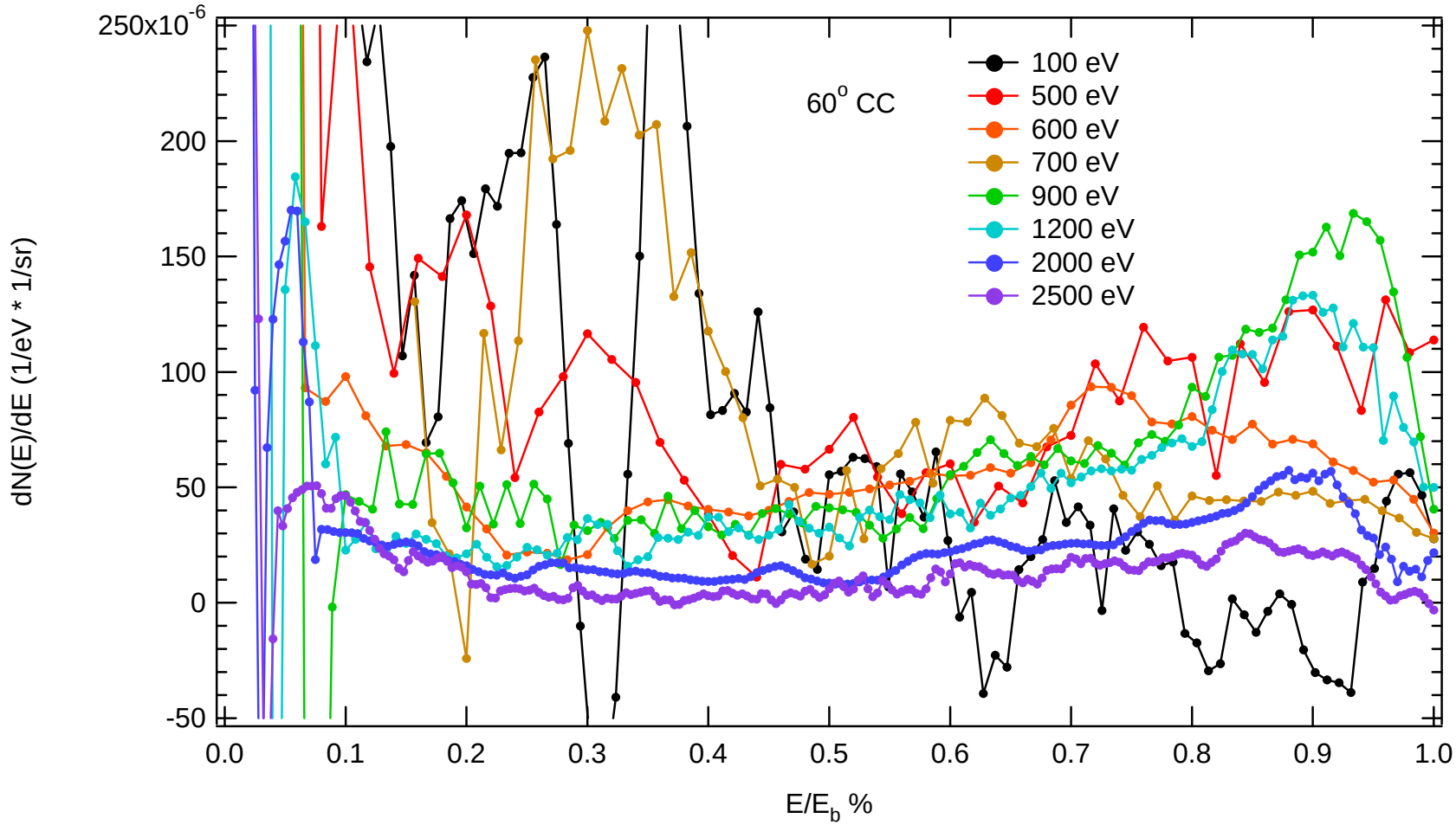

Figure E-27 Normalized AR Energy Spectra at 60° Counter-Clockwise emission for selected beam energies.

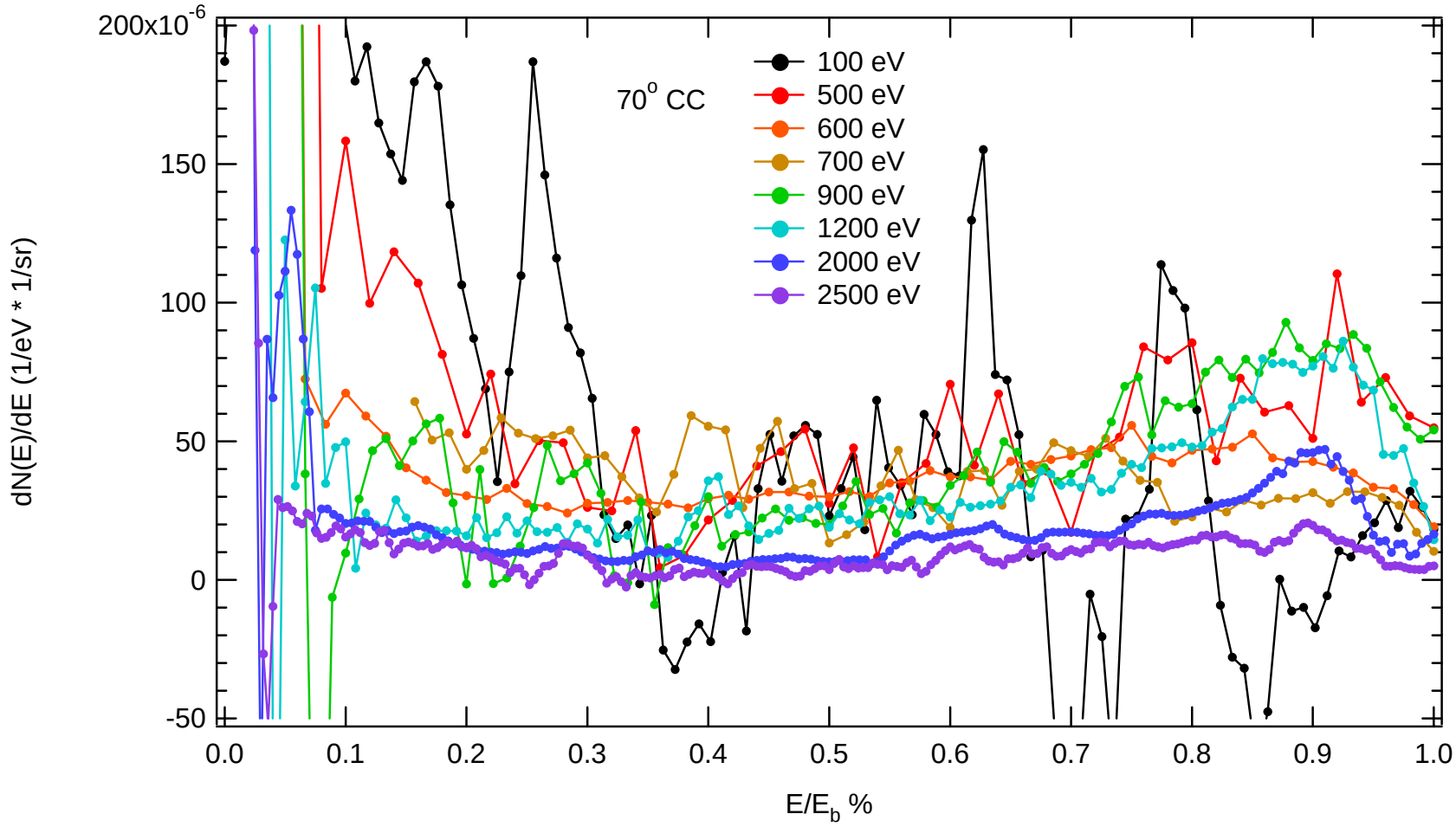

Figure E-28 Normalized AR Energy Spectra at 70° Counter-Clockwise emission for selected beam energies.

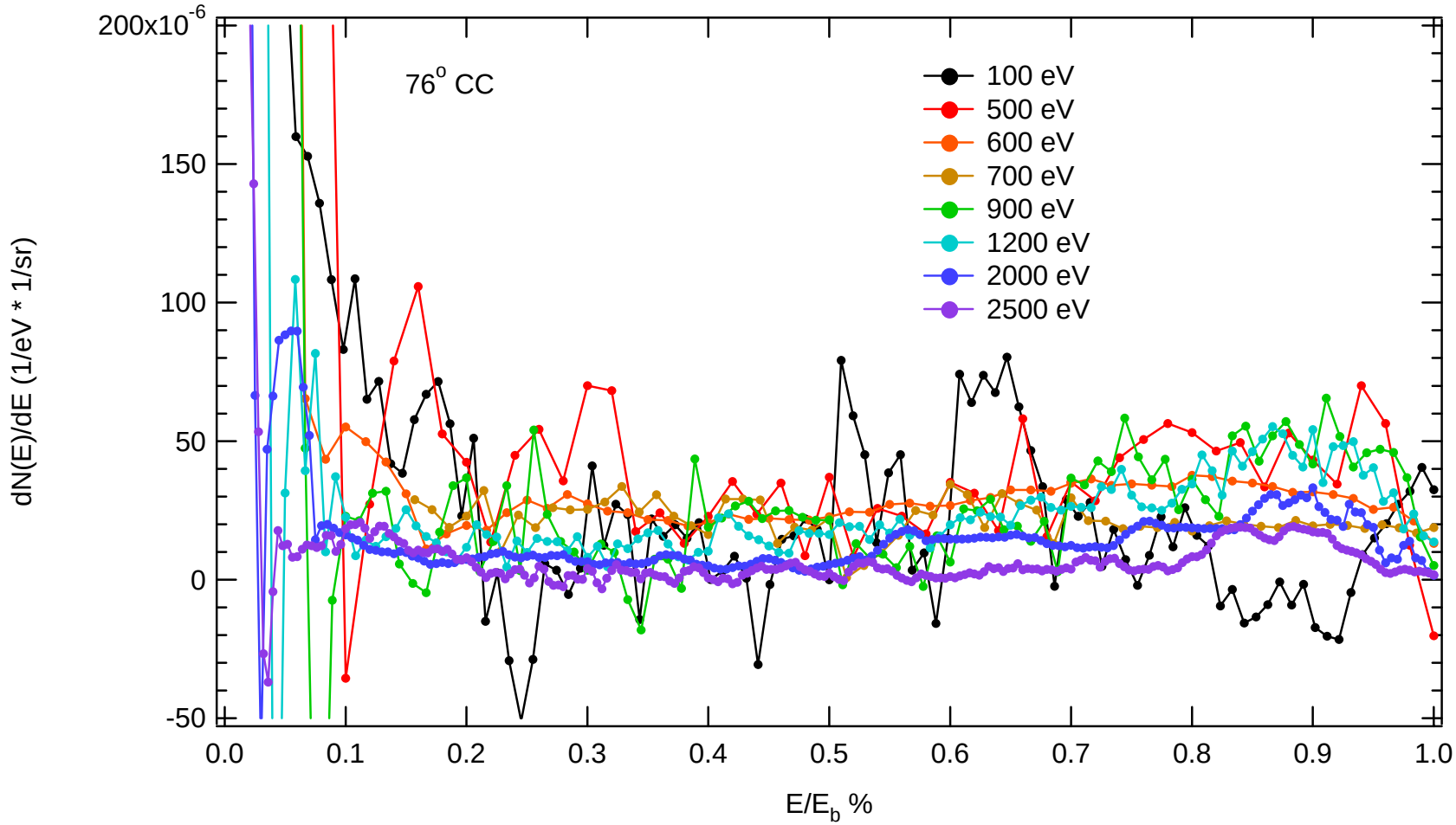

Figure E-29 Normalized AR Energy Spectra at 76° Counter-Clockwise emission for selected beam energies.

E-5(C) High Energy 0.1 eV resolution Spectra (E_b resolved)

The 0.1 eV step size has been used to resolve the positions and intensities of the Elastic and Plasmon peaks. The figures Fig. E-30 through Fig. E-35 span the energy range from ~20 eV below the incident beam energy, E_b, to the beam energy. The selected incident beam energies are 100 eV, 500 eV, 900 eV, 1200 eV, 2000 eV, and 2500 eV and the yields are given in units of $eV^{-1} * sr^{-1}$ on the y-axis and in units of volts on the x-axis. No Clockwise emission angle spectra were taken for E_b = 100 eV.

There are many minute errors in the spectra. The largest error is addressed as the green portion of E_b = 100 eV spectra from 86.8 eV to 88.3 eV. It is invalid because the incident beam current went to zero during that span of time. This is the first inkling that the E-gun filament was becoming heavily degraded due to such high filament currents while using comparatively low accelerating voltages. At this time, the filament was replaced and the steppermotor and controller were installed before further high-energy resolution spectra were measured.

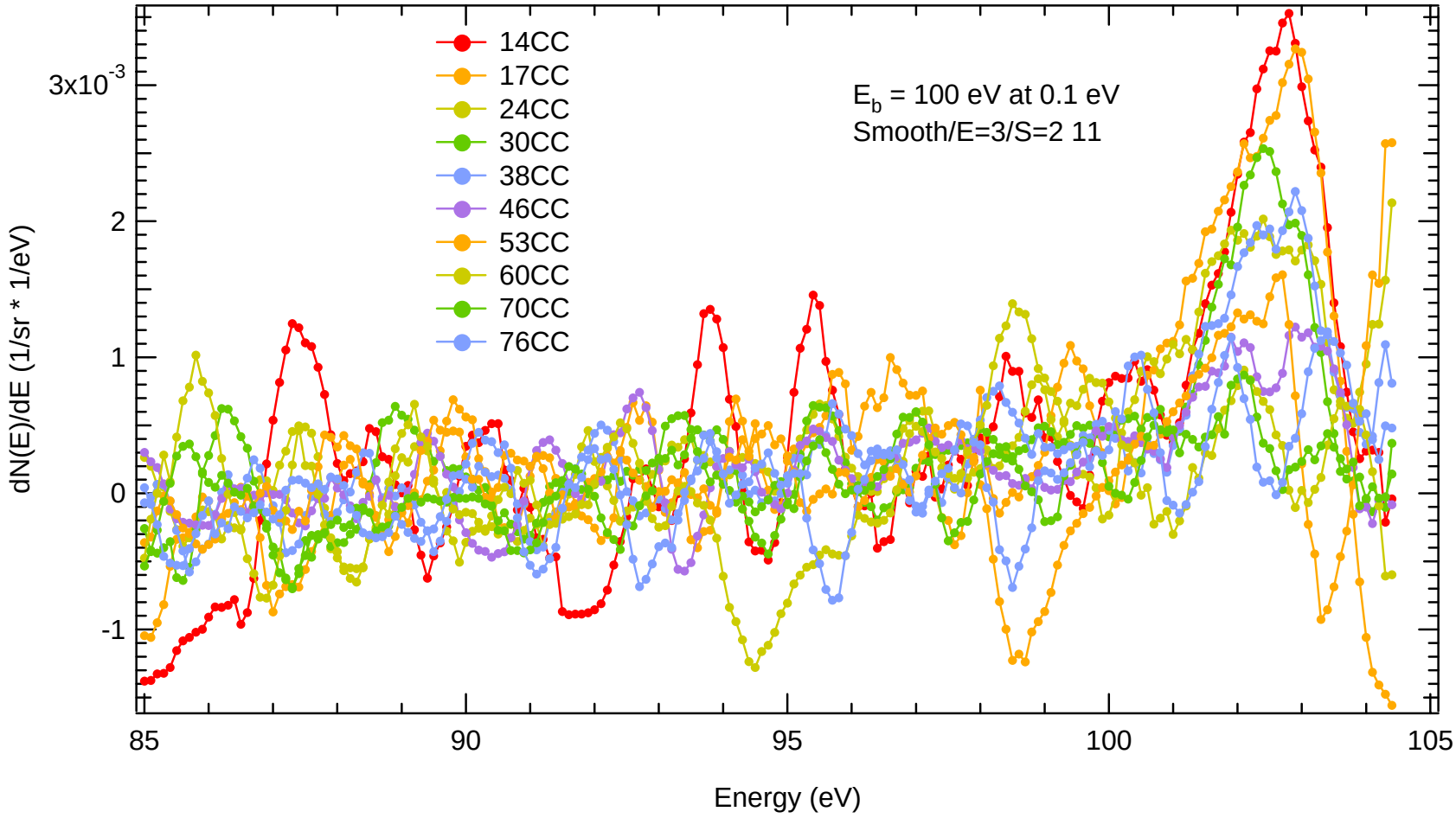

Figure E-30 Fine energy resolution for 100 eV incident beam energy.

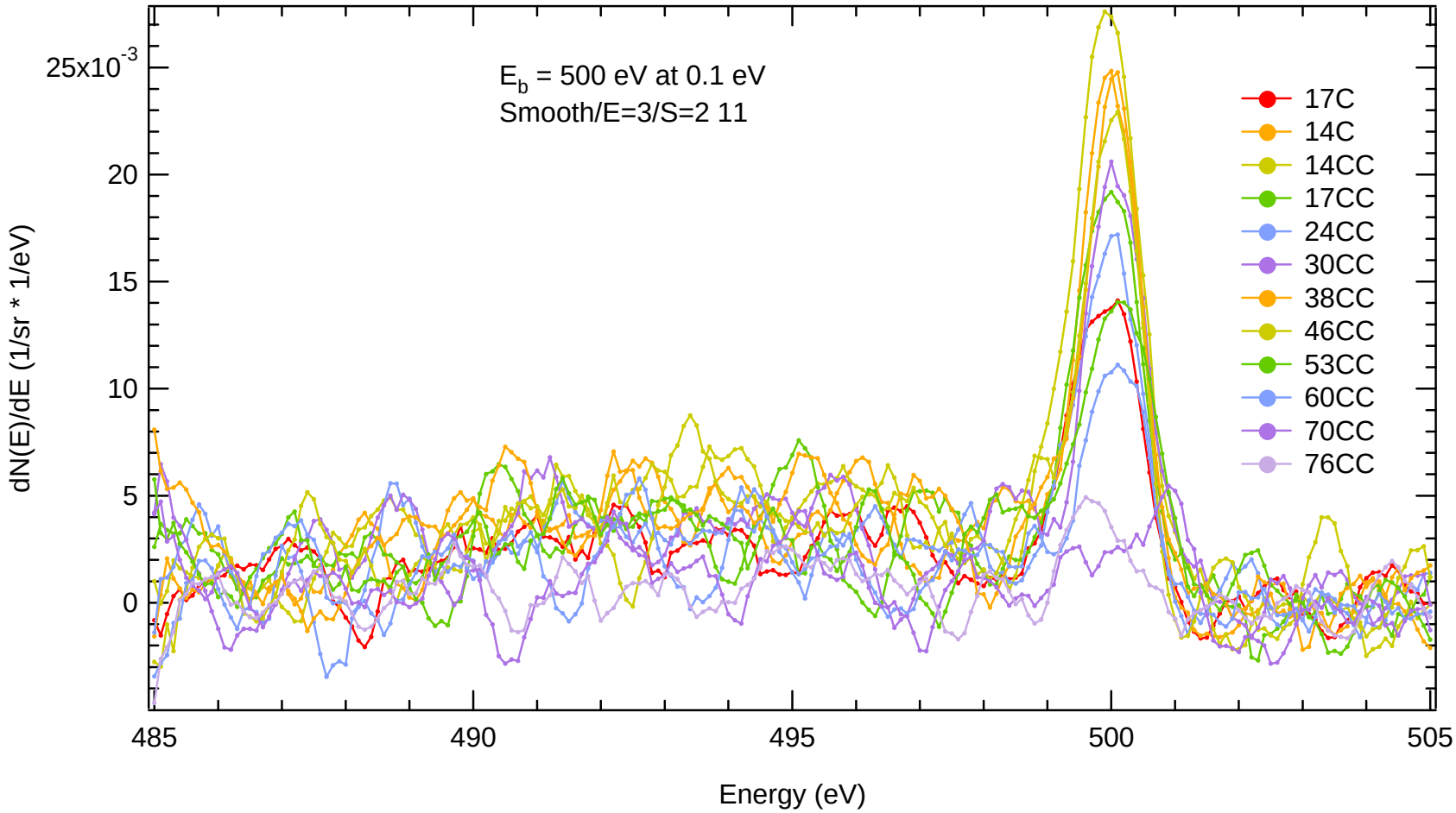

Figure E-31 Fine energy resolution for 500 eV incident beam energy.

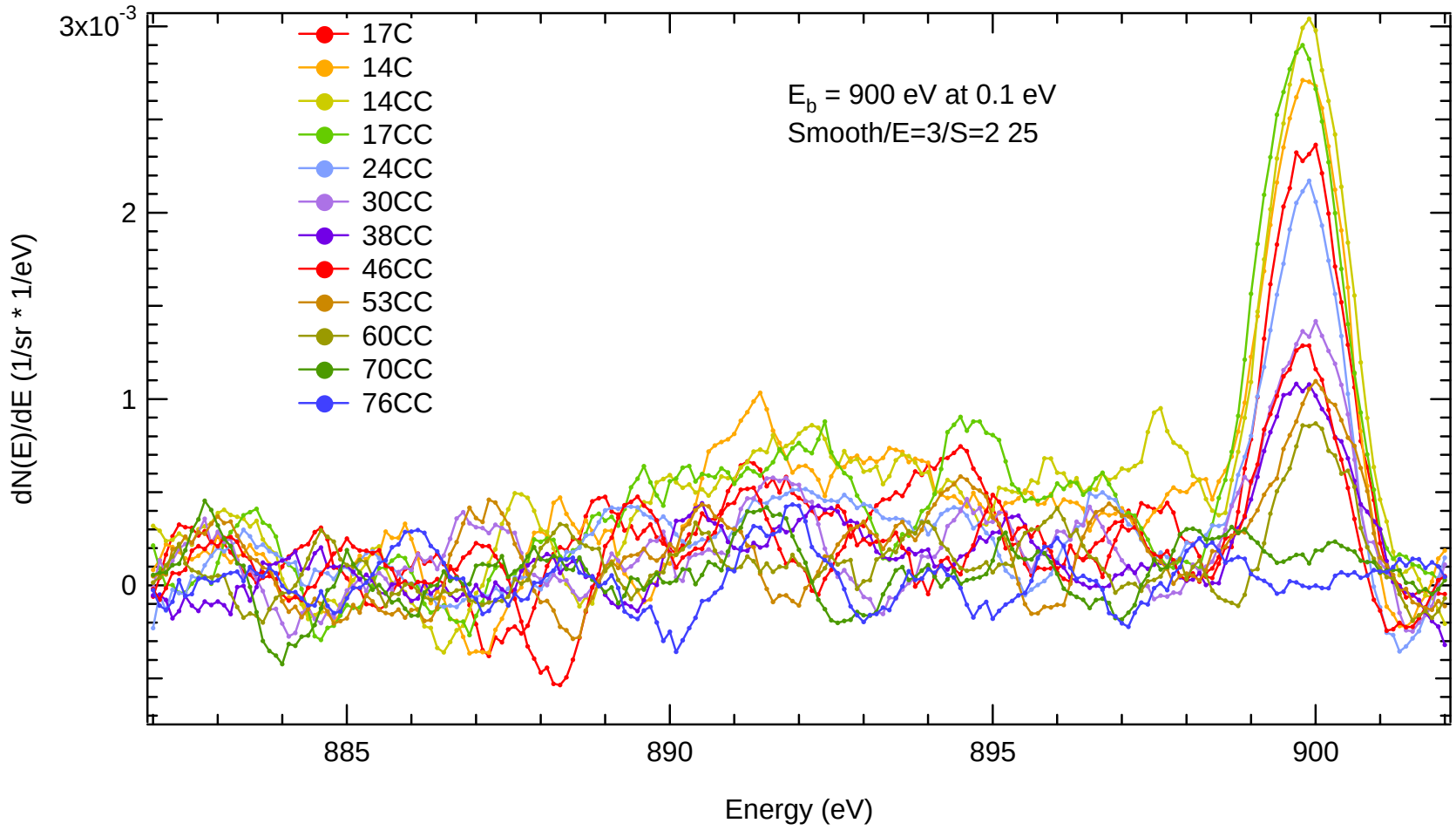

Figure E-32 Fine energy resolution for 900 eV incident beam energy.

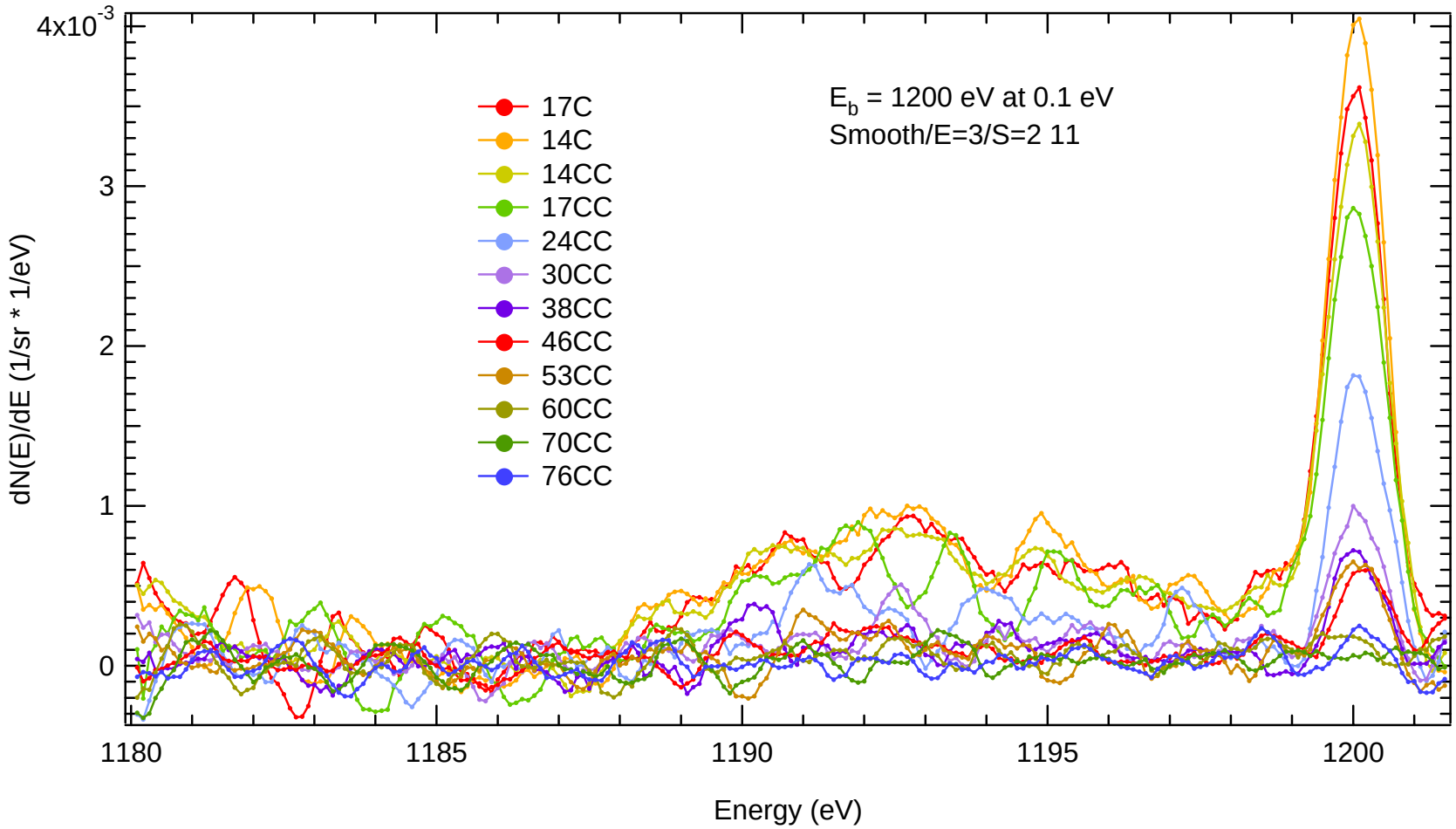

Figure E-33 Fine energy resolution for the 1200 eV incident beam energy.

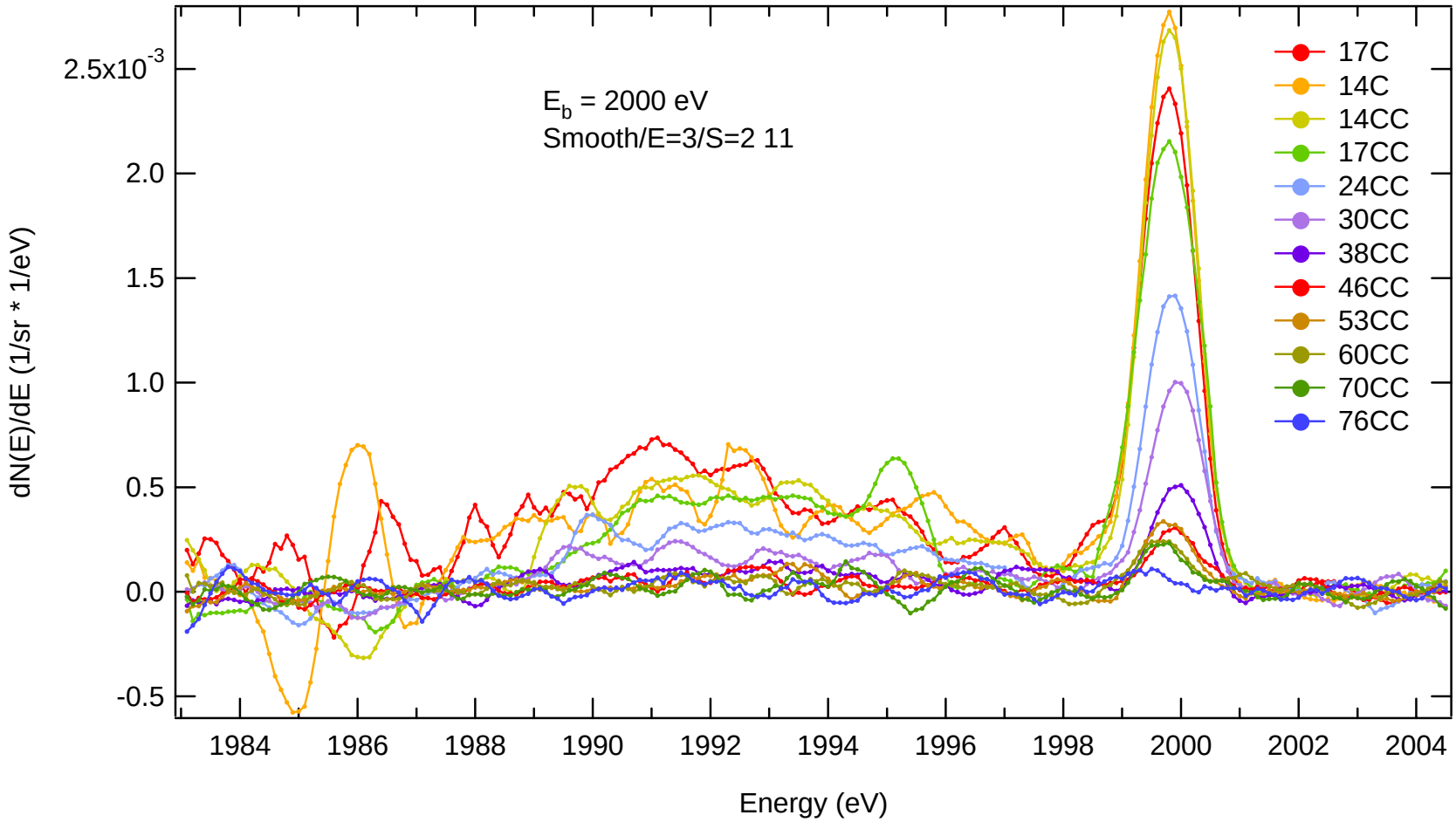

Figure E-34 Fine energy resolution for the 2000 eV incident beam energy.

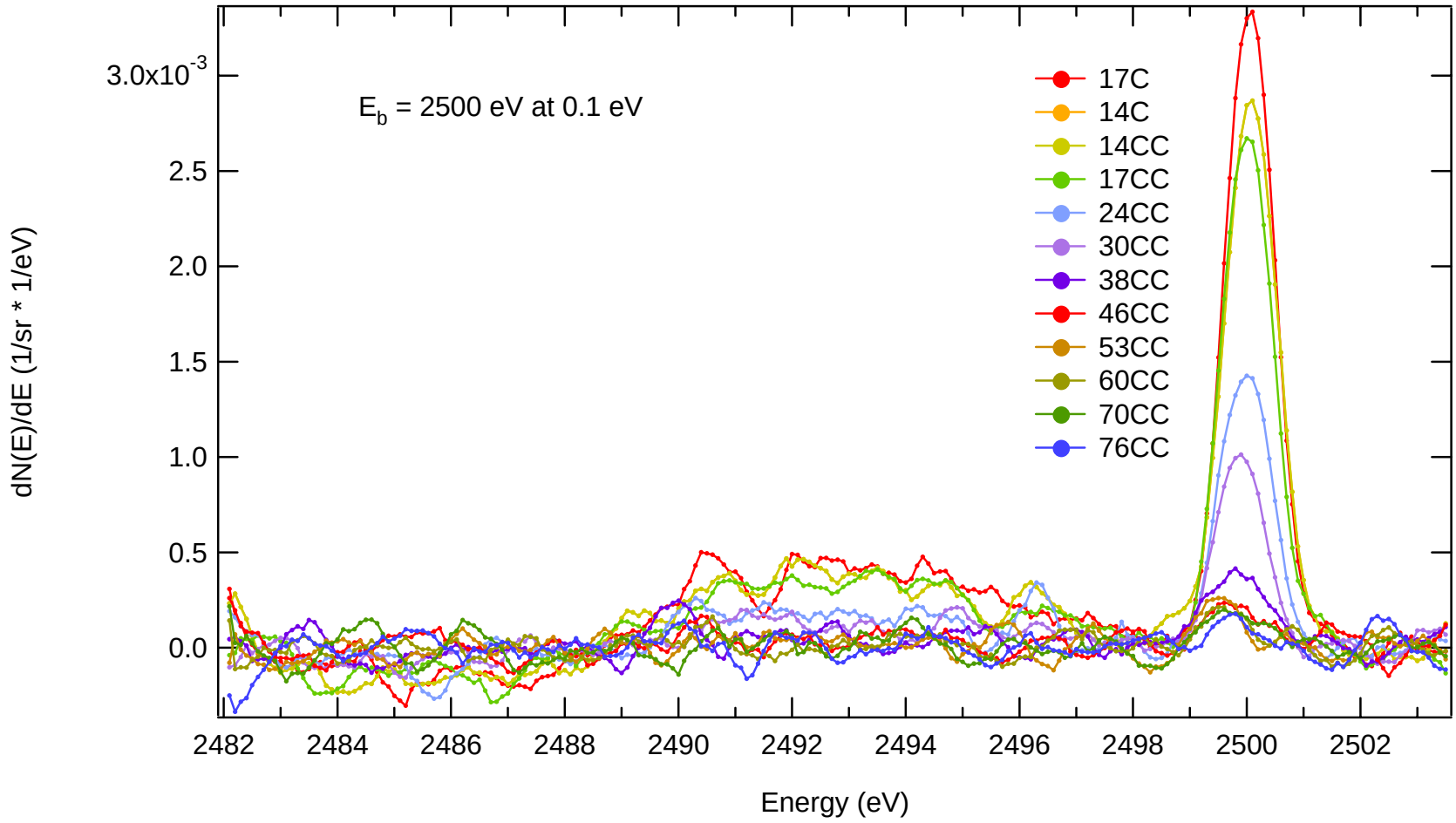

Figure E-35 Fine energy resolution for the 2500 eV incident beam energy.

E-5(D) High Energy 0.1 eV resolution Spectra (Angle Resolved)

The Elastic ER angular distributions are shown in Figure E-36 through Figure E-47. These spectra have all been shifted by the incident electron beam energy, E_b, so that the x-axis origin is the location of E_b. These spectra have been taken at 0.1 eV step size. This is a re-organization of the E_bR spectra in the last section, where all the electron beam energy data have been grouped together for each particular angle. The range is recalibrated to set the Elastic Peak at the origin.

No normalization has taken place.

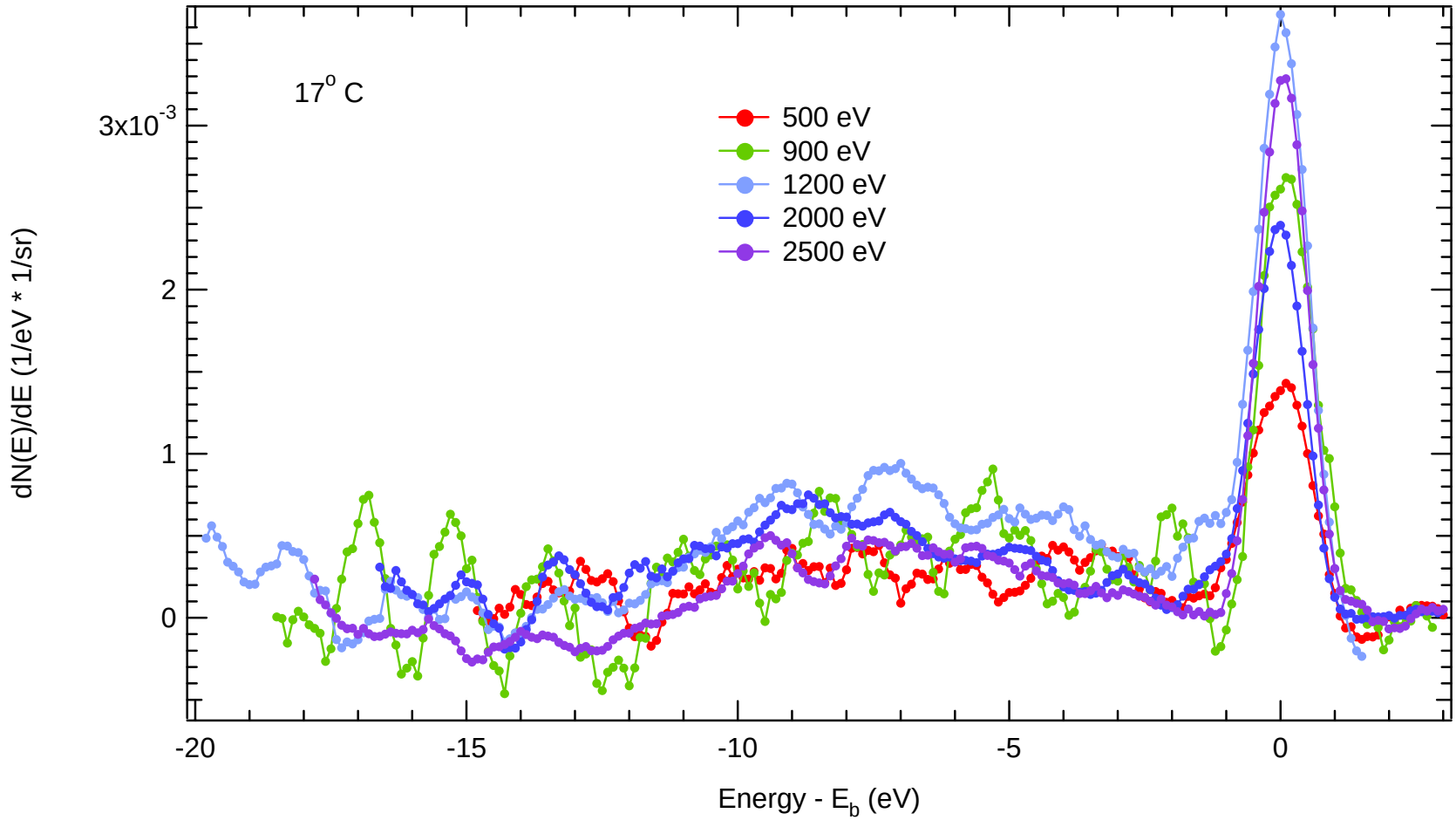

Figure E-36 Elastic AR Energy Spectra at 17° Clockwise emission for selected beam energies.

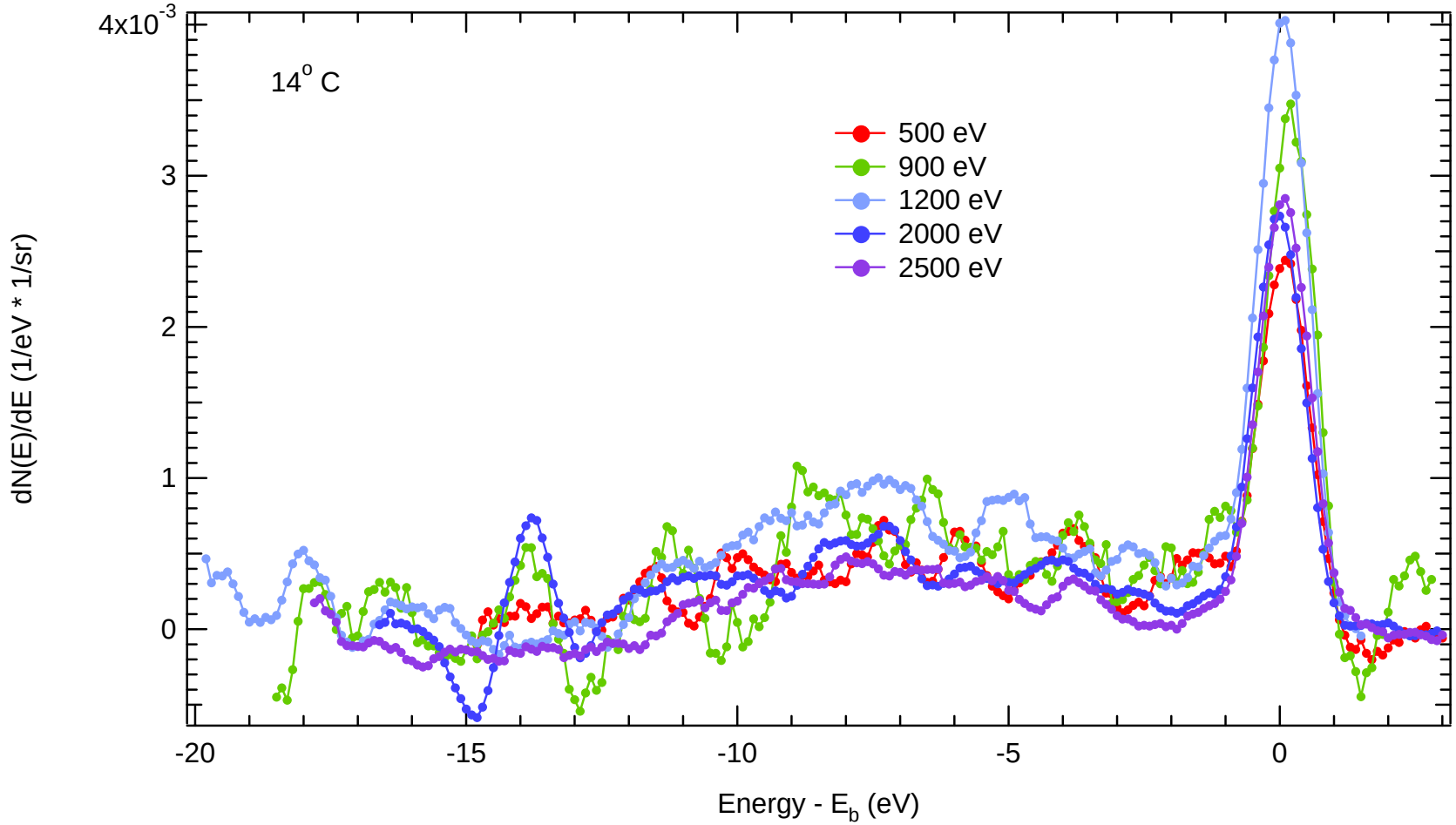

Figure E-37 Elastic AR Energy Spectra at 14^{o} Clockwise emission for selected beam energies.

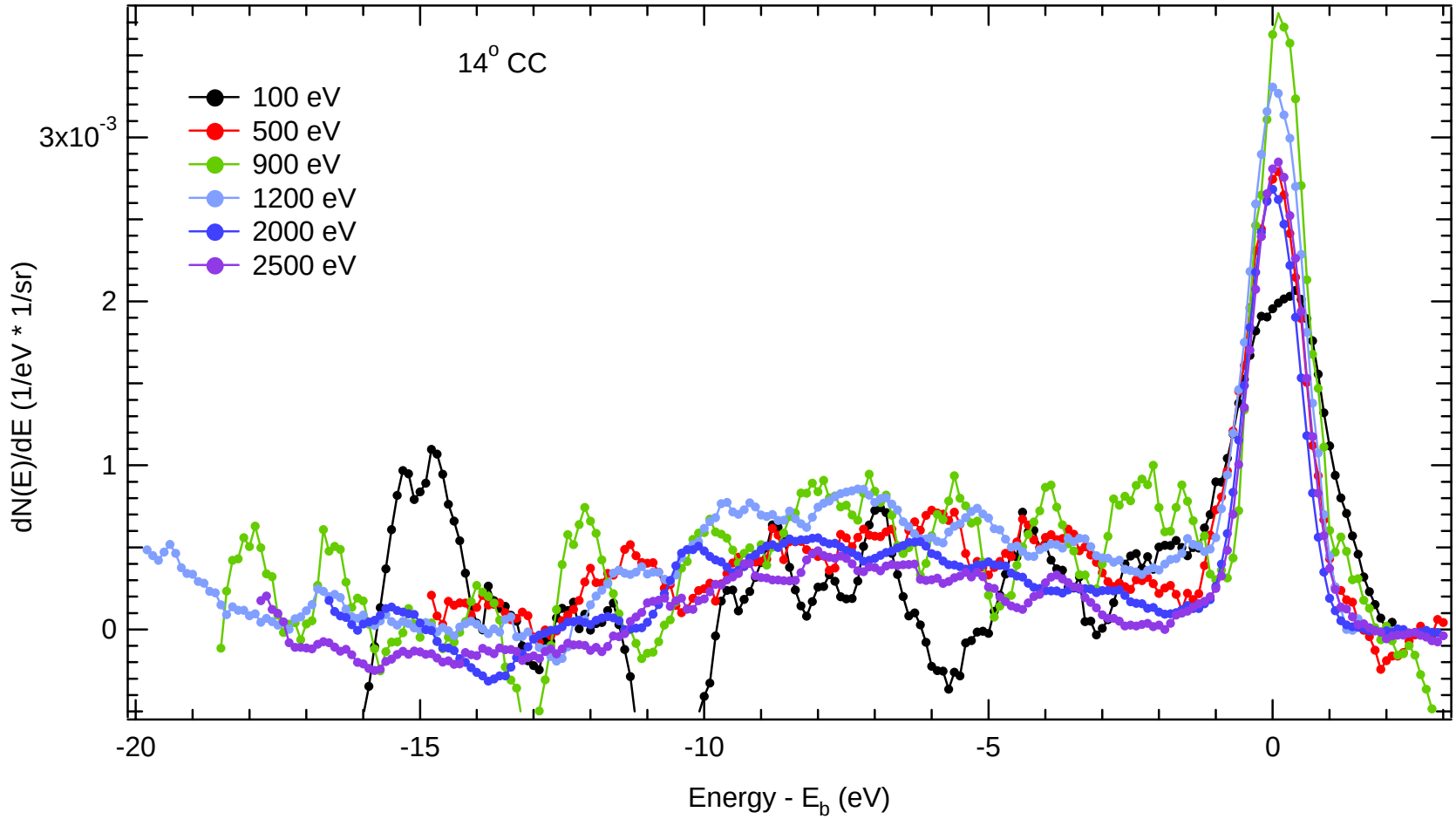

Figure E-38 Elastic AR Energy Spectra at 14° Counter-Clockwise emission for selected beam energies.

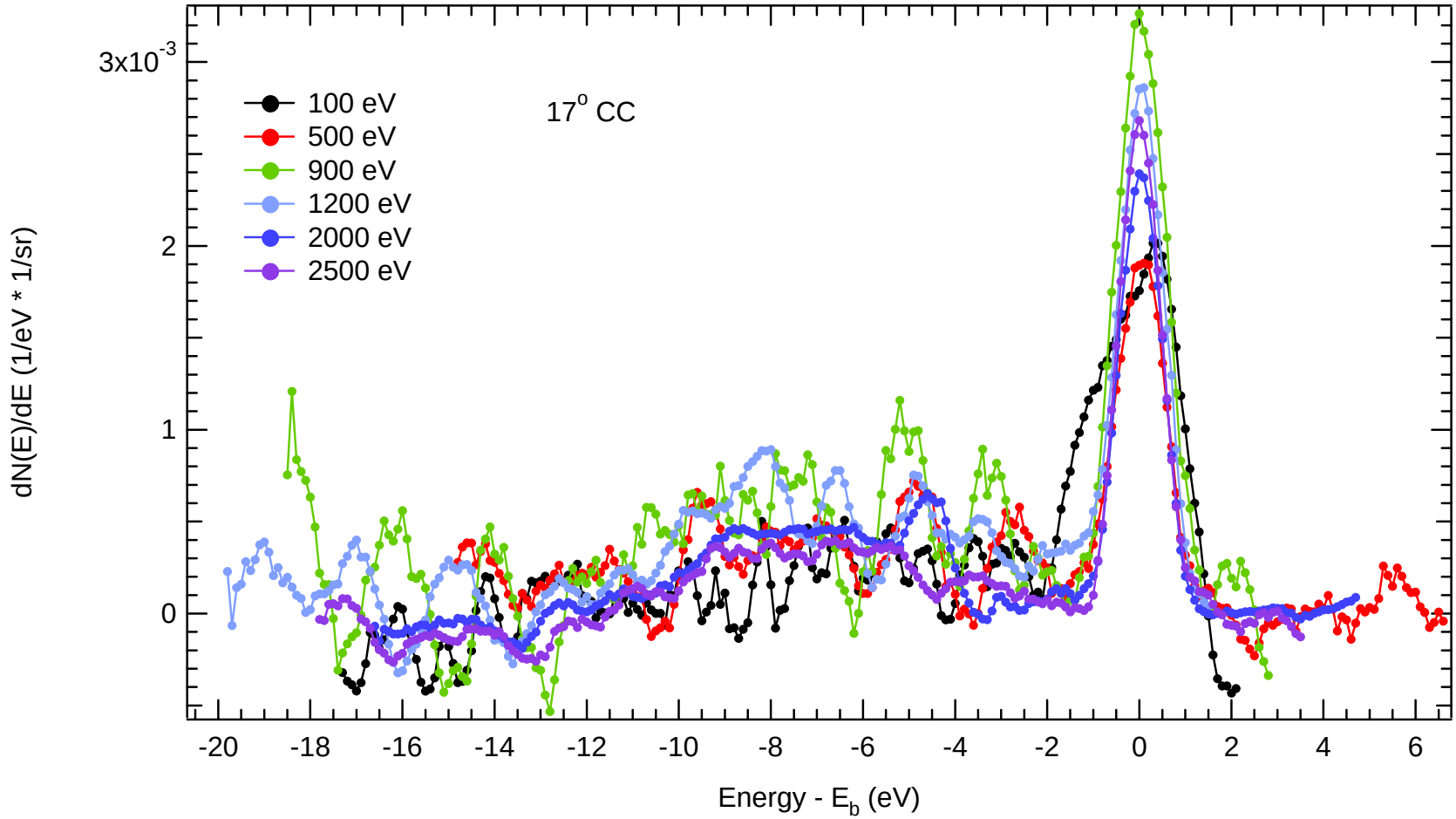

Figure E-39 Elastic AR Energy Spectra at 17° Counter-Clockwise emission for selected beam energies.

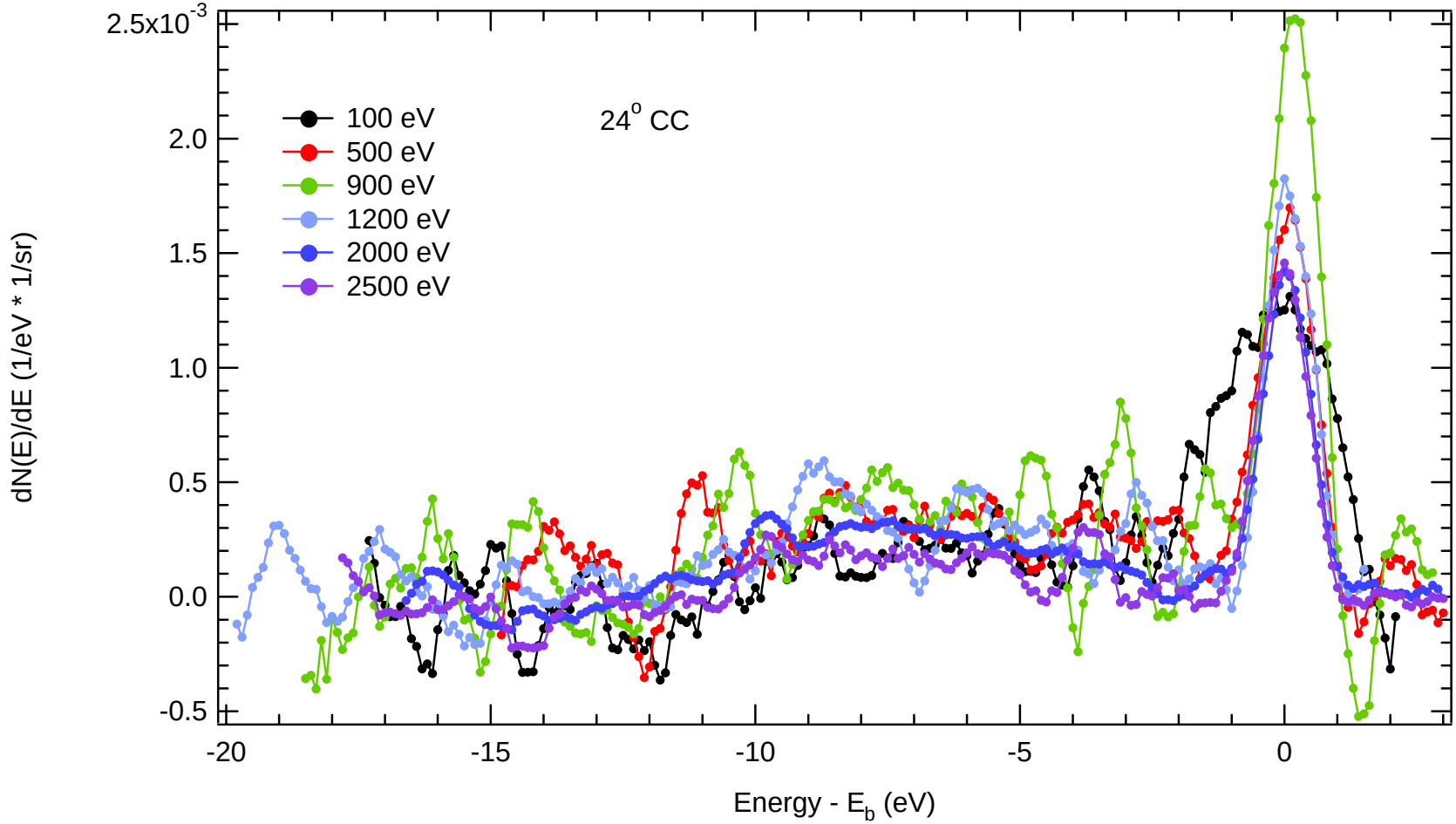

Figure E-40 Elastic AR Energy Spectra at 24° Counter-Clockwise emission for selected beam energies.

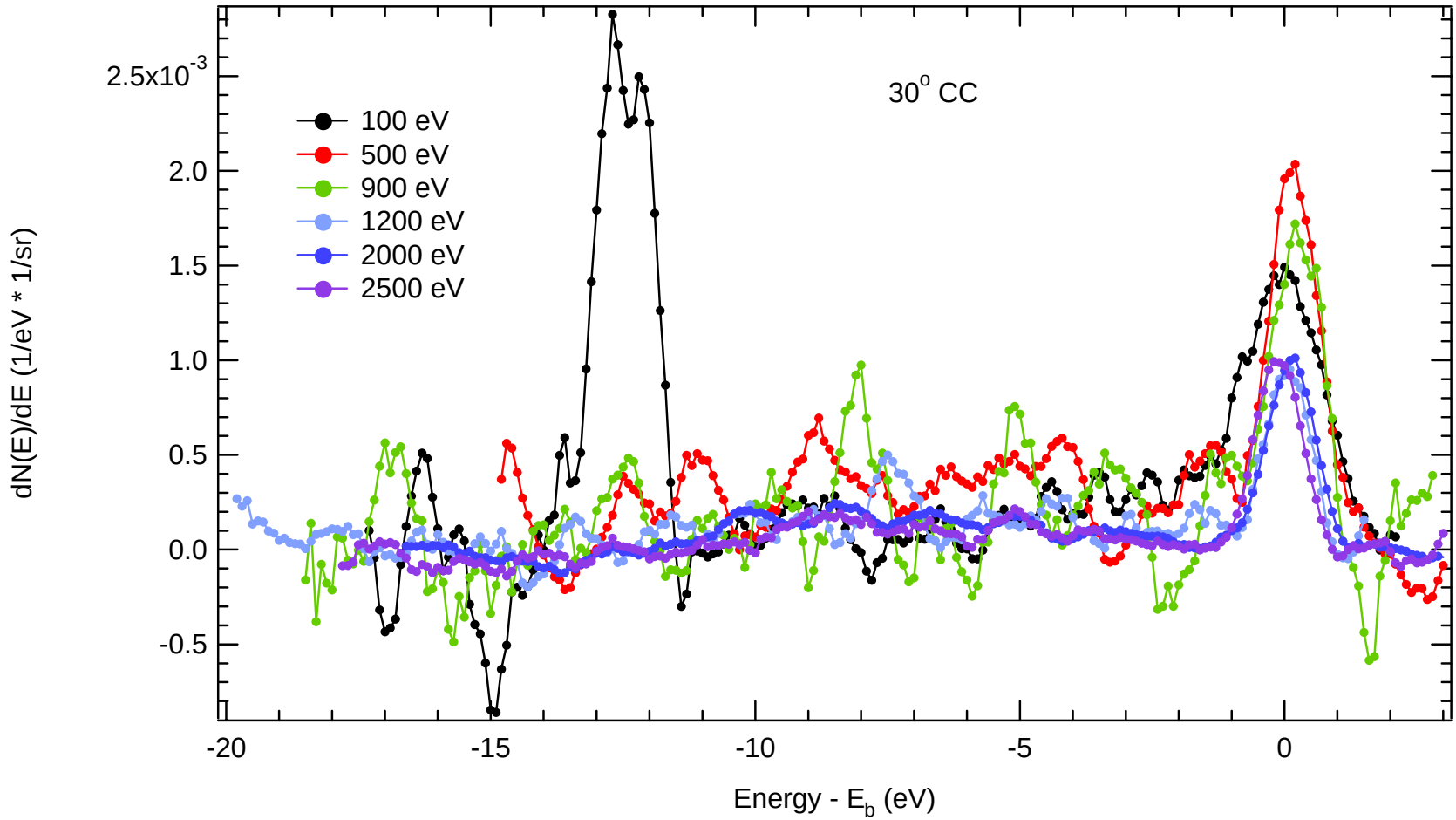

Figure E-41 Elastic AR Energy Spectra at 30° Counter-Clockwise emission for selected beam energies.

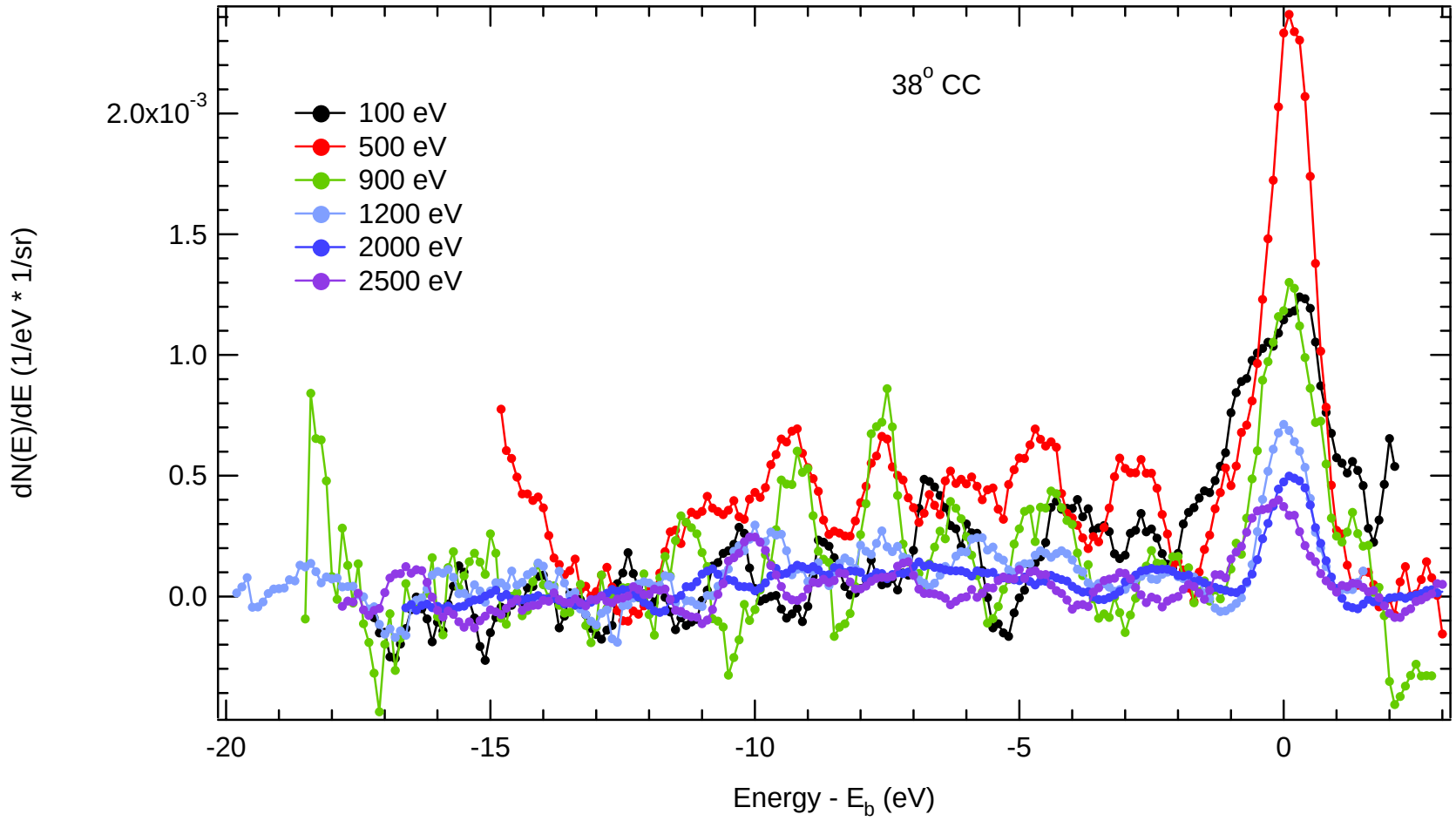

Figure E-42 Elastic AR Energy Spectra at 38° Counter-Clockwise emission for selected beam energies.

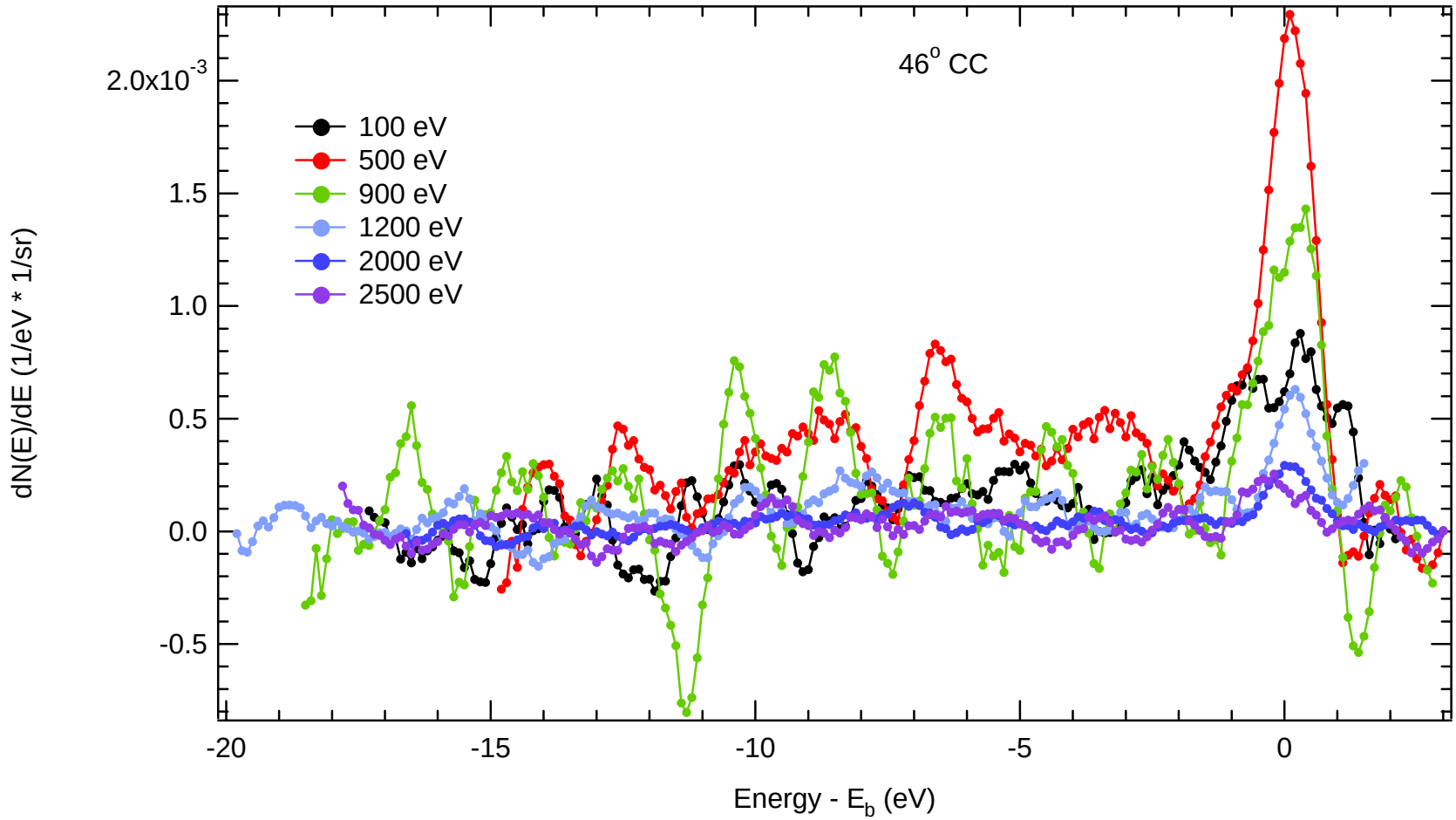

Figure E-43 Elastic AR Energy Spectra at 46° Counter-Clockwise emission for selected beam energies.

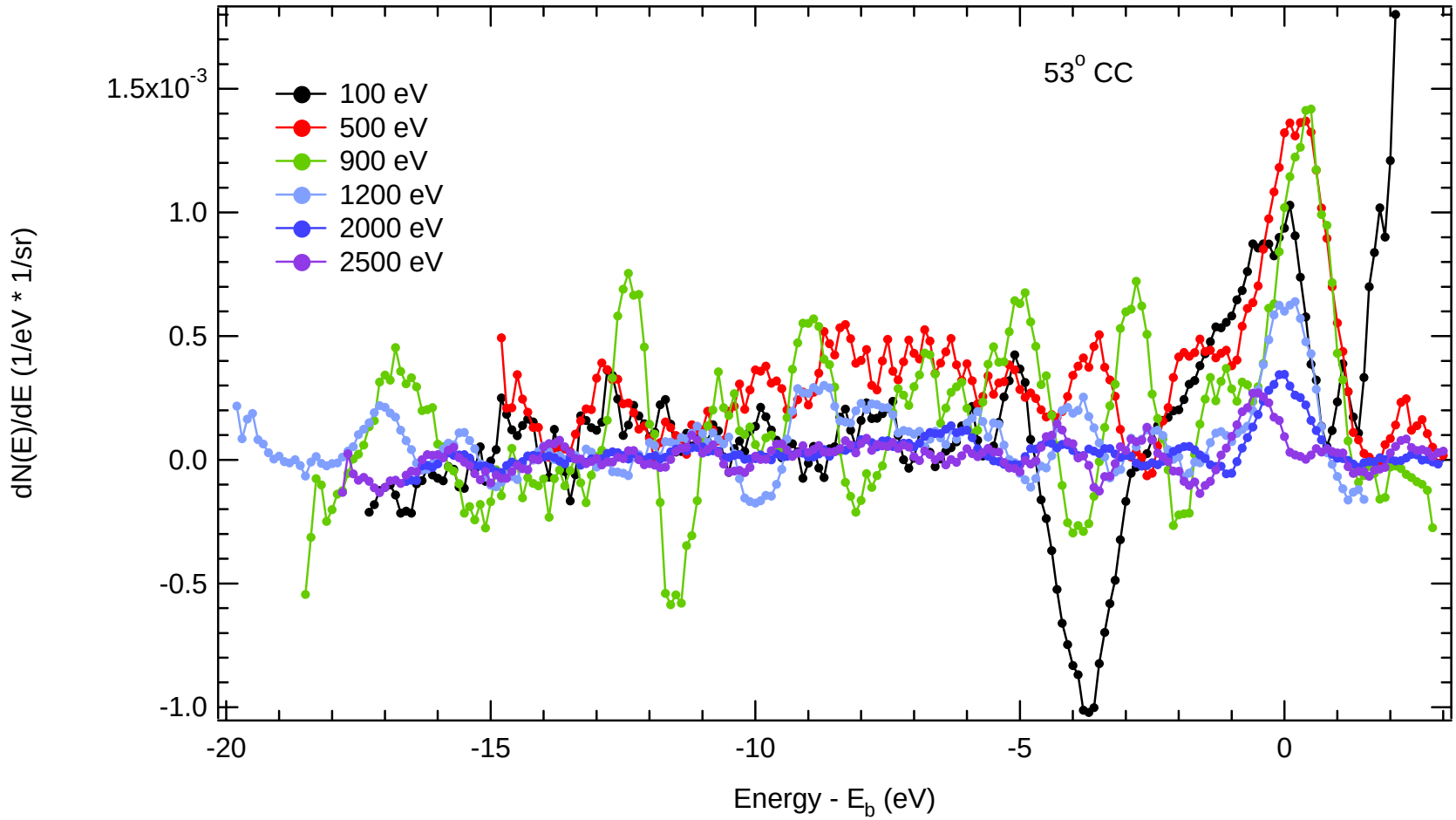

Figure E-44 Elastic AR Energy Spectra at 53° Counter-Clockwise emission for selected beam energies.

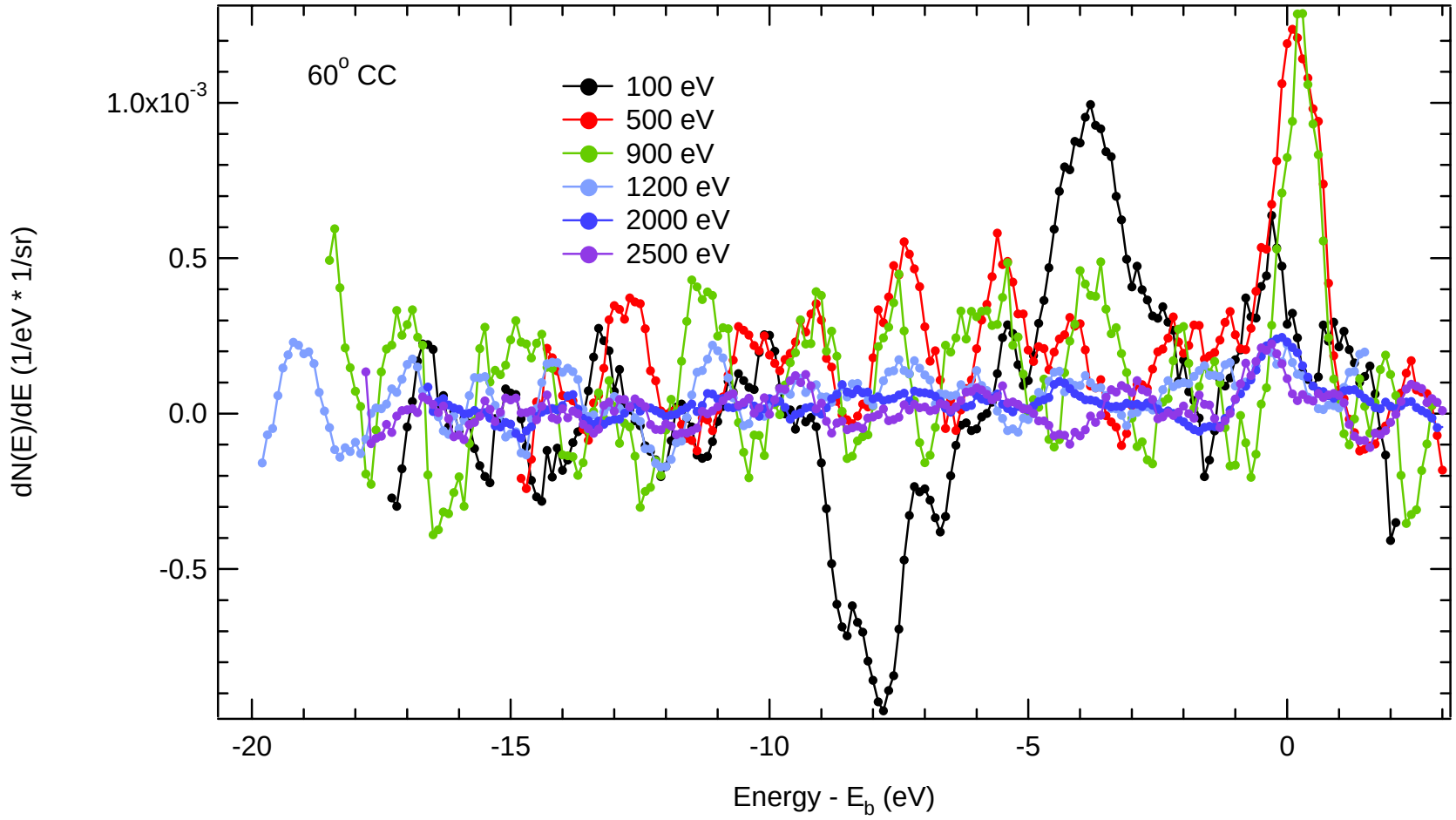

Figure E-45 Elastic AR Energy Spectra at 60° Counter-Clockwise emission for selected beam energies.

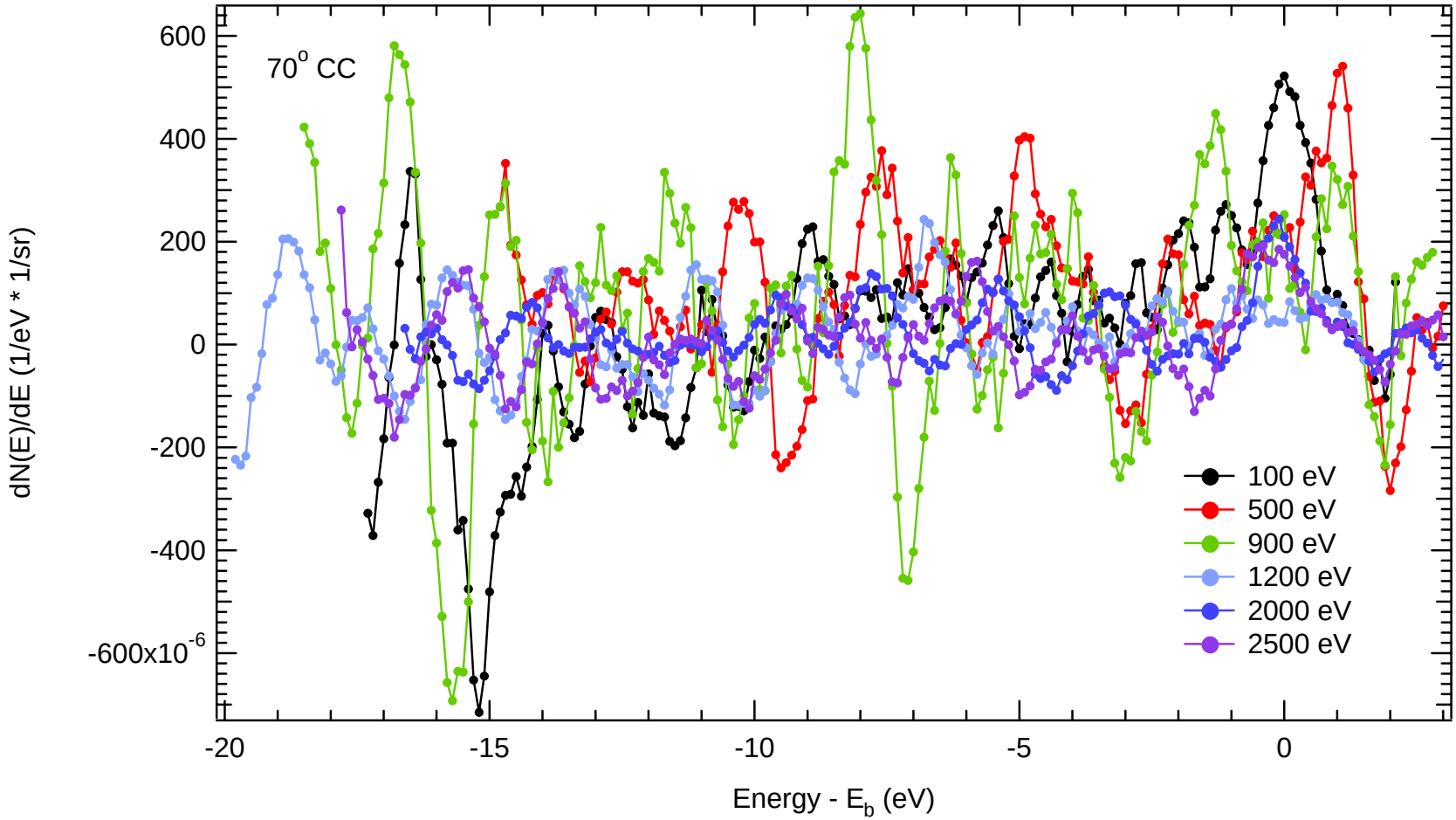

Figure E-46 Elastic AR Energy Spectra at 70° Counter-Clockwise emission for selected beam energies.

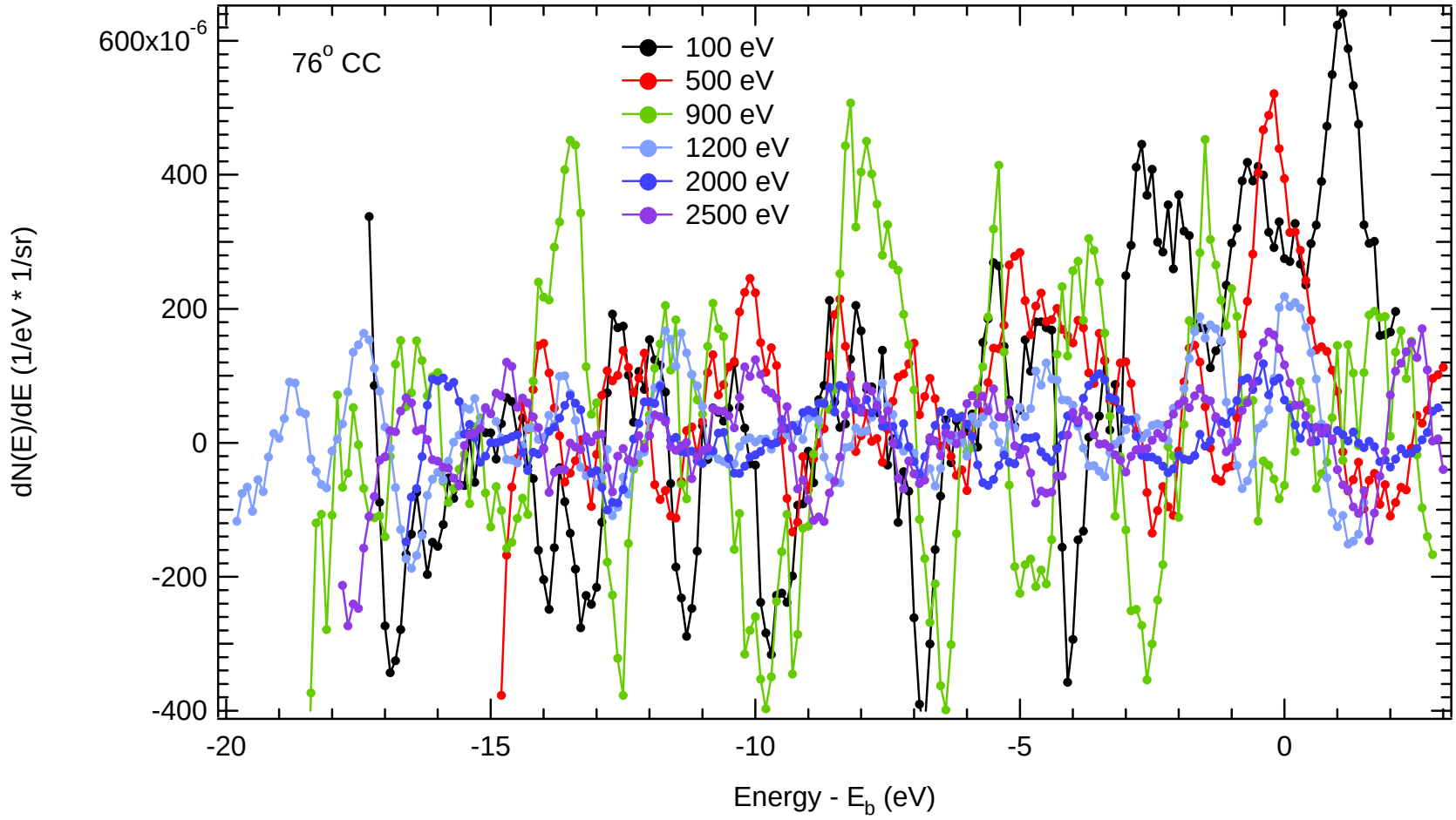

Figure E-47 Elastic AR Energy Spectra at 76° Counter-Clockwise emission for selected beam energies.

E-5(E) High Energy 1 eV resolution Spectra (E_b Resolved)

A zoom of the high-energy portion of the spectra is given at 1 eV resolution. The energy emissions span from the incident beam energy, E_b, to ~200 eV below E_b. The graphs are Fig. E-48 through Fig. E-54 for the same selected E_b's as those measured in coarse energy resolution. From these portions of spectra, the energy positions and yield intensities of three key points of interest are measured, tabulated, and compared. The key points consist of the elastic peak, the Elastic—BSE boundary minimum, and the BSE Peak (Chap. 5.1 and 5.4)

The Elastic Peak Intensity is different for the 1 eV and 0.1 eV resolutions. The 0.1 eV resolution Intensity is an order of magnitude higher than that of the 1 eV resolution Intensities, but since the widths of the 1 eV resolution Elastic Peaks are an order of magnitude smaller than those of the 0.1 eV resolution, the product of the intensity by the width are comparable. The Integrated areas of the Elastic Peaks measured at 0.1 eV and 1 eV resolution are compared in Chap. 5.1.

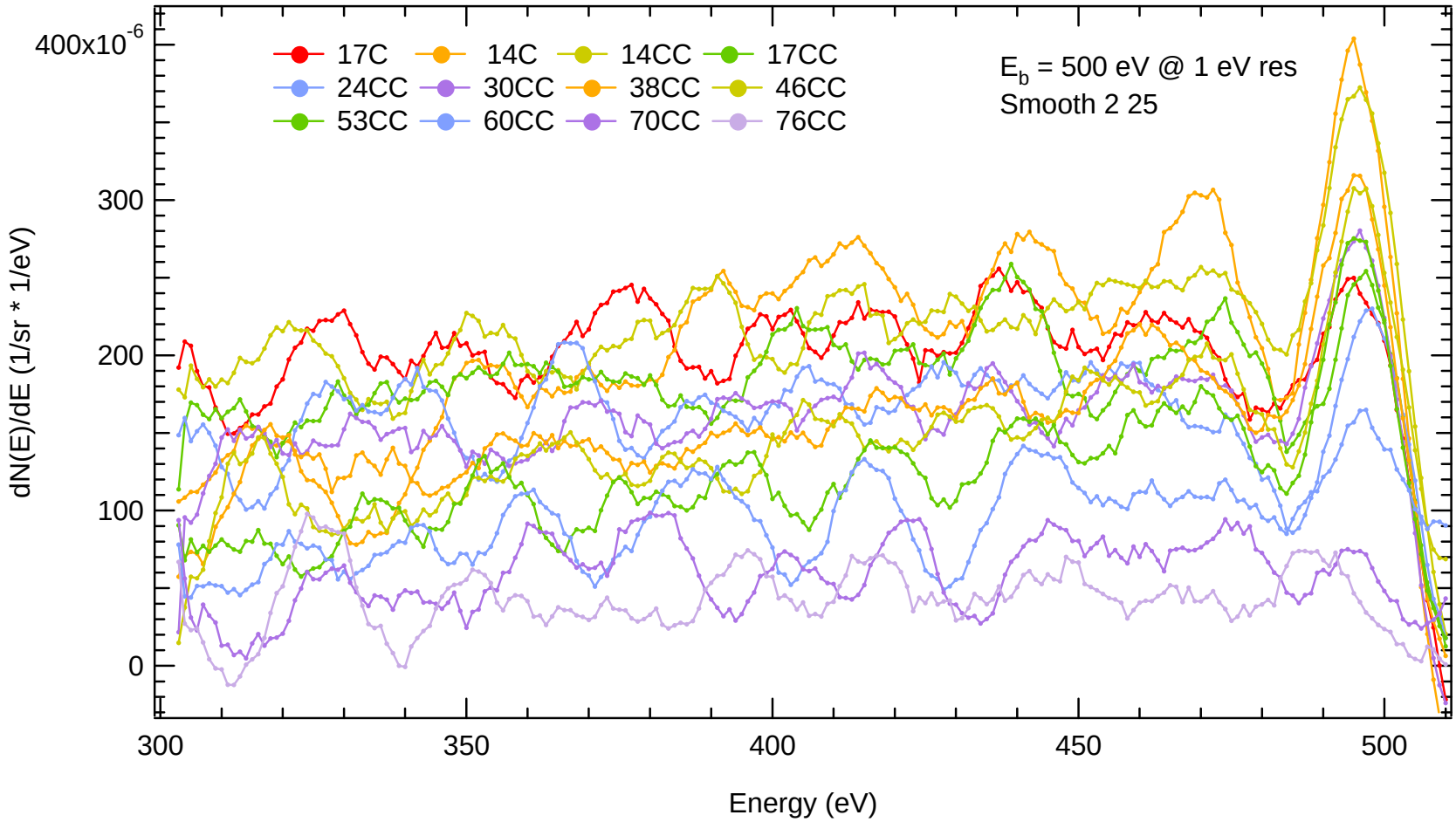

Figure E-48 BSE and Elastic Peaks measured with the 1 eV resolution for 500 eV Incident Beam Energy.

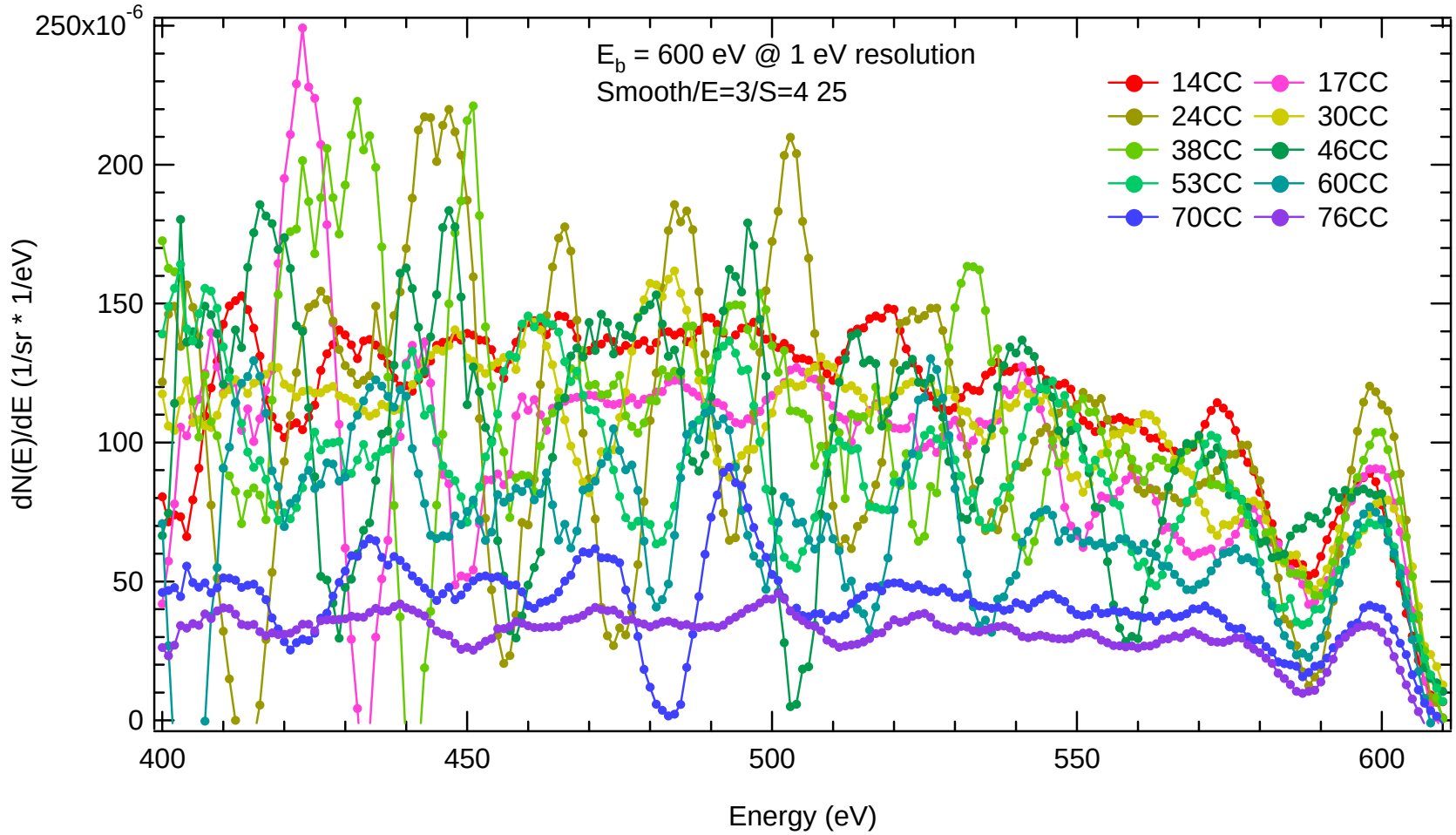

Figure E-49 BSE and Elastic Peaks measured with the 1 eV resolution for 600 eV Incident Beam Energy.

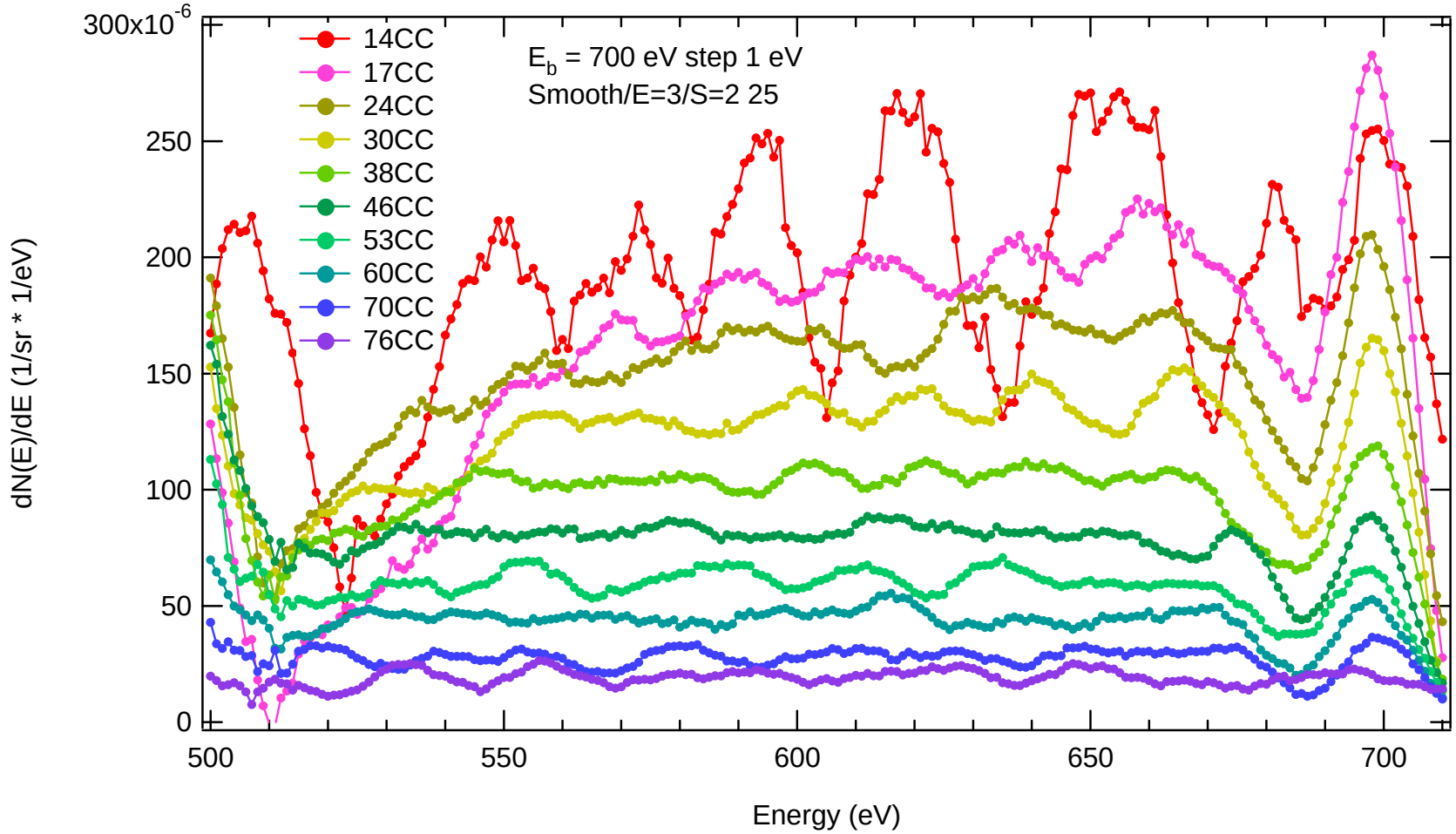

Figure E-50 BSE and Elastic Peaks measured with the 1 eV resolution for 700 eV Incident Beam Energy.

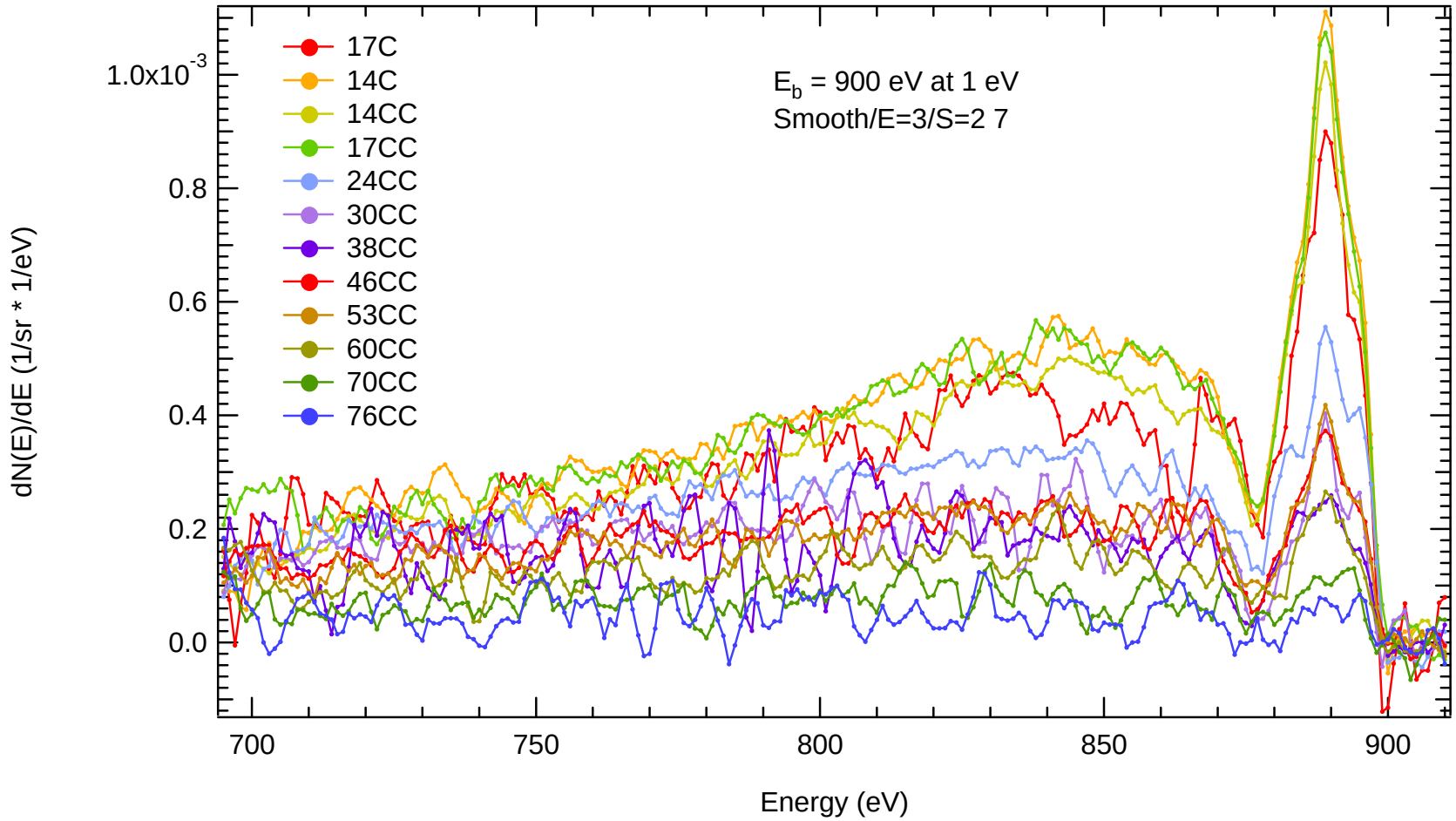

Figure E-51 BSE and Elastic Peaks measured with the 1 eV resolution for 900 eV Incident Beam Energy.

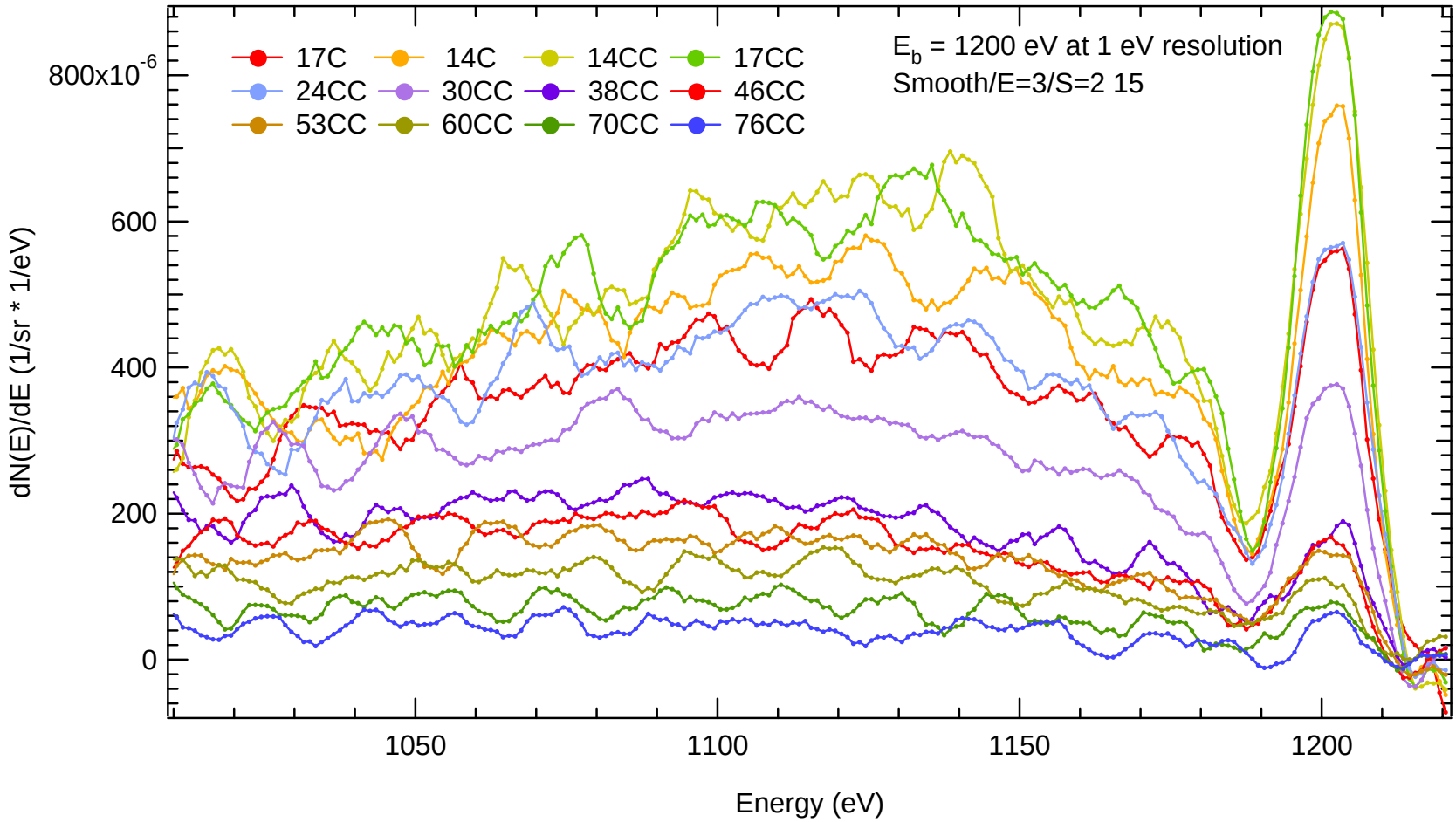

Figure E-52 BSE and Elastic Peaks measured with the 1 eV resolution for 1200 eV Incident Beam Energy.

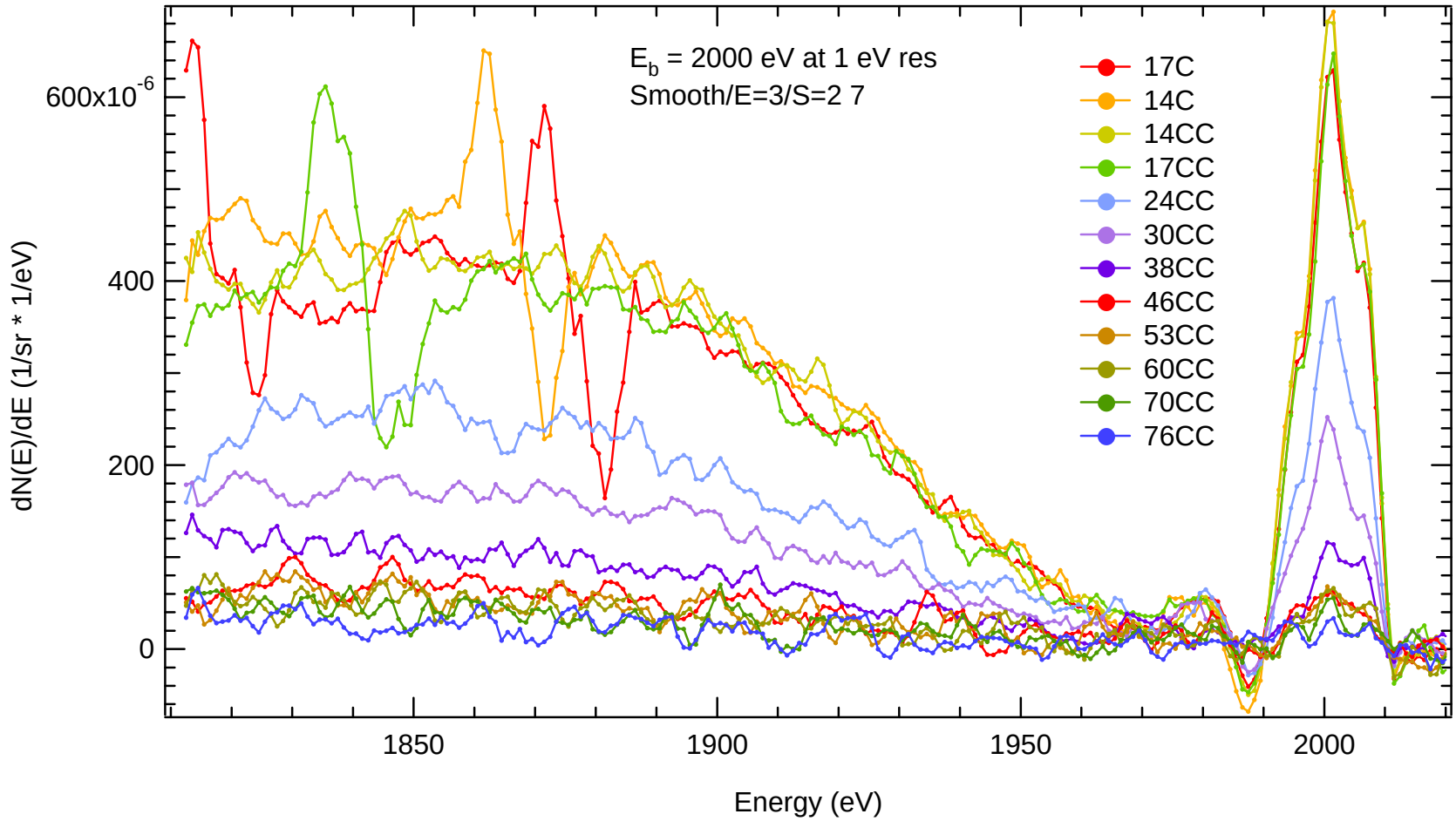

Figure E-53 BSE and Elastic Peaks measured with the 1 eV resolution for 2000 eV Incident Beam Energy.

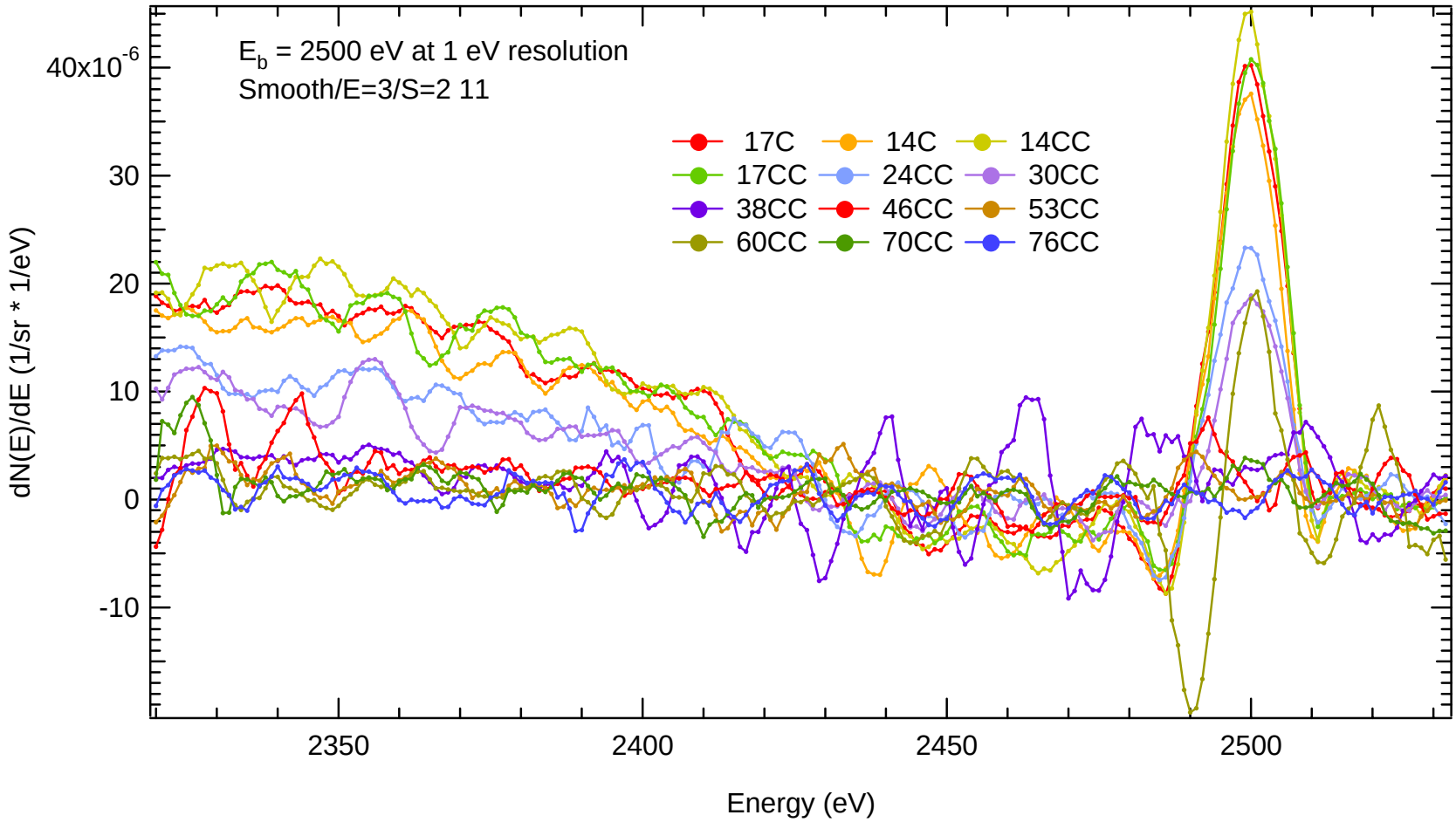

Figure E-54 BSE and Elastic Peaks measured with the 1 eV resolution for 2500 eV Incident Beam Energy.

E-5(F) High Energy 1 eV resolution Spectra (Angle Resolved)

The high energy AR angular spectra are shown in Fig. E-55 through Fig. E-66. These spectra have all been shifted by the electron beam energy so that the x-axis origin is the electron beam energy value. These spectra have been taken at 1 eV step size.

Comparison of the AR spectra to those using 0.1 eV resolution (section E-5(D)) show a noticeable difference in elastic peak width and height. This is because the derivative process Chap. 3.2(d) always involved the same number of neighboring data points regardless of the energy resolution.

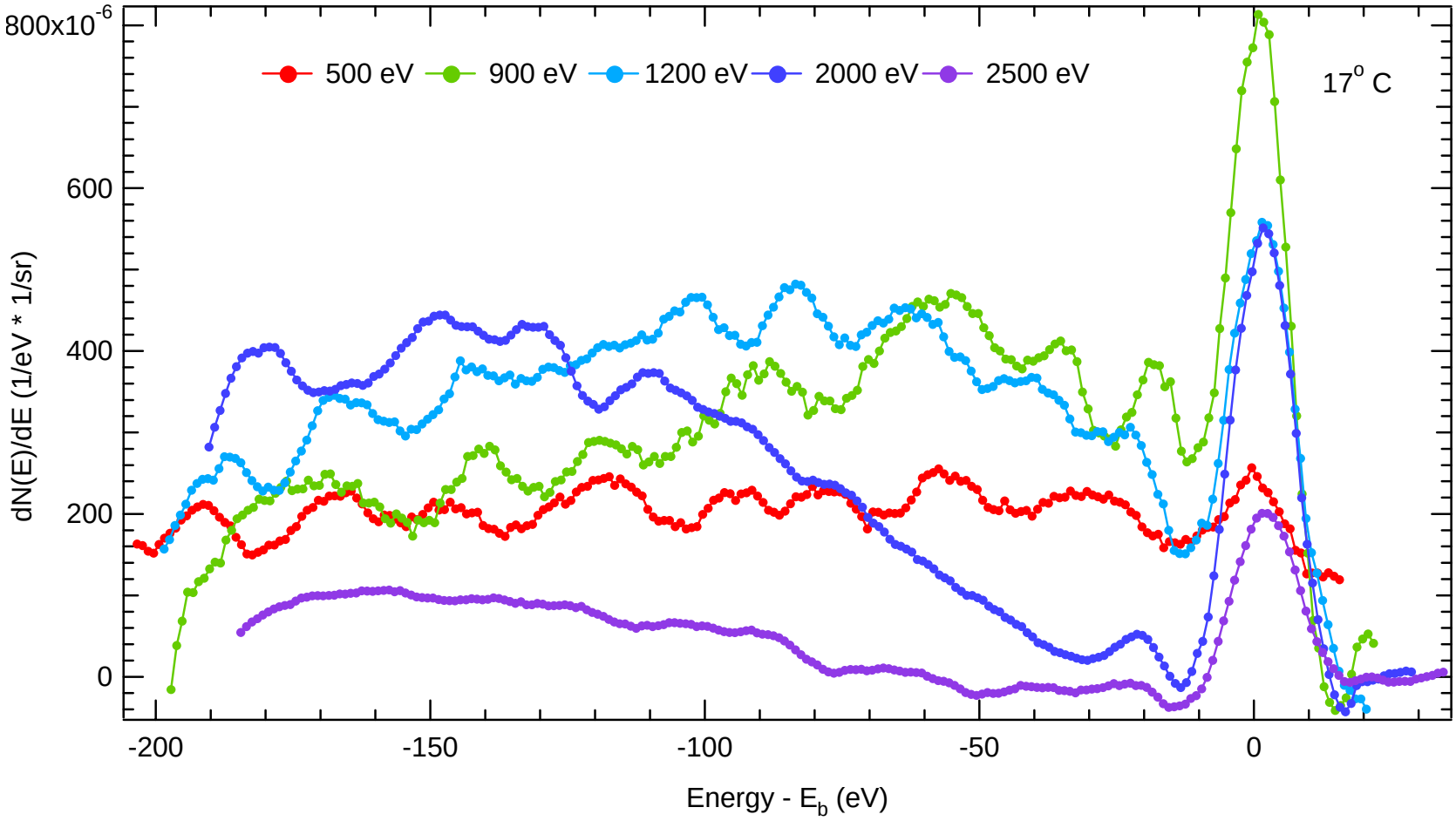

Figure E-55 Angular Resolved BSE and Elastic Peaks measured using the 1 eV resolution at 17^{o} Clockwise emission and selected beam energies.

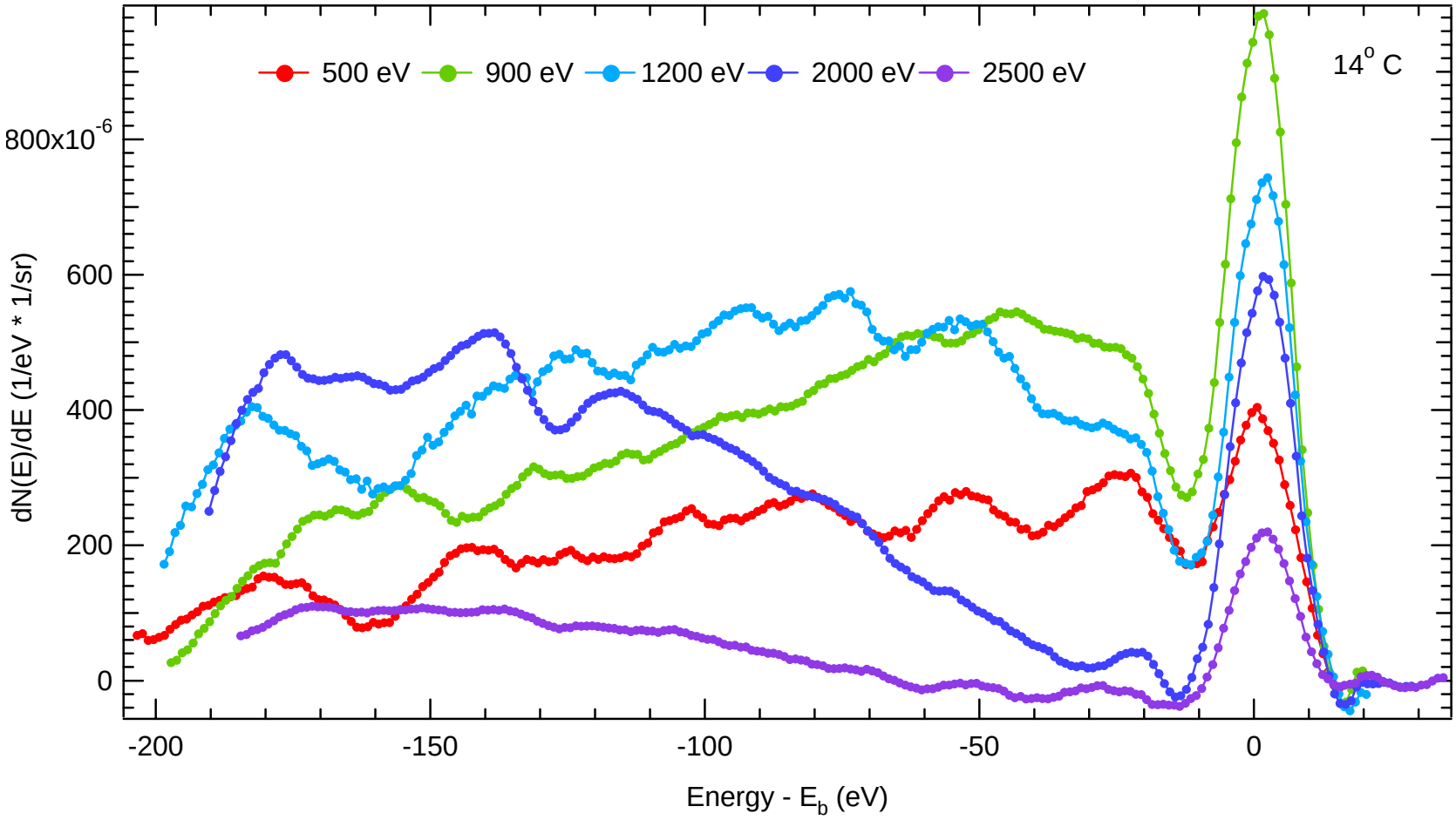

Figure E-56 Angular Resolved BSE and Elastic Peaks measured using the 1 eV resolution at 14° Clockwise emission and selected beam energies.

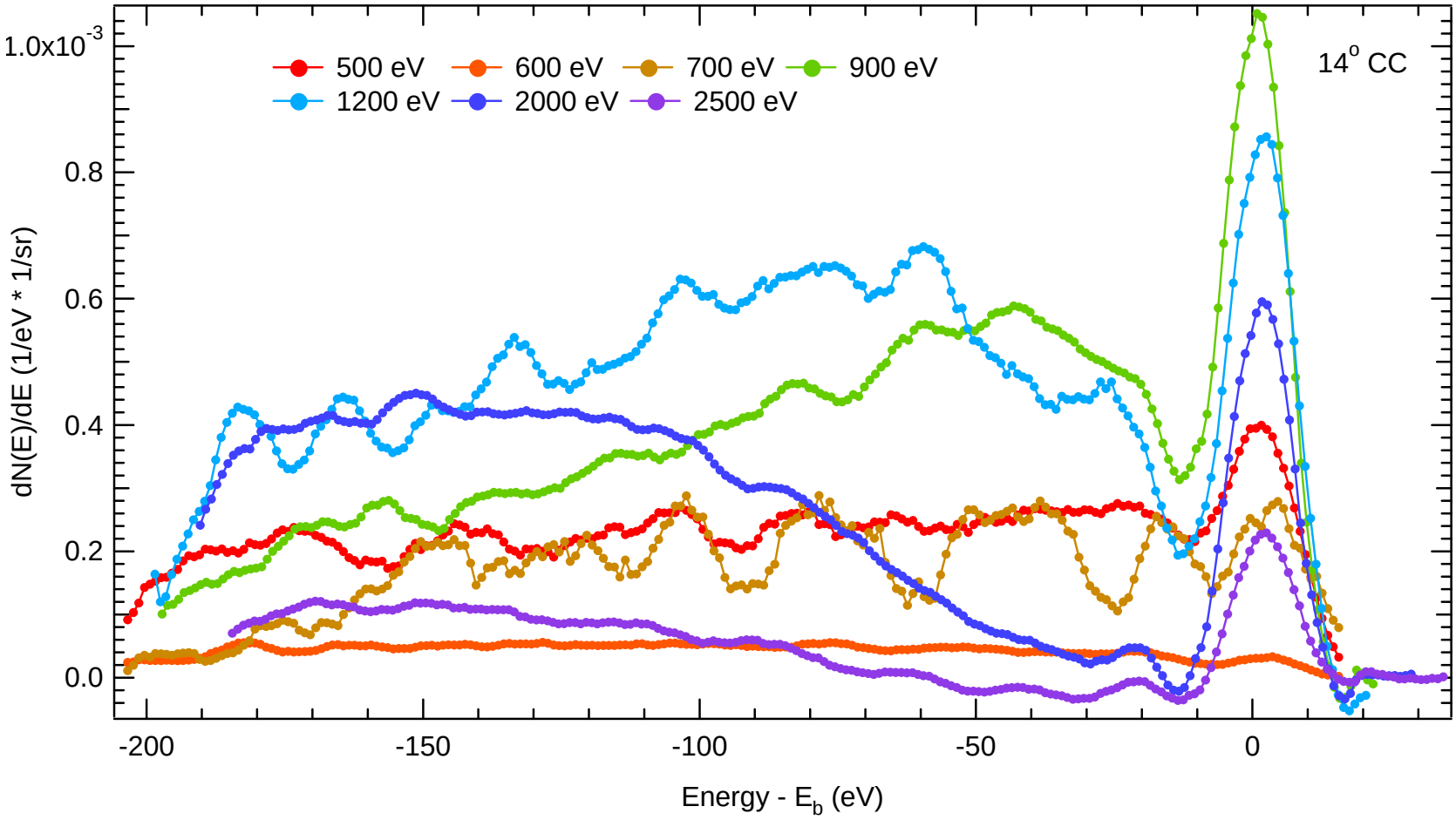

Figure E-57 Angular Resolved BSE and Elastic Peaks measured using the 1 eV resolution at 14° Counter-Clockwise emission and selected beam energies.

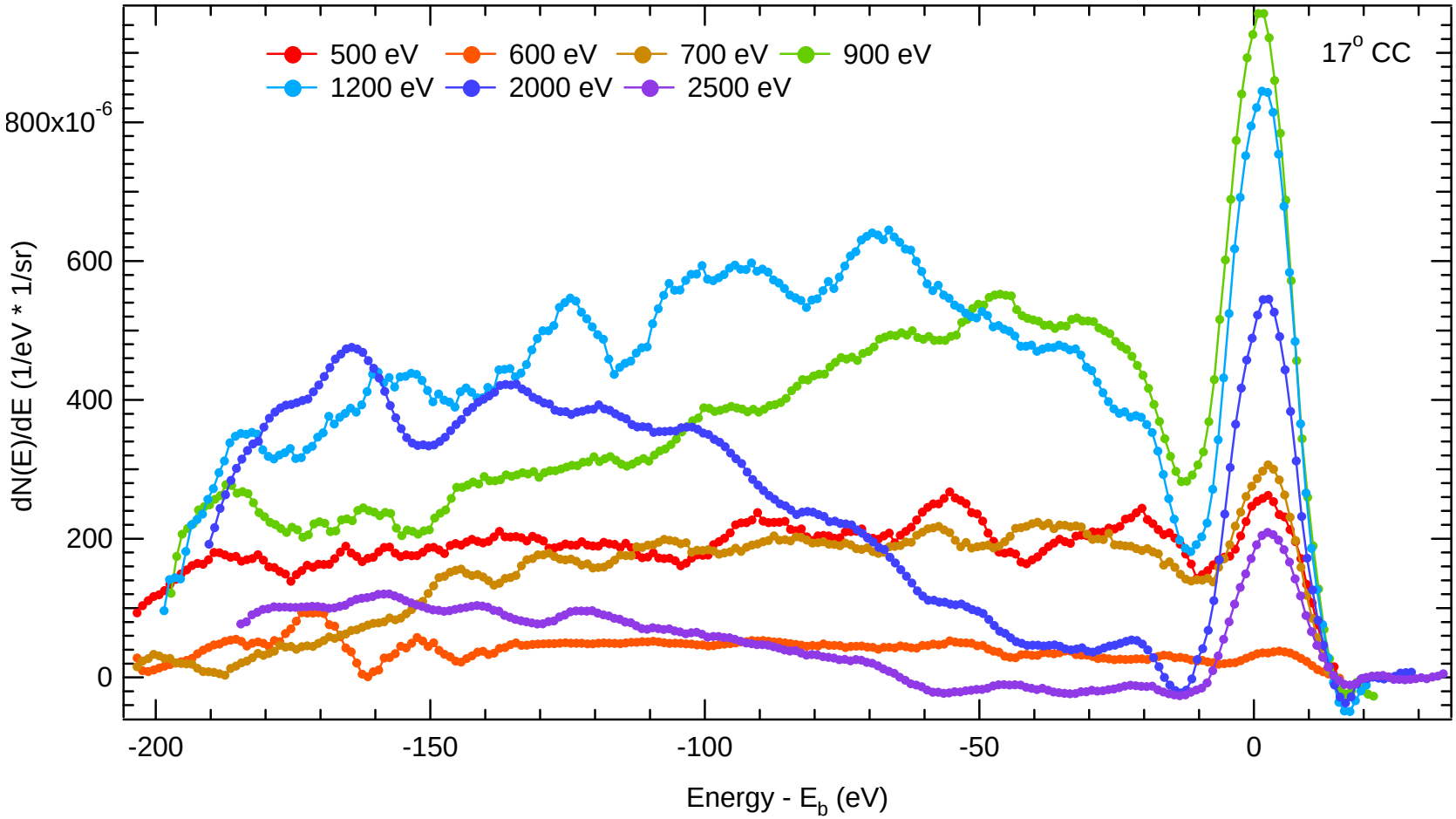

Figure E-58 Angular Resolved BSE and Elastic Peaks measured using the 1 eV resolution at 17° Counter-Clockwise emission and selected beam energies.

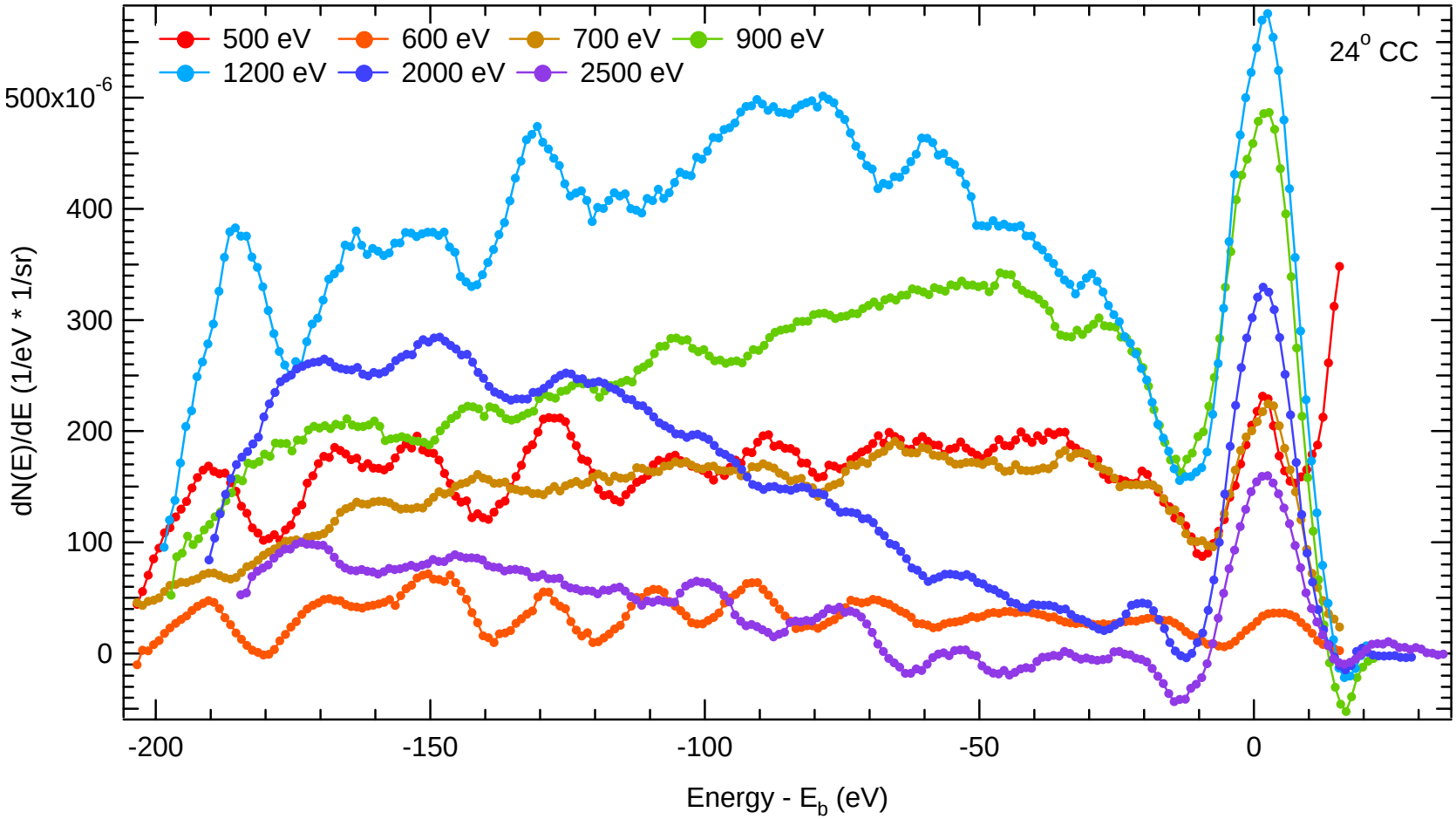

Figure E-59 Angular Resolved BSE and Elastic Peaks measured using the 1 eV resolution at 24° Counter-Clockwise emission and selected beam energies.

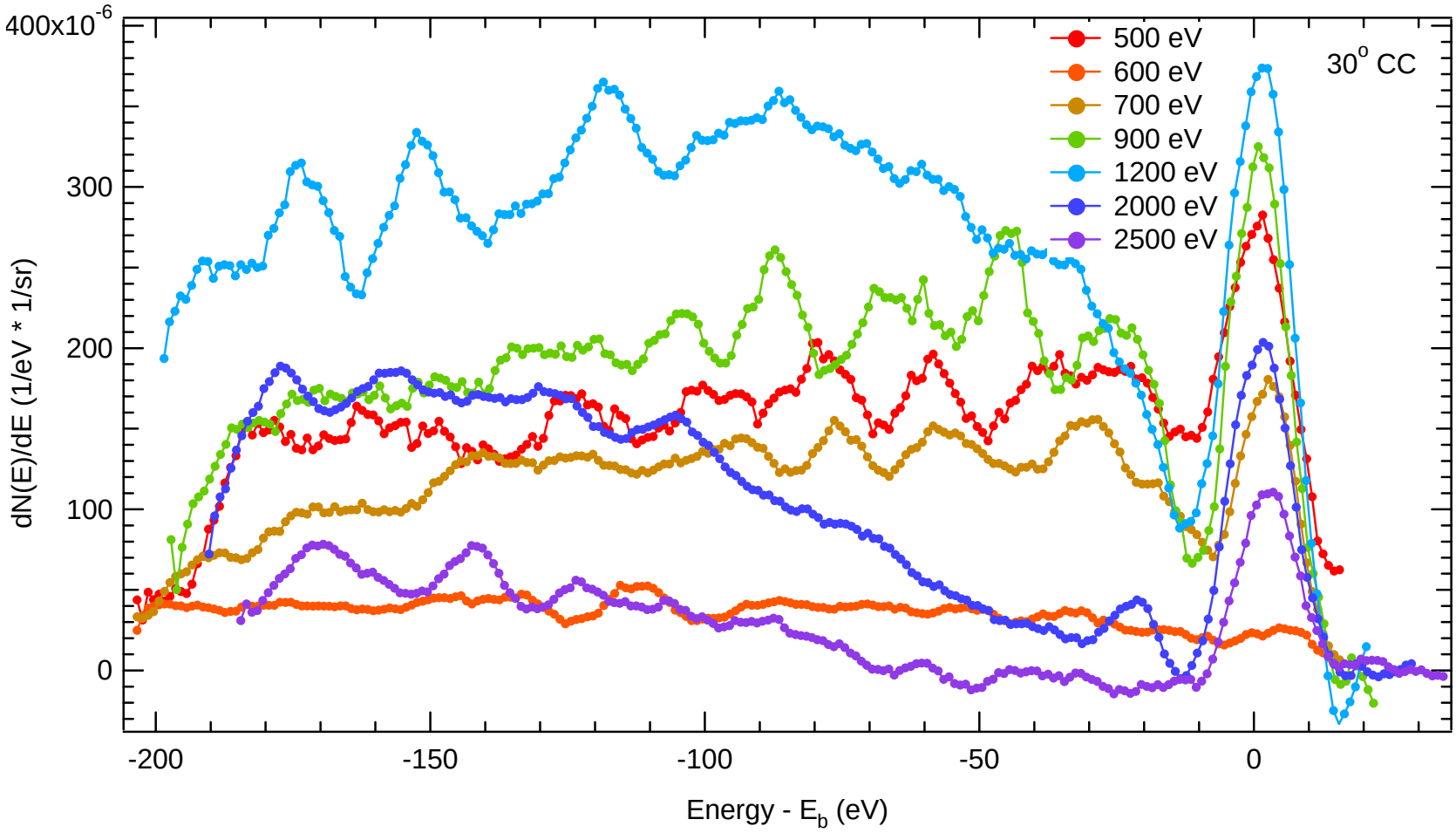

Figure E-60 Angular Resolved BSE and Elastic Peaks measured using the 1 eV resolution at 30^{o} Counter-Clockwise emission and selected beam energies.

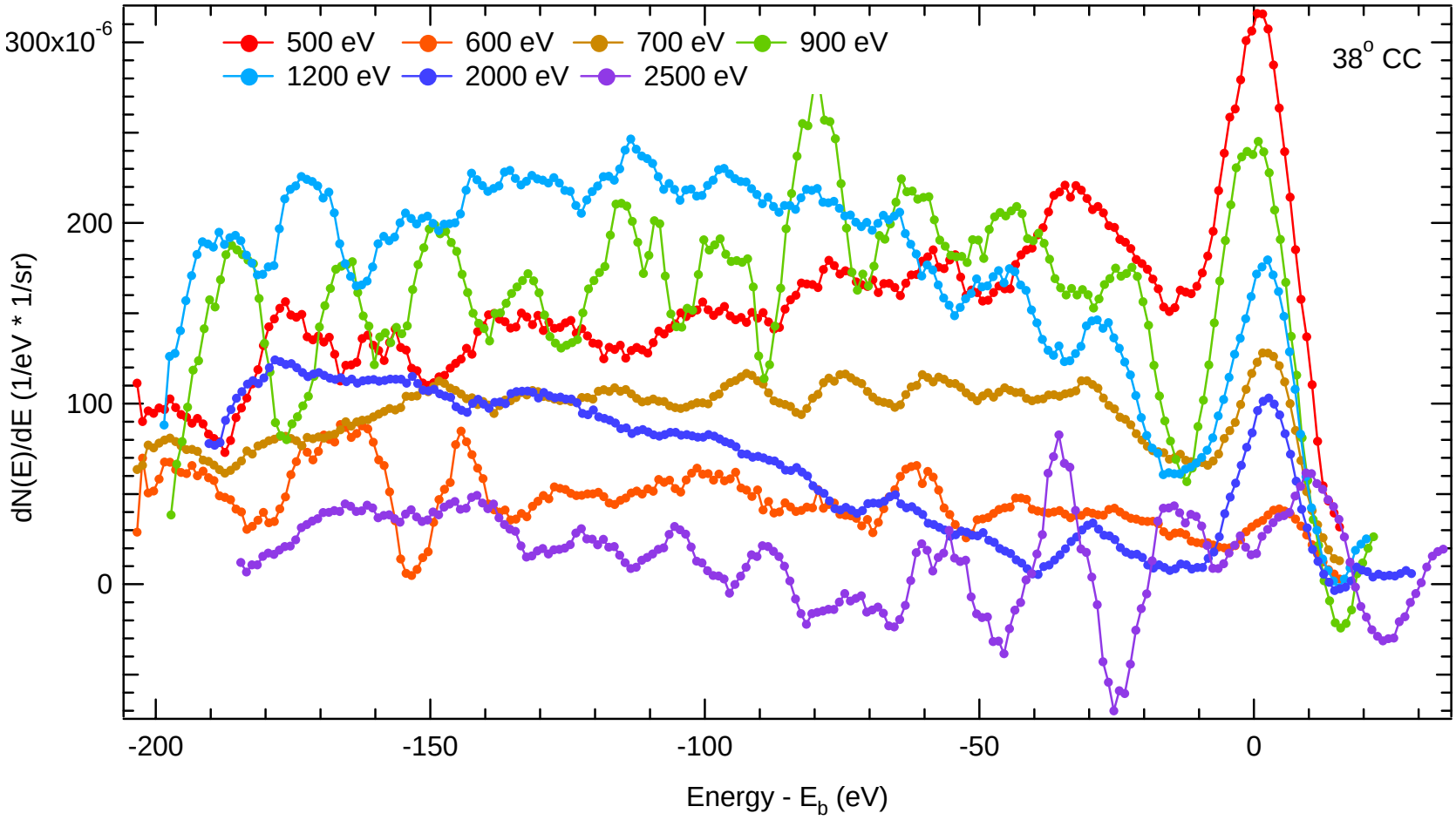

Figure E-61 Angular Resolved BSE and Elastic Peaks measured using the 1 eV resolution at 38° Counter-Clockwise emission and selected beam energies.

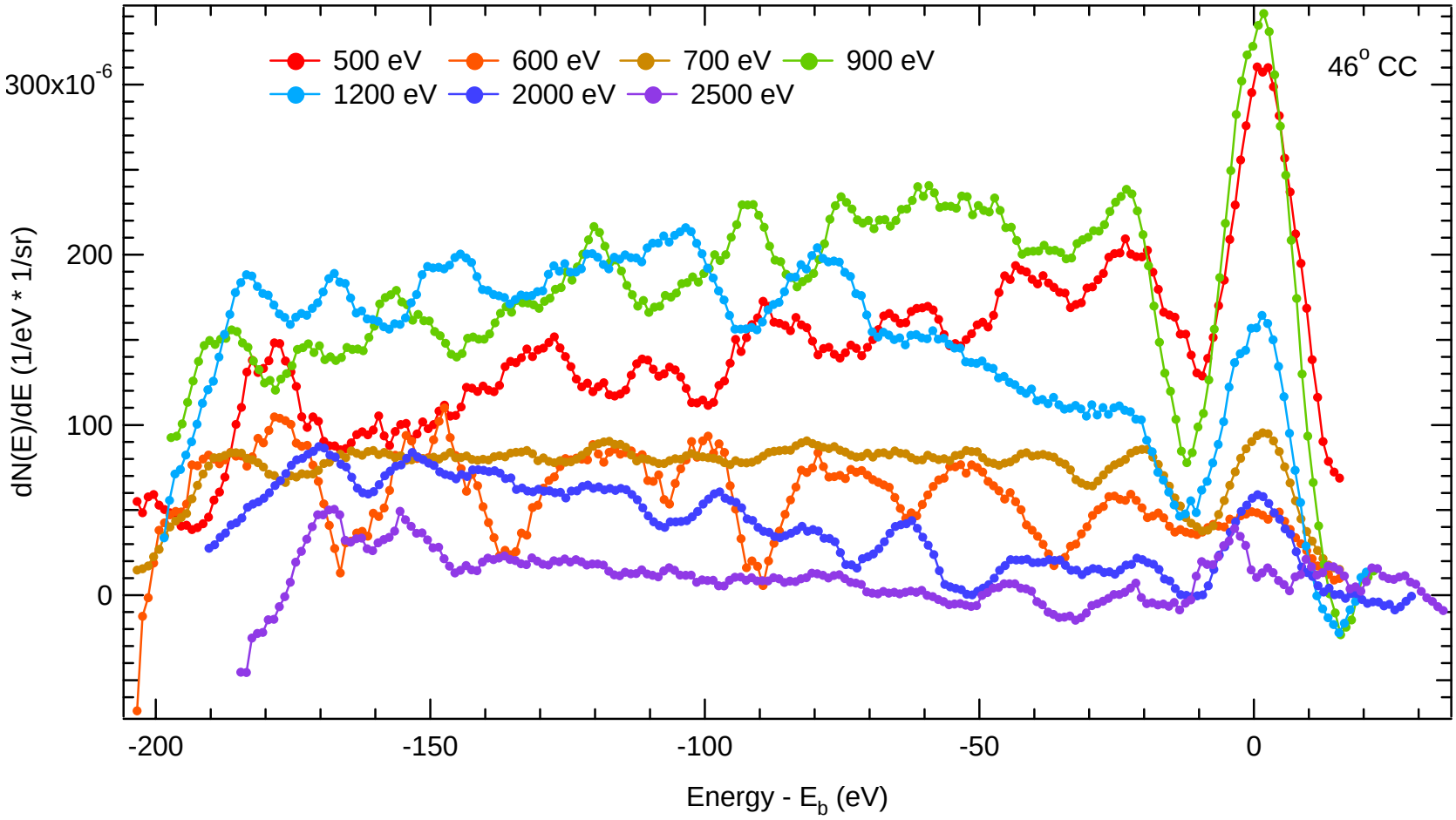

Figure E-62 Angular Resolved BSE and Elastic Peaks measured using the 1 eV resolution at 46° Counter-Clockwise emission and selected beam energies.

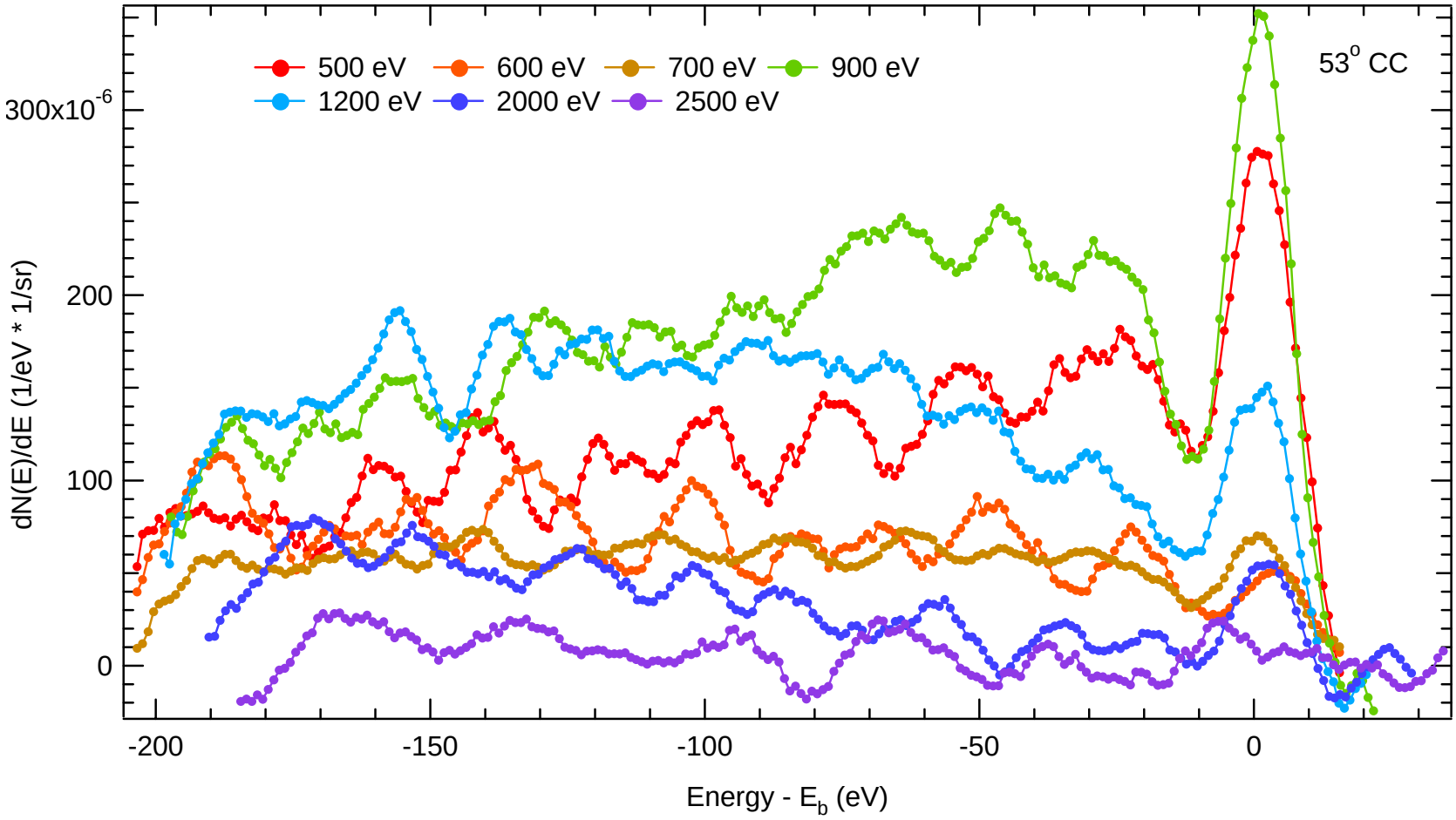

Figure E-63 Angular Resolved BSE and Elastic Peaks measured using the 1 eV resolution at 53° Counter-Clockwise emission and selected beam energies.

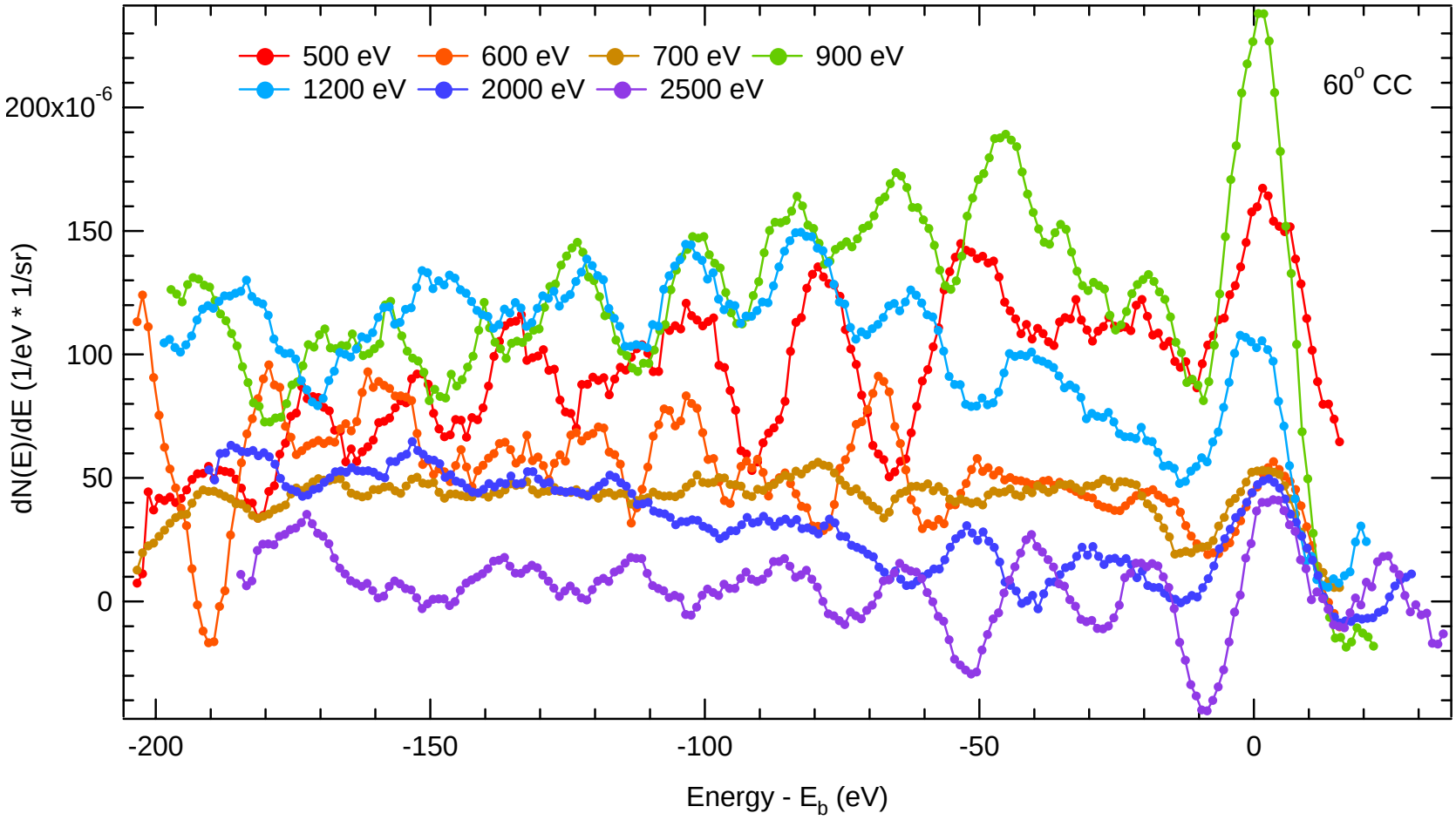

Figure E-64 Angular Resolved BSE and Elastic Peaks measured using the 1 eV resolution at 60° Counter-Clockwise emission and selected beam energies.

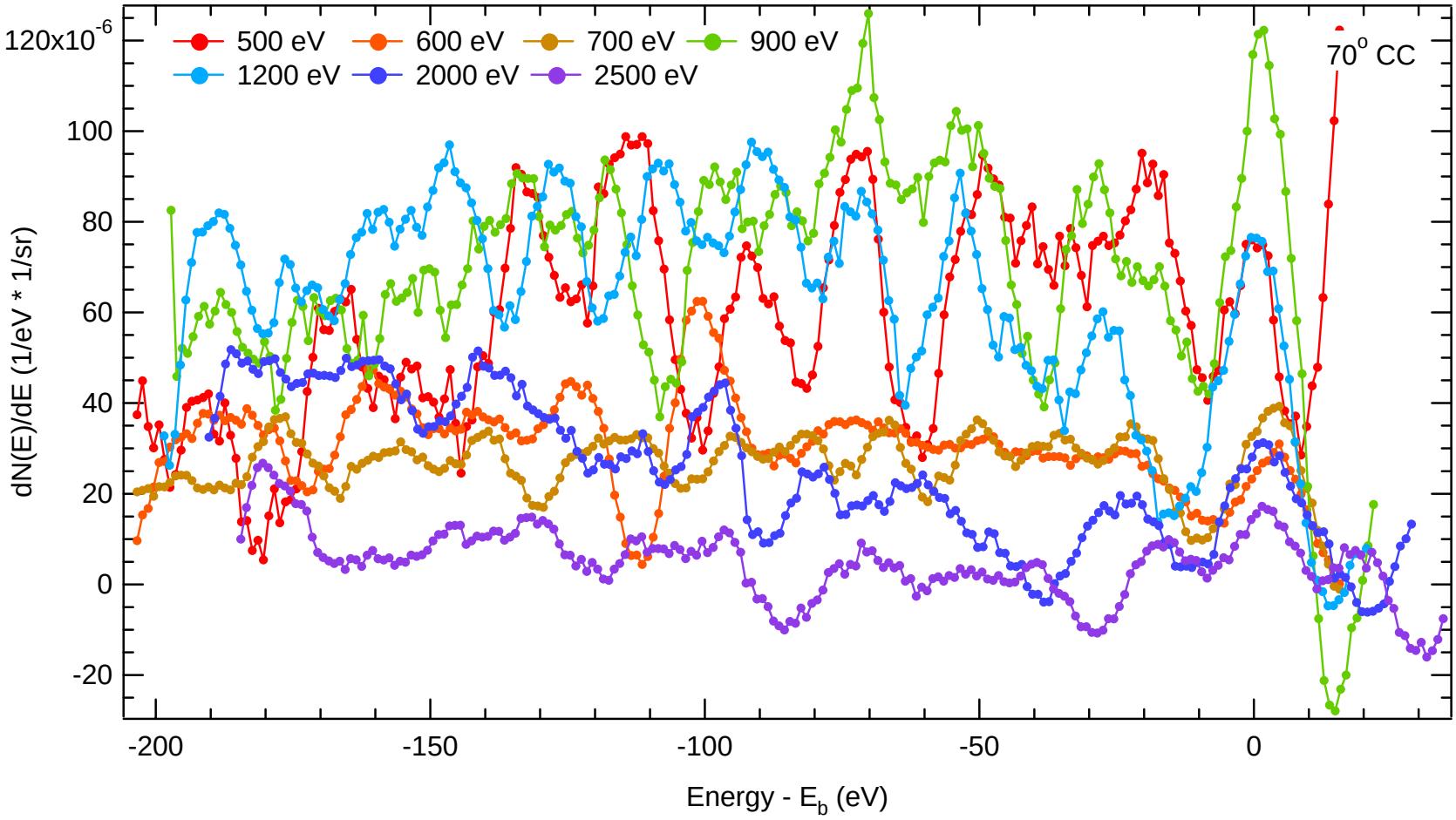

Figure E-65 Angular Resolved BSE and Elastic Peaks measured using the 1 eV resolution at 70° Counter-Clockwise emission and selected beam energies.

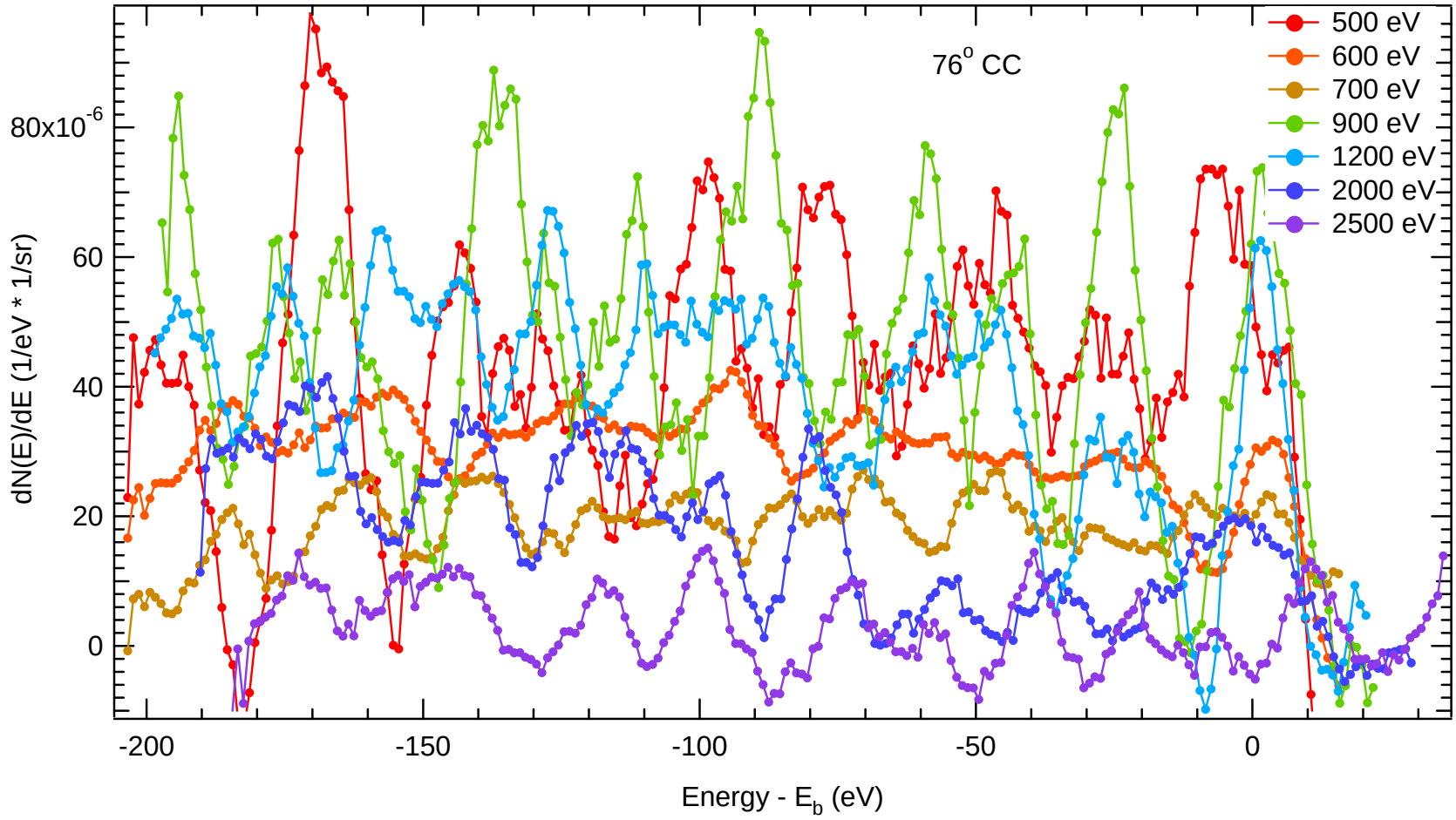

Figure E-66 Angular Resolved BSE and Elastic Peaks measured using the 1 eV resolution at 76° Counter-Clockwise emission and selected beam energies.

E-5(G) Low Energy 1 eV resolution Spectra (E_b resolved)

The low energy E_b—resolved spectra are shown in Fig. E-67 through Fig. E-73. The step size of 1 eV is used to bias the RD for the 1 eV resolution zoom. The incident beam energies used are E_b = 500 eV, 700 eV, 900 eV, 1200 eV, 2000 eV, and 2500 eV. The energy range spans ~220 eV, and incident beam energy, E_b, spectra are shown together. The importance of showing these fine energy resolution spectra is two fold. First is to extract statistics about the SE peak location and intensity for comparison to the 0.1 eV resolution SE peak location and yield intensity. Second is to show the shape of these spectra without smoothing such as in the 10 eV resolution spectra.

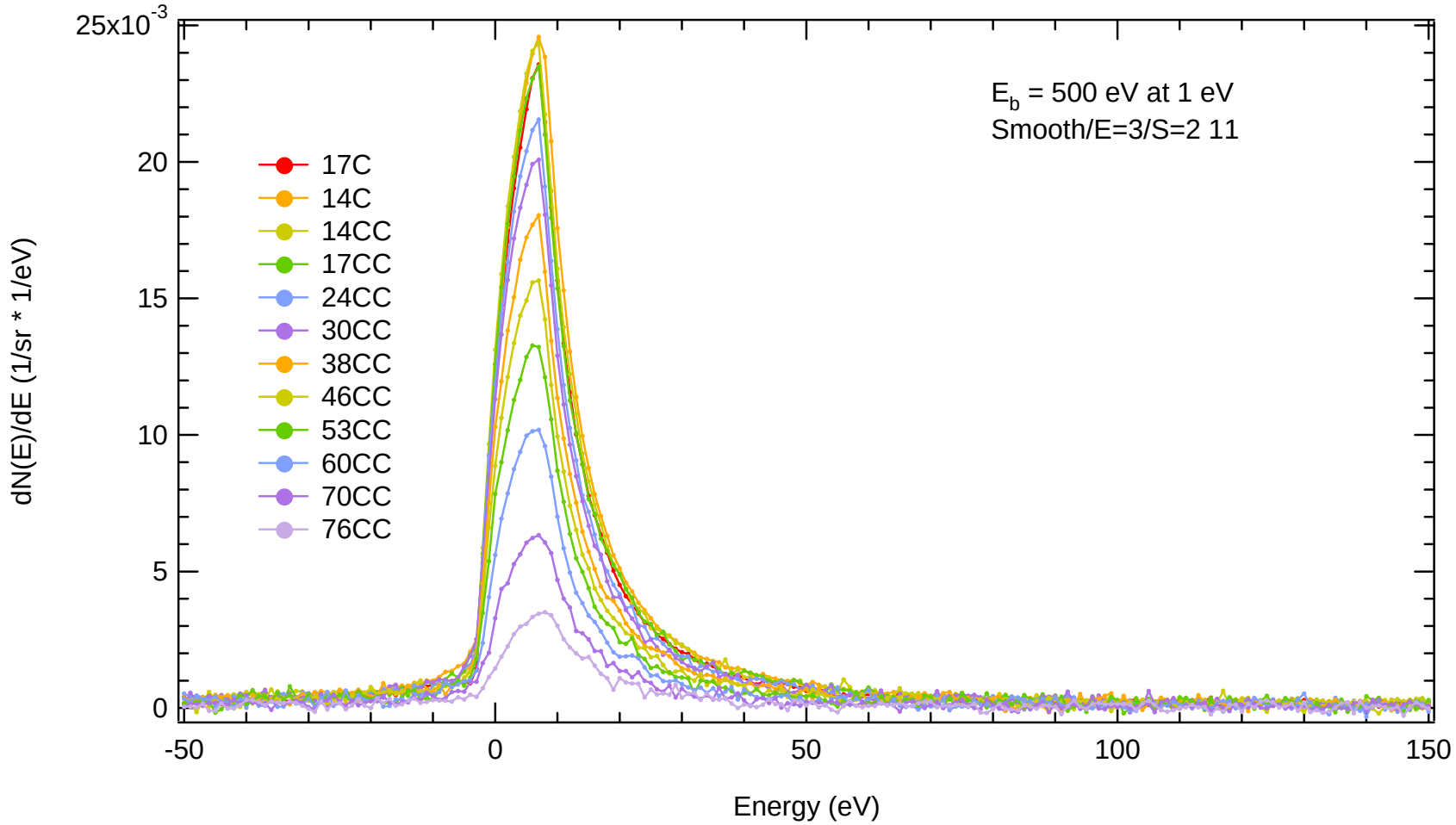

Figure E-67 SE peak resolved in 1 eV at 500 eV incident beam energy for selected emission angles.

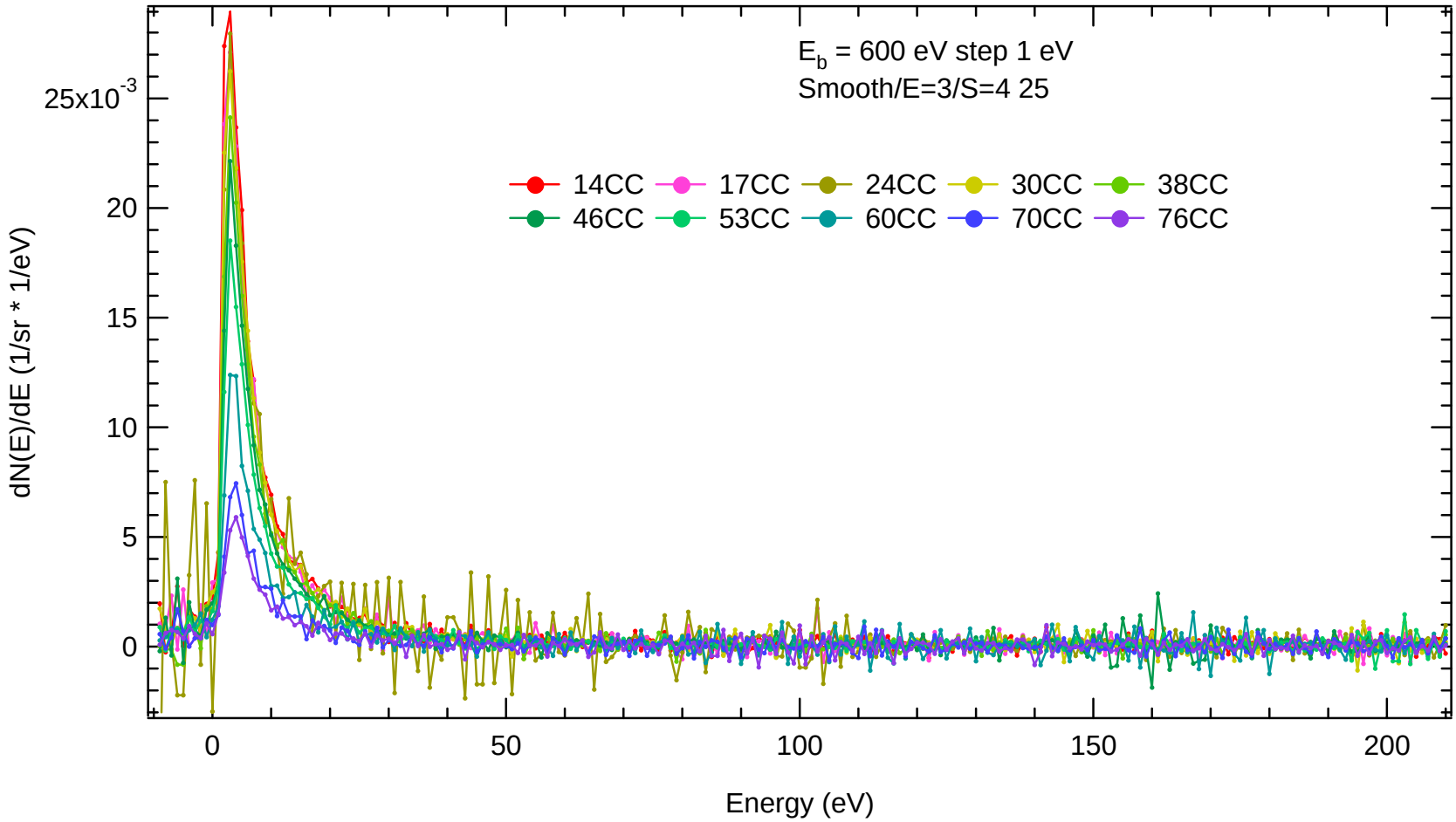

Figure E-68 SE peak resolved in 1 eV at 600 eV incident beam energy for selected emission angles.

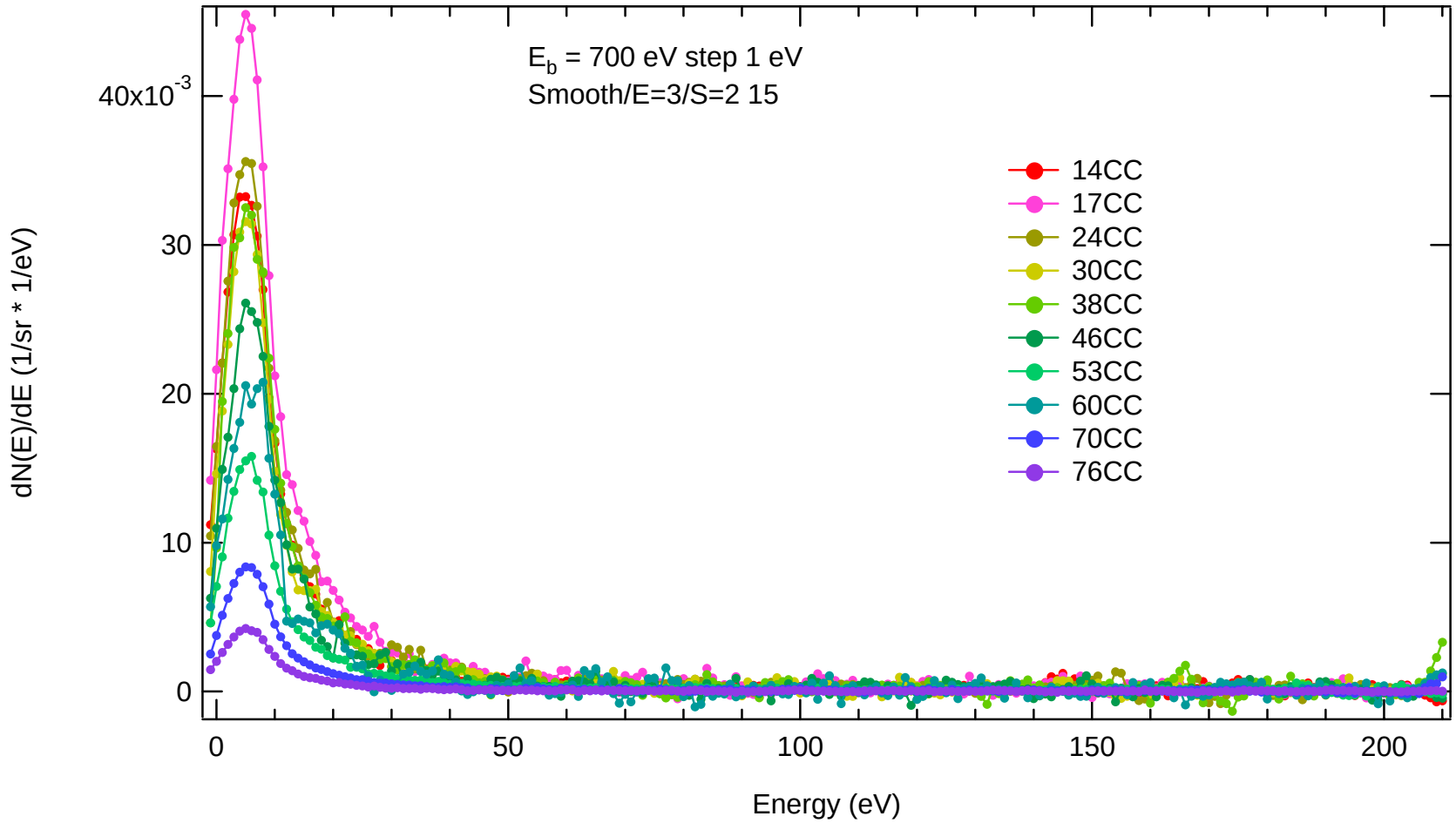

Figure E-69 SE peak resolved in 1 eV at 700 eV incident beam energy for selected emission angles.

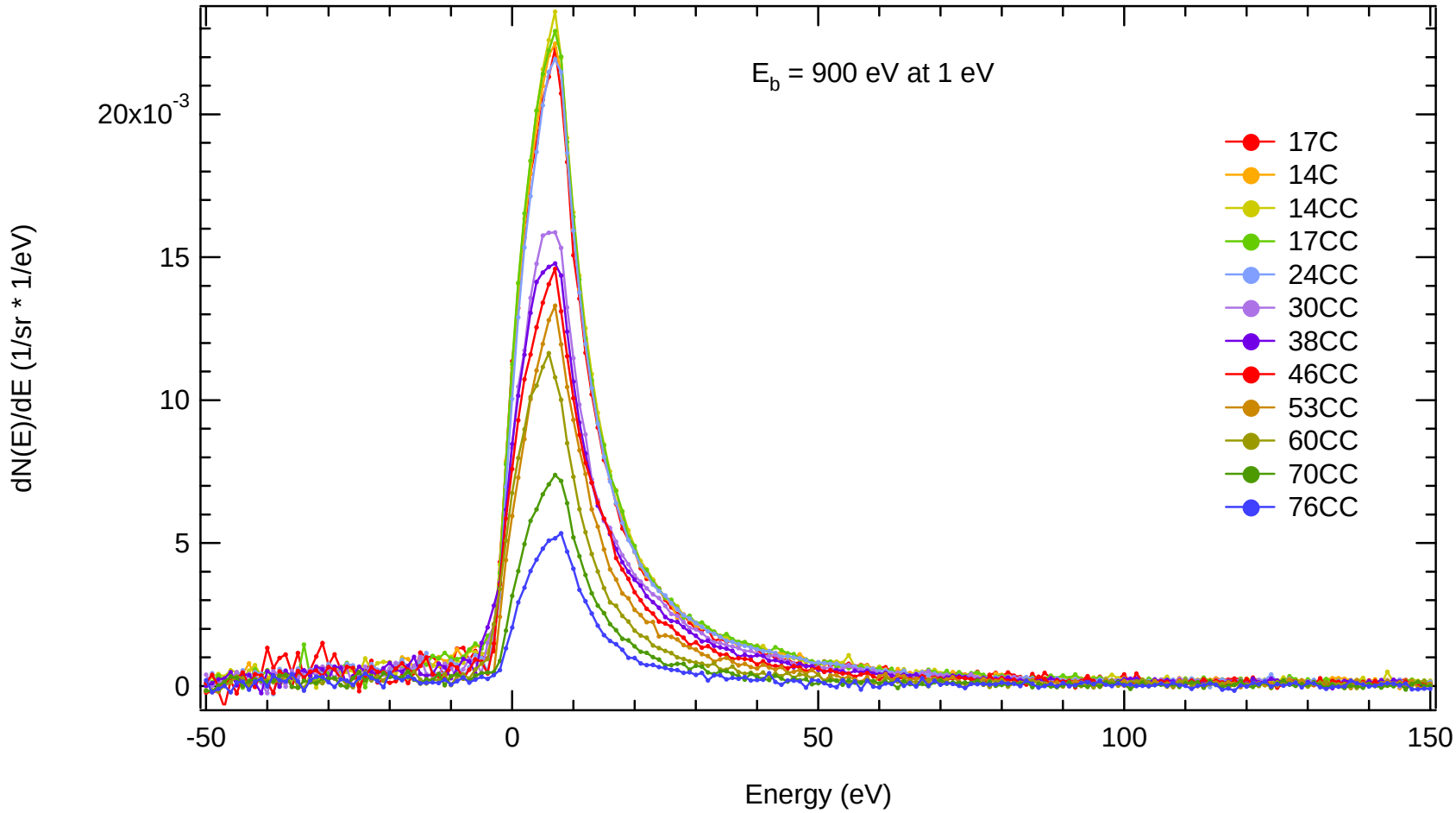

Figure E-70 SE peak resolved in 1 eV at 900 eV incident beam energy for selected emission angles.

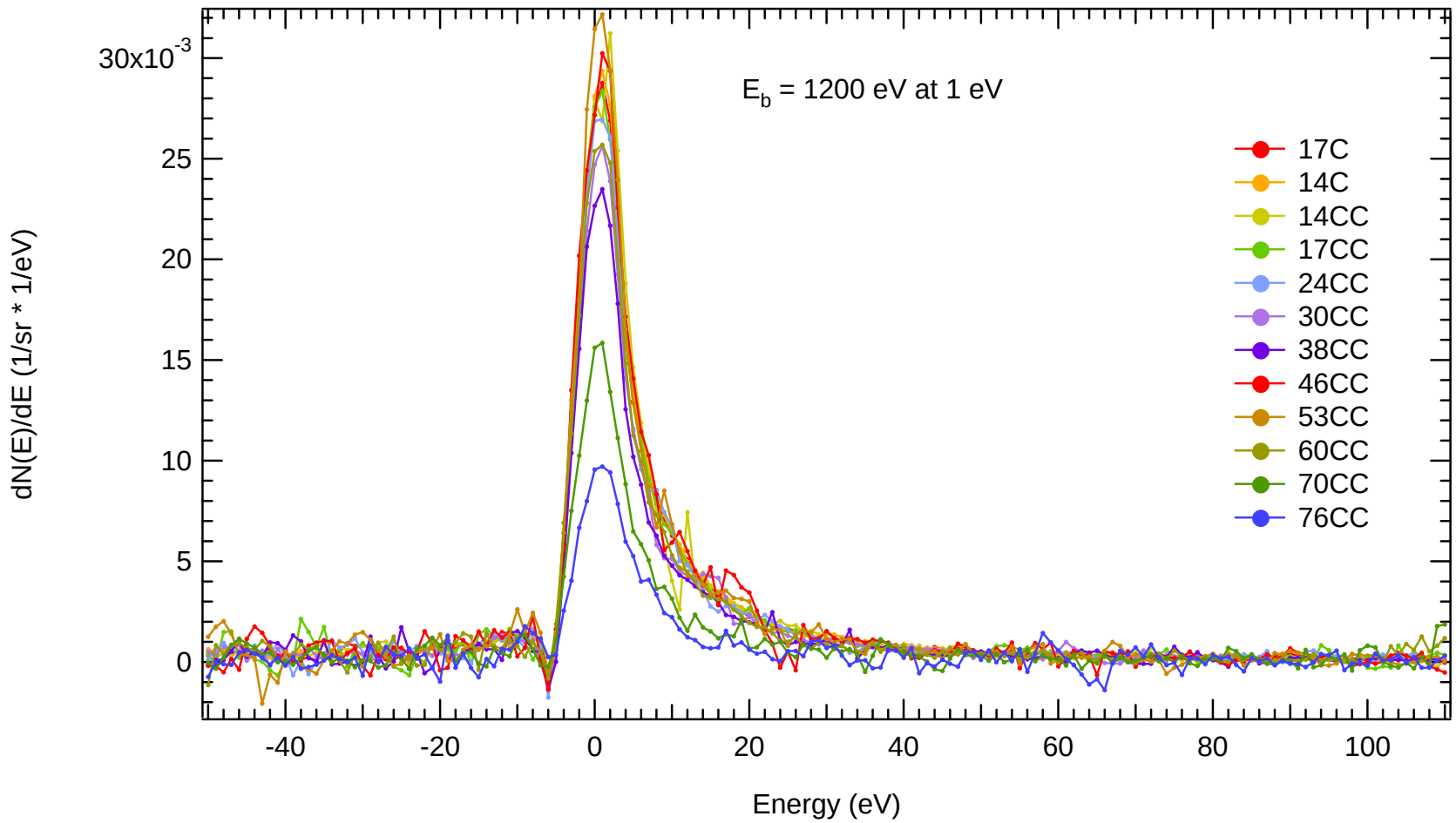

Figure E-71 SE peak resolved in 1 eV at 1200 eV incident beam energy for selected emission angles.

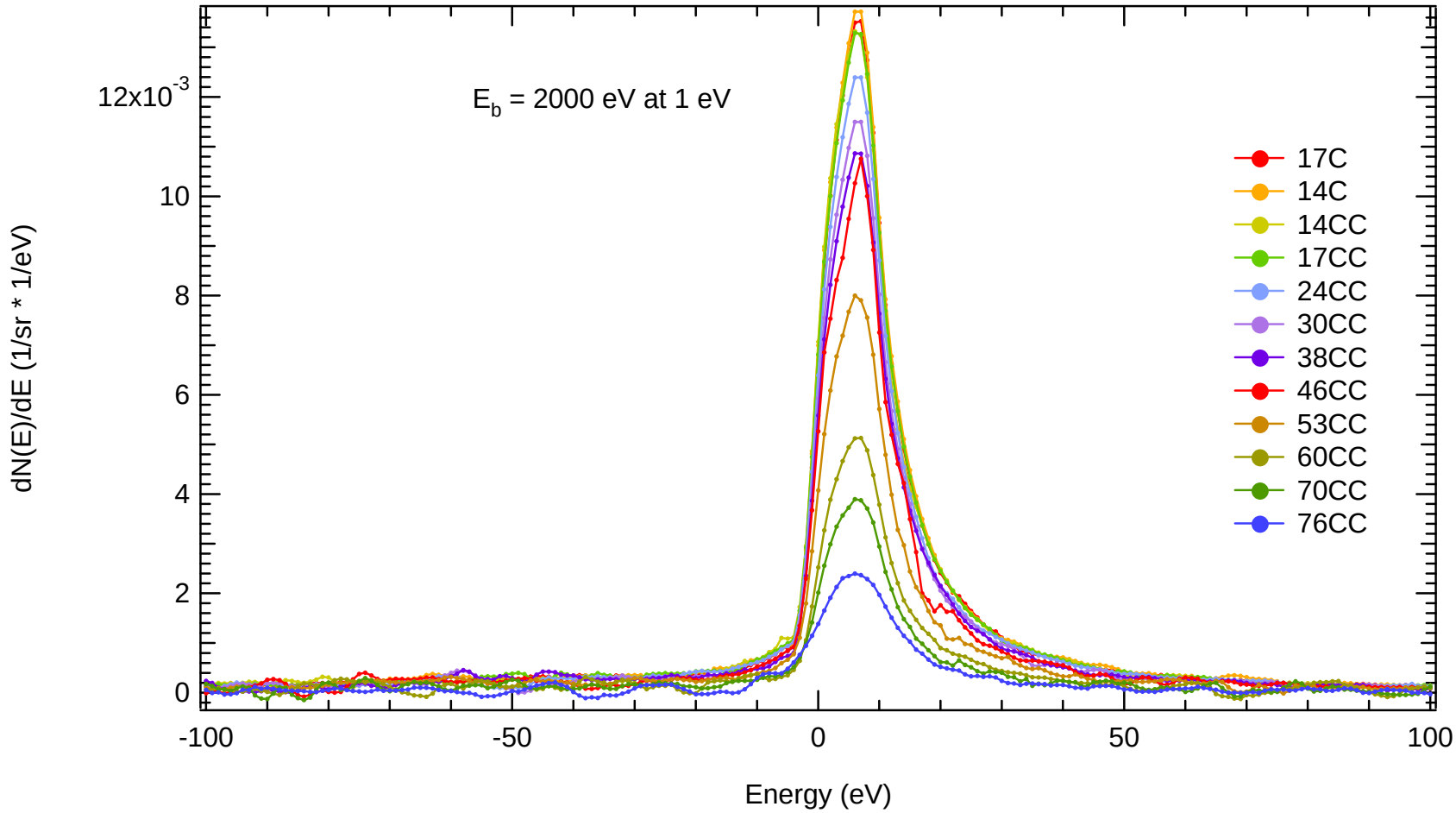

Figure E-72 SE peak resolved in 1 eV at 2000 eV incident beam energy for selected emission angles.

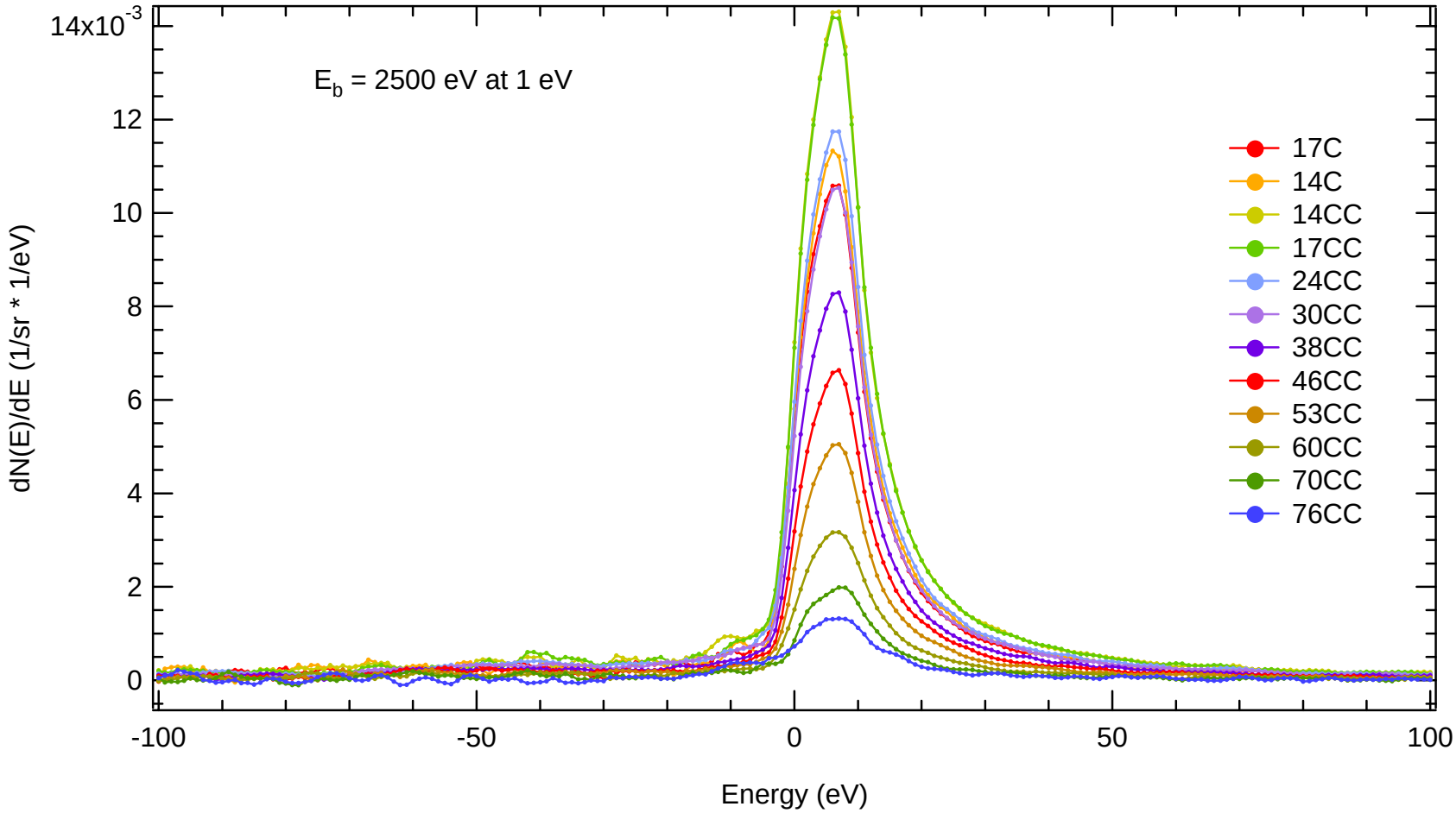

Figure E-73 SE peak resolved in 1 eV at 2500 eV incident beam energy for selected emission angles.

E-5(H) Low Energy 1 eV resolution Spectra (Angle Resolved)

The low energy AR angular spectra are shown in Fig. E-74 through Fig. E-85.

Notice that all of these spectra have peak energies between 3 and 4 eV. This is because these spectra have been calculated using the sliding derivative technique, which, in affect, smoothes the spectra by 10 data points. The sharpness of the SE peak, the intensity of the SE peak, and the energy location of the SE peak are all sacrificed for an optimum calculation of the SE yield. For studies which rely on these peak features, it is suggested to use the higher resolution energy ranges (0.1 eV or 0.01 eV).

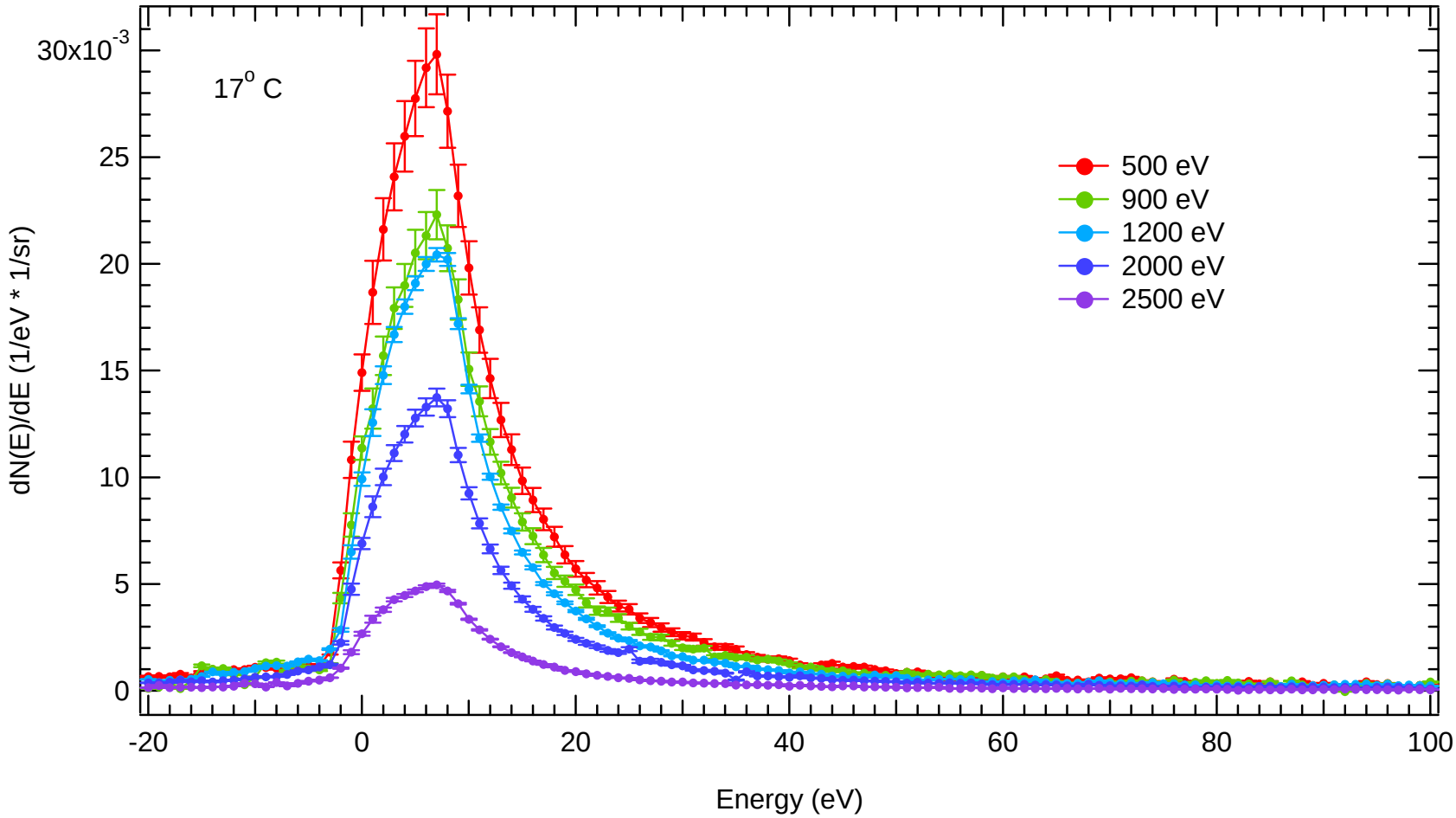

Figure E-74 SE peak resolved in 1 eV at 17 ^{o} Clockwise emission for selected incident beam energies.

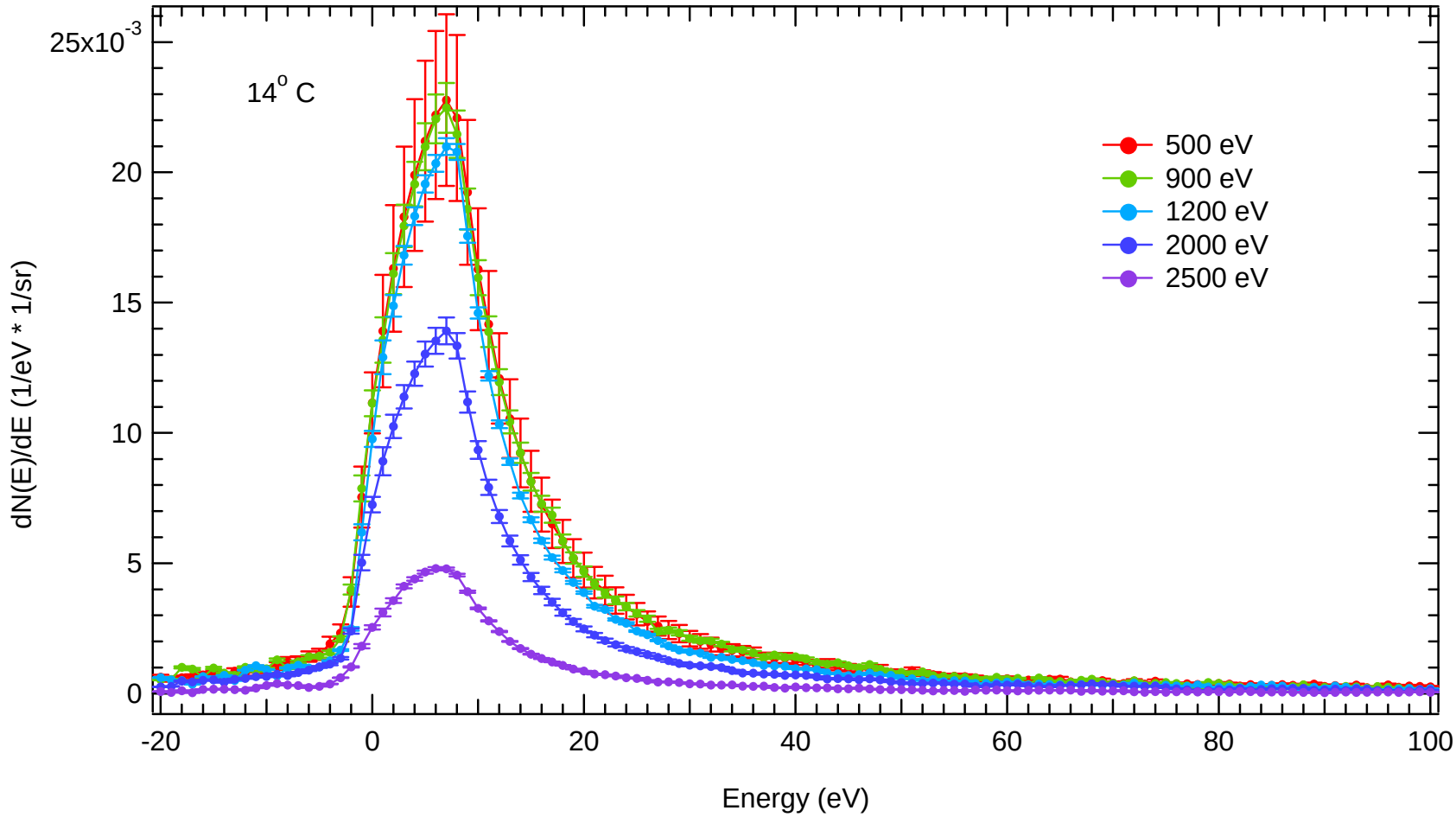

Figure E-75 SE peak resolved in 1 eV at 14 ^{o} Clockwise emission for selected incident beam energies.

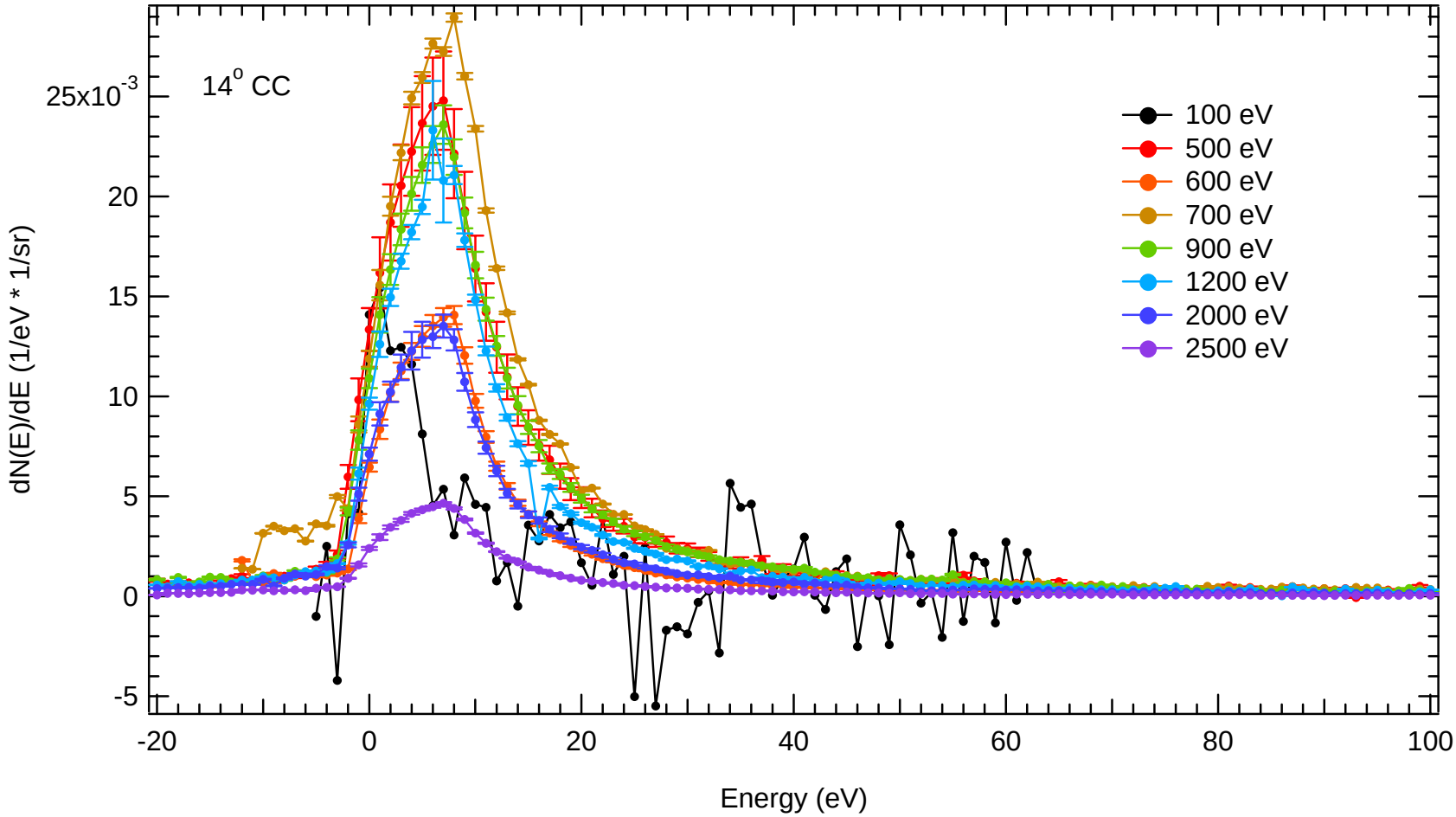

Figure E-76 SE peak resolved in 1 eV at 14 ° Counter-Clockwise emission for selected incident beam energies.

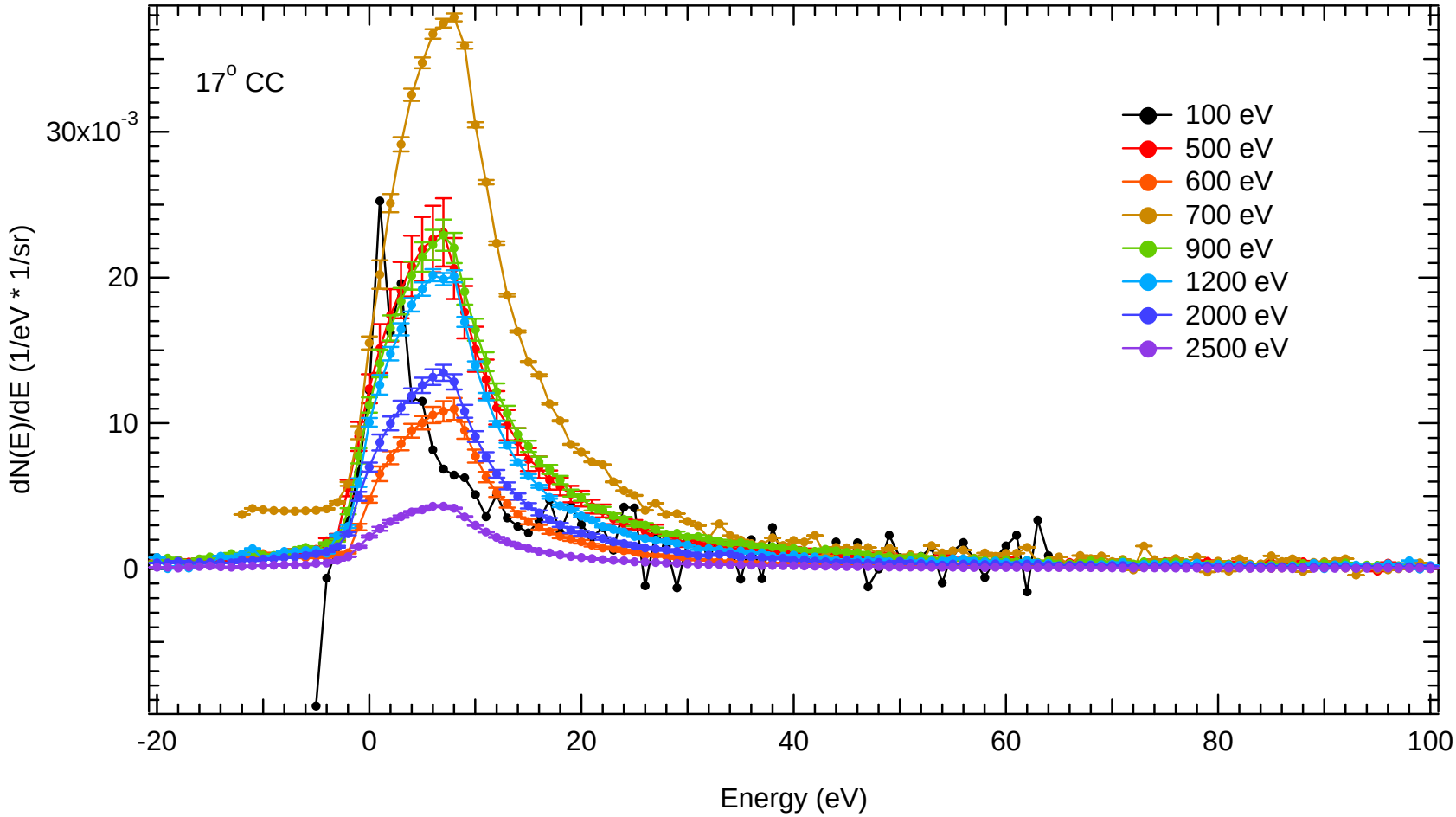

Figure E-77 SE peak resolved in 1 eV at 17 ° Counter-Clockwise emission for selected incident beam energies.

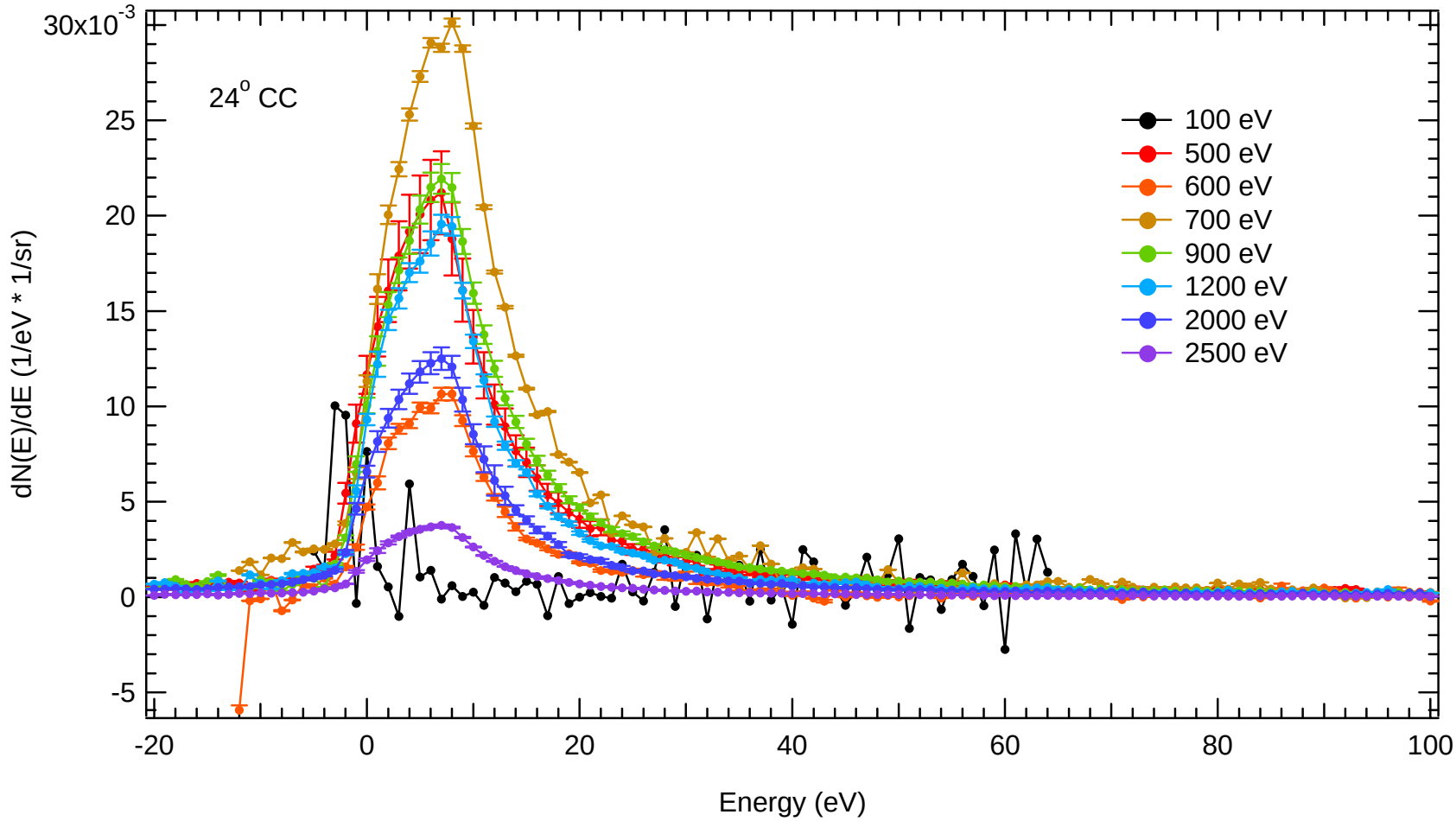

Figure E-78 SE peak resolved in 1 eV at 24 ^{o} Counter-Clockwise emission for selected incident beam energies.

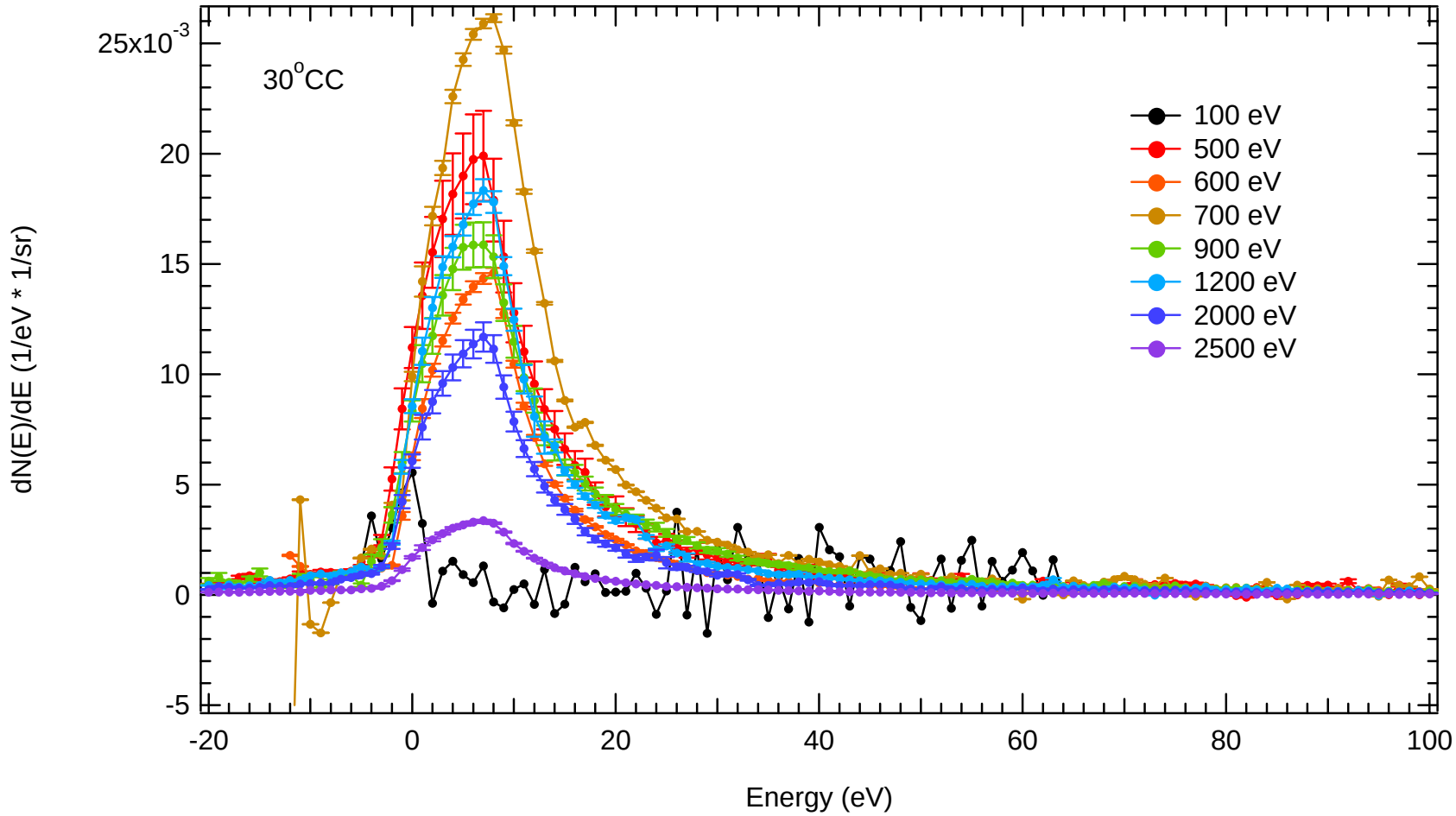

Figure E-79 SE peak resolved in 1 eV at 30 ^{o} Counter-Clockwise emission for selected incident beam energies.

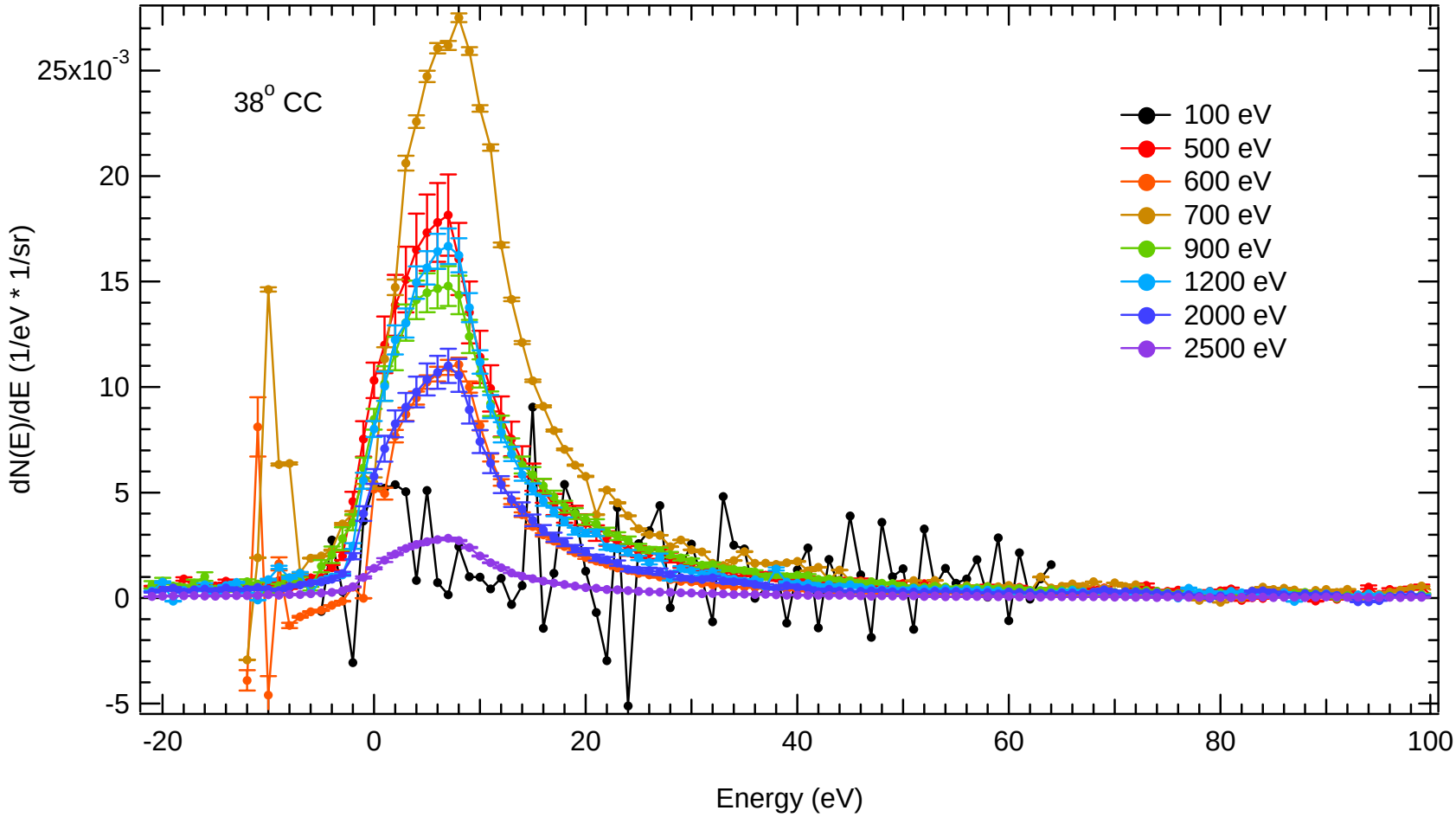

Figure E-80 SE peak resolved in 1 eV at 38 ^{o} Counter-Clockwise emission for selected incident beam energies.

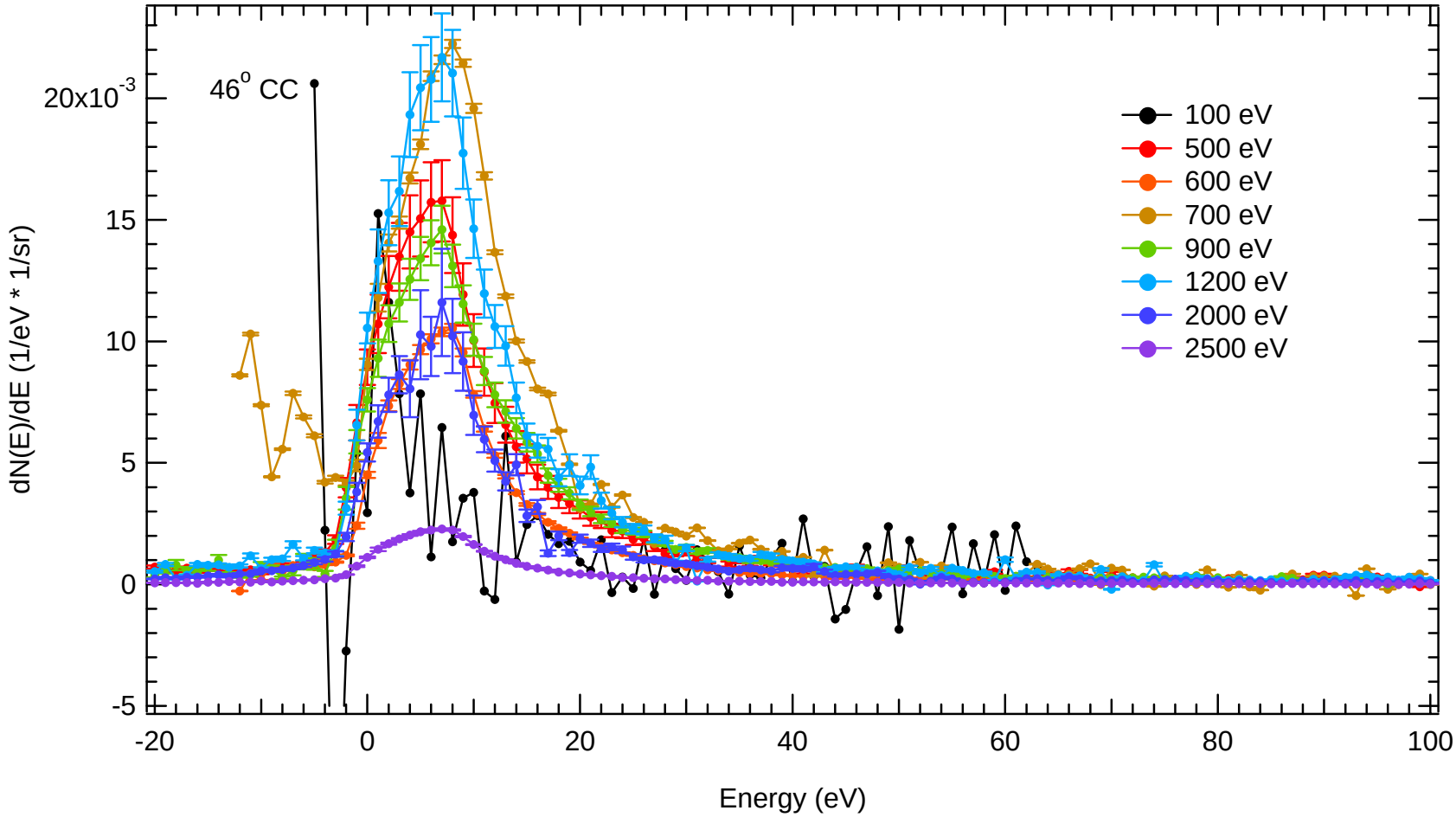

Figure E-81 SE peak resolved in 1 eV at 46 ° Counter-Clockwise emission for selected incident beam energies.

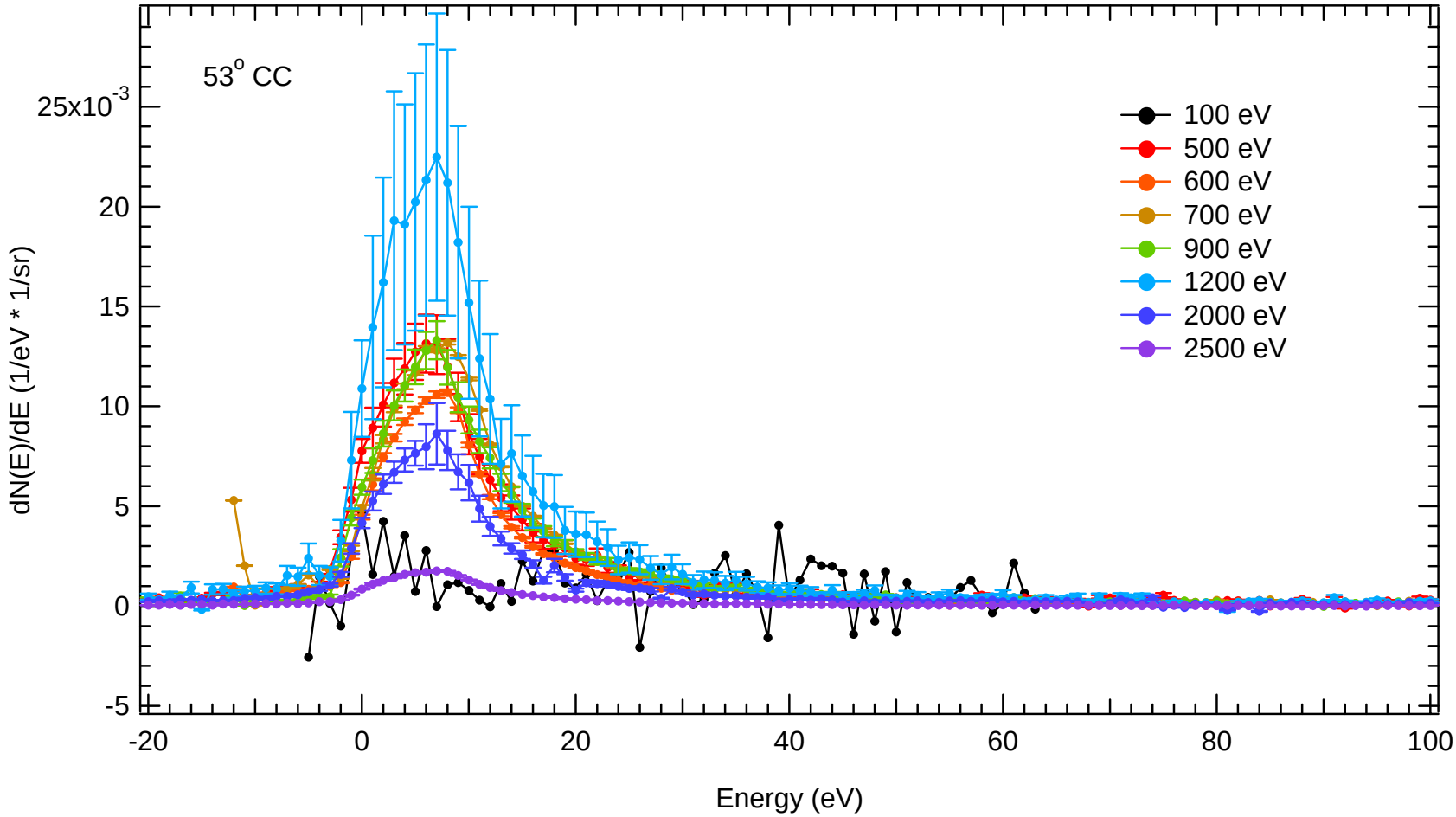

Figure E-82 SE peak resolved in 1 eV at 53 ° Counter-Clockwise emission for selected incident beam energies.

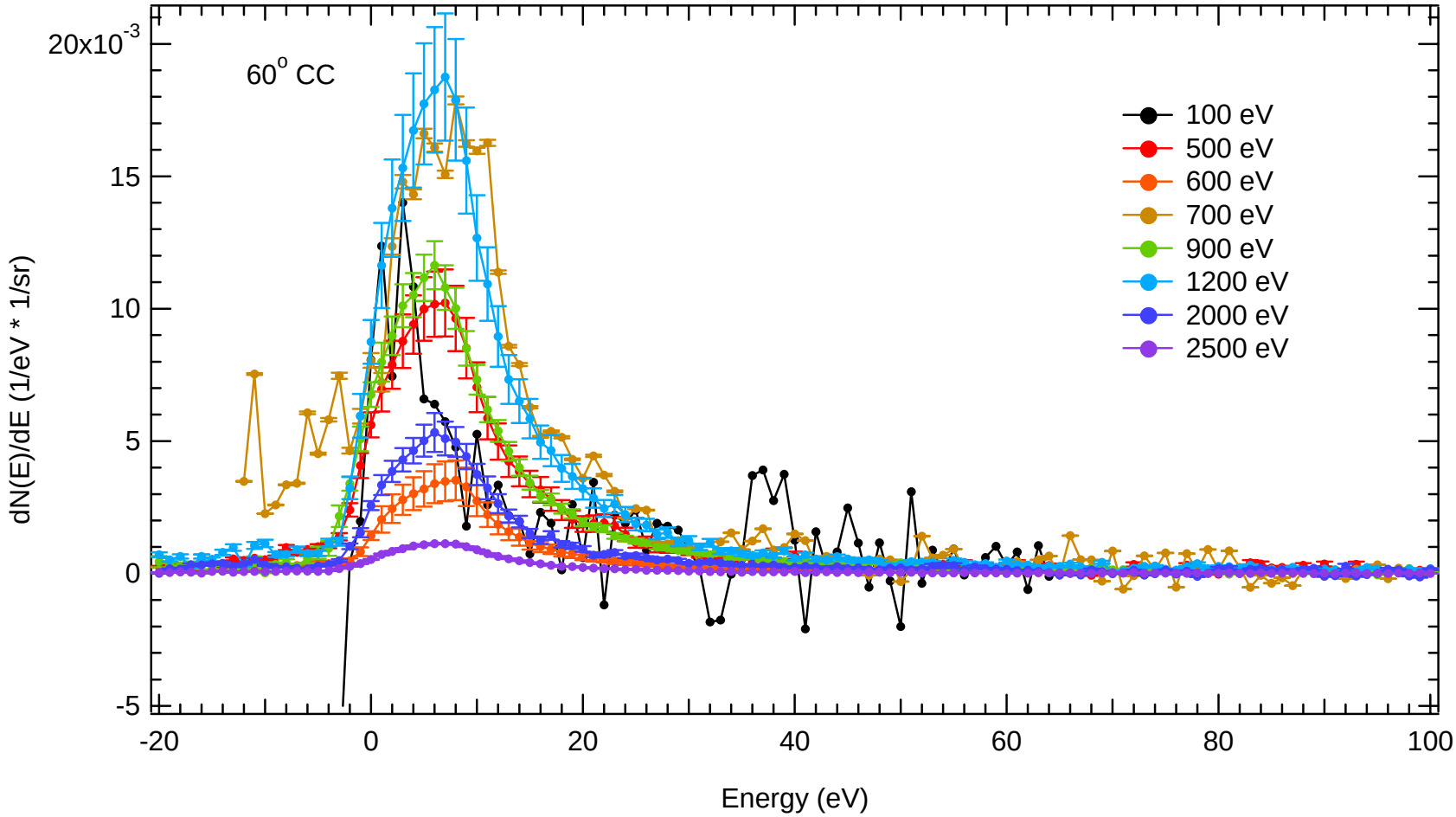

Figure E-83 SE peak resolved in 1 eV at 60 ° Counter-Clockwise emission for selected incident beam energies.

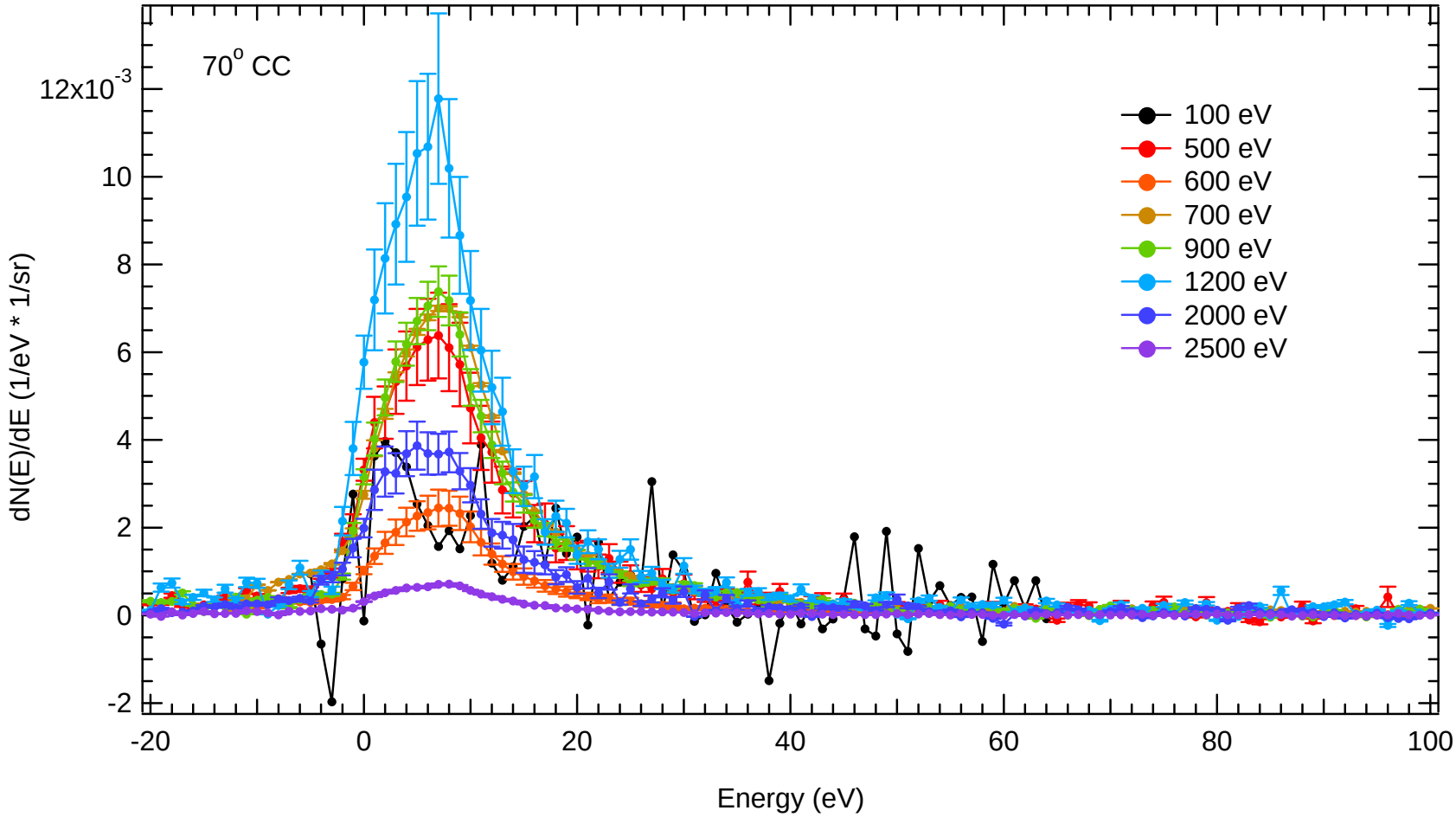

Figure E-84 SE peak resolved in 1 eV at 70 ° Counter-Clockwise emission for selected incident beam energies.

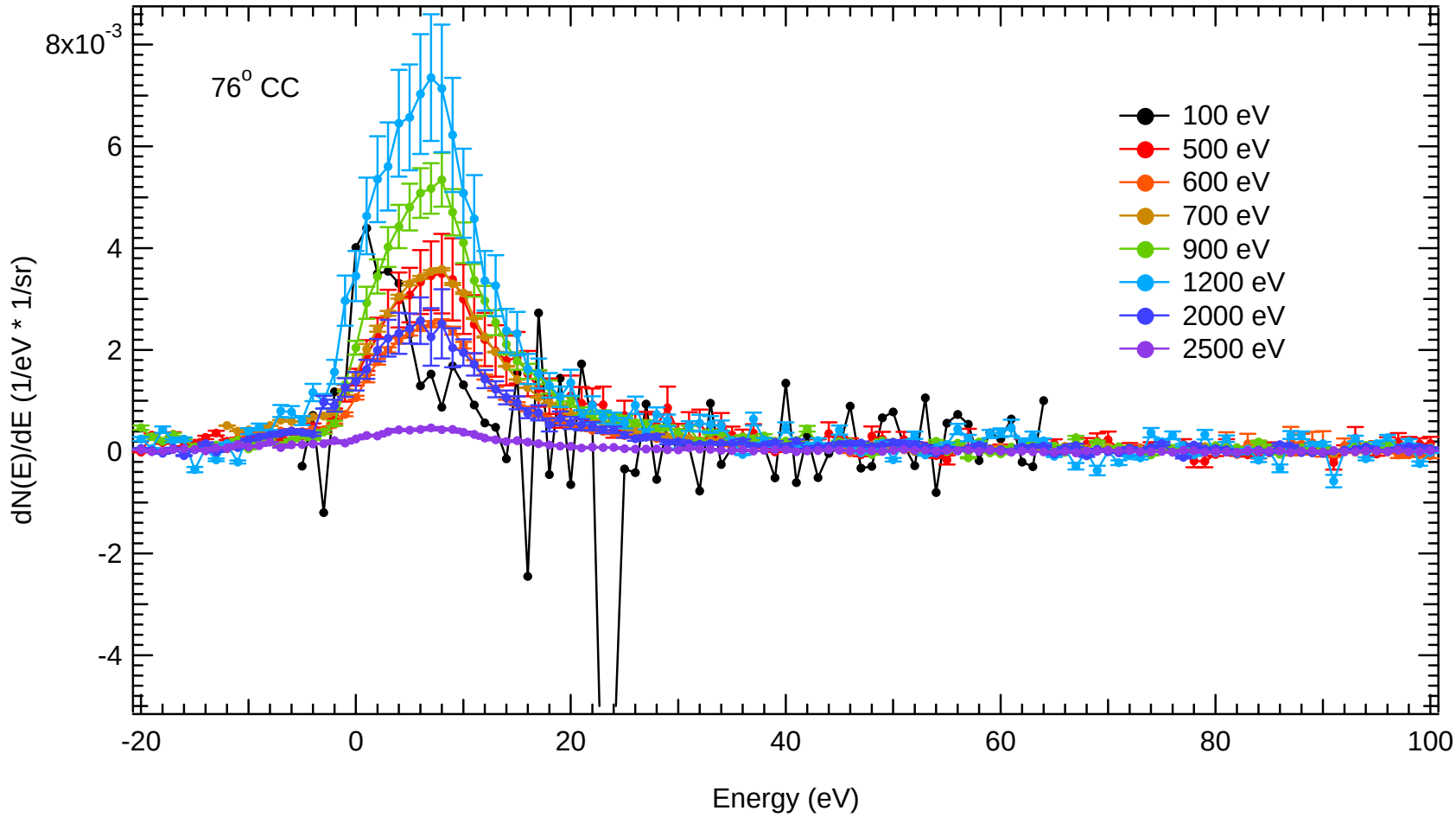

Figure E-85 SE peak resolved in 1 eV at 76 ^{o} Counter-Clockwise emission for selected incident beam energies.

E-5(I) Low Energy 0.1 eV resolution Spectra (E_b Resolved)

The 0.1 eV step size has been used to resolve the positions and intensities of the SE peak. The figures Fig. E-86 through Fig E-89 span the energy range ~20 eV within the vicinity of the SE peak.

The fine resolution spectra of the SE Peak have also been resolved at 0.1 eV. Though the Elastic peak has been resolved at the finest 0.01 eV resolution [Chap. 3], the finest energy resolution spectra of the SE peak are resolved at 0.1 eV.

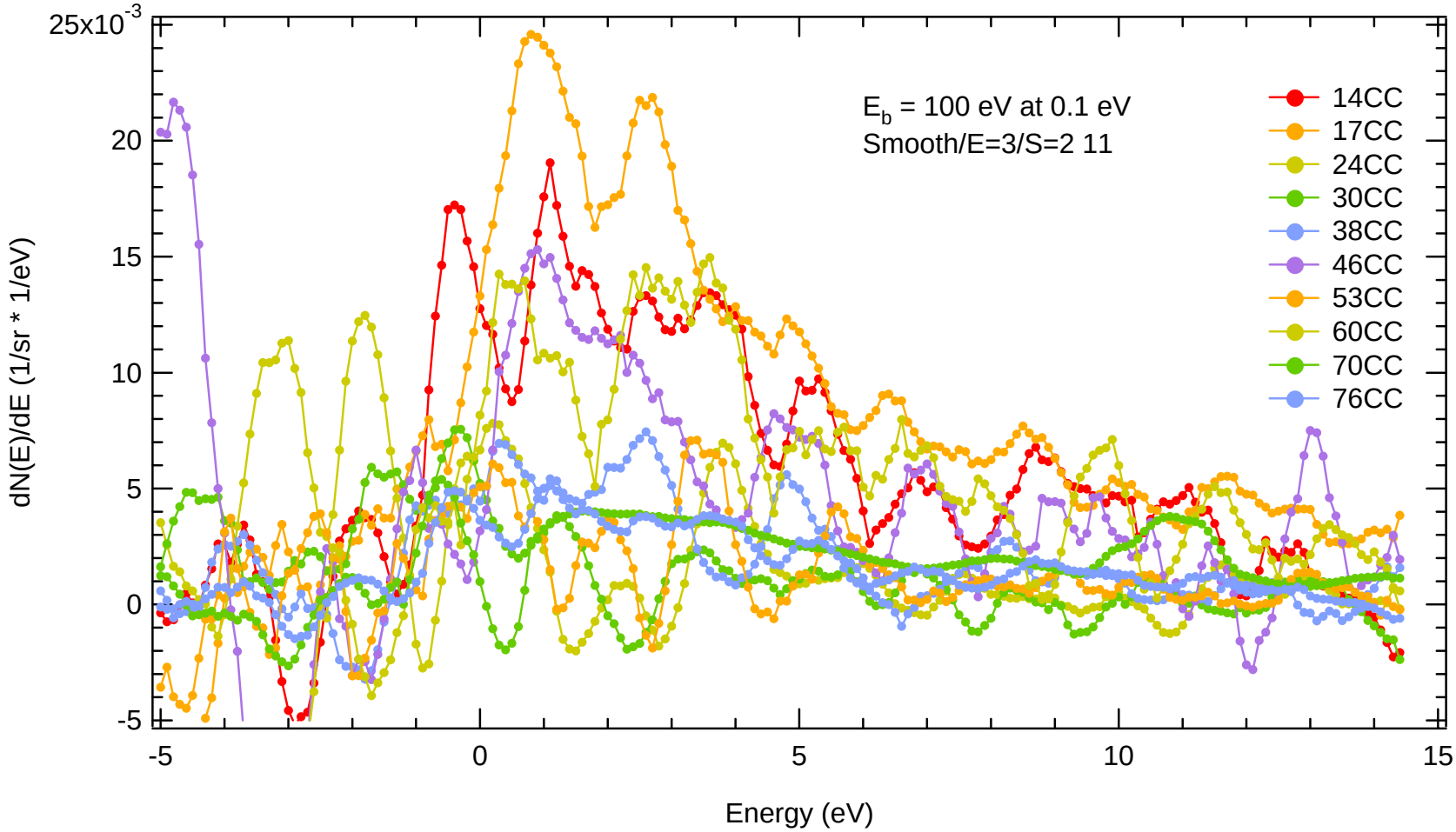

Figure E-86 SE peak resolved at 0.1 eV for 100 eV incident beam energy given in selected emission angles.

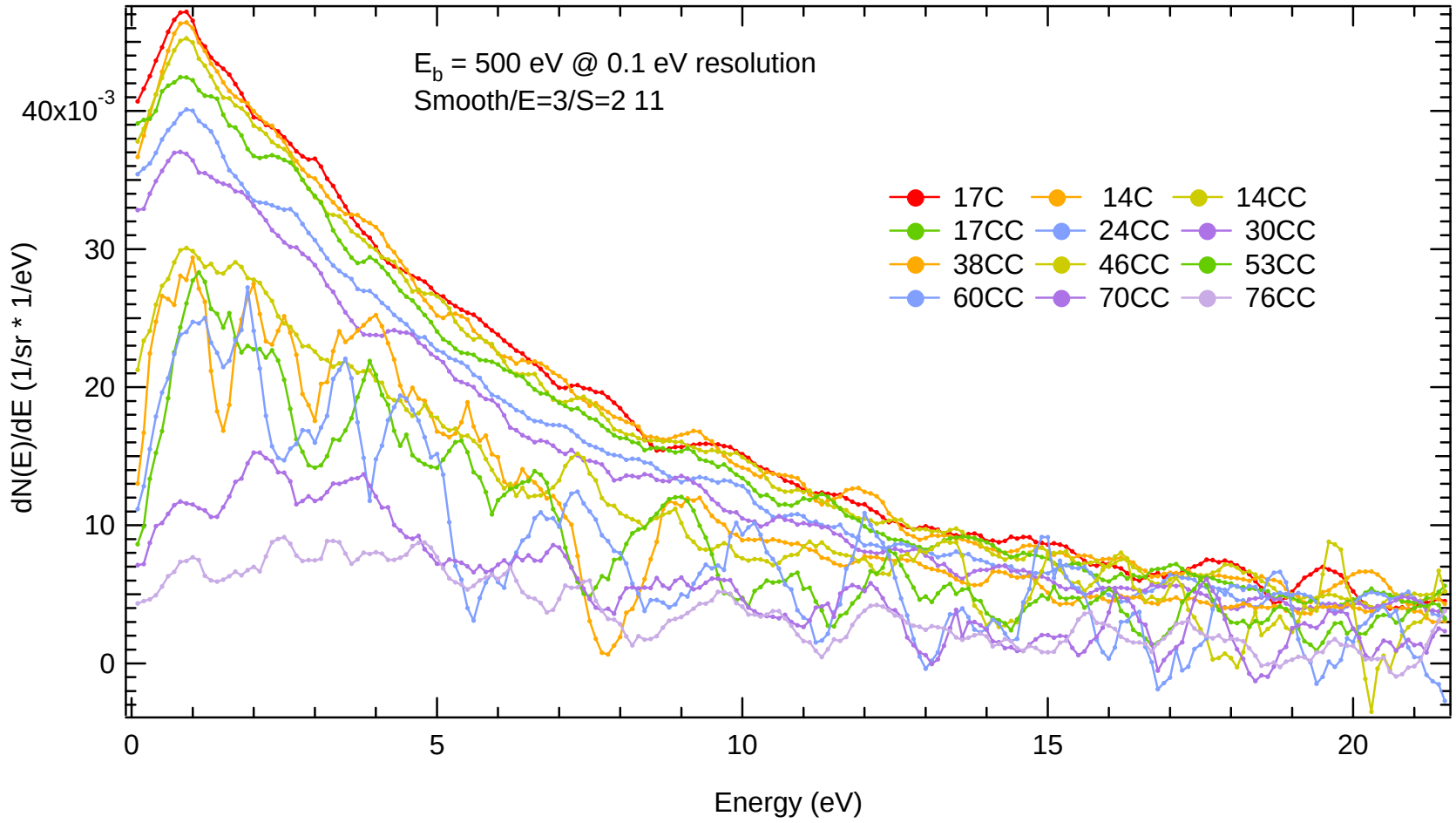

Figure E-87 SE peak resolved at 0.1 eV for 500 eV incident beam energy given in selected emission angles.

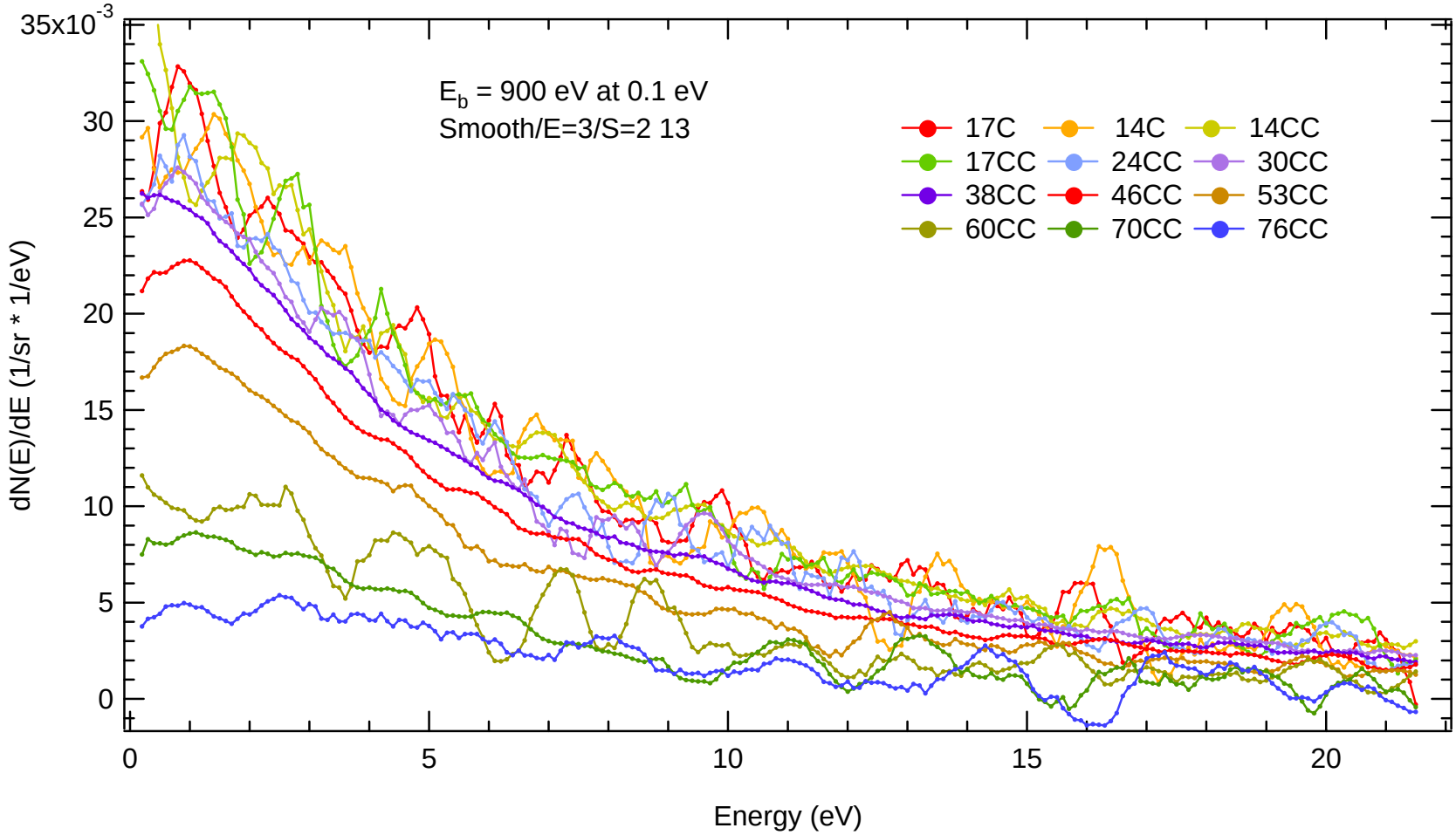

Figure E-88 SE peak resolved at 0.1 eV for 900 eV incident beam energy given in selected emission angles. D3501

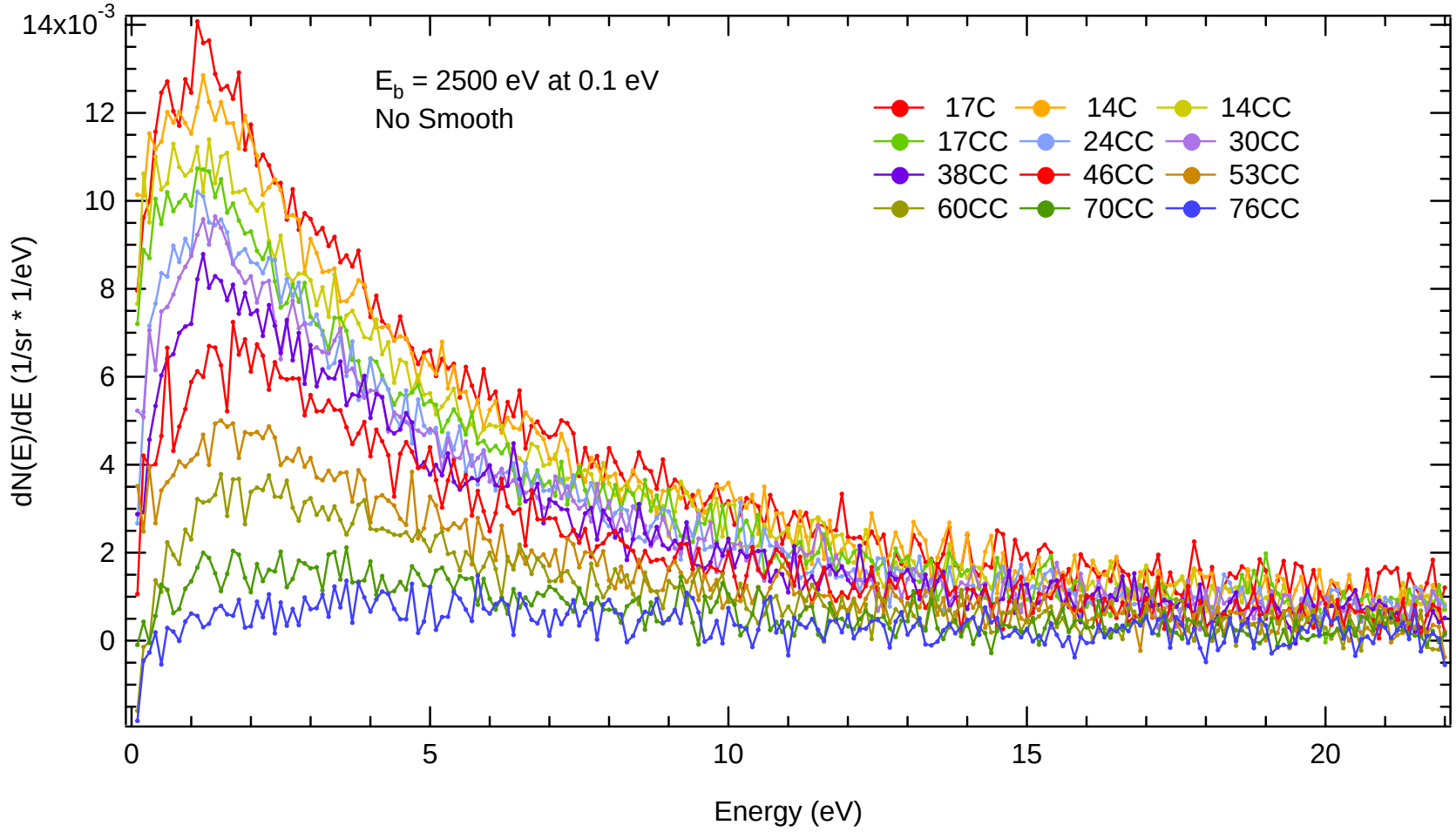

Figure E-89 SE peak resolved at 0.1 eV for 2500 eV incident beam energy given in selected emission angles.

E-5(J) Low Energy 0.1 eV resolution Spectra (Angle Resolved)

The SE spectra measured using the 0.1 eV resolution are shown in Fig. E-90 through Fig. E-101. Each graph compares a single emission angle at incident beam energy measurements of E_b = 500 eV, 900 eV, and 2500 eV. The idea is that the SE region can be measured with high resolution, but the calculation of the slope can be quite tricky. Though the E_b = 100 eV have been measured for the Counter-Clockwise angle emissions, some of the spectra seem to be not so good. This is most likely because the incident electron beam current stability is effected by large filament currents. The electron gun design can not sufficiently maintain such high stable filament currents without degrading.

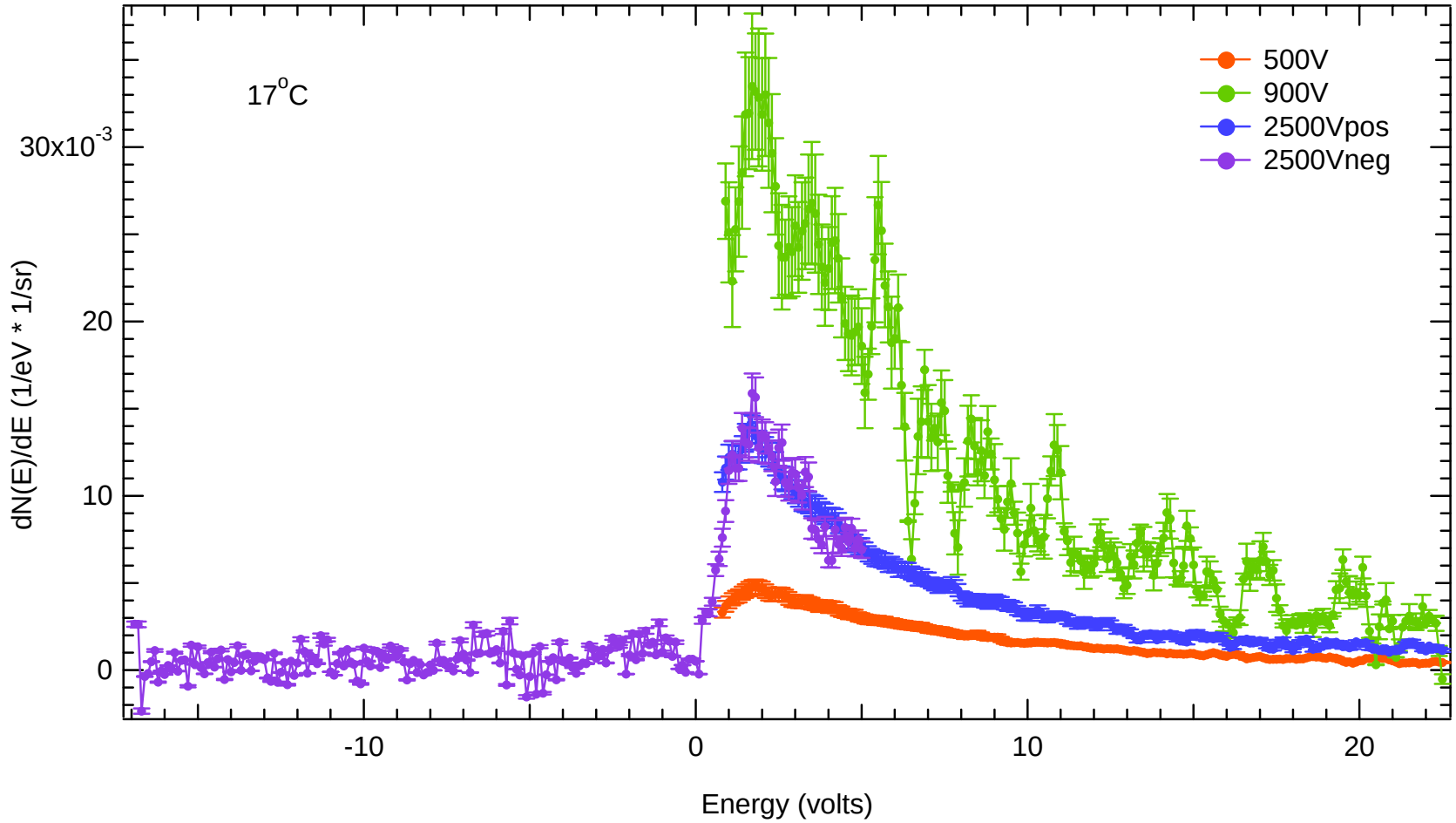

Figure E-90 SE peak resolved in 0.1 eV at 17 ° Clockwise emission for 500, 900, and 2500 eV incident beam energies.

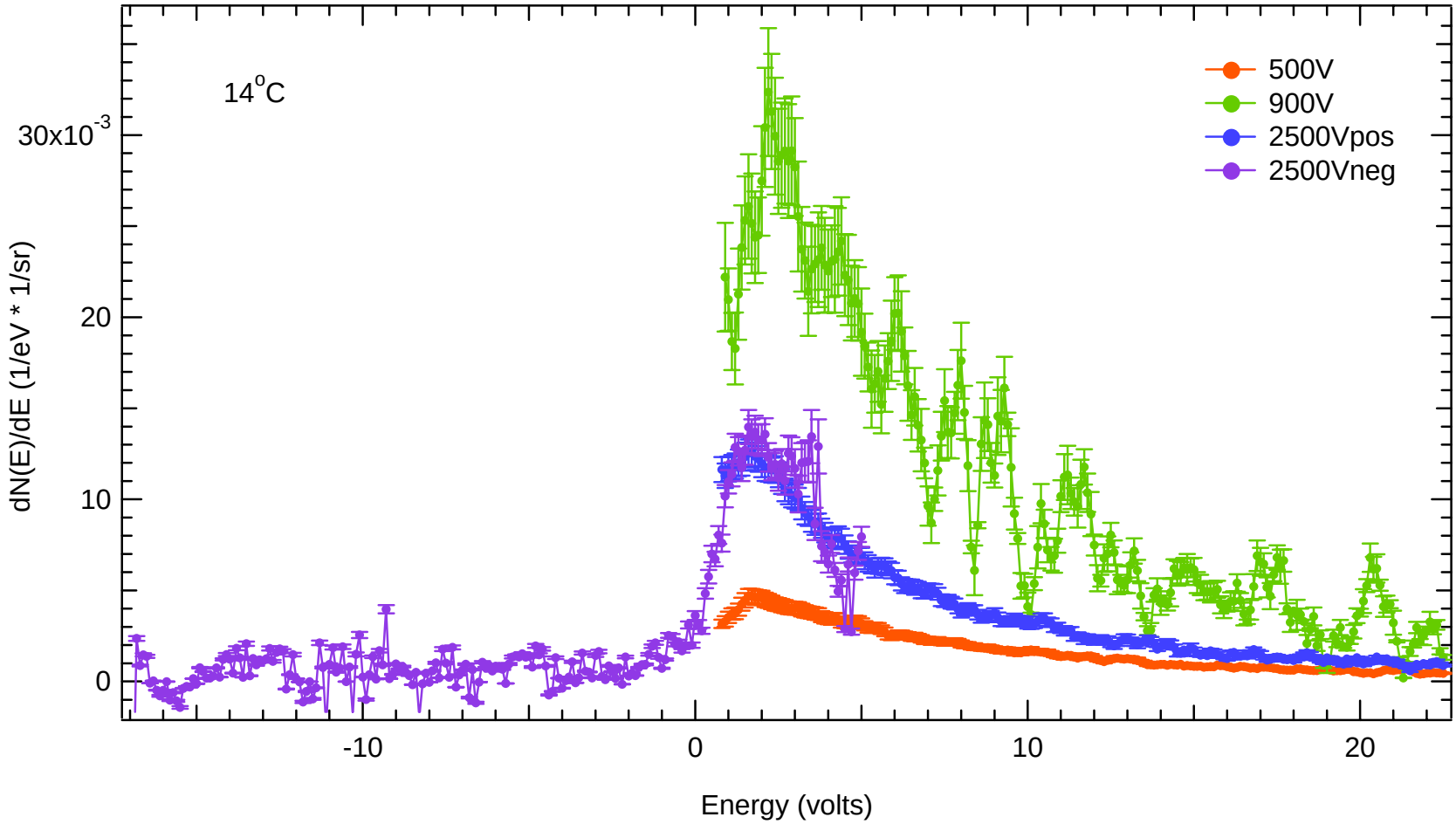

Figure E-91 SE peak resolved in 0.1 eV at 14 ° Clockwise emission for 500, 900, and 2500 eV incident beam energies.

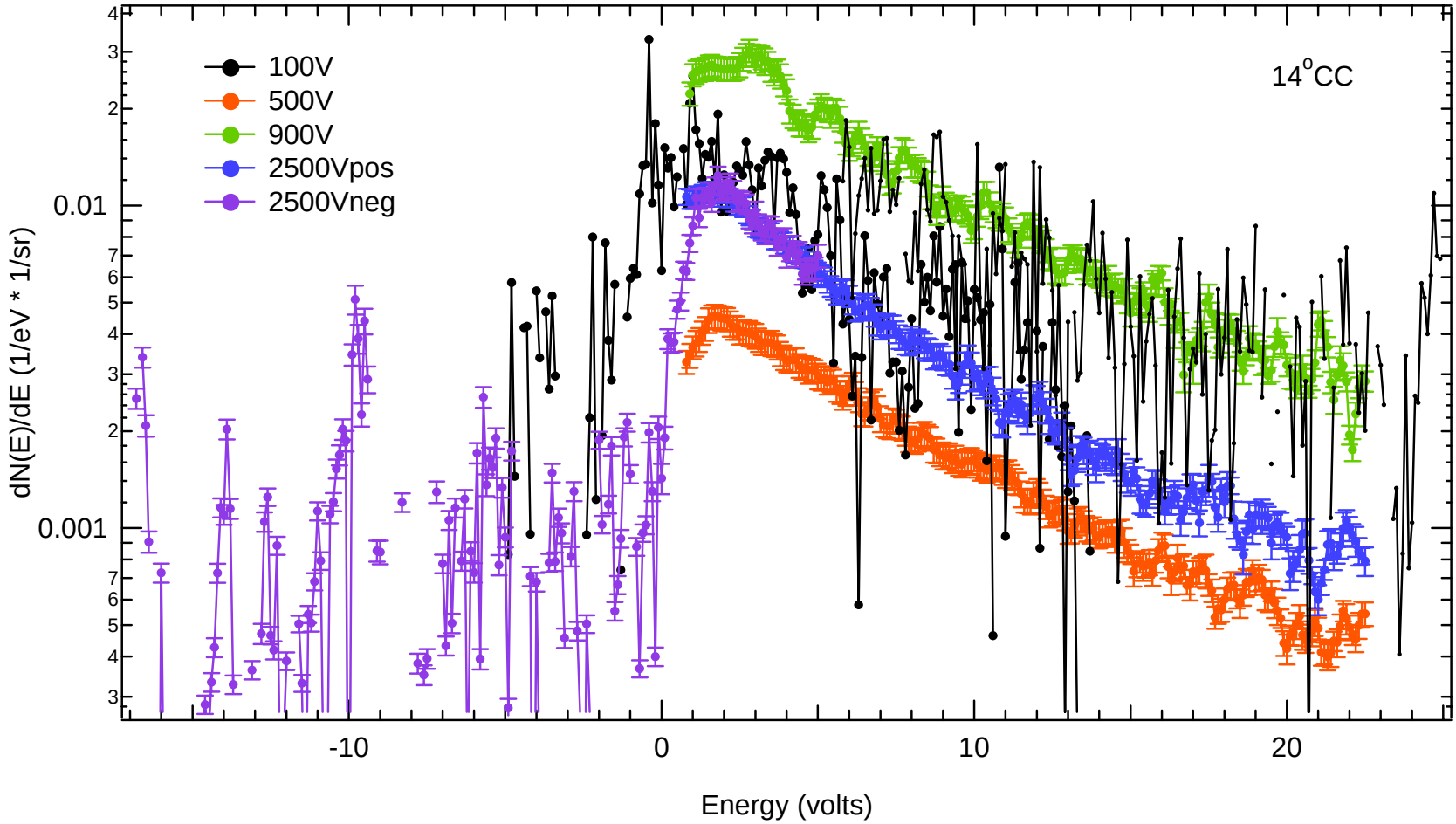

Figure E-92 SE peak resolved in 0.1 eV at 14 ^{o} Counter-Clockwise emission for 500, 900, and 2500 eV incident beam energies.

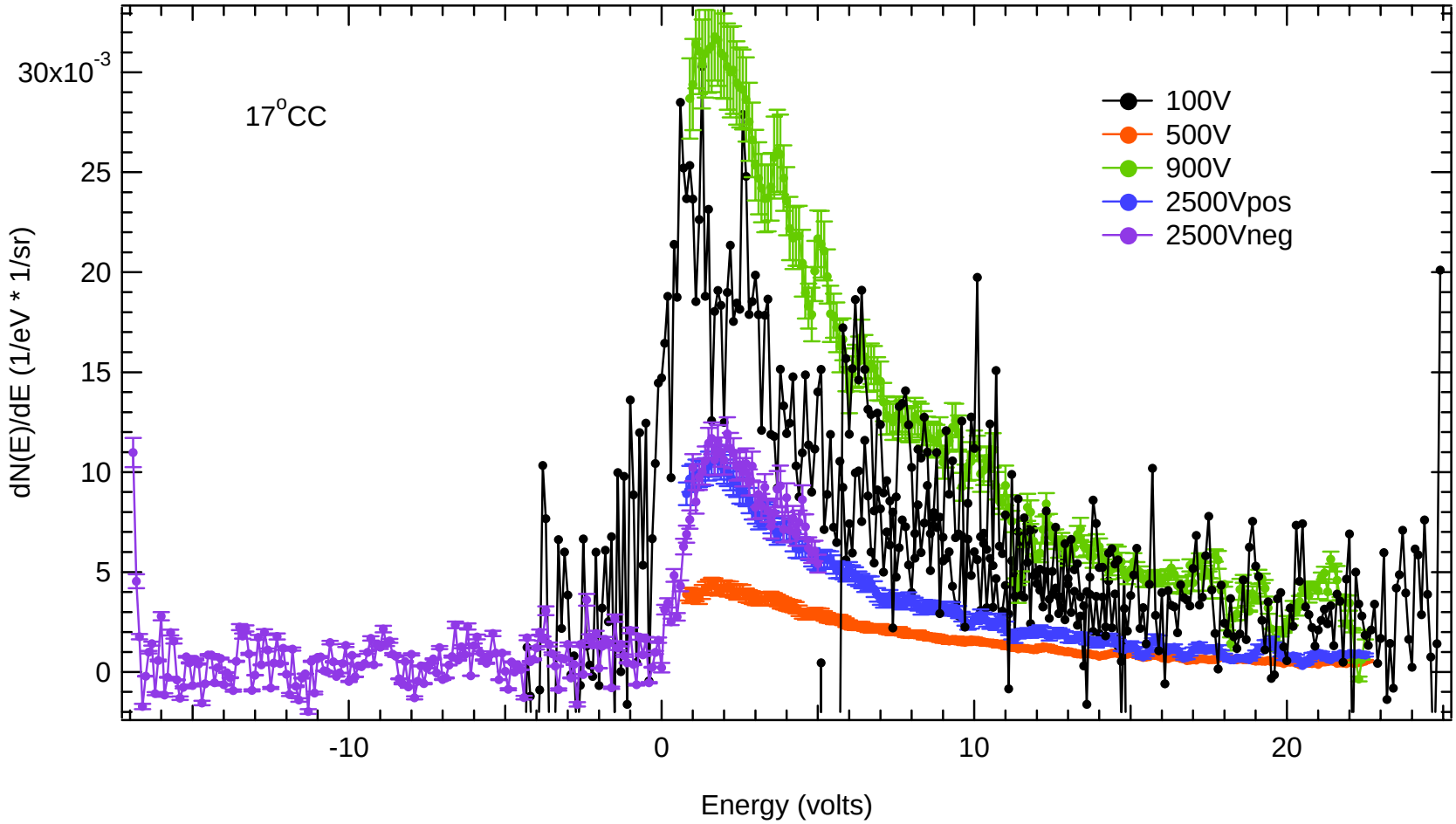

Figure E-93 SE peak resolved in 0.1 eV at 17 ° Counter-Clockwise emission for 500, 900, and 2500 eV incident beam energies.

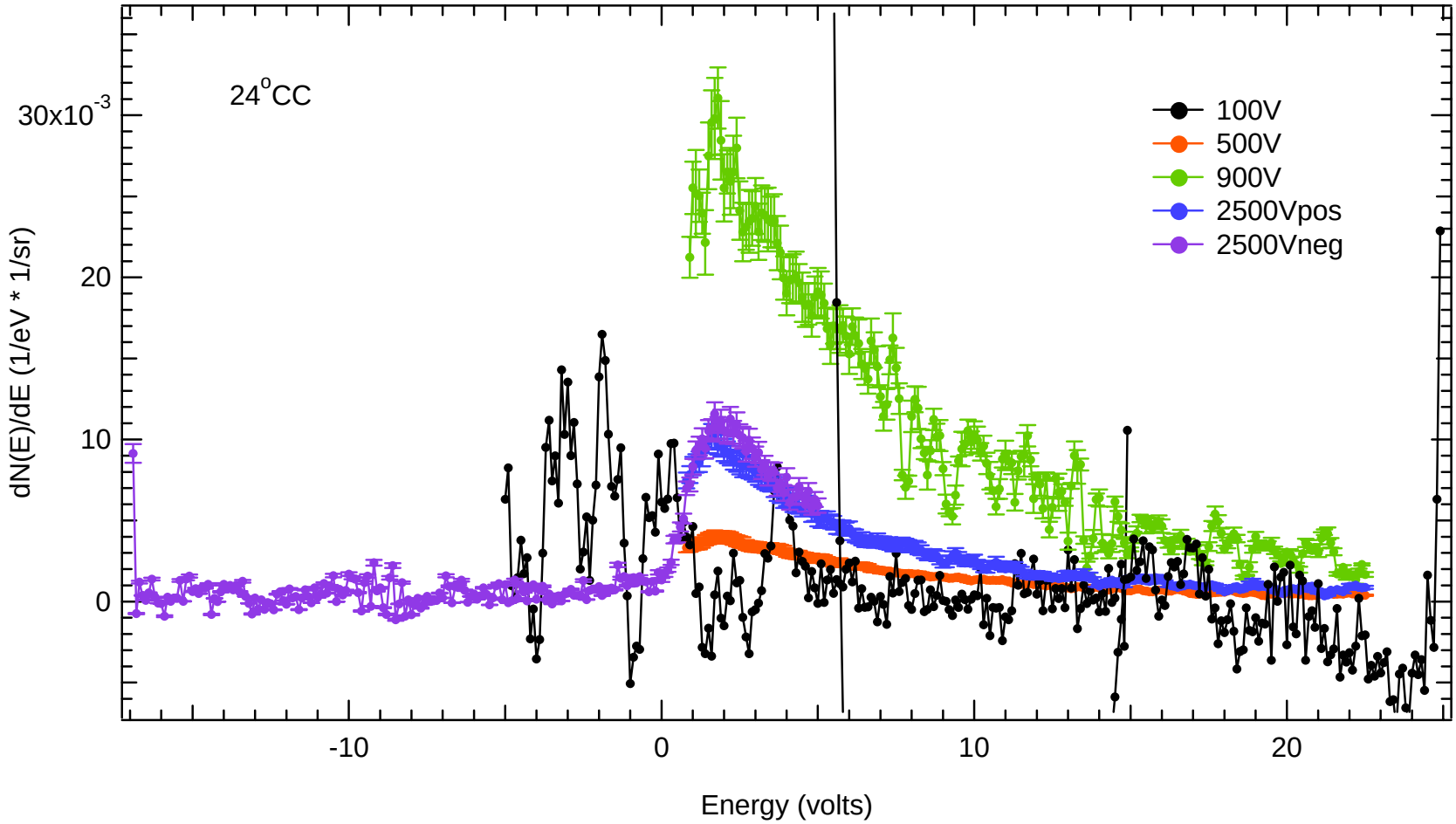

Figure E-94 SE peak resolved in 0.1 eV at 24 ° Counter-Clockwise emission for 500, 900, and 2500 eV incident beam energies.

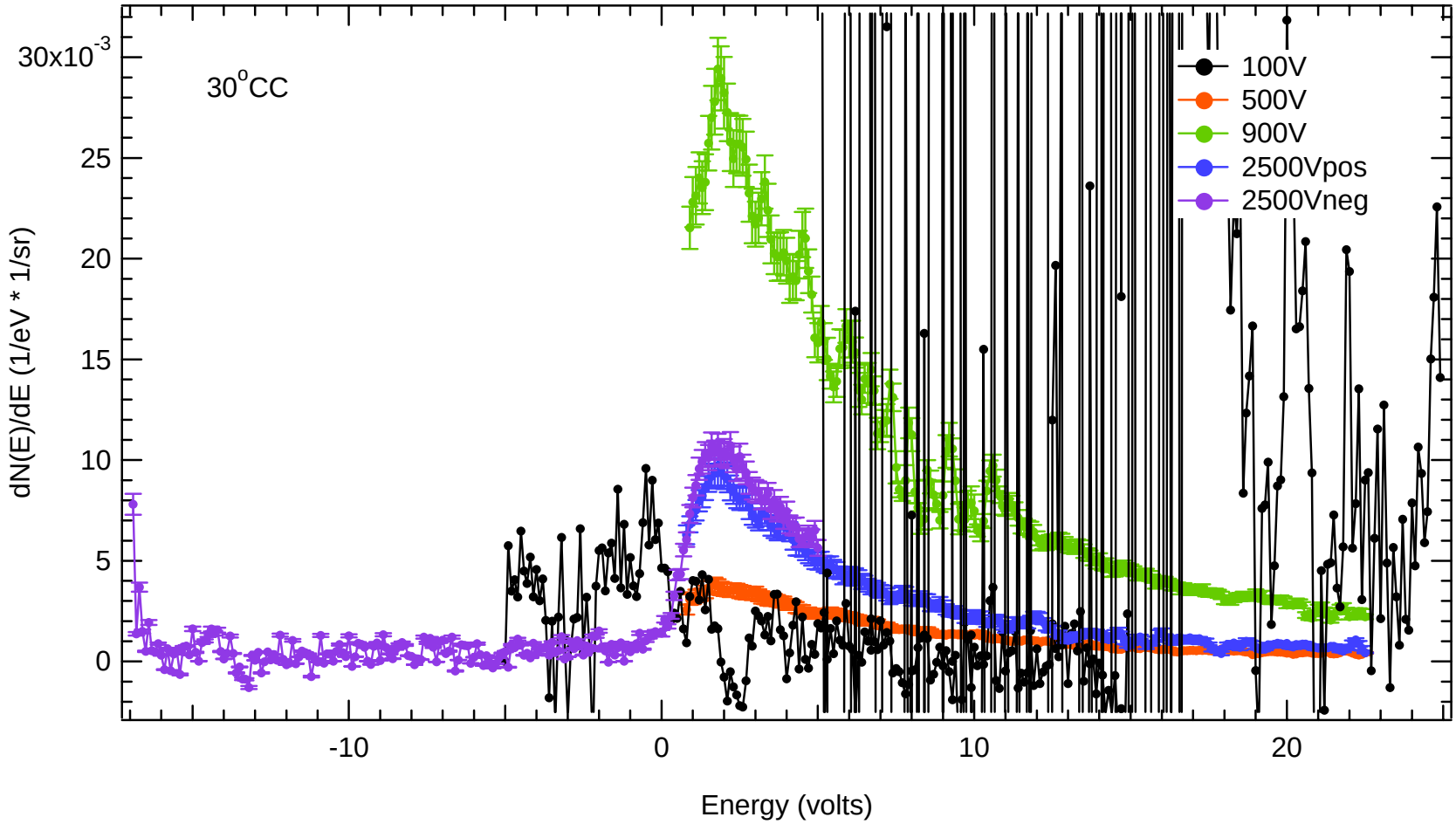

Figure E-95 SE peak resolved in 0.1 eV at 30 ° Counter-Clockwise emission for 500, 900, and 2500 eV incident beam energies.

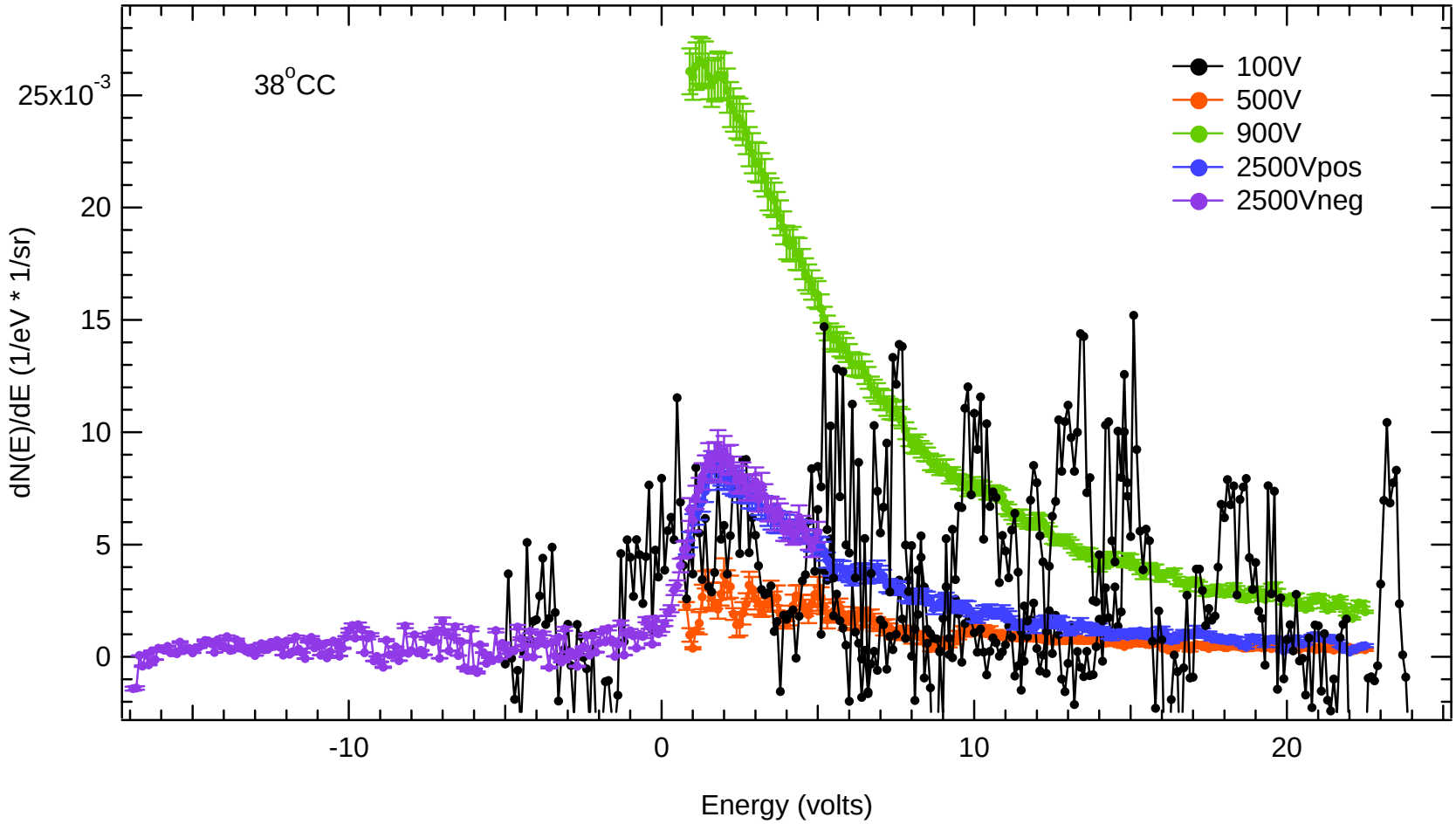

Figure E-96 SE peak resolved in 0.1 eV at 38 ° Counter-Clockwise emission for 500, 900, and 2500 eV incident beam energies.

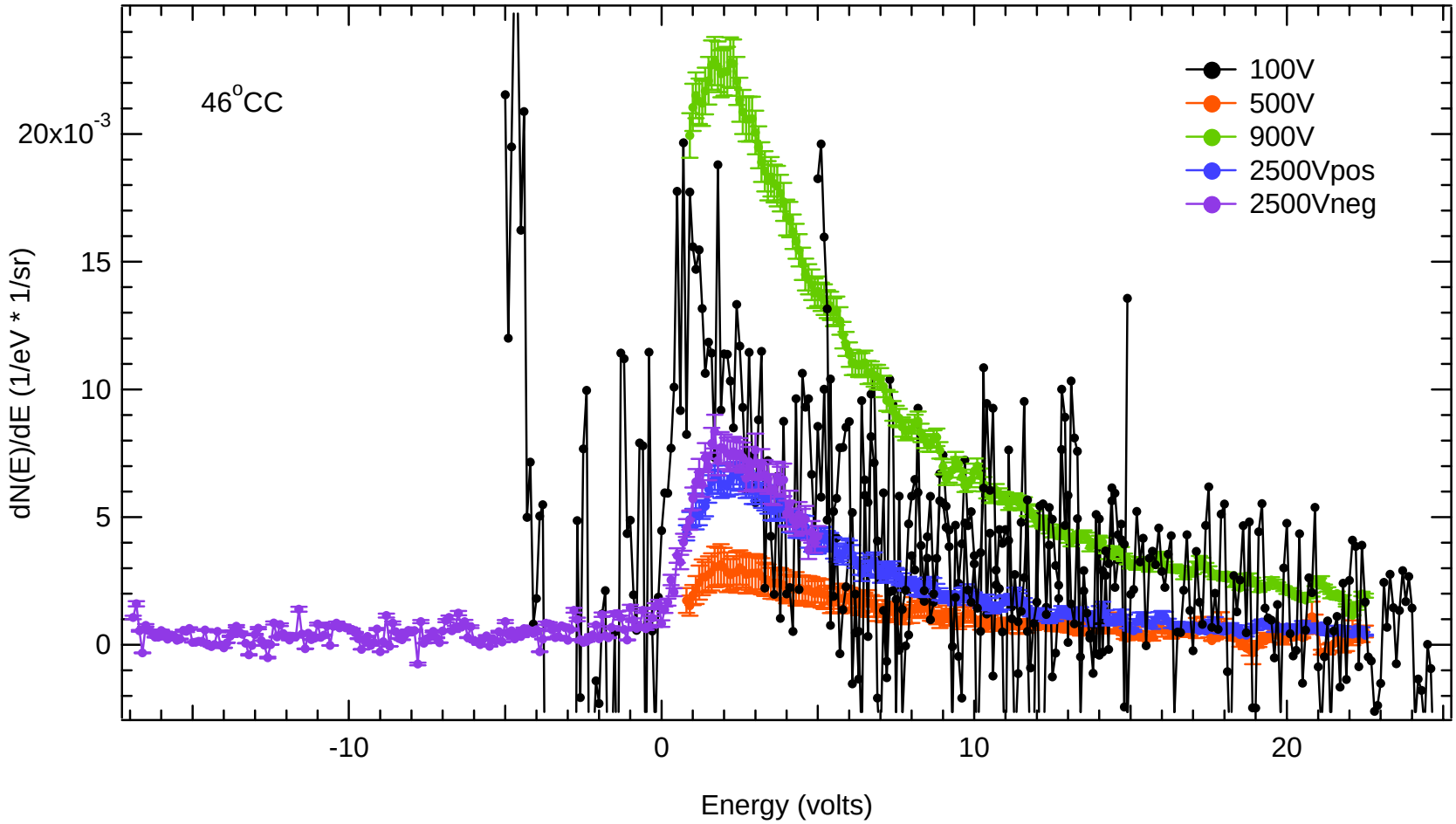

Figure E-97 SE peak resolved in 0.1 eV at 46 ° Counter-Clockwise emission for 500, 900, and 2500 eV incident beam energies.

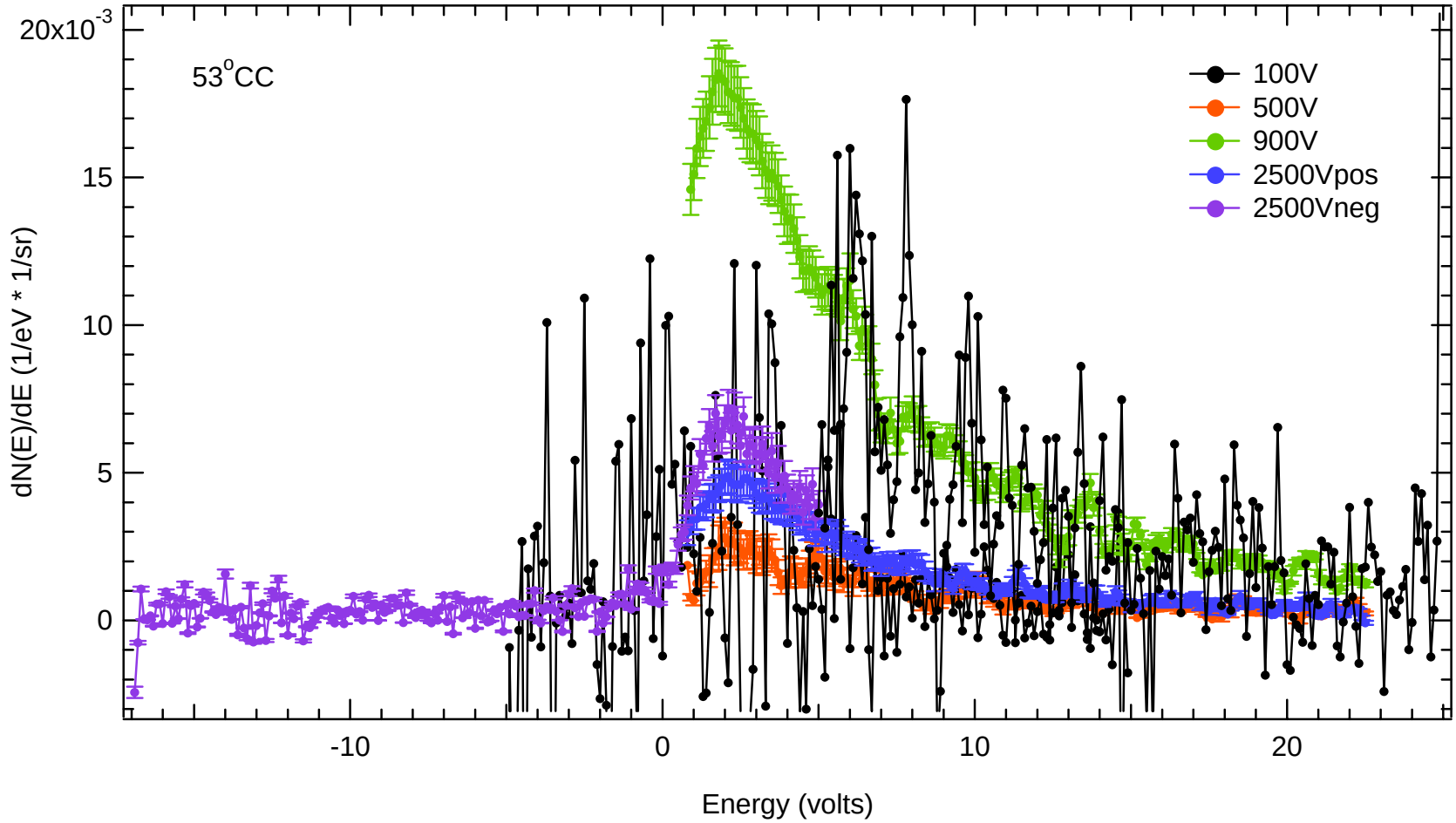

Figure E-98 SE peak resolved in 0.1 eV at 53 ^{o} Counter-Clockwise emission for 500, 900, and 2500 eV incident beam energies.

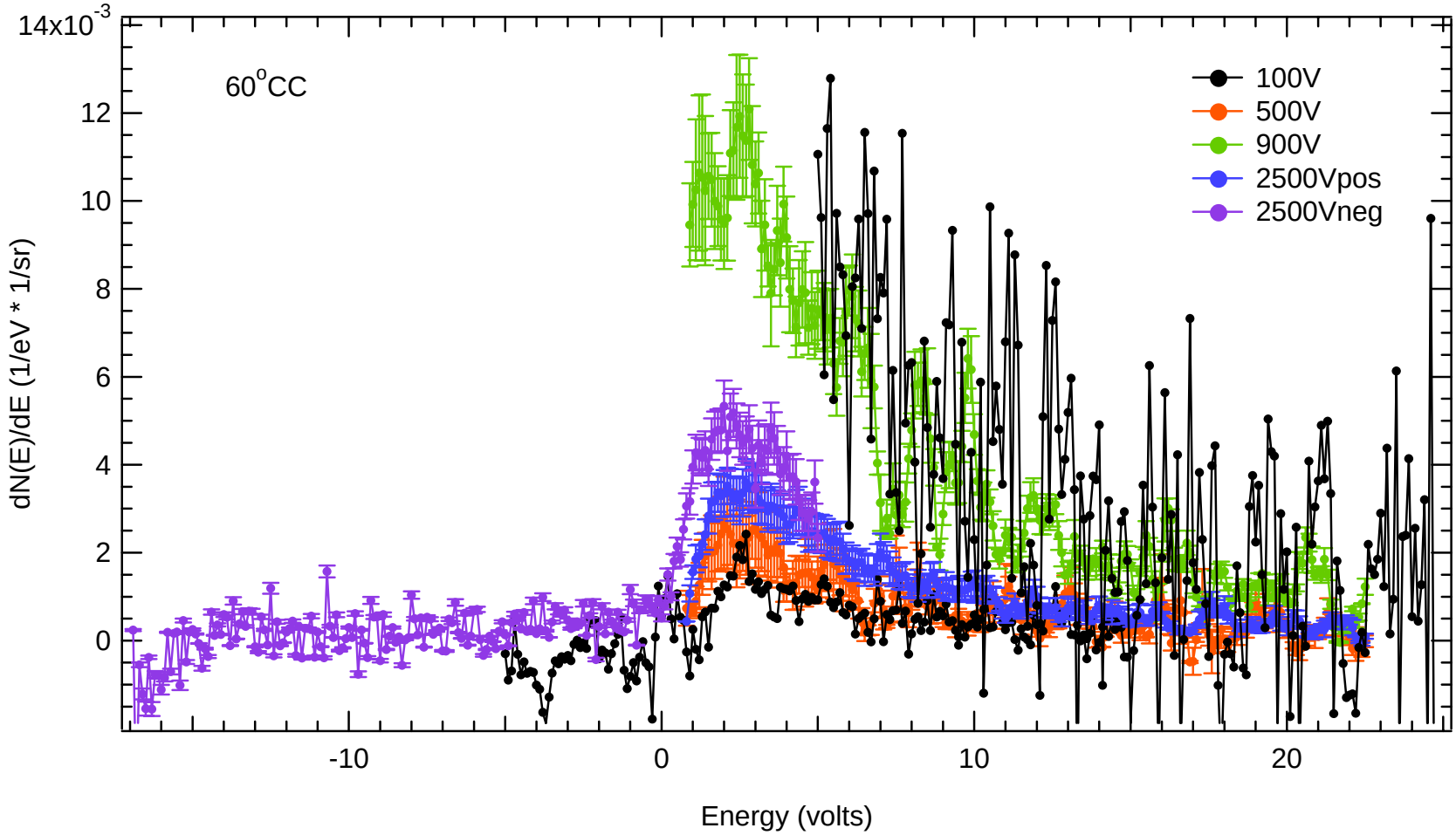

Figure E-99 SE peak resolved in 0.1 eV at 60 ° Counter-Clockwise emission for 500, 900, and 2500 eV incident beam energies.

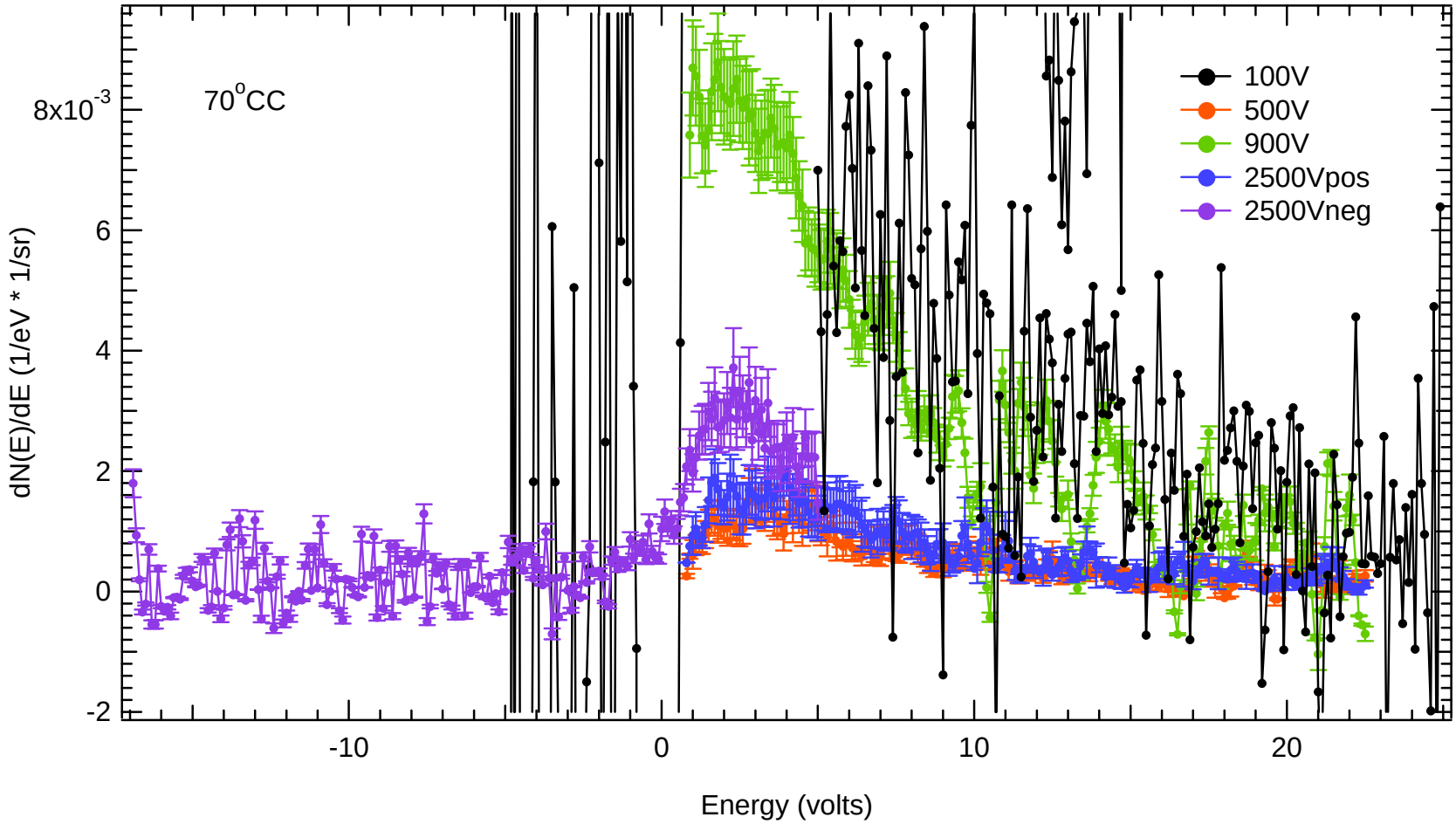

Figure E-100 SE peak resolved in 0.1 eV at 70 ° Counter-Clockwise emission for 500, 900, and 2500 eV incident beam energies.

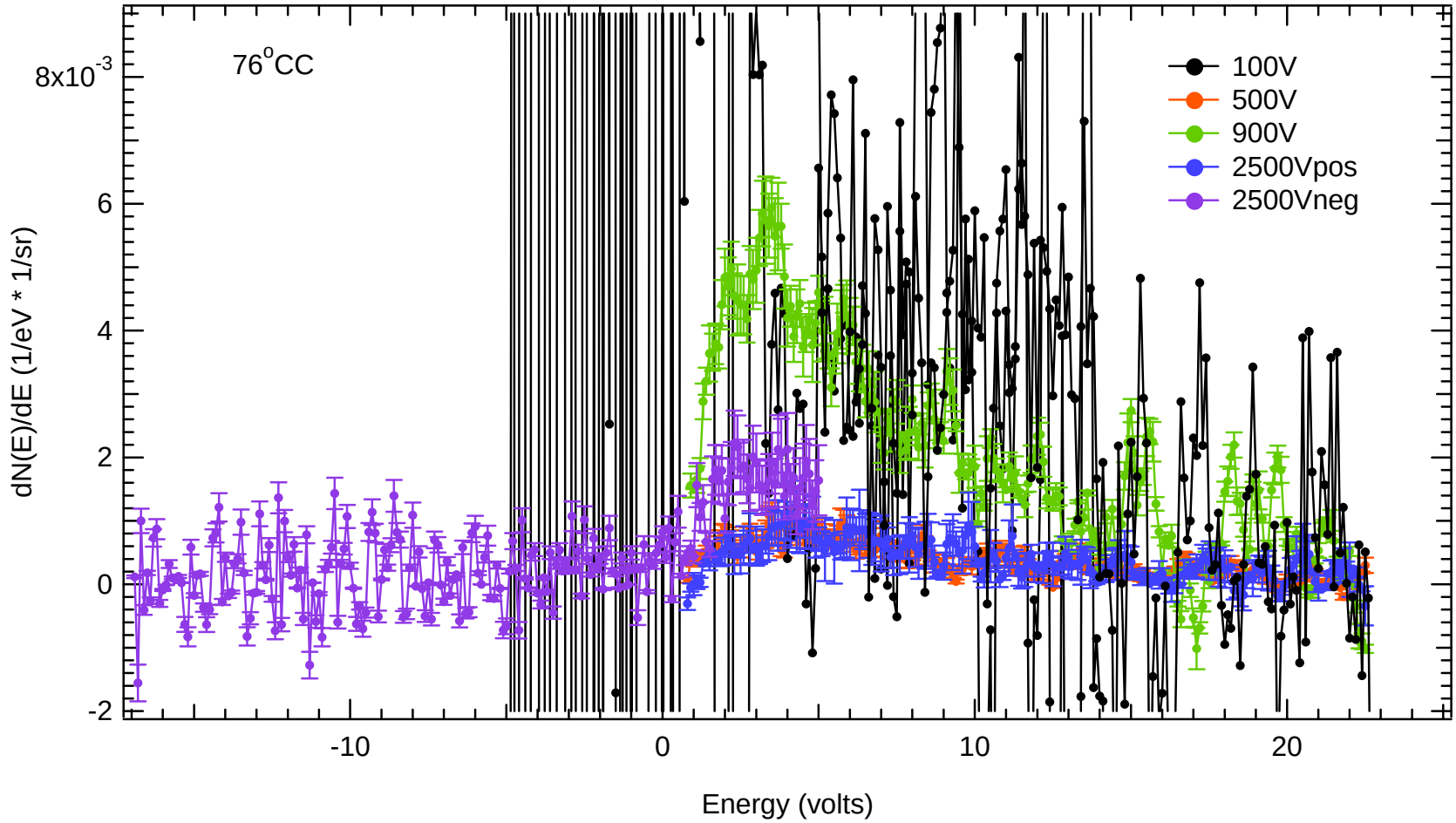

Figure E-101 SE peak resolved in 0.1 eV at 76° Counter-Clockwise emission for 500, 900, and 2500 eV incident beam energies.